PHYS A EV W

VOLUME 83

THE PHYSICAL REVIEW

A journal of experimental and theoretical physics established by E. L. Nichols in 1893

Published by the American Institute of Physics
for the
AMERICAN PHYSICAL SOCIETY

Officers

President

C. C. LAURITSEN
California Institute of Technology
Pasadena, California

Vice-President

J. H. VAN VLECK
Harvard University
Cambridge, Massachusetts

Secretary

K. K. DARROW
Bell Telephone Laboratories
Office:
Columbia University
New York 27, New York

Treasurer

G. B. PEGRAM
Columbia University
New York 27, New York

*Local Secretary
for the Pacific Coast*

J. KAPLAN
University of California at Los Angeles
Los Angeles, California

Managing Editor

S. A. GOUDSMIT
Brookhaven National Laboratory
Upton, Long Island
New York

BOARD OF EDITORS

Editor

S. A. GOUDSMIT

Assistant Editor

S. PAFFENBARGER

Associate Editors

J. BARDEEN	HARVEY BROOKS	M. GOLDHABER
T. BONNER	R. F. CHRISTY	R. HOFSTADTER
R. G. HERB	C. L. CRITCHFIELD	A. W. LAWSON
W. E. LAMB, JR.	M. DEUTSCH	A. PAIS
A. J. F. SIEGERT	T. H. JOHNSON	R. SERBER
W. E. STEPHENS	BRUNO ROSSI	C. H. TOWNES

Manuscripts for publication should be submitted to S. A. Goudsmit, Brookhaven National Laboratory, Upton, Long Island, New York. Authors' institutions are requested to pay a publication charge of $8 per page which, if honored, entitles them to 100 free reprints. Instructions will be sent with galley proofs.

Proof and all correspondence concerning papers in the process of publication should be addressed to the Publication Manager, American Institute of Physics, 57 East 55 Street, New York 22, New York.

Subscription Price

United States and Canada $25.00
Elsewhere $27.00

Back Numbers[1]

Yearly back number rate when complete year is available:
Prior to 1949: $20.00
Thereafter: $27.00
Single copies: $2.00 each, prior to July, 1929;
$1.00 each, July, 1929–December, 1941;
$2.00 each, January, 1942–December, 1946;
$1.00 each, January, 1947–December, 1948;
$1.25 each, thereafter.
General index, 1893–1920: $4.00

Subscriptions, remittals, and orders for back numbers should be addressed to the American Institute of Physics, 57 East 55 Street, New York 22, New York.

Changes of address in the case of members of the American Physical Society should be addressed to the Treasurer; in the case of other subscribers to the American Institute of Physics.

[1] Set Series: Inquire of Physics Department, Cornell University, Ithaca, New York.

The Physical Review is published semi-monthly at Prince and Lemon Streets, Lancaster, Pennsylvania.

Entered as second-class matter March 6, 1947, at the Post Office at Lancaster, Pennsylvania, under the Act of March 3, 1879.

Acceptance for mailing at special rate of postage provided for in paragraph (d-2), section 34.40, P. L. & R. of 1948, authorized January [illegible]

THE
PHYSICAL REVIEW

A journal of experimental and theoretical physics established by E. L. Nichols in 1893

SECOND SERIES, VOL. 83, NO. 3 AUGUST 1, 1951

Excited States of Si^{29} from an Investigation of the $P^{31}(d,\alpha)Si^{29}$ and $Si^{28}(d,p)Si^{29}$ Reactions*†

P. M. ENDT,‡ D. M. VAN PATTER, W. W. BUECHNER, AND A. SPERDUTO
Physics Department and Laboratory for Nuclear Science and Engineering, Massachusetts Institute of Technology, Cambridge, Massachusetts

(Received April 12, 1951)

The alpha-particle groups from a thin target of zinc phosphate bombarded by 1.81-Mev deuterons have been studied with a high resolution magnetic spectrograph. Eight of the alpha-groups observed have been assigned to the previously unreported $P^{31}(d,\alpha)Si^{29}$ reaction, corresponding to the ground state and seven excited states of Si^{29} in a region of excitation of 0 to 5 Mev.

From a similar investigation of the proton groups from thin targets of silicon dioxide bombarded by 1.81-Mev deuterons, ten $Si^{28}(d,p)Si^{29}$ proton groups were observed, corresponding to the ground state and nine excited states of Si^{29}. The positions of the excited states found from the $P^{31}(d,\alpha)Si^{29}$ reaction agreed within the experimental error with those obtained from the $Si^{28}(d,p)Si^{29}$ reaction. The excited states observed in Si^{29} are at 1.282, 2.038, 2.436, 3.073, 3.623, 4.078, 4.840, 4.897, and 4.934 Mev.

I. INTRODUCTION

TWO low-lying levels[1] of Si^{29} at 1.2±0.2 and 2.35 Mev are excited by the beta-decay of Al^{29}. The evidence for low excited states of Si^{29} from nuclear reactions has been previously confined to the $Si^{28}(d,p)Si^{29}$ reaction. The spectrum of protons from natural silicon targets bombarded by deuterons was first reported by Pollard and Humphreys.[2] However, only an arbitrary assignment of the proton groups was possible because of the presence of three isotopes in the targets: Si^{28}, 92 percent; Si^{29}, 5 percent; and Si^{30}, 3 percent. Recently, Motz and Humphreys[3] have investigated the (d,p) reaction for the three silicon isotopes using enriched targets and range measurements. They report levels in Si^{29} at 1.29, 2.06, 2.43, 3.08, 3.60, 4.09, and 4.87 Mev. Three of these levels were found previously by Allan and Wilkinson[4] at 1.29, 2.02, and 2.41 Mev, using a natural silicon target.

Gamma-rays from the capture of slow neutrons by natural silicon have been measured by Kinsey and his co-workers[5] using a pair spectrometer. The assignment of the gamma-rays is again complicated by the presence of the three silicon isotopes, and it cannot be made with certainty until the excited states of Si^{29}, Si^{30}, and Si^{31} are established from other nuclear reactions.

In contrast to the reactions involving silicon targets, the particle groups from $P^{31}(d,\alpha)Si^{29}$ can be unambiguously associated with the energy levels of Si^{29}. Phosphorus occurs naturally as a single isotope; and, while this reaction has not been reported, the ground-state Q-value can be estimated as 8.4±0.3 Mev from reported Q-values for the $Si^{28}(d,p)Si^{29}$ and $Si^{28}(\alpha,p)P^{31}$ reactions of 6.16±0.06 Mev[4] and −2.23±0.25 Mev.[6] The high Q-value of the $P^{31}(d,\alpha)Si^{29}$ reaction makes possible the investigation of a large region of excitation of Si^{29}.

In measurements of the type described in the following section, greater accuracy and better resolution are usually obtained with (d,p) rather than (d,α) reactions. This is largely a result of problems associated with the target. In general, for a given target thickness, the yields are greater from the (d,p) reactions, and in addition the loss and spread of energy because of the

* This work has been supported by the joint program of the ONR and AEC.

† This work was reported at the meeting of the American Physical Society in Chicago, November, 1950. Phys. Rev. **81**, 317 (1951).

‡ On leave from Physisch Laboratorium der Rijks-Universiteit, Utrecht, The Netherlands.

[1] Seidlitz, Bleuler, and Tendam, Phys. Rev. **76**, 861 (1949).

[2] E. Pollard and R. F. Humphreys, Phys. Rev. **59**, 466 (1941).

[3] H. T. Motz and R. F. Humphreys, Phys. Rev. **80**, 595 (1950).

[4] H. R. Allan and C. R. Wilkinson, Proc. Roy. Soc. (London) **A194**, 131 (1948).

[5] B. B. Kinsey (private communication).

[6] O. Haxel, Z. Physik **35**, 840 (1935).

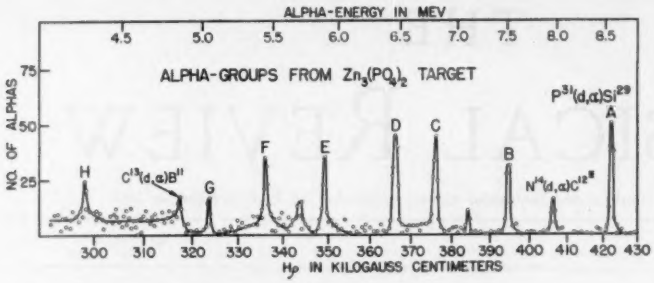

FIG. 1. Alpha-particle groups observed from a zinc-phosphate target bombarded by 1.81-Mev deuterons.

target thickness and surface are less for protons than for alpha-particles. Thus, to determine the levels in Si^{29}, we have investigated both the alpha-particles from phosphorus targets and the protons from silicon targets bombarded with deuterons, the results from the phosphorus being used to identify the proton groups from the Si^{28} isotope.

In addition to providing two independent determinations of the energies of the excited states of Si^{29}, the present measurements are of interest regarding the question[2] as to whether, for different reactions where the residual nucleus is the same, the same energy levels are excited.

II. EXPERIMENTAL PROCEDURE

The charged particles from the phosphorus and silicon targets were analyzed in the magnetic field of a 180-degree annular magnet. The analysis was at 90 degrees to the incident deuteron beam. The essential details of the experimental arrangement have been described previously,[7,8] and recent improvements in precision of measurements and calculations have been discussed in detail.[9]

In order to make a preliminary search for the $P^{31}(d,\alpha)Si^{29}$ ground-state group, a 300-kev phosphorus target was prepared by melting in a bunsen-burner flame a small amount of metaphosphoric acid on a platinum backing. A more extensive survey of the $P^{31}(d,\alpha)Si^{29}$ alpha-groups was made using a 20-kev thick zinc-phosphate target prepared by evaporation onto a platinum backing.

TABLE I. $P^{31}(d,\alpha)Si^{29}$ reaction.

Group	Q-value (Mev)	Relative intensity	Si^{29} level
A	8.170±0.020	1.0	0
B	6.885±0.020	0.9	1.286±0.010
C	6.126±0.020	1.0	2.044±0.014
D	5.727±0.020	1.4	2.443±0.015
E	5.086±0.020	0.6	3.084±0.016
F	4.539±0.020	0.9	3.631±0.017
G	4.080±0.020	0.4	4.090±0.018
H	3.221±0.020	0.6	4.949±0.020

[7] Buechner, Strait, Stergiopoulos, and Sperduto, Phys. Rev. **74**, 1569 (1948).
[8] Buechner, Strait, Sperduto, and Malm, Phys. Rev. **76**, 1543 (1949).
[9] Strait, Van Patter, Buechner, and Sperduto, Phys. Rev. **81**, 747 (1951).

Two targets of quartz were prepared by evaporation in vacuum onto platinum sheets. These targets were 50- and 5-kev thick for the $Si^{28}(d,p)Si^{29}$ ground-state group at 1.81-Mev bombarding energy. The thick target served for rough location of the $Si^{28}(d,p)Si^{29}$ groups, and the thin target was used for the accurate determination of Q-values.

The spectra of alpha-particles and protons were obtained by exposing a series of nuclear-track plates successively over a wide range of analyzing-magnet field strengths. The observed track-density distributions were then normalized to the same beam exposure and area of plate counted in order to make the intensities of the particle groups comparable throughout the region surveyed. Proton groups with energies less than 3.6 Mev were recorded in the presence of deuterons elastically scattered from the platinum backing of the target by covering the nuclear-track plates with thin aluminum foils sufficiently thick to stop the scattered deuterons.

For most of the surveys, a deuteron bombarding energy of 1.81 Mev was used, although in some cases other voltages were used either as a check on the assignment of a particular group or to change the relative positions of the groups of interest and those due to contaminations.

III. RESULTS

$P^{31}(d,\alpha)Si^{29}$ Reaction

The alpha-particle groups with energies from 4.1 to 8.9 Mev observed from the 20-kev zinc-phosphate target bombarded by 1.81-Mev deuterons are shown in Fig. 1. Several proton groups were also observed but are not plotted in the figure. A total of twelve alpha-groups of varying intensities is indicated. Eight of these groups were assigned to the $P^{31}(d,\alpha)Si^{29}$ reaction and are designated by the letters A through H. The remaining four groups were attributed to target contaminants of C^{13}, N^{14}, and Na^{23}. The two $Na^{23}(d,\alpha)Ne^{21}$ groups, occurring at $H\rho$ values of 344 and 384 kilogauss-cm, were identified from a comparison with the alpha-groups observed from a sodium-iodide target at the same bombarding energy. The background of alpha-particles between peaks appeared to increase at lower

$H\rho$ values, which can be largely accounted for by the presence of alpha-particles from polonium contamination in the target and camera chambers.

In Table I are listed the measured Q-values for the $P^{31}(d,\alpha)Si^{29}$ alpha-particle groups and the resulting positions of the Si^{29} levels. The observed relative intensities at 1.81-Mev deuteron bombarding energy are also given. Because of variations in target thickness and secondary electron emission with bombardment, these relative intensities are only approximate.

For reasons that have been mentioned, it is more convenient to obtain accurate values for the Si^{29} levels from the $Si^{28}(d,p)Si^{29}$ reaction. Hence, no intensive effort was made to use a thinner target or to eliminate the effects of surface contaminants. Although various checks indicated that the effects due to these causes were not serious, a rather large uncertainty has been assigned to the measured Q-values in order to allow for these possible sources of error.

$Si^{28}(d,p)Si^{29}$ Reaction

In Fig. 2 are shown the proton groups with energies from 2.75 to 8.0 Mev observed from a 5-kev normal SiO_2 target bombarded by 1.81-Mev deuterons. As is indicated in the figure, three of these groups have been assigned to the $N^{14}(d,p)N^{15*}$ reaction,[10] and four others have been shown as arising from contaminants of D^2, C^{12}, C^{13}, and O^{16}. The identification of the two proton groups of low intensity at $H\rho$ values of 341 and 368 kilogauss-cm has not been definitely established. These groups have not been observed from targets prepared from SiO_2 obtained from the Stable Isotopes Division of the AEC at Oak Ridge in which the Si^{29} and Si^{30} contents were enriched relative to Si^{28}. It is concluded that they are not associated with any of the silicon isotopes and probably arise from some unknown contaminant in the quartz used for preparing the normal SiO_2 targets.

TABLE II. Q-values for $Si^{28}(d,p)Si^{29}$ groups and energy levels in Si^{29}.

Group	Rel Int	Q-value (Mev)	Si^{29} level ($Si^{28}(d,p)Si^{29}$)	Si^{29} level ($P^{31}(d,\alpha)Si^{29}$)	Si^{29} level[2]
A	1.0	6.246±0.010	0	0	0
B	1.4	4.964±0.008	1.282±0.007	1.286±0.010	1.29±0.04
C	1.2	4.208±0.008	2.038±0.007	2.044±0.014	2.06±0.04
D	0.8	3.810±0.007	2.436±0.007	2.443±0.015	2.43±0.04
E	0.5	3.173±0.007	3.073±0.007	3.084±0.016	3.08±0.05
F	0.4	2.623±0.006	3.623±0.007	3.631±0.017	3.60±0.05
G	0.3	2.168±0.007	4.078±0.008	4.090±0.018	4.09±0.06
—	0.6	1.406±0.008	4.840±0.010	—	—
—	0.4	1.349±0.008	4.897±0.010	—	—
H	4.3	1.312±0.008	4.934±0.010	4.949±0.020	4.87±0.10

The remaining ten groups have been assigned to the $Si^{28}(d,p)Si^{29}$ reaction. The relative intensities of these groups were the same from both normal SiO_2 targets and from SiO_2 targets enriched in Si^{29} and Si^{30}. It is interesting to note that many of these groups have often been observed from targets other than SiO_2, including the phosphate targets used for the $P^{31}(d,\alpha)Si^{29}$ reaction. In these cases, they appear to arise from a surface contamination due to the use of silicone stopcock grease in the vacuum system. On the basis of the assignment to the $Si^{28}(d,p)Si^{29}$ reaction, the Q-values of these groups have been calculated and are tabulated in Table II. Table II also lists the observed relative intensities and the energy levels in Si^{29} to which these groups correspond.

As has been mentioned, it is possible to check the assignment of these groups to the Si^{28} isotope, since the levels in Si^{29} calculated on this assumption should agree with the values obtained from the $P^{31}(d,\alpha)$ reaction. The positions of the Si^{29} levels obtained from this latter reaction are also included in Table II. It can be seen that there is agreement within the experimental error between the positions of the levels corresponding to the proton groups marked *A* through *H* in Fig. 2 and those corresponding to the alpha-particle groups marked *A*

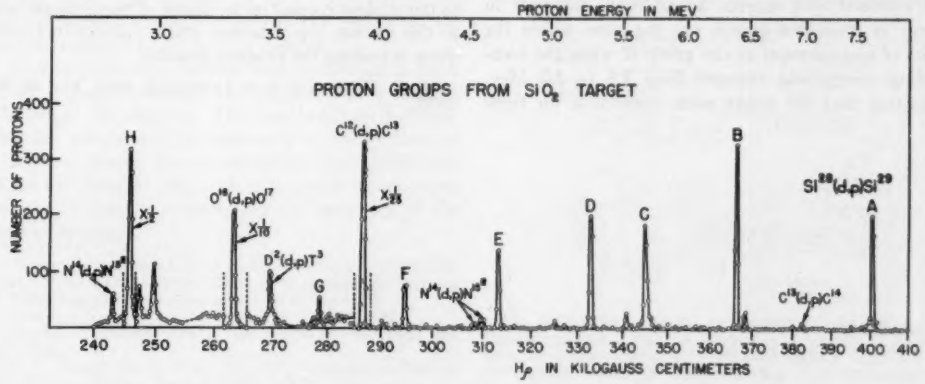

FIG. 2. Proton groups observed from a natural quartz target bombarded by 1.81-Mev deuterons.

[10] R. Malm and W. W. Buechner, Phys. Rev. **80**, 771 (1950).

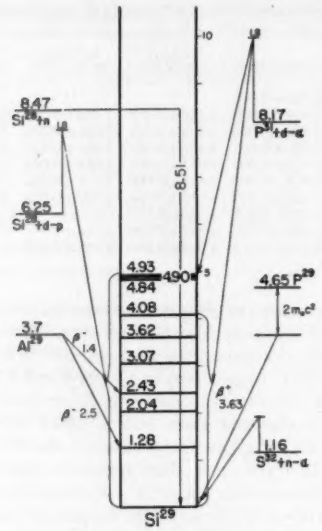

FIG. 3. Energy-level diagram for Si^{29}.

through H in Fig. 1. The discrepancy of 15 kev for the levels corresponding to the two groups marked H can be attributed to the uncertainty in determining the peak position of the $P^{31}(d,\alpha)Si^{29}$ group H in the presence of a high background. The fact that no $P^{31}(d,\alpha)Si^{29*}$ alpha-particle groups were observed which would correspond to the proton groups at 247.4 and 249.7 kilogauss-cm does not rule out the possibility that these groups may be assigned to Si^{28}, since they are approximately one-tenth the intensity of proton group H. The intensities of these two groups were found to be the same, relative to the group H, from both normal SiO_2 and enriched SiO_2 targets. In addition, the shift in energy of these two groups was the same within the limits of measurement as the group H when the bombarding energy was changed from 1.8 to 2.0 Mev, indicating that the target mass responsible for these two groups does not differ by more than five mass units from Si^{28}.

IV. CONCLUSIONS

An investigation of the $P^{31}(d,\alpha)Si^{29}$ and $Si^{28}(d,p)Si^{29}$ reactions by magnetic analysis has shown eight particle groups from both reactions which correspond to the ground state of Si^{29} and the same seven excited states. The positions of the excited states found from the two reactions agree within the experimental error. However, the results from the $Si^{28}(d,p)Si^{29}$ reaction are considered to be more accurate. Two additional proton groups were observed for which no corresponding alpha-particle groups were found. However, their low intensity, relative to the other proton groups, and the presence of a high background in the corresponding portions of the alpha-particle spectrum prevent the elimination of the possibility that alpha-particle groups may have been present which were associated with the excitation of these two additional states in Si^{29}. An energy-level diagram for Si^{29}, incorporating these results, is shown in Fig. 3.

The positions of the Si^{29} levels found from these measurements are in good agreement with the recently reported range measurements of Motz and Humphreys,[3] which are included in Table II. However, the present ground-state $Si^{28}(d,p)Si^{29}$ Q-value of 6.246 ± 0.010 Mev is definitely higher than their value of 6.18 ± 0.09 Mev and the earlier value of 6.16 ± 0.06 Mev found by Allan and Wilkinson.[4] A verification of the higher figure is obtained by subtracting the deuteron binding energy of 2.226 ± 0.003 Mev[11] from the gamma-ray of 8.51 ± 0.04 Mev observed by Kinsey *et al.*[5] from the neutron capture of natural silicon. This calculation leads to a predicted Q-value of 6.28 ± 0.04 Mev for $Si^{28}(d,p)Si^{29}$.

This work was carried out while one of the authors (P.M.E.) was at the High Voltage Laboratory under the auspices of the 1950 M.I.T. Foreign Students Summer Project. We wish to express our appreciation to the student committee in charge of the program and to the various organizations which collaborated with them in making the program possible.

[11] R. C. Mobley and R. A. Laubenstein, Phys. Rev. **80**, 309 (1950).

Neutron-Proton Scattering in the Energy Range of 18 to 21 Mev*

EWART M. BALDWIN
Carnegie Institute of Technology, Pittsburgh, Pennsylvania
(Received February 19, 1951)

The relative cross sections for neutron-proton scattering in the neutron energy range of 18 to 21 Mev were measured by means of a proportional counter telescope at the laboratory proton recoil angles of 15 degrees and 44 degrees 24 minutes, respectively. From these data a ratio of 1.06±0.16 for neutrons scattered in the center-of-mass system in the backward direction to those scattered in the sideways direction was computed.

INTRODUCTION

NEUTRON–PROTON scattering experiments carried out in the neutron energy range of 10 to 30 Mev include those of Fowler[1] at 27 Mev and a set of experiments in the vicinity of 12 to 15 Mev by various investigators.[2–4] The results of all the experiments in the range of 12 to 15 Mev, with the exception of the experiments by Amaldi, indicated isotropic, or nearly isotropic scattering. The results of Amaldi indicated a high anisotropy in favor of neutrons scattered in the sideways direction in the center-of-mass system. At 27 Mev Fowler found an anisotropy in favor of the neutrons scattered in the backward direction.

It was the purpose of this experiment to contribute data in the neutron energy interval between 18 and 21 Mev. In this experiment the detection of recoil protons, scattered by neutrons, from a polyethylene foil was accomplished by use of a proportional counter telescope which selected protons in a given energy range and in a given direction.

The telescope consisted of an array of four cylindrical proportional counters (see Fig. 1). Lead sleeves of $\frac{1}{8}$-inch wall thickness were inserted in the brass counters to stop protons produced in the brass walls. Lead was used because of its very low (n,p) cross section.[5] The central wire of each counter was made of 0.0032-inch nickel, which was shielded at each end by 0.06-inch Inconel tubing to keep the sensitive region of the counter confined to the central portion.

An evacuated fore-chamber was constructed in front of the counter telescope and separated from it by a 0.003-inch Al partition. The front end of this fore-chamber was sealed by 0.006-inch Al foil in front of which was placed the scattering foil. The dimensions of the forechamber were such as to place the scattering foil at the position required by the geometry of the counter telescope.

The output of each counter was fed successively through a preamplifier, linear amplifier, coincidence analyzer channel, scaler, and mechanical recorder. The mixing of all four channels and the selection of coincidence and anticoincidence pulses was done in the coincidence analyzer. The triple coincidence and anticoincidence outputs were each fed to a scaler and mechanical recorder.

The output of a parallel plate thorium fission neutron monitor[6] was likewise fed through a preamplifier, linear amplifier, scaler, and mechanical recorder. The selection of pulse height was done by a discriminator incorporated in the scaler circuit.

The source of high energy neutrons was the University of Pittsburgh cyclotron. This is a conventional cyclotron of 47-inch pole diameter. For this problem, neutrons were obtained from the (α,n) reaction with an alpha-beam and a beryllium target. The cyclotron was capable of giving alpha-particles an energy of approximately 30 Mev, and with the positive Q of 6 Mev for $Be^9(\alpha,n)C^{12}$ the resulting neutron energy spectrum extended to approximately 36 Mev.

Data was taken at the proton recoil angles of 15 degrees and 44 degrees 24 minutes, measured in the laboratory system. For these runs the counter system was filled with a mixture of argon and 3 percent carbon dioxide at a pressure of 20 cm of mercury. A counter

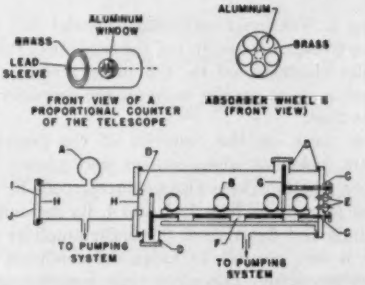

FIG. 1. Schematic diagram of the counter telescope. A—mechanical vacuum gauge, B—proportional counter, C—Wilson seals, D—rubber gaskets, E—Stupakoff seals, F—Lucite block, G—absorber wheel, H—aluminum foil, I—polyethylene foil, J—lead foil.

* This work was carried out in partial fulfillment of the requirements for the degree of Doctor of Science at the Carnegie Institute of Technology and was supported in part by the ONR.

[1] Brolley, Coon, and Fowler, Phys. Rev. **79**, 227 (1950).

[2] Amaldi, Bocciarelli, Foretti, and Trabacch, Naturwiss. **30**, 582 (1942).

[3] C. F. Powell and G. P. S. Occhidini, *Fundamental Particles* (The Physical Society, London, 1947), p. 150.

[4] J. S. Laughlin and P. G. Kruger, Phys. Rev. **73**, 197 (1948).

[5] B. Cohen, "Nuclear reactions," thesis, Carnegie Institute of Technology (1950) (to be published).

[6] B. Rossi and H. Staub, *Ionization Chambers and Counters* (McGraw-Hill Book Company, Inc., New York, 1949), p. 207.

voltage of approximately 840 volts was found satisfactory for operation of the counters in the proportional range.

PRELIMINARY TESTS AND CALIBRATION

In order to check the functioning of the electronic gear before and after each run, a signal from a pulse generator was fed into the input circuits of the preamplifiers. This pulse was a negative square pulse of approximately 2 microseconds duration, and approximated in shape the proton pulses fed from the proportional counters.

By allowing this pulse generator to trigger the electronic system it was possible to check the behavior of

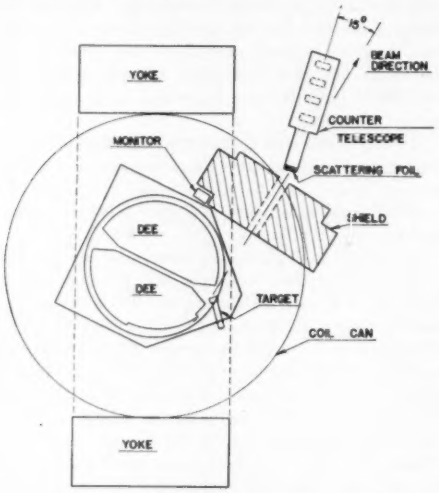

FIG. 2. Cyclotron and counter telescope.

all amplifier channels, the mixing circuit, and the scalers.

Using a Tektronix oscilloscope Model 511 it was possible to measure and record the outputs of the linear amplifier channels fed by the pulse generator. This afforded a check on the gains of the amplifiers from time to time.

As a check on the behavior of the proportional counters, polonium alpha-sources were placed on the absorber wheels. These alpha-sources could be placed in front of counters Nos. 1, 3, and 4. By measuring the amplitude and duration of the linear amplifier output pulses it was possible to judge the condition of the counter gas filling. This alpha-pulse measurement was an added check on the electronic system. Also by measuring the amplitude of these output pulses, and knowing the alpha-energy loss in the counter, the discriminator bias of the coincidence analyzer could be set to count pulses produced by protons up to a certain maximum energy.

Owing to the finite length of time required for the collection of the ions in the proportional counters, it was necessary to adjust the gate widths of the univibrator in each of the four analyzer channels to the following values: 2.0 microseconds for channels Nos. 1, 2, 3 and 6.0 microseconds for channel No. 4. Also a delay of 2.2 microseconds was introduced between the coincidence output and the anticoincidence input.

In order to position the telescope for the experiment it was necessary to know accurately the position of the cyclotron target. To take advantage of the maximum beam intensity it was necessary to know the horizontal angular distribution of the neutron beam.

An angular distribution of the neutron beam, obtained from the reaction $Be^9(\alpha,n)C^{12}$, was taken with silver threshold detectors placed a few inches apart on a horizontal circle of 75-cm radius centered at the target. This distribution, like some of those encountered by Falk,[7] had two maxima about 27 degrees apart. The maximum farther from the cyclotron yoke was chosen for the scattering experiment.

An accurate survey of the cyclotron target was made after the removal of one of the side plates from the cyclotron vacuum chamber. A horizontal axis, passing through the target at a point where the internal beam strikes the target cup, and passing through the neutron beam maximum, was taken as the reference line. The vertical projection of this axis was marked on the cyclotron coil can and on the floor.

The counter telescope was orientated with respect to this horizontal axis, and pivoted at a point 125 cm from the cyclotron target about a vertical axis passing through the center of the scattering foil. The scattering angles were marked on the floor of the cyclotron room, and the telescope was positioned by means of plumb bob and ruler. The error in angular location of the telescope was less than $\frac{1}{4}$ degree.

To avoid blocking the individual proportional counters by an excessive number of proton pulses, and to avoid a high accidental triple coincidence rate, it was necessary to shield the counter system from the direct neutron beam. This was accomplished by building a cement shield 2 feet thick and 4 feet wide between the counter telescope and the cyclotron target. This shield was constructed from cement blocks of 4 inches×8 inches×16 inches dimensions. The shield was built on the lower cyclotron coil can and extended to the lower surface of the upper coil can. An aperture of 4 inches ×5 inches through the shield allowed the neutron beam from the cyclotron target to strike the surface of the scattering foil (see Fig. 2). This shield was effective in reducing the individual counter rates by a factor of 10 over that obtained without a shield.

To prevent those protons produced in the shield from entering the telescope, a lead foil of approximately $\frac{1}{16}$-inch thickness was placed directly in front of the

[7] C. Falk, Phys. Rev. **83**, 499 (1951).

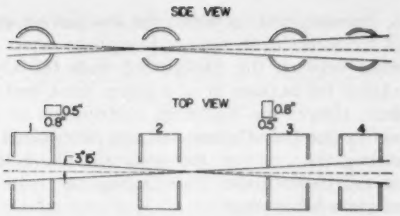

FIG. 3. Counter aperture geometry.

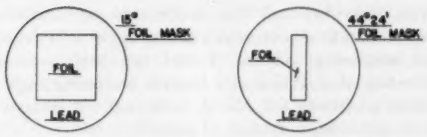

FIG. 4. Lead mask apertures for scattering foils.

scattering foil. Lead was used because of its low (n,p) cross section.[5]

EXPERIMENTAL PROCEDURE

In order to select the recoil protons scattered at a given angle by neutrons in the energy range of 18 to 21 Mev from those scattered by the rest of the neutron spectrum, two sets of proton energy absorbers were required. One set was located in front of counter No. 1, and the other set between counters Nos. 3 and 4.

The Al absorber thickness for the front set was chosen so that protons produced by 18-Mev neutrons on the inside (telescope side) of the polyethylene, and traveling normal to that surface, would enter counter No. 3 with an energy of approximately 0.2 Mev. The thickness of the rear Al absorber set was adjusted so that protons produced by 21-Mev neutrons on the outside surface (target side) of the polyethylene, and traveling normal to that surface, would just enter counter No. 4 with less than 0.1 Mev.

To calculate the thickness of the Al absorbers, the energy loss in the counter gas and the energy loss in the polyethylene scatterer, it was necessary to have an accurate set of range energy curves. The curves used for aluminum and argon were taken from the compilation of range-energy curves published in 1949 by the University of California Radiation Laboratory, Berkeley, California.[8] The calculations of Hirschfelder and Magee[9] were used for polyethylene.

Different thicknesses of polyethylene foil were required for different scattering angles in order to choose identical segments of the neutron spectrum. The thickness of the polyethylene was chosen so that those protons produced on the outside surface of the foil by neutrons of a predetermined energy, and traveling along a normal through the foil, would lose sufficient energy to emerge from the inside surface with the minimum proton energy, i.e., the energy of a proton produced on the inside surface by an 18-Mev neutron. At the proton recoil angle of zero degrees this predetermined neutron energy chosen to produce the above mentioned protons was 19.60 Mev. For all other angles the proton energy was given by $E_p = E_n \cos^2\theta$, where E_p equals the proton energy in Mev, E_n equals the neutron energy in Mev, and θ was the proton recoil angle in the laboratory system.

At the proton recoil angles of 15 degrees and 44 degrees 24 minutes the polyethylene thicknesses were 53.27 mg/cm² and 15.27 mg/cm², respectively.

Protons leaving the foil at angles of several degrees with the normal can be detected by the counter system. This small angular spread produced a corresponding spread in the neutron energy interval and, owing to the $\cos^2\theta$ relation, this energy spread became greater with increasing proton recoil angle. In order to match as closely as possible neutron energy spectra at various proton recoil angles it was necessary to construct the defining counter apertures (rear aperture No. 1, front aperture counter No. 3) as rectangular slits, and to introduce a third set of apertures directly behind the scattering foil (see Figs. 3 and 4). This third set of apertures was cut from ⅛-inch lead plate and was designed to constrict the angular spread at the two recoil proton angles, chosen for the experiment, to values which gave approximately the same spread in the neutron energy interval.

Making use of the polyethylene range-energy curves, the $E_p = E_n \cos^2\theta$ relation, and the counter aperture

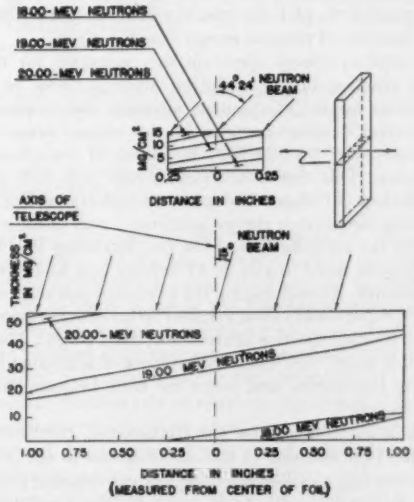

FIG. 5. Distribution in scattering foil of these neutrons which produce protons emerging from scattering foil with minimum proton energy.

[8] Aron, Hoffman, and Williams, UCRL-121, second revision (1949).

[9] J. Hirschfelder and J. Magee, Phys. Rev. **73**, 207 (1948).

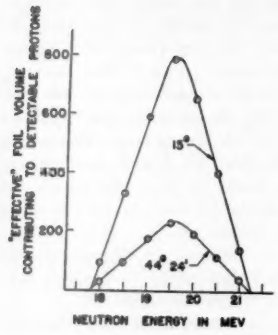

FIG. 6. "Effective" scattering foil volume *versus* neutron energy.

geometry, it was possible to trace the volume of scattering foil contributing to those protons which emerged from the inside scattering surface with a given energy and which were produced by neutrons of a given energy. The volume of such a portion of the foil was equal to the cross-sectional area which was effective for neutrons of that given energy, times the vertical height of the foil modified by the vertical aperture contributions. Furthermore, since both foils had the same vertical height and the same vertical aperture dependence, it was sufficient for any comparison to plot only the cross-sectional areas of the scattering foil contributing to the above mentioned protons (see Fig. 5). Such calculations and graphs were compiled for the scattering foils used at the angles of 15 degrees and 44 degrees 24 minutes.

By measuring the areas enclosed for a given neutron energy responsible for protons in the detectable range it was possible to plot the effective cross-sectional areas as a function of neutron energy (see Fig. 6).

A neutron energy spectrum was measured for the (α,n) reaction of the cyclotron alpha-particles on a beryllium target. The neutron intensity was measured at several neutron energies in the energy range of approximately 9 to 21 Mev by means of the counter telescope. This spectrum checked very well with the predictions of Cohen.[5] The spectrum is plotted in Fig. 7.

Using the neutron energy spectrum it was possible to weight the contributions of the two scattering foils for the proton recoil angles of 15 degrees and 44 degrees 24 minutes. By multiplying the effective cross-sectional area (proportional to foil volume) *versus* neutron energy curve by its respective neutron spectrum weight, it was possible to get the "effective" volume of scattering foil at the two angles, and hence the ratio between them (see Fig. 8).

In order to determine the background, contributed by the (n,p) reaction in the carbon atoms in the polyethylene foil, a carbon foil of equivalent stopping power was deposited on a lead foil of $\frac{1}{16}$-inch thickness. When the polyethylene foil was removed for a background count, it was replaced by this lead-carbon foil. It was found, however, that to within the few percent error in this measurement it was not possible to detect the difference between the background with the above lead-carbon foil in place or with just a blank lead foil in place. Hence, the scattering contribution of the protons in the polyethylene foil was determined by subtracting the counting rate with the above lead-carbon foil present from the counting rate with the polyethylene foil in place.

DISCUSSION OF RESULTS

The ratio between the neutron-proton scattering cross section at a neutron scattering angle of θ_1 degrees from scattering foil No. 1 and the neutron-proton scattering cross section at a neutron scattering angle of θ_2 from scattering foil No. 2, both angles measured in the center-of-mass system, is given by

$$R=\frac{\sigma(\theta_1)}{\sigma(\theta_2)}=\frac{N_1}{N_2}\cdot\frac{d\Omega_2'}{d\Omega_1'}\cdot\frac{\text{effective } f_2}{\text{effective } f_1},$$

where N_1 and N_2 are the number (normalized to the monitor) of protons scattered at the angles of $(180-\theta_1)$ and $(180-\theta_2)$ degrees, respectively; $d\Omega_1'$ and $d\Omega_2'$ are the elements of scattering solid angles in the center-of-mass system into which these recoil protons are scattered; and effective f_1 and effective f_2 are proportional to the "effective" number of target nuclei presented by the foils No. 1 and No. 2.

The ratio N_1/N_2 comes directly from the experimental data and has a value of 6.5 ± 1.0. This value is

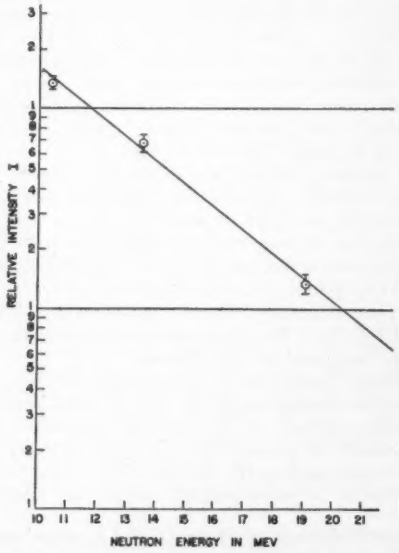

FIG. 7. Neutron energy spectrum from Be(α,n) reaction.

obtained from six separate sets of runs, using

$$\frac{N_1}{N_2}=\frac{\sum[(N_1/N_2)_i/e_i]}{\sum(1/e_i)}\pm\frac{\sqrt{n}}{\sum(1/e_i)}=6.5\pm1.0,$$

where e_i is the probable error in the ith ratio, $(N_1/N_2)_i$, and n is the number of sets.

From the relation $d\Omega'_{cm}=4\cos\theta d\Omega_{lab}$ between an element of solid angle in the laboratory system and an element of solid angle in the center-of-mass system, we have $d\Omega_2'/d\Omega_1'=0.547$.

The ratio of the "effective" volume of scattering foil for a proton scattering angle of 15 degrees to the "effective" volume of scattering foil for a proton scattering angle of 44 degrees 24 minutes is equivalent to the ratio of the areas under the neutron-spectrum weighted curves shown in Fig. 8. This ratio has a value of 0.298 ± 0.10.

Hence, the product of these three factors is

$$R=1.06\pm0.16.$$

The results of this experiment seem to be consistent with the existing data, provided that the results of Amaldi are discounted in favor of the predominance of corresponding data presented by numerous other investigators. That is, there does not appear to be any high degree of anisotropy in the neutron-proton scattering at this energy range.

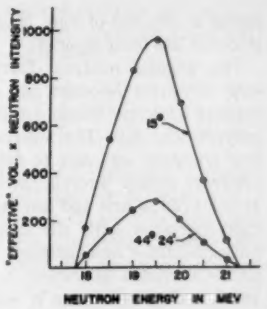

FIG. 8. Spectrum-weighted neutron energy intervals.

The author wishes to express his appreciation for the guidance and help given him by Professors R. B. Sutton, E. C. Creutz, H. C. Corben, and L. Wolfenstein, and is indebted to Dr. M. Foss for his active interest in the problem. He also wishes to express his thanks to Dr. A. J. Allen and the cyclotron staff of the University of Pittsburgh for their cooperation, to Dr. B. Cohen for his helpful suggestions, and to Dr. C. E. Falk and Dr. A. Lasday for their help in construction of equipment and operation of the cyclotron.

PHYSICAL REVIEW VOLUME 83, NUMBER 3 AUGUST 1, 1951

(d,n) Reactions with 15-Mev Deuterons. Part I. Angular Distributions*†

C. E. FALK‡
Carnegie Institute of Technology, Pittsburgh, Pennsylvania
(Received February 8, 1951)

Nine elements are bombarded with 15-Mev deuterons from a cyclotron. The resulting angular distributions of 9.25- to 13.1-Mev neutrons are measured by means of a four-proportional counter telescope and also by threshold detectors. It is observed that all the measured angular distributions are peaked in the forward direction, some showing a peak at 0° and others peaks at 10°–15° with respect to the deuteron beam. Different methods of production of neutrons from (d,n) reactions are discussed, and it is shown that most of the observed neutrons are produced by a stripping process.

INTRODUCTION

ALTHOUGH the interaction between high energy deuterons (~200 Mev) and nuclei has been thoroughly investigated and explained,[1–3] the nature of the interaction at medium deuteron energies is not clear. Several investigations[4–7] have not produced sufficient evidence to determine whether stripping,[3] which explained the high energy reaction, can account for the nature of the yields in d,n and d,p reactions.

The deuteron beam of the University of Pittsburgh cyclotron was used to investigate the characteristics of the yields of (d,n) reactions. These experiments can be divided into two groups: the investigation of the angular distributions of neutrons produced by 15-Mev deuterons, which is reported here, and the study of neutron energy spectra and neutron yields from d,n reactions, which will be reported in Part II. The integrated interpretation of all the data will be pre-

* Assisted by the ONR.
† This work was carried out in partial fulfillment of the requirements for the degree of Doctor of Science at the Carnegie Institute of Technology.
‡ Now at Brookhaven National Laboratory, Upton, Long Island, New York.
[1] A. C. Helmholtz, Phys. Rev. **72**, 1003 (1947).
[2] R. Serber, Phys. Rev. **72**, 1008 (1947).
[3] S. Dancoff, Phys. Rev. **72**, 1017 (1947).
[4] R. B. Roberts and P. H. Abelson, Phys. Rev. **72**, 76 (1947).
[5] Falk, Creutz, and Seitz, Phys. Rev. **76**, 322 (1948).
[6] P. Ammiraju, Phys. Rev. **76**, 1421 (1949).
[7] R. Gove, Phys. Rev. **78**, 344 (1950).

sented at the end of Part II after all the experimental evidence has been reported.

The angular neutron distributions were measured with threshold detectors and also with a proportional counter telescope[8] which detected proton recoils from a polyethylene foil. The apparatus, which consisted of four counters, was able to detect neutrons within any arbitrary energy interval through the use of absorbers in front of the first and last counter. The telescope was then operated with the counters in a coincidence-anticoincidence arrangement. By placing the telescope or the detectors at various angles with respect to the incident deuteron beam it was possible to obtain the neutron angular distributions.

APPARATUS

Thick internal cyclotron targets were used in all experiments. These targets were of the rotating cup

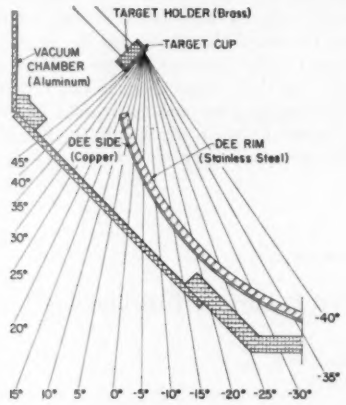

FIG. 1. Horizontal cross section of cyclotron dee and vacuum chamber showing attenuating materials encountered by neutrons coming from the target.

type with most metals machined directly as cups. In the case of a gold a heavy layer was sprayed onto a copper cup.

Silver was used as the threshold detector, since the $Ag^{107}(n,2n)Ag^{106}$ reaction had a sufficiently high threshold[9] of ~11 Mev and the 24.5-minute half-life of Ag^{106} was convenient for counting. The detectors were 2″ long cylinders with an o.d. of 1″ and a thickness of 0.020″. The cylindrical form made it convenient to slip the detectors over the G-M tubes.

The counter telescope construction is described by E. Baldwin.[8] The geometry of the detected beam is defined by circular apertures cut into the walls of the counters which have their axes at right angles to the direction of detection. This system of circular apertures permitted only protons within a 10° circular cone to pass from the polyethylene foil through all the counters.

As the experiments were performed inside the cyclotron room it was necessary to discriminate against γ-ray pulses. However, it was important that the electronic discriminators were set low enough to make detection of the high energy proton pulses possible. For this reason the size of pulses produced by polonium α-particles were measured. From range-energy relationships it was possible to calculate how much energy the α-particles would lose in the counter and also how much energy would be lost by the fastest protons. Subsequently, it was possible to determine the minimum discriminator voltage by direct proportionality. Actually, it was possible to set the discriminators at $\frac{1}{4}$ of the height of the smallest proton pulse and still prevent γ-ray pulses from being counted.

As the accidental counting rate is proportional to the cube of the individual counting rate, it was important to keep the latter as low as possible. For this reason a shield consisting of 20 to 30 cement blocks (4″×8″ ×16″) was placed between the counter telescope and the cyclotron. However, it was found that when the telescope was placed in such a position that it pointed along the direction of the opening of the shield, the single-counter counting rate was still much too high. This can be understood if one considers that the neutron flux coming through the opening of the shield would not only irradiate the polyethylene foil but also the aluminum absorbers and the center portion of the brass counters in the telescope. It was found that when the telescope was placed at an angle of 15° with respect to the neutron beam, most neutrons would miss the bulk of the telescope. (The experimental arrangement was similar to the one shown in Fig. 2 of the preceding paper[8] except that the telescope is oriented at 15° away from the cyclotron yoke.) After these precautions had been taken, the deuteron beam was kept at such an intensity that the counting rate of the single counters was small enough to make the number of accidentals negligible.

EXPERIMENTAL PROCEDURE

All experiments on angular distributions were run with the absorbers of the telescope set to detect neutrons from 9.25 Mev to 13.1 Mev. Before and after every run the equipment underwent tests to check the consistency of the gain of the amplifiers and the counting ability of the scalers. The telescope and shield were moved to different angles and the relative neutron intensity per unit monitor count was measured. A thorium fission chamber of the Rossi-Staub type[10] was used as a monitor. It was assumed that the number of fissions would be proportional to the number of deuterons striking the target. The threshold for thorium

[8] For details of telescope construction see E. Baldwin, Phys. Rev. **83**, 495 (1951).

[9] G. C. Baldwin and H. W. Koch, Phys. Rev. **67**, 1 (1945).

[10] B. Rossi and H. Staub, *Ionization Chambers and Counters* (McGraw-Hill Book Company, Inc., New York, 1949), p. 207.

fission being 1.1 Mev,[11] this would be true only if the neutron spectrum remained constant during the run. Neutron spectra measurement showed this to be the case. The monitor was cross checked by measuring the actual deuteron current striking the target.

At each angle, measurements were taken without the polyethylene foil in place in order to determine the background. This measured the number of protons produced by (n,p) reactions in the aluminum foil, absorbers, and the gas mixture. However, it did not measure those protons produced by (n,p) reactions in the carbon of the polyethylene. In order to measure these a carbon layer corresponding to the carbon in the polyethylene was placed in front of the counters. It was found that the number of protons produced in the carbon was so small that it could not be measured within the experimental error. By making measurements at different angles the angular distributions in the laboratory system were obtained. However, attenuation corrections have to be made. As can be seen from Fig. 1, the neutrons produced in the target have to traverse the cyclotron vacuum chamber to reach the neutron detectors. Thus, the detected neutrons have to traverse various thicknesses of aluminum, copper, and stainless steel and are consequently attenuated to varying extents before they are actually observed.

The attenuation was calculated by using the total scattering cross section σ_T, which can be broken up into two parts, $\sigma_T=\sigma_{CN}+\sigma_E$. σ_{CN} is the cross section for the formation of the compound nucleus and σ_E the elastic scattering cross section. It has been shown[12,13] that at energies used in this experiment one obtains $\sigma_{CN}=\sigma_E$. Thus, both of these processes had to be considered.

The neutrons produced by the compound nucleus are emitted almost isotropically and usually at lower energies. However, the elastically scattered neutrons are diffracted and are thus scattered predominantly in the forward direction. Their angular distribution is given by[12]

$$B=d\sigma_E/d\omega=R^2[J_1(R\theta/\lambda)/\theta]^2,$$

where R is the radius of the scattering nucleus, θ is the angle of scattering, λ is the De Broglie wavelength of the incoming neutron, and J_1 is a bessel function of the first order. The angular distribution of the elastically scattered neutrons is thus very dependent on the energy of the incident neutron and the radius of the scattering nucleus. Using 11-Mev neutrons the distribution falls to half-intensity at $\theta=0.375$ radian for copper and $\theta=0.490$ radian for aluminum. Because of this anisotropic distribution some of the elastically scattered neutrons will be scattered into the detector. The magnitude of this effect has been calculated for one case, the angular distribution of neutrons produced by deuterons impinging on a copper target, by graphically integrating the following expression:

$$K=\int_0^{\varphi} Bd\theta \Big/ \int_0^{2\pi} Bd\theta,$$

where K is the fraction of the elastically scattered neutrons which are scattered into the detectors and φ is the angle subtended by the detector as seen from the scatterer. Results of this calculation showed that the error introduced by neglecting this effect is small enough not to alter the shape of the curves to any noticeable extent.

The above discussion is valid for the measurements which were made with the counter telescope, as in

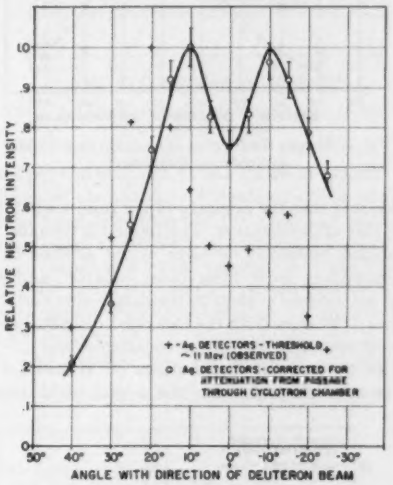

FIG. 2. Angular distribution of neutrons from 15-Mev deuterons or beryllium.

that case where the cement shield prevents elastically scattered neutrons from all parts of the cyclotron from being radiated into the telescope. When threshold detectors are used, there is, of course, no shield in front of them, and then only a fraction of the total cross section should be used for the attenuation calculations, as an appreciable fraction of the elastically scattered neutrons are essentially scattered back into some detectors.

However, the fact that the data obtained with the counter telescope (which does not count scattered-in neutrons) is in good agreement with the threshold detector data (using the same attenuation corrections as those used for the telescope data) shows that the effect of the scattered-in neutrons is very small.

It should be kept in mind, however, that either attenuation calculation procedure is only an approxi-

[11] W. E. Shoupp and L. E. Hill, Phys. Rev. **75**, 785 (1949).
[12] E. Amaldi *et al.*, International Conference on Fundamental Particles and Low Temperatures, Phys. Soc. (London) **1**, 97 (1947).
[13] H. Bethe, Phys. Rev. **57**, 352, 1125 (1940).

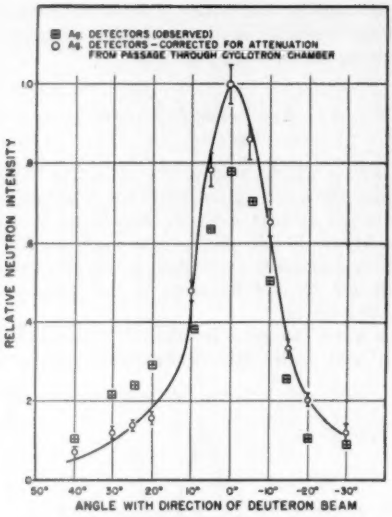
Ag DETECTORS (OBSERVED)
Ag DETECTORS – CORRECTED FOR ATTENUATION FROM PASSAGE THROUGH CYCLOTRON CHAMBER
RELATIVE NEUTRON INTENSITY
ANGLE WITH DIRECTION OF DEUTERON BEAM

FIG. 3. Angular distribution of neutrons from 15-Mev deuterons on magnesium.

mation and that the accuracy of the results will depend upon this approximation. The proof for "double" and single-peak existence, however, is not affected by this approximation, as in most cases "double" and single peaks are already evident in the data before correction. Figures 2–10 show both the measured distributions and the ones corrected for this attenuation effect.

After the angular distributions of Al and Co (the first being single-peaked and the second double-peaked)

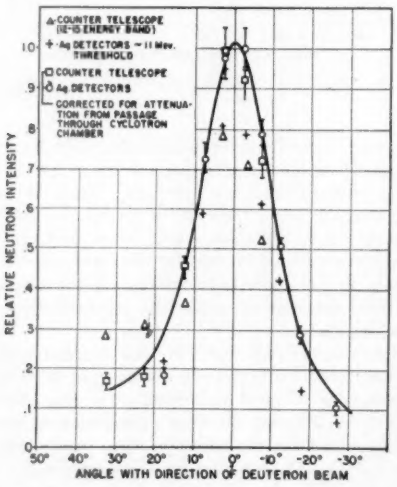
COUNTER TELESCOPE (E=E ENERGY BAND)
Ag DETECTORS – 11 Mev. THRESHOLD
COUNTER TELESCOPE
Ag DETECTORS
CORRECTED FOR ATTENUATION FROM PASSAGE THROUGH CYCLOTRON CHAMBER
RELATIVE NEUTRON INTENSITY
ANGLE WITH DIRECTION OF DEUTERON BEAM

FIG. 4. Angular distribution of neutrons from 15-Mev deuterons on aluminum.

had been measured with the counter telescope, the measurements were repeated with Ag threshold detectors. As can be seen from Figs. 4 and 6, the agreement between the results of the two methods is good. Consequently, the remaining angular distributions were measured only with Ag detectors, as this was the least time consuming method.

Attention is called to the fact that the direction of the deuteron beam was not exactly known within 5°. Thus, it was assumed to be at the center of symmetry of the angular distribution. The orientation of the center of symmetry with respect to the cyclotron varied slightly from run to run; and, consequently, the attenuation corrections are not always identical at the same angle with respect to the deuteron beam.

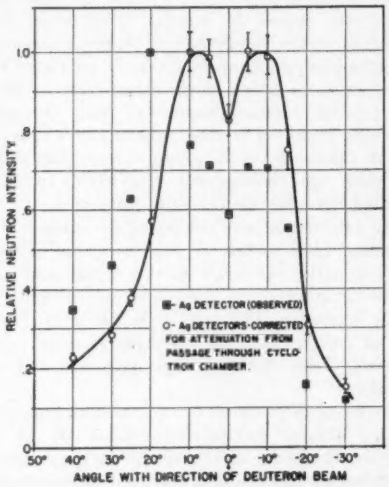
RELATIVE NEUTRON INTENSITY
Ag DETECTOR (OBSERVED)
Ag DETECTORS-CORRECTED FOR ATTENUATION FROM PASSAGE THROUGH CYCLOTRON CHAMBER.
ANGLE WITH DIRECTION OF DEUTERON BEAM

FIG. 5. Angular distribution of neutrons from 15-Mev deuterons on titanium.

As the changes due to the transformation into the center-of-mass system are so slight that no change of the distributions is apparent, all distributions are plotted in laboratory system coordinates.

RESULTS—DISCUSSION

As can be seen from Figs. 2–10 all angular distributions show definite preferred directions. For some elements this preferred direction is that of the deuteron beam. Thus, Mg, Al, Mo, and Ag produce "single" peaks in the neutron distribution. Other targets, such as Be, Ti, Co, Cu, and Au show preferred directions at some angle (usually about 12°–15°) with respect to the deuteron beam. The neutron angular distributions resulting from this appear to be "double" peaked. These experimental results for Be and Al are in good

agreement with the recent work by Holt.[14] His neutron angular distributions produced by 8.2-Mev deuterons show also a "double" peak in Be and a "single" peak in Al.

When deuterons interact with nuclei, deuterons can be produced by three different processes: neutron ejection from a compound nucleus formed by the deuteron, stripping, and electric disintegration of the deuteron in flight. Considering neutron production from compound nuclei, the statistical theory of the compound nucleus predicts that, at the energies used in this experiment, the angular distribution of the neutrons should be isotropic,[15] or show a very wide and small peak in the forward direction.[16] As the measured peaks have a maximum to minimum intensity ratio of at least

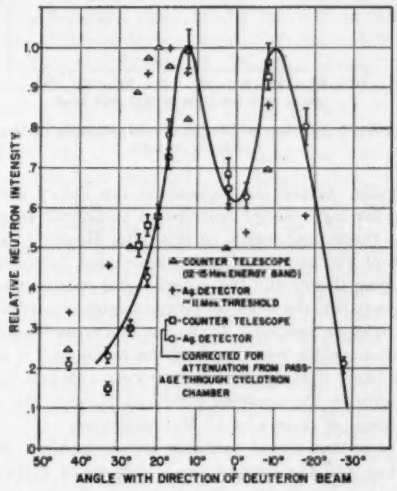

FIG. 6. Angular distribution of neutrons from 15-Mev deuterons on cobalt.

4, it is difficult to see how a compound nucleus can account for the majority of the observed neutrons.

Another method of neutron production through deuteron-induced reactions is stripping. This process has been demonstrated experimentally,[1] and a satisfactory model has been given by Serber.[2] However, this model, which explained the process with 190-Mev deuterons, has to be modified if it is applied to 15-Mev deuterons. While the coulomb effect of the target nucleus on the incoming deuteron becomes much more important at these low energies, the Serber model simply modified for coulomb effect still predicts "single" peaks in the angular distribution of neutrons. Stripping at relatively low energies (~10 Mev) has been recently

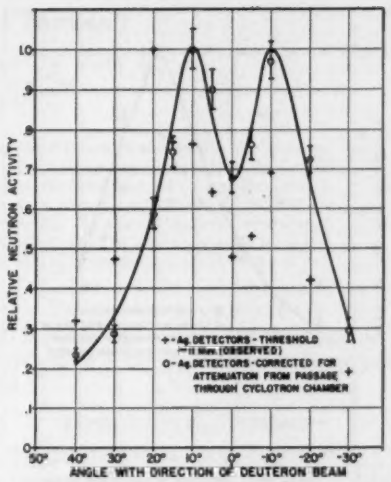
RELATIVE NEUTRON ACTIVITY
ANGLE WITH DIRECTION OF DEUTERON BEAM
Ag DETECTORS - THRESHOLD
Ag DETECTORS - CORRECTED FOR ATTENUATION FROM PASSAGE THROUGH CYCLOTRON CHAMBER

FIG. 7. Angular distribution of neutrons from 15-Mev deuterons on copper.

worked out theoretically. It was shown by Butler[17] that the shape of the angular distributions of the neutrons or protons are determined by the spins and parities of the target and residual nuclei. Thus, an angular momentum change of 0 in the production of the residual nucleus will produce a "single" peaked neutron distribution, a change of $\Delta l=1$ will produce a slight "double" peak, and a change of $\Delta l=2$ a very pronounced "double" peak. This explains why the shape of the observed

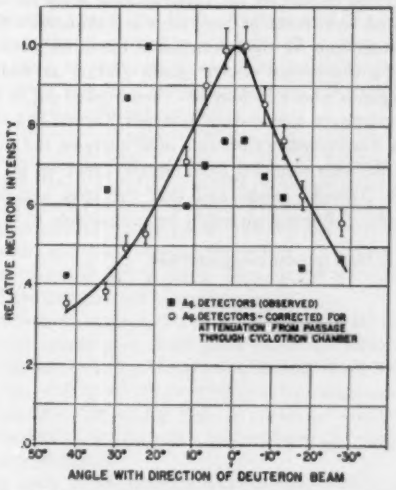
RELATIVE NEUTRON INTENSITY
ANGLE WITH DIRECTION OF DEUTERON BEAM
Ag DETECTORS (OBSERVED)
Ag DETECTORS - CORRECTED FOR ATTENUATION FROM PASSAGE THROUGH CYCLOTRON CHAMBER

FIG. 8. Angular distribution of neutrons from 15-Mev deuterons on molybdenum.

[14] J. H. Holt, Proceedings of the Harwell Nuclear Physics Conference (September, 1950), p. 52.
[15] V. Weisskopf, Phys. Rev. **52**, 295 (1937).
[16] L. Wolfenstein, Phys. Rev. **78**, 322 (1950).
[17] S. T. Butler, Phys. Rev. **80**, 1095 (1950).

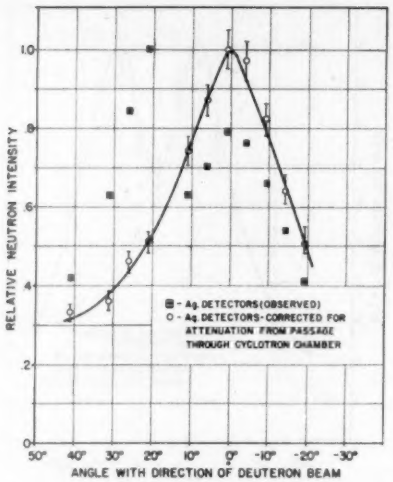
RELATIVE NEUTRON INTENSITY
ANGLE WITH DIRECTION OF DEUTERON BEAM
■ - Ag. DETECTORS (OBSERVED)
○ - Ag. DETECTORS - CORRECTED FOR ATTENUATION FROM PASSAGE THROUGH CYCLOTRON CHAMBER

FIG. 9. Angular distribution of neutrons from 15-Mev deuterons on silver.

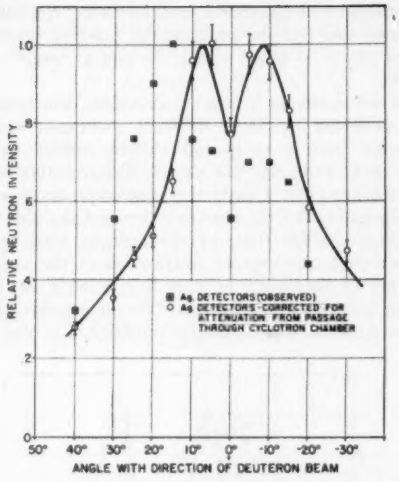
RELATIVE NEUTRON INTENSITY
ANGLE WITH DIRECTION OF DEUTERON BEAM
■ Ag. DETECTORS (OBSERVED)
○ Ag. DETECTORS - CORRECTED FOR ATTENUATION FROM PASSAGE THROUGH CYCLOTRON CHAMBER

FIG. 10. Angular distribution of neutrons from 15-Mev deuterons on gold.

angular distributions seems to vary irregularly with Z. As the deuteron energies in this experiment (15.0 $\pm$1Mev) are great enough to have the absorbed proton produce many excited states in the residual nucleus, one would expect all the angular distributions to be a mixture of the $\Delta l=0$, 1, and 2 distributions and thus be "single" peaked and rather wide. The fact that some of the distributions show sharp "single" peaks while others are even "double" peaked seems to indicate that the cross section for the production of some particular excited level must be very large as compared with the cross sections for the formation of the other levels.

The theory for electric disintegration at deuteron energies of about 15 Mev has been worked out in detail for relatively low energy neutrons. Guth[18] has shown that if one considers neutrons of all energies, the angular distributions resulting from electric break-up do show wide "double" peaks and that the cross section for electric disintegration might be comparable to that for stripping. As the assumptions in the theory are not valid for high energy neutrons, it is difficult to apply these theoretical results to this data. However, in the light of the good qualitative agreement between the stripping theory and the experimental results reported in this paper, the work on proton angular distributions and spectra resulting from d,p reactions,[19] and the neutron spectra resulting from d,n reactions,[20] it seems very likely that the stripping process accounts for the majority of the neutrons produced through the bombardment of targets by 15-Mev deuterons.

The author wishes to thank Dr. A. J. Allen, Mr. J. Nechaj, and the crew of the University of Pittsburgh cyclotron for their cooperation and the use of the cyclotron, Drs. E. Creutz, L. Wolfenstein, and F. Seitz for their experimental and theoretical guidance, Drs. E. Baldwin and A. Lasday for their help throughout the experiment, and Dr. B. Cohen for many helpful discussions.

[18] E. Guth (private communication).

[19] H. Gove, Phys. Rev. **78**, 344 (1950).

[20] C. Falk and B. Cohen (to be published).

Absorption of 280-Mev Photons*†

J. W. DeWire, A. Ashkin, and L. A. Beach
Cornell University, Ithaca, New York

(Received April 16, 1951)

Total cross sections for 280-Mev photons have been measured for a number of elements. The source of photons was the bremsstrahlung spectrum of 310-Mev upper limit, which was obtained from the Cornell synchrotron. P hotons above 250 Mev were detected by a pair spectrometer and the transmission through various samples determined. The measured cross sections in units of cm^2/g are 0.01060, 0.0284, 0.0528, 0.0776, 0.1069, and 0.1148 for Be, Al, Cu, Sn, Pb, and U, respectively. The probable statistical errors range from 0.9 to 1.4 percent. These values are lower than the theoretical values by a fraction which is roughly proportional to Z^2 and is about 10 percent for Pb, in agreement with other results obtained at lower energies.

INTRODUCTION

DURING the past several years a number of investigators have determined total cross sections for photons above 10 Mev in various materials, following the initial experiments of Delsasso, Fowler, and Lauritsen.[1] In each case the experiment consisted of measuring the transmission of the photons through known thicknesses of metals. Adams[2] obtained values at 11.0, 13.7, and 19.1 Mev, using the continuous photon spectrum from a 22-Mev betatron and various threshold detectors employing the (γ,n) reaction. Walker[3] determined cross sections for the 17.6-Mev photons from $Li^7(p,\gamma)Be^8$ reaction, using an electron pair spectrometer as a detector. Lawson[4] made similar measurements at 88 Mev, detecting the highest energy photons from a 100-Mev betatron with a pair spectrometer. These experimental results in general show good agreement with the theory for absorbers of low atomic number but significantly low cross sections for the heavy elements. In this paper measurements of cross sections for photons of 280 Mev are described. It will be seen that the results show a similar relation to the theoretical values as those at lower energies.

The method used in this work was to measure the transmission through various metal samples of the photons in the upper energy region of the continuous spectrum from the Cornell synchrotron. The cross sections in the 300-Mev region vary slowly with energy, making it possible to use photons of a rather wide energy spread. However, as Lawson has pointed out,[4] if the energy width is too large, photons which produce effects in the absorber can reappear in the beam either directly or through secondary processes with energies within the sensitive region of the detector. The strength of this effect depends not only on the width of the energy band but also on the geometry. Calculations based on our experimental arrangement indicate that for a bremsstrahlung spectrum with an upper energy limit of 310 Mev, the region above 250 Mev could be used with reductions in the cross section no larger than 0.5 percent.

EXPERIMENTAL EQUIPMENT

A schematic plan of the equipment involved in this experiment is shown in Fig. 1. The slowly diverging beam from the synchrotron passes through the following components:

1. An ionization chamber monitor.
2. A collimating slit in a 6-inch lead wall. Slit dimensions—$\frac{1}{16}$ inch high by 1 inch wide.
3. Another monitor chamber identical to the first.
4. An open region about 30 inches long in which the absorbers are placed.
5. A second lead slit, $\frac{1}{4}$ inch high by 1 inch wide.
6. A region of magnetic field of 10^4 gauss, extending 15 inches along the path.
7. A third lead slit, $\frac{1}{2}$ inch by $1\frac{1}{2}$ inches by 6 inches.
8. A $\frac{1}{4}$-mil gold pair-forming radiator in the magnetic field of the pair spectrometer.

The region from the front of the second slit to the exit from the spectrometer is evacuated to prevent the appearance of electrons in the beam after they have been swept out by the first magnet, which has been aptly called the broom magnet.

The monitor chambers are multiple parallel plate ionization chambers containing air at atmospheric pressure. Each chamber consists of eleven aluminum plates $\frac{1}{32}$ inch thick and 3 inches square, spaced $\frac{1}{2}$ inch apart. Alternate plates are connected to a 270-volt potential and to a condenser which integrates the charge collected during a run. This charge is measured by a balanced electrometer tube circuit.

The broom magnet serves to insure that the spectrometer counts only those pairs which are formed in the gold radiator. Its effectiveness is illustrated by the fact that with the radiator removed the background in the spectrometer under typical operating conditions is decreased by as much as a factor of twenty when the broom is energized.

The heart of the equipment is the pair spectrometer. It is built around a magnetic field in a region shown by the outline in the schematic plan and having a height of 4 inches. Electron pairs formed in the radiator are

* Assisted by the joint program of the ONR and AEC.
† The results given in this paper were contained in Phys. Rev. **82**, 447 (1951).
[1] Delsasso, Fowler, and Lauritsen, Phys. Rev. **51**, 391 (1937).
[2] G. D. Adams, Phys. Rev. **74**, 1707 (1948).
[3] R. L. Walker, Phys. Rev. **76**, 527 (1949).
[4] J. L. Lawson, Phys. Rev. **75**, 433 (1949).

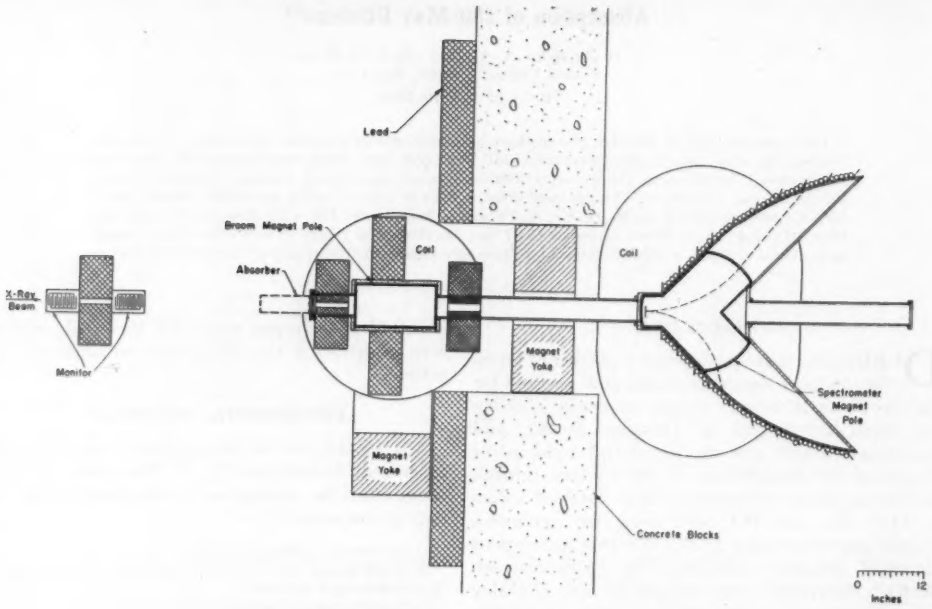

FIG. 1. Schematic plan of the experimental equipment.

separated by the field and pass through the evacuated chamber and a $\frac{1}{16}$-inch aluminum window to the various G-M counters. There are 42 counters on each side of the spectrometer, connected together in 9 groups covering 9 equal momentum intervals. The lowest momentum interval on each side is not covered by counters because of obvious limitations in the design. Since the electrons emerge from the radiator very nearly in the direction of the photon beam, it is desirable to provide a type of focusing wherein particles of a given momentum and direction, but coming from a laterally extended source, are brought to a focus. This was done by cutting off the magnet poles at 45° to the beam direction and placing the counters along the edges. In order to keep the size of the magnet within reason, the poles were cut off as shown causing the higher momentum orbits to leave the region of the field entirely before reaching the counters. The positions of these counters were determined by plotting orbits and finding an empirical curve of focus.

The pairs produced in the radiator are recorded by counting coincidences[4] between pairs of counters on opposite sides of the spectrometer. All the counters of a group are connected in parallel. Each group is connected to a preamplifier which sends pulses to a master coincidence circuit. The purpose of this circuit is to record all coincidences corresponding to the same total momentum of the electron and positron in one output channel. The number of pulses recorded in each output channel is then a measure of the number of photons in the energy increment defined by the momentum width of a counter group. For a given setting of the spectrometer magnet, all the energy response increments are isosceles triangles of equal width and variable heights which can be calculated from the geometry of the spectrometer and the pair production cross section. The resolving time of the coincidence circuit is approximately one microsecond. A desirable feature of the circuit is an anticoincidence action by which the coincidence circuit is rendered insensitive for about 1.5 microseconds whenever two pulses from one side of the spectrometer appear within the resolving time of the circuit. This eliminates recording ambiguous events involving more than one pair of electrons.

CALIBRATION OF THE SPECTROMETER

The energy calibration of the spectrometer involved not only finding an absolute calibration figure to be used in setting the field in future use but also laying out the equal momentum intervals for the counters. This can be done by measuring the magnetic field at many points, then using these data to plot the various orbits. Fortunately, a simpler method was found, based on the fact that a flexible wire held under tension in a magnetic field and carrying an electric current will assume a shape identical to the orbit of a charged particle.[5] If one can neglect the weight of the wire, then the relation

[5] J. Loeb, Compt. rend. 222, 488 (1946).

between the various parameters is

$$T/i = H\rho,$$

where T is the tension in the wire in dynes, i is the current in absolute emu, and $H\rho$ is the usual representation of the momentum of the represented particle in gauss-cm. Using this technique the absolute calibration can be made in terms of easily measured quantities.

This method was applied to the spectrometer in the manner shown in Fig. 2. The wire[6] was attached at the radiator position to a pivot post which was free to turn about a vertical axis and could be set to the direction of the beam by means of a simple optical lever. By setting the various parameters to predetermined values the momentum intervals were marked off. The internal consistency in the data showed the individual momentum determinations to be accurate to 0.5 percent. After the boundaries of the momentum intervals were marked off, they were adjusted slightly by fitting their positions to a smooth curve. A standard flip coil, mutual inductance, and fluxmeter combination was calibrated against the wire for setting the field of the spectrometer. A field of 14.2 kilogauss is just sufficient to bend a 300-Mev electron into the top counter group.

EXPERIMENTAL PROCEDURE

The program for each cross-section determination consisted of a series of twenty-minute runs, with or without the absorber, in which the high energy photons were counted by the spectrometer. The region of the synchrotron spectrum which was used is shown in Fig. 3, where a plot of the resolution triangles for the three output channels in which data were recorded is superimposed on the photon energy spectrum. The energy end point was determined by the spectrometer to be 310±5 Mev. The internal consistency of the data obtained in the separate channels provided a rigid check on the stability of the synchrotron energy and the spectrometer magnetic field. In no case did the results in the individual channels differ from the mean by more than twice the standard deviation.

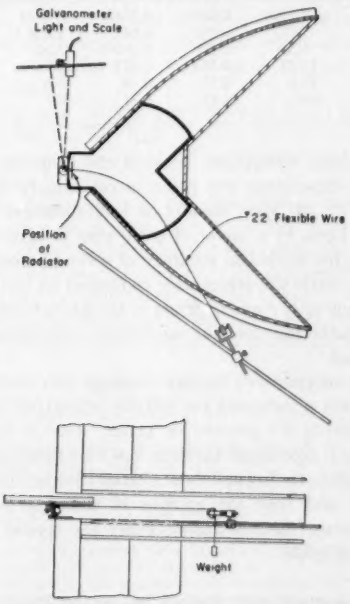

FIG. 2. Experimental arrangement for calibrating the spectrometer.

[6] A very suitable wire is No. 22 "anti-precession" wire made by Sperry Gyroscope Company. It is made of 2-mil strands of cadmium copper.

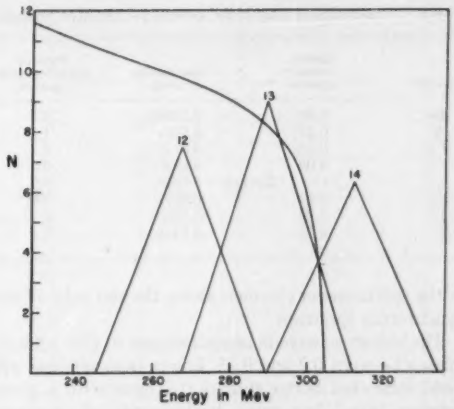

FIG. 3. Spectrometer resolution triangles used in the absorption experiments, superimposed on the photon spectrum from the synchrotron.

The spectrometer records not only true coincidences but also chance coincidences between single particles not related to the same photon. In addition the anti-coincidence feature eliminates some of the true pairs. These effects were separated by using the fact that the true coincidence counting rate is proportional to the beam intensity, while the other effects vary as the square of the intensity. Measurements of the coincidence counting rate for various beam intensities verified this behavior. In the absorption experiments the accidental effects were corrected for by using data obtained at beam intensities three to six times the normal running intensity. The corrections to the cross section were somewhat less than five percent. These accidental effects are magnified by the time dependence of the beam which occurs in pulses about thirty microseconds wide at a rate of thirty per second. It is possible to extend the time width of the beam considerably, but under these conditions the energy stability is probably not very good.

A small background, less than the statistical error, was subtracted from the data. The amount of this background was determined from the residual counts

TABLE I. Experimental total cross sections for 280-Mev photons.

Absorber	Approx. transmission		Cross section (cm^2/g)	Probable statistical error (percent)
Be	0.30		0.01060	1.2
Al	0.22		0.0284	1.2
Cu	0.25		0.0521	1.5
	0.08		0.0530	0.9
		Average	0.0528	0.9
Sn	0.23		0.0776	1.0
Pb	0.20		0.1069	1.2
U	0.24		0.1148	1.4

in the spectrometer channels above the end point of the synchrotron spectrum.

The absorbers were in general chosen to give a transmisson between 0.2 and 0.25. Lower transmissions will yield somewhat better statistical accuracy for a given running time,[7] but small backgrounds of unknown nature become important.

The purity of the samples, with the exception of beryllium and uranium, was determined spectroscopically by the New England Spectrochemical Laboratories, and further chemical analyses in doubtful cases were performed in this laboratory.[8] The only significant impurity was in the aluminum sample, which contained 0.6 percent iron. The correction for this to the cross section amounted to 0.4 percent.

The beryllium absorber was in the form of three blocks of metal which were obtained from the Brush Beryllium Company.[9] Samples of this metal were analyzed by the Brush Company and also by the National Spectrographic Laboratory. The following significant impurities were found:

Beryllium oxide	1.2 percent,
Magnesium	0.4 percent,
Iron	0.08 percent.

The effect of these impurities is to increase the observed cross section by 1.5 percent.

The uranium absorber was borrowed from the AEC.[10] Its stated purity is greater than 99.85 percent.

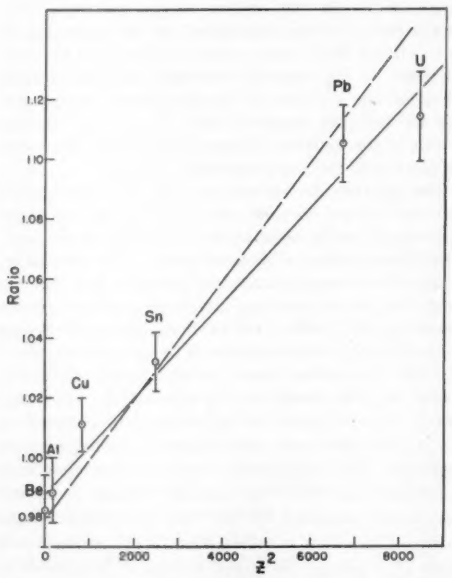

FIG. 4. Ratios of the theoretical to experimental total cross sections plotted as a function of the squares of the atomic numbers of the absorbers. The solid line is fitted to the data; the dashed line is a fit to Lawson's data at 88 Mev.

[7] J. Rainwater and W. W. Havens, Phys. Rev. **70**, 136 (1946); M. E. Rose and M. M. Shapiro, Phys. Rev. **74**, 1853 (1948).

[8] We are indebted to Mrs. Jane Levin for these analyses.

EXPERIMENTAL RESULTS

The experimental cross sections are given in Table I. The corrections for impurities have been made to the results. The two measurements on copper were made with different absorber thicknesses to check on the exponential absorption. Another check on this aspect of the experiment was made in preliminary measurements at 200 Mev. Results on lead absorbers varying in thickness by a factor of three were in agreement to within the statistical accuracy of several percent.

TABLE II. Theoretical cross sections for 280-Mev photons.

Absorber	Nuclear pairs	Electron pairs	Compton	Total (barns/atom)	Total (cm^2/g)
Be	0.1110	0.0311	0.0138	0.1559	0.01041
Al	1.117	0.096	0.045	1.258	0.02805
Cu	5.33	0.206	0.100	5.64	0.0533
Sn	15.27	0.343	0.172	15.78	0.0800
Pb	39.8	0.55	0.28	40.6	0.1182
U	49.7	0.61	0.32	50.6	0.1280

The statistical errors were computed on the basis of the number of counts. Errors in the background and in the correction for the accidental coincidences are included.

The accumulated monitor readings with and without absorbers represented the relative integrated beam intensities to 0.5 percent or better. This is based on excellent agreement between the two monitors, indicating that the beam did not change its direction during a run and that the amount of radiation scattered backwards from the absorber into the second monitor was negligible.

[9] These blocks were obtained on loan by Professor B. D. McDaniel through the courtesy of the Division of Research of the AEC. We wish to thank Professor McDaniel and the AEC for making them available to us.

[10] We are indebted to Dr. D. J. Pflaum and others in the AEC for lending us the uranium.

DISCUSSION

The absorption of photons in this energy region is due essentially entirely to pair production in the Coulomb fields of the atomic nuclei and electrons, and Compton scattering. The Compton cross section is given by the well-known Klein-Nishina formula.[11] The cross section for pair production in the nuclear field has been calculated by Bethe and Heitler,[12] using the Born approximation and screening corrections based on the Fermi-Thomas atomic model. Calculations on pair production in the electronic field have been made by Wheeler and Lamb[13] and others.[14] The results of Wheeler and Lamb are used here, as in Lawson's paper, since they apply particularly to the high energy region.

The calculated cross sections are given in Table II. The nuclear pair cross sections were derived from curves for air and lead plotted by Dr. P. V. C. Hough[15] from the differential cross-section plots of Rossi and Greisen.[16] Bethe[17] has pointed out a convenient method for finding the cross section for any element at any energy from a curve for one element over all energies. The cross section according to the Bethe-Heitler theory can be expressed as

$$\phi/\bar{\phi} = F(\gamma) - (28/27)\log Z,$$

where $\bar{\phi} = Z^2 r_0^2/137$ and $\gamma = WZ^{\frac{1}{3}}$, W being the energy of the photon. This relation provided a simple method of computing the cross sections from the data for air and lead. It was found that the air and lead curves gave values of the function F which differed by about 1.5 percent; an average value was used in computing the cross sections.

The electronic pair cross sections were found by multiplying the nuclear cross sections by the quantity $1.12/Z$, which is predicted by the Wheeler and Lamb calculations.

In Fig. 4 the ratios of the calculated to measured cross sections are plotted against Z^2. The solid line is fitted to the data. The dashed line is a fit to the ratios obtained by Lawson at 88 Mev.[18] The difference in the slopes of the two lines shows a trend toward a smaller correction to the Born approximation at high energies, in agreement with the prediction of Bess[19] on the related bremsstrahlung process. However, this difference can hardly be considered significant in view of the statistical uncertainty. Measurements at still higher energies are needed to check this effect.

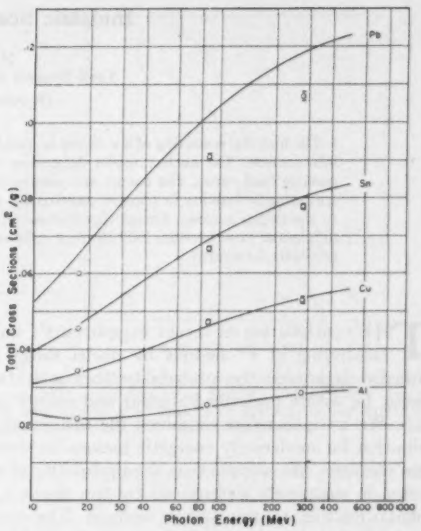

FIG. 5. Total cross sections for photons in the elements for which the most data exist. The curves are the theoretical cross sections. The points at 17.6 Mev are due to Walker; those at 88 Mev to Lawson; those at 280 Mev to the work described in this paper.

The cross section for beryllium is in agreement with the theory, in contrast to Lawson's measurement at 88 Mev which gave a cross section about five percent higher than theory. At present this discrepancy is not understood.

The high energy photon cross sections are summarized in the graph of Fig. 5, where the theoretical curves and experimental points are plotted for the elements for which the most data exist. The results of Adams[2] have not been included, since some corrections for geometry were not applied directly to his experimental values. They are in agreement with Walker's data at 17 Mev.[3] The plots clearly show the good agreement between experiment and theory for the light elements and the well-established difference for the heavy elements, which has been attributed to the inadequacy of the Born approximation.

We are indebted to Professor R. R. Wilson for his generous contributions, particularly to the design of the spectrometer. Much of the development of electronic circuits was done by Mr. L. F. Walker. We are also indebted to Dr. J. S. Levinger and Mr. M. Camac for some calculations on the properties of the spectrometer and collimating system.

[11] W. Heitler, *The Quantum Theory of Radiation* (Oxford University Press, London, 1944), p. 157.
[12] H. Bethe and W. Heitler, Proc. Roy. Soc. (London) **146**, 83 (1934).
[13] J. A. Wheeler and W. E. Lamb, Phys. Rev. **55**, 858 (1939).
[14] F. Perrin, Compt. rend. **197**, 1100 (1933); K. M. Watson, Phys. Rev. **72**, 1060 (1947); P. Nemirovsky, J. Phys. U.S.S.R. **11**, 94 (1947); A. Borsellino, Helv. Phys. Acta **20**, 136 (1947); V. Vortruba, Phys. Rev. **73**, 1468 (1948).
[15] We are indebted to Dr. Hough for computing these data.
[16] B. Rossi and K. Greisen, Revs. Modern Phys. **13**, 240 (1941).
[17] H. A. Bethe, private communication.
[18] See reference 4. The dashed line is not identical to the one drawn by Lawson. It is based on theoretical data computed as described in this paper and is shifted upward by less than one percent.
[19] L. Bess, Phys. Rev. **77**, 550 (1950).

Inelastic Scattering of π-Mesons

M. H. JOHNSON
Naval Research Laboratory, Washington, D. C.
(Received March 21, 1951)

The inelastic scattering of a π-meson is considered the result of an elastic collision between a meson and a free nucleon. The nuclear model determines the initial nucleon momentum distribution and limits the possible final states. The energy and angular distribution of scattered mesons is obtained in terms of the scattering probability in relative coordinates, which depends only on the momenta of the meson relative to the struck nucleon. Energy distributions of the scattered mesons, calculated for several cases from the differential cross section, indicate that collisions in which the meson loses most of its kinetic energy are relatively infrequent.

THE continuation of recent experiments[1,2] on the scattering of π^- mesons by nuclei should empirically determine the probability that a scattered meson be within prescribed angular and energy intervals. We have therefore examined the theoretical distribution for moderately energetic mesons incident on free nucleons. We assume that the probability of scattering is completely determined by the meson's momenta relative to the struck nucleon. The nuclear model influences the scattering only by fixing the nucleon's initial momentum distribution and by suppressing final states incompatible with nuclear structure. We shall see that the predominant collisions are those in which the meson does not lose a major fraction of its initial energy.

The meson's momenta[3] in the center-of-mass reference frame are given by

$$\mathbf{p}=\mathbf{p}_1-E_1(E_1+E_2)^{-1}(\mathbf{p}_1+\mathbf{p}_2), \tag{1a}$$

$$\mathbf{p}'=\mathbf{p}_1'-E_1(E_1+E_2)^{-1}(\mathbf{p}_1'+\mathbf{p}_2'). \tag{1b}$$

The velocity in the Lorentz transformation to the center-of-mass reference frame is $c^2(E_1+E_2)^{-1}(\mathbf{p}_1+\mathbf{p}_2)$. Terms containing the square of the velocity have been omitted from Eq. (1); the greatest error is 5 percent of p_1 for a 100-Mev meson. Conservation of energy and momentum require that $p'=p$ and that θ, the angle between $\mathbf{p}'$ and $\mathbf{p}$, be given by

$$\cos\theta=1-|\mathbf{p}_1'-\mathbf{p}_1|^2(2p^2)^{-1}=1-q^2(2p^2)^{-1}. \tag{2}$$

The meson's change in momentum, $\mathbf{p}_1'-\mathbf{p}_1$, is designated by $\mathbf{q}$.

The differential scattering cross section may be written

$$d\Phi(\mathbf{p}')=\sigma(p,\cos\theta)\delta(p'-p)(4\pi p'^2)^{-1}d\mathbf{p}', \tag{3}$$

where σ depends only on p and θ. The restriction of $\mathbf{p}'$ to the surface $p'=p$ has been expressed by the Dirac delta-function. If $g(p_2)d\mathbf{p}_2$ is the probability that the nucleon's initial momentum is in the volume element $d\mathbf{p}_2$, the differential cross section for collisions in which $\mathbf{p}_1'$ lies in the volume element $d\mathbf{p}_1'$ can be obtained by averaging the reaction rate over $g(p_2)$. Thus

$$d\Phi(\mathbf{p}_1')=(E_1+E_2)(4\pi E_2p_1)^{-1}d\mathbf{p}_1' \times\int p^{-1}g(p_2)\sigma(p,\cos\theta)\delta(p'-p)d\mathbf{p}_2. \tag{4}$$

By changing the variable of integration from $\mathbf{p}_2$ to $\mathbf{p}$ through the relation

$$\mathbf{p}_2=-\mathbf{p}+E_2(E_1+E_2)^{-1}(\mathbf{p}_1+\mathbf{p}_2), \tag{5}$$

and by using the defining properties of the delta-function, Eq. (4) can be reduced to

$$d\Phi(\mathbf{p}_1')=(E_1+E_2)^4(4\pi E_1^3E_2p_1q)^{-1}d\mathbf{p}_1' \times\int g(p_2)\sigma(p,\cos\theta)dS. \tag{6}$$

In Eq. (6) dS is an element of area in the surface $p'=p$. Certain values of the nucleon's final momentum $\mathbf{p}_{2e}'$, may be incompatible with the possible nuclear states. The corresponding values of $\mathbf{p}$,

$$\mathbf{p}_e=\mathbf{p}_1-E_1(E_1+E_2)^{-1}(\mathbf{p}_1'+\mathbf{p}_{2e}'), \tag{7}$$

must be omitted from the integration in Eq. (6).

TABLE I. Range of scattering angles for various energy losses. Meson scattering with an energy change from 100 Mev to the value shown in the first column takes place at scattering angles greater than ψ_l. The number of collisions is reduced by the exclusion principle at scattering angles between ψ_{el} and ψ_{eu}.

Scattered meson energy	cp_1'	ψ_e	ψ_{eu}	ψ_{el}
100 Mev	195 Mev	0°	—	0°
95	189	6	150°	7
90	182	12	130	16
85	176	18	110	28
80	169	23	87	47
70	156	33	—	—
60	143	43	—	—
50	128	53	—	—
40	113	63	—	—
30	96	75	—	—
20	77	90	—	—
10	54	117	—	—

[1] H. Bradner and B. Rankins, Phys. Rev. **80**, 916 (1950).
[2] Bernardini, Booth, Lederman, and Tinlot, Phys. Rev. **80**, 924 (1950); **82**, 105 (1951). G. Bernardini, Phys. Rev. **82**, 313(T) (1951).
[3] Notation: E, m, and $\mathbf{p}$ are total energy, mass, and momentum; subscripts 1 and 2 designate meson and nucleon; unprimed and primed letters refer to quantities before and after collision; $\mathbf{dp}$ stands for the volume element $dp_xdp_ydp_z$.

Consider a nuclear model in which A nucleons within a sphere of radius $1.5\times10^{-13}A^{\frac{1}{3}}$ cm constitute a degenerate Fermi gas occupying a volume $Ah^3/4$ in phase space. Then

$$g(p_2)=3(4\pi p_{2m}^2)^{-1} \qquad p_2<p_{2m}, \tag{8a}$$

$$g(p_2)=0 \qquad p_2>p_{2m}, \tag{8b}$$

where $p_{2m}=1.05\times10^{-14}$ g cm/sec. Moreover, all final states with $p_2'<p_{2m}$ are excluded by the Pauli principle; for example, since $p_1'>p_1$ implies $p_2'<p_2$, all collisions with $p_1'>p_1$ are suppressed.

In the space of the relative momentum, $\mathbf{p}$, the surface $p'=p$ intersects the volume $p_2<p_{2m}$ in a circle A. The intersection is real only if

$$p_1'\geq[(E_2-E_1)p_1-2E_1p_{2m}](E_1+E_2)^{-1}, \tag{9}$$

which defines the least energy a scattered meson can have. Moreover, with a value of p_1' satisfying Eq. (9) the interesection is real only if q lies in the interval

TABLE II. Comparison of energy distributions.

		Most probable energy loss	Fraction losing more than 50 Mev	Integrated cross section*
$\psi=90°$	Constant cross section	20 Mev	0.24	0.80
	π^- on neutrons	20	0.22	0.97
	π^- on protons	20	0.23	0.62
$\psi=180°$	Constant cross section	42	0.42	0.58
	π^- on neutrons	40	0.41	0.75
	π^- on protons	44	0.43	0.42

* The quantity tabulated is $4\pi\sigma_0^{-1}\int\frac{d\Phi(E_1',\psi)}{d\Omega dE_1'}dE_1'$.

$q_u\geq q\geq q_l$, where

$$q_u=[p_{2m}^2+E_2E_1^{-1}(p_1^2-p_1'^2)]^{\frac{1}{2}}+p_{2m}, \tag{10a}$$

$$q_l=[p_{2m}^2+E_2E_1^{-1}(p_1^2-p_1'^2)]^{\frac{1}{2}}-p_{2m}. \tag{10b}$$

The limiting scattering angles, ψ_u and ψ_l, are obtained by inserting q_u and q_l into the relation

$$\sin\tfrac{1}{2}\psi=\tfrac{1}{2}(p_1p_1')^{-\frac{1}{2}}[q^2-(p_1'-p_1)^2]^{\frac{1}{2}}. \tag{11}$$

The angles ψ_l are shown in Table I for a 100-Mev meson; ψ_u does not exist for a 100-Mev meson.

The surface $p'=p$ intersects the volume $p_2'<p_{2m}$ in a circle B. The intersection is real only if

$$p_1'^2\geq p_1^2-E_1E_2^{-1}p_{2m}^2, \tag{12}$$

which requires that the meson's energy loss be less than the maximum initial kinetic energy of a nucleon. Moreover, with a value of p_1' satisfying Eq. (12) the intersection is real only if q lies in the interval $q_{eu}\geq q\geq q_{el}$, where

$$q_{eu}=p_{2m}+[p_{2m}^2-E_2E_1^{-1}(p_1^2-p_1'^2)]^{\frac{1}{2}}, \tag{13a}$$

$$q_{el}=p_{2m}-[p_{2m}^2-E_2E_1^{-1}(p_1^2-p_1'^2)]^{\frac{1}{2}}. \tag{13b}$$

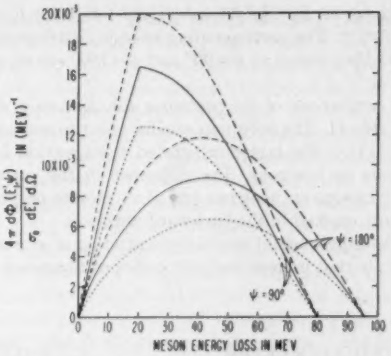

FIG. 1. Energy distribution of scattered mesons: solid curve for a constant scattering cross section; dashed curve for π^- mesons on neutrons or π^+ mesons on protons; dotted curves for π^+ mesons on neutrons or π^- mesons on protons.

The limiting scattering angles, ψ_{eu} and ψ_{el}, found from Eq. (11), are shown in Table I for a 100-Mev meson.

To proceed further, the dependence of σ on p and θ must be specified. The simplest possibility is that σ is a constant σ_0. The integral in Eq. (6) is then proportional to the area between circles A and B. If $\mathbf{p}_1'$ lies within the solid angle $d\Omega$, the differential cross section becomes

$$d\Phi(E_1',\psi)=(\tfrac{3}{4})\sigma_0(E_1+E_2)^2 \times(cE_1E_2p_1^2)^{-1}E_1'UdE_1'd\Omega/4\pi, \tag{14}$$

where

$$U=(qp_{2m}^2)^{-1}p_1'^2[p_{2m}^2 -\tfrac{1}{4}(E_2(E_1q)^{-1}(p_1^2-p_1'^2)-q)^2], \tag{14a}$$

if $\psi_{el}\geq\psi\geq\psi_l$ or if $\psi_u\geq\psi\geq\psi_{eu}$, and

$$U=(E_1qp_{2m}^2)^{-1}E_2p_1'^2(p_1^2-p_1'^2), \tag{14b}$$

if $\psi_{eu}\geq\psi\geq\psi_{el}$. When circle B is not a real intersection, Eq. (14a) applies in the entire interval $\psi_u\geq\psi\geq\psi_l$. The cross section is always zero outside the last-named interval. The energy distributions of a 100-Mev meson at $\psi=90°$ and at $\psi=180°$ are shown in Fig. 1.

A possible dependence[4] of σ on p and θ is

$$\sigma=\sigma_0[1-E_1^{-1}(\tfrac{1}{2}c^2q^2+m_1^2c^4)(c^2p^2+m_1^2c^4)^{-\frac{1}{2}}], \tag{15}$$

where the upper sign applies to collisions of π^- mesons with neutrons or π^+ mesons with protons and the lower sign applies for collisions of π^+ mesons with neutrons or π^- mesons with protons. In the integration in Eq. (6), a negligible error is made if p is replaced by the value it has at the center of circle A. Consequently, the cross section is given by Eq. (14) multiplied by

[4] To the same approximation as Eq. (1), the form of σ in Eq. (15) is that given by weak coupling meson field theory for a pseudoscalar meson. M. Peshkin, Phys. Rev. 81, 425 (1951); Ashkin, Simon, and Marshak, Prog. Theor. Phys. 5, 634 (1950).

the factor $1-E_1^{-1}(\frac{1}{2}c^2q^2+m_1^2c^4)(\frac{1}{4}c^2q^2+E_2^2(E_1+E_2)^{-2}c^2p^2+m_1^2c^4)^{-\frac{1}{2}}$. The corresponding energy distributions for a 100-Mev meson at $\psi=90°$ and $\psi=180°$ are shown in Fig. 1.

A comparison of the preceding calculations is shown in Table II. The only noteworthy effect introduced by Eq. (15) is the larger integrated cross section for π^- mesons on neutrons. The difference in the scattering of π^- mesons on neutrons and of π^- mesons on protons is most marked in the backward direction.

The experimental results for scattering of π^- mesons[2] indicate that in most inelastic collisions the meson loses 80 percent or more of its initial kinetic energy. It is quite evident that this result cannot be reconciled with the assumptions underlying Eq. (14). The relatively frequent occurrence of large energy losses suggest that a transfer of momentum from the struck nucleon to the rest of the nucleons takes place during the collision. If such a transfer tended to lower the kinetic energy of the struck nucleon before the re-emission of the meson, the qualitative features of the experimental results might be reproduced.

Note added in proof:—I am indebted to Mr. Petschek and Dr. Marshak for completely verifying the derivation of Eq. (14).

PHYSICAL REVIEW VOLUME 83, NUMBER 3 AUGUST 1, 1951

Masses of Light Nuclei from Nuclear Disintegration Energies*

C. W. LI, WARD WHALING, W. A. FOWLER, AND C. C. LAURITSEN
Kellogg Radiation Laboratory, California Institute of Technology, Pasadena, California
(Received April 16, 1951)

Values of the atomic masses from n^1 to F^{20} have been derived from the Q-values of nuclear reactions with a procedure of statistical adjustment. Tables are given of several fundamental mass differences, the most probable Q-values, and the atomic masses. Some disparity with the mass spectroscopic results is noted.

I. INTRODUCTION

THE large number of accurate Q-values that have become available in the past two years now make it possible for the first time to calculate the masses of the light nuclei directly in terms of O^{16}, without recourse to mass spectroscopic results. Since there are many more reactions than unknown masses, the masses are considerably overdetermined, and some adjustment procedure must be used to solve for the most probable masses. A general least-squares solution becomes exceedingly complex when so many independent variables are involved, and we have used the simpler but essentially equivalent procedure introduced by Tollestrup, Fowler, and Lauritsen.[1] The large number of reactions which interconnect the light nuclei provide many cross-checks on the internal consistency of the experimental data. By an approximate least-squares adjustment of the experimental Q-values we first obtain a numerically self-consistent set of Q-values which we regard as the most probable Q-values. The results are significant in the sense that the required amounts of adjustment are well within the experimental errors. This consistent set of Q-values determines a unique set of mass values which it seems reasonable to regard as the most probable masses. Probable errors in the masses are calculated by a straightforward compounding of gaussian errors.

II. EXPERIMENTAL Q-VALUES

The experimental Q-values used in deriving the masses are listed in the second column of Table I with a reference to the source of each entry in the last column. We have attempted to include as much data as possible for which high accuracy is claimed. Measurements of many different types are included, but all range measurements have been omitted because of the relatively large experimental uncertainties and the uncertainty of the empirical range-energy relation. The extensive magnetic analysis work by Buechner's group at the Massachusetts Institute of Technology accounts for more than one-fourth of the entries in Table I. The other values come from many different laboratories, and the good consistency is very gratifying.

Only those measurements with the smallest probable error have been included. The dividing line was arbitrarily set at 30 kev; with a few exceptions noted subsequently, all measurements with a probable error less than 30 kev are listed in Table I. With this criterion of selection, it has actually turned out that except for five cases, all of the measurements included have a probable error of 15 kev or less. The error of most of the measurements are much better than 1 percent except for those with Q-values below 1 Mev. But it should be mentioned that the calculation of the nuclear masses from Q-values is a linear and additive operation, and consequently absolute errors and not percentage errors are significant. A low energy reaction should not be excluded because of a large percentage error in its measured Q-value.

Several measurements have been omitted even though a small error was claimed; a list of references to these omitted values is appended to Table I. Many of these measurements, such as the early values for the photodisintegration threshold of deuterium, are known to

* Assisted by the joint program of the ONR and AEC.
[1] Tollestrup, Fowler, and Lauritsen, Phys. Rev. 78, 372 (1950).

involve experimental error. A few others have been omitted because of inconsistency with other direct and indirect measurements of the same Q-value by methods that are believed to be more reliable. For example, the β-spectrum end point for $C^{11}(\beta^+)B^{11}$ gives a Q-value of 2.003 ± 0.005 Mev (To 40). From the well-established n^1-H^1 mass difference and the accurately known threshold for $B^{11}(p,n)C^{11}$, we calculate a Q-value of 1.980 ± 0.003 Mev; the discrepancy is several times the probable errors. We believe that the neutron threshold measurement is more reliable and have omitted the beta spectrum measurement from the table. In addition, measurements of Q-value ratios, such as $H^2(\gamma,n)H^1/Be^9(\gamma,n)Be^8$, have been omitted. There are accurate measurements of each of these reactions alone and the ratios have been omitted to avoid increased complexity in the manipulation of the data.

Because of the method of weighting the data, the inclusion of additional data with large probable errors would have a negligible effect on the average Q-values used. For lack of a better alternative, the stated errors have been assumed in every case to have similar significance as an indication of experimental accuracy. They are all regarded as the conventional 50 percent "probable error." On the basis of this assumption, different measurements of the same Q-value have been averaged together, weighting each value inversely as the square of the probable error. Inverse reactions or reactions giving the same Q-value have been averaged together; for example, items 2, 3, and 4 in Table I all give the binding energy of the deuteron and have been averaged together. These weighted average values are listed in column 3 of Table I and are used as the experimental Q-values in subsequent calculations. The probable error $\bar{P}$ in the average Q-value $\bar{Q}\pm\bar{P}$ is calculated by both internal and external consistency, and the larger of the two is used:

$$1/\bar{P}_{\text{int}}^2=\sum_i(1/P_i^2),$$

$$\bar{P}_{\text{ext}}=0.67\left(\frac{\sum_i w_i(Q_i-\bar{Q})^2}{(n-1)\sum_i w_i}\right)^{\frac{1}{2}};\quad w_i=\frac{1}{P_i^2}.$$

For only two reactions in Table I is $\bar{P}_{\text{ext}}$ greater than $\bar{P}_{\text{int}}$; this is interpreted as an indication that experimental physicists are overly cautious in assigning probable errors.

Energy standards and fundamental constants used in the calculation of a Q-value from the experimental data change slightly with time. Corrections should be made to conform to the best values of these constants, but a complete revision of this kind has not been undertaken in the present work. In a few cases which came to our attention, this correction has been made as noted in the footnotes to Table I.

III. NUCLEAR CYCLES AND FUNDAMENTAL MASS DIFFERENCES

Figure 1 illustrates graphically the interconnections between the light nuclei which are of interest in this discussion. Each line connecting two nuclei represents a reaction in which one of the nuclei is the target nucleus, the other the residual nucleus. The reactions can be divided into two classes. The first class, indicated by dotted lines, contains reactions which are independent, at the present stage of investigation, in the sense that they are not equivalent to any combination of other reactions. The second class, indicated by solid lines, contains those reactions any one of which can be constructed by a suitable combination of two or more of the other reactions in this class. For example, the reaction $Be^9(d,\alpha)Li^7$ is equivalent to the sum of the two reactions $Be^9(p,\alpha)Li^6$ and $Li^6(d,p)Li^7$ and belongs in the second class: $C^{13}(d,\alpha)B^{11}$ belongs in the first class because there is no other path between C^{13} and B^{11} at the present time.

From these reactions in the second class one can construct many equivalent nuclear cycles or combinations of reactions with the same sum. These cycles are useful in that: (1) They give better experimental values of certain fundamental mass differences than the direct determination. For example, compare the direct determination of the $n-H^1$ mass difference from the neutron beta-decay with the equivalent cycles listed in Table II, Group 2. (2) These cycles provide a test of the internal consistency of the Q-values. This is useful in judging the statistical consistency of experimental input data and is used in Sec. IV as a basis for a statistical adjustment of the Q-values.

Table II contains all of the independent and simplest nuclear cycles in addition to three direct determinations: $n(\beta^-)H^1$, $H^1(n,\gamma)H^2$, and $H^2(d,p)H^3$. The cycles fall into five groups with the respective sums: (1) zero, (2) $n-H^1$, (3) $n+H^1-H^2$, (4) $2H^2-H^1-H^3$, and (5) $2H^2-He^4$. We emphasize the fact that the cycles we have used are linearly independent, which means that none of the cycles are obtained by a combination of two others. The first choice of the independent cycles is arbitrary, although it is desirable that they be as simple as possible to keep the probable errors small. However, the cycles which can subsequently be constructed by a combination of the original cycles should not be used for statistical reasons. A cycle which is used more than once is thereby given a statistical weight greater than is justified by its probable error.

With the exception of Group 1, each of the groups of cycles in Table II determines the most probable value of a fundamental mass difference. The eight independent cycles in Group 2 each determine an experimental value of the $n-H^1$ mass difference when the experimental Q-values are substituted in the cycle. This value is listed opposite each cycle, with a probable error computed from the probable error P_i of the N Q-values in the cycle:

$$P_{\text{cycle}}=\left(\sum_{i=1}^{N}P_i^2\right)^{\frac{1}{2}}.$$

From these eight determinations of $n-H^1$ the weighted average is calculated, weighting each value inversely as the square of its probable error. This average value of $n-H^1$ is then assumed to be the most probable value of this fundamental mass difference. The second cycle, for which the best accuracy is claimed, largely determines the weighted mean value. Omitting this cycle, the weighted average is 782.7 kev. The arithmetic average of the eight values is 784.0 kev. Leaving out the fifth cycle, which seems high, the arithmetic average becomes 782.2 kev.

The probable error in the weighted average value of $n-H^1$ has been calculated from internal consistency and external consistency; both values are listed in Table II. A closer examination of the data reveals that the weighted average is mainly determined by cycles 2, 3, and 4, each of which contains a threshold measurement calibrated against the $Li^7(p,n)Be^7$ threshold at 1.882±0.002 Mev. In view of this correlation of the input data the probable error of the weighted average has been set at 1 kev.

The remaining groups of cycles in Table II have been treated in the same way. The only difference is that in the last two cycles of Group 5 which give the $2H^2-He^4$ mass difference, the quantity $n+H^1-H^2$ occurs. The weighted mean of this difference from Group 3, 2.225 ±0.002 Mev has been substituted as the experimental value of this quantity in these two cycles.

The good internal consistency of the nuclear data is evident from the good agreement of the cycle sums. Each reaction in the second class appears in at least one cycle, and each cycle is a check on the consistency of the data.

IV. THE ADJUSTED Q-VALUES

The 43 reactions in the second class contain only 25 nuclei, including O^{16}. Thus the masses are overdetermined, and some adjustment procedure must be adopted to solve for a unique set of mass values. We have assumed that the most probable set of Q-values is that numerically self-consistent set which is obtained by the least squares adjustment of the experimental Q-values. This self-consistent set of Q-values determines a unique set of mass values which we regard as the most probable

TABLE I. Nuclear reaction energies used in evaluating masses

Reaction	Experimental Q value (Mev)	Weighted mean of experimental Q (Mev)	Adjusted value of Q (Mev)	Ref.*
$n(\beta^-)H^1$	0.783 ±0.013[a]		0.7823±0.001	Ro 50*p*
$H^1(n,\gamma)H^2$	2.230 ±0.007			Be 50*g*
$H^2(\gamma,n)H^1$	−2.226 ±0.003	$H^1(n,\gamma)H^2$=	2.225 ±0.002	Mo 50*p*
$H^2(p,n)2H^1$	−2.225 ±0.010	2.227 ±0.003		Sm 50*b*
$H^2(n,\gamma)H^3$	6.251 ±0.008		6.257 ±0.004	Ki 50*p*
$H^2(d,n)He^3$	3.265 ±0.009[b]		3.268 ±0.004	To 49*a*
$H^2(d,p)H^3$	4.036 ±0.012[b]	4.031 ±0.005	4.032 ±0.004	To 49*a*
	4.030 ±0.006			St 51
$H^3(\beta^-)He^3$	0.0186±0.0002	0.0185±0.0002	0.0185±0.0002	Je 49, Sl 49
	0.0183±0.0003			Cu 49*b*
	0.0180±0.0005			Gr 49
	0.0190±0.0005			Ha 49*b*
$H^3(p,n)He^3$	−0.7637±0.001	$H^3(p,n)He^3$=		Ta 49*c*
$He^3(n,p)H^3$	0.766 ±0.010	−0.7637±0.001	−0.7638±0.001	Fr 50
$He^6(\beta^-)Li^6$	3.215 ±0.015		(unadjustable)	Pe 50
$Li^6(p,\alpha)He^3$	4.017 ±0.012[b]	4.019 ±0.005	4.016 ±0.005	To 49*b*
	4.021 ±0.006			St 51
	3.97 ±0.03			Bu 50*e*
$Li^6(d,p)Li^7$	5.019 ±0.007		5.020 ±0.006	St 51
$Li^7(p,n)Be^7$	−1.6457±0.002	−1.6453±0.001[c]		He 49
	−1.6450±0.002		−1.6452±0.001	Sh 49*d*
$Li^7(p,\alpha)\alpha$	17.340 ±0.014	17.339 ±0.009	17.337 ±0.007	St 51
	17.338 ±0.011			Wh 50*e*
$Li^7(d,p)Li^8$	−0.187 ±0.010	−0.188 ±0.006	(unadjustable)	Pa 50
	−0.188 ±0.007			St 51
$Be^8(\alpha)\alpha$	0.101 ±0.010[d]	0.091 ±0.004	0.096 ±0.004	He 49*b*
	0.089 ±0.005			To 49*b*
$Be^9(\gamma,n)Be^8$	−1.666 ±0.002		−1.666 ±0.002	Mo 50*p*
$Be^9(n,\gamma)Be^{10}$	6.797 ±0.008		6.810 ±0.006	Ki 50*a*
$Be^9(p,n)B^9$	−1.852 ±0.002		(unadjustable)	Ri 50
$Be^9(p,d)Be^8$	0.558 ±0.003	0.559 ±0.002	0.559 ±0.002	To 49*b*
	0.562 ±0.004			St 51
$Be^9(p,\alpha)Li^6$	2.121 ±0.007[b]	2.133 ±0.007	2.132 ±0.006	To 49*b*
	2.142 ±0.006			St 51
$Be^9(d,p)Be^{10}$	4.585 ±0.008	4.588 ±0.006	4.585 ±0.005	St 51
	4.591 ±0.008			Kl 51
$Be^9(d,t)Be^8$	4.597 ±0.013		4.591 ±0.004	St 51
$Be^9(d,\alpha)Li^7$	7.150 ±0.008	7.153 ±0.006	7.152 ±0.005	St 51
	7.151 ±0.010			Wh 50*e*
	7.191 ±0.024			Kl 51
$Be^{10}(\beta^-)B^{10}$	0.553 ±0.015	0.556 ±0.003	0.556 ±0.003	Fu 49*b*
	0.545 ±0.010			Be 50

TABLE I.—*Continued.*

Reaction	Experimental Q value (Mev)	Weighted mean of experimental Q (Mev)	Adjusted value of Q (Mev)	Ref.[a]
	0.555 ±0.005			Fe 50
	0.560 ±0.005			Hu 50[b]
$B^{10}(n,\alpha)Li^7$	2.793 ±0.027	2.789 ±0.009	2.793 ±0.003	Ha 50ρ
	2.788 ±0.010			Je 50, El 48
$B^{10}(p,\alpha)Be^7$	1.148 ±0.006	1.150 ±0.003	1.148 ±0.003	Br 50a
	1.152 ±0.004			Va 50
	1.147 ±0.010			Bu 50
$B^{10}(d,p)B^{11}$	9.235 ±0.011		9.234 ±0.009	St 51
$B^{11}(p,n)C^{11}$	−2.762 ±0.003		(unadjustable)	Ri 50
$B^{11}(p,\alpha)Be^8$	8.567 ±0.011	8.570 ±0.009	8.575 ±0.006	St 51
	8.574 ±0.014			Li 51
$B^{11}(d,p)B^{12}$	1.136 ±0.005		(unadjustable)	St 51
$B^{11}(d,\alpha)Be^9$	8.018 ±0.007		8.016 ±0.006	Va 51ρ
$C^{12}(n,\gamma)C^{13}$	4.948 ±0.008		4.948 ±0.004	Ki 50a
$C^{13}(d,n)N^{14}$	−0.281 ±0.003		−0.280 ±0.003	Bo 49c
$C^{13}(d,p)C^{14}$	2.716 ±0.005	2.723 ±0.005	2.723 ±0.004	St 51
	2.732 ±0.006			Kl 51
$C^{13}(p,n)N^{13}$	−3.003 ±0.003		−3.003 ±0.002	Ri 50
$C^{13}(d,p)C^{14}$	5.91 ±0.03	5.941 ±0.004	5.944 ±0.004	Cu 50
	5.948 ±0.008			St 51
	5.940 ±0.004			Li 51
$C^{13}(d,t)C^{12}$	1.310 ±0.006	1.310 ±0.003	1.309 ±0.003	St 51
	1.310 ±0.003			Li 51
$C^{13}(d,\alpha)B^{11}$	5.160 ±0.010	5.163 ±0.005	(unadjustable)	St 51
	5.164 ±0.006			Li 51
$C^{14}(\beta^-)N^{14}$	0.154 ±0.003	0.155 ±0.001	0.155 ±0.001	Le 47a
	0.152 ±0.005			Le 48a
	0.1563±0.001			Co 48c
	0.155 ±0.002			Be 48b
	0.1575±0.005			An 49b
	0.155 ±0.001			Fe 49
	0.155 ±0.001			Wa 50b
$C^{14}(p,n)N^{14}$	−0.620 ±0.009	$C^{14}(p,n)N^{14}$ [m]		Sh 49a
$N^{14}(n,p)C^{14}$	0.630 ±0.006	−0.628 ±0.004	−0.627 ±0.001	Fr 50
	0.630 ±0.010			St 48a
$N^{13}(\beta^+)C^{13}$	2.220 ±0.006	2.222 ±0.004	2.221 ±0.002	Ly 39
	2.224 ±0.005			Ho 50
$N^{14}(n,\gamma)N^{15}$	10.823 ±0.012		10.833 ±0.007	Ki 50a
$N^{14}(d,p)N^{15}$	8.615 ±0.009		8.608 ±0.007	St 51
$N^{15}(p,\alpha)C^{12}$	4.960 ±0.007	4.961 ±0.005	4.961 ±0.005	St 51
	4.961 ±0.006			Li 51
$N^{15}(d,\alpha)C^{13}$	7.681 ±0.009		7.684 ±0.006	St 51
$O^{15}(\beta^+)N^{15}$	2.705 ±0.005		(unadjustable)	Pe 49ρ
$O^{16}(d,n)F^{17}$	−1.614 ±0.010[n]		(unadjustable)	He 48a
$O^{16}(d,p)O^{17}$	1.917 ±0.005	1.917 ±0.004	1.918 ±0.004	St 51
	1.918 ±0.008			Kl 51
$O^{16}(d,\alpha)N^{14}$	3.112 ±0.006	3.116 ±0.004	(unadjustable)	St 51
	3.119 ±0.005			Wh 51
$O^{18}(p,n)F^{18}$	−2.453 ±0.002		−2.453 ±0.002	Ri 50ρ
$F^{18}(\beta^+)O^{18}$	1.657 ±0.015		1.671 ±0.002	Bl 49a
$F^{19}(p,\alpha)O^{16}$	8.113 ±0.030	8.118 ±0.009	8.124 ±0.007	Ch 50
	8.118 ±0.009			St 51
$F^{19}(d,p)F^{20}$	4.373 ±0.007		(unadjustable)	St 51
$F^{19}(d,\alpha)O^{17}$	10.050 ±0.010		10.042 ±0.007	St 51[f]

[a] The recoil energy of the proton included.
[b] Probable error recalculated according to the systematic procedure outlined in Brown, Snyder, Fowler, and Lauritsen, Phys. Rev. **82**, 159 (1951).
[m] −1.6457 ±0.002 Mev has been used as a standard in many of the experimental Q-values in this table. This corresponds to a threshold energy of 1.882 ±0.002 Mev.
[d] Recalculated with recent values of ThC″ gamma-ray energy and $Be^9(\gamma,n)Be^8$ threshold.
[n] Corrected to $Li^7(p,n)Be^7$ threshold = 1.882 Mev.
[f] References to values omitted from the table: Me 49a, Ki 39d, My 42, Wi 45, Ar 48, Al 40a, Ro 48b, To 40, Si 44, Si 45a.
[a] The designation in the last column of the table refers to the reference list in Hornyak, Lauritsen, Morrison, and Fowler, Revs. Modern Phys. **22**, 364 (1950). In addition:

Ha 50ρ Hanna, Phys. Rev. **80**, 530 (1950).
Ki 50ρ Kinsey and Bartholomew, Phys. Rev. **80**, 918 (1950).
Kl 51 Klema and Phillips, Phys. Rev. **83**, 212 (1951), and thesis, Rice Institute (1950).
Li 51 Li and Whaling, Phys. Rev. (to be published), and Phys. Rev. **82**, 122 (1951).
Mo 50ρ Mobley and Laubenstein, Phys. Rev. **80**, 309 (1950).
Pe 49ρ Perez-Mendez and Brown, Phys. Rev. **76**, 689 (1949).
Ri 50ρ Richards and Smith, Phys. Rev. **80**, 524 (1950).
Ro 50ρ Robson, Phys. Rev. **81**, 297 (1951).
St 51 Strait, Van Patter, Buechner, and Sperduto, Phys. Rev. **81**, 747 (1951).
Va 51ρ Van Patter, Sperduto, Huang, Strait, and Buechner, Phys. Rev. **81**, 233 (1951).
Wh 51 Whaling and Li (private communication).

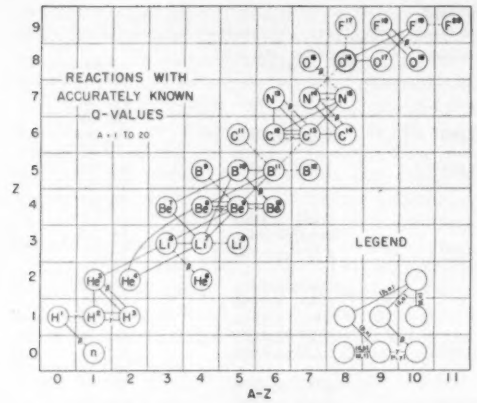

FIG. 1. The nuclear reactions with accurately known Q-values at the present time are represented on this chart by lines connecting target nucleus and residual nucleus.

masses. By numerical self-consistency we mean that the Q-values satisfy all the conditions set by the cycles in Table II, that all equivalent cycles have the same sum.

TABLE Ia. Summary of the adjustments of the interlinked Q-values below O^{16}.

Amount of adjustment	Number of cases
0 (kev)	11
1	10
2	4
3	5
4	1
5	2
6	2
7	1
8	0
9	0
10	1
11	0
12	0
13	1
unadjustable	2
Total	40

Sign of adjustment	Number of cases
0	11
+	11
−	16
unadjustable	2
Total	40

Ratio of the adjustment to the probable error of the experimental Q	Number of cases
0 or up to 1/5	17
between 1/5 and 1/2	10
between 1/2 and 1	9
5/4	1
13/8	1
unadjustable	2
Total	40

More specifically, we have assumed that the set of most probable Q-values, $[Q_i^{adj}]$ is that numerically self-consistent set which satisfies the condition $\sum_i (1/P_i^2)(Q_i^{adj} - Q_i^{exp})^2$ be a minimum, where $[Q_i^{exp}]$ is the set of experimental Q-values. For the most general treatment the sum above would be taken over all of the reactions in the second class. Because of the large number of independent variables we have found it convenient to consider the cycles one at a time. The sum is taken over only those reactions included in one cycle, and the cycles are adjusted for numerical consistency one at a time. This treatment deviates from a complete least-squares adjustment in that the sum above is broken up into many partial sums to be minimized separately, and in disregarding the fact that many of the Q-value measurements are not observationally independent; for example, many measurements have used a common energy standard, such as the Po-alpha energy.

TABLE Ib. Q-values adjustable by more than one cycle.

Reaction	Experimental $\bar{Q}$	Q adjusted from one cycle	From which cycle	Final adjusted value
$H^3(d,n)He^4$	3.265 ±0.009	3.268 ±0.004 3.267 ±0.008	$n-H^1$ $2H^2-He^4$	3.268 ±0.004
$Li^6(d,p)Li^7$	5.019 ±0.007	5.019 ±0.006 5.020 ±0.006	zero $2H^2-He^4$	5.020 ±0.006
$Li^7(p,\alpha)\alpha$	17.339 ±0.009	17.334 ±0.007 17.341 ±0.008	$2H^2-He^4$ $2H^2-He^4$	17.337 ±0.007
$Be^9(d,p)Be^{10}$	4.588 ±0.006	4.588 ±0.005 4.582 ±0.006	$n-H^1$ $n+H^1-H^2$	4.585* ±0.005
$Be^9(d,\alpha)Li^7$	7.153 ±0.006	7.153 ±0.005 7.152 ±0.005 7.151 ±0.006 7.152 ±0.006	zero $n-H^1$ $2H^2-He^4$ $2H^2-He^4$	7.152 ±0.005
$B^{10}(n,\alpha)Li^7$	2.789 ±0.009	2.795 ±0.003 2.790 ±0.006 2.791 ±0.008	zero $n-H^1$ $2H^2-He^4$	2.793* ±0.003
$B^{11}(d,\alpha)Be^9$	8.017 ±0.006	8.015 ±0.006 8.017 ±0.006	zero $2H^2-He^4$	8.016 ±0.006
$C^{13}(d,p)C^{13}$	2.723 ±0.005	2.722 ±0.005 2.723 ±0.004 2.723 ±0.004 2.722 ±0.004	zero $n-H^1$ $n+H^1-H^2$ $2H^2-H^1-H^2$	2.723 ±0.004
$N^{14}(n,p)C^{14}$	0.628 ±0.004	0.627 ±0.001 0.627 ±0.004	$n-H^1$ $2H^2-He^4$	0.627 ±0.001
$N^{13}(\beta^+)C^{13}$	2.222 ±0.004	2.221 ±0.002 2.222 ±0.003	$n-H^1$ $n-H^1$	2.221 ±0.002
$N^{14}(n,\gamma)N^{15}$	10.823 ±0.012	10.834 ±0.007 10.832 ±0.009	$n+H^1-H^2$ $2H^2-He^4$	10.833 ±0.007
$N^{15}(d,\alpha)C^{13}$	7.681 ±0.009	7.683 ±0.006 7.686 ±0.008	zero $2H^2-He^4$	7.684 ±0.006

* Shifted by half-kev from the weighted mean.

Since all of the reactions in the second class can be brought into a numerically consistent system simply by altering the Q-values until all the equivalent cycles have a common sum, this adjustment procedure is very simple in practice. For example, consider the first cycle in Group 1 of Table II. The cycle sum should be zero, but the sum of the experimental Q-values is 7 kev. This 7-kev discrepancy has been divided into three parts, proportional to the square of the probable error of the three Q-values in the cycle, and these increments have

been subtracted from the respective Q-values. The sum of the adjusted Q-values is now zero. Similarly, the other zero cycles are adjusted so that the sum is zero for each cycle.

A similar adjustment procedure has been applied to the cycles in Group 2 of Table II. In this case the cycle sum is $n-H^1$, and the weighted average value of this difference, discussed in Sec. III, is the value to which the cycle is fitted. The remaining groups of cycles are treated in exactly the same way. With a few exceptions noted below, these adjusted Q-values are listed in the fourth column of Table I.

The probable error of an adjusted Q-value is a function of the probable errors of all of the Q-values in the cycle as well as the probable error of the cycle sum. It can be shown that P_1*, the probable error in the adjusted value of $Q_1 \pm P_1$, is given by

$$(P_1^*)^2 = P_1^2\left[1-\frac{P_1^2}{\sum_i P_i^2}+\frac{P_1^2}{\sum_i P_i^2}\frac{P_e^2}{\sum_i P_i^2}\right],$$

where P_e is the probable error in the weighted mean of the cycle sum, and P_i refers to the probable error in the experimental Q-value for one of the reactions in the cycle. The sums in the denominator are taken over all of the reactions in the cycle. P_e is, of course, zero for the zero cycles and is negligible for the $n-H^1$ and $n+H^1-H^2$ cycles. As can be seen from the expression for P^* above, the probable error in an adjusted Q-value may be much smaller than the probable error in the corresponding experimental Q-value. For example, the probable error in the adjusted Q-value $F^{18}(\beta^+)O^{18}$ is only 2 kev, although the probable error in the experimental value is 15 kev. The adjusted value and its probable error are determined largely by the inverse reaction $O^{18}(p,n)F^{18}$ for which the probable error is only 2 kev.

It should be noted that in calculating Q-values for reactions not listed in the table, smaller probable errors can usually be obtained by using combinations of reactions listed in the table rather than by using the masses and their probable errors. For example, the Q-value for $N^{14}(d,\alpha)C^{12}$ can be calculated directly from

TABLE II. Nuclear cycles and fundamental mass differences.

Cycle	Mass difference from experimental Q (Mev)
Group 1. Nuclear cycles giving a sum of zero	
$B^{11}(p,\alpha)Be^8$, $Be^9(p,d)Be^8$, $B^{11}(d,\alpha)Be^9$	0.007 ±0.012
$Be^9(p,\alpha)Li^6$, $Li^6(d,p)Li^7$, $Be^9(d,\alpha)Li^7$	0.001 ±0.012
$N^{15}(p,\alpha)C^{12}$, $C^{12}(d,p)C^{13}$, $N^{15}(d,\alpha)C^{12}$	0.003 ±0.011
$B^{10}(n,\alpha)Li^7$, $Li^7(p,n)Be^7$, $B^{10}(p,\alpha)Be^7$	0.006 ±0.010
$F^{19}(p,\alpha)O^{16}$, $O^{16}(d,p)O^{17}$, $F^{19}(d,\alpha)O^{17}$	0.015 ±0.014
Group 2. $n-H^1$	
$n(\beta^-)H^1$	0.783 ±0.013
$H^3(p,n)He^3$, $H^3(\beta^-)He^3$	0.7822±0.001
$C^{13}(p,n)N^{13}$, $N^{13}(\beta^+)C^{13}$	0.781 ±0.005
$C^{14}(p,n)N^{14}$, $C^{14}(\beta^-)N^{14}$	0.783 ±0.004
$O^{18}(p,n)F^{18}$, $F^{18}(\beta^+)O^{18}$	0.796 ±0.015
$H^2(d,p)H^3$, $H^2(d,n)He^3$, $H^3(\beta^-)He^3$	0.7845±0.010
$C^{13}(d,p)C^{13}$, $C^{13}(d,n)N^{13}$, $N^{13}(\beta^+)C^{13}$	0.782 ±0.007
$B^{10}(n,\alpha)Li^7$, $Be^9(d,\alpha)Li^7$, $Be^9(d,p)Be^{10}$, $Be^{10}(\beta^-)B^{10}$	0.780 ±0.013
Weighted mean of $n-H^1=0.7823\pm0.001$ ($p_e=0.24$ kev, $p_i=0.95$ kev, $p_e/p_i=0.25$)	
Group 3. $n+H^1-H^2$	
$H^1(n,\gamma)H^2$	2.227 ±0.003
$H^2(d,p)H^3$, $H^2(n,\gamma)H^3$	2.220 ±0.009
$Be^9(p,d)Be^8$, $Be^9(\gamma,n)Be^8$	2.225 ±0.003
$Be^9(d,p)Be^{10}$, $Be^9(n,\gamma)Be^{10}$	2.209 ±0.010
$C^{12}(d,p)C^{13}$, $C^{12}(n,\gamma)C^{13}$	2.225 ±0.009
$N^{14}(d,p)N^{15}$, $N^{14}(n,\gamma)N^{15}$	2.208 ±0.015
Weighted mean of $n+H^1-H^2=2.225$ ±0.002 ($p_e=1.2$ kev, $p_i=1.9$ kev, $p_e/p_i=0.63$)	
Group 4. $2H^2-H^1-H^3$	
$H^2(d,p)H^3$	4.031 ±0.005
$Be^9(p,d)Be^8$, $Be^9(d,t)Be^8$	4.038 ±0.013
$C^{12}(d,p)C^{13}$, $C^{12}(d,t)C^{12}$	4.033 ±0.006
Weighted mean of $2H^2-H^1-H^3=4.032$ ±0.004	
Group 5. $2H^2-He^4$	
$Li^7(p,\alpha)He^4$, $Be^8(\alpha)\alpha$, $Be^9(p,d)Be^8$, $Be^9(d,\alpha)Li^7$	23.842 ±0.012
$N^{15}(d,\alpha)C^{12}$, $C^{12}(d,p)C^{13}$, $C^{13}(p,n)N^{13}$, $N^{14}(n,\gamma)N^{15}$	23.817 ±0.016
$B^{10}(n,\alpha)Li^7$, $Be^9(d,\alpha)Li^7$, $B^{11}(d,\alpha)Be^9$, $B^{10}(d,p)B^{11}$ with $n+H^1-H^2$*	23.842 ±0.017
$Li^7(p,\alpha)He^4$, $Li^6(d,p)Li^7$, $Li^6(p,\alpha)He^3$ $H^2(d,n)He^3$ with $n+H^1-H^2$*	23.829 ±0.015
Weighted mean of $2H^2-He^4=23.834$ ±0.007	

* $n+H^1-H^2=2.225\pm0.002$ Mev from the weighted mean in Group 3.

TABLE III. Table of atomic masses.

A mass number		$M-A$, mass defect (Mev)	M, atomic mass from nuclear data (amu)[a]	Atomic mass from mass spectroscopy[b]	Bethe[c]
n	1	8.3638 ±0.0029	1.008 982 (±3)		1.008 93
H	1	7.5815 ±0.0027	1.008 142 (±3)	1.008 165 (±4)	1.008 123
H	2	13.7203 ±0.006	2.014 735 (±6)	2.014 778 (±8)	2.014 708
H	3	15.8271 ±0.010	3.016 997 (±11)		3.017 02
He	3	15.8086 ±0.010	3.016 977 (±11)		3.017 00
He	4	3.6066 ±0.014	4.003 873 (±15)	4.003 944 (±19)	4.003 90
He	6	19.065 ±0.025	6.020 474 (±27)		6.020 90
Li	6	15.850 ±0.021	6.017 021 (±22)		6.016 97
Li	7	16.969 ±0.024	7.018 223 (±26)		7.018 22
Li	8	23.296 ±0.028	8.025 018 (±30)		8.025 02
Be	7	17.832 ±0.024	7.019 150 (±26)		7.019 16
Be	8	7.309 ±0.027	8.007 850 (±29)		8.007 85
Be	9	14.007 ±0.028	9.015 043 (±30)		9.015 03
Be	10	15.560 ±0.026	10.016 711 (±28)		10.016 77
B	9	15.076 ±0.029	9.016 190 (±31)		9.016 20
B	10	15.004 ±0.026	10.016 114 (±28)		10.016 18
B	11	11.909 ±0.022	11.012 789 (±23)		11.012 84
B	12	16.912 ±0.020	12.018 162 (±22)		12.019 0
C	11	13.889 ±0.022	11.014 916 (±24)		11.014 95
C	12	3.542 ±0.015	12.003 804 (±17)	12.003 842 (±6)	12.003 82
C	13	6.958 ±0.013	13.007 473 (±14)		13.007 51
C	14	7.153 ±0.010	14.007 682 (±11)		14.007 67
N	13	9.179 ±0.013	13.009 858 (±14)		13.009 88
N	14	6.998 ±0.010	14.007 515 (±11)	14.007 564 (±7)	14.007 51
N	15	4.528 ±0.011	15.004 863 (±12)		15.004 89
O	15	7.233 ±0.012	15.007 768 (±13)		15.007 8
O	16		16.000 000 (standard)		16.000 000
O	17	4.221 ±0.006	17.004 533 (±7)		17.004 50
F	17	6.970 ±0.011	17.007 486 (±11)		17.007 5
F	19	4.149 ±0.014	19.004 456 (±15)		19.004 50
F	20	5.914 ±0.017	20.006 352 (±19)		

[a] 1 amu = 931.152 Mev.
[b] A. O. Nier, Phys. Rev. **81**, 624 (1950).
[c] H. A. Bethe, *Elementary Nuclear Theory* (John Wiley and Sons, New York, 1947). Errors omitted here.

TABLE IV. Fundamental mass spectroscopic doublets.

	Computed from nuclear data (mMU)[a]	From mass spectroscopy
$2H^1-H^2$	1.5494±0.0024	1.5519±0.0017[b]
$2H^2-He^4$	25.596 ±0.008	25.612 ±0.009[c], 25.604±0.009[d]
$3H^2-\frac{1}{4}C^{12}$	42.302 ±0.016	42.373 ±0.040[c]
$C^{12}H_4^1-O^{16}$	36.372 ±0.019	36.478 ±0.022[c]
$C^{12}H_2^1-N^{14}$	12.573 ±0.012	12.586 ±0.013[c]

[a] 1 amu =931.152 Mev, J. W. M. DuMond and E. R. Cohen, Phys. Rev. 82, 555 (1951).
[b] T. R. Roberts, Phys. Rev. 81, 624 (1951).
[c] A. O. Nier and T. R. Roberts, Phys. Rev. 81, 507 (1951).
[d] H. Ewald, Z. Naturforsch. 5, 1 (1950).
[e] A. O. Nier (private communication, computed from other doublets, not measured directly).

the masses of the four nuclei involved: 13.5697±0.024 Mev; using the Q-values for $N^{14}(d,p)N^{15}$ and $N^{15}(p,\alpha)C^{12}$, one obtains 13.569±0.009 Mev.

Some reactions appear in more than one cycle and in some cases the adjusted value from one cycle does not agree with the adjusted value from another cycle. Table Ib lists these reactions, with the adjusted values obtained from the different cycles containing the reaction. For the final adjusted value we have taken the weighted mean of the several adjusted values from the different cycles. The probable error assigned to this final adjusted value is the probable error of the most accurate preliminary adjusted value. These final adjusted values, listed in the last column of Table Ib, have been substituted back in the original cycles, and the remaining Q-values in the cycles readjusted to yield numerical consistency as before. This last adjustment is very small, never more than 4 kev, and we have neglected any small effect this small adjustment might have on the probable error of the adjusted Q-value. The final adjusted values are listed in the fourth column of Table I, together with the ones not requiring readjustment, and are used in subsequent calculation, referred to as "adjusted values."

V. THE ATOMIC MASSES

The calculation of the mass values from the adjusted Q-values is straightforward. The H^1 mass is given in terms of O^{16} by

$$H^1=\tfrac{1}{16}O^{16}+\tfrac{1}{16}[-9Q_a+10Q_b+5Q_c-(Q_1-Q_2-Q_3+Q_4+Q_5+Q_6+Q_7-Q_8)]\times 1.07394 \text{ mMU}$$

$Q_a=n-H^1$(Mev) $Q_2=C^{14}(\beta^-)N^{14}$ $Q_6=Be^9(p,\alpha)Li^6$

$Q_b=n+H^1-H^2$ $Q_3=C^{13}(d,p)C^{14}$ $Q_7=Li^6(p,\alpha)He^3$

$Q_c=2H^2-He^4$ $Q_4=C^{13}(d,\alpha)B^{11}$ $Q_8=H^2(d,n)He^3$

$Q_1=O^{16}(d,\alpha)N^{14}$ $Q_5=B^{11}(d,\alpha)Be^9$.

The probable error is the square root of the sum of the squares of the probable errors of all the reactions in the chain above, with the appropriate factors. The error will depend slightly on the particular chain chosen; in general, the most direct chain gives the smallest probable error. The value of the mass however, does not depend on the particular chain, all chains are equivalent when the adjusted Q-values are used. The four mass differences in Table II give immediately the n^1, H^2, H^3, and He^4 masses, and the remaining masses are calculated from the remaining Q-values. The results are listed in Table III. It is clear from the foregoing expression for the proton mass that the quantity determined by the Q-values is $M-A$, the mass defect in energy units. These mass defects are included in Table III. They are convenient to use in calculating Q-values, and are independent of the conversion factor from energy units to mass units.

The most recent mass spectroscopic values for H^1, H^2, He^4, C^{12}, and N^{14} are also listed in Table III. The mass spectroscopic values are consistently larger by more than the probable error. We have examined our experiments in detail for a source of systematic error that would account for this discrepancy. One might suspect some of the energy standards which are used in the calibration of the nuclear measurements. However, an error of this sort would tend to put all of the Q-values in error in the same direction, too high or too low. In this case the error in the masses would be proportional to the mass defect.

We have not found any single Q-value which could be changed to bring the two mass systems into agreement. Because of the interconnection of the Q-values in the second class, it is not possible to change one Q-value without changing a great many others. It should be noted that all of the Q-values in the chain that determine the proton mass, and hence also H^2, H^3, and He^4, are of this second class except $C^{13}(d,\alpha)B^{11}$ and $O^{16}(d,\alpha)N^{14}$. Because of the critical importance of these two reactions and the fact that they cannot be checked by a combination of other reactions at the present time, it would be desirable to have further independent measurements of these two Q-values, as well as precise measurements of other reactions which would form combinations equivalent to these two reactions.

Recent values of the mass spectroscopic doublets are listed in Table IV along with the values of these doublets calculated from the nuclear data. The agreement between the $2H^1-H^2$ and $2H^2-He^4$ and $C^{12}H_2^1-N^{14}$ doublets is good, and the disparity between the two mass systems apparently arises from the poor agreement for the $C^{12}H_4^1-O^{16}$ and $3H^2-\frac{1}{4}C^{12}$ doublets. Further measurements of these doublets would be desirable.

It is a pleasure to acknowledge the helpful interest of Dr. A. V. Tollestrup and Professors R. F. Christy and T. Lauritsen in this work. We are indebted to Professor W. W. Buechner of the Massachusetts Institute of Technology for making his results available to us before publication, and to Professor K. T. Bainbridge of Harvard University for valuable criticism and discussion of the mass spectrographic results.

Neutron Capture γ-Rays from Fluorine, Sodium, Magnesium, Aluminum, and Silicon

B. B. KINSEY, G. A. BARTHOLOMEW, AND W. H. WALKER*
Division of Atomic Energy, National Research Council of Canada, Chalk River, Ontario, Canada
(Received April 20, 1951)

The energies and the absolute intensities of the γ-rays produced by neutron capture in fluorine, sodium, magnesium, aluminum, and silicon have been measured with the aid of a pair spectrometer. Direct transitions to the ground states of the product nuclei are predominant in the γ-ray spectra of fluorine and aluminum. The neutron binding energy in F^{20} is 6.63±0.03 Mev and in Al^{28}, 7.724±0.010 Mev. The γ-ray representing the direct transition to the ground state of Na^{24} was not detected. The interpretation of the magnesium spectrum presents some difficulties. A weak γ-ray with the binding energy of a neutron in Mg^{25} was detected, but none could be found to correspond to the direct transition to the ground state in Mg^{24}. In silicon, most captures are due to Si^{28} which produces Si^{29} by the emission of two γ-rays in cascade. Very weak γ-rays representing direct transitions to the ground states in Si^{29} and Si^{30} were detected. Their energies are 8.51±0.04 (Si^{29}) and 10.55±0.05 Mev (Si^{30}).

I. EXPERIMENTAL ARRANGEMENT

THE spectra of γ-rays of neutron capture are being explored with a pair spectrometer. A diagram of the experimental arrangement is shown in Fig. 1. The neutron-capturing sample under investigation is placed in a high neutron flux near the reacting core of the Chalk River pile. A block of bismuth, 5 inches thick, is located in the experimental hole between the sample and the reactor to reduce the γ-radiation from the latter to negligible proportions. Two cylindrical lead collimators in the hole limit the field of view of the spectrometer so that only the central portion of the neutron-capturing sample is visible. In this way the γ-radiations from the aluminum lining in the hole are eliminated. A cylinder, containing a mixture of boric acid and paraffin, and a sheet of cadmium prevent the escape of neutrons from the hole.

II. ENERGY AND RELATIVE INTENSITY MEASUREMENTS

The γ-ray spectrum is obtained by plotting the coincidence counting rate of the pair spectrometer against the strength of the magnetic field, a homogeneous γ-ray being revealed by a peak of characteristic shape. The energy of a γ-ray is determined from the distance between the inner edges of the slits which define the aperture of the counters, the value of the magnetic field obtained by the linear extrapolation of the high energy edge of the coincidence peak, and a small additive correction.[1]

The line width of the spectrometer, defined as the width of a coincidence peak at half maximum, is determined by the ratio of the widths of the slits to the distance separating them. The line width, in energy units, is nearly independent of the γ-ray energy, and for most of the present work it was 130 kev. The γ-ray spectrum of aluminum, however, was studied with a line-width of 65 kev.

The relative intensities of the γ-rays producing the coincidence spectrum are determined from the peak coincidence counting rates and from calculated values of the efficiency of the spectrometer as a function of the γ-ray energy. The results are then corrected for the absorption of the γ-ray in the boron-paraffin cylinder and for self-absorption in the sample. The relative intensities given by this method have been verified by a direct determination with an ionization chamber of the intensities of the 2.75-Mev γ-ray produced by the decay of Na^{24} and of the 7.4-Mev neutron capture radiation from lead. The counting efficiency rises very rapidly with energy, at 3 Mev nearly as the fifth power. At 3 Mev the efficiency is very low, and for this reason it is difficult to detect and measure γ-rays with a lower energy unless they are exceptionally intense. At higher energies the instrument is much more efficient, and it is easy to measure very weak radiations.

In Figs. 2, 3, 4, 5, 6, 7, 9, 12 and 15, the ordinates of the γ-ray spectra are the coincidence counting rates observed, uncorrected for absorption or for the variation of the efficiency of the spectrometer. The errors given in the curves represent the statistical errors of counting. When the counting rates were very low, it was necessary to average the counting rates obtained for several adjacent values of the magnetic field, and these averages are indicated in the spectra by horizontal lines drawn through representative points. The abscissas are adjusted so that the extrapolated limits of the high energy edges of the coincidence peaks are equal to the energies of the γ-rays which have been calculated from the magnetic field corresponding to these limits and include the additive correction mentioned above.

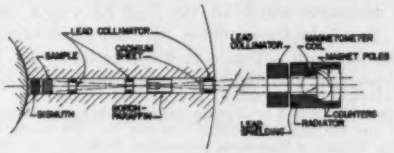

FIG. 1. General arrangement of apparatus.

* Now at McMaster University, Hamilton, Ontario
[1] The method of energy measurement and the calculation of the efficiency of this instrument will be fully described elsewhere.

III. ABSOLUTE INTENSITY MEASUREMENTS

The absolute intensities of the capture γ-rays of sodium, i.e., the number of photons produced per neutron captured, have been determined from the intensities measured relative to that of the 2.75-Mev γ-ray of Na^{24}. Since one photon of 2.75 Mev is produced per capture when radioactive equilibrium is established between Na^{24} and the neutrons producing it, the ratio of the intensities of the capture radiations to that of the 2.75-Mev γ-ray is equal to the number of photons produced per capture.

In principle, the absolute intensities of the capture radiations produced by any other material can be determined by mixing a weighed amount of it with a weighed amount of a sodium compound, provided that the capture cross sections of both are known. Let N be the number of atoms of this material in the container, σ its capture cross section, N_0 and σ_0 the similar quantities for sodium, and let the intensity in photons per second be I_r; then

$$I_r/I_0 = N\sigma P_r T_r / N_0 \sigma_0 T_0, \qquad (1)$$

P_r being the number of photons of the γ-ray, r, emitted per capture, and T_r the fraction which escape from the sample in the direction of the spectrometer. The transmission coefficients T are easily calculated, and P_r may be determined therefore from the intensity ratio and from known or measurable quantities.

In practice, such comparisons are difficult because the coincidence counting rate produced by the Na^{24} γ-ray is very low even if kilogram amounts of sodium compounds are used. We have used, therefore, the 9.0-Mev capture γ-ray of nickel as a substandard. Nickel is more suitable than other materials as a substandard for intensity comparisons, because the coincidence spectrum consists mainly of a 9.0-Mev peak which is exceptionally strong and can be easily measured when nickel is used in very small quantities. The absolute intensity of this γ-ray was determined in a separate experiment in which a small weighed amount of nickel sesquioxide was mixed uniformly with a weighed amount of sodium fluoride. The result obtained was 0.43 photon per capture, assuming that the capture cross sections of sodium and nickel are respectively 0.47[2] and 4.8 barns.[3]

Provided the cross sections of sodium and of the sample element are known with sufficient precision, the reliability of the nickel method depends on the calculated efficiency of the spectrometer and on the statistical accuracy of measurement of the coincidence peaks. There is reason to believe, however, that this method gives intensities which are too high for γ-rays near 5 Mev. As will be shown below, the intensities obtained for the strongest silicon γ-rays are certainly too high by 30 percent. Too high an intensity might correspond to too high a value for the absorption cross section of sodium or too low a value for silicon. Neither of these quantities is likely to be in serious error, for the absorption and the activation[4] cross sections of sodium agree within the limits of experimental error (20 percent), and the cross section of silicon, determined from the reactivity of a pile, owing to the possible presence of impurities, is generally more likely to be too high than too low. We conclude that the calculated efficiency of the spectrometer, which seems to give the correct ratio of efficiency at 7.38 and 2.75 Mev, gives too low results between these values. Unfortunately, we have so far found no way of checking the efficiency at energies other than these.

Another method for making the nickel comparison may be applied to samples with low capture cross sections. The neutron flux in a reactor decreases in a radial direction outwards from the center. The change in the flux over the length of a sample is small, and, in the case of weakly absorbing materials, there is no variation of the flux on a plane through the sample and perpendicular to the axis of the hole. Consequently, if, instead of mixing nickel oxide with the sample, two nickel sheets are fixed to the front and back faces of the container, the nickel capture radiation produced is proportional to the average value of the neutron flux in the weakly absorbing sample, and the intensity ratio obtained should be equal to that found when an equivalent amount of the oxide is mixed with the material. For magnesium, aluminum, and silicon it has been more convenient to make the intensity comparison in this way, and for the latter element an identical result was obtained with that found using the nickel mixture.

In using the sheet method we assume that the absorption of neutrons in the material is so low that the distribution of the neutron flux is not disturbed by the presence of the sample. This assumption seems to be justified for samples containing a few hundred grams of the absorbing element for which the cross section is small compared with one barn. Using a lead sample, for which the cross section is about 200 mb, we have found by a direct measurement with manganese foils within the material that the neutron flux is uniform to 5 percent. In this experiment, the lead sample was of similar size to those used in the pile and was exposed to a uniform neutron flux in a paraffin-lined enclosure.

For samples containing about the same number of atoms with cross sections in excess of one barn, the flux at the center of the sample is considerably less than that at the ends and the nickel sheet method will indicate intensities which are too low. In this case, the mixture method is essential; the result is then given by Eq. (1) and depends to a small extent only (in fact, to the second order of small quantities) on the axial variation of the flux and the self-absorption of the capture radiation.

[2] This cross section is a mean value of that of Colmer and Littler and the values quoted in Circular No. 499 of the U. S. National Bureau of Standards, September, 1950.

[3] F. C. W. Colmer and D. J. Littler, Proc. Phys. Soc. (London) **A63**, 1175 (1950).

[4] Seren, Friedlander, and Turkel, Phys. Rev. **72**, 888 (1947).

IV. FRACTION OF γ-RAYS OBSERVED

A check on the intensity measurements may be obtained from a consideration of the total energy detected in the form of capture radiation.

The fraction of the total binding energy which is not promptly emitted in the form of capture γ-radiation is negligible, for that which may be delayed by the production of an isomeric state is usually small compared with the neutron binding energy and the amount of internal conversion is of the order of 0.1 percent. Consequently, the sum of the products of the γ-ray energies with their intensities, in photons per capture, should be very nearly equal to the binding energy. Any difference observed represents the energy emitted as γ-rays with energies below the limit of detection by the pair spectrometer. If E_m is the lower limit of detection, and if B is the neutron binding energy, the sum of the intensity-weighted energies is

$$S=\sum_{E_m}^{B} P(E)E \lesssim B. \tag{2}$$

For the elements which are the subject of the present paper, the quantities S/B are usually near unity.

If the spectrum contains unresolved components, the contribution to the total energy radiated must be calculated on the assumption of a continuous spectrum. Let $q(E)$ be the counting rate at energy E, C a quantity proportional to the number of captures in the sample, and $\epsilon(E)$ the relative efficiency of the spectrometer at energy E. Then the counting rate is given by

$$q(E)=kCT(E)\epsilon(E)\nu(E)A,$$

where k is a constant, $\nu(E)$ is the number of photons emitted per capture per unit energy range at E, and A is the area under the coincidence peak of a homogeneous γ-ray with unit peak height at energy E. The counting rate of the 9-Mev nickel γ-ray is given by:

$$q_1=0.43C_1T_1\epsilon_1k.$$

The absolute intensity of the continuous spectrum emitted by the sample may then be calculated by combining these equations. Hence:

$$\nu(E)=\frac{q(E)}{q_1}\frac{C_1}{C}\frac{T_1\epsilon_1}{T(E)\epsilon(E)}\frac{0.43}{A}. \tag{3}$$

The coincidence spectrum obtained with a homogeneous γ-ray contains a tail extending to low energies, which for various reasons it has not been possible to study in detail below an energy less than that of the extrapolated limit by four or five times the width of the peak. To this extent, the area under a coincidence peak is roughly independent of the energy of the γ-ray; the average value of A for a line-width of 130 kev was found to be 135 kev. Using Eq. (3), the sum of the intensity-weighted energies for an unresolved spectrum

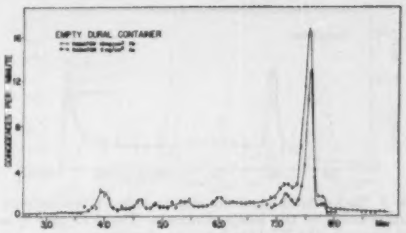

FIG. 2. Coincidence spectrum produced by an empty Dural container. A part of the peak near 4 Mev is due to bismuth capture radiations.

is

$$S'=\int_{E_m}^{B}\nu(E)EdE \lesssim B. \tag{4}$$

Equation (3) is derived on the assumption that the resolution of the instrument is such that $\nu(E)$ does not vary much over a range of energy equal to the width of the peak of a homogeneous γ-ray. For most of the light elements this assumption is certainly untrue. Further, no account is taken in Eq. (3) of the long tail at the lower energy side of a coincidence peak. The tails of the higher energy peaks will contribute appreciably—and by an unknown amount—to the background counting rate at lower energies and the contribution to the γ-ray spectrum and to (4) will be greatly exaggerated by the rapidly decreasing sensitivity of the instrument at low energies. Consequently, the value of the integral S' will generally be too high.

V. SAMPLE CONTAINER

Compounds of fluorine and sodium were irradiated in Dural containers, four inches in diameter and six inches long. The container itself produces a γ-ray spectrum, in which the radiations of aluminum are prominent. This spectrum must be subtracted from that obtained when the container is full of the material to be studied. From each ordinate of the combined spectrum is subtracted the contribution of the empty container scaled so that the peaks due to the 7.72-Mev aluminum γ-ray coincide. The container spectrum, Fig. 2, was obtained with a somewhat thicker radiator (15 mg/cm² of lead) than that normally used (5 mg/cm² of gold). Apart from the higher counting rate, the difference in the shape of coincidence spectra obtained with these two radiator thicknesses is negligible for the purposes of making this subtraction. The strong peak at 7.72 Mev and the weaker peaks at 4.7 and at 6.1 Mev are due to aluminum. Two small peaks appear on the tails of the peak at 7.72 Mev. The γ-ray at 7.9 Mev is due to the copper, and that at 7.2 Mev to the manganese component in the Dural.

Magnesium and aluminum were available in the form

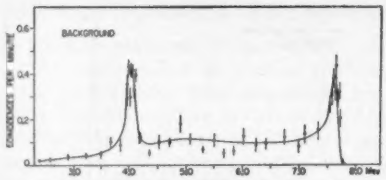

FIG. 3. Background spectrum due to hole containing only the bismuth block and the lead collimators. The 4.17-Mev γ-ray is due to bismuth; the 7.7-Mev γ-ray to aluminum.

of metallic cylinders,[5] and for this reason it was not necessary to place them in containers. The γ-rays of these elements are superposed on radiation produced by the reactor filtered through the bismuth block (Fig. 1), and the radiation emitted by the block itself. This background spectrum, shown in Fig. 3, was obtained from measurements made without a sample. To within 10 percent the ordinates of Fig. 3 correspond to the same pile power as that used in the study of magnesium, aluminum, and silicon. The peak at 4.17 Mev in Fig. 3

TABLE I. Energies and intensities of sodium capture γ-rays.

γ-ray	Energy in Mev	Intensity in photons per 100 captures
A	6.41±0.03	20
B	5.61 0.03	7.5
C	5.13 0.03	1.8
F	3.96 0.03	20
G	3.85 0.05	11
H	3.60 0.03	10
I	3.56 0.05	20

is due to the γ-ray of bismuth[6] and that at 7.7 Mev to aluminum.

Silicon has been studied in a container of a new design consisting of an aluminum tube with end walls of Bakelite. Since the field of view of the spectrometer covers the central parts of the sample only, aluminum γ-rays do not then contribute appreciably to the spectrum. The capture γ-rays produced by the Bakelite ends are extremely weak and cannot be detected under these conditions.

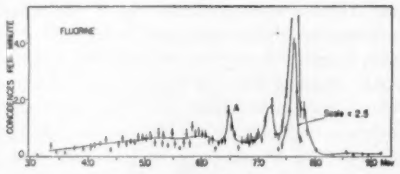

FIG. 4. Coincidence spectrum produced by fluorine (as Teflon) in a Dural container.

[5] For the provision of magnesium and aluminum metal of exceptional purity we are indebted to the Division of Physical Metallurgy, Department of Mines and Technical Surveys, Ottawa.

[6] Kinsey, Bartholomew, and Walker, Phys. Rev. **82**, 380 (1951).

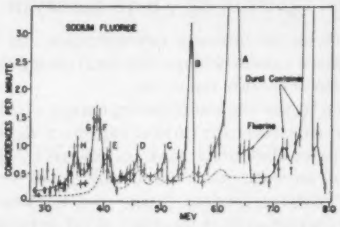

FIG. 5. Coincidence spectrum produced by sodium fluoride in a Dural container. Line-width: 130 kev. The contribution to this spectrum below 7 Mev produced by the container and the bismuth block is shown by the dotted line.

VI. FLUORINE

Fluorine capture radiation was investigated from 2.5 Mev to 10.4 Mev using a sample of about 1700 grams

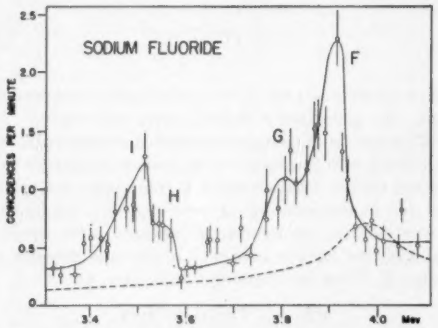

FIG. 6. Coincidence spectrum produced by sodium fluoride showing details between 3.4 and 4.0 Mev. Line-width: 130 kev. The contribution of the Dural container and the bismuth radiation is shown by the dotted line.

of Teflon (C_2F_4) in a Dural container. The results are shown in Fig. 4. Only one γ-ray, *A*, was resolved above the background due to the container. This γ-ray has an

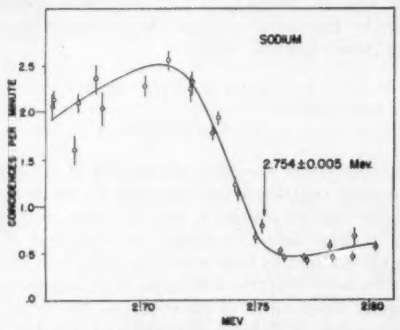

FIG. 7. Coincidence spectrum produced by sodium fluoride between 2.65 and 2.80 Mev. The peak represents the 2.75-Mev γ-ray emitted by Na^{24} in radioactive equilibrium.

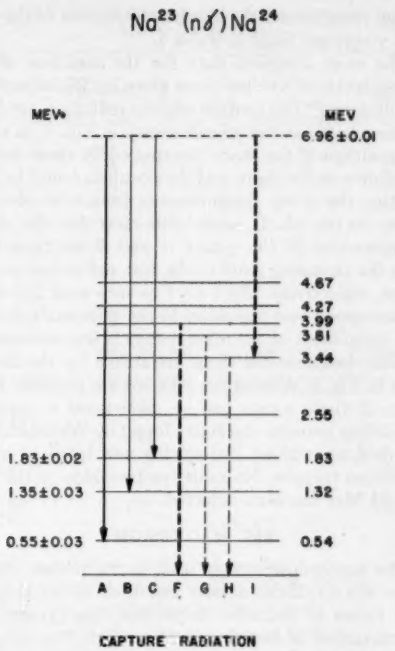

FIG. 8. Decay scheme for the capture γ-rays of sodium. The energy levels are drawn to scale according to the results of Whitehead and Heydenburg (reference 13) (right hand figures). The energies of the first three excited states of Na^{24}, obtained by subtracting the γ-ray energies from 6.96 Mev, are shown on the left.

energy of 6.63±0.03 Mev, which agrees with the binding energy of 6.5 Mev, obtained from the results of Bower and Burcham,[7] and with 6.52±0.08 Mev, obtained from those of Allen and Rall[8] from studies of the energy balance in the (d,p) reaction. The background due to the container was too high to permit a search for γ-rays of lower energy.

The absolute intensity of the 6.63-Mev γ-ray, in photons per capture in fluorine, has been estimated in two ways. In the first method, the peak coincidence counting rate was compared with that of the 6.797-Mev γ-ray[9] of beryllium. Assuming that the capture cross sections of fluorine and beryllium are the same (9 millibarns) and taking into account the number of fluorine and beryllium atoms in the two samples, the absorption of the γ-rays in the samples and in the boron-paraffin plug used to remove the neutrons from the beam, and the energy dependence of the counting efficiency in the spectrometer, we find that the intensity of the fluorine γ-ray is 0.27±0.10 of that of the beryllium γ-ray. Only one γ-ray has been detected in the beryllium capture spectrum and, assuming that that γ-ray is emitted at the rate of one photon per capture, the intensity of the fluorine γ-ray is 0.27±0.10 photon per capture.

In the second method, the intensity of the fluorine γ-ray emitted by sodium fluoride was compared with the intensity of the 2.75-Mev γ-ray emitted by Na^{24} in radioactive equilibrium with the neutrons producing it (see Fig. 5). The fluorine γ-ray is partially obscured by the strong sodium γ-ray at 6.41 Mev, and only a rough estimate of its intensity is possible. The result is 0.42±0.10 photon per capture.

The results of the two methods are in rough agreement; taking a mean value, we conclude that the 6.63-Mev fluorine γ-ray is emitted in 0.35±0.10 photon per capture. The neutron captures which do not result in the emission of this γ-ray must produce others which, on account of their low intensity or lower energy, are not detected.

TABLE II. Energies and intensities of magnesium capture γ-rays.

γ-ray	Energy in Mev	Intensity in photons per 100 captures
A	9.26±0.04	1
B	8.16 0.03	9
C	7.37 0.08	0.5
D	7.15 0.04	1
E	6.75 0.04	2.5
F	6.39 0.05	5
G	5.73 0.04	1
H	5.50 0.04	7
I	5.05 0.07	9
J	3.92 0.03	94
K	3.45 0.07	16
L	2.83 0.05	39

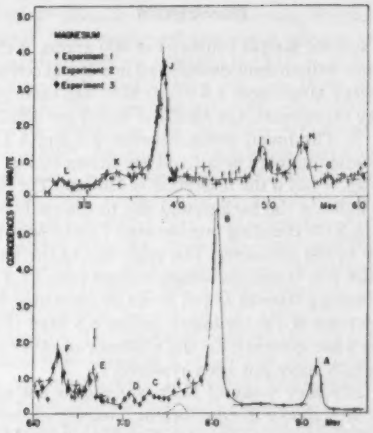

FIG. 9. Coincidence spectrum produced by magnesium compiled from a combination of results. Line-width: 130 kev. The contribution due to bismuth is shown by the dotted line near 4.1 Mev, and that due to a small amount of aluminum, near 7.7 Mev. No coincidence peaks were discovered between that of the γ-ray *A* and 12.5 Mev.

[7] J. C. Bower and W. E. Burcham, Proc. Roy. Soc. (London) **A173**, 379 (1939).
[8] R. C. Allen and W. Rall, Phys. Rev. **78**, 337A (1950).
[9] Kinsey, Bartholomew, and Walker, Can. J. Phys. **29**, 1 (1951).

VII. SODIUM

The sodium sample consisted of 900 grams of chemically pure sodium fluoride enclosed in a Dural container. The energy range from 2.8 to 8.0 Mev was examined in a survey experiment, the results of which are illustrated in Fig. 5. The broad peaks between 3.3 and 4.2 Mev were studied in more detail and are shown in Fig. 6. In both Figs. 5 and 6 the resolution is 130 kev. The dotted curves indicate the background due to the container.

In Fig. 5 the counting rate between 7 and 8 Mev is due entirely to the container. The peak due to the fluorine γ-ray lies just above the strong sodium peak at A. The peak counting rates at D and E can be accounted for by the spectrum of the container. Below 3.3 Mev (Fig. 5) there is some evidence for the existence of other radiations which have not been resolved.

The 2.75-Mev γ-ray of Na^{24}, which does not appear in Fig. 5, is shown in equilibrium intensity in detail in Fig. 7. Its energy was found to be 2.754 ± 0.005 Mev, in agreement with recent measurements. Wolfson[10] has obtained the value 2.755 ± 0.005 Mev by comparison with the 1.33-Mev γ-ray of Co^{60}. Bishop and coworkers[11] found 2.757 ± 0.004 Mev by comparison with the ThC″ γ-ray which was assumed to be 2.618 ± 0.004 Mev.

The binding energy of the neutron in the Na^{24} nucleus may be derived from the Q value of the (d,p) reaction by adding the binding energy of the deuteron obtained by Bell and Elliott.[12] The Q value obtained by Whitehead and Heydenburg[13] was 4.76 Mev in agreement with earlier results obtained by Murrell and Smith.[14] Recently, the M.I.T. group have obtained a value of 4.731 ± 0.009 Mev for the same quantity.[15] From this we deduce that the neutron binding energy in Na^{24} is 6.961 ± 0.012 Mev. No γ-ray with this energy has been found; however, the coincidence peak due to a weak γ-ray at this energy might be hidden beneath the tail of the aluminum γ-ray in the spectrum of the container.

TABLE III. Abundances, cross sections, and binding energies of magnesium isotopes.

Target nucleus	Abundance percent	Contribution to capture cross section in millibarns	Binding energy or product nucleus in Mev
Mg^{24}	78.6	52 ± 6[a]	7.334±0.012
Mg^{25}	10.1		10.93 ±0.10
Mg^{26}	11.3	5.4[b]	6.44 ±0.10

[a] See reference 3. [b] See reference 4.

The energies and the absolute intensities of the capture γ-rays are listed in Table I.

The most complete data for the positions of the energy levels of Na^{24} are those given by Whitehead and Heydenburg.[13] The neutron capture radiations are fitted to these levels in the scheme shown in Fig. 8, in which the positions of the levels determined by these authors are shown on the right, and the positions found by subtracting the γ-ray measurements from 6.96 Mev are shown on the left. It seems quite clear that the proper interpretation of the γ-rays A and B are transitions from the capturing state to the first and second excited states, respectively. The γ-ray C is very weak but seems to correspond to a transition to the third excited state. The assignment of the other γ-rays is less obvious and possible locations for them are shown by the broken lines in Fig. 8. Alternative schemes are possible. However, all these γ-rays can be understood in terms of transitions between the states found by Whitehead and Heydenburg without introducing new levels at higher excitation energies. No radiative transition to the level at 2.55 Mev has been detected.

VIII. MAGNESIUM

The magnesium sample used in the present experiment was a cylinder of pure metal, six inches long and four inches in diameter. Impurities were present in a concentration of less than 0.02 percent. The elements which produce exceptionally strong homogeneous γ-rays, *viz.*, Mn, Fe, Ni, and Cu, were present to the extent of only a few parts per million and measurements of the intensities of the γ-rays from these elements show that the impurities of these elements in the magnesium sample could not contribute appreciably to the spectrum observed.

Three sets of measurements were made to obtain the capture γ-ray spectrum shown in Fig. 9. Coincidence peaks were looked for up to 12.5 Mev but none were found above the energy of peak A. In experiments Nos. 1 and 2 the bismuth block placed between the sample and the reactor was contained in a Dural cylinder with a Dural end wall facing the sample. Radiations produced by neutron capture in the Dural were transmitted through the sample with sufficient intensity to obscure the magnesium spectrum in the region from 6.8 to 7.8 Mev and the results in this energy range have been omitted in Fig. 9. The Dural contribution to the coincidence spectrum below 7 Mev is negligible. In experiment No. 3, the bismuth block was replaced by another which was so constructed that no Dural was exposed to the field of view of the spectrometer. The spectrum, in this case, is nearly free from unwanted radiations. In plotting Fig. 9 the three sets of data were normalized to the same pile power. Except for a few isolated points the results coincide within the statistical error.

The energies and intensities of the resolved magnesium radiations are listed in Table II. These γ-rays

[10] J. L. Wolfson, Phys. Rev. **78**, 176 (1950).
[11] Bishop, Collie, Halban, Hedgran, Siegbahn, DuToit, and Wilson, Phys. Rev. **80**, 211 (1950).
[12] R. E. Bell and L. G. Elliott, Phys. Rev. **79**, 282 (1950).
[13] W. D. Whitehead and N. P. Heydenburg, Phys. Rev. **79**, 99 (1950).
[14] E. B. Murrell and C. L. Smith, Proc. Roy. Soc. (London) **A173**, 410 (1939).
[15] Strait, Van Patter, Buechner, and Sperduto, Phys. Rev. **81**, 747 (1951).

TABLE IV. Energies of the excited states of Mg^{25} and Mg^{26} in Mev.

Mg^{25}					
Schelberg[a] *et al.* $Al^{27}(d,\alpha)Mg^{25}$	French and Treacy[b] $Al^{27}(d,\alpha)Mg^{25}$	Pollard[c] *et al.* $Al^{27}(d,\alpha)Mg^{25}$	Allan[d] *et al.* $Mg^{24}(d,p)Mg^{25}$	Bleuler and Zünti[e] $Na^{25}(\beta^-)Mg^{25}$
0.57±0.05	0.58		0.58	
0.96 0.05	0.94	0.81	0.98	1.0
1.63 0.04	1.54	1.58		
1.97 0.05	1.87			
2.74 0.04		2.54		
3.36 0.04				
4.01 0.05				
4.81 0.05				
5.48 0.05				
5.95 0.05				

Mg^{26}			
Motz[f] $Na^{23}(\alpha,p)Mg^{26}$	Humphreys and Pollard[g] $Na^{23}(\alpha,p)Mg^{26}$	Livingston and Bethe[h] $Na^{23}(\alpha,p)Mg^{26}$	Alburger,[i] γ-rays following $Na^{23}(\alpha,p)Mg^{26}$
	0.23		
0.44			
	0.60		
	1.18		
1.91	1.92		1.85
		2.2	
2.85	2.75		2.80
		4.0	
		5.0	

[a] Schelberg, Sampson, and Cochran, Phys. Rev. **80**, 574 (1950).
[b] See reference 18.
[c] Pollard, Sailor, and Wyly, Phys. Rev. **75**, 725 (1949).
[d] See reference 17.
[e] E. Bleuler and W. Zünti, Helv. Phys. Acta **20**, 195 (1947).
[f] See reference 22.
[g] R. F. Humphreys and E. Pollard, Phys. Rev. **59**, 924 (A) (1941).
[h] See reference 24.
[i] D. E. Alburger, Phys. Rev. **73**, 1014 (1948).

are superposed on a relatively high background. The contribution to the spectrum due to the background of bismuth and pile radiation (Fig. 3) is very small and for the same pile power the two prominent peaks are shown by the dotted lines in Fig. 9. After subtracting this contribution and using Eq. (3) the γ-ray spectrum of Fig. 10 was obtained.

The contribution of the γ-rays of Table II to the energy radiated per capture [Eq. (2)] is $S=7.5$ Mev. If, as seems likely, the calculated efficiency curve of the spectrometer gives too high intensities near 5 Mev, this is a low result and may indicate that a portion, at least, of the background is due to unresolved radiations. The integral [Eq. (4)] of Fig. 10 is $S'=17$ Mev. This very high result must be due to the effect of the tails of the peaks due to homogeneous γ-rays, as pointed out in an earlier paragraph.

The neutron binding energies of the magnesium isotopes can be computed from the energy release in a number of nuclear reactions. Only the neutron binding energies of Mg^{25}, Mg^{26}, and Mg^{27} are relevant to the present work.

The neutron binding energy of Mg^{25} can be obtained from the energy balance of the $Mg^{24}(d,p)Mg^{25}$ reaction. For this quantity Allan and Wilkinson[16] have found 5.03±0.05 Mev and Allan, Wilkinson, Burcham, and Curling[17] have confirmed this value using a target of separated Mg^{24}. More recently, the M.I.T. group[15] have obtained 5.094±0.010 Mev for the same quantity. Another value consistent with this result can be obtained by subtracting the Q's of the $Al^{27}(d,\alpha)Mg^{25}$ and $Al^{27}(p,\alpha)Mg^{24}$ reactions. For the former quantity, French and Treacy[18] obtained 6.62±0.05 Mev and for the latter, they have quoted an unpublished value of Freeman of 1.58±0.01 Mev. The difference, 5.04±0.05 Mev, agrees with the results of Allan and Wilkinson and of the M.I.T. work quoted above. A more accurate value for the Q of the $Al^{27}(d,\alpha)Mg^{25}$ reaction has been obtained recently by the M.I.T. group;[15] it is 6.694 ±0.010 Mev. The difference between the Q's of the two reactions then becomes 5.114±0.014 Mev, which is in close agreement with the value 5.094±0.010 Mev. When the binding energy of the deuteron[12] is added to the average of these two quantities, the neutron binding energy of Mg^{25} is found to be 7.334±0.012 Mev.

The neutron binding energy of Mg^{26} cannot be obtained from the energy balance of the (d,p) reaction with Mg^{25} for the group of protons which should

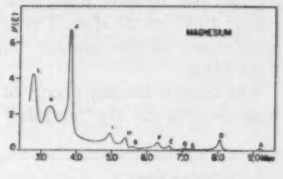

FIG. 10. Corrected γ-ray spectrum from magnesium.

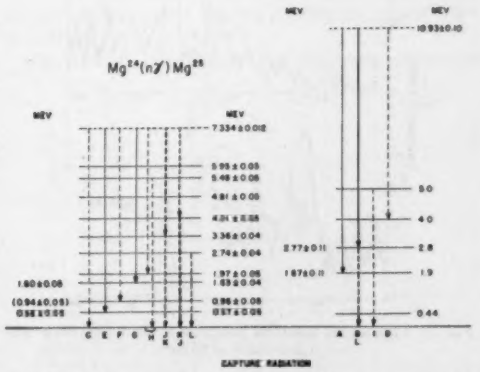

FIG. 11. Decay scheme for the capture γ-rays of magnesium. The level system of Mg^{26} (right-hand figures) is that obtained by Schelberg, Sampson, and Cochran (reference a, Table IV); that of Mg^{25} was obtained from various sources. The positions of the energy levels determined from γ-ray measurements are given on the left.

[16] H. R. Allan and C. A. Wilkinson, Proc. Roy. Soc. (London) **A194**, 131 (1948).

[17] Allan, Wilkinson, Burcham, and Curling, Nature **163**, 210 (1949).

[18] A. P. French and P. B. Treacy, Proc. Phys. Soc. (London) **A63**, 665 (1950).

produce the ground state of Mg^{26} has never been detected. The neutron binding energy, however, can be computed by the addition of the following equations, using the masses of the light nuclei given by Tollestrup, Fowler, and Lauritsen:[19]

$$Mg^{26}+d=Mg^{27}+p+4.21\pm0.1 \text{ Mev},^{17}$$

$$Mg^{27} = Al^{27} +2.64\pm0.05 \text{ Mev},^{20}$$

$$Al^{27}+d=Mg^{25}+\alpha+6.694\pm0.010 \text{ Mev}.^{15}$$

The result is 11.01 ± 0.12 Mev.

An independent estimate may be made from the following equations:

$$Mg^{24}+d=Mg^{25}+p+5.104\pm0.010 \text{ Mev},$$

$$Na^{23}+d=Na^{24}+p+4.731\pm0.009 \text{ Mev},^{15}$$

$$Na^{24} = Mg^{24} +5.53\pm0.01 \text{ Mev},^{21}$$

$$Na^{23}+\alpha=Mg^{26}+p+1.66\pm0.09 \text{ Mev}.$$

The Q value of the last equation, 1.66 ± 0.09 Mev, is a weighted average of the results of Motz,[22] Merhaut,[23] and the value quoted by Livingston and Bethe.[24] For the neutron binding energy of Mg^{26}, we obtain the result: 10.85 ± 0.10 Mev. The mean value for the two calculations of the neutron binding energy is 10.93 ± 0.10 Mev.

The neutron binding energy of Mg^{27} may be obtained from the Q of the $Mg^{26}(d,p)Mg^{27}$ reaction. According to Allan *et al.*,[17] this quantity is 4.21 ± 0.1 Mev, whence the neutron binding energy of Mg^{27} is 6.44 ± 0.1 Mev.

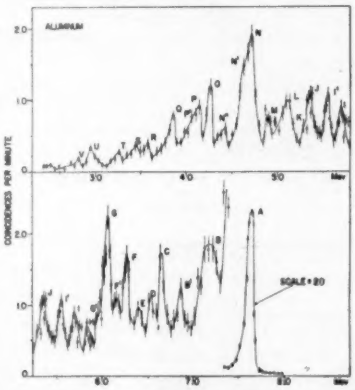

FIG. 12. Coincidence spectrum produced by pure aluminum with a line width of 65 kev.

TABLE V. Energies and intensities of aluminum capture γ-rays.

γ-ray	Energy (Mev)		Difference energy (Mev)		Possible difference γ-ray	Intensity in photons per 100 captures
A	7.724	±0.010	0.00			35
B	7.34	0.04	0.38	±0.04		0.7
B'	6.98	0.04	0.74	0.04		0.7
C	6.77	0.02	0.95	0.02		1.4
D	6.61	0.03	1.11	0.03		0.4
E	6.50	0.03	1.22	0.03		0.4
F	6.33	0.02	1.39	0.02		2
F'	6.22	0.03	1.50	0.03		0.7
G	6.13	0.02	1.59	0.02		2
G'	6.01	0.05	1.71	0.05		0.7
H	5.89	0.04	1.83	0.04		1.0
I	5.78	0.03	1.94	0.03		1.4
I'	5.60	0.02	2.12	0.02		3
J	5.41	0.03	2.31	0.03		3
K	5.32	0.03	2.40	0.03		1.0
L	5.21	0.02	2.51	0.02		3
M	4.94	0.05	2.78	0.05	*V*	1.4
N	4.79	0.02	2.93	0.02		9
N'	4.66	0.05	3.06	0.05	*U*	7
N''	4.45	0.02	3.27	0.02	*T*	3
O	4.29	0.02	3.43	0.02	*S*	8
P	4.16	0.02	3.56	0.02	*R*	6
P'	4.06	0.04	3.66	0.04		3
Q	3.88	0.02	3.84	0.02	*Q*	8
R	3.62	0.02	4.10	0.02		6
S	3.46	0.02	4.26	0.02		4
T	3.29	0.02	4.43	0.02		5
U	3.02	0.05	4.70	0.05		15
V	2.84	0.03	4.88	0.03		13

The results of the binding energy calculations, the abundances of the magnesium isotopes and their contributions to the total neutron absorption cross section, are summarized in Table III.

Only two of the magnesium capture γ-rays have energies which might be identified with the neutron binding energies. A weak γ-ray is indicated at *C* in Fig. 9, for which the energy is 7.37 ± 0.08 Mev in agreement with the binding energy of the neutron in Mg^{25}. The statistics, however, are not good enough to establish its presence with certainty. No γ-ray near 11 Mev has been found to correspond with the neutron binding energy in Mg^{25} (10.93 Mev). A γ-ray with an energy of 11 Mev would have been detected if its intensity were 0.2 quantum per 100 captures or greater. The γ-ray *F*, which has an energy of 6.39 ± 0.05 Mev, may represent the transition to the ground state in Mg^{27}. The intensity of this γ-ray is of the order of 0.05 photon per capture. Now the total absorption cross section of magnesium[9] is 58 ± 6 mb, and the contribution to this cross section due to the capture of neutrons in Mg^{26} is[4] 5.4 ± 1.0 mb, i.e., about 10 percent of the total. If, then, the γ-ray *F* is due to capture in Mg^{26}, it must account for about one-half of the cross section due to that isotope. As will be shown below, an alternative explanation for *F* is possible.

The energies of the excited states of Mg^{25} and Mg^{26} have been measured in a number of ways and by different authors; the results are summarized in Table IV.

[19] Tollestrup, Fowler, and Lauritsen, Phys. Rev. **78**, 372 (1950).
[20] Benes, Hedgran, and Hole, Arkiv. Mat. Astron. Fysik **35**, No. 12 (1949). The errors in the decay energies of Mg^{27} and Al^{28} are not given in the text of that paper and those quoted above are our estimates. Motz and Humphreys (see reference 30), quoting these results, give much larger errors.
[21] K. Siegbahn, Phys. Rev. **70**, 127 (1946).
[22] H. T. Motz, private communication.
[23] O. Merhaut, Physik. Z. **41**, 528 (1940).
[24] M. S. Livingston and H. A. Bethe, Revs. Modern Phys. **9**, 245 (1937).

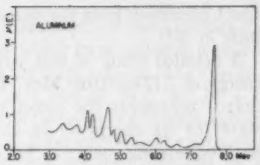

FIG. 13. Corrected γ-ray spectrum from aluminum.

The positions of the excited states of Mg^{25} appear to be well defined by the measurements listed in Table IV. Our present knowledge of Mg^{26} is less satisfactory; in that isotope only two levels, near 1.9 and 2.8 Mev, have been detected and measured by more than one experimenter. These levels were also reported by Pollard and Humphreys[25] in an investigation of the $Mg^{25}(d,p)Mg^{26}$ reaction, but it is doubtful if their results really refer to Mg^{26} for Allan and co-workers,[17] using a target of separated Mg^{25}, failed to detect any proton groups which could not be ascribed to the $Mg^{24}(d,p)Mg^{25}$ reaction. The level energies in the third column are the results of König[26] and of May and Vaidyanathan,[27] corrected by Livingston and Bethe.[24] The existence of the two levels at 4 and at 5 Mev has not been confirmed.

No excited states are known in Mg^{27}. Allan and co-workers[17] have studied the $Mg^{26}(d,p)Mg^{27}$ reaction using magnesium enriched in Mg^{26}, but did not report groups with energy less than that of the ground-state group for which the Q is 4.21 Mev.

In Fig. 11 an attempt has been made to fit the capture γ-rays into a level scheme based on the excitation energies listed in Table IV. In those cases where there seems to be little doubt of the γ-ray assignment the transition is represented by a full line and the level energy obtained from the γ-ray energies and the value of the binding energy in Table III is given on the left of the diagram. The level energies shown on the right are those reported by Schelberg, Sampson, and Cochran for Mg^{25}, and by Motz, and Livingston and Bethe for Mg^{26}.

Only the γ-rays A and B can be fitted with certainty into this scheme. They have energies greater than the binding energies of Mg^{25} and Mg^{27} and they must be due, therefore, to Mg^{26}. Assuming that the neutron binding energy of Mg^{26} is 10.93±0.10 Mev, these γ-rays can be accounted for in terms of transitions to excited states at 1.67±0.11 and 2.77±0.11 Mev, values which are in agreement with those given in Table IV. The strong γ-ray L appears to be the product of the transition from the latter state to the ground state. One other possible location for L is shown in the Mg^{25} scheme and yet others are possible which involve transitions between intermediate excited states.

There is little doubt concerning the assignment of the γ-rays E and G. Assuming that the neutron binding energy is that given in Table III and subtracting from this quantity the energies of these γ-rays, we obtain excited states in Mg^{25} at 0.58±0.05 and 1.60±0.05 Mev in good agreement with the level energies reported by Schelberg *et al.* In a similar manner, the γ-ray F, which, as pointed out above, can represent the ground-state transition in Mg^{27}, can also be accounted for by a transition in Mg^{25} leading to an excited state at 0.94 ±0.05 Mev. It is possible that contributions to the coincidence peak at F are made by both these transitions; this point, however, can only be settled after more accurate measurements have been made of the energy of the γ-ray F and the binding energies of Mg^{25} and Mg^{27}.

The γ-ray H can be fitted into the decay scheme for

TABLE VI. Energies of the excited states of Al^{28} in Mev.

Whitehead and Heydenburg[a]	Pollard, Sailor, and Wyly[b]	Allan and Wilkinson[c]	Allan and Clavier[d]	Present work
1.01	1.03	1.00	1.00	0.95±0.02
1.37				1.39 0.02
1.65	1.57	1.48		1.59 0.02
2.23	2.16	2.15	2.15	2.12 0.02
2.67	2.61			2.51 0.02
3.03	2.97			
3.33	3.41			
3.64				
4.03	3.90			
	4.47			
4.78	4.72			
	4.88			
5.02	5.16			
5.26				
	5.44			
5.68	5.76			
				6.98 0.04
				7.34 0.04

[a] See reference 13.
[b] See reference c, Table IV.
[c] See reference 16.
[d] See reference 28.

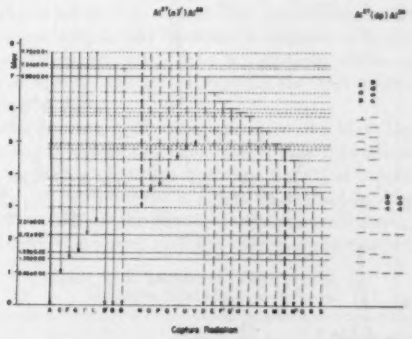

FIG. 14. Decay scheme for the capture γ-rays of aluminum. The positions of the energy levels of Al^{28} obtained from (d,p) reactions is given on the right; W and H: Whitehead and Heydenburg (reference 13); P, S and W: Pollard, Sailor, and Wyly; A and W: Allan and Wilkinson (reference 16); A and C: Allan and Clavier (reference 28). The positions of the energy levels obtained from the γ-ray measurements are shown on the left.

[25] E. C. Pollard and R. F. Humphreys, Phys. Rev. **59**, 466 (A) (1941).
[26] A. König, Z. Physik **90**, 197 (1934).
[27] A. N. May and R. Vaidyanathan, Proc. Roy. Soc. (London) **A155**, 519 (1936).

Mg^{25} in two ways. The γ-ray I is less easy to fit into a scheme for Mg^{25} and probably represents the de-excitation of the 5-Mev level in Mg^{26}.

The γ-ray J is remarkable in that its intensity, with the exception of that of L, is five times as great as that of any other radiation in the spectrum. The measured intensity of J is nearly one quantum per capture unless two γ-rays of equal energy contribute to the coincidence peak observed. This intensity is clearly much too high. While it is possible for J to originate in a cascaded pair of γ-rays in Mg^{26}, both components must possess the same energy for the profile of the coincidence peak has the width characteristic of a monochromatic γ-ray.

The sum of the energies of γ-rays J and K is 7.37 $\pm$0.09 Mev in agreement with the energy of γ-ray C. This suggests that J is produced by capture of neutrons in Mg^{24}. The level energies given by Schelberg *et al.* provide two possible routes for such a cascade process and these are shown in Fig. 11. However, while a considerable γ-ray intensity is associated with the peak at K, the energy is not well defined and it is not possible to choose between these alternatives.

IX. ALUMINUM

The sample was a cylinder of the pure metal, six inches long and four inches in diameter. Impurities were believed to be present in a total concentration of less than 0.01 percent by weight. The coincidence spectrum obtained with a line-width of 65 kev is shown in Fig. 12. There is only one stable isotope in aluminum, Al^{27}; hence the entire spectrum is due to the de-excitation of Al^{28}. The most significant feature of the spectrum is the predominance of the γ-ray A which corresponds to a direct transition from the capturing state to the ground state in Al^{28}.

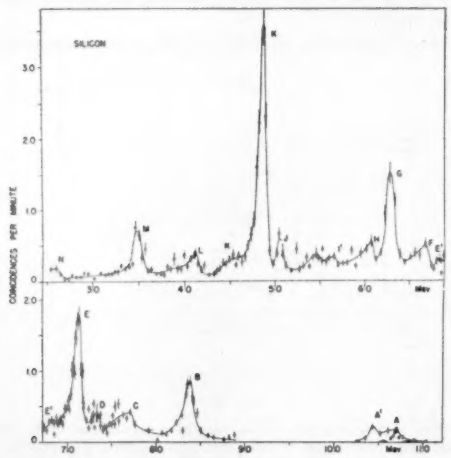

FIG. 15. Coincidence spectrum of silicon. The coincidence peak with an end point near 10.8 Mev is due to nitrogen; the measurements represented by the full circles were made under similar conditions with the silica sample withdrawn.

A detailed study of this γ-ray shows that it has an energy of 7.724$\pm$0.010 Mev. There can be little doubt that it represents the direct transition to the ground state for its energy is in good agreement with the neutron binding energy in Al^{28} deduced from the energy balance in the (d,p) reaction. From the Q value obtained by Allan and Clavier,[28] the neutron binding energy found by the addition of the binding energy of the deuteron, is 7.73 Mev; from Allan and Wilkinson,[16] 7.69 Mev; from Pollard, Sailor, and Wyly, 7.68 Mev; and from Whitehead and Heydenburg,[13] 7.95 Mev. Recently, accurate measurements have been made by Enge, Van Patter, Buechner, and Sperduto,[29] using a magnetic method of analysis; they find a Q value of 5.494$\pm$0.010 Mev, which is equivalent to a neutron binding energy of 7.724$\pm$0.012 Mev, in very good agreement with our measurements. These authors have found an excited state in Al^{28} only 31 kev above the ground state. The γ-ray A may well consist of two components which differ in energy by this amount, but the resolution of Fig. 12 is not sufficient to reveal them.

TABLE VII. Energies and intensities of silicon capture γ-rays.

γ-ray	Energy in Mev	Intensity in photons per 100 captures
A'	10.55$\pm$0.05	0.4
B	8.51 0.04	4
C	7.79 0.05	1
D	7.36 0.08	2
E	7.18 0.03	9
E'	6.88 0.03	0.7
F	6.76 0.04	4
G	6.40 0.03	19
H	6.11 0.05	4
I'	5.70 0.04	2
I	5.52 0.05	2
J	5.11 0.04	9
K	4.95 0.03	112
K'	4.60 0.08	4
L	4.20 0.03	19
M	3.57 0.06	94
N	2.69 0.05	65

The absolute intensity of the γ-ray A was measured by the nickel method. Assuming that the cross section of aluminum is 212 mb we find that the intensity of this γ-ray is 0.35 photon per capture. The predominance of this γ-ray in the aluminum spectrum is well shown in Fig. 13, which is the corrected γ-ray spectrum obtained from Eq. (3), for a line width of 130 kev.

The energies and the intensities of the aluminum γ-rays are listed in Table V. The first column contains the designation of the γ-ray according to Fig. 12, the second, its energy, and the third the difference between its energy and that of the γ-ray A (the binding energy). In some cases, these differences represent the energies

[28] H. R. Allan and C. A. Clavier, Nature **158**, 832 (1946).
[29] Enge, Van Patter, Buechner, and Sperduto, Phys. Rev. **81**, 317 (1951).

of known excited states. The fourth column contains the designation of the γ-rays which have an energy nearly equal to the difference in the third column. The energies of a pair of γ-rays, such as V and M, or U and N', add to give the energy of A, and these γ-rays, therefore, may be in cascade. The fifth column contains the intensity of the γ-rays in photons per capture, obtained by a comparison of the intensity relative to that of the γ-ray A.

The positions of the energy levels of Al^{28} at the present time are known only from the results of investigations of the (d,p) reaction. The results of four investigators are listed in Table VI. There is general agreement on the positions of the excited states up to 3 Mev, but above this energy agreement is less satisfactory. The experiments of Whitehead and Heydenburg seem to have been performed with a greater resolution than that of Pollard, Sailor, and Wyly; and above 3 Mev, for this reason, their results are to be preferred although their Q value for the ground-state transition in the (d,p) reaction differs widely from the rest.

With the aid of these results, and with that of similar data kindly furnished by Dr. D. M. Van Patter, the capture γ-rays have been fitted into the decay scheme shown in Fig. 14. This can be done with some assurance for the higher energy γ-rays since they probably represent transitions from the capturing state to levels up to 3 Mev. Of these, the γ-rays, C, F, G, I', and L represent transitions to the first five excited states given by Whitehead and Heydenburg. The remaining γ-rays in this energy range, from B at 7.34 to K at 5.32 Mev, cannot be emitted by the capturing state. The broad coincidence peak B, which must represent more than one γ-ray, is of interest, for it is unlikely that it represents transitions from the capturing level to a group near 0.4 Mev, no level at this energy having been detected in the (d,p) process. The γ-rays B must, therefore, be direct transitions from levels with high excitation to the ground state. These levels must be excited by transitions of only 0.4 Mev from the capturing state.

The strong γ-ray N has an energy of 4.79±0.02 Mev. It could be ascribed to a transition between the 7.72-Mev level and a state known to exist near 3.0 Mev, or it could represent the transition between a level at 4.78 Mev to the ground state. The latter level was found by Whitehead and Heydenburg and is produced by a strong group of protons from the (d,p) reaction.

The relatively strong γ-rays, O, P, and Q can be accounted for in terms of transitions to levels rather less well established between 3.4 and 3.9 Mev. The remaining γ-rays are harder to interpret in a reliable way. The lower energy γ-rays are poorly resolved, and while some of them can be accounted for as transitions to the ground state from known excited states, in many cases there are other alternatives. A distinction between these alternatives cannot be made on the basis of the present data

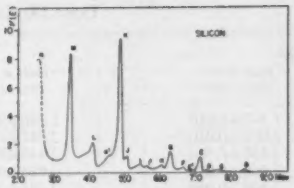

FIG. 16. Corrected γ-ray spectrum from silicon.

The positions of the energy levels deduced from the differences between the γ-ray energies and the binding energy has been included in the fifth column of Table VI where the identification is clear.

The contribution of the aluminum γ-rays to the total energy radiated is 6.7 Mev per capture. This low result, like that obtained with magnesium, suggests that many γ-rays are emitted with escape detection. The integrated energy [Eq. (4)] is 10.2 Mev.

X. SILICON

The silicon source consisted of chemically pure silicic acid. The amount of silicon in the material used was estimated by driving off the water in chemical combination at 1000°C and assuming that the remainder was pure silica, SiO_2. Impurities were present in too low a concentration to affect the gamma-ray spectrum. Two separate surveys of the spectrum were made with the two types of sample container described above. The Dural spectrum seriously interfered with that of the silicon, and the results of the first experiment (with Dural end walls in the container) could only be used to confirm the energy measurements of the stronger γ-rays obtained from the second.

The silicon spectrum is shown in Fig. 15, which contains the results of the second experiment only. The region from 8.8 to 10 Mev is not covered, since the first experiment revealed the presence of no radiations above background in this region. One interesting feature of this spectrum is that radiation A appears to be double. The low energy component is a genuine silicon γ-ray, for its energy is in agreement with the neutron binding energy of Si^{30}.

The more energetic component, at 10.8 Mev, has the binding energy of a neutron in N^{15}. That nitrogen in the air in the experimental hole (see Fig. 1) is indeed the origin of the γ-ray A, is shown in Fig. 15 by the full circles which are the results of measurements made with the same pile power with the silicon sample withdrawn

TABLE VIII. Abundances, cross sections, and binding energies of silicon isotopes.

Target	Abundance percent	Contribution to cross section in millibarns	Binding energy product nucleus of in Mev
Si^{28}	92.2		8.476±0.013
Si^{29}	4.7	156[a]	10.53 ±0.10
Si^{30}	3.1	4[b]	6.597±0.014

[a] Reference 3. [b] Reference 4.

TABLE IX. Energies of the excited states of Si^{29}, Si^{30}, and Si^{31} in Mev.

Si^{29}							
Endt *et al.*[a] $Si^{28}(d,p)Si^{29}$		Endt *et al.*[a] $P^{31}(d,\alpha)Si^{29}$		Motz, Humphreys[b] $Si^{28}(d,p)Si^{29}$	Allan, Wilkinson[c] $Si^{28}(d,p)Si^{29}$	Seidlitz *et al.*[d] $Al^{29}(\beta)Si^{29}$	
1.273±0.010		1.286±0.020		1.29±0.04	1.29	1.25±0.20	
2.022±0.010		2.044±0.020		2.06±0.04	2.00		
2.426±0.010		2.443±0.020		2.43±0.04	2.41	2.35±0.20	
3.066±0.010		3.084±0.020		3.08±0.05			
3.620±0.010		3.631±0.020		3.60±0.05			
		4.090±0.020		4.09±0.06			
4.934±0.010		4.959±0.020		4.87±0.10			
Si^{30}							
Pollard, Humphreys[e] $Si^{29}(d,p)Si^{30}$	Motz, Humphreys[b] $Si^{29}(d,p)Si^{30}$	Landon[f] $Si^{29}(d,p)Si^{30}$	Livingston, Bethe[g] $Al^{27}(\alpha,p)Si^{30}$	Benson[h] $Al^{27}(\alpha,p)Si^{30}$	Brolley *et al.*[i] $Al^{27}(\alpha,p)Si^{30}$	Merhaut[j] $Al^{27}(\alpha,p)Si^{30}$	Alburger[k] γ-rays $Al^{27}(\alpha,p)Si^{30}$
0.9							
1.0							
2.8	2.4 ±0.2	2.4	2.28	2.28		2.24	
3.6	3.91±0.15	3.7	3.58	3.66	3.49	3.40	3.5±0.3
			4.75	4.6			
	5.00±0.15	5.0					
	5.7 ±0.2				5.44		
					7.18		
					8.20		
					9.26		
					9.87		
					10.86		
Si^{31}							
	Motz, Humphreys[b] $Si^{30}(d,p)Si^{31}$		Metzger *et al.*[l] $P^{31}(n,p)Si^{31}$		Van Patter *et al.*[m] $Si^{30}(d,p)Si^{31}$		
	0.73±0.15		0.7±0.2		0.763±0.011		
	1.23±0.15						
	1.73±0.15				1.701±0.10		
	2.33±0.15						

[a] See reference 31.
[b] See reference 30.
[c] See reference 16; the 4.16-Mev Q-value obtained by these authors is assumed to correspond to the excited state at 2.00 Mev in Si^{29}, following Motz and Humphreys.
[d] Seidlitz, Bleuler, and Tendam, Phys. Rev. **76**, 861 (1949).
[e] See reference 25.
[f] H. H. Landon, Phys. Rev. **78**, 338 (A) (1950).
[g] See reference 24.
[h] See reference 36.
[i] See reference 35.
[j] O. Merhaut, Z. Physik **115**, 77 (1940).
[k] See reference i, Table IV.
[l] Metzger, Alder, and Huber, Helv. Phys. Acta **21**, 278 (1948).
[m] See reference 34.

from the hole. Both the peak coincidence counting rate of A and its energy have the values to be expected of the ground-state γ-ray produced by capture in nitrogen.

The energies and intensities of the silicon radiations are given in Table VII. The intensities were determined by the nickel calibration method. The corrected γ-ray spectrum of silicon is shown in Fig. 16.

The stable silicon isotopes are Si^{28}, Si^{29}, and Si^{30}. The binding energy of Si^{29} may be obtained from the Q-value of the (d,p) reaction after addition of the binding energy of the deuteron. For the former, Allan and Wilkinson[16] obtained 6.16±0.06 Mev and Motz and Humphreys[30] have obtained 6.18±0.09 Mev. Recently, the M.I.T. group[31] have found the more accurate value 6.246±0.010 Mev, from which it may be deduced that the binding energy of Si^{29} is 8.476±0.013 Mev.

The group of protons producing the ground state of Si^{30} in the reaction $Si^{29}(d,p)Si^{30}$ has recently been measured by Motz and Humphreys,[30] who find a Q value of 8.36±0.10 Mev, which is equivalent to a binding energy in Si^{30} of 10.59±0.10 Mev. The same quantity may be estimated from the Q's of other reactions in two ways with an accuracy better than that obtained from the (d,p) measurements. By adding the equations:

$$P^{31}+d=Si^{29}+\alpha+8.170\pm0.020 \text{ Mev},^{31}$$

$$Si^{30}+d=Si^{31}+p+4.364\pm0.010 \text{ Mev},^{15}$$

$$Si^{31}=P^{31}+1.50\pm0.02 \text{ Mev},^{32}$$

the neutron binding energy of Si^{30} is found to be 10.60 ±0.06 Mev. Again, the addition of the following equations:

$$Si^{30}+d=Al^{28}+\alpha+3.120\pm0.010 \text{ Mev},^{15}$$

$$Si^{28}+d=Si^{29}+p+6.246\pm0.010 \text{ Mev},^{31}$$

$$Al^{28}=Si^{28}+4.81\pm0.05 \text{ Mev},^{20}$$

leads to a neutron binding energy of 10.37±0.06 Mev. This result is appreciably less than the previous one and the discrepancy may arise from an overestimate of the decay energy of Al^{28}. For this quantity, the result used above, *viz.*, that obtained by Benes *et al.*,[20] is much

[30] H. T. Motz and R. F. Humphreys, Phys. Rev. **80**, 595 (1950).
[31] Endt, Van Patter, and Buechner, Phys. Rev. **81**, 317 (1951).
[32] H. W. Newson, Phys. Rev. **51**, 624 (1937).

higher than that obtained by Bleuler and Zünti, but it should be much more accurate.

The neutron binding energies of Si^{29} and Si^{30} may also be calculated from the masses obtained by Duckworth and his associates[33] and from the mass of the neutron given by Tollestrup, Fowler, and Lauritsen. For the binding energy of Si^{29} we obtain 8.46±0.15 Mev, and for that of Si^{30}, 10.95±0.19 Mev. The first of these values is in good agreement with that obtained from the (d,p) reaction, but the second is much higher.

The Q values obtained for the $Si^{30}(d,p)Si^{31}$ reaction are in good agreement. Motz and Humphreys[30] obtained 4.33±0.15 Mev, and more recently the M.I.T. group[34] have found 4.364±0.010 Mev. The latter figure leads to 6.597±0.012 Mev for the neutron binding energy in Si^{31}. Allan and Wilkinson[16] obtained 4.16 ±0.06 Mev, a value which, as pointed out by Motz and Humphreys,[30] is probably due to $Si^{28}(d,p)Si^{29}$.

The binding energies of the silicon isotopes relevant to the present discussion are collected in Table VIII. For the binding energies of Si^{29} and Si^{31} we have chosen the M.I.T. values as probably the most accurate; for that of Si^{30}, we have taken a weighted mean of all the results calculated above.

The most energetic silicon γ-ray, A' in Table VII, has an energy of 10.55±0.05 Mev and clearly corresponds to the ground-state transition in Si^{30}. The γ-ray B, with an energy of 8.51±0.05 Mev, is probably the ground-state transition in Si^{29} for its energy is in agreement with the neutron binding energy of that isotope. However, this identification cannot be regarded as established, for there is good evidence for the existence of an excited state in Si^{30} near 2.3 Mev (Table IX), and it is not impossible that B may be associated with a transition to this level following capture in Si^{29}. The only γ-ray near 6.6 Mev which would correspond to a transition to the ground state in Si^{31}, is the γ-ray F (6.76±0.04 Mev). This would seem to have too high an energy. The intensity of F is only 4 photons per 100 captures, which is what is to be expected if all the energy produced by capture in Si^{30} were concentrated in one γ-ray. Thus, unless a large proportion of the captures in Si^{30} produced the 6.6-Mev γ-ray, the capture radiation of that isotope would probably not be detected by the present apparatus. No γ-rays leading to the excited states of Si^{31} (see Table IX) can be identified in Fig. 15.

The energies of the excited states of the silicon isotopes are listed in Table IX, and in Fig. 17 an attempt has been made to fit the capture γ-rays to the known levels of Si^{29} and Si^{30}. The positions of the excited states of Si^{29} have been obtained by Endt *et al.*,[31] in two different reactions and the results are consistent within themselves and with those of other experimenters. In Si^{30}, there is general agreement about the existence of levels

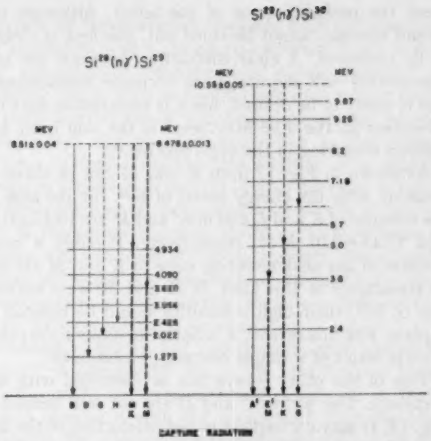

FIG. 17. Decay scheme for the capture γ-rays of silicon. The positions of the energy levels of Si^{29} are those obtained by Endt and co-workers (reference 31), from a study of the (d,p) reaction. The energies of the levels of Si^{30} from 7.18 Mev upwards, are those given by Brolley, Sampson, and Mitchell (reference 35), and below that energy, a mean value of the results of various experimenters.

near 2.3 and 3.6 Mev, and some evidence for another near 4.6 Mev. There is a well-established level near 5.0 Mev and another, according to Motz and Humphreys, at 5.7 Mev. From 5.4 Mev upwards a series of levels have been reported by Brolley, Sampson, and Mitchell[35] of which the energies are based on results obtained by Benson.[36]

The outstanding feature of Figs. 15 and 16 is the strength of the two γ-rays K and M, which have a comparable intensity and are much stronger than any others in the spectrum. The sum of the energies of these two γ-rays is 8.52±0.07 Mev, which is in very good agreement with that of the γ-ray B and with the neutron binding energy in Si^{29}. It follows that the greater part of the silicon capture cross section is due to Si^{28} and leads to the emission of these two γ-rays. They can be fitted into the scheme of Fig. 17 in two ways. (1) The γ-ray K, 4.95±0.03 Mev, can represent a transition to the ground state from the level with the energy of 4.934±0.010 Mev (see Table IX). The γ-ray M, 3.57±0.06 Mev, could therefore, represent a transition from the capturing state to this level; subtracting the energy of that level from the binding energy (Table VIII) we obtain 3.542±0.015 Mev, which differs from that of M by only 28 kev. (2) M may also be identified with a transition to the ground state from the level at 3.620±0.010 Mev. K could then be due to the transition from the capturing state to this level; the energy difference in this case is 4.856±0.015 Mev. This quantity is less than the energy of K by nearly 100 kev or three

[33] Duckworth, Preston, and Woodcock, Phys. Rev. **79**, 188 (1950). H. E. Duckworth and R. S. Preston, Phys. Rev. **79**, 402 (1950).
[34] Van Patter, Enge, and Buechner, Phys. Rev. **82**, 304 (1951).
[35] Brolley, Sampson, and Mitchell, Phys. Rev. **76**, 624 (1949).
[36] B. B. Benson, Phys. Rev. **73**, 7 (1948).

times the probable error of the latter. Although the second scheme cannot be ruled out, the first is clearly to be preferred. A clear distinction between the two alternatives will require more accurate measurement and is much to be desired, for it is remarkable that the excitation of the 4.93-Mev level is the one most frequently occurring in the (d,p) process.[30]

As shown in Fig. 17 both K and M can be made to combine with the energy levels of Si^{30}, for the sum of the energies of K and I, and of E' and M are 10.47 ± 0.06 and 10.45 ± 0.07 Mev, respectively. Possibly a small fraction of the peak counting rates of K and M are due to transitions of this kind. If K and M were entirely due to Si^{30}, their high intensities would be difficult to explain. For this reason, it is better to assume that they are the result of a simple cascade process in Si^{29}.

Few of the other γ-rays can be identified with any certainty. The γ-rays C and D are not well defined in Fig. 15. D may correspond to the production of the first excited state in Si^{29}; if this is true, the energy of this excited state is 1.12 ± 0.09 Mev which is not in good agreement with the value found by Endt *et al.*, *viz.*, 1.273 ± 0.010 Mev. The γ-rays G and H correspond to transitions leading to excited states at 2.08 ± 0.05 and 2.36 ± 0.06 Mev, respectively, in only fair agreement with the positions of the energy levels given in Table IX. A part of G may also be associated with L, for the sum of L and G is 10.60 ± 0.05 Mev, in agreement with the neutron binding energy of Si^{30}. This assignment would introduce a level at 6.4 Mev which is not substantiated by any other evidence.

It is clear from a consideration of Table VII and Fig. 17 that the sum of the intensities of the γ-rays emitted by silicon exceeds the rate of neutron capture. The sum of the energies of the γ-rays of Table VII is $S=15.5$ Mev, which greatly exceeds the highest binding energy in the Si isotopes. The computation of S ignores the unresolved background; when this is taken into account, the integrated energy is $S'=23$ Mev.

XI. DISCUSSION

The large number of γ-rays observed from aluminum seems remarkable at first sight. However, the resolution used in this case (65 kev) was twice that employed with the other elements. The relative simplicity of the spectra obtained from magnesium and silicon may be due to the lower neutron capture rate used with these elements (18 percent of the aluminum capture rate for magnesium and 7 percent for silicon). If it had been possible to increase the amount of sample material to give a capture rate similar to that of aluminum, it is possible that the low intensity backgrounds of Figs. 9 and 15 could have been examined with 65-kev resolution and many more γ-rays would have been detected. However, this is not true of sodium, where the neutron capture rate was about 50 percent of that of the aluminum sample.

The sharp contrast between the strong transitions to the ground states in fluorine and aluminum and the weak transitions in sodium, magnesium, and silicon calls for some comment.

The relatively high absolute intensity of the fluorine γ-ray and the existence[8] of numerous excited states in F^{20} between the ground state and the neutron binding energy, suggest, by analogy with the aluminum spectrum, that the 6.63-Mev γ-ray is predominant in the spectrum of fluorine. This would place fluorine among the few nuclei which produce, in the product nuclei, strong transitions leading directly to the ground states.[37] The capturing state of F^{20} which is responsible for the emission of the γ-ray must have a spin of 0 or 1 and even parity, for it seems to be established from a consideration of the spin (1/2) and magnetic moment of F^{19} and of the angular correlation of the γ-rays and α-particles in the $F^{19}(p,\alpha)O^{16}$ reaction,[38] that the parity of F^{19} is even. Recently, a weak β-transition has been observed[39] between the ground states of F^{20} and Ne^{20} and if this transition is second forbidden, as its intensity would indicate, the parity of the ground state of F^{20} is even and the spin is 2 or 3. It follows that the 6.63-Mev γ-ray produces no change in parity and therefore is of the magnetic dipole or electric quadrupole type. This capture γ-ray is one of the very few for which it is possible, at the present time, to determine the order of multipolarity on the basis of experimental rather than theoretical evidence.

The strong transition to the ground state of Al^{28} seems to be of the same multipole order as that of the γ-ray from F^{20}, for recently, Butler,[40] from a consideration of the angular distribution of the protons, has shown that the production of Al^{28} in its ground state from the (d,p) reaction occurs with the transfer of a neutron with zero orbital angular momentum. The spin of Al^{27} being 5/2, it follows that the spin of Al^{28} is 2 or 3, and its parity is the same as that of Al^{27}. These results are consistent with the β-disintegration of Al^{28} for the β-rays which pass to the ground state of Si^{28} have not been detected and must be at least first forbidden.

It seems possible to account for the absence, or weakness, of the ground-state transition which follows the capture of neutrons in sodium in terms of the high angular momentum which would be radiated in that γ-ray. The spin of the level responsible for the first neutron resonance in sodium at 3 kev is 2 units[41] and it is probable that this state is the one most frequently excited by neutrons at thermal energies. Now the half-life and β-decay energy of Na^{24} correspond to a first-forbidden transition which is followed by the successive emission of two γ-rays from excited states in Mg^{24}. The spin of the uppermost state excited in this sequence is probably 4 and that of the lower state, probably 2 units.

[37] Kinsey, Bartholomew, and Walker, Phys. Rev. **78**, 481 (1950).
[38] Barnes, French, and Devons, Nature **166**, 145 (1950).
[39] R. M. Littauer, Phil. Mag. **41**, 1214 (1950).
[40] S. T. Butler, Phys. Rev. **80**, 1095 (1950).
[41] Hibdon, Muehlhause, Selove, and Woolf, Phys. Rev. **77**, 730 (1950).

Recently, Grant[42] has attempted to detect the β-transition to the lower level of Mg^{24} and has shown that it must be at least three degrees more forbidden than that to the higher level. He has concluded that the decay of Na^{24} is consistent, on the current theories of β-disintegration, only with the observed β-decay being of the allowed-unfavored type, the spin of Na^{24} in its ground state being 5 units. If this is true, it follows that the capture γ-ray producing Na^{24} in its ground state must radiate 3 units of angular momentum. This should be sufficient to forbid its emission to a high degree. The parity change, however, associated with this radiation cannot be directly determined.

The weakness of the magnesium and silicon ground-state γ-rays are difficult to explain in terms of changes in parity or spin. The spin of the even isotopes of magnesium being zero, and that[43] of Mg^{25} being 5/2, a minimum of two units of angular momentum must be radiated in the direct transition to the ground state. That required for the ground-state transition in Mg^{26} is two or three depending on the orientation of the spin of Mg^{25} at the resonance responsible for the thermal neutron capture. The spin changes involved in the silicon γ-rays are not known, for the spin of Si^{29} is not established with certainty. If the spin[44] of Si^{29} is 1/2, spin changes alone will not account for the weakness of the ground-state transition in Si^{29} due to the capture of neutrons in Si^{28}. The same is true in Si^{30}, for the intensity of the ground-state γ-ray (A') is weak compared with that of the other γ-rays ascribed to this isotope. Probably for both magnesium and silicon, the origin of the weakness of the ground state γ-rays is to be found in specific properties of the ground states other than those concerned with spin and parity.

The recent measurements on the angular distribution of the (d,p) reaction in aluminum would seem, at first sight, to provide a clue to the solution of this problem. As pointed out above, Butler[40] has shown that Al^{28} is formed in its ground state by addition to Al^{27} of a neutron without orbital angular momentum. Now if we consider an extreme independent particle model of the nucleus, in which the motions of the nucleons are still independent at excitation energies in the neighborhood of the neutron binding energy, and if, in addition, we assume that the spin of the ground state of an odd nucleus is determined by the total angular momentum of the odd nucleon, it follows that the resonance responsible for the capture of a thermal neutron must correspond to a configuration in which the neutron enters an s-orbit, for the neutron can contribute no orbital angular momentum. Both the capturing state and the ground state in Al^{28} contain s-orbits for the unpaired neutron and from experiment we know that the transition between them is a probable one. This unusual combination of circumstances suggests that the condition for the emission of a strong ground-state γ-ray is that the ground-state configuration should contain an s-neutron orbit. Such an hypothesis clearly cannot apply to those heavier nuclei which produce strong ground-state γ-rays and to which, according to the current theories of shell structure, the addition of a neutron produces a change of parity. It also does not account for the intensities of the ground-state γ-rays of fluorine and of the silicon isotopes. However, it does seem to explain the weakness of the magnesium ground-state γ-rays and those of other elements for which the shell structure theories indicate that there is no difference in parity between adjacent isotopes.

The spin of Mg^{25} is 5/2 and, from the shell scheme of Mayer,[45] is presumably due to the 13th neutron being in a $d_{5/2}$-orbit, the subshell being completed in Mg^{26}. This is consistent with the assumption that the 13th proton in the aluminum isotopes is in a $d_{5/2}$-orbit for the positron decay of Al^{25} and Al^{26}, which are both super-allowed, occur without the emission of γ-radiation, showing that the wave function of the odd neutron and proton are very similar. Thus the weakness of the ground-state γ-ray in Mg^{25} and the failure to detect the corresponding γ-ray in Mg^{26} may be explained on the hypothesis discussed above as being due to a transition between an s- and a d-neutron orbit.

The capture of neutrons by Mg^{26} might be expected to follow a course similar to that of Al^{27}, for the latter differs from the former only by the presence of a proton. We have already discussed the possibility that the γ-ray produced by the direct transition to the ground state in Mg^{27} may be a strong one, and we have pointed out that further measurements are required to settle this point. If the 15th neutron in Mg^{27} is in an s-orbit, the forbidden nature of the β-decay of that nucleus to the ground state of Al^{27} is easily understood, and this mode of disintegration, like the similar one in Al^{28}, is at least first and probably second forbidden.

If the spin of Si^{29} is 1/2 and the 15th and 16th neutrons in Si^{29} and Si^{30} are in s-orbits, strong ground-state γ-rays might be expected from these nuclei contrary to the results of experiment. The value 1/2 for the spin of Si^{29} is consistent with the assumption that the proton in the phosphorus isotopes is in a similar orbit, for the spin of P^{31} (which has an even number of neutrons) is 1/2 and the super-allowed positron disintegration of P^{29} shows that the orbit of the 15th proton in that nucleus is identical with that of the 15th neutron in Si^{29}. If, on the contrary, we assume that the neutron in Si^{29} is in a $d_{3/2}$-orbit, it follows that the odd proton in the phosphorus isotopes must change from a $d_{3/2}$ to an $s_{1/2}$-level at P^{31}. The possibility of such re-arrangements has been discussed by Nordheim.[46]

While there is, as yet, no confirmation of this re-ar-

[42] P. J. Grant, Proc. Phys. Soc. (London) **63**, 1298 (1950).
[43] Crawford, Kelly, Schawlow, and Gray, Phys. Rev. **76**, 1527 (1949).
[44] Townes, Mays, and Dailey, Phys. Rev. **76**, 700 (1949).
[45] M. G. Mayer, Phys. Rev. **78**, 16 (1950).
[46] L. W. Nordheim, Phys. Rev. **75**, 1894 (1949).

rangement in the phosphorus isotopes, there is evidence that the configuration of the odd proton changes in the fluorine isotopes with increasing neutron content. For the super-allowed positron disintegrations of F^{17} and F^{18} suggest that the unpaired protons in these nuclei are converted into neutrons in the same orbit in the corresponding oxygen isotopes. But the spin[40] of O^{17} is probably 3/2 or 5/2 showing that the unpaired proton in F^{17} is in a *d*-orbit. The spin of F^{19}, however, which has an even number of neutrons, is 1/2 and its parity and magnetic moment clearly show that the unpaired proton in this isotope is in an *s*-orbit. The strength of the fluorine ground-state transition is difficult to explain on the basis of the hypothesis discussed above. If the forbidden nature of the β-decay between the ground states of F^{20} and Ne^{20} means that the spin of the former nucleus is 2 or 3 units, one would expect that the odd neutron in F^{20} is in a $d_{3/2}$-orbit and that the addition of a neutron to F^{19} should produce a weak ground-state γ-ray. Therefore, the criterion for a strong ground-state γ-ray suggested by aluminum, *viz.*, that in the ground state of the product nucleus, the last neutron should be an *s*-orbit, does not appear to be generally applicable. Information about the spin of the ground state of F^{20}, possibly obtained by the angular distribution of the protons from the (d,p) reaction, and a confirmation of the spin of Si^{29} would contribute to the solution of this problem.

The assistance of A. Papineau in making measurements and drawing figures is gratefully acknowledged.

PHYSICAL REVIEW VOLUME 83, NUMBER 3 AUGUST 1, 1951

Secondary Emission of Electrons from Liquid Metal Surfaces

JAMES J. BROPHY
Physics Department, Illinois Institute of Technology, Chicago, Illinois
(Received April 13, 1951)

The secondary emission ratio as a function of primary energy is determined for targets of bismuth, gallium, lead, and mercury for the metals in both the liquid and solid state. The secondary emission characteristics for liquid surfaces are shown to be very nearly like those for solid surfaces, and in general the shape of the secondary efficiency curves for these materials are similar to those for other pure metals. A comparison of the observed maximum secondary ratios with predicted values is made.

I. INTRODUCTION

THE secondary emission characteristics of many pure metals in the solid state have been well investigated by many workers. For these targets the secondary emission ratio as a function of primary energy shows a broad maximum of about two secondaries per primary for primary energies in the range of 300 to 500 electron volts. However, the characteristics for targets in the liquid state have not been examined. The purpose of this paper is to report the results of such an investigation on targets of bismuth, gallium, lead, and mercury.

Since a good vacuum must be maintained above the surface being examined, metals with appreciable vapor pressures near their melting points must be avoided. This requires that targets be selected that have their melting and boiling points separated by a large temperature difference. For practical reasons, metals with high melting points cannot be used, since it is desired to carry out the work in a Pyrex envelope. Finally, the alkali metals were abandoned because of their chemical activity. These considerations reduced the possible target materials to four: bismuth, gallium, lead, and mercury. These metals are easily melted, have very low vapor pressures in the liquid state, and are not extremely active chemically.

II. EXPERIMENTAL TECHNIQUE

The experimental tube designed to carry out this work is shown in Fig. 1. The electron gun system consists of a tungsten filament surrounded by a nickel anode cylinder covered at one end except for a three-millimeter aperture. The rear end of the cylinder is covered by a disk attached to the negative filament lead to prevent the escape of electrons in this direction. Two nickel disks with four-millimeter apertures are mounted coaxially with the cylinder. Electrons emitted by the filament escape through the first aperture and are focused on the target by electric fields set up by the disks. The potential of the middle electrode is negative with respect to the other disks. The use of this electron lens system produces a primary beam very homogeneous in energy because secondary electrons produced on the electrodes are prevented from becoming part of the beam. Secondaries produced at the first aperture are returned to the cylinder because of the negative potential gradient in the first space. Few secondaries are produced at the second aperture since the net energy of the primary electrons at this point is very low. Finally, because of the focusing action no primaries strike the last disk and no secondaries are produced here.

A nickel cylinder open at both ends is positioned

immediately above the target surface to act as a secondary collector. The target is located at the very bottom of the tube and is inserted in the molten state through a side arm. The envelope is of Pyrex, and leads through the glass wall are graded seals of tungsten to corex to Pyrex. Supporting wires are of nickel.

Potentials were supplied to the electrodes by means of a standard circuit. The potential of the anode cylinder was maintained at one-third of the total primary accelerating voltage from filament to target. The potential of the central focusing disk could be varied to focus the beam on the target. This condition was checked by the use of a fluorescent target. The potential required for minimum spot size on the fluorescent target (diameter about two millimeters) was found to agree satisfactorily with that calculated assuming the lens system to be three simple aperture lenses in contact. The dioptry of such an aperture lens is given in the literature.[1] Investigation indicated that the secondary collector was collecting all of the secondaries when its potential was thirty volts positive with respect to the target. Primary currents of the order of one to ten microamperes were employed and the currents to the target and collector were measured by two vacuum tube dc microammeters.[2]

The experimental tube was sealed through a reentrant cold trap to a single stage mercury diffusion pump with especially small clearance at the jet. An RCA type 1949 hot cathode ionization gauge was included in the pumping line near the experimental tube. The entire vacuum system was mounted on a tiltable stand which could be tipped about 40 degrees from the vertical. The purpose of this tilting stand was to pour the molten material from a side reservoir into the experimental tube. This design allowed the use of an all-glass, rigid, high vacuum system together with the necessary flexibility required to insert the target under a high vacuum. The movable system was connected by means of a short length of rubber tubing to a second mercury diffusion pump fastened to a stationary stand. This pump in turn was backed by a rotary mechanical pump. The extremely low fore-pressures produced by the stationary pump and the low clearance at the jet of the first pump combine to produce small likelihood of contamination by materials diffusing from the high pressure side of the first pump into the low pressure region of the experimental tube.

The pumps were kept running for at least 50 hours before any data was taken and also during the experimental runs. During the preliminary pumping period the experimental tube was baked for eight hours in an electric oven at temperatures of 500°C. The nickel electrodes in the tube could be degassed with a high frequency induction heater while the tube was in the oven. While the experimental tube was being backed the electrodes were brought to a cherry red, the short piece of exposed glass tubing between the tube and the cold trap was severely torched with a Bunsen burner, and the target in the side reservoir was melted and remelted several times. At the end of the baking period and at the beginning of the experimental run the pressure as indicated by the ion gauge was 2×10^{-7} mm of Hg.

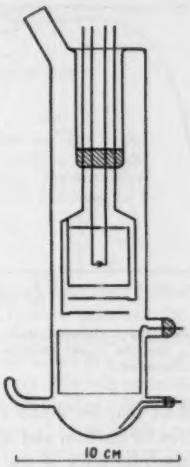

FIG. 1. The experimental tube.

At this time the target material was melted and poured into the experimental tube. The temperature of the target was stabilized just above its freezing point by means of a small electric heater (for the bismuth and lead targets) or a bath of alcohol and snow (for the mercury target). It was found that because the melting point of gallium is so near room temperature and because of its relatively large heat of fusion, this target would stay in either the liquid or solid state for many hours, once it was put in such a state, without the aid of any external agent. Primary and secondary currents as a function of primary energy were recorded for the liquid target and then the target was allowed to freeze. (The alcohol-snow mixture was replaced by one of acetone-dry ice for the mercury target.) The data was repeated for the solid target and then the target was remelted. This process was repeated several times always obtaining excellent correlation after melting and remelting.

III. RESULTS

The results obtained are shown in Fig. 2 and Fig. 3, where the secondary ratio is plotted as a function of the primary energy for the liquid surfaces. In general, the secondary efficiency curves are similar to those obtained from other pure metals. The curves for the solid targets are not shown since it was found that they were very nearly identical with those for the liquid targets. There was some indication that δ for solid mercury is uniformly about four percent greater than that for the liquid, while δ for solid bismuth is about three percent

[1] P. L. Copeland, Am. J. Phys. **10**, 236 (1942).
[2] R. S. Anderson, Am. J. Phys. **18**, 119 (1950).

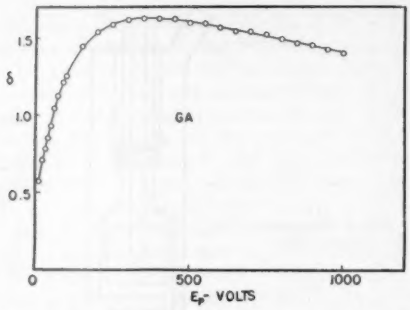

FIG. 2. Secondary emission ratio, δ, as a function of primary energy, E_p, for the liquid gallium target. The curve for solid gallium is the same.

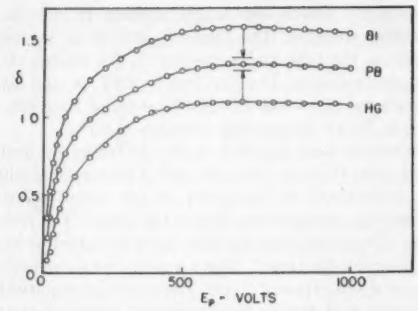

FIG. 3. Secondary emission ratio, δ, as a function of primary energy, E_p, for the bismuth, lead, and mercury targets in the liquid state. The ordinates for bismuth have been raised the amount indicated, while those for mercury have been lowered. The results for the solid targets are very similar to these.

smaller than that for liquid bismuth. The liquid and solid curves for gallium and lead were identical within the experimental error of the apparatus, estimated to be about two percent.

The maximum secondary ratios given by mercury, lead, and bismuth increase with atomic number. This order agrees with a regularity pointed out recently by Sternglass.[3] The magnitudes of the maximum ratios check fairly satisfactorily also. The maximum δ for gallium however is about 30 percent greater than would be expected on the basis of Sternglass' regularity. It is seen that the maximum in the case of gallium ($Z=31$) is very sharp as compared for the maxima of lead (82), mercury (80), and bismuth (83), the last of which are very similar. These results are in line with the correlation between variation of secondary emission and atomic number first pointed out by Copeland.[4]

[3] E. J. Sternglass, Phys. Rev. **80**, 925 (1950).
[4] P. L. Copeland, Phys. Rev. **46**, 167 (1934).

The results of this investigation indicate that the secondary emission characteristics of liquid metal surfaces are very similar to those of targets in the solid state. If as postulated in the quantum-mechanical treatment of secondary emission, the lattice spacing is an important parameter, it must be that this parameter influences the result through the size of the unit cell rather than through a long-range order within the target material. The secondary efficiency curves of gallium, bismuth, lead, and mercury are shown to be generally similar to the curves for other pure metals. Finally, the magnitudes of the maximum secondary ratios of bismuth, lead, and mercury fit satisfactorily into the general scheme of the ratios for other elements, while that due to gallium does not appear to do so.

The author wishes to express his appreciation to Dr. P. L. Copeland, who suggested this investigation and who has been most gracious in devoting his time to many helpful discussions.

The Half-Life of Tritium by Absolute Counting*

W. M. JONES
University of California, Los Alamos Scientific Laboratory, Los Alamos, New Mexico
(Received April 2, 1951)

Results of a measurement of the half-life of tritium by absolute counting are presented. The method consisted of the mass spectrometric analysis of a hydrogen-tritium mixture enriched in tritium, the dilution of some of this material with hydrogen in a known way to a countable level of activity, and the counting of a portion of the diluted gas in a Geiger counter of known effective volume. The half-life was found to be 12.41 with uncertainties of plus 0.15 and minus 0.25 year.

ANALYSIS, DILUTION, AND MEASUREMENT OF THE TRITIUM

THE initial hydrogen-tritium mixture, enriched in tritium, came from a system of Hertz pumps which has been set up in this Laboratory by Dunn, Mosley, Potter, and Robinson. Unfortunately, it was not possible to utilize this material until some time after it became available, and it became slightly contaminated with hydrogen during this interval. The sample was freed from substances other than hydrogen by forming uranium hydride with well-outgassed and finely divided uranium and then pumping off residual gases. This procedure was repeated several times. The tritium was finally evolved into a Pyrex bulb. This gas was immediately analyzed with a mass spectrometer, a portion subjected to a first-stage dilution with pure hydrogen, and the remaining enriched material again analyzed.

The enriched material was analyzed on a 60° Nier-type mass spectrometer. The various species were brought to focus by varying the magnetic field, and the instrument was operated without the source magnet. The gas was admitted to the spectrometer through a molecular leak. The analyses made just before and just after the first-stage dilution gave 98.17 and 98.21 atomic percent tritium, respectively. A preliminary analysis of a synthetic hydrogen-tritium mixture, of known composition showed that the mass 2 to mass 4 ratio is not in error by more than about two percent due to discrimination effects. A similar conclusion was later reached with a hydrogen-deuterium mixture of known composition.

Preliminary experiments had been made in regard to the effect of the tritium radioactivity on stopcock grease in introducing contamination by formation of hydrogen and other gases, principally methane. In these experiments the situation normally encountered was intentionally greatly magnified and indicated that undesirable effects would be completely negligible for the few hours which elapsed between the final purification of the tritium and the first dilution stage. The diluted gas was protected from contact with stopcock grease by means of mercury.

The dilution of the tritium with pure hydrogen was carried out in three stages in order to reduce the activity to a suitable level. At each stage a known amount of the gas richer in tritium, contained in a volume of about 2 cc, was allowed to mix with a known amount of pure hydrogen contained in a bulb of about 500-cc capacity. Both volumes had been accurately calibrated with mercury. In the determination of the amounts of gases, temperatures were estimated to 0.01°C. In the pressure measurements meniscus positions were estimated to 0.001-cm Hg, appropriate reductions to international centimeters of Hg were made, and small corrections were made for non-ideal gas behavior. The pure hydrogen was present at a higher pressure so that some mixing occurred on connecting the two vessels. In addition, the larger vessel could be cooled with liquid nitrogen to facilitate mixing. At each stage the cycle of cooling and warming was repeated ten times, and as a final precaution the gas was allowed to stand overnight. It was necessary to insure that contamination from a previous stage did not falsify the dilution procedure. For this reason the first-stage dilution was made in a different vacuum system from the remaining two stages, since it was thought that contamination would not be removable to a degree suitable for the last stage. Decontamination consisted in passing hydrogen or water through the apparatus for many hours. For the final stage of dilution new standard volumes were calibrated in order to remove any uncertainty with regard to contamination. Effectiveness of decontamination was checked by the counting of hydrogen gas which had stood for several hours in contact with the apparatus.

Pressure and temperature measurements on some diluted gas in the small calibrated volume mentioned were used to determine the amount of the gas to be transferred to a counter. In order to check on how well gas was transferred, three different systems, presenting much different surface areas, were employed. The first two systems involved Toepler pumps which differed by a factor of eight in volume. In the third arrangement the gas was allowed to distribute itself between the counter, the small calibrated volume, and a small additional connecting volume of capillary tubing. Since about 98 percent of the gas went into the counter and since all volumes involved were known, the amount of

* This paper is based on work performed under University of California Contract with the AEC.

gas in the counter was accurately known. There seemed to be no systematic differences in the half-life determinations using the different methods of transfer. The transfer systems were pretreated with hydrogen and with some of the diluted tritium gas, since some preliminary results on the untreated glass of the transfer system presenting the largest surface had indicated that a small amount of activity (not more than about ½ percent of the material used in a counting measurement) was assumed by the glass. Apparently, however, an approximately stationary state of saturation was reached by the surface during the course of the experiments reported here, since the effects of prolonged pumping or exposure to D_2 for a few hours did not give half-life values differing in a consistent way from values obtained without so treating the transfer system.

COUNTERS AND COUNTING MEASUREMENTS

Two counters of identical construction were used during the experiments with no difference in results. The counters were about 15 inches long, and their construction has been previously described.[1] The partial pressure of the hydrogen-tritium mixture in the counter was slightly over 1-mm Hg, and to this 93 percent argon–7 percent ethyl alcohol quencher was added in such a way that no tritium escaped. The final pressure was usually 10-cm Hg. The counting rate due to tritium was usually about 45 counts per second. Dead time corrections were in all cases less than 1.5 percent and were made on the basis of a measured dead time of 3.0×10^{-4} sec. Corrections were made for background, which was usually monitored by means of a third similar counter with which the main counters were intercompared periodically.

It was necessary to find the fraction of the disintegrations which gave rise to counts. This may be taken as the ratio of an effective volume of the counter to the total volume occupied by gas. The effective volume may be regarded in first approximation as being bounded by the cylinder wall and by planes which are perpendicular to the counter axis at the points where the central wire emerges from its shields. The length of unshielded wire L should be replaced, however, by $L-\epsilon$, where ϵ is determined by such factors as the nature of the electric field, the geometry of the counter ends, the counter filling, and the particle range. If the counter contains a radioactive gas of decay constant λ present at a density of ρ nuclei per unit volume in a counter of effective cross section A, then the counting rate for a counter of wire length L will be

$$R_L=A\rho\lambda(L-\epsilon). \tag{1}$$

By simultaneously filling two counters, identical except for their wire lengths L, with a mixture of quencher and diluted tritium, ϵ was found to be 0.9_8 and 1.0_8 cm at quencher pressures of approximately 10 and 20 cm Hg, respectively. The longer effective lengths of the same type counters for the gas counting of carbon fourteen[1] are probably due to a greater contribution from the counter ends by the longer range C^{14} β-particles. It is shown below that the effective cross section of the counter is the same as the geometrical cross section to within experimental errors. The use of counters of different dimensions in absolute gas counting appears to be due to Libby *et al.*[2] and has also been used by others.[1,3–5]

The counters were sometimes, but not always, allowed to stand in a hydrogen atmosphere to minimize possible adsorption effects. The presence of the tritium in the counter for the exposure time of an experiment did not appear to raise backgrounds. This observation does not preclude the possibility of adsorption during a measurement. Some experiments were made which might have uncovered such an effect. In experiment 10, extra hydrogen equal to that normally present was added with no effect. In addition, the higher pressure of quencher in experiment 5 and the added alcohol in experiment 13 did not show any effect, although these experiments were primarily performed for other reasons (see below). In addition, one of the two counters was considerably older, had been more often used than the other, and probably had a surface more susceptible to adsorption. However, the same half-life is given by both counters within experimental errors, suggesting that loss of counts by surface adsorption of material does not constitute a serious error. Gas adsorbed on the wall might still contribute to the counting rate, since even those β-particles which are directed toward the wall rather than the volume of the counter may be backscattered or cause the emission of secondary electrons. Any serious effects due to slow absorption are unlikely, since the counting rate was constant to within experimental error over a 2-day period in a preliminary experiment. In experiment 5 the quencher was increased to 20-cm Hg in order to see whether any significant number of β-particles had failed to produce a count at the lower pressure because of their motion toward the wall after having been produced at a distance from the wall of the order of or less than a mean free path for ion pair formation. No such effect was observed, probably because of backscattering, secondary emission, and the short mean free path for the low energy tritium β-particles. The effective and geometrical cross sections of the counter are thus closely the same. It was considered possible, although not likely, that the absence of an effect in experiment 5 might be owing to a balancing decrease in counting rate due to greater electron attach-

[1] W. M. Jones, Phys. Rev. **76**, 885 (1949).

[2] Anderson, Libby, Weinhouse, Reid, and Grosse, Phys. Rev. **72**, 931 (1947).

[3] Hawkins, Hunter, Mann, and Stevens, Phys. Rev. **74**, 696 (1948).

[4] W. B. Mann and G. B. Parkinson, Rev. Sci. Instr. **20**, 41 (1941).

[5] Engelkemeier, Hamill, Inghram, and Libby, Phys. Rev. **75**, 1825 (1949).

ment or recombination at the higher pressure. Since argon and hydrogen give no trouble with electron attachment, while the alcohol might, the amount of alcohol present in experiment 13 was made more than twice that normally present with no indication of an effect. In experiment 17 a small amount of air was added without effect on the half-life obtained, while a mass spectrometric analysis of quencher gas from which the alcohol had been frozen out showed the oxygen content to be less than 0.01 percent. Thus, electron attachment does not seem to be an important factor. Recombination of the electrons and positive ions should be negligible at the pressures prevailing in the counter. In experiment 12 the 0.005-in. Kovar wire was replaced by one of wolfram on the chance that some take-up or evolution of gas during a counter discharge might be occurring, but such behavior does not appear to be significant.

The plateaus were definite, but their length was considerably shortened by the presence of the hydrogen. An experiment was therefore performed to verify that the operating voltage had been properly chosen and that the hydrogen was not causing any additional effect on counting rate. A uranium foil was taped to the counter and counted with hydrogen plus quencher in the counter and with quencher alone, in which case a much longer plateau region was obtained. Several counting rate measurements were taken in each situation, and the ratio of the counting rate with H_2 to that without H_2 was found to be 1.003 ± 0.004. Two different high voltage supply-scaler circuits were used with no apparent difference in results, and no detectable change in counting rate was found by use of a shorter cable to the counter. A small correction to the half-lives, amounting to a little over 1 percent in the last experiments, was made to allow for tritium decay subsequent to the time of analysis.

DISCUSSION OF ERRORS AND COMPARISON WITH OTHER WORK

The probable error from the data of Table I is 0.04 year. There is a negligible uncertainty associated with the mass spectrometric analysis, the errors from measurements in the three stages of dilution may correspond to 0.01 yr, and the fraction of the disintegrations counted, as determined by measurement of ϵ, contributes an estimated uncertainty of 0.02 yr. Uncertainties of 0.01 yr and 0.02 yr may arise from the dead time and background corrections. On this basis a probable error of about 0.05 yr is estimated. Because of uncertainty in each of the experiments performed to uncover sources of absolute error and because of unknown errors, a larger estimate of uncertainty seems appropriate. The half-life of tritium, as given by this work, is taken to be 12.41 years with uncertainties of plus 0.15 and minus 0.25 year.

TABLE I. Summary of experiments.

Experiment	Half-life, years	Experiment	Half-life, years
1	12.41	10	12.32
2	12.37	11	12.44
3	12.49	12	12.50
4	12.42	13	12.32
5	12.38	14	12.42
6	12.34	15	(counter developed leak)
7	12.38	16	12.52
8	12.30	17	12.47
9	12.38		
		Average	12.41 years
		pe	0.04 year

The above value may be compared with the three most recent published values of the half-life. These values are in agreement within their stated limits of error.

The decay of the current from an ionization chamber containing tritium gas was used to obtain a value of 10.7 ± 2 years.[6] The precision uncertainty was much lower than the error quoted, which was stated to arise from uncertainties due to possible tritium absorbtion and to the effect of the He^3 produced.

The production of He^3 from two samples of tritium gas over a period of a few months gave a value of 12.1 ± 0.5 years.[7]

Measurement of the steady-state rate of diffusion of He^3 from a thin-walled quartz capsule containing a known amount of tritium as water gave a value of 12.46 ± 0.2 years.[8] In a subsequent and more detailed account[9] the uncertainty was given as 0.1 year.

A precise determination of the tritium half-life by measurement of the He^3 growth has been in progress for some time and will be reported soon.

I thank F. J. Dunn, J. R. Mosley, R. M. Potter, and E. S. Robinson, who provided the enriched tritium-hydrogen gas.

[6] Goldblatt, Robinson, and Spence, Phys. Rev. **72**, 974 L (1947).
[7] A. Novick, Phys. Rev. **72**, 972 L (1947).
[8] Jenks, Ghormley, and Sweeton, Phys. Rev. **75**, 701 L (1949).
[9] Jenks, Sweeton, and Ghormley, Phys. Rev. **80**, 990 (1950).

Dependence of Magnetic Shielding of Nuclei upon Molecular Orientation

NORMAN F. RAMSEY
Harvard University, Cambridge, Massachusetts
(Received February 8, 1951)

An expression is calculated for the dependence of the magnetic shielding of nuclei in linear molecules upon the magnetic quantum number of the molecule. The expression for the dependence upon orientation is shown to consist of two different terms. The first of these is directly related to the spin-rotational magnetic interaction constant of the molecule. Since the interaction is known experimentally in the important case of molecular hydrogen, this term can directly be evaluated from the experimental measurements. The other term is proportional to $(3\zeta^2-r^2)/r^5$ averaged over the electron coordinates in the molecule. This term can be calculated from the wave function of the hydrogen molecule. For molecular hydrogen, the dependence of the nuclear shielding upon the molecular orientation is in principle measurable. Such a measurement, combined with the theory of the paper, provides an important check on the molecular hydrogen wave function.

I. INTRODUCTION

IN an earlier paper,[1] the theory of magnetic shielding of nuclei in molecules was presented. In that paper, the magnetic shielding expression was averaged over all orientation states of the molecule, since such averaging automatically takes place in the high precision measurements by the methods of nuclear resonance absorption[2] and induction.[3] However, in molecular beam resonance experiments, particularly with molecular hydrogen,[4,5] the nuclear moments are separately measured in states with different magnetic quantum numbers for the rotational angular momentum. Therefore, there is need for a theory of the dependence of the magnetic shielding of the molecule upon the rotational magnetic quantum number. For simplicity, the discussion will be limited to $^1\Sigma$ linear molecules, since experimentally molecules of this type are those of greatest interest.

II. THEORY

In Eq. (9) of the previous paper[1] it was shown that the shielding constant σ_λ for a molecule in orientation λ was given by

$$\sigma_\lambda=(e^2/2mc^2)(0\lambda|\sum_k(x_k^2+y_k^2)/r_k^3|0\lambda)+\mu_0\sum_{n\lambda}{}'[1/(E_n-E_0)][H_{0\lambda n\lambda'}L_{n\lambda'0\lambda}+L_{0\lambda n\lambda'}H_{n\lambda'0\lambda}], \quad (1)$$

where the quantities are defined in the previous paper.

If for λ one writes σ when the molecule has its axis perpendicular to the magnetic field and π when the axis is parallel, and if ξ, η, and ζ form a cartesian coordinate system attached to the molecule with the ζ-axis being along the internuclear line and with origin at the nucleus for which the shielding is calculated, the above gives

$$\sigma_\sigma=(e^2/2mc^2)(0|\sum_k(\xi_k^2+\zeta_k^2)/r_k^3|0)+\mu_0\sum_{n\lambda}{}'[1/(E_n-E_0)][H_{0\sigma n\lambda'}L_{n\lambda'0\sigma}+L_{0\sigma n\lambda'}H_{n\lambda'0\sigma}], \quad (2)$$

$$\sigma_\pi=(e^2/2mc^2)(0|\sum_k(\xi_k^2+\eta_k^2)/r_k^3|0). \quad (3)$$

In the last equation the complicated second set of terms does not enter because a linear molecule is cylindrically symmetric about its axis as a result of which L has only diagonal matrix elements about that axis since by definition it is then proportional to the ζ-component of orbital angular momentum. From Eq. (18) of the previous paper,[1] and with the notation of Eq. (19) of that paper, (2) above can be expressed as

$$\sigma_\sigma=\frac{e^2}{2mc^2}\left(0\left|\sum_k\frac{\xi_k^2+\zeta_k^2}{r_k^3}\right|0\right)-\left(\frac{e^2}{4mc^2}\right)\left(\frac{I}{M\mu_N}\right)\left(\sum_i\frac{2Z_iM\mu_N}{Ia_i}-\frac{H_r}{J}\right). \quad (4)$$

If σ_{JM} is the average value of σ_λ when the molecule is in a rotational state specified by total rotational angular momentum quantum number J and rotational magnetic quantum number M,

$$\sigma_{JM}=Av_{\lambda JM}(\sigma_\lambda)=Av_{\lambda JM}(\sin^2\theta_\lambda\sigma_\sigma+\cos^2\theta_\lambda\sigma_\pi) \quad (5)$$

as in Eq. (15) of the earlier paper.[1] For any specified rotational state wave function of the average of $\sin^2\theta_\lambda$ and $\cos^2\theta_\lambda$ may readily be evaluated. Alternatively, (5) may be rewritten as

$$\sigma_{JM}=\tfrac{2}{3}\sigma_\sigma+\tfrac{1}{3}\sigma_\pi-\tfrac{1}{3}(\sigma_\sigma-\sigma_\pi)Av_{sJM}(3\cos^2\theta_\lambda-1). \quad (6)$$

For a rotator, however,[6]

$$Av_{\lambda JM}(3\cos^2\theta_\lambda-1)=-\frac{2}{(2J-1)(2J+3)}\{3(\mathbf{J})_z^2-\mathbf{J}^2\}, \quad (7)$$

[1] N. F. Ramsey, Phys. Rev. **78**, 699 (1950).
[2] Purcell, Torrey, and Pound, Phys. Rev. **69**, 37 (1946).
[3] F. Bloch, Phys. Rev. **70**, 460 (1946).
[4] Kellogg, Rabi, Ramsey, and Zacharias, Phys. Rev. **57**, 691 (1940).
[5] Kolsky, Phipps, Ramsey, and Silsbee, Phys. Rev. **79**, 883 (1950); **80**, 843 (1950).
[6] H. A. Bethe, *Handbuch der Physik*, Vol. 24, p. 557, Eq. (65.38).

where $\mathbf{J}$ is the rotational angular momentum vector in units of $\hbar$ and $(\mathbf{J})_s$ is the component of this vector in the direction of the magnetic field. Therefore,

$$\sigma_{JM}=\tfrac{2}{3}\sigma_\sigma+\tfrac{1}{3}\sigma_\pi+\frac{2}{3(2J-1)(2J+3)}\times\{3M^2-J(J+1)\}\{\sigma_\sigma-\sigma_\pi\}. \quad (8)$$

From the combination of Eqs. (3), (4), and (8), together with the fact that the problem is symmetrical in ξ_k and η_k, while r_k^2 is the sum of ξ_k^2, η_k^2, and ζ_k^2, one obtains

$$\sigma_{JM}\Big/\left(\frac{e^2}{3mc^2}\right)=\left(0\left|\sum_k\frac{1}{r_k}\right|0\right)+\left(\frac{3M^2-J(J+1)}{2(2J-1)(2J+3)}\right)\left(0\left|\sum_k\frac{3\zeta_k^2-r_k^2}{r_k^3}\right|0\right)-\left(\frac{3M^2-J(J+1)}{2(2J-1)(2J+3)}+\frac{1}{2}\right)\left(\frac{I}{M\mu_N}\right)\times\left(\sum_i\frac{2Z_iM\mu_N}{Ia_i}-\frac{H_r}{J}\right). \quad (9)$$

Equation (9) gives the desired dependence of the shielding on the orientation of the molecule. If Eq. (9) is averaged over all values of M_J, the previously derived shielding formula is obtained.

The case of greatest interest experimentally is that of $J=1$, in which case (9) gives

$$\frac{\sigma_{1,\pm1}-\sigma_{1,0}}{e^2/3mc^2}=\frac{3}{10}\left(0\left|\sum_k\frac{3\zeta_k^2-r_k^2}{r_k^2}\right|0\right)-\frac{3}{10}\left(\frac{I}{M\mu_N}\right)\left(\sum_i\frac{2Z_iM\mu_N}{Ia_i}-H_r\right). \quad (10)$$

As discussed in the previous paper,[1] the second terms in Eqs. (4), (9), and (10) in the case of molecular hydrogen can be completely determined experimentally from the measured values[5] of the spin-rotational interaction constant H_r and from the known values of the other fundamental quantities involved. With the numerical values used in the analogous step in the previous paper, except with the improved value[6] of 13.40 ± 0.04 gauss for $H_r\mu'/MJ$, (10), for example, becomes

$$\sigma_{1,\pm1}-\sigma_{1,0}=\frac{e^2}{10mc^2}\left(0\left|\sum_k\frac{3\zeta_k^2-r_k^2}{r_k^3}\right|0\right)-(0.339\pm0.005)\times10^{-5}. \quad (11)$$

III. CONCLUSION

Although a completely theoretical evaluation of the magnetic shielding of a nucleus in a linear molecule of a given rotational state from Eq. (9) would be very difficult in general, the work is tremendously simplified in those cases for which the second term in (4) can be experimentally evaluated from a measurement of H_r. In particular, for molecular hydrogen, where H_r is known, the difference $\sigma_{1,\pm1}-\sigma_{1,0}$ is given by (11). A sensitive measurement of the difference of the apparent nuclear magnetic moment of hydrogen in the rotational states of magnetic quantum number 0 and ±1 should determine $\sigma_{1,\pm1}-\sigma_{1,0}$. Equation (11) shows that such a determination directly gives an experimental value for the average value of the quantity $\Sigma_k(3\zeta_k^2-r_k^2)/r_k^3$. This quantity is closely similar to $\Sigma_k(3\zeta_k^2-r_k^2)/r_k^5$ which must be calculated theoretically in determining the deuteron quadrupole moment from the experimental data. Consequently, a precision measurement of the difference $\sigma_{1,\pm1}-\sigma_{1,0}$ would provide a valuable experimental check on the wave function used to calculate the deuteron quadrupole moment from the experimental data. In some molecular beam experiments now in progress at Harvard[5] the difference $\sigma_{1,\pm1}-\sigma_{1,0}$ should be experimentally observable, though it should not be measured with precision in the present apparatus.

A Comparison of Several Nuclear Absolute Voltage Determinations*

WILLIAM J. STURM† AND VIRGIL JOHNSON‡
University of Wisconsin, Madison, Wisconsin
(Received April 23, 1951)

An evaluation of the consistency between the absolute voltage determination of the threshold energy of the $Li^7(p,n)Be^7$ reaction as measured by Herb, Snowdon, and Sala and earlier independent absolute alpha-particle energy measurements has been made. The experimental comparison was affected by employing the natural alpha-particles from polonium and radium C′, the energy of which has been measured absolutely by several authors using magnetic deflection methods. In this experiment the alpha-particles from these substances have been electrostatically deflected in the 90° cylindrical electrostatic analyzer at the University of Wisconsin. Alpha-particle line measurements were analyzed by numerical integration of resolution and source functions and in themselves contributed negligibly to the uncertainties of the comparison. The resulting alpha-particle energies, evaluated by comparison with the energy of the $Li^7(p,n)Be^7$ threshold, agree with earlier measurements, and indicate that within the limits of accuracy of the experiments, all determinations give identical results.

INTRODUCTION

SEVERAL accurate measurements of the absolute energies of the alpha-particles emitted by radium C′ and polonium have been made by electrostatic and magnetic deflection techniques.[1] Briggs' most recent precision measurement was made using improved apparatus as well as better values for the e/m for the alpha-particle and claims an accuracy of 7 parts in 100,000. More recently, further nuclear energy measurements have been made to establish a series of reference voltages using, among others, the energy of the $Li^7(p,n)Be^7$ threshold.[2] Herb, Snowdon, and Sala[3] as a result of their recent absolute measurements, placed the energy of the threshold for this reaction at 1.882 Mev absolute ± 0.1 percent.

This paper reports a comparison of absolute measurements of Herb with earlier absolute measurements of alpha-particle energies. This was accomplished by comparing the proton energy of the $Li(p,n)$ threshold with the energies of the radium C′ and polonium alpha-particles. All were measured on a modification of the electrostatic analyzer[4] used by Herb, Snowdon, and Sala in their absolute voltage determinations. The analyzer as used for this experiment employed a narrower gap, and was supplied with high voltage from an electronic source in place of the battery supply of the earlier work.

APPARATUS

The cylindrical electrostatic analyzer used for these measurements deflects the proton beam from the University of Wisconsin electrostatic generator, and the alpha-particles used in this experiment, through a 90° arc (Fig. 1). Curved metal plates were used to provide the radial electric field for the deflection of the particles and were separated by $\frac{3}{16}$-in. gap. These plates were made by the same manufacturer and produced with the same tolerance requirements as were Herb's original $\frac{5}{16}$-in. set. An electronic high voltage supply,[5] controlled and measured by a standard cell checked for constancy at the University of Wisconsin Standards Laboratory, provided up to 25 kev ± 0.01 percent to each of the analyzer plates. Provision was made for measuring the lithium (p,n) threshold and alpha-spectra alternately while retaining identical analyzer geometry, slit settings and consequently resolving power for the comparative results desired here. A multiple heated target housing[6] provided a simple method for bringing any one of a group of several lithium foils into the proton beam. Neutrons from the lithium (p,n) reaction were detected by means of a BF_3 long counter placed immediately behind the target.

A scintillation counter (Fig. 1) was employed to detect the polonium and radium C′ alpha-particles as they emerged from the exit slit of the analyzer. This counter was an RCA 931-A photomultiplier tube. The fluorescent screen, a ZnS compound (RCA 33-A-20A lot No. 484), was simply dusted on the glass surface of the tube to form a sensitive area for particle detection. The tube was mounted in brass housing which, involving an O-ring to seal the junction at the tube base, permitted the glass portion of the phototube to be introduced into the vacuum system of the analyzer.

EXPERIMENTAL PROCEDURE

Lithium oxide targets were prepared by evaporation of metallic lithium on tantalum foils. Oxidation occurred

* Work supported by the AEC and the Wisconsin Alumni Research Foundation.
† AEC Predoctoral fellow; now at Oak Ridge National Laboratory, Oak Ridge, Tennessee.
‡ Now at Midwest Research Institute, Kansas City, Missouri.
[1] E. Rutherford and H. Robinson, Phil. Mag. **28**, 552 (1914); I. Curie, Ann. phys. **3**, 344 (1925); Compt. rend. **175**, 220 (1925); G. H. Briggs, Proc. Roy. Soc. (London) **A118**, 549 (1928); S. Rosenblum and G. Dupony, J. phys. et radium **4**, 262 (1933); G. H. Briggs, Proc. Roy. Soc. (London) **157**, 183 (1936); Collins, McKenzie, and Ramm, Nature **167**, 682 (1951).
[2] J. E. Hill and G. E. Valley, Phys. Rev. **55**, 678A (1939); Haxby, Shoupp, Stephens, and Wells, Phys. Rev. **58**, 1035 (1940); A. O. Hanson and D. L. Benedict, Phys. Rev. **65**, 33 (1944).
[3] Herb, Snowdon, and Sala, Phys. Rev. **75**, 246 (1949); see also Shoupp, Jennings, and Jones, Phys. Rev. **76**, 502 (1949).
[4] Warren, Powell, and Herb, Rev. Sci. Instr. **18**, 559 (1947).
[5] R. Henkel and B. Petree, Rev. Sci. Instr. **20**, 729 (1949).
[6] Bender, Shoemaker, and Powell, Phys. Rev. **71**, 905 (1947).

when the targets were exposed to air. Six foils were prepared, each used for one threshold measurement, the thinnest being a barely visible deposit.

Three of the polonium sources were prepared by electrodeposition by the Canadian Radium and Uranium Corporation. A fourth foil was prepared at this laboratory by evaporating part of the commercially prepared deposit on to a blank nickel foil in an effort to determine the effect of the age of the source upon the nature of the spectrum at the position of the alpha-particle line. These sources of strengths, varying from 0.25 to 3.0 millicurie, were deposited on nickel metal strips and covered one 0.050×0.250-in. face of a 0.050×0.250×0.750-in. strip of the metal.

The RaC′ source was prepared at the Radium Laboratory of the State of Wisconsin General Hospital. The active deposit of RaC′ was produced by exposing one centimeter at the end of a 0.020-in. diameter platinum wire to approximately 250 millicuries of radon over mercury for 40 minutes. In order to increase the strength of the deposit a cylinder of copper mesh 1 cm in diameter was fitted about the platinum wire and raised to a positive potential of 300 volts with respect to the wire. The strength of the RaC′ source at the beginning of the first measurement was about 25 millicuries.

A sequence of 13 measurements, selected in order to minimize variations in time and change in the experiment arrangements, alternated alpha-line and lithium (p,n) threshold measurements. The resolution selected in each case was the optimum one chosen in view of the strengths of the alpha-particle sources. Because these measurements did not themselves represent an absolute measurement, it was not necessary to measure accurately the spacings of the analyzer plates, or to measure the absolute value of the voltages on the plates.

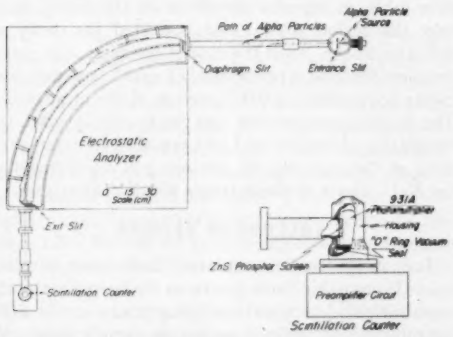

FIG. 1. Schematic diagram of the cylindrical electrostatic analyzer. Alpha-particle sources were placed at the entrance slit, and detection was accomplished by scintillation counting. Insert: The housing for the photomultiplier showing phosphor screen and method of producing vacuum seal.

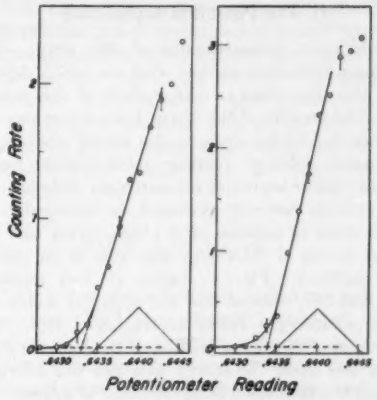

FIG. 2. The $Li^7(p,n)Be^7$ threshold, showing neutron yield in arbitrary units plotted as a function of potentiometer voltage. Six determinations were used to establish the position of the threshold on the potentiometer axis. Triangles represent the width and approximate shape of the incident proton spectrum at the potentiometer setting corresponding to the position of the apex.

(a) $Li^7(p,n)Be^7$ Thresholds

Six measurements of the $Li(p,n)$ threshold were made, each on a different lithium target. Targets were maintained at a temperature of 250° to 300° Centigrade at all times, and a liquid air trap was mounted in the vacuum system near the targets in order to avoid contamination of the lithium foils. The theoretical resolutions[4] for all of the threshold measurements was the same, 1000. The proton beam strength measured at the target was essentially constant during each run, and varied from 0.1 to 0.25 microampere for the various threshold measurements. The beam intensity for each point on the curves was measured by means of a current integrator circuit, and counting rates were recorded in arbitrary units of neutrons per microampere of proton beam. Each measurement represented the average of two cycles of data, taken in all cases in opposite directions and in equal current intervals over the range of proton energy shown (Fig. 2). The proton energy is proportional to the voltage applied to the plates and is reported here in terms of the reading of the potentiometer which controlled the voltage to the plates. The consistency of the results is not quite as great as that of Herb, all six points here lying within 0.04 percent of the mean threshold value. However, since each target upon repeated measurements gave a more constant threshold than the group would indicate, and since no systematic variation could be found, it was felt desirable to take the mean of a number of measurements as the closest approach to duplicating the value obtained by Herb. Combining these results with Herb's work, the potentiometer reading 0.64330 was taken to correspond to the energy 1.882 Mev absolute.

(b) The Polonium Alpha-Line

Preliminary measurements of the shape of the polonium alpha-line showed that its width depended upon the cleanliness of the surface of the polonium layer. The breadth of the line at $\frac{1}{2}$ maximum was in one instance halved by cleaning the source in a sequence of organic solvents (carbon tetrachloride, benzene, acetone) before beginning measurement of the spectrum. This process, however, produced no measurable effect in the shape or position of the high energy side of the line. A survey of the energy spectrum of the polonium alpha-particles (Fig. 3) taken at two resolutions, 1000 and 667, showed that the apparent width of the line depended upon resolution employed. However, the projection of the linear portion of the high energy side of the line upon the energy axis was not affected by varying the resolution over the range of interest in this experiment. It was considered essential, therefore, to locate the position of this projection as the prime datum for the determination of the energy of the alpha-particle. Corrections which were applied to account for the

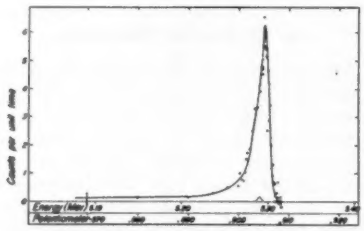

FIG. 3. The spectrum of polonium alpha-particles in the region of the line at 5.298 Mev. The resolution for this measurement was 1000.

width of the resolution function will be described subsequently. A significant rise of the background counting rate in time was observed, the rate of increase varying from one count per minute per 15 hours to one count per minute per hour. It was consequently necessary to decontaminate the alpha-detector frequently during the runs, and to make a frequent record of the background counting rate.

The results obtained showed a very constant value for the potentiometer setting corresponding to the energy of the projection of the high energy side of the alpha-line. All five determinations of this point lay within 0.004 percent of the mean value and the width of the toe of curve again corresponded roughly to the value of the resolution used. Sources of varying strengths and methods of production were used to determine whether diffusion into the nickel support influenced this value. One energy measurement, made immediately upon completion of the deposition in order to assure that any time dependent diffusion into the support was minimized, yielded a result indistinguishable from the others in this series.

(c) The Radium C′ Line

Most of the considerations discussed in evaluating the high energy extrapolation for the polonium line occurred in the case of RaC′. The source was cleaned in organic solvents and introduced into the vacuum system of the analyzer within 30 minutes of its preparation. The analyzer resolution was 667 for the radium C′ measurements. Since the rate of alpha-particle emission was not constant, but followed the characteristic curve of growth of RaC from the parent substances, and since the manner of deposition was not known with sufficient accuracy to make a theoretical calculation satisfactory for correcting the data, a monitor method was used to evaluate the source strength continuously. A second scintillation counter was set up and a second source of RaC′ was prepared by removing some of the deposit from the original source. The monitor counter was a second RCA 931A photomultiplier and zinc sulfide screen; the screen was, in this case, covered with a 0.0005-in. aluminum foil, and the tube was painted with an opaque layer of black lacquer. The monitor source was mounted 2 cm from the aluminum foil and thus, by aluminum and air absorption, all radon and RaA alpha-particles were removed without detection. During the measurement of the RaC′ line, both the monitor and the scintillation counter on the analyzer recorded data for identical intervals. It was consequently possible to correct analyzer data either point by point in proportion to the total number of counts observed by the monitor, or by plotting the monitor data as a function of time. The second alternative was chosen as the more accurate. The monitor curves measured during each run showed decay periods in good agreement with the value calculated from the periods of the parent substances and indicate that the period of growth was completed before the measurements were begun.

Each RaC′ curve was the result of two cycles of data taken in opposite directions on the energy scale over the region shown, and corrected for decay as indicated above. As in the case of polonium, the extrapolation intercept is reproducibly located, both measurements lying within ± 0.003 percent of the mean value. The second measurement was made shortly after the completion of the first and was preceded by remeasurement of the analyzer slit settings and replacement of the RaC′ source at the entrance slit of the analyzer.

ANALYSIS OF RESULTS

The measurements reported here were directed toward comparing three points on the energy scale, the experimental determinations being made on the same instrument and under comparable experimental conditions. The first, that of the $Li^7(p,n)Be^7$ threshold, was taken to be the extrapolation of the linear portion of the neutron yield curve upon the energy axis and was measured in the same manner as was done by Herb *et al.*[3]

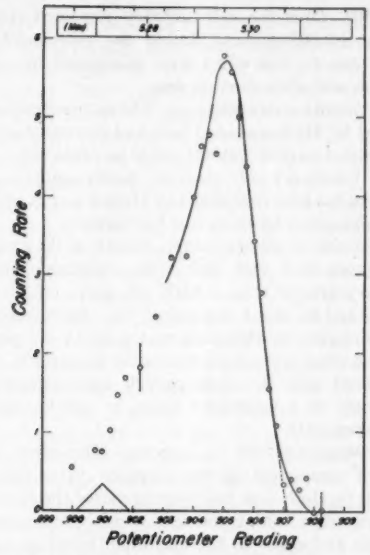

FIG. 4. The polonium alpha-line measured with a resolution of 1000. Curve represents the result of fitting the observed data with a combination of exponential source function and triangular resolution function. The period of the exponential was 1.05 times the base width of the triangle.

The second and third were the positions of the natural alpha-particle lines from polonium and RaC′. Since these energy values in the nonrelativistic region depend linearly upon the voltage applied to the deflctor plates, the first approximation to the energy is directly proportional to the setting of the potentiometer which determines this plate voltage. Analysis, then, involve determination of the potentiometer settings corresponding to these points from the data of the last sections, and conversion of these values to equivalent energies.

Li(p,n) threshold determinations were made under conditions which, using much of the same apparatus, duplicated closely the experimental conditions of Herb's measurements. Because of the nature of the quantitative definition of this threshold, a simple evaluation of the six extrapolated potentiometer values obtained here was taken to correspond to the absolute energy value of the threshold assigned by Herb. This potentiometer setting, 0.64330 was thus taken to correspond to the energy 1.882 Mev on the absolute scale, and the energies of the alpha-particle lines were calculated from this fiducial point.

The determination of the energy of the polonium alpha-particle line was not as direct, however, and involved assumptions about the nature of the resolution and source functions. A curve of the alpha-particle spectrum in the region of the polonium line was measured with resolution 1000 and attempts were made to fit the portion in the vicinity of the line with various combinations of resolution and source functions —triangular, gaussian, and truncated triangular resolution functions were used in combination with exponential and finite "delta-functions" source functions. Exponential functions increased with energy and terminated abruptly at the energy of the alpha-particle line. The alpha-intensity measured in the potentiometer setting P will be given by

$$Y(P)=\int f(P)g(P)dP,$$

where $f(P)$ is the source function, $g(P)$ the resolution function, and $Y(P)$ the intensity measured. That curve which fitted the observed prototype data best (Fig. 4) was a combination of the triangular resolution function and exponential source function and was found to yield a value for the base width of the resolution function indistinguishable from the theoretical resolutions. The period of the exponential for this curve was 1.05 times the triangular base width and the position of the alpha-line was $P_0=0.90583$ potentiometer. And since an extrapolation value of the high energy linear position of this curve was $P_e=0.90710$ potentiometer, we take P_0 for polonium alpha-particle measurements made at a resolution 1000 as given by

$$P_0=P_e-0.00127,$$

in which P_0 is the extrapolated value of the alpha-line for the mean of the 5 measurements, 0.90708 potentiometer. Thus P_0, the potentiometer reading corresponding to the energy of the line, is 0.90581.

From the electrostatic analyzer relations between the applied voltage and the particle energy, given in terms of the geometrical parameters of the analyzer[4] we have

$$V'=2V_0(1-\gamma)d/b,$$

in which $\frac{1}{2}V'$ is the positive voltage supplied to the positive analyzer plate (the negative plate is charged

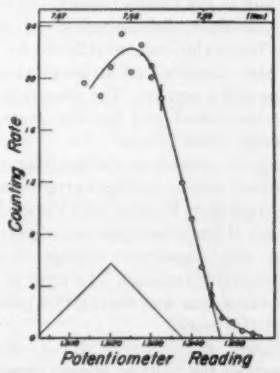

FIG. 5. The high energy side of the RaC′ alpha-particle line. The average extrapolated potentiometer reading, 1.3147, corresponds to an energy of 7.683 Mev absolute.

to the same value), V_0 is the particle energy in volts, d is the separation of the plates, and b is the mean radius of the plates. The value of γ is determined by

$$\gamma = eV_0/2m_0c^2,$$

where eV_0 is the particle energy, m_0 the rest mass, and c the velocity of light. Since V' is directly proportional to the potentiometer reading P_e', we can replace V' by kP_e' and determine k from the known values of P_e' (0.64330) and V_0 (1.882 Mev absolute) for lithium. Thus $k = 2.7141 \times 10^4$. Introducing this value for k, together with $P_0' = 0.90581$ and the mass of the alpha-particle into the above expression we find the energy of the polonium alpha-line to be 5.298-Mev absolute.

The third point established on this energy scale was the position of the RaC′ alpha-line. Two measurements of this line were made (Fig. 5) at the same resolution, 667. However, because of the short half-life of RaC′, a prototype curve was made at this resolution using the polonium alpha-particle line. This prototype line was fitted as already discussed and was again fitted best by a curve of intensity resulting from a combination of an exponential source function and triangular resolution function. For this curve the value of P_0 was found to be 0.90600 potentiometer; and since the value of P_e from the curves was 0.90710, the difference $P_e - P_0$ was 0.00110 potentiometer units. This difference was increased in the ratio of the potentiometer readings corresponding to the extrapolated linear portions, P_e for RaC′ and that for polonium, and was subtracted from P_e for RaC′. Thus for RaC′

$$P_0 = 1.31467 - 0.00159 = 1.31308.$$

And the energy of the RaC′ alpha-particle calculated as in the last section is 7.683 Mev absolute.

ESTIMATION OF ERRORS

A consideration of the limitations upon the accuracy of the various factors which enter into the determination of these energies and which are used in evaluating the probable errors in the results follows:

(a) The absolute determination of the Li(p,n) threshold.—This value was established by Herb *et al.* to be 1.882 Mev absolute with an uncertainty evaluated by him to be ±0.1 percent. The uncertainty was conservatively determined and for the purposes of this paper we accept these values.

(b) Leakage to ground on the analyzer plates.—For all data reported here no leakage current was detectable on the microammeters in series with the analyzer plates. Assuming that 0.5 microampere was detectable in this manner, the only significant voltage drop was that across the protective resistors. The error in the voltage due to this cause was less than 0.004 percent and is negligible for this work.

(c) Constancy of the standard cell.—Each of two determinations of the voltage showed three-day variations of less than 2 in 10^5, and measurements made at the beginning and end of the series differed by less than 5 in 10^5. Thus the cell probably remained constant within ±0.005 percent during the experiment, and errors due to this effect were minimized by cycling neutron and alpha-particle data.

(d) Potentiometer settings.—The same potentiometer as used by Herb was used here and its contribution to the error, 1 part in 150,000, could be neglected.

(e) Constancy of analyzer power supply.—This problem has been considered by Henkel and Petree[5] and the value given by them is ±0.01 percent.

(f) Width of slit apertures.—Width of the entrance, diaphragm and exit slits were measured with an accuracy greater than ±0.005 cm, and were probably reproduced to about this value. The determination of the resolution on this basis was good to ±5 percent, and the effect upon final evaluation of particle energy influenced only the alpha-particle measurements and that only in a secondary sense, as will be discussed (j) subsequently.

(g) Magnetic field in analyzer.—The effect of the vertical component of the magnetic value has been treated by Herb *et al.* We have estimated the error from this source by taking the field within the analyzer as uniform and equal to the maximum found at any interior point during the earlier work (0.3 gauss) and as wholly in the vertical direction which is that of greatest effect. Only the difference in the correction for a 2-Mev proton and a 5.3-Mev alpha-particle is significant here and is less than 0.01 percent. Likewise, the difference in correction for a 2-Mev proton and for a 7.7-Mev alpha-particle is less than 0.02 percent, and was considered in evaluating the resultant probable error.

(h) Relativistic effects.—The complete expression for the energy of an alpha-particle in terms of the voltage at the analyzer plates is given by

$$V' = 2V_0(1 - \gamma + 2\gamma^2 \cdots)\left(\frac{d}{b} + \frac{1}{12}\frac{d^3}{b^3} \cdots\right).$$

Since the value of d/b is 4.69×10^{-3}, terms in d^3/b^3 and higher order will produce negligible correction. However, terms in γ produce a change as great as 0.04 percent in the alpha-line energies and were introduced into the calculation. Terms in γ^2 and higher produced negligible effects.

(i) Determination of slope of linear portions of curves.—The effect of statistical uncertainty upon the determination of the position of the linear portion of the curve has been determined by Bessel's method for several typical curves. The uncertainty in the extrapolations thus evaluated prove to be less than ±0.004 percent. However, assigning to each point on the curve a statistical uncertainty of $\pm N^{\frac{1}{2}}$, where N is the total number of particles detected for the point considered, and extrapolating through the extreme values thus computed, indicated that the errors could be as great as ±0.01 percent. The latter value was used in estimating the total error.

(j) The width and shape of the resolution function.—The shape of the resolution function, as long as symmetry is preserved, does not alter the extrapolated potentiometer values significantly; however, the width of this function must be established in the case of alpha-particle data. From the curve analysis in the manner indicated earlier, we conclude that the uncertainty in the extrapolated values arising from the width of this function is less than ±0.01 percent. An additional uncertainty due to setting the slits, as discussed in (f), produced an error of 5 percent in the width of the resolution function, and affected the energy determinations by ±0.005 percent. A total error of ±0.015 percent seemed to be the maximum expected from these causes.

(k) The assumption of an exponential source function.—To determine the error arising from this cause several other types of source functions were considered. As one extreme, a source "delta-function," having a width corresponding to the sum of the natural width of the alpha-particle line and the degradation in energy occurring in the source itself, was integrated numerically with the gaussian and triangular resolution functions used earlier. This was compared with the results of integrating similarly a rectangular block source function extending down to zero energy and showed that a range of ±0.015 percent in energy would include both possibilities as well as the exponential case assumed. A rather conservative value of ±0.02 percent was taken for this uncertainty.

(l) Degradation of alpha-particle energy at the source.—For the thickest source used, assuming a stopping power of 4.5 relative to air and a density of 9.5 for Po, the greatest loss of energy possible is of the order of 200 electron volts, and is a negligible error. Because of the method of evaluating the alpha-particle line position by extrapolation of the high energy side of the line, diffusion into the source, unless a large fraction of the alpha-emitter diffused thus, was not a significant factor. This was established experimentally by producing a fresh source on nickel and measuring it immediately. No error in these measurements was taken to arise from this cause.

The uncertainties *b* through *l* are those which arise un the determination of the potentiometer voltage corresponding to the extrapolated alpha-lines. If these errors are assumed to be random, the combined probable error in this determination is ±0.03 percent for the Po and ±0.036 percent for RaC′. In establishing the potentiometer reading corresponding to the Li(p,n) threshold, many of the errors discussed above (b through e) were again operative. If the distribution of threshold measurements is assumed random and if the uncertainty of 0.1 percent in Herb's measurement is included, the probable error in the evaluation of the particle energies is ±0.103 percent. And our final results for the energy of the alpha-particles are

RaC′ energy = 7.683±0.008-Mev absolute,

Po alpha-energy = 5.298±0.005-Mev absolute.

DISCUSSION OF RESULTS

In order to compare the results obtained here with the independent absolute alpha-measurements made of the Po and RaC′ alpha-particle lines by magnetic deflection techniques, we have selected for the comparison the latest value of Briggs[1] for the RaC′ alpha-energy and that of Rosenblum and Dupouy[1] for the Po alpha-energy. Introducing the current values[7] for the electronic charge, alpha-particle mass and the Faraday, changes Briggs' value of e/m for the alpha-particle by 0.001 percent, and hence his value for the RaC′ energy insignificantly. The value he reported for the energy of the RaC′ line was 7.6802-Mev absolute ±0.007 percent.

For the Po alpha-line, Rosenblum's values for H have been reconverted using more recent values of the constants and the energy was converted to the absolute scale. The energy thus computed, 5.297 Mev with an experimental error of less than 0.2 percent, agrees very well with the value of 5.298 Mev reported in Halloway and Livingston.[8] This latter value was obtained by recalculation of the data of Lewis and Bowden[9] in terms of Briggs' absolute energy for the RaC′ line.

Thus within the accuracy of the experiments, present values for the alpha-particle energies agree with the earlier independent magnetic deflection measurements. Since these determinations were made electrostatically and energies assigned by comparison with the absolutely determined Li(p,n) threshold energy, it is clear that all methods yield consistent results for the energy of these alpha-particles. Consequently, it appears improbable that a systematic error as large as 0.1 percent has been made in either magnetic or electrostatic absolute determinations and that it is reasonable to accept the precision of both with increased confidence.[10]

The writer wishes to acknowledge his indebtedness to Professor H. T. Richards for suggesting the problem and for his interest and advice throughout the course of the experiment, and to Professor R. G. Herb for several valuable discussions and his interest in this problem.

---

[7] J. W. M. DuMond and E. R. Cohen, Revs. Modern Phys. **20**, 82 (1948).

[8] M. G. Halloway and M. S. Livingson, Phys. Rev. **54**, 18 (1938).

[9] W. W. Lewis and B. V. Bowden, Proc. Roy. Soc. (London) **145**, 235 (1934).

[10] *Note added in proof:*—It may be of interest to make the inverse comparison as well, accepting the claimed accuracy (0.007 percent) of Briggs' measurement of the RaC′ alpha-energy, and use the present measurements (accuracy 0.036 percent) to fix the Li(p,n) threshold. Although the small uncertainty in Briggs' absolute energy may be optimistic, the $Li^7(p,n)Be^7$ threshold thus calculated from data of the present comparison is 1.8813 ±0.0007 Mev absolute. (The polonium alpha-energy becomes 5.296±0.002 Mev.) Combining this threshold value with the other accurate absolute determinations, 1.8822±0.0019 Mev absolute (reference 3), and 1.8816±0.0019 Mev absolute (HSS, reference 3), yields an unweighted mean of 1.8816 Mev absolute. An uncertainty of 0.05 percent (0.0009 Mev) assigned to this mean value will generously overlap all three of the absolute and independent determinations of the threshold.

Optical Absorption and Photoconductivity in Barium Oxide*

W. W. TYLER† AND R. L. SPROULL
Cornell University, Ithaca, New York
(Received October 30, 1950)

Measurements of the optical absorption and photoconductivity in BaO single crystals are reported. The threshold photon energy for both processes is 3.8 ev, and the absorption constant at higher energies is at least 10^5 cm^{-1}. A second increase in the absorption constant begins at about 4.8 ev and is not accompanied by photoconductivity. The observed dependence of photoconductivity on temperature and electric field strength indicates space charge effects in limiting current flow. The onset of absorption at 3.8 ev is thought to be due to the production of excitons, with the accompanying photoconductivity due to thermal dissociation of excitons or exciton ionization of impurity centers.

I. INTRODUCTION

CATHODES coated with mixtures of barium oxide and strontium oxide have great practical importance, having been used for many years as low temperature sources of electrons in vacuum tubes. The aggregates of small oxide particles comprising the cathodes are not well understood, although much effort has been devoted to their study.[1] One aim of the present work was to approach an understanding of the oxide cathode by studying the fundamental electronic properties of a simpler system, a single crystal of BaO. Knowledge of the location and separation of energy bands in the BaO lattice and the identification of impurity levels should assist in an understanding of thermionic emission, activation, poisoning, and other phenomena of oxide-coated cathodes.

In addition to its practical importance as an electron emitter, BaO is of quite general interest. At present, very little is known about the electronic properties of crystals of the divalent alkaline earth oxide group. Most of the present theory of processes in ionic crystals has been developed[2] on the basis of studies of the properties of alkali halide crystals. This theory can be tested and perhaps influenced by an equivalent understanding of the properties of the divalent oxides.

II. PREPARATION OF CRYSTAL SAMPLES

Single crystals of the alkali halide group occur naturally or may be grown artificially with relative ease. The alkaline earth oxides do not occur naturally and are difficult to grow artificially because of their high melting temperatures and chemical activity at these temperatures. In addition, BaO is unstable in the atmosphere, combining with H_2O to form the hydroxide. This fact presents problems in the growth, manipulation, and study of the crystals.

The crystals used in the work presented here were all grown[3] from the vapor phase at a temperature of approximately 1500°C. This method of growth produced clusters of small BaO crystals from which single crystals could be extracted or larger, multicrystalline plates cut with a high speed silicon carbide saw. The largest single crystals used in this work were approximate cubes with edges of the order of 1 mm. Preparation of the crystal samples and mounting of these samples for experimental work was done in a dry box desiccated by porous BaO or with a liquid nitrogen cold trap.

The growth of BaO crystals from pressed BaO powder is a purifying process. However, the chemical purity of the crystals obtained is still limited principally by the purity of the starting material.[4] During growth, variable amounts of molybdenum are added to some crystals due to evaporation from the furnace heater. The total impurity content, estimated from spectroscopic analysis is at most 0.4 percent for the crystals used. Except for several crystals heavily dosed with molybdenum (Run 27), the major impurities are strontium (0.2 percent) and calcium (0.05 percent).

III. OPTICAL ABSORPTION MEASUREMENTS

Absorption measurements on single crystals and multicrystalline plates were made with the samples mounted in an airtight absorption cell with quartz windows. Mounting and sealing were done in the dry box. The ratio of light intensity passing through the cell windows and sample to that passing through the windows alone gives the transmittance of the sample. A Hanovia hydrogen discharge tube and a Bausch and Lomb quartz monochromator provided fairly continuous monochromatic radiation through the spectral region

* This work has received support from a Frederick Gardner Cottrell Grant by the Research Corporation and from the ONR.
† Now at the Knolls Atomic Power Laboratory of the General Electric Company, Schenectady, New York.
[1] See review articles by J. P. Blewett, J. Appl. Phys. **10**, 668, 831 (1939); **17**, 643 (1946); A. S. Eisenstein, *Advances in Electronics* (Academic Press, Inc., 1948), Vol. 1, pp. 1–64.
[2] N. F. Mott and R. W. Gurney, *Electronic Processes in Ionic Crystals* (Oxford University Press, 1940); F. Seitz, *The Modern Theory of Solids* (McGraw-Hill Book Company, Inc., New York, 1940).
[3] Details of the method of growth will soon be published in Rev. Sci. Instr.
[4] Utilizing seed crystals of cleaved MgO and purer BaO powder as raw material, W. C. Dash, in this laboratory, has recently obtained larger BaO crystals of higher purity. The above data on crystal size and purity pertains to the crystals used for the measurements reported subsequently. Checks using the purer crystals now available indicate that the results to be reported are to a large extent intrinsic to the BaO lattice and independent of impurity content.

from 4000A to 2000A. An RCA 1P28 photomultiplier tube and sensitive dc amplifier were used to detect light energy. The resolution of the system was such that the half-intensity width of the Hg 3650A line was 70A; the resolution improves for shorter wavelengths as the dispersion of the quartz prisms increases.

Figure 1 shows transmission data for a single crystal of BaO. Within the wavelength resolution the transmission cutoff was the same for samples of different impurity content from four different crystallizing runs. Absorption in BaO crystals begins quite abruptly at about 3.8 ev or 3250A. Beyond 3100A, the absorption constant is at least as great as 300 cm^{-1}. Crystals cannot be cleaved into thin enough specimens to measure the absorption constant in this region, so evaporated BaO films must be used. Figure 1 also shows a transmission curve for a MgO crystal.[5] Studies of ultraviolet optical absorption in MgO were first reported by Brice and Strong.[6] It is notable that even for thinner samples, the transmission cutoff for BaO is much sharper than for

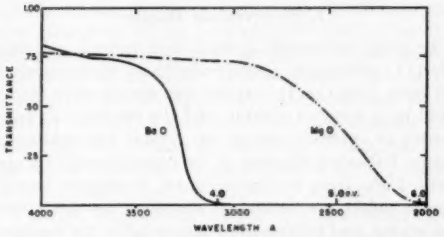

FIG. 1. Optical transmittance of BaO and MgO crystals. The BaO crystal is 0.38 mm thick. The MgO crystal is 1.2 mm thick.

MgO. For three MgO samples studied, the absorption constant at 2100A is only about 15 cm^{-1} and may in part be due to impurity centers.[7] As neither the MgO nor the BaO samples had optically polished surfaces, the relative values of transmittance in the 4000A region are not significant.

The results of optical absorption measurements on BaO films have been reported.[8] The threshold for absorption in films occurs at about 3.8 ev, in agreement with single crystal studies. Figure 2 shows the absorption constant as a function of wavelength. Taft and Dickey[9] have confirmed location of the optical absorption edge in BaO at 3.8 ev by measuring the photoelectric emission from very thin metallic films deposited on the surface of BaO layers.

[5] Obtained from the Norton Company, Niagara Falls, Ontario, Canada.
[6] R. T. Brice and J. Strong, Phys. Rev. **47**, 255 (1935); J. Opt. Soc. Am. **25**, 207 (1935).
[7] J. P. Molnar and C. D. Hartman, Phys. Rev. **79**, 1015 (1950).
[8] W. W. Tyler, Phys. Rev. **76**, 1887 (1949).
[9] E. A. Taft and J. E. Dickey, Phys. Rev. **78**, 625 (1950).

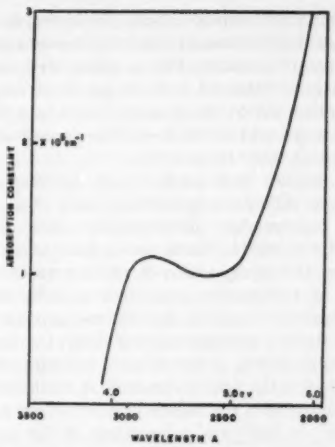

FIG. 2. Absorption constant of BaO as a function of wavelength. The curve represents the average of data from three thin films of BaO on quartz; the original data is from reference 8.

IV. PHOTOCONDUCTIVITY MEASUREMENTS

A. Direct Current Measurements

Preliminary measurements of photoconductivity in BaO crystals using steady-state dc detection methods have been reported.[10] Although it had been shown by early workers[11] that single pulse ballistic measurements of photoconductivity were easier to interpret than steady-state measurements, it was felt that the BaO crystals available were too small for successful ballistic-type measurements. For the dc measurements, the crystal was mounted in vacuum between nickel electrodes across which a dc potential of about 300 v was applied. The crystals used in the dc experiments were

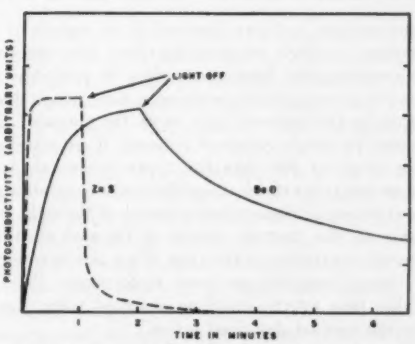

FIG. 3. Photoconductivity as a function of time for crystals of BaO and ZnS (sphalerite). Illumination begins at time=0. The current decay in BaO after illumination ceases is approximately exponential.

[10] W. W. Tyler, Phys. Rev. **76**, 179 (1949).
[11] F. C. Nix, Revs. Modern Phys. **4**, 723 (1932).

about 0.5 mm×0.5 mm×0.5 mm. The hydrogen arc and Bausch and Lomb monochromator were used to provide monochromatic radiation. Photocurrents were measured using a parallel-balanced electrometer circuit employing two Victoreen VX-41 input tubes. Currents of the order of 10^{-14} amp could be detected. The dc measurements were made at room temperature.

Initial studies were made on six different crystals from three different crystallizing runs. For all the samples, appreciable photocurrents were measured from 3300A to 2100A. The dc measurements are characterized by the superposition of photocurrents on dark currents of comparable magnitude and by the long times required to obtain equilibrium current values. Figure 3 shows a recorder trace of current *vs* time for a BaO crystal during a two-minute exposure to 3000A light and after the light is removed. A similar measurement is shown for a zinc sulfide (sphalerite) crystal. This time effect in BaO was independent of the particular

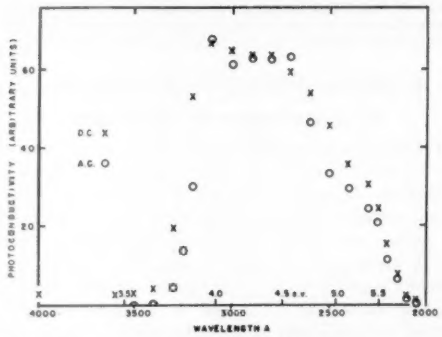

FIG. 4. Photoconductivity as a function of wavelength. The illumination spectrum is given in Fig. 7. The dc data are for crystal No. 6; the ac data are for crystal No. 7.

crystal studied and was observed in all regions of the spectrum in which photoconductivity was observed. The exceptionally long time effect is probably not caused by a change in the semiconduction current due to heating by the incident light, since the observed time required to attain constant currents is greater by a factor of about 100 than the approximate calculated time necessary for thermal equilibrium to be established. The exponential decay after removal of the light may be due to the thermal release of trapped electrons. However, no studies of the time effect as a function of the crystal temperature were undertaken. (No detectable time effects could be observed using the ac detection method described below.)

Figure 4 shows the wavelength dependence of the dc photoconductivity in BaO. Measurements for a different crystal using the ac detection system are shown for comparison. Both curves represent room temperature photocurrents, uncorrected for spectral variations in intensity of the light source. The dc data represent approximate steady-state values, taken 2 minutes after exposure, with time allowed for complete recovery between readings. Ordinates for the two curves are arbitrarily matched. Except for the long wavelength "tail" on the dc curve, the wavelength dependence for the two methods agrees within experimental error. The higher the impurity content of the crystal, the larger the dark current observed with dc detection. In some cases (e.g., crystal No. 7 of Fig. 4, 0.05 percent molybdenum), large concentrations of impurities precluded dc photoconductivity measurements.

The dc system was checked by observing photoconductivity in small crystals of zinc sulfide (sphalerite) and diamond. The results indicate approximate agreement with published data[12,13] taken using ballistic techniques. Several attempts were made to observe photoconductivity in crystals of MgO. Although MgO absorbs appreciably between 2500A and 2000A (Fig. 1), no photoconductivity could be detected at any wavelength in this region.

B. Alternating Current Measurements

1. Experimental Details

To avoid the complications of dark currents and time effects in subsequent photoconductivity measurements, the light falling on the crystal was square-wave modulated by a rotating shutter, and the resultant ac component of current through the crystal was measured. Figure 5 shows a diagram of the experimental arrangement. Light from the hydrogen arc is chopped into 33 square pulses per second, is dispersed by the monochromator, and falls on the BaO crystal in the vacuum. A dc voltage is maintained across the crystal, and ac current components are coupled to the preamplifier through the capacitor C (0.05 μf). After amplification the signal goes to the phase-sensitive detector which rectifies and detects only ac voltages in synchronism with an auxiliary signal generated by the phototube on the periphery of the chopper disk. Control of the relative phases of the two signals is obtained by moving the phototube along the periphery of the disk. The use of phase-sensitive detection gives a convenient and stable method of attaining a narrow band-pass and consequent high signal-to-noise ratio.

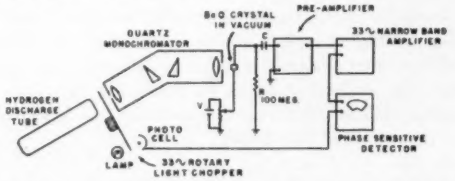

FIG. 5. Diagram of ac photoconductivity apparatus. The input impedance of the preamplifier is a resistance of 2000 megohms; C is 0.05 μf. For other details, see text.

[12] B. Gudden and R. W. Pohl, Z. Physik **17**, 331 (1923).
[13] B. Gudden and R. W. Pohl, Z. Physik **3**, 123 (1920).

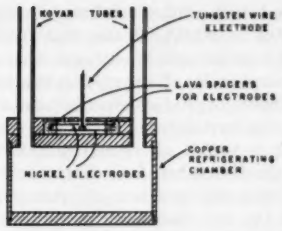

FIG. 6. Crystal mount for photoconductivity measurements as a function of temperature. The "tungsten wire electrode" is a 0.003-in. tungsten wire connecting to a 0.050-in. oxidized tungsten rod, 0.020-in. long, which is pressed onto the upper surface of the crystal by a light coil spring and glass support. The crystal lies between this rod and the lower nickel electrode.

The preamplifier consists of two parallel-balanced Victoreen VX-41 electrometer tubes which are battery powered and spring suspended to minimize the effects of microphonics. It is essentially an impedance transformer, having a voltage gain of about one-half. The basic design of the narrow band parallel-balanced amplifier is largely due to Roess,[14] who has presented a good discussion of the problems involved in building low frequency narrow band amplifiers. Phase-sensitive detection is obtained by connecting each phase of the "push-pull" output from the amplifier to one of the grids of a 6SL7; the cathodes are tied together and driven by the auxiliary phase signal. A microammeter and *RC* circuit with a time constant of about 1 second are connected between the plates of the 6SL7.

The 20-db down band width of amplifier and detector is about one cycle, with the maximum gain at 33 cps. The relative response at 60 cps is at least 60 db below the maximum, and no trouble is experienced with 60-cycle "pick-up." At 33 cps with maximum gain, full-scale deflection of the output meter represents 2×10^{-6} v rms at the input of the preamplifier. The noise level for the system with preamplifier and 100-megohm input resistor, but without the BaO crystal, is about 7×10^{-7} v. Output readings are approximately linear over an 80-db range of input voltage. Actually, the limitation on the magnitude of minimum photocurrents detectable is due to noise in the dark current of the BaO crystals. Currents measured for the data shown below were of the order of 10^{-14} to 10^{-12} ampere, with signal to noise ratios of the order of 10 to 1000.

The crystal mount used for ac photoconductivity measurements was designed to allow measurements from room temperature to near liquid nitrogen temperatures. Figure 6 shows the crystal mount, electrodes, and refrigerating chamber. The nickel electrode on which the crystal rests is held at a positive dc potential with respect to ground; the parallel nickel electrode above the crystal is at ground potential. Through a hole in the top electrode, a tungsten electrode is spring loaded on the crystal. To increase the thermal isolation of the sample, the small tungsten electrode is sealed to a glass rod and welded to a 0.003-in. wire which runs through the glass rod and through a Kovar-glass seal in the vacuum head to the input of the preamplifier. Thick copper plates above the electrodes and crystal are attached to the refrigerating chamber and serve to maintain the temperature of crystal and electrodes at approximately the temperature of the chamber. A copper-constantan thermocouple attached to the top electrode just above the crystal is used for temperature measurements. With liquid nitrogen in the cylinder, the lowest temperature recorded was $-180°$C. The crystal temperature is estimated to be within 5° of the electrode temperature.

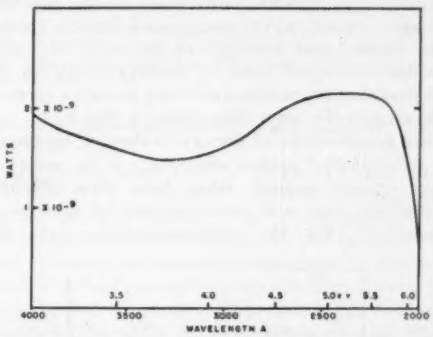

FIG. 7. Spectral energy distribution for light source and monochromator. The source is a Hanovia No. 71-3 hydrogen discharge tube in a quartz envelope operated at 3000 v ac, 0.3 amp. The Bausch and Lomb quartz monochromator is used with a constant width of both slits of 0.5 mm. The energy is determined by an RCA Cs-Sb phototube C-7120 calibrated against a thermopile.

The light source used for most of the measurements of both optical absorption and photoconductivity is a quartz, water-cooled, hydrogen discharge tube[15] similar to one described by Kistiakowsky.[16] The spectral energy distribution for this lamp is shown in Fig. 7. Due to the low light level, this calibration could not be obtained directly using a vacuum thermopile. Instead, a Cs–Sb phototube with a quartz window[17] was calibrated against the thermopile at high light levels using a high pressure mercury arc for light source. The sensitivity of the electrometer circuit used with the phototube was then increased by a factor of 10^3 and the hydrogen arc calibrated against the phototube. The error in relative values of the spectral distribution is probably less than 5 percent. The errors in absolute energy values are dif-

[14] L. C. Roess, Rev. Sci. Instr. **16**, 172 (1945). We are indebted to Dr. H. B. DeVore, RCA Laboratories, Princeton, New Jersey, for valuable discussions of problems relating to low frequency narrow band amplifiers.

[15] Hanovia Chemical and Manufacturing Company, No. 71-3.

[16] G. B. Kistiakowsky, Rev. Sci. Instr. **2**, 549 (1931).

[17] We are indebted to Dr. R. W. Engstrom, RCA Tube Division, Lancaster, Pennsylvania, for supplying us with this tube.

ficult to estimate and may be as much as 50 percent. The single crystals used in the ac experiments were about 1 mm×1 mm×1 mm.

2. *Experimental Results*

The lower curve, Fig. 8, shows the photoconduction current as a function of wavelength. The upper curve represents the same data normalized to a constant number of photons per second in each wavelength interval, using the spectral energy distribution shown in Fig. 7. The correction of the data changes the shape of the curve so slightly that the data below are presented without this normalization. The absolute magnitude of the quantum efficiency is difficult to estimate because of lack of knowledge of the mean range of the charge carriers. The ordinates in Fig. 8 are calculated on the assumption that the carriers freed by photon absorption remain free until striking an electrode. The ordinates thus represent lower limits for the quantum efficiency. At 4.0 ev, the quantum efficiency is greater than 5×10^{-2} and probably of the order of unity. (Evidence presented below in connection with Fig. 12 will show that the quantum efficiency probably appreciably exceeds the lower limit given by Fig. 8.)

The general shape of the curves showing photoconductivity plotted against wavelength is the same for seven crystals studied, taken from three different crystallizing runs, and containing varying amounts of impurities.[18] For the photoconductivity data the monochromator slit width was 0.5 mm, giving resolution of about 80A at 3000A. Within this resolution, the threshold for photoconductivity was coincident with that for absorption for all the crystals studied. Figure 9 shows thresholds for photoconductivity and absorptance plotted for two crystals from the same crystallizing run. Due to the fact that all crystal samples used were exposed to the atmosphere for a short time, while being transferred from the dry box to the vacuum, one might expect that the data shown in Fig. 9 are characteristic of a film of $Ba(OH)_2$ which must form on the BaO crystal surfaces. However, $Ba(OH)_2$ does not absorb appreciably anywhere in the region from 4000A to 2000A. This was convincingly demonstrated during the film study[8] by observation of the transmittance of BaO films as they were converted to $Ba(OH)_2$ films.

Although the optical absorption in BaO is quite insensitive to temperature change,[8] the magnitude of photoconduction currents is quite sensitive to temperature. Figure 10 shows photoconductivity as a function of wavelength for several temperatures. The shape of the wavelength dependence is the same at each temperature investigated. Crystals with different impurity content show different temperature dependence, the purer crystals showing detectable photoconductivity at lower temperatures. Figure 11 shows temperature dependence of photoconductivity at fixed wavelength and fixed field strength for two crystals, No. 9 and No. 11. Crystal No. 9 contains about 0.05 percent Mo in addition to Sr and Ca impurities; crystal No. 11 is relatively free of Mo. Photoconductivity could not be observed below −120°C for any of the crystals studied. The peak in the temperature dependence of photoconductivity shown for crystal No. 11 at −10°C has been observed for only two samples and is probably not significant.

It should be emphasized that the data shown represent steady-state currents and that the temperature dependence observed is probably not intrinsic to BaO. Lenz,[19] studying steady-state photoconductivity in diamond and zincblende, noted temperature dependence of the same nature as that observed in BaO. As a result

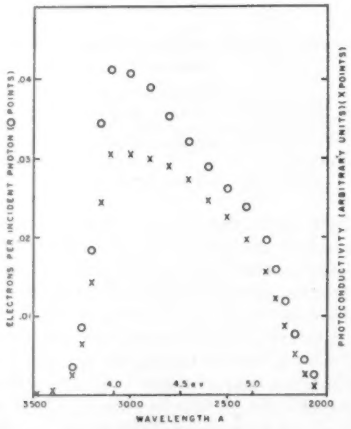

FIG. 8. Correction of data to constant number of photons incident per second at each wavelength. The crosses are the original data on BaO crystal No. 9. The circles are the data corrected by using Fig. 7. The quantity "electrons per incident photon" is intended only as a lower limit to the quantum efficiency, since the electric field was not large enough to give saturation currents.

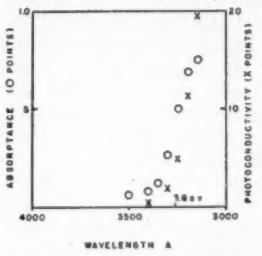

FIG. 9. Comparison of thresholds for absorptance and photoconductivity of a BaO crystal.

[18] As mentioned in footnote 4, the principal features of the observed wavelength dependence of both optical absorption and photoconductivity are believed to be intrinsic to the BaO lattice. However, using the larger crystals of higher purity, only recently available, and employing greater resolution, the slight peak in the photoconductivity indicated in Fig. 4 and Fig. 10 at about 4.0 ev appears considerably sharper and higher relative to the rest of the curve.

[19] H. Lenz, Ann. Physik **77**, 449 (1925).

of later work using ballistic techniques, Lenz[20] attributed this observed temperature dependence in diamond to the temperature dependence of space charge effects. In the present work, a few measurements have been made at liquid air temperatures using the ballistic technique. The signal-to-noise ratio was poor because of the small energy absorbed in each pulse of light, but the experiments serve to confirm the space charge interpretation of the temperature dependence of photoconductivity.

Figure 12 shows photoconductivity as a function of the strength of the dc field across a BaO crystal, for various temperatures. It is apparent that even for fields of the order of 15,000 v per cm there is no evidence for saturation of the photoconduction current. Higher fields cannot be applied because of the abrupt rise of noise in the dark current. The failure to draw saturation currents in any of the crystals studied indicates that

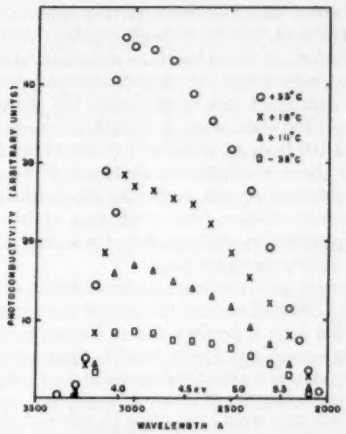

FIG. 10. The ac photoconductivity for BaO crystal No. 9 at various temperatures.

the charge carriers do not remain free until they strike an electrode; therefore, the quantum efficiency computed for Fig. 8 is only a lower limit and the actual quantum efficiency is considerably larger.

Like the temperature dependence, the field dependence of photoconductivity is impurity sensitive. Curves of the type shown in Fig. 12 are in general slightly concave upward but become more nearly straight lines for the crystals of highest purity. Again this behavior suggests the existence of a large space charge in the crystals of higher impurity concentration, probably due to trapping of photoconduction electrons at impurity centers. Techniques have not yet been developed for the inclusion of controlled amounts of impurity in BaO crystals, and, therefore, no systematic correlation between either temperature dependence or field dependence of photoconductivity and impurity content can be presented.

[20] H. Lenz, Ann. Physik **83**, 941 (1927).

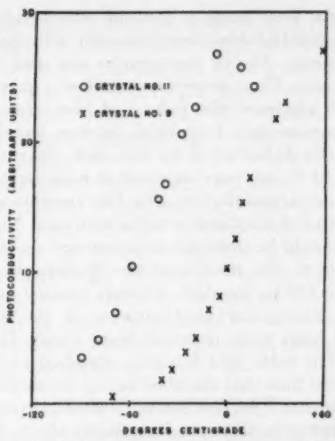

FIG. 11. The ac photoconductivity as a function of temperature. The wavelength in both cases is 3000A, and the potential difference across the crystals (each about $\frac{1}{4}$ mm thick) is 500 v. Crystal No. 11 is of higher purity.

The crystal mount used for the above measurements was designed to minimize the effect of external photoelectric currents. However, the field dependence and temperature dependence described above constitute the best evidence that the currents measured in this work are true photoconductivity currents. The currents are so small that the smallest fields used would collect all electrons released by the external photoelectric effect. Furthermore, there is no reason to believe that external photoelectric currents should disappear at low temperatures.[21]

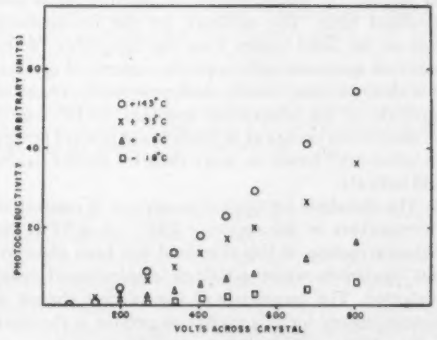

FIG. 12. The ac photoconductivity as a function of electric field strength at various temperatures. The BaO crystal is No. 8, 0.56 mm thick in the direction of the field. Illumination is by a medium pressure mercury arc at 3140A.

[21] Using a 1000-watt H-6 Hg arc as light source, photocurrents could be measured from BaO crystals at any strong Hg line in the visible region of the spectrum. The quantum efficiency for this

Attempts were made to measure photoconductivity in evaporated BaO films simultaneously with absorption measurements. The dc electrometer was used for this measurement. Films were evaporated[8] on a quartz plate on which platinum electrodes had been coated. The electrodes were each 1 cm long and were separated by 1 mm. After deposition of the film, dark currents of the order of 10^{-11} amp were observed at room temperature with 67 v dc across the film. The dark currents were not linear with film thickness or stable with time. No photocurrents could be observed superimposed on the large dark current. On decreasing the temperature of the film to -150°C, the dark currents became negligible ($<10^{-14}$ amp), and photocurrents of the order of 5×10^{-14} amp were observed from about 3100A to 2500A. The total light intensity absorbed in the film was greater than that absorbed during the single crystal measurements. Film photocurrents were independent of voltage between electrodes for voltages above 200. The very small magnitude of film currents and the independence of field strength probably indicate that the film is made up of very small crystals, with interfaces between these crystals decreasing the mobility of charge carriers. The large room temperature dark currents are probably due to surface and interface semiconduction in the film. The presence of detectable photocurrents in films at -150°C is consistent with the fact that the temperature dependence of photoconductivity observed in single crystals is not intrinsic.

V. CONCLUSIONS

A detailed interpretation of these experiments will not be attempted here. The experimental conclusions and a brief analyses of their relation to other experiments and to the properties of BaO follow.

1. The fundamental optical absorption band begins at a photon energy of about 3.8 ev. The band edge has been located by measurements on both crystals and evaporated films. The evidence for the fundamental nature of the band comes from the invariance of the absorption spectrum with impurity content of crystals and with irradiation history, and, principally, from the magnitude of the absorption constant ($>10^5$ cm^{-1}). This absorption occurs at a much lower photon energy than estimates[22] based on x-ray data for similar oxides would indicate.

2. The threshold for optical absorption is insensitive to temperature in the region -150°C to $+30$°C. No systematic motion of this threshold has been observed under conditions where a 0.02-ev displacement could be detected. The magnitude of the average change in minimum energy for this excitation process is therefore less than 10^{-4} ev/°C in this temperature range.

3. The threshold for photoconduction occurs at the same energy as for optical absorption. This statement applies to photoconduction with quantum efficiency of the order of 0.01 or more. Small photoelectric or photoconduction currents are observed at longer wavelengths, but these have not been investigated in detail; the optical absorption constant is so small in this region that impurities or F-centers probably provide the electrons.

4. A second rise in the optical absorption begins at about 4.8 ± 0.2 ev. At this energy the photoconductivity is decreasing with increasing photon energy. Such behavior has been ascribed[23] to limitation of photoconduction currents by recombination when the absorption of light takes place in a very thin layer at the surface of a crystal. Such an explanation does not appear reasonable in the present problem for two reasons: (a) The absorption constants at 4.5 and 5.2 ev are the same, but photoconductivities differ by greater than a factor of two; (b) A rough quantitative theory of the variation of recombination rate with absorption constant predicts that the photoconductivity would fall toward zero much less rapidly than the observations indicate. (The data show a decrease of more than a factor of 100 from 4.1 to 6.2 ev.) It should be observed that the above considerations are based on the assumption of a perfect crystal, neglecting the possibility that the quantum efficiency for production of free charge may depend on the distance from the surface at which photon absorption takes place.

It appears quite possible that two different excitation processes could be causing the optical absorption. (The absorption edge is perhaps due to exciton production, with the second rise due to band-to-band transitions.) One would have a threshold energy of 3.8 ev, a peak at 4.1 ev, and it would fall slowly to nearly zero at 6.2 ev; this absorption would be accompanied by photoconductivity. The second process would have a threshold at about 4.8 ± 0.2 ev and would not be accompanied by photoconductivity of comparable quantum efficiency. However, we know of no proposed explanation for an absorption process unaccompanied by photoconductivity at higher energy than the photoconduction threshold.

5. The magnitude of the photoconduction current is a sensitive function of temperature, a function of impurity content, and a nonlinear function of the applied electric field. In each case the dependence is such that the existence of space charge in the crystal is suggested. The positive holes left in the filled band after the excitation of electrons may or may not be mobile. If mobile, they may be trapped, and then the rate of release from traps would be an exponential function of temperature. The same statement applied to the excited electrons. Except for the possibility of recombination or complete transit of the crystal, any motion of electrons and holes

photoeffect is less than for photoconductivity currents from 3300A to 2100A by a factor of at least 10^6. These photocurrents did not disappear at -180°C and may be external photoelectric currents. Using the lower intensity hydrogen arc source, no currents were detectable except the photoconduction currents in the region of strong optical absorption.

[22] N. F. Mott and R. W. Gurney, reference 2, pp. 76–78, 101.

[23] N. F. Mott and R. W. Gurney, reference 2, p. 104.

results in a space charge reduction of the field in the crystal. Since the electrons are probably more mobile than the holes, the temperature dependence of photoconductivity probably represents the variation with temperature of the rate of release of electrons from traps.

6. The excitation process responsible for the observed light absorption may be either the creation of a free electron and hole or the creation of an exciton. Mott[24] has attributed the first (lowest energy) fundamental absorption bands in the alkali halides to exciton creation. Such excitons in BaO would probably be thermally dissociated at room temperature.[25] The present experiments cannot distinguish between a band-to-band electronic transition, which enables an electron to move freely immediately after the absorption of light, and a transition to an exciton state, which would be quickly dissociated to yield an electron moving freely. Experiments with single, short light pulses (to reduce the effects of space charge) should be performed down to liquid hydrogen temperatures to distinguish between these processes.

Another way in which photoconductivity could result from the creation of excitons has recently been demonstrated by Apker and Taft.[26] They showed that excitons produced by absorption in the first fundamental absorption band in KI may ionize F-centers, giving rise to electrons in the conduction band. Such a process may contribute to photoconductivity in BaO, competing with thermal dissociation of excitons in the production of conduction electrons.

[24] N. F. Mott, Trans. Faraday Soc. **34**, 500 (1938).

[25] Mott has estimated in Proc. Phys. Soc. (London) **A167**, 384 (1938), the extent to which dissociation of excitions may contribute to photoconductivity. If one inserts the value 4 for the optical dielectric constant and 34 for the static dielectric constant (recently measured in this laboratory) into Mott's estimation (p. 390), one finds that temperatures much below liquid air temperature would be required to prevent dissociation of excitons in BaO. This contrasts with the behavior of NaCl, which has a lower dielectric constant and in which optical absorption without photoconductivity has been observed at room temperature by Ferguson (Phys. Rev. **66**, 220 (1944)).

VI. ACKNOWLEDGMENTS

The authors are indebted to Dr. Arnold R. Moore and Mr. S. S. Stevens for valuable assistance in this work and are especially grateful for many discussions with Professor J. A. Krumhansl on the interpretation of these experiments.

[26] L. Apker and E. Taft, Phys. Rev. **79**, 964 (1950).

PHYSICAL REVIEW VOLUME 83, NUMBER 3 AUGUST 1, 1951

Low Energy Photomeson Production in Hydrogen

S. D. DRELL
Stanford University, Stanford, California

(Received February 8, 1951)

Berkeley experiments have revealed the general features of the neutral and charged π-meson photoproduction cross sections for gamma-rays incident on protons. In particular, approximate equality of the π^0 and π^+ production cross sections has been observed. This has proved difficult to account for theoretically. Calculations based on a weak coupling perturbation treatment of the meson-nucleon interaction predict the π^0 production to be reduced by $\sim(\mu/M)^2$ relative to π^+ production for energies at which the Berkeley experiments are performed ($\sim$320 Mev). In this paper we avoid the perturbation theory approximation of weak nucleon-meson coupling. By means of a canonical transformation of the type introduced by Bloch and Nordsieck, we obtain a solution to the hamiltonian equation that involves no assumption concerning the largeness or smallness of $g^2/4\pi$. The approximations involved are neglect of nucleon recoil and treatment of spin and charge matrices as classical unit vectors. Handling the electromagnetic field by standard perturbation theory, we use this solution to calculate the matrix elements for photoproduction. In evaluating the matrix elements we must use a finite source cutoff to compensate neglect of nucleon recoil. We obtain qualitative agreement with the observed equality of π^0 and π^+ production cross sections with a choice of $g^2/4\pi\sim 1-2$ and of source radius of the order of a nucleon Compton wavelength. Calculation of the anomalous nucleon magnetic moments corroborates a choice of these constants in this range. We also obtain an angular distribution and energy dependence for the production cross sections in accord with observation.

I. INTRODUCTION

EXTENSIVE experimental work at Berkeley has established the following general features of the photomeson production process, for gamma-rays of energy up to 320 Mev incident on protons:

1. The cross sections for production of neutral and charged pi-mesons by 320-Mev bremsstrahlung are approximately equal, ($\sigma_T\sim 10^{-28}$ cm^2).[1,*]

2. The production cross sections are approximately isotropic in the center-of-mass frame.[2]

3. The excitation function for the production of neutral mesons is steeper than for the production of charged mesons.[3]

This paper attempts to arrive at an understanding of these features of neutral and charged photomeson production within the framework of the present formulation of meson field theory. From the point of view of

[1] Steinberger, Panofsky, and Steller, Phys. Rev. **78**, 802 (1950). J. S. Steller and W. K. H. Panofsky, Phys. Rev. **81**, 649 (1951). I wish to thank Professor R. Serber for calling my attention to this result.

[*] *Note added in proof.*—Later data indicate a reduction in π^0 production by a factor of roughly three relative to π^+ production.

[2] Steinberger, Panofsky, and Steller, Phys. Rev. **78**, 802 (1950); K. A. Brueckner, Phys. Rev. **79**, 641 (1950) (see p. 645).

[3] J. S. Steller and W. K. H. Panofsky, Phys. Rev. **81**, 649 (1951); J. Steinberger and A. Bishop, Phys. Rev. **78**, 494 (1950).

meson theory these are very simple processes, involving only the interaction of a single nucleon and its associated meson field with quanta. Thus, a theoretical understanding of the Berkeley observations would be very desirable. It is apparent from the experimental observation 1 (large magnitude of the π^0 production cross section) that any theoretical attempt at an explanation of this process must lie outside the perturbation-weak coupling approximation. This is because there is no direct interaction between neutral mesons and electromagnetic radiation. For charged meson production the gamma-ray can directly interact with and eject a π^+ meson, in a lowest order perturbation calculation ($\sim e^2g^2$). For neutral meson production in this same order the process is described by an interaction of the gamma-ray with the proton magnetic moment, followed by π^0 emission[1,4] For gamma-energies up to several times the production threshold of roughly 150 Mev, we would expect the π^0 photoproduction cross section to be reduced relative to that for π^+ mesons by $\sim(\mu/M)^2$. Perturbation calculations bear out this prediction.[5]

However, we may avoid the assumption of weak coupling between the proton and meson field and view this process along lines more closely related with the notion of the compound nucleus, as applied to the calculation of low energy photoprocesses in heavy nuclei. The physical nucleon—a Dirac particle with its associated meson field—is described in its initial state by momentum, spin, and isotopic spin vectors $\mathbf{p}_i$, $\boldsymbol{\sigma}_i$, and $\boldsymbol{\tau}_i$. After absorbing a gamma it emits a π-meson, recoiling with $\mathbf{p}_f$, $\boldsymbol{\sigma}_f$, and $\boldsymbol{\tau}_f$, as directed by conservation of energy, momentum, angular momentum, and charge. The difference between π^+ and π^0 production is derived from the fact that the proton changes its charge state upon emitting a π^+, but $\boldsymbol{\tau}$ remains unchanged for π^0 emission. However, if the meson field couples with the nucleon spin, we may expect an appreciable spin change $\Delta\boldsymbol{\sigma}$ to accompany both the π^+ and π^0 photoproduction processes and hence comparable cross sections for them. Nucleon velocity effects are considerably smaller at this energy. This is analogous to the considerations that apply in treating the (γ,p) and (γ,n) processes in heavy nuclei.[6] In the nuclear photoprocess, on the other hand, there is a coulomb barrier that is responsible for a drastic reduction in the number of protons emitted, relative to the number of neutrons. No coulomb effects operate in this process of meson production from protons. On the basis of the preceding discussion, we are motivated to renounce perturbation theory, at least as far as meson-nucleon coupling is concerned. In order to obtain the desired coupling of the meson field with the nucleon spin, we resort to a pseudoscalar formulation of the meson field. Brueckner's[2] analysis of the charged meson production data argues strongly for this choice. Our calculation of the π^0 production process on the basis of a scalar meson field, which does not directly couple with the nucleon spin, further substantiates it by predicting much too small a cross section. Yang[7] and others have presented convincing arguments against a vector meson field in a charge symmetric formulation.

II. DESCRIPTION OF CALCULATIONS AND RESULTS

We give a brief description of the method, approximations, and results of this calculation. A nucleon, described by the one-particle Dirac equation, is coupled with a quantized, charge symmetric pseudoscalar meson field. Pseudovector coupling is assumed. No approximation is made concerning the largeness or smallness of the coupling strength $g^2/4\pi$. Following the Bloch-Nordsieck[8] argument, we replace the hamiltonian by its positive energy part. The approximation involved here is neglect of the change in the nucleon velocity upon interaction with the quantum and meson fields.[9] Treating the spin and charge (isotopic spin) vectors $\boldsymbol{\sigma}$ and $\boldsymbol{\tau}$ classically, we can write down an exact solution to the equation of motion. The wave function is obtained by means of a canonical transformation of the type introduced by Bloch and Nordsieck[8] for the radiation field, and applied by Lewis, Oppenheimer, and Wouthuysen[10] to meson problems.

Handling the electromagnetic field by standard perturbation theory, we use this solution to calculate the matrix elements for transitions from an initial state in which one gamma-ray is present to a final state with one free meson. The results are readily compared with Foldy's[11] perturbation calculation of π^+ production on the basis of pseudoscalar meson theory with pseudovector coupling, in which nucleon recoil is neglected. Expanding our matrix element for π^+ production in a power series in g, we find that the leading term, of the order eg, agrees with Foldy's calculation. The matrix element we calculate for π^0 production is of the order eg^3. It diverges linearly unless a finite-source cutoff is used to compensate the neglect of nucleon recoil. We obtain qualitative agreement with the observed equality of π^0 and π^+ photoproduction cross sections with a choice of nucleon-meson coupling constant of the order of unity ($g^2/4\pi\sim1-2$) and of the source radius of the order of the nucleon Compton wavelength. In agreement with observations 2 and 3 above, the calculated cross sections are roughly spherically symmetric in the center-of-mass system, and the excitation function for π^0 production is steeper than for π^+ production. Brueckner[2] has given a detailed discussion of the rela-

[4] G. Araki, Prog. Theor. Phys. **5**, 507 (1950).
[5] K. A. Brueckner and K. M. Watson give a more complete discussion of this point in Phys. Rev. **79**, 187 (1950).
[6] MDDC 1175 (LLA 24), U. S. Government Printing Office.
[7] C. N. Yang, Phys. Rev. **77**, 242 (1950).
[8] F. Bloch and A. Nordsieck, Phys. Rev. **52**, 54 (1937).
[9] The effect of recoil is reduced by the order of the meson, proton mass ratio for energies at which the Berkeley experiments operate.
[10] Lewis, Oppenheimer, and Wouthuysen, Phys. Rev. **73**, 127 (1948).
[11] L. L. Foldy, Phys. Rev. **76**, 372 (1949). See also Feshbach and Lax, Phys. Rev. **76**, 134 (1949).

tion between the angular distribution and the nature of the interaction of the gamma-ray with the nucleon spin, or moment, on the basis of a pseudoscalar meson field theory. The difference in behavior of the excitation function for charged and neutral meson production indicates that different production mechanisms dominate near threshold. For π^+ production the quantum field interacts with the meson charge and nucleon spin, as indicated by the first term of Eq. (6) following. This matrix element is independent of emitted meson momentum, and the cross section increases linearly with the π^+ momentum. This mechanism does not operate for π^0 production. In the latter case the nucleon spin recoils as the emitted π^0 field carries away angular momentum. Hence, the matrix element varies with a first power and the cross section with the cube of the emitted π^0 momentum at threshold.

We also use the same calculational procedure to determine the anomalous nucleon magnetic moments. We wish to learn from this calculation if we obtain qualitative agreement with the observed value of $|\Delta\mu_N| \sim 2\mu_0$ with the choice of $k_{\max}$ and $g^2/4\pi$ made in the photoproduction calculation. Within the uncertainties in the values of these parameters and in our classical treatment of spin, we find that we do.

III. CALCULATION

A. Wave Funtion

We write the hamiltonian for a Dirac particle of mass M' and momentum $\mathbf{p}$, interacting via pseudovector coupling with a charge symmetric pseudoscalar meson field,

$$H=\boldsymbol{\alpha}\cdot\mathbf{p}+\beta M'+\tfrac{1}{2}\sum_{\alpha=1}^{3}\sum_{\mathbf{k}}\omega_k(P_{\mathbf{k}\alpha}^2+Q_{\mathbf{k}\alpha}^2)+(g/2^{\frac{1}{2}}\mu L^{\frac{1}{2}})\sum_{\alpha=1}^{3}\sum_{\mathbf{k}}(\boldsymbol{\sigma}\cdot\mathbf{k}+\omega_k\gamma_5)(\tau_\alpha/\omega_k^{\frac{1}{2}})\times(Q_{\mathbf{k}\alpha}\cos\mathbf{k}\cdot\mathbf{r}-P_{\mathbf{k}\alpha}\sin\mathbf{k}\cdot\mathbf{r}). \quad (1)$$

In Eq. (1), $P_{\mathbf{k}\alpha}$ and $Q_{\mathbf{k}\alpha}$ are the canonically conjugate momentum and amplitude for mode $(\mathbf{k}\alpha)$ of the meson field. They are defined by a fourier expansion of the meson field,

$$\varphi_\alpha(\mathbf{r})=(1/L^{\frac{1}{2}})\sum_{\mathbf{k}}(1/\omega_k^{\frac{1}{2}})(P_{\mathbf{k}\alpha}\cos\mathbf{k}\cdot\mathbf{r}+Q_{\mathbf{k}\alpha}\sin\mathbf{k}\cdot\mathbf{r}). \quad (2)$$

The meson mass is μ; ω_k is $(k^2+\mu^2)^{\frac{1}{2}}$; $g^2/4\pi$ is the dimensionless coupling constant, L^3 the normalization volume; $\boldsymbol{\alpha}$, β, $\boldsymbol{\sigma}$, and $\gamma_5=\gamma_1\gamma_2\gamma_3\gamma_4$ are the usual Dirac matrices; τ_α is the isotopic spin vector; $\alpha=3$ describes the neutral charge state of the meson field. We use units of $\hbar=c=1$. We neglect the nucleon recoil by replacing the velocity operator $\boldsymbol{\alpha}$ by the value $\mathbf{v}$ of the nucleon velocity. If we assume that the nucleons travel with slow, nonrelativistic velocities $v<1$, as is the case for the Berkeley experiments, we may in addition replace β by one and neglect the γ_5 term in the interaction. In this approximation, the hamiltonian expression (1) reduces to[12]

$$H=\mathbf{v}\cdot\mathbf{p}+M'+\tfrac{1}{2}\sum_{\alpha,\mathbf{k}}\omega_k(P_{\mathbf{k}\alpha}^2+Q_{\mathbf{k}\alpha}^2)+(g/2^{\frac{1}{2}}\mu L^{\frac{1}{2}})\times\sum_{\alpha,\mathbf{k}}(\tau_\alpha\boldsymbol{\sigma}\cdot\mathbf{k}/\omega_k^{\frac{1}{2}})(Q_{\mathbf{k}\alpha}\cos\mathbf{k}\cdot\mathbf{r}-P_{\mathbf{k}\alpha}\sin\mathbf{k}\cdot\mathbf{r}). \quad (3)$$

If we treat the spin and charge vectors classically, so that we can commute the different components of $\boldsymbol{\sigma}$ and $\boldsymbol{\tau}$ among themselves, we can write down an exact solution to the wave equation,

$$H\psi(Q,\mathbf{r})=E\psi(Q,\mathbf{r}).$$

The normalized eigenfunction is

$$\psi(Q,\mathbf{r})=L^{-\frac{1}{2}}\exp i\{(g/2^{\frac{1}{2}}\mu L^{\frac{1}{2}})\sum_{\mathbf{k},\alpha}(\tau_\alpha\boldsymbol{\sigma}\cdot\mathbf{k}/\omega_k^{\frac{1}{2}})\sin\mathbf{k}\cdot\mathbf{r}\times[Q_{\mathbf{k}\alpha}+\tfrac{1}{2}(g/2^{\frac{1}{2}}\mu L^{\frac{1}{2}})(\tau_\alpha\boldsymbol{\sigma}\cdot\mathbf{k}/\omega_k^{\frac{1}{2}})\cos\mathbf{k}\cdot\mathbf{r}]+M\mathbf{v}\cdot\mathbf{r}\}\prod_{\alpha\mathbf{k}}h_{m_{\alpha\mathbf{k}}}[Q_{\mathbf{k}\alpha}+(g/2^{\frac{1}{2}}\mu L^{\frac{1}{2}})\times(\tau_\alpha\boldsymbol{\sigma}\cdot\mathbf{k}/\omega_k^{\frac{1}{2}})\cos\mathbf{k}\cdot\mathbf{r}], \quad (4)$$

and the corresponding eigenvalue is

$$E=M+\sum_{\mathbf{k},\alpha}\omega_k(m_{\alpha k}+\tfrac{1}{2}). \quad (5)$$

The method of obtaining this solution by means of a canonical transformation is given in references 8 and 10. The $m_{\alpha k}$ are the numbers of free mesons of wave number $\mathbf{k}$, energy ω_k, and charge state α. The $h_{m_{\alpha k}}$ are normalized harmonic oscillator wave functions. The nucleon-meson field coupling manifests itself in a displacement of the origin of the field oscillators whose coordinates now depend on the spin and charge states. Neglected in Eqs. (4) and (5) are terms of order $(\mathbf{v}\cdot\mathbf{k})/\omega_k<1$. The mass parameter M in Eqs. (4) and (5) represents the mass of the physical nucleon $-1836\,m_0$. It is related to the mass constant M' in Eq. (3) by

$$M=M'-(g^2/4\mu^2L^3)\sum_{\mathbf{k},\alpha}[\tau_\alpha^2(\boldsymbol{\sigma}\cdot\mathbf{k})^2/\omega_k^2].$$

This mass renormalization is discussed for the electromagnetic case in reference 8 and by Pauli and Fierz.[13] The infinite sum is related to the self-energy problem of field theory. We do not discuss this further here, since our nonrelativistic treatment is not valid for large k. We shall employ cutoffs when infinite sums arise, corresponding to a finite size nucleon of radius $\sim 1/k_{\max}$. These infinities are the same as those which obscure standard perturbation calculations with neglect of recoil.

B. Matrix Element

Interaction with the electromagnetic field will induce transitions of the nucleon-meson system between dif-

[12] A more detailed treatment following the Bloch-Nordsieck argument (Eqs. (4) through (9) of reference 8) yields this same result for slow nucleons.

[13] W. Pauli and M. Fierz, Nuovo cimento **15**, 1 (1938).

ferent stationary states as described by Eq. (4). In contrast with the situation for the meson field, the coupling with the quantum field is weak ($e^2=1/137$), and we treat it by perturbation theory. We calculate the matrix element for the system to absorb a quantum of momentum $\mathbf{K}$ and make a transition from an initial state with velocity, spin, and isotopic spin $\mathbf{v}_i$, $\boldsymbol{\sigma}_i$, $\boldsymbol{\tau}_i$, and with no free mesons (all $m_{\alpha\mathbf{k}}=0$) to a final state with $\mathbf{v}_f$, $\boldsymbol{\sigma}_f$, $\boldsymbol{\tau}_f$, and with one free meson of momentum $\mathbf{k}'$ and charge α' ($\alpha'=3$ for π^0 production). The perturbing terms in the hamiltonian are

$$H'=(ge)/(2^{\frac{1}{2}}\mu)\mathbf{A}\cdot\boldsymbol{\sigma}(\varphi_1\tau_2-\varphi_2\tau_1)$$
$$-e\int\mathbf{A}\cdot(\varphi_2\,\mathbf{grad}\varphi_1-\varphi_1\,\mathbf{grad}\varphi_2)d\mathbf{r}. \quad (6)$$

We neglect the interaction of the nucleon with quanta because of its heavy mass and slow velocity. This is consistent with our other approximations. We introduce the fourier analysis, Eq. (2), for the meson field. Expanding the vector potential $\mathbf{A}$ in plane waves, we write $L^{-\frac{1}{2}}((2\pi)^{\frac{1}{2}}/K^{\frac{1}{2}})\boldsymbol{\epsilon}_{\mathbf{K}}{}^{\lambda}\exp(i\mathbf{K}\cdot\mathbf{r})$ for annihilation of a photon of momentum $\mathbf{K}$ and polarization $\lambda(=1,2)$, so that Eq. (6) reads

$$H'=(ge/2^{\frac{1}{2}}\mu L^3)(2\pi/K)^{\frac{1}{2}}\boldsymbol{\epsilon}_{\mathbf{K}}{}^{\lambda}\cdot\boldsymbol{\sigma}\sum_{\mathbf{k}}1/\omega_k{}^{\frac{1}{2}}$$
$$\times[(\tau_2P_{\mathbf{k}1}-\tau_1P_{\mathbf{k}2})\cos\mathbf{k}\cdot\mathbf{r}+(\tau_2Q_{\mathbf{k}1}-\tau_1Q_{\mathbf{k}2})\sin\mathbf{k}\cdot\mathbf{r}]$$
$$-(ie/2L^{\frac{1}{2}})(2\pi/K)^{\frac{1}{2}}\sum_{\mathbf{k}}[\boldsymbol{\epsilon}_{\mathbf{K}}{}^{\lambda}\cdot\mathbf{k}/(\omega_k\omega_{\mathbf{k}+\mathbf{K}})^{\frac{1}{2}}]$$
$$\times(P_{\mathbf{k}1}-iQ_{\mathbf{k}1}+P_{-\mathbf{k}1}+iQ_{-\mathbf{k}1})$$
$$\times(P_{(-\mathbf{k}-\mathbf{K})2}-iQ_{(-\mathbf{k}-\mathbf{K})2}$$
$$+P_{(+\mathbf{k}+\mathbf{K})2}+iQ_{(+\mathbf{k}+\mathbf{K})2}). \quad (7)$$

We use the following properties of canonical coordinates u and v and of hermite polynomials of zero order:

$$[v,e^{iqu}]=ae^{iqu},\quad vh_0(u+c)=(i/\sqrt{2})h_1(u+c),$$
$$uh_0(u+c)=(1/\sqrt{2})h_1(u+c)-ch_0(u+c).$$

We then write for the matrix element for production of a meson of momentum $\mathbf{k}'$ and charge α'

$$\text{M.E.}=(e/L^{9/2})(2\pi/K)^{\frac{1}{2}}\int d\mathbf{r}\prod_{\mathbf{k}\alpha}dw_{\mathbf{k}\alpha}\exp[-iM(\mathbf{v}_f-\mathbf{v}_i)\cdot\mathbf{r}-2i\sum_{\mathbf{k}\alpha}\beta_{\mathbf{k}\alpha}w_{\mathbf{k}\alpha}]h_{1\mathbf{k}'\alpha'}(f)\prod_{\mathbf{k}\alpha}{}'\,h_{0\mathbf{k}\alpha}(f)$$
$$\times\Big\{(g/2^{\frac{1}{2}}\mu L^{\frac{1}{2}})\boldsymbol{\epsilon}_{\mathbf{K}}{}^{\lambda}\cdot\boldsymbol{\sigma}\sum_{\mathbf{q}}\omega_q{}^{-\frac{1}{2}}\exp[i(\mathbf{K}-\mathbf{q})\cdot\mathbf{r}][\tau_2h_{1\mathbf{q}1}(i)\prod_{\mathbf{k}\alpha}{}'\,h_{0\mathbf{k}\alpha}(i)-\tau_1h_{1\mathbf{q}2}(i)\prod_{\mathbf{k}\alpha}{}'\,h_{0\mathbf{k}\alpha}(i)]$$
$$-i\sum_{\mathbf{q}}\frac{\boldsymbol{\epsilon}_{\mathbf{K}}{}^{\lambda}\cdot\mathbf{q}}{(\omega_q\omega_{\mathbf{q}+\mathbf{K}})^{\frac{1}{2}}}\Big(\frac{g\tau_1\boldsymbol{\sigma}\cdot\mathbf{q}}{\mu(\omega_qL)^{\frac{1}{2}}}\exp[-i\mathbf{q}\cdot\mathbf{r}]\prod_{\mathbf{k}\alpha}h_{0\mathbf{k}\alpha}(i)+h_{1-\mathbf{q}1}(i)\prod_{\mathbf{k}\alpha}{}'\,h_{0\mathbf{k}\alpha}(i)\Big)$$
$$\times\Big(\frac{g\tau_2\boldsymbol{\sigma}\cdot(\mathbf{q}+\mathbf{K})}{\mu(\omega_{\mathbf{q}+\mathbf{K}}L)^{\frac{1}{2}}}\exp[i(\mathbf{q}+\mathbf{K})\cdot\mathbf{r}]\prod_{\mathbf{k}\alpha}h_{0\mathbf{k}\alpha}(i)-h_{1(\mathbf{q}+\mathbf{K})2}(i)\prod_{\mathbf{k}\alpha}{}'\,h_{0\mathbf{k}\alpha}(i)\Big)\Big\}, \quad (8)$$

where

$$w_{\mathbf{k}\alpha}=Q_{\mathbf{k}\alpha}+(g/2^{\frac{1}{2}}\mu L^{\frac{1}{2}})\frac{[(\tau_\alpha\boldsymbol{\sigma})_f+(\tau_\alpha\boldsymbol{\sigma})_i]\cdot\mathbf{k}}{\omega_k{}^{\frac{1}{2}}}\cos\mathbf{k}\cdot\mathbf{r},$$
$$\beta_{\mathbf{k}\alpha}=(g/2^{\frac{1}{2}}\mu L^{\frac{1}{2}})\frac{[(\tau_\alpha\boldsymbol{\sigma})_f-(\tau_\alpha\boldsymbol{\sigma})_i]\cdot\mathbf{k}}{\omega_k{}^{\frac{1}{2}}}\sin\mathbf{k}\cdot\mathbf{r}.$$

Above, $h(i)\{h(f)\}$ refers to initial {final} spin and charge values in the arguments of the hermite polynomials, and $\prod_{\mathbf{k}\alpha}{}'$ denotes a product for all values of $\mathbf{k}$ and α excluding the one written immediately to the left of it.

In evaluating this matrix element an essential difference is observed between the charged and neutral meson production calculations. The operation of charged meson field amplitudes φ_1, φ_2 in Eq. (6) on the initial state function has introduced $h_{1\mathbf{k}1}(i)$ and $h_{1\mathbf{k}2}(i)$ into the integrand of Eq. (8). They can connect directly with $h_{1\mathbf{k}'\alpha'}(f)$ for $\mathbf{k}=\mathbf{k}'$ and $\alpha'=1$ or 2. This set of direct terms is present for charged meson production but does not contribute to the π^0 process, for which $\alpha'=3$.

We write

$$\text{M.E.}(\gamma,\pi_1)=\text{M.E.}_D+\text{M.E.}_I, \quad (9)$$
$$\text{M.E.}(\gamma,\pi_0)=\text{M.E.}_0, \quad (10)$$

where M.E.$_D$ denotes these direct terms, and M.E.$_I$ and M.E.$_0$ differ only in isotopic spin $\boldsymbol{\tau}$. We use the generating functions for hermite polynomials[8] to carry through analytically the integrations in Eq. (8). We observe the integrals to dictate momentum conservation[14]

$$M\mathbf{v}_i+\mathbf{K}=M\mathbf{v}_f+\mathbf{k}'. \quad (11)$$

Energy conservation reads

$$\tfrac{1}{2}Mv_i{}^2+K=\tfrac{1}{2}Mv_f{}^2+\omega_{k'}. \quad (12)$$

[14] For this reason it is preferable not to treat the nucleon as a delta-function source at the origin. The calculational result would be the same, since we neglect velocity terms.

We obtain

$$\text{M.E.}_D=(ge i/\mu L^3)(\pi/2K\omega_{k'})^{\frac{1}{2}}$$
$$\times\{\exp\textstyle\sum_{k\alpha}(-g^2/8\mu^2L^3\omega_k^3)[\boldsymbol{\Delta}(\tau_\alpha\boldsymbol{\sigma})\cdot\mathbf{k}]^2\}$$
$$\times\left[\boldsymbol{\varepsilon}_K^\lambda\cdot\boldsymbol{\sigma}\tau_2-\frac{2\boldsymbol{\varepsilon}_K^\lambda\cdot\mathbf{k}'\boldsymbol{\sigma}\cdot(\mathbf{k}'-\mathbf{K})}{\omega_{k'-K}^2}\tau_2\right.$$
$$\left.-\frac{\boldsymbol{\varepsilon}_K^\lambda\cdot\mathbf{k}'\boldsymbol{\Delta}(\tau_2\boldsymbol{\sigma})\cdot(\mathbf{k}'-\mathbf{K})}{\omega_{k'-K}^2}\right]; \quad (13)$$

$$\text{M.E.}_I=\boldsymbol{\Delta}(\tau_1\boldsymbol{\sigma})\cdot\mathbf{k}'\text{M.E.}'; \quad (14)$$

$$\text{M.E.}_0=\boldsymbol{\Delta}(\tau_3\boldsymbol{\sigma})\cdot\mathbf{k}'\text{M.E.}'; \quad (15)$$

$$\text{M.E.}'=-(g^3ei/\mu^3L^3)(\pi/2K\omega_{k'}{}^3)^{\frac{1}{2}}$$
$$\times\{\exp\textstyle\sum_{k\alpha}(-g^2/8\mu^2L^3\omega_k^3)[\boldsymbol{\Delta}(\tau_\alpha\boldsymbol{\sigma})\cdot\mathbf{k}]^2\}$$
$$\times L^{-3}\sum_{\mathbf{k}}\frac{\boldsymbol{\varepsilon}_K^\lambda\cdot\mathbf{k}}{\omega_k{}^2\omega_{k+K}{}^2}[\tau_1\boldsymbol{\sigma}\cdot\mathbf{k}+\tfrac{1}{2}\boldsymbol{\Delta}(\tau_1\boldsymbol{\sigma})\cdot\mathbf{k}]$$
$$\times[\tau_2\boldsymbol{\sigma}\cdot(\mathbf{k}+\mathbf{K})+\tfrac{1}{2}\boldsymbol{\Delta}(\tau_2\boldsymbol{\sigma})\cdot(\mathbf{k}+\mathbf{K})]. \quad (16)$$

We must introduce a high momentum cutoff $k_{\max}$ to compensate neglect of nucleon recoil in the hamiltonian expression, Eq. (3), in order to prevent the exponential factor in Eqs. (13) and (16) from vanishing. The exponential factor is quite sensitive to the cutoff, since the exponent diverges quadratically for large $k_{\max}>\mu$. However it will not affect our discussions of the relative π^0 and π^+ production rates, or of the angular distributions and excitation functions. We see quite clearly in this exponential factor the essential difference between this work and the Bloch-Nordsieck calculation for soft bremsstrahlung in electron scattering. The exponent in the quantum field calculation—Eq. (28) of reference 8—diverges logarithmically for long wavelengths ($k\to 0$) so that the matrix elements vanish even when a finite source cutoff is introduced. Hence, the probability for emission of any finite number of quanta is zero. However, we observe that the exponents in Eqs. (13) and (16) above vanish for $k\to 0$. Because of the finite rest mass μ of a meson, this would be true even without the factor k^2 that appears in the numerator of the exponent as a consequence of the derivative coupling in our choice of hamiltonian Eq. (1). Energy conservation as expressed by Eq. (12) limits the number of mesons emitted by an externally perturbed nucleon, in contrast to the Bloch-Nordsieck result for massless quanta. The ultraviolet catastrophe associated with $k_{\max}\to\infty$ is ameliorated by methods taking the nucleon recoil into account, and it is removed by the renormalization techniques. We do not investigate this question further but remark here that a reasonable choice for $k_{\max}$ suffices to establish qualitative accord with experimental observation 1.

We consider matrix element (13) for production of π_1 mesons. Charge vector τ_2 goes to $\sqrt{2}\tau^+=(\tau_1+i\tau_2)/\sqrt{2}$ for π^+ production. Noting that g in this calculation corresponds to Foldy's[11] $(4\pi)^{\frac{1}{2}}g$, we see that the first two terms of Eq. (13), apart from the exponential factor, agree with his matrix element calculated with straightforward application of second-order perturbation theory and with neglect of nucleon recoil. Their absolute square, averaged over quantum polarizations and summed over spin $\boldsymbol{\sigma}$, treated as a classical unit vector, yields

$$\frac{4\pi^2e^2(g^2/4\pi)}{\mu^2K\omega_{k'}L^6}\left(1-\frac{2\mu^2k'^2\sin^2\theta}{\omega_{k'-K}^4}\right)$$
$$\times\exp\textstyle\sum_{k\alpha}(-g^2/4\mu^2L^3\omega_k^3)[\boldsymbol{\Delta}(\tau_\alpha\boldsymbol{\sigma})\cdot\mathbf{k}]^2, \quad (17)$$

where θ is the angle between the emitted meson and the incident photon. Performing the final state sum, we obtain a π^+ cross section in qualitative agreement with the experimental observations 1, 2, and 3 on π^+ production. For low meson energies, the cross section is roughly isotropic in the center-of-mass frame and has a linear excitation function. Brueckner[2] gives a more detailed discussion of the main features of π^+ production. These general qualitative features of π^+ production will not be seriously altered by inclusion of the third term in Eq. (13). As indicated in the work of Foldy and Brueckner, choice of $(g^2/4\pi)\sim 0.1$ to 0.4 gives a general agreement with the experimentally observed production cross section of $\sim 10^{-28}$ cm^2. We see here that

$$\Gamma^2\equiv(g^2/4\pi)\exp\textstyle\sum_{k\alpha}(-g^2/4\mu^2L^3\omega_k^3)[\boldsymbol{\Delta}(\tau_\alpha\boldsymbol{\sigma})\cdot\mathbf{k}]^2$$
$$\approx(g^2/4\pi)\exp\{-(g^2/4\pi)(k_{\max}/\mu)^2|\boldsymbol{\Delta}(\tau\boldsymbol{\sigma})|^2/4\pi\}$$

is roughly $\sim 1/10$ for a reasonable choice of $(g^2/4\pi)\sim 1-2$, and of $k_{\max}|\boldsymbol{\Delta}(\tau\boldsymbol{\sigma})|\sim 5\mu$. We calculate for the square of matrix element (15), averaged over quantum polarization and summed over spin,

$$\langle|\text{M.E.}_D|^2\rangle_{\text{Av}}=\frac{\pi^2e^2\Gamma^2}{2\mu^2K\omega_{k'}L^6}\left(\frac{\boldsymbol{\Delta}\boldsymbol{\sigma}\cdot\mathbf{k}'}{\omega_{k'}}\right)^2(g^2/4\pi)^2$$
$$\times\left(\frac{1}{3\pi}\frac{K}{\mu}\frac{k_{\max}}{\mu}\right)^2.$$

We see this to indicate a meson production mechanism of magnitude comparable with that operating in charged meson production as described in Eq. (17). It is responsible for the entire contribution to neutral meson production,[15] which process is thus predicted to have an isotropic cross section in the center-of-mass system and a rapidly rising excitation function proportional to the cube of the emitted π^0 momentum.

In this paragraph we attempt to get a hold on the error introduced by the treatment of the spin and

[15] A contribution to neutral meson production from the interaction of a gamma-ray with the Dirac magnetic moment of the nucleon is neglected. The contribution of this matrix element is proportional to eg and increases with the cube of the emitted π^0 momentum near threshold. It is reduced relative to Eq. (15) by the ratio μ/M, and its neglect is consistent with our approximations.

charge vectors, σ and τ, as classical unit vectors in this calculation. The first two terms of matrix element (13) which contribute to charged meson production are linear in σ and τ. We verify by comparison with a perturbation calculation, in which σ and τ are treated quantum mechanically as matrices with noncommuting components, that, to lowest order in g, the classical treatment gives the same results. However, in expressions (15) and (16) we see that the matrix element for π^0 production contains three σ and τ vectors. It may be thought that neglect of the commutation relations might introduce serious error. In order to attempt a rough estimate we calculate the π^0 cross section by fourth-order perturbation theory, with neglect of nucleon recoil. To order eg^3, the matrix element thus calculated is five times as large as our results here. In connection with these higher order processes in a perturbation calculation, Brueckner and Watson[5] have observed that they give the predominant contribution for pseudoscalar coupling, yielding a cross section compatible with experiment, for $(g^2/4\pi)\sim 10$.

IV. SUMMARY AND DISCUSSION

To summarize, we have performed a nonperturbation calculation of the photomeson production process. We treat the interaction of a quantized charge-symmetric pseudoscalar meson field pseudovectorially coupled with a Dirac nucleon. Nucleon recoil is neglected, and spin and charge operators σ and τ are treated as classical unit vectors. We use a finite source cutoff with a radius of approximately the nucleon Compton wavelength in order to compensate neglect of nucleon recoil. Because of uncertainties connected with the choice of the coupling parameter $g^2/4\pi$, the cut-off radius $1/k_{\max}$, and the spin reorientation $\Delta\sigma$, we can give no reliable quantitative results. However, it appears possible to establish qualitative agreement with the experimental observations listed in the opening paragraph. No physical assumptions outside of the structure of standard meson theory are necessary. The results supply additional evidence in favor of coupling between nucleons and mesons that is of intermediate strength ($g^2/4\pi \sim 1-2$) and that involves the nucleon spin. If we consider a scalar meson with no spin coupling, there occurs a $\Delta v<1$ in place of $\Delta\sigma$ in matrix element (15) for π^0 production, and the cross section for π^0 production is calculated to be considerably too small to agree with experiment. In addition, the electric dipole angular distribution calculated on the basis of a scalar theory conflicts with observation.

We can further corroborate our results by considering the anomalous magnetic moments of the neutron and proton. We calculate the matrix element of Eq. (6) between initial and final states with no free mesons and with the same σ, τ. We represent the vector potential with a slow space variation $\mathbf{A}_q \exp(i\mathbf{q}\cdot\mathbf{r})$. Under these conditions the entire contribution to the matrix element (8) results from the second term of Eq. (6) and is calculated to be

$$-(g^2/4\pi)(4/15\pi)(M/\mu)(k_{\max}/\mu)(i\tau_1\tau_2\boldsymbol{\sigma}\cdot\mathbf{A}_q\boldsymbol{\sigma}\cdot\mathbf{q})\mu_0, \quad (18)$$

where $\mu_0=e/2M$ is one nuclear magneton. Because of our classical treatment of σ and τ, we cannot assign an unambiguous numerical value to this matrix element. We note, however, that the magnitude of the magnetic field strength is $B=qA_q$, so that we can set an upper limit of $(g^2/4\pi)(4/15\pi)(M/\mu)k_{\max}/\mu)\mu_0$ for the calculated anomaly. For the choice of constants specified in the discussion of the photoprocess ($k_{\max}\sim M$; $(g^2/4\pi)\sim 1$ to 2), the anomalous magnetic moments are calculated to be not greater than four to eight nuclear magnetons.[16]

The value of the method of calculation discussed in this paper lies in the fact that it avoids the often unjustified perturbation approximation. It is severely limited to low energy processes, in which it is possible to neglect nucleon recoil, and to discussions not totally obscured by the self-energy infinities which can be handled only by the new covariant subtraction techniques. With neglect of nucleon recoil, we get the familiar $1/r^3$ singularity when we calculate the two-nucleon interaction. We write the Bloch-Nordsieck transformed equation, for two nucleons of mass M_1 and M_2 at $\mathbf{r}_1$ and $\mathbf{r}_2$ (and a pseudoscalar meson field),

$$\{\mathbf{v}_1\cdot\mathbf{p}_1+M_1+\mathbf{v}_2\cdot\mathbf{p}_2+M_2+\tfrac{1}{2}\sum_{k\alpha}\omega_k(P_{k\alpha}^2+Q_{k\alpha}^2)$$
$$+(g^2/2\mu^2L^3)\tau_1\tau_2(\boldsymbol{\sigma}_1\cdot\mathbf{grad}_1)(\boldsymbol{\sigma}_2\cdot\mathbf{grad}_2)$$
$$\times\textstyle\sum_k \omega_k^{-2}\exp[i\mathbf{k}\cdot(\mathbf{r}_2-\mathbf{r}_1)]-E\}u(Q,\mathbf{r})=0.$$

This is just the wave equation with the potential term calculated on the basis of second-order perturbation theory. Transforming back to the original canonical coordinates, we have the exact solution. However, one must take into account the nucleon recoil[17] in order to remove the objectionable $1/r^3$ singularity in the potential and to prevent the system from collapsing. The method should prove of value in application to other simple scattering, absorption, and production processes involving a one-nucleon system or a phenomenologically described many-nucleon configuration.

It is a pleasure to thank Professor L. I. Schiff for his constructive comments and for his friendly and helpful interest.

[16] Matrix element (18) may be in error because of a classical treatment of spin. However, the same spin factor occurs in the matrix elements for π^0 production and for the anomalous magnetic moment. (See Eq. (16).) We may expect this classical approximation to introduce a similar error into both calculations and thus not affect the above argument.

[17] G. Araki, Phys. Rev. **75**, 1101 (1949); L. Van Hove, Phys. Rev. **75**, 1519 (1949); S. M. Dancoff, Phys. Rev. **78**, 382 (1950).

The Range and Straggling of Protons between 35 and 120 Mev*

N. BLOEMBERGEN† AND P. J. VAN HEERDEN
Nuclear Laboratory, Harvard University, Cambridge, Massachusetts
(Received March 12, 1951)

The range of protons in aluminum, copper, and lead has been determined with a photographic method, using the internal beam of the 95-in. synchrocyclotron of Harvard University. The method allows the simultaneous determination of the range, straggling, and the energy distribution of the protons in the internal beam. The latter was shown to have a half-width of 12 Mev. The experimental results for the range show slight, but significant deviations from tabulated values. Results for the straggling agree well with theory, if the effect of multiple scattering in the absorber is taken into account.

I. INTRODUCTION

THE energy loss, and, therefore, the range of heavy charged particles in matter, is almost completely determined by ionization and excitation of atoms. For energies below 10 Mev, there is abundant experimental material for the range of charged particles, and Bethe's formula[1] for the energy loss per unit path,

$$-dE/dx=(4\pi NZz^2e^4/mv^2)[\log(2mv^2/I)-\log(1-\beta^2)-\beta^2], \quad (1)$$

describes the results well. Calculations based on Eq. (1) have been extended to higher energies,[2,3] and ranges in many substances have been tabulated up to 10,000 Mev. These tables are often used in the determination of the energy of a particle by means of its range, but the only experimental check, reported recently[4] during the course of this work, is for protons of 345 Mev. It is true that no large deviations from the tabulated values are to be expected, since Bethe's formula is well fitted to the experimental data below 10 Mev and the underlying assumptions are even better fulfilled at higher energies, as long as energy losses by meson production and radiation can be neglected. But the mean ionization potential, I, has not been calculated precisely by the theory, and usually a rather arbitrary assumption like the approximate relation[2] $I=11.5Z$ is made. The quantity I should be determined from experiment. Small differences of our observed ranges from the tabulated values[2] lead to different values for I. These results will be given in Sec. III after the description of a new method by which they have been obtained.

In a final section the energy distribution of the protons in the internal beam of the synchrocyclotron will be discussed. It is an important factor in the interpretation of experiments with the internal beam and should always be taken into account.

II. EXPERIMENTAL METHOD

The beam hitting a target in a synchrocyclotron is not monoenergetic. The energy of the protons is defined in the following way. The particles are scattered into a narrow forward cone by coulomb forces in a thin tungsten target which is placed inside the dee. The protons are refocused by the magnetic field of the cyclotron according to their momentum in the horizontal plane. There is no focusing for the small vertical component of the motion. The protons which are scattered slightly downward hit the plateholder assembly located three inches below the medium plane of the cyclotron on a radius about 180° from the scatterer. A sketch of the situation is given in Fig. 1.

For each setting of the target, an interval of about 20 Mev can be covered at the plate, where the protons are selected according to energy. Both target and plateholder could be moved inward to obtain data at lower energies. The target was set at about 40 in., 35 in., 30 in., and 25 in., and each time the photographic plates covered a distance of 10 in. inward from the target radius. The position of the target and the plate was measured with a precision of 0.5 mm.

The magnetic field was calibrated along several radii to one part in ten thousand with the magnetic resonance of the Li^7 nuclei.[5] It appeared that the field values were reproducible to within 0.05 percent by adjusting the regulated magnet current to a standard value. Thus, the field was not recalibrated during each

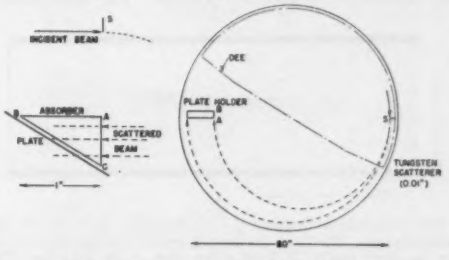

FIG. 1. Schematic diagram showing the positions of target, absorber, and photographic plate inside the tank of the cyclotron.

* Assisted by the joint program of the ONR and AEC.
† Society of Fellows.
[1] M. S. Livingston and H. A. Bethe, Revs. Modern Phys. **9**, 261 (1937).
[2] Aron, Hoffman, and Williams, Report AECU-663, UCRL-121 (1949).
[3] J. H. Smith, Phys. Rev. **71**, 32 (1947).
[4] C. J. Bakker and E. Segrè, Phys. Rev. **81**, 489 (1951).
[5] We are indebted to Mr. G. D. Watkins and Mr. U. E. Kruse for carrying out this calibration.

run. The energy can then be calculated from the Hr values with an accuracy of 0.2 percent at 40 in. and 0.3 percent at 25 in.

The range was determined by means of a tapered absorber which the protons had to traverse before they would hit the photographic emulsion of the Kodak commercial film. The intensity of the internally scattered beam would produce a convenient density after an exposure of a few seconds. Once the direction of the incoming protons was checked with a nuclear track plate, all data were taken with the unsensitive commercial film which was clamped between the plateholder and the absorber. The film could easily be changed by pulling the plateholder assembly out of the tank through a vacuum lock.

The absorbers were 10 in. long and had a triangular cross section with angles of 30° and 60°. The protons would enter the absorber perpendicular to the narrowest edge, which is about 0.5 in. high. The absorbers were made from electrolytic aluminum (measured density: 2.701 g/cm³), electrolytic copper (8.857 g/cm³), and chemically pure lead (11.32 g/cm³). The position of the absorber edge was marked on the film with a light source. In the case of lead, which had no sufficiently sharp edges, light marks were obtained through small drilled holes. After exposure and processing, the plates would show an appearance such as is schematically represented in Fig. 2. The r-direction represents the direction of increasing radius, thus increasing energy, and the y-direction increasing thickness of the absorber. There is a rather sharp slanting edge above which the plate is blank. No protons are able to traverse the absorber there.

The photographic density D was measured along lines in the y-direction for various values of r. A typical microphotometer curve is given in Fig. 3. From the density the number of protons, N, hitting a unit area of the plate can be calculated with the formula,

$$D=Ga[1-\exp(-Na)], \qquad (2)$$

where G is the number of grains per cm² emulsion with an average cross section a; furthermore, $D_M=Ga$ is the maximum attainable density.[6] The assumption underlying Eq. (2) is that every grain traversed by a proton is made developable. This is not true for fast protons which produce a smaller density. But the registrogram in Fig. 3 shows that the density is nearly constant over a considerable distance near the end of the range, so that there formula (2) can be applied. Nuclear track plates are not as good in this respect. The smaller grains in these plates cause the density to decrease more rapidly, as the proton energy is increased. Since our experimental density was always smaller than unity ($D/D_M<\frac{1}{8}$), the approximate relation that N is proportional to D was used. The relative error in N is smaller than 10 percent. In this way an integral range curve can be obtained from Fig. 3. Examples are shown in Figs. 4 and 5. The distance from the absorber edge to the point where the number of protons has dropped to 50 percent multiplied by the cosine of the absorber angle gives the value for the mean range. The cosine was checked at many points in the absorber with a traveling microscope to eliminate machining inaccuracies. The uncertainty in the mean range is estimated at less than 0.003 cm.

FIG. 2. Facsimile drawing of a photographic plate used in the measurements. The black horizontal lines at the top and bottom are the light marks, indicating the edge of the absorber. The slanting line indicates where the protons reach the end of their range. For further explanation see text.

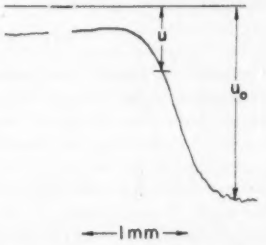

FIG. 3. Photometer curve of a plate along a line of constant r. The deflection u_0 corresponds to the blank plate; the deflection u is somewhere in the straggling part of the range. The photographic density is defined as $D=^{10}\log(u_0/u)$. The edges of the absorber fall far outside the diagram, which contains only a small portion in the y-direction across the slanting line of the plate in Fig. 2.

The straggling parameter s is simultaneously obtained, as indicated in Figs. 4 and 5. At lower energies (below 60 Mev), the straggling is enhanced by imperfect focusing. The focusing condition—at $\pi(1-n)^{-\frac{1}{2}}$ radians from the target—is not critical, since the protons emerge in a narrow cone with an aperture of about 1° from the thin scatterer. At 40 in. the plate was exactly in focus at 185° from the scatterer. Unfortunately, the geometry of the tank made it impossible to align plate and target at 180° for the smallest radii. In this case the plate was actually 20° out of focus. This caused an energy spread of about 0.6 percent and an apparent increase in the straggling of 50 percent. Straggling data below 60 Mev have, therefore, been omitted.

Corrections from not perfect normal incidence of the protons on the absorber and from the small contribution of the vertical component of the motion to the

[6] H. Yagoda, *Radioactive Measurement with Nuclear Emulsions* (John Wiley and Sons, Inc., New York, 1949), p. 22.

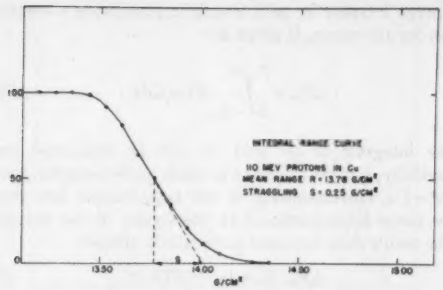

FIG. 4. Integral range curve for 110-Mev protons.

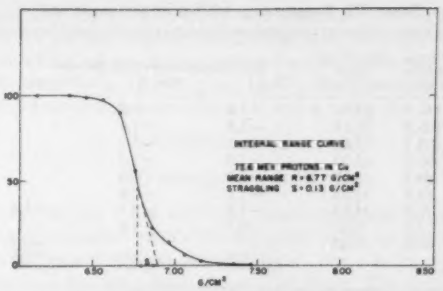

FIG. 5. Integral range curve for 75-Mev protons.

energy are smaller than 0.1 percent. About 10 percent of the protons are scattered inelastically or absorbed in nuclear reactions. But the effect of these processes on the range is negligible, as is also the effect of the curvature of the path through the absorber in the magnetic field.

The range can also be obtained from experiments with flat absorbers. Only protons with an energy sufficiently large to penetrate the absorber will reach the film. At smaller radii the film will be blank. The film is photometered in the r-direction, and a value for the energy with a mean range equal to the thickness of the absorber can be obtained. The photometer curve has to be corrected for the radial distribution in the number of protons (compare Sec. IV).

Strictly speaking, the curves obtained by the first method should be corrected for the vertical distribution in the number of protons. Over the small region of the absorber of interest in the experiments, this distribution is practically constant.

TABLE I. Range-energy relation for protons in copper.

Proton energy (Mev)	Theoretical range (grams/cm²)	Experimental correction (%) Run I	Run II	Run III	Flat abs.
113.7	14.79	+0.5	+0.5	+0.6	
111.3	14.24	+1.0	+0.8	+1.0	
108.3	13.58	+0.6	+0.7	+1.0	
102.1	12.26	+1.7	+1.8	+2.7	
99.8	11.78	+1.2	+0.7	+1.9	
96.2	11.19	0.0	+0.2	+0.5	
		+0.9±0.5	+0.7±0.2	+1.3±0.6	
89.8	9.79	+1.4	+1.6	+1.5	+1.0
86.9	9.24	+1.9	+1.5	+2.4	
84.0	8.71	+1.2	+1.5	+1.4	+1.3
79.1	7.84	+2.1	+1.6	+2.6	
76.1	7.32	+2.1	+2.6	+2.4	
73.0	6.81	+1.0	+1.7	+1.1	
		+1.6±0.4	+1.8±0.3	+1.9±0.6	+1.2
65.2	5.55				+2.2
					+1.2
55.7	4.23				+0.5
44.0	2.79				+1.2
					+1.3±0.4

III. RESULTS

The experimental results for the mean range in copper are listed in Table I. It is seen that there is a small but significant difference from the theoretical values obtained by interpolation in the tables of Aron, Hoffman, and Williams.[2] The experimental range is about 1 percent larger at the higher energies, and 1.5 percent at the lower. The mean of the absolute deviations has been listed. It is believed that the deviations from the mean are due to errors in the plateholder setting and in the measurement of absorber thickness. The deviations are in agreement with the estimated errors in the range and energy determination. The error could undoubtedly be reduced by a factor of 3 by a more painstaking definition of the geometry.

The data for aluminum are shown in Table II. The theoretical values are taken from Smith.[3] Again a

TABLE II. Range-energy relation for protons in aluminum.

Proton energy (Mev)	Theoretical range (grams/cm²)	Experimental correction (percent)
75.84	6.057	+0.1
75.70	6.041	+1.4
73.05	5.660	+0.7
72.94	5.657	+1.8
66.10	4.750	+0.5
65.78	4.711	+0.7
62.10	4.248	+0.5
61.79	4.205	+1.0
56.96	3.650	+1.2
56.68	3.626	+1.4
		+0.9±0.4
52.33	3.136	+1.4
52.08	3.106	+2.4
47.67	2.646	−0.3
		−1.1
44.86	2.372	+0.9
		+1.1
42.57	2.153	+2.5
		+1.1
39.66	1.907	+1.4
		+0.3
37.16	1.700	+3.7
		+2.4
34.96	1.511	+2.9
		+1.3
		+1.4±1.0

TABLE III. Range-energy relation for protons in lead.

Proton energy (Mev)	Theoretical range (grams/cm²)	Experimental correction (percent) Run I	Run II	Flat abs.
114.1	20.83	−1.0	−0.3	
106.6	18.54	−1.4	−1.4	
104.1	17.81	−1.5	−1.1	
95.3	15.30	−1.0	−1.0	
89.1	13.55	−0.7	0.0	
82.4	11.93	−1.1	−0.8	
78.9	11.12	−1.1	−0.9	−1.4
72.1	9.47	−0.5	−1.0	
62.5	7.42			−0.1
		-1.0 ± 0.3	-0.9 ± 0.4	-0.8 ± 0.7

difference of 1 percent to 1.5 percent is observed. Finally, Table III shows the results for lead. Here the range is 1 percent smaller than the tabulated value.

The differences must be attributed to the average ionization potential. The value of this quantity derived from experiment and the relative mass stopping power at 75 Mev, with copper taken as reference, are given in Table IV. The ratio of the mass stopping powers for Cu and Pb agrees well with the value of Bakker and Segrè[4] at 300 Mev, but there is a discrepancy for the ratio of Al and Cu outside the limits of error of the two experiments. We think our value 1.221 to have a possible error of 1 percent, while Bakker and Segrè give 1.143 to be correct within 2 percent.

Our range measurements for Al, however, yield a value for I_{exp} in fair agreement with Wilson's measurement.[7] He derives for the mean ionization potential of Al 150 ± 5, while we get 159 ± 5.

Consequently, our values of I_{exp} at 100 Mev for Cu and Pb are substantially larger than those at 300 Mev reported by Bakker and Segrè.

The last column in Table IV gives the values I_{corr}, if the effect of multiple scattering of protons traversing the absorber is taken into account. Since the particles will not follow a straight line through the absorber, the real range will be larger than the measured one.

The mean square deviation in angle from the normal direction at a distance (R_0-x) in the absorber is given by[8-10]

$$\langle\vartheta^2(x)\rangle_{Av}=\int_{-R_0}^{-x}4\pi Ne^4Z^2G(pv)^{-2}dx^1, \tag{3}$$

where N is the number of nuclei per cc with charge Z, p and v the momentum and the velocity of the proton, and G is a numerical factor for which various authors derive different expressions.[9] We take a simple one from Rossi

$$G=2\ln181Z^{-1}.$$

When the protons arrive at the end of their range R_0, which point we take as the origin of x, then the total average increase in path length, representing a correction for the range, is given by

$$\Delta R_{Av}=\frac{1}{2}\int_{-R_0}^{0}\langle\vartheta^2(x)\rangle_{Av}dx. \tag{4}$$

The integrals in (3) and (4) can be evaluated numerically, but we can use the crude approximation that $p^2v^2=Cx$, corresponding to the approximate law that the range is proportional to the square of the energy. The result then becomes particularly simple;

$$\Delta R_{Av}/R_0=4\pi Ne^4Z^2GC^{-1}. \tag{5}$$

The relative correction for the range is independent of the proton energy, and is larger for elements with high Z. The values $\Delta R_{Av}/R_0$, using Eq. (5), are given in Table V, and the corresponding corrections in the ionization potential have been included in I_{corr} in Table IV. Similar corrections should probably be applied to the ionization potential obtained from experiments at lower energies. If a more correct relation $p^2v^2=Cx^\alpha$, with α between 1.1 and 1.2 is used, then the relative correction would become even more important at lower energies.

TABLE IV. Experimental values for the mass stopping power and mean ionization potential.

Element	Relative mass stopping power at 70 Mev	Energy (Mev)	I_{exp} (ev)	I_{corr} (ev)
Al	1.221	50–75	159	161
		35–50	162	164
Cu	1.000	90–115	355	365
		50–90	365	375
Pb	0.747	70–115	895	970

The correction has not been applied to the experimental range, since the real range will not be observed.

The calculations are valid only when $\langle\vartheta^2\rangle_{Av}\ll1$. During the last part of the track this condition is not satisfied. For protons of 100 Mev, however, the energies below 10 Mev contribute only 5 percent to ΔR_{Av}. The influence of this last part of the range can be neglected.

It is more serious that our estimate ignores the correlation between angular deviations at different distances x in each individual proton track. It may turn out that the distribution in ΔR is not normal. More precise calculations should be based on detailed distribution functions given by Fermi, Snyder, and Scott.[10]

The effect of multiple scattering on the straggling is even larger. Obviously, individual tracks will deviate more or less from the straight path. Assuming now that the distribution in ΔR is normal, it seems reasonable to take the root-mean-square deviation equal to $\gamma\Delta R_{Av}$, where γ is of the order of unity. This causes an additional straggling, which has to be added quadratically to the straggling, caused by fluctuations in the specific ionization along the individual tracks. This latter

[7] R. R. Wilson, Phys. Rev. **60**, 749 (1941).
[8] B. Rossi and K. Greisen, Revs. Modern Phys. **13**, 249 (1941).
[9] Groetzinger, Berger, and Ribe, Phys. Rev. **77**, 584 (1950).
[10] W. T. Scott and H. S. Snyder, Phys. Rev. **78**, 223 (1950).

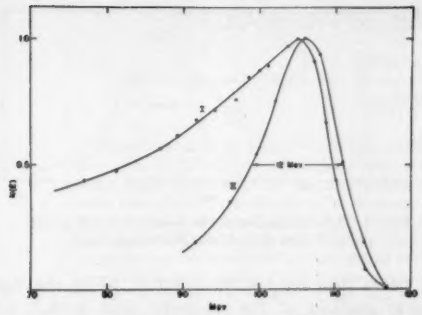

FIG. 6. The distribution of proton energies in the internal beam, hitting a beryllium target $\frac{1}{4}$ in. thick, (curve I) and a tungsten target 0.01 in. thick, (curve II). Both targets were at a 40-in. radius.

effect can be calculated with formulas given by Livingston and Bethe. It is expressed in a straggling parameter s, defined as the difference between the mean and extrapolated range. The corrected straggling is then given by

$$s^2_{\text{corr}}=\tfrac{1}{2}\pi\gamma^2(\Delta R_m)^2+s^2. \tag{6}$$

The values of s and s_{corr} are compared with the experimental values s_{exp} in Table V. We have put $\frac{1}{2}\pi\gamma^2=1$. It is seen that the agreement between theory and experiment becomes very good if the effect of multiple scattering is taken into account. Otherwise, there would be rather large deviations, of 30 percent, outside the experimental error of 10 percent for the heavy element. An important factor in these straggling experiments was that the aperture of the scattered beam is only 0.7°. Therefore, no appreciable increase in straggling can arise from the finite aperture.

IV. THE ENERGY DISTRIBUTION IN THE INTERNAL BEAM

This distribution can be obtained from the same photograph, represented in Fig. 2, as the range. The film is now photometered for various values of r. The maximum density is not the same for all values of r, since the number of protons hitting a unit area of the plate depends on the energy. This number $n(r, y)$ is related to the measured density by Eq. (2). We are interested, however, in $N(E)$, the number of protons per unit energy interval at the scatterer. Let $f(\varphi)d\varphi$ be the vertical angular distribution from the scatterer, for which we can take a gaussian with a mean square deviation $\langle\varphi^2\rangle_{Av}=\frac{1}{2}\langle\vartheta^2\rangle_{Av}$ given by Eq. (3). The relationship between the variables φ, E and r, y is given by

$$\begin{aligned}\varphi&=2y/[\pi(r+r_0)],\\ E&=\text{constant}\times(r+r_0)^2,\end{aligned} \tag{7}$$

where r_0 and r are the radial positions of the target and the location in the photographic plate, measured from the center in opposite directions, and y is the distance of the plate from the median plane. The transformation jacobian is readily seen to be a constant. Hence,

$$N(E)f(\varphi)=Kn(r, y), \tag{8}$$

where K is a constant, and $f(\varphi)$ is related to the energy by Eq. (3). But under our experimental conditions $f(\varphi)$ did not vary by more than 10 percent. For thick targets the calculation of $\langle\varphi^2\rangle_{Av}$ is not reliable, since one does not know the actual path of the protons hitting the edge of the target. In principle, $f(\varphi)$ could be determined experimentally by photometering a photographic film without absorber in the vertical direction.

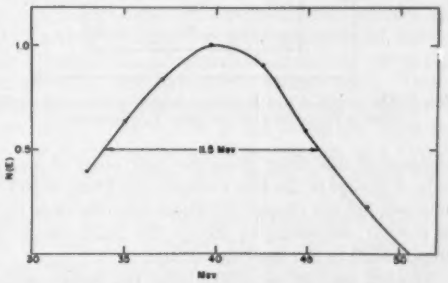

FIG. 7. The distribution of proton energies in the internal beam, hitting a tungsten target (0.01 in. thick) at a 25-in. radius.

In Fig. 6, the distributions $N(E)$ for a beryllium target, $\frac{1}{4}$ in. thick, and a tungsten target, 0.01 in. thick, at a 40-in. radius are given and in Fig. 7 the distribution for the same tungsten target at 25 in. The width of the distribution is about 12 Mev, independent of the radius, and the maximum is about 12 Mev below the maximum energy, corresponding to the equilibrium orbit at the target radius.

Calculations show that multiple traversals with corresponding energy loss cannot explain the distribution for the thin target. A change in the vertical aperture of the cyclotron by clippers did not effect the distribution nor did the use of thinner targets. The broad tail of the distribution of the thick beryllium target, however, must undoubtedly be ascribed to this cause. Light elements with small scattering favor multiple traversals and a corresponding energy spread by ioniza-

TABLE V. The range correction for multiple scattering and the straggling parameter.

Element	Energy (Mev)	$\Delta R_m/R_0$	s (g/cm²)	s_{corr} (g/cm²)	s_{exp} (g/cm²)
Al	75.8	0.23%	0.084	0.085	0.088
Cu	110.		0.225	0.24	0.25
	72.6	0.53%	0.12	0.125	0.13
Pb	106.6		0.30	0.41	0.37
	95.0	1.5%	0.235	0.32	0.32

tion loss. For reliable results the distribution should be checked in each experiment with the internal beam.[11]

The energy distribution for thin targets represents, probably, a distribution in the amplitudes of radial oscillations which originate near the center of the cyclotron, the average amplitude being 2.5 in. The distribution did not change by more than 20 percent in width under a variation of operating conditions, like tank pressure and firing time of the ion source in the modulation cycle.[12] Rainwater[13] gives three possible reasons for radial oscillation. First, starting the ions off center, and second, azimuthal inhomogeneities in the magnetic field, which could have only a very small effect in our case. There remains the third possibility, that the dc bias field of the dee causes the radial oscillation. An

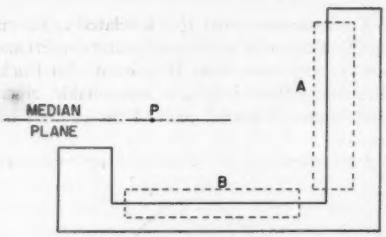

FIG. 8. The targets A and B used to determine the radial oscillations in the beam near the point P, where $n=0.2$.

estimate of this effect gives the right order of magnitude. A change in dee-bias voltage from 2000v to 1000v, however, did not change the distribution by more than 10 percent. According to theory, the width should be proportional to the dee-bias voltage.

Another method of determining the radial oscillations was recently suggested at Harwell,[14] using a *C*-shaped target as represented in Fig. 8. Only particles with small vertical oscillations will pass the edge.

[11] D. Bodansky and N. F. Ramsey, Phys. Rev. **82**, 831 (1951); and Birge, Kruse, and Ramsey, Phys. Rev. **83**, 274 (1951).

[12] Under the rather special conditions of an experiment by Birge, Kruse, and Ramsey (see reference 11) a reduction in the width of 35 percent was found.

[13] J. Rainwater, mimeographed notes, "Some factors involved in the theory and operation of an F.M. cyclotron."

[14] M. Snowden, Proceedings of the Harwell Nuclear Physics Conference (1950).

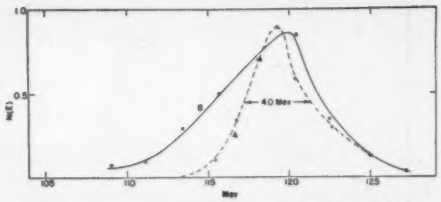

FIG. 9. The distribution of the proton energies at the point P, according to the Harwell method.

The beam then reaches the point P, where the logarithmic gradient of the magnetic field $n=0.2$, and starts blowing up. The blown-up beam will at least partially hit the horizontal target B, but many particles will still hit the vertical target A beyond the point P. It was assumed that the beam will only blow up if the equilibrium orbit reaches the point P. Therefore, target A would be hit by all particles with a radial amplitude larger than the distance AP.

We have applied this method. The carbon activity of the polyethylene target A was measured as a function of the distance PA and differentiated. The activity of sections of target B at different distances from P was also measured. The two distributions which should be approximately the same are represented in Fig. 9. It is seen that the distribution so obtained does not agree with our previous results. The basic assumption that the orbit will blow up when the equilibrium radius is at $n=0.2$ is not justified. By analyzing a particular orbit, it was found that a proton may acquire a considerable, vertical deflection when it spends a couple of revolutions near P, where the gradient in the field is large, even though its equilibrium orbit may be at a radius which is 3 in. smaller. Furthermore, some particles with very small radial amplitudes should not blow up at all and always hit target A. The method can only be applied near the point P and seems to depend critically on the behavior of the magnetic field near the edge of the poles. Therefore, the method of 180° focusing is more reliable.

The authors wish to thank Professor N. F. Ramsey for stimulating discussions and Mr. A. C. Grant and other members of the cyclotron crew for their cooperation during the bombardments.

The Microwave Spectra of the Deutero-Ammonias*†

M. T. Weiss and M. W. P. Strandberg
Research Laboratory of Electronics, Massachusetts Institute of Technology, Cambridge, Massachusetts
(Received March 14, 1951)

Measurements of the inversion-rotation spectra of the deutero-ammonias have been made in the 4000-Mc/sec to 80,000-Mc/sec region. Fifty lines of NH_2D and NHD_2 have been measured and identified by means of the Stark effect. As expected, our results show that for these molecules, only simultaneous rotational and inversion transitions can be observed. Thus, corresponding to each $J_\tau \rightarrow J_{\tau'}$ transition two absorption lines can be observed, separated by either twice the rotational energy separation or twice the inversion splitting of the levels involved. From our observations the inversion splittings of the partially deuterated molecules can be calculated and are found to be in good agreement with the Dennison and Uhlenbeck inversion doubling theory. Thus, the inversion splittings for the ammonia molecules are approximately as follows: 24,000 Mc/sec for NH_3; 12,000 Mc/sec for NH_2D; 5000 Mc/sec for NHD_2; 2000 Mc/sec for ND_3. Our results are also in agreement with the structural parameters of ammonia as given by Herzberg. The sign of the nuclear quadrupole coupling constant was also measured and found to be negative, as expected. The centrifugal distortion for both rotation and inversion states has been experimentally determined.

INTRODUCTION

AMMONIA has occupied a unique position in microwave spectroscopy; and, because of its usefulness in a wide variety of spectroscopic investigations, it has perhaps the most intensively studied spectrum in the microwave region. However, most of the previous work has been confined to the inversion spectrum of NH_3, with very little effort expended to investigate the microwave spectra of the deutero-ammonias. This is somewhat surprising, since the partially deuterated ammonias can supply a considerable amount of useful and interesting information which cannot be obtained from the NH_3 microwave spectrum. Thus, since the finite NH_3 microwave absorption frequency is not due to rotational transitions, because of the symmetric top K degeneracy, but only to inversion transitions, the rotational constants cannot be obtained. Similarly, although the magnitude of the nuclear electric quadrupole coupling constant, eQq, has been obtained from the NH_3 hyperfine spectrum, its sign can be determined only by observing the NH_2D or NHD_2 spectrum. Furthermore, it should be of great interest to investigate in detail the unique microwave spectrum of these molecules in which simultaneous inversion and rotational transitions take place.

The first to investigate the microwave spectra of the deutero-ammonias was Kyhl[1] at M.I.T. in 1947. He identified a 9515-Mc/sec absorption as caused by NHD_2. More recently, Lyons[2] and a group at the National Bureau of Standards became interested in the low frequency deutero-ammonia spectrum for use in the construction of an "atomic" clock. They have reported a number of lines from 3000 Mc/sec to 17,000 Mc/sec but have given no proper interpretation of this spectrum.

ROTATIONAL ENERGY LEVELS

In this paper a description will be given of the detailed investigation of the microwave spectra of NH_2D and NHD_2. Both of these molecules are asymmetric rotors; thus, for each J rotational quantum number value there are $2J+1$ energy levels. These various levels are frequently denoted by a subscript τ which ranges from $-J$ to J and labels the levels in order of increasing energy. King, Hainer, and Cross[3] also designate these levels by means of a double subscript $K_{-1}K_1$, where $\tau = K_{-1} - K_1$. For a prolate symmetric top, K_{-1} is the quantum number for the projection of J on the principal axis of least moment of inertia, while for an oblate symmetric rotor K_1 represents the projects of J on the principal axis of greatest moment of inertia.

The rotational energy levels of a polyatomic molecule are determined by the usual three reciprocal moments of inertia, a, b, and c, where $a \geqslant b \geqslant c$. Both NH_2D and NHD_2 have a pyramidal structure with the nitrogen atom at the apex of the pyramid. For these pyramid types of molecules which have two equal atoms and one different atom on the base, one can show that the principal moments of inertia I_{zz}, I_1, and I_2 can be obtained from the following equations: (See Fig. 1).

$$\frac{I_{zz}}{mr^2} = \frac{\beta(2+\alpha)}{2+\alpha+\beta} + \frac{2\sin^2\tfrac{1}{2}\theta}{(2+\alpha+\beta)^2} \times [3\alpha(\alpha+2) - \beta(\beta+2) + 2\alpha\beta], \quad (1a)$$

$$(I_{xx}+I_{yy})/2mr^2 = (I_{zz}/2mr^2) + 2\sin^2\tfrac{1}{2}\theta, \quad (1b)$$

$$\frac{I_{xx}-I_{yy}}{2mr^2} = \frac{\beta(2+\alpha)}{2(2+\alpha+\beta)} - \frac{\sin^2\tfrac{1}{2}\theta}{3(2+\alpha+\beta)^2}[9\alpha(\alpha+2) + 5\beta(\beta+2) + 2\alpha\beta(11+2\alpha+2\beta)], \quad (1c)$$

* This work has been supported in part by the Signal Corps, The Air Materiel Command, and ONR.

† Presented at the New York Meeting of Americal Physical Society, February 1-3, 1951 [Phys. Rev. 82, 326(A) (1951)]; also Phys. Rev. 81, 286 (1951).

[1] R. L. Kyhl, M.I.T. Physics Department thesis (1947).

[2] Lyons, Kessler, Rueger, and Nuckols, Phys. Rev. 81, 297, 630 (1951).

[3] King, Hainer, and Cross, J. Chem. Phys. 11, 27 (1943).

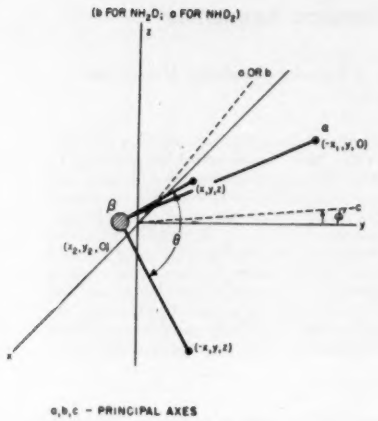

FIG. 1. Molecular geometry.

$$\frac{I_{xy}^2}{mr^2}=\frac{(1-\alpha)^2(2\beta)^2}{3(2+\alpha+\beta)^2}[\sin^2\tfrac{1}{2}\theta-(4/3)\sin^4\tfrac{1}{2}\theta], \quad (1d)$$

$$I_{1,2}=\tfrac{1}{2}(I_{xx}+I_{yy})\pm\{[\tfrac{1}{2}(I_{xx}-I_{yy})]^2+I_{xy}^2\}^{\frac{1}{2}}, \quad (1e)$$

$$\phi=\tan^{-1}[-(I_{xx}-I_2)/I_{xy}], \quad (1f)$$

where α = mass ratio of the unique atom in the base of the pyramid to the mass of one of the two equal atoms, β = mass ratio of apex atom to one of the two equal atoms, r = distance from apex to corner of pyramid, θ = corner to apex to corner angle, and ϕ = angle between the geometric symmetry axis and a principal axis of inertia.

The values of r and θ for ammonia have been determined from the infrared data of NH_3 and ND_3 and are given by Herzberg[4] as follows: $r(N-H)=1.014\times10^{-8}$ cm and θ = H−N−H angle = 106.78°. These values, although not fully accurate for the partially deuterated molecules, because of different zero-point vibrations, should still permit good preliminary calculations.

The rigid rotor energy value of the J_τ level can be expressed by

$$W(J_1\tau)=\tfrac{1}{2}(a+c)J(J+1)+\tfrac{1}{2}(a-c)E_\tau^J(\kappa), \quad (2)$$

where $E_\tau^J(\kappa)$ is a function of the asymmetry parameter which is defined by $\kappa=(2b-a-c)/(a-c)$ and can vary from −1 to +1. Values of the reduced energies $E_\tau^J(\kappa)$ are given by King, Hainer, and Cross for values of J from 0 to 12 in intervals of κ of 0.1. For intermediate values of κ, five-point lagrangian interpolation is required to obtain sufficient accuracy.

SELECTION RULES

The pure rotational selection rules on J for these molecules are $\Delta J=0, \pm1$, while the selection rules on the change in the subscripts $K_{-1}K_1$ depend upon the orientation of the dipole moment with respect to the principal axes of inertia. For NH_2D and NHD_2 the dipole moment is only about 10° from the c axis (axis of largest moment of inertia); thus, only c-type transitions will give the intense lines. These transitions require that the K_1 subscript shall not change during the transition.

However, since these ammonia molecules can also undergo inversion, an additional over-all species selection rule must also be considered. This selection rule can be determined from a consideration of the matrix elements of the electric dipole moment, referred to a fixed coordinate system. By considering the symmetry properties of the rotational and inversion wave functions it will be shown that a rotational transition cannot take place without a simultaneous inversion transition, and, similarly, that an inversion transition must be accompanied by a rotational transition. Thus, let us consider the space-fixed Z component of the matrix element of μ_g, the molecule-fixed g component of the dipole moment. This matrix element is given by

$$|\mu_{oj}|_Z=\int\psi_{ro}^*\psi_{io}^*\langle\mu_g\rangle_{nev}\Phi_{gZ}\psi_{rj}\psi_{ij}d\tau$$

$$=\int\psi_{ro}^*\Phi_{gZ}\psi_{rj}d\tau_r\int\psi_{io}^*\langle\mu_g\rangle_{nev}\psi_{ij}d\tau_i, \quad (3)$$

where ψ_r is the rotational wave function, ψ_i is the inversion wave function, and the subscripts o and j indicate the initial and final states, respectively. Also, Φ_{gZ} is the direction cosine between the g and Z axes and $\langle\mu_g\rangle_{nev}$ is the dipole moment averaged over the nuclear, electronic, and vibrational wave functions.

In order that the integral

$$\int\psi_{io}^*\langle\mu_g\rangle_{nev}\psi_{ij}d\tau_i=\langle\mu_g\rangle_{nevi} \quad (4)$$

(which is the average value of the dipole moment as seen by the rotating molecule) should have a non-zero value, the integrand must not change sign upon reflection in a plane perpendicular to the g axis. Since μ_r is a linear function of the coordinates, it does change sign. Therefore, ψ_{io} and ψ_{ij} must have different symmetry properties for this reflection. For the ammonia molecules, a reflection in a plane perpendicular to the dipole moment is equivalent to an inversion, so that the initial and final inversion wave functions must have opposite symmetry properties for inversion. We have thus shown that an inversion transition must take place during a rotational transition to make $|\mu_{oj}|_Z$ different from zero.

The dipole matrix element can now be written as

$$|\mu_{oj}|_Z=\langle\mu_g\rangle_{nevi}\int\psi_{ro}^*\Phi_{gZ}\psi_{rj}d\tau_r. \quad (5)$$

Therefore, the dipole moment matrix element is now in

[4] G. Herzberg, *Infrared and Raman Spectra* (D. Van Nostrand Company, Inc., New York, 1945).

the same form as that for a normal rotational transition, and is subject to the normal rotational selection rules. We have therefore shown that the dipole matrix element will be different from zero only if both rotational and inversion transitions take place, subject to the usual rotational selection rules and to the restriction that the symmetry to inversion must change during the transition. The above argument is, of course, also valid for NH_3; but, because of the K degeneracy of the symmetric rotor energy levels, there is no observable energy change between a K^+ level to a K^- level. With an asymmetric molecule, this K degeneracy is removed so that the inversion transition is affected by an observable amount by the simultaneous rotational transition. The above selection rules are equivalent to the over-all species selection rule $+\leftrightarrow-$ given by Herzberg.[4]

The resulting inversion-rotation energy level diagram is given in Fig. 2, which shows that for a given $J_\tau \rightarrow J_{\tau'}$ transition, instead of one absorption line two lines result because of the inversion splitting. The separation between the two absorption frequencies will be equal to the sum of the inversion splittings of the two levels involved, if the pure rotational separation frequency ν_r is larger than the inversion splitting, as shown in Fig. 2(a). On the other hand, if the inversion splitting is larger than the pure rotational energy difference, then the separation between the resulting two absorption lines is equal to twice the pure rotational frequency, as shown in Fig. 2(b). Thus, one can determine the pure rotational frequency ν_r and the pure inversion frequency ν_i by measuring the two absorption lines corresponding to a $J_\tau \rightarrow J_{\tau'}$ transition.

INVERSION DOUBLING THEORY

The theoretical study of inversion doubling in ammonia has been carried out in detail by a large number of investigators. For our purposes, the Dennison and

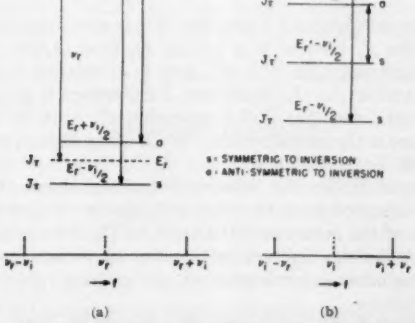

FIG. 2. Rotation-inversion energy levels: (a) $\nu_r > \nu_i$, (b) $\nu_i > \nu_r$.

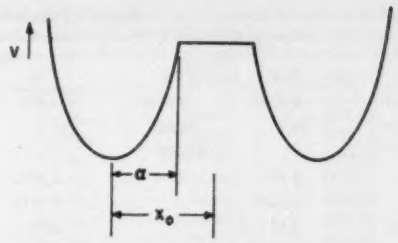

FIG. 3. Dennison and Uhlenbeck's potential well.

Uhlenbeck[5] treatment of this problem is the simplest, and still gives surprisingly accurate results. As is well known, ammonia has a double minimum potential because of its pyramidal structure which permits two equivalent positions of equilibrium for the nitrogen atom, one on either side of the plane of the hydrogen atoms. Dennison and Uhlenbeck treated this problem of a particle in a two-minima potential field by means of the WKB method and showed that each level is split into two, corresponding to the two wave functions, $\psi_{\text{symmetrical}}$ and $\psi_{\text{antisymmetrical}}$. In order to evaluate Δ, the inversion splitting, Dennison and Uhlenbeck chose a particular potential curve consisting of two equal parabolas connected by a straight line, as shown in Fig. 3. The splitting is then evaluated explicitly as a function of the length of the joining line $2(x_0-\alpha)$ and the distance between the two minima $2x_0$. Thus, one obtains

$$\Delta_0/\nu_1 = (2\alpha/\pi^{\frac{1}{2}}) \exp[-\alpha^2 - 2(x_0-\alpha)(\alpha^2-1)^{\frac{1}{2}}], \quad (6a)$$

$$\Delta_1/\nu_1 = [(4\alpha^3-4\alpha)/\pi^{\frac{1}{2}}] \times \exp[-\alpha^2 - 2(x_0-\alpha)(\alpha^2-3)^{\frac{1}{2}}], \quad (6b)$$

$$x_0 = (4\pi^2\mu\nu_1/h)^{\frac{1}{2}}q; \quad V = \alpha^2 h\nu_1/2, \quad (6c)$$

where Δ_0 = line splitting of ground state, Δ_1 = line splitting of excited state, q = height of ammonia pyramid $= 0.38\times10^{-8}$ cm, μ = reduced mass, V = height of potential hill, and α and x_0 are dimensionless parameters adjusting the height of the potential barrier and the position of the minimum of the potential well to the observed data.

Since Δ_0 and ν_1 are known for NH_3, one can calculate x_0 and V, the potential height. This latter is calculated to be 1793.36 cm^{-1} and should remain the same for the deuterated ammonias as well, since the isotopic change should not affect the electronic structure. In calculating the reduced mass for NH_2D and NHD_2, one can make use of the fact that the vibrational frequency is inversely proportional to the square root of the reduced mass at least to the first order. One thus obtains Table I, which gives the calculated and observed values. In this table the observed values of Δ_0 are those calculated for the $J=0$ level, as indicated later.

[5] D. M. Dennison and G. E. Uhlenbeck, Phys. Rev. 41, 313 (1932).

TABLE I. Calculated and observed inversion values.

	NH_3		NH_2D		NHD_2		ND_3	
	Calc.	Obs.	Calc.	Obs.	Calc.	Obs.	Calc.	Obs.
Δ_0 cm^{-1}	0.7935	0.7935	0.402	0.406	0.172	0.1705	0.068	
Δ_1 cm^{-1}	30.4	35.84	15.5	19.7	6.8	9.84	2.8	3.4
ν_1 cm^{-1}		950.16		884		813		747.3
x_0	3.173		3.2896		3.4302		3.5778	
α	1.9429		2.0143		2.1004		2.1908	
μ Amu	2.47		2.87		3.385		4.20	

A comparison of the calculated and observed values of the inversion splitting in the ground state of NH_2D and NHD_2 indicates that the Dennison and Uhlenbeck theory is surprisingly accurate (the agreement is better than 1 percent) even for the unsymmetrical molecule in which the motion of the nitrogen atom is not precisely along the axis of the pyramid. Furthermore, when one considers that the potential energy depends somewhat upon the distance between the hydrogen atoms, as well as being a function of the displacement of the nitrogen atom from its equilibrium position, one can marvel at the agreement obtained by using the simple one-dimensional potential function. These calculations also predict that the ND_3 inversion frequencies should occur near 0.068 cm^{-1}.

The limitations of the above theory become apparent, however, when one compares the calculated and observed values of Δ_1, the inversion splitting in the excited parallel vibrational state. As can be seen from Table I here the agreement is only fair, with the calculated values for all four of the ammonia molecules being too low by approximately 20 percent. This discrepancy is not excessive, considering the simple theory used, and was not pursued further, since our main interest is in the ground-state splitting.

TABLE IIa. Calculated and observed inversion splittings for NH_2D (Mc/sec).

Transition	Calculated ν_i	Observed ν_i
$2_{02}\rightarrow 2_{12}$	12,099	12,096.44
$3_{03}\rightarrow 3_{13}$	12,114	12,117.37
$4_{04}\rightarrow 4_{14}$	12,184	12,190*
$5_{05}\rightarrow 5_{15}$	12,306	12,307.40
$6_{06}\rightarrow 6_{16}$	12,475	12,473.47
$7_{07}\rightarrow 7_{17}$	12,692	12,685*
$8_{08}\rightarrow 8_{18}$	12,955	12,952.02
$9_{09}\rightarrow 9_{19}$	13,267	13,269.12
$10_{0,10}\rightarrow 10_{1,10}$	13,625	13,640*
$11_{0,11}\rightarrow 11_{1,11}$	14,030	14,070*
$7_{16}\rightarrow 7_{26}$	11,148	
$8_{17}\rightarrow 8_{27}$	11,186	
$10_{19}\rightarrow 10_{29}$	11,400	
$9_{27}\rightarrow 9_{37}$	10,167	

* Probable value; see text.

INVERSION AS A FUNCTION OF ROTATIONAL LEVEL

The Dennison and Uhlenbeck theory outlined above does not, however, take into account the variation of the inversion splitting with rotational levels. For NH_3, this variation was treated by Sheng, Barker, and Dennison,[6] who based their analysis upon the centrifugal force distortion of the ammonia potential function. Their equation for the inversion frequency is

$$\nu_i=\Delta_0-A[J(J+1)-K^2]+BK^2, \tag{7}$$

where Δ_0, A, and B are all positive numbers and J and K are the usual rotational quantum numbers. This equation has been found to be quite accurate for NH_3 although higher order terms have since been introduced for greater accuracy. The form of this equation should also be valid for the deuterated molecules although K^2 must now be redefined, since it is no longer a good quantum number for asymmetric rotors. For K, the angular momentum along the symmetry axis for a symmetric top, one can substitute P_c which is the angular momentum along the c axis. For NH_2D and NHD_2, the c axis is about 10 degrees from the symmetry axis.

One can calculate $\langle P_c^2\rangle$, the average squared momentum about the c axis, from the following equations, as given by Bragg and Golden:[7]

$$\langle P_b^2\rangle=dE(\kappa)/d\kappa, \tag{8a}$$

$$2\langle P_a^2\rangle=J(J+1)+E(\kappa)-(1+\kappa)\langle P_b^2\rangle, \tag{8b}$$

$$\langle P_c^2\rangle=J(J+1)-\langle P_a^2\rangle-\langle P_b^2\rangle. \tag{8c}$$

From calculations it is seen that $\langle P_c^2\rangle$ is nearly the same for the J_τ level as it is for the $J_{\tau'}$ level; hence, an average value for $\langle P_c^2\rangle$ was used in calculating ν_i for the various $J_\tau\rightarrow J_{\tau'}$ transitions. Furthermore, it should be mentioned that $\langle P_c^2\rangle$ is approximately equal to the square of the second subscript in the King, Hainer, and Cross[3] J_{K-1K_1} notation.

Table II lists the "observed" (calculated from the two observed lines) inversion splittings for six lines for each of the molecules NH_2D and NHD_2. Since only a single line was observed for the other transitions listed, no accurate determination of the splitting could be

[6] Sheng, Barker, and Dennison, Phys. Rev. **60**, 786 (1941).
[7] J. K. Bragg and S. Golden, Phys. Rev. **75**, 735 (1949).

made. However, in some cases a fairly accurate calculation can be made of the pure rotational separation of the two levels involved by using the centrifugal distortion theory. In these cases, the inversion frequency can be calculated by taking the difference between the calculated rotational frequency and the observed absorption frequency. Values so obtained are marked by an asterisk.

Table II also lists the inversion frequency calculated from the previous equation relating ν_i to J and $\langle P_c^2 \rangle$. The values of Δ_0, A, and B were calculated by a least squares process to fit the "observed" inversion frequencies, resulting in the following equations for ν_i:

for NH_2D,

$$\nu_i = 12{,}181.6 - 76.7 - [J(J+1) - \langle P_c^2 \rangle] + 23.6\langle P_c^2 \rangle; \quad (9a)$$

for NHD_2,[7a]

$$\nu_i = 5110.9 - 26[J(J+1) - \langle P_c^2 \rangle] + 8.1\langle P_c^2 \rangle; \quad (9b)$$

for NH_3,

$$\nu_i = 23{,}785.75 - 151.450[J(J+1) - K^2] + 59.892K^2 + 0.49569(J^2+J-K^2)^2 - 0.37674K^2(J^2+J-K^2) + 0.06554K^2. \quad (9c)$$

By comparing the values for the inversion frequencies, as calculated from the above equations with the "observed" values, one can see that there is close agreement. The discrepancies, which vary from a few Mc/sec to about 25 Mc/sec, can be partially attributed to the fact that the value of the inversion splitting of the two rotational levels involved in the observed transitions are not identical. Furthermore, higher order terms were neglected; and these can be of importance for the high J transitions, as seen from the equation for NH_3.

In the above equations for ν_i, the values for Δ_0, the extrapolated inversion splitting for $J=0$, have previously been discussed and shown to agree very well with calculations based on the Dennison and Uhlenbeck[5] theory. Theoretical calculations for A and B, on the other hand, involve a very complicated numerical integration which was not carried through for the deuterated molecules. Significant empirical relations for determining the scaling factor for A and B, in going from the light to heavier molecules, could not be obtained.

EXPERIMENTAL RESULTS

A total of 35 NH_2D and NHD_2 lines, whose Stark components permitted positive identification, were measured and identified in the frequency region 7000 Mc/sec to 80,000 Mc/sec. These line frequencies, together with their intensities, are listed in Tables III and IV. It is to be noted that for each of the two molecules six pairs of lines were observed for $J_r \rightarrow J_{r'}$ transitions, whereas only a single line was measured for each of the other transitions listed. Although a number of other lines were observed and measured, they are not listed, because no positive identification could be made, usually because of interference of strong nearby lines. The 13,923.95-Mc/sec line listed in Table IV is tentatively assigned the $9_{27} \rightarrow 9_{37}$ transition in NHD_2 because of definite Stark evidence. However, the measured frequency is several hundred megacycles from the calculated value. Therefore, no definite assignment can be given for this line until a further experimental search is made for the other $9_{27} \rightarrow 9_{37}$ NHD_2 line in the 5000-Mc/sec region.

[7a] The accuracy of this equation has been improved by the low frequency measurements of K. Sawyer in this laboratory. See the Appendix.

TABLE IIb. Calculated and observed inversion splittings for NHD_2 (Mc/sec).

Transition	Calculated ν_i	Observed ν_i
$1_{01} \rightarrow 1_{11}$	5093	5083.11
$2_{02} \rightarrow 2_{12}$	5086	5089.11
$3_{03} \rightarrow 3_{13}$	5095	5098.99
$4_{04} \rightarrow 4_{14}$	5122	5126*
$5_{14} \rightarrow 5_{24}$	4822	4824.49
$6_{15} \rightarrow 6_{25}$	4809	4795.59
$8_{28} \rightarrow 8_{38}$	4325	4355.35

* Probable value; see text.

CENTRIFUGAL DISTORTION AND STRUCTURAL PARAMETERS

From the above observed data, one should be able to calculate the rotational and structural constants $(a-c)$ and κ for NH_2D and NHD_2. However, to do so, account must be taken of the fact that centrifugal distortion

TABLE III. List of observed NH_2D lines.

Transition	Frequency Mc/sec	Intensity 10^{-6} cm^{-1}
$2_{02} \rightarrow 2_{12}$	49,962.85±0.10	685
$2_{02} \rightarrow 2_{12}$	74,155.73±0.15	594
$3_{03} \rightarrow 3_{13}$	18,807.74±0.05	157
$3_{03} \rightarrow 3_{13}$	43,042.48±0.10	275
$4_{04} \rightarrow 4_{14}$	25,023.88±0.05	108
$5_{05} \rightarrow 5_{15}$	7562.06±0.05	30.2
$5_{05} \rightarrow 5_{15}$	17,052.74±0.05	51.4
$6_{06} \rightarrow 6_{16}$	10,842.62±0.05	57.6
$6_{06} \rightarrow 6_{16}$	14,104.32±0.05	32.5
$7_{07} \rightarrow 7_{17}$	12,154.57±0.05	61.8
$8_{08} \rightarrow 8_{18}$	12,784.10±0.05	41.2
$8_{08} \rightarrow 8_{18}$	13,119.94±0.05	14.5
$9_{09} \rightarrow 9_{19}$	13,217.78±0.05	43.3
$9_{09} \rightarrow 9_{19}$	13,320.46±0.05	14.7
$10_{8,10} \rightarrow 10_{1,10}$	13,626.80±0.05	45.5
$11_{8,11} \rightarrow 11_{1,11}$	14,069.73±0.05	48.9
$7_{16} \rightarrow 7_{26}$	29,186.99±0.05	193
$8_{17} \rightarrow 8_{27}$	18,254.38±0.05	47.6
$10_{19} \rightarrow 10_{29}$	12,399.24±0.05	22.5
$9_{27} \rightarrow 9_{37}$	33,909.34±0.05	87.1

TABLE IV. List of observed NHD_2 lines.

Transition	Frequency Mc/sec	Intensity 10^{-9} cm^{-1}
$1_{01}\rightarrow1_{11}$	57,674.76±0.15	396.0
$1_{01}\rightarrow1_{11}$	67,841.52±0.15	273.0
$2_{02}\rightarrow2_{12}$	28,560.90±0.05	86.3
$2_{02}\rightarrow2_{12}$	38,739.13±0.10	343.0
$3_{03}\rightarrow3_{13}$	8283.92±0.05	20.1
$3_{03}\rightarrow3_{13}$	18,481.91±0.05	50.1
$4_{04}\rightarrow4_{14}$	9517.55±0.05	30.0
$5_{14}\rightarrow5_{24}$	28,677.86±0.05	15.0
$5_{14}\rightarrow5_{24}$	38,326.84±0.10	13.4
$6_{15}\rightarrow6_{25}$	7801.38±0.05	5.51
$6_{16}\rightarrow6_{25}$	17,392.56±0.05	55.0
$8_{26}\rightarrow8_{36}$	20,608.77±0.05	17.4
$8_{26}\rightarrow8_{36}$	29,319.47±0.05	71.0
$9_{27}\rightarrow9_{37}$*	13,923.95±0.05	6.24

* Tentative assignment.

will change the rotational absorption frequencies from the values calculated on a rigid rotor basis. To accomplish this, use was made of the centrifugal distortion theory developed by Lawrance and Strandberg.[8] According to their work, the effect of centrifugal distortion on the energy of a given state can be expressed, to the first order, as

$$dW=P_a^2da+P_b^2db+P_c^2dc. \quad (10)$$

By expressing P_a^2, P_b^2, and P_c^2 in terms of J, κ, and $E(\kappa)$, as given previously, and by postulating that

$$\tfrac{1}{4}da=A_aP_a^2+A_bP_b^2+A_cP_c^2 \quad (11)$$

with similar expressions for db and dc, they obtained the following equation for dW:

$$dW=L(dE/d\kappa)^2+M(dE/d\kappa)E+N(dE/d\kappa)J(J+1)+QE^2+REJ(J+1)+SJ^2(J+1)^2, \quad (12)$$

where the E's are the reduced energies. The frequency correction, owing to centrifugal distortion, can now be obtained by subtracting dW_1, the correction to one energy level, from dW_2, the correction to the other level involved in the transition. For $\Delta J=0$ transitions, the frequency correction becomes

$$d\nu_{12}=L[(dE_2/d\kappa)^2-(dE_1/d\kappa)^2]+M[(dE_2/d\kappa)E_2-(dE_1/d\kappa)E_1]+NJ(J+1)[(dE_2/d\kappa)-(dE_1/d\kappa)]+Q[E_2^2-E_1^2]+RJ(J+1)[E_2-E_1]. \quad (13)$$

This equation was applied to the spectrum of formaldehyde, which is nearly a symmetric top. Therefore, E and $(dE/d\kappa)$ could be approximated with good accuracy by means of rather simple expressions. In our case, no similar accurate approximations could be made; thus, our calculations involve the complete equation as given above.

The evaluation of the structural parameters and of the centrifugal distortion constants can now be undertaken. We shall first discuss the NH_2D molecule. A first approximation to $(a-c)/2$ and to κ was made by assuming zero centrifugal distortion for the $J=2$, and 3 transitions. Since the rigid rotor frequencies can be obtained in closed form in terms of $(a-c)/2$ and κ, one can easily solve for these parameters. These values were then changed slightly, to give an amount of centrifugal distortion which would best fit the distortion equation given above. The constants for this equation were evaluated by means of a least-squares process to fit the six $J_\tau\rightarrow J_{\tau'}$ transitions for which both rotation-inversion lines were observed. It is to be noted that in all of these transitions the K_{+1} subscript is the same as the J-value.

The final choice for the rotational constants is $(a-c)/2=74{,}350\pm150$ Mc/sec and $\kappa=-0.315\pm0.002$ for the NH_2D molecule. These are not equilibrium values but are effective values including zero-point vibration. With a knowledge of $(a-c)$ and κ and with the aid of the equations it is possible to determine the effective values of θ, the corner-to-apex-to-corner angle of the ammonia pyramid, and r, the nitrogen-to-hydrogen distance. For NH_2D the following values were obtained: $\theta=107.3°\pm0.2°$ and $r=(1.008\pm0.004)$A.

For NHD_2, a procedure similar to that used for NH_2D resulted in the following choice for the rotational constants of this molecule: $\frac{1}{2}(a-c)=55{,}200\pm100$ Mc/sec and $\kappa=-0.1385\pm0.002$. This corresponds to an effective value for θ of $107°\pm2°$ and for r of (1.016 ±0.008)A. Considering that zero-point vibration will cause the effective values of θ and r to differ slightly for the different isotopic ammonias, these values are in good agreement with the following average NH_3 and ND_3 values given by Herzberg: $\theta=106.78°$ and $r=1.014$A.

Tables V and VI list the centrifugal distortion as observed and as calculated from a "best-fit" equation, and a comparison indicates that there is fairly good agreement. The rigid rotor frequencies listed in these tables were calculated, using 5-point lagrangian interpolation in the King, Hainer, and Cross tables. This type of interpolation gives an accuracy to the fifth decimal place, which is equivalent in our case to a frequency accuracy of about one Mc/sec. In Table VI, listing the NHD_2 centrifugal distortion, it is to be noted that for several transitions, centrifugal distortion tends to raise the transition frequency rather than lower it, as is more usual. This does not violate any stability principle, since each energy level is lowered by the centrifugal distortion with the lower energy level involved in the transition being affected more than the upper energy level, thus resulting in an increase in the transition energy.

[8] R. B. Lawrance and M. W. P. Strandberg, Phys. Rev. **83**, 363 (1951).

ABSORPTION COEFFICIENTS

For pressure broadened microwave spectrum lines the method of Van Vleck and Weisskopf can be used to calculate the absorption coefficients. One can show that with the usual simplifying assumptions permissible for microwave lines, the expression for the absorption coefficient α for our asymmetric molecules, measured at the peak of resonance, is given by

$$\alpha=\frac{8\pi^2}{3ckT}\frac{n}{\Delta\nu}\frac{\nu^2\mu^2\lambda\exp[-W_i/kT]}{(kT/h)^{\frac{1}{2}}(\pi/abc)^{\frac{1}{2}}}g, \qquad (14)$$

where α=power absorption coefficient in cm^{-1}, n=no. of molecules of absorbing gas per cm^3, $\Delta\nu$=half-width of absorption line at half-intensity and taken to be 29 Mc/sec for a pressure of 1 mm of Hg at room temperature, W_i=energy of lower state involved in the transition, ν=frequency of absorption line, μ=dipole moment, λ=line strength calculated by Cross, Hainer, and King, and g=statistical weight factor due to nuclear spin. All other symbols have their usual meanings.

The statistical weight factor due to nuclear spin can be determined from the following considerations. For the NH_2D molecule, an inversion followed by a rotation about the a axis (see Fig. 1) is equivalent to an interchange of the two hydrogen atoms. Since these are Fermi particles, the parity of the over-all wave function must change for the above operation. Therefore, for those states in which the inversion and the rotation about the a axis (frequently denoted by C_2^a) are both symmetric or both antisymmetric (i.e., for lower inversion state and K_{-1} even or upper inversion state and K_{-1} odd), only the antisymmetric spin wave function will occur so that the over-all wave function will be antisymmetric. Similarly, for the lower inversion state and K_{-1} odd or upper inversion state and K_{-1} even, only the symmetric spin wave function will occur. One can now determine the ratio of the statistical weights of the symmetrical to antisymmetrical spin states by the same argument used for calculating the alternation of intensities for homonuclear diatomic molecules. This ratio is found to be $(I+1):I$, where I is the nuclear spin. Therefore, for NH_2D the nuclear weight factor g is $\frac{3}{4}$ or $\frac{1}{4}$ for symmetric or antisymmetric spin states, respectively.

In the case of NHD_2 the reasoning must involve an inversion followed by a rotation about the b axis rather than about the a axis, since for this molecule it is the b axis which is the symmetry axis passing through the NDD plane. The symmetry for the operation C_2^b (rotation about the b axis) is determined by the product $K_{-1}K_1$; and since the deuteron is a Bose particle, an inversion followed by C_2^b must not change the parity of the over-all wave function. Therefore, the statistical weight factor for NHD_2 is determined as follows. For a lower inversion state and C_2^b even, or for a higher inversion state and C_2^b odd, only the symmetric states will occur, while for other combinations, only the antisymmetric spin states will occur. Thus, g for NHD_2 is $\frac{2}{3}$ or $\frac{1}{3}$ for symmetric or antisymmetric spin states, respectively.

Values for the absorption coefficients for the various observed lines are listed in Tables III and IV. Experimentally, no absolute intensity measurements were made although approximate estimates were made by relative comparison with known NH_3 lines and with the known sensitivity of the spectroscope. The correlation of these rough estimates and the calculated values are good. The relative intensities of the high and low frequency components of a given $J_\tau\rightarrow J_{\tau'}$ transition were also checked experimentally and found to agree with the calculated ratios.

TABLE V. Centrifugal distortion correction for NH_2D; $\frac{1}{2}(a-c)=74{,}350$; $\kappa=-0.315$.

Transition	Rigid rotor ν Mc/sec	Observed ν Mc/sec	Observed $\Delta\nu$ Mc/sec	Best fit $\Delta\nu$ Mc/sec
$2_{02}\rightarrow 2_{12}$	62,150.95	62,059.29	91.7	91.9
$3_{03}\rightarrow 3_{13}$	31,178.52	30,925.11	253.4	253.4
$4_{04}\rightarrow 4_{14}$	13,054.85			225.7
$5_{05}\rightarrow 5_{15}$	4879.07	4745.34	133.4	133.4
$6_{06}\rightarrow 6_{16}$	1699.19	1630.85	68.3	68.7
$7_{07}\rightarrow 7_{17}$	564.23			33.9
$8_{08}\rightarrow 8_{18}$	181.19	167.92	13.3	12.4
$9_{09}\rightarrow 9_{19}$	56.43	51.34	5.1	5.7
$10_{0,10}\rightarrow 10_{1,10}$	27.48			5.4
$11_{0,11}\rightarrow 11_{1,11}$	5.32			3.9

Distortion equation:

$$\Delta\nu=-4.083[(dE_2/d\kappa)^2-(dE_1/d\kappa)^2]+43.43[(dE_2/d\kappa)E_2-(dE_1/d\kappa)E_1]+47.25[(dE_2/d\kappa)-dE_1/d\kappa]J(J+1)=241.1[E_2^2-E_1^2]-264.7[E_2-E_1]J(J+1)$$

TABLE VI. Centrifugal distortion correction for NHD_2; $\frac{1}{2}(a-c)=55{,}200$; $\kappa=-0.1385$.

Transition	Rigid rotor ν Mc/sec	Observed ν Mc/sec	Observed $\Delta\nu$ Mc/sec	Best fit $\Delta\nu$ Mc/sec
$1_{01}\rightarrow 1_{11}$	62,845.20	62,758.14	87.1	87.9
$2_{02}\rightarrow 2_{12}$	33,874.03	33,650.02	224.0	222.1
$3_{03}\rightarrow 3_{13}$	13,540.01	13,382.92	157.1	160.0
$4_{04}\rightarrow 4_{14}$	4454.36			63.4
$5_{14}\rightarrow 5_{24}$	33,898.32	33,502.35	396.0	396.0
$6_{15}\rightarrow 6_{25}$	12,716.15	12,596.97	119.2	118.4
$8_{26}\rightarrow 8_{36}$	24,944.05	24,964.12	−20.1	−20.0
$9_{27}\rightarrow 9_{37}$	9060.80			−181.3

Distortion equation:

$$d\nu=-0.296618[(dE_2/d\kappa)^2-(dE_1/d\kappa)^2]-16.56467[(dE_2/d\kappa)E_2-(dE_1/d\kappa)E_1]+2.33861J(J+1)[(dE_2/d\kappa)-dE_1/d\kappa]-65.6743[E_2^2-E_1^2]+11.44885[E_2-E_1]J(J+1)$$

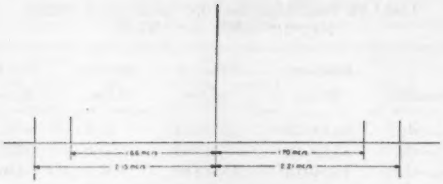

FIG. 4. Observed quadrupole structure.

SIGN OF NUCLEAR QUADRUPOLE COUPLING CONSTANT

The value of the nuclear electric quadrupole coupling constant eqQ has been measured for NH_3 and should be the same for the deuterated molecules, since it merely involves the nuclear quadrupole moment of the N^{14} nucleus. However, owing to the fact that the microwave spectrum of NH_3 is caused by transitions between states having the same rotational structure, the resulting quadrupole pattern is completely symmetrical and does not permit a determination of the sign of the quadrupole coupling constant.

With partially deuterated ammonia, rotational levels are not degenerate, so that a sign determination can be made with high resolution equipment. To accomplish this, the hyperfine structure of the $4_{04}\rightarrow 4_{14}$ transition of NH_2D occurring at 25,023.88 Mc/sec was investigated, using a high resolution microwave spectroscope developed by Eshbach. The theoretical asymmetry in the quadrupole pattern was calculated, using essentially the theory discussed by Loomis and Strandberg,[9] with the magnetic correction of Henderson[10] applied. Our results (Fig. 4) show that the quadrupole coupling constant is negative and is in agreement with the accepted value of -4.10 Mc/sec for eqQ. The sign has long been assumed negative both from considerations of the probable electronic structure of the ammonia molecule, as discussed by Townes and Dailey,[11] and from the negative value of eqQ for NF_3 as measured by Sheridan and Gordy.[12]

TABLE VII. Observed ND_2H lines.

Transition	Frequency Mc/sec	Intensity 10^{-9} cm^{-1}
$5_{05}\rightarrow 5_{15}$	6461.09±0.05	8.4
$6_{06}\rightarrow 6_{16}$	5581.08±0.05	12.2
$6_{06}\rightarrow 6_{16}$	4860.20±0.05	4.6
$7_{07}\rightarrow 7_{17}$	5392.07±0.05	4.7
$7_{07}\rightarrow 7_{17}$	5197.56±0.05	8.8
$8_{08}\rightarrow 8_{18}$	5414.15±0.05	8.9
$8_{08}\rightarrow 8_{18}$	5364.03±0.05	4.4
$9_{09}\rightarrow 9_{19}$	5507.75±0.05	3.6
$9_{09}\rightarrow 9_{19}$	5494.98±0.05	7.1
$10_{0,10}\rightarrow 10_{1,10}$	5635.18±0.05	6.0
$10_{0,10}\rightarrow 10_{1,10}$	5631.97±0.05	3.0
$11_{0,11}\rightarrow 11_{1,11}$	5787.16±0.05	2.3
$11_{0,11}\rightarrow 11_{1,11}$	5786.44±0.05	4.6
$12_{0,12}\rightarrow 12_{1,12}$	5962.30±0.20	3.4
		1.7
$13_{0,13}\rightarrow 13_{1,13}$	6161.86±0.20	
$14_{0,14}\rightarrow 14_{1,14}$	6387.23±0.20	

[9] C. C. Loomis and M. W. P. Strandberg, Phys. Rev. **81**, 798 (1951).
[10] R. S. Henderson, Phys. Rev. **24**, 107, 626 (1948).

EXPERIMENTAL TECHNIQUES

The partially deuterated ammonias were synthesized by a method involving the following reaction:

$$Mg_3N_2+6H_2O\rightarrow 3Mg(OH)_2+2NH_3.$$

The magnesium nitride was made by heating magnesium powder in a closed Vykor crucible with a Meker burner. The top layer of white magnesium oxide was then removed and the remaining magnesium nitride was placed in an evacuated vessel. By adding a mixture of deuterated and ordinary water, various quantities of NH_3, NH_2D, NHD_2, and ND_3 were evolved. Presumably, partially deuterated ammonia could also be made by adding heavy water to ordinary ammonia.

TABLE VIII. Inversion splittings for ND_2H (Mc/sec).

Transition	Calculated	Observed
$5_{05}\rightarrow 5_{15}$	5156	5145*
$6_{06}\rightarrow 6_{16}$	5226	5220.64
$7_{07}\rightarrow 7_{17}$	5301	5294.81
$8_{08}\rightarrow 8_{18}$	5396	5389.09
$9_{09}\rightarrow 9_{19}$	5504	5501.35
$10_{0,10}\rightarrow 10_{1,10}$	5628	5633.57
$11_{0,11}\rightarrow 11_{1,11}$	5771	5786.80
$12_{0,12}\rightarrow 12_{1,12}$	5932	5962.30
$13_{0,13}\rightarrow 13_{1,13}$	6102	6161.86
$14_{0,14}\rightarrow 14_{1,14}$	6291	6387.23

* Value calculated from only one line.

The Stark modulation spectroscope used in this investigation is the result of development of the entire microwave spectroscopy group at the Research Laboratory of Electronics and has been described by Weiss *et al.*[13] The high resolution spectroscope used to measure the quadrupole hyperfine structure was built by Eshbach and is to be described in a forthcoming paper. Recently, a low frequency spectroscope has been constructed to investigate the ammonia spectrum, between 3000 Mc/sec and 7000 Mc/sec. Sawyer has undertaken this investigation, and his results are reported in the Appendix.

APPENDIX

K. SAWYER

The absorption transitions of ND_2H which were observed below 6500 Mc/sec and identified are listed in Table VII. Intensity

[11] C. H. Townes and B. P. Dailey, J. Chem. Phys. **17**, 782 (1949).
[12] J. Sheridan and W. Gordy, Phys. Rev. **79**, 513 (1950).
[13] Weiss, Strandberg, Lawrance, and Loomis, Phys. Rev. **78**, 202 (1950).

calculations are made with an assumed line half-width of 29.2 Mc/sec at 1 mm Hg. The transitions are paired for all transitions found, except in the case of the $5_{05}-5_{15}$ line, where the lower frequency component lies in the 3800-Mc/sec region. Corresponding inversion splittings are listed in Table VIII. The $5_{05}-5_{15}$ inversion is not truly an observed splitting, since it is calculated from the position of the pure rotation transition.

The agreement between observed and calculated values is good at low values of J. Above $J=11$ the calculated value rapidly falls below the observed value, indicating the need of higher order terms.

In the case of high J transitions, the rotational transition frequency is so slight that the lines are close doublets. Above $J=11$ measurements were made at the maximum intensity of the unresolved doublet. For all transitions above $J=7$, the centrifugal distortion is so slight that the five-place tables of the reduced energy caused errors in excess of the distortion. Table IX gives the calculated and observed rotational energy differences. The centrifugal distortion was calculated, using equation for Table VI above.

TABLE IX. Rotational transitions (Mc/sec).

Transition	Frequency Rigid rotor	Frequency Observed	Distortion Observed	Distortion Calculated
$5_{05}\rightarrow5_{15}$	1314.31			−2.40
$6_{06}\rightarrow6_{16}$	361.56	360.44	1.12	0.70
$7_{07}\rightarrow7_{17}$	95.50	97.25	−1.75	−2.56
$8_{08}\rightarrow8_{18}$	24.29	25.06	−0.77	
$9_{09}\rightarrow9_{19}$	6.07	6.37	−0.30	
$10_{0,10}\rightarrow10_{1,10}$	1.66	1.60	0.06	
$11_{0,11}\rightarrow11_{1,11}$		0.36		

PHYSICAL REVIEW VOLUME 83, NUMBER 3 AUGUST 1, 1951

Centrifugal Distortion in Asymmetric Molecules. II. HDS

R. E. HILLGER* AND M. W. P. STRANDBERG
Research Laboratory of Electronics, Massachusetts Institute of Technology, Cambridge, Massachusetts†

(Received March 6, 1951)

A perturbation method for relating the theory of centrifugal distortion in asymmetric top molecules to observed microwave Q branch, *a* or *c* type transitions, is presented. The formula for the distortion correction is expressed in terms of the total angular momentum, J, the symmetry axis momentum of the nearest symmetric top, K, and five distortion constants. The formula yields a satisfactory fit to the observed spectrum of HDS ($\kappa\simeq-0.5$). The electric dipole moment is determined as 1.02±0.02 debye. The inertia defect and distortion constants are calculated. The effective structure for the HDS molecule so determined is in agreement with infrared determinations.

INTRODUCTION

THE vibration-rotation energies of polyatomic molecules have been derived to a second order of approximation for special cases by a number of authors. In general, the method followed has been equivalent to that of Wilson and Howard.[1] This work may be summarized by stating that the rotational term values of a molecule depend upon these quantities: the equilibrium structure of the molecule, the normal frequencies of vibration, and the nonvanishing coefficients of the anharmonic (cubic) terms in the expression for the binding potential energy of the molecule. Nielsen[2] has calculated the matrix elements for the rotational energy including, to second order, vibration-rotation energies.

Unfortunately the correction of centrifugal distortion in asymmetric top rotational term values is, in general, an inconvenient process. The explicit diagonalization of the reduced energy matrix may be accomplished for only a relatively few low J terms, when the asymmetry coefficient and the six centrifugal distortion coefficients are included as unknowns. Since the experimental data are best used to evaluate the centrifugal distortion coefficients, the diagonalization of the reduced energy matrix for each trial value of these coefficients is awkward for comparison with experiment.

A method of arriving at an explicit form of the formula for centrifugal distortion correction terms to the rigid rotor frequencies has been demonstrated.[3] This paper will discuss a method of determining centrifugal distortion correction factors in terms of the general centrifugal distortion matrix elements.

I. THEORY

The method used here is that of determining the centrifugal distortion correction in terms of rigid rotor frequencies specifically for Q branch "*a*" type or "*c*" type transitions. This dependence may be determined explicitly in terms of quantum or pseudo-quantum numbers and the rigid rotor absorption frequency, by a modified application of conventional perturbation theory.

To review briefly, the reduced energy matrix is diagonal in J and M; the nonvanishing elements in K (i.e., P_z) are $(K|H|K)$, $(K|H|K\pm2)$, and $(K|H|K\pm4)$.

* Now associated with Snow and Schule, Inc., Cambridge, Massachusetts.

† This work was supported in part by the Signal Corps, the Air Materiel Command, and ONR.

[1] E. B. Wilson, Jr., and J. B. Howard, J. Chem. Phys. **4**, 262 (1936).

[2] H. H. Nielsen, Phys. Rev. **60**, 794 (1941).

[3] R. B. Lawrance and M. W. P. Strandberg, Phys. Rev. **83**, 363 (1951).

TABLE I. Identification of parameters.

	I^r	II^r	III^r
x	b	c	a
y	c	a	b
z	a	b	c
F	$\frac{1}{2}(\kappa-1)$	0	$\frac{1}{2}(\kappa+1)$
G	1	κ	-1
H	$-\frac{1}{2}(\kappa+1)$	1	$\frac{1}{2}(\kappa-1)$
κ		$\frac{2b-a-c}{a-c}$	

These elements have been given by Nielsen[2] explicitly in terms of the molecular parameters.

The reduced energy matrix $E(\kappa)$ may be set up for a given value of J, the order of which is $(2J+1)$ since $-J \leqslant K \leqslant J$. This matrix may immediately be factored to four submatrices as in the case of the rigid rotor.[4] Explicitly these submatrices in terms of the original energy elements are:

$$E^{\pm}=\left\|\begin{array}{c|cccccc} a_{00} & \sqrt{2}a_{02} & \sqrt{2}a_{04} & 0 & \cdots & \cdots & \cdots \\ \hline \sqrt{2}a_{02} & a_{22}\pm a_{2,-2} & a_{24} & a_{26} & 0 & \cdots & \cdots \\ \sqrt{2}a_{04} & a_{24} & a_{44} & a_{46} & a_{48} & 0 & \cdots \\ 0 & a_{26} & a_{46} & a_{66} & a_{68} & a_{6,10} & \cdots \\ \cdots & \cdots & \cdots & \cdots & \cdots & \cdots & \cdots \end{array}\right\|, \quad (1)$$

where E^- has the same elements as E^+ after the first row and column have been deleted, and

$$0^{\pm}=\left\|\begin{array}{cccccccc} a_{11}\pm a_{1,-1} & a_{13}\pm a_{1,-3} & a_{15} & 0 & \cdots & \cdots & \cdots \\ a_{13}\pm a_{1,-3} & a_{33} & a_{35} & a_{37} & 0 & \cdots & \cdots \\ a_{15} & a_{35} & a_{55} & a_{57} & a_{59} & 0 & \cdots \\ 0 & a_{37} & a_{57} & a_{77} & a_{79} & a_{7,11} & \cdots \\ \cdots & \cdots & \cdots & \cdots & \cdots & \cdots & \cdots \end{array}\right\|. \quad (2)$$

In deriving these, use has been made of the relations

$$a_{K,K}=a_{-K,-K}$$

and

$$a_{K,K+2}=a_{K+2,K}=a_{-K,-K-2}=a_{-K-2,-K}$$
$$a_{K,K+4}=a_{K+4,K}=a_{-K,-K-4}=a_{-K-4,-K}. \quad (3)$$

The matrices are presented in the general notation of King, Hainer, and Cross[5] (hereinafter referred to as KHC) so that the identification of explicit energy levels is immediately obtained from their work, and hence will not be duplicated here. The difference between KHC's matrices and those given above is that the latter give the entire energy of the molecule including distortion corrections.

[4] Obviously there is no loss in generality in considering only the reduced energy matrix since it contains the entire complexity of the asymmetric rotor problem. The addition of $\frac{1}{2}(a+c)J(J+1)$ to $E(\kappa)$ yield the total energy.

[5] King, Hainer, and Cross, J. Chem. Phys. 11, 27 (1943).

The matrix elements for the rotational reduced energy are given explicitly by Nielsen[6] as

$$(K|H|K)=(R_0 \mp R_1 K+R_2K^2+R_3K^4), \quad (4)$$

$$(K|H|K\pm 2)=\{f(J,K\pm 1)\}^{\frac{1}{2}} \times\{R_4-[K^2+(K\pm 2)^2]R_5(a-c)/2\}, \quad (5)$$

$$(K|H|K\pm 4)=\{[f(J,K\pm 1)] \times[f(J,K\pm 3)]\}^{\frac{1}{2}}R_6(a-c)/2, \quad (6)$$

where

$$R_0=\tfrac{1}{2}F(a-c)J(J+1)-\tfrac{1}{2}D_J(1-c)J^2(J+1)^2,$$
$$R_1=2Z_c\textstyle\sum_r \zeta_r e_r, \quad R_3=-\tfrac{1}{2}D_K(a-c),$$
$$R_2=\tfrac{1}{2}(G-F)(a-c)-\tfrac{1}{2}D_{JK}(a-c)J(J+1),$$
$$R_4=\tfrac{1}{4}H(a-c)+\tfrac{1}{2}\delta_J(a-c)J(J+1),$$
$$f(J,n)=[J(J+1)-n(n-1)][J(J+1)-n(n+1)], \quad (7)$$

and D_J, D_{JK}, D_K, δ_J, R_5, and R_6 are the six centrifugal distortion terms dependent upon the vibration frequencies and molecular structure parameters. R_1 arises from internal angular momentum and is hereafter neglected. a, b, and c are defined as the effective reciprocal moments of inertia of the molecule which when corrected for zero point vibration yield the equilibrium values, a_e, b_e, and c_e.[7] The latter are defined as the reciprocal moments of inertia the molecule would have if the atoms were located at the exact minima of the molecular binding potential, and may be expressed

$$a_e=h/(8\pi^2 I_{aa}^e) \text{ cps},$$
$$b_e=h/(8\pi^2 I_{bb}^e) \text{ cps},$$
$$c_e=h/(8\pi^2 I_{cc}^e) \text{ cps},$$
$$a \geq b \geq c. \quad (8)$$

Planck's constant has been factored from all elements to reduce them to frequency units. The I^r representation is used for a-type Q branch transitions and the III^r representation for c-type transitions. The actual definition of H, F, and G in terms of a, b, and c are determined by the type of representation used. Table I has been prepared from KHC for this purpose. Further discussion of this point is given later. In the I^r representation a-type transitions are between term levels of E^+ and E^-, or 0^+ and 0^-. Similarly for the III^r representation, c-type transitions are given by the same selection rules.

[6] Nielsen's choice of phase factor for P_s and P_g differs from KHC. We have modified Nielsen's results to agree with KHC by changing the sign of the $(K|H|K\pm 2)$ elements. Either choice of phase yields identical results for the $(K|H|K)$ and $(K|H|K\pm 4)$ elements. In any case the modification is purely formal. Note that Nielsen's D_J, D_{JK}, D_K, δ_J, R_5, and R_6 have been normalized to $\frac{1}{2}(a-c)$.

[7] This is not quite correct, for there still remains a small correction due to vibration-rotation interaction which is dependent neither on vibration quantum number (zero point vibration), nor rotational quantum number (centrifugal distortion) i.e., Nielsen's x_0, y_0, and z_0.

The energy matrices (1) and (2) show clearly that the symmetric top K-degeneracy is removed in the Kth level by a perturbation of order K. To illustrate, consider the $E^{\pm}$ matrix. The 0^+ level is a singlet level (nondegenerate in zero order). The 2^+ level is split from the 2^- level because of the second-order coupling with the 0^+ level through the off-diagonal elements $\sqrt{2}a_{02}$. The term $a_{2,-2}$ is neglected for the moment since it is only a centrifugal distortion correction and small compared to the absorption energy. Both $K=2$ levels are perturbed almost equally by the $4^{\pm}$ levels. So the $K=2$ degeneracy is removed in second order. The $4^{\pm}$ degeneracy is removed due to a second-order coupling with the $2^{\pm}$ levels. Since the $2^{\pm}$ degeneracy is removed in second order, the $4^{\pm}$ degeneracy is removed in fourth order, and so on. The degeneracy of the levels K^+ and K^- is thus eliminated in Kth order due to the progressively greater splitting of the $(K-2)^{\pm}$ and $(K-4)^{\pm}$, etc., levels.

Observation of this fact simplifies the calculation of the effect of including centrifugal distortion terms in the matrix. We postulate that the matrix has been progressively diagonalized by second-order perturbation theory beginning with the next to the lowest K level in the matrix. Thus the new diagonal elements of the $K-2$ levels, $(a_{K-2,K-2})_p^{\pm}$, are assumed nondegenerate. The amount by which the levels are split is of course closely related to the absorption frequency ν_{K-2}. It differs slightly from the absorption frequency since the $K^{\pm}$ levels, which will eventually have their degeneracy removed, will further perturb the diagonal $K-2$ elements. The latter effect is taken into account by writing:[5]

$$(a_{K-2,K-2})_p^{+}-(a_{K-2,K-2})_p^{-} \cong \nu_{K-2}[1-a_{K,K-2}^2/(a_{K,K}-a_{K-2,K-2})^2].$$

This of course reduces to ν_{K-2} in the region where second-order perturbation is applicable, i.e., where

$$a_{K,K-2}^2/(a_{K,K}-a_{K-2,K-2})^2 = H^2f(J,K-1)/64(G-F)(K-1)^2 \ll 1. \quad (10)$$

By similar reasoning the interaction of the K level with the $K+2$ level is negligibly small, thus

$$E^{\pm} \cong a_{K,K-2}^2/a_{K,K}^{\pm}-(a_{K-2,K-2}^{\pm})_p + a_{K,K-4}^2/a_{K,K}^{\pm}-(a_{K-4,K-4}^{\pm})_p \quad (11)$$

and hence

$$\nu_K \cong \nu_{K-2}a_{K,K-2}^2/(a_{K,K}-a_{K-2,K-2})^2 + \nu_{K-4}a_{K,K-4}^2/(a_{K,K}-a_{K-4,K-4})^2. \quad (12)$$

The term involving $a_{K,K-4}$ is second order in a centrifugal distortion correction, and hence may be neglected.

The terms above are then written separating the rigid rotor contributions from the centrifugal distortion contributions.

$$\nu_K=(\nu_K)_{\text{rigid}}\left\{1+\frac{2\delta_{K,K-2}}{a_{K,K-2}'} - \frac{2(\delta_{KK}-\delta_{K-2,K-2})}{(a_{KK}'-a_{K-2,K-2}')}+D_{K-2}\right\} \quad (13)$$

where:

$$a_{K,K-2}=a'_{K,K-2}\ (\text{rigid})+\delta_{K,K-2}\ (\text{distortion}),\ \text{etc.}$$

$$\nu_{K-2}=(\nu_{K-2})_{\text{rigid}}\ (1+D_{K-2})$$

and D_{K-2} is the centrifugal distortion contribution to ν_{K-2}.

The term D_{K-2} is of course a similar term to that given above, but now in terms of D_{K-4}, and so on. Finally, also, for low K values (1, 2, 3) the fourth off-diagonal terms, $(K|H|K'\pm 4)$, must be considered. When Eq. (13) is properly summed, using Eqs. (4), (5), (6), and (7), it may be written for odd and even K's as follows:

$$\begin{aligned}\nu_o(J_K)=\nu_r(J_K)\{&1+2KJ(J+1)\delta_J/H\\ &+(K-1)J(J+1)D_{JK}/(G-F)\\ &+\tfrac{3}{8}K(K^2+2)[D_K/(G-F)-2R_6/H]\\ &+[16(G-F)/H^2R_6-4D_K/(G-F)]_{K(\text{even})}\\ &+[64(G-F)/H^2R_6]_{K(\text{odd})\geq 3}\\ &-[2D_K/(G-F)]_{K(\text{odd})}\}. \quad (14)\end{aligned}$$

This is our desired equation.

It is well to reconsider the restrictions of this formula. First, one must stay away from the diagonal of perturbation divergence, i.e.,

$$\frac{H^2f(J,K-1)}{64(G-F)^2(K-1)^2} \ll 1. \quad (15)$$

Further discussion of this point is given in reference 3. Equation (14) is used to correct for the distortion in the observed microwave spectrum of HDS. Though this molecule is quite asymmetric ($\kappa \simeq -0.5$) the convergence criterion given above is satisfied for the observable levels. It is to be noted, however, that though the convergence criterion is satisfied even for the observed high J high K lines, it may not be satisfied for the low K terms of the same J value. In other words, the convergence of a level J_K may be assured, but the convergence of the splittings of the J_{K-2}, J_{K-4}, etc., may not be satisfactory. Such convergence is postulated in the derivation of Eq. (14). Since the distortion of the J_K transition is composed of its own

[5] The rigid rotor frequency is not calculated so crudely, of course. Such an approximation is only justified since we are interested in the *additional* contribution due to centrifugal distortion to an accuracy of a few percent.

terms, plus those of the lower order transitions, i.e., J_{K-2}, J_{K-4}, etc., each of these lower order contributions must be in turn calculable by this method to achieve Eq. (14). This is certainly not the case in general. We only note that the contributions from the lower order K's diminish rapidly with decreasing K so that little error is caused as long as the main terms, the $K-2$, and possibly $K-4$ terms, meet the convergence requirement.

Second, it may be noted again that the above analysis is appropriate to Q-branch "a" and "c" type transitions. The type of transition covered is governed through F, G and H, by the representation used: I^r for "a" type and III^r for "c" type transitions. The value of K in Eq. (14) corresponds to the KHC index K_{-1} or K_{+1} for "a" and "c" type transitions respectively.

The restriction given above is not as drastic as may be first surmised, for molecules having significant distortion ("light" molecules) and yet a microwave spectrum will, in general, satisfy it.

Finally, this analysis could be extended with more difficulty to P and R branches. At present such an extension seems of little general importance, since molecules with P or R branches in the microwave region will generally have large moments of inertia, and consequently small centrifugal distortion correction; or they will be nearly symmetric tops (only one small moment of inertia), and hence symmetric top formulas may be reasonably applied; or the qualitative analysis of reference 3 may also be used.

II. CENTRIFUGAL DISTORTION OF HDS

The experimental values of the rotational absorption frequencies of HDS[32], observed for the first time in the microwave region, and identified by the Stark effect, are given in Table III. This data is now to be fitted to the distortion formula Eq. (14). The rigid rotor frequency is given by:

$$\nu_r(J_K)=\tfrac{1}{2}(a-c)[\Delta E(\kappa)]. \tag{16}$$

The process of fitting will be described briefly. A study of Eqs. (14) and (16) shows that there are seven adjustable parameters, i.e., the five distortion constants and $\frac{1}{2}(a-c)$ and κ. Fairly accurate values of the latter two constants are obtained from low J transitions. Assuming these are correct, the distortion constants are determined using the experimental frequencies and the method of least squares. The process is then reversed; $\nu(J_K)$ is calculated from the distortion constants just evaluated and compared with the observed $\nu_o(J_K)$. Discrepancies are attributed to the fact that the $\nu_r(J_K)$, as determined from $\frac{1}{2}(a-c)$ and κ, are not exactly correct. Therefore, slight variations in $\frac{1}{2}(a-c)$ and κ are made and the computations repeated until an entirely consistent set of results is obtained.

TABLE II. κ, $\frac{1}{2}(a-c)$ and distortion constants of hydrogen deuterium sulfide.

$\frac{1}{2}(a-c)=3.2664$ cm^{-1}
$\kappa=-0.47767$
$R_6=-2.808\times10^{-4}$ cm^{-1}
$\delta_J=+2.531\times10^{-5}$ cm^{-1}
$D_{JK}=+9.133\times10^{-4}$ cm^{-1}
$D_K=(-1.64\times10^{-4}$ cm$^{-1})$*
$R_6=+0.695\times10^{-5}$ cm^{-1}

* Assumed.

The actual computations would seem to be quite laborious, but fortunately, Eq. (14) lends itself to an analytical simplification which reduces the computations involved by a large factor. Taking values of $\frac{1}{2}(a-c)$ and κ, $\nu_r(J_K)$ is calculated for each value of J_K. K in the present case is the KHC K_{-1} index for the asymmetric rotor. The differences $\nu_o(J_K)-\nu_r(J_K)$ are taken and when finally the correct values of $\nu_r(J_K)$ are found, these differences will be the centrifugal distortion corrections. The following ratios are formed for each line

$$a(J_K)=[\nu_o(J_K)-\nu_r(J_K)]/\nu_r(J_K). \tag{17}$$

Now, if the differences $a((J+1)_K)-a(J_K)$ are taken between lines of equal K_{-1}, the only distortion terms remaining are those which are a function of J. With slight rearrangement, a series of equations are obtained

$$\frac{a((J+1)_K)-a(J_K)}{2(J+1)}=\left[\frac{D_{JK}}{(G-F)}+2\frac{\delta_J}{H}\right]K-\frac{D_{JK}}{(G-F)}$$
$$=AK+B, \tag{18}$$

which represents a straight line as a function of K. The values of the constants A and B are taken as those which best fit this linear relationship and are found by the method of least squares. It turns out that if $\frac{1}{2}(a-c)$ and κ as chosen are almost correct, then the values of A and B are essentially independent of $\nu_r(J_K)$. Since $\frac{1}{2}(a-c)$ and κ are known to three figure accuracy from low J transitions, the above computation need only be carried out once or twice during the process of fitting.

A and B thus determine the J dependence of distortion and when substituted back into Eq. (14), a new series of equations are obtained involving only K dependent and constant terms. These can be written

$$a_K=a(J_K)-J(J+1)(AK+B)$$
$$=\tfrac{2}{3}K(K^2+2)\left[\frac{D_K}{(G-F)}-\frac{2R_6}{H}\right]$$
$$+\left[\frac{16(G-F)}{H^2}R_6-\frac{4D_K}{(G-F)}\right]_{K(\text{even})}$$
$$+\left[\frac{64(G-F)}{H^2}R_6\right]_{K(\text{odd})\geq3}-\left[\frac{2D_K}{(G-F)}\right]_{K(\text{odd})} \tag{19}$$

where the "even" and "odd" notations indicate the terms which are present for even and odd values of K respectively. By taking the differences, $a_{K+2}-a_K$, the

TABLE III. Comparison of calculated and observed frequencies for hydrogen deuterium sulfide (in Mc/sec).

Initial state	Final state	Distortion correction	Calculated frequency	Observed frequency ±0.05 Mc/sec	Obs.-Calc. frequency
$1_{1,1}$	$1_{1,0}$	−73.43	51,073.30	51,073.27	−0.03
$2_{1,1}$	$2_{1,0}$	−49.61	11,283.73	11,283.83	+0.10
$3_{2,2}$	$3_{2,1}$	−220.38	53,204.97	53,200.93	−4.04
$4_{2,2}$	$4_{2,1}$	−125.09	10,862.97	10,861.07	−1.90
$5_{2,3}$	$5_{2,2}$	−411.22	40,917.57	40,929.20	+11.63
$6_{4,3}$	$6_{4,2}$	−177.27	7939.65	7936.74	−2.91
$7_{4,4}$	$7_{4,3}$	−516.94	27,557.68	27,566.31	+8.63
$8_{4,5}$	$8_{4,4}$	−1111.14	75,545.79	75,551.73	+5.94
$9_{5,5}$	$9_{5,4}$	−529.15	17,209.60	17,212.61	+3.01
$10_{5,6}$	$10_{5,5}$	−1123.07	47,906.66	47,905.36	−1.30
$11_{6,6}$	$11_{6,5}$	−476.79	10,233.30	10,235.81	+2.51
$12_{6,7}$	$12_{6,6}$	−1008.25	28,843.69	28,842.84	−0.85

coefficient of the K dependent term and the correct value of κ may be determined. There is insufficient data to evaluate all the constants unambiguously, therefore the value of D_K is assumed to be known (see Section IV) since, in the case of HDS, it involves the smallest centrifugal distortion correction. Equation (19) for $K=1$ then determines the value of $\frac{1}{2}(a-c)$, R_6 is calculable from the K-dependent term, and R_8 results from the final remainder. It is at this point that the experimental data do not agree with the theory. The theory indicates that the remaining terms in R_8 should show a four-to-one alternation with K odd or even respectively, since $D_K/(G-F)$ is practically negligible. Experimentally, the remainder is a constant for any value of $K\geq 2$ for HDS. Since this disagreement has not been resolved, the remainder, for purposes of fitting the experimental data, has been arbitrarily chosen to be $16(G-F)R_6/H^2$. Obviously, the constant terms become less and less important as J and K become large, i.e., for $J=12$, $K=6$, the three J and K dependent terms account for over 99 percent of the centrifugal distortion correction.

The results of the equation fitting are summarized in Tables II and III.

The data presented in Table IV is quite consistent with no apparent systematic errors. For this reason, it is felt that the fitting is quite good and that the constants given in Table III truly represent the centrifugal distortion parameters of HDS.

III. CALCULATION OF THE INERTIA DEFECT AND THE EFFECTIVE ROTATIONAL CONSTANTS

The study of the rotational absorption spectrum of HDS yielded accurate values of $(b-c)$ and $\frac{1}{2}(a-c)$, but to obtain the effective rotational constants a, b, and c another equation is required. If a $\Delta J=+1$ transition were observed and corrected for centrifugal distortion, the problem would be solved since $(a+c)$ would then be known. In the absence of this experimental data, one must resort to other means. Fortunately, another method is available because HDS is a planar molecule and hence the effective moments of inertia can be expressed in terms of the inertia defect Δ, as follows:

$$I_{aa}^{v}+I_{bb}^{v}-I_{cc}^{v}=\Delta. \tag{20}$$

With a knowledge of the molecular force constants and vibrational frequencies obtained from infrared data, Δ can be computed with a fair degree of accuracy. Since Δ is a small correction term amounting to only a few percent of the rotational constants, an error as large as ten to twenty percent may be permissible in the calculation of Δ and not affect the final results more than one percent. In addition, Darling and Dennison[9] and Nielsen[2] have pointed out that Δ is independent to second-order approximation of the anharmonic force constants, and therefore only the harmonic terms in the potential energy function need be considered.

The necessary normal coordinates and vibrational frequencies are determined from existing infrared and Raman spectra data. The physical parameters of HDS are taken to be identical with H_2S,[10] an assumption which should be quite valid.

On the basis of Slater-Pauling valence forces, the kinetic and potential energy functions can be expressed directly in terms of the directed valence coordinates δr_1, δr_3, and $\delta\gamma$ which refer respectively to small displacements from equilibrium positions in the sulfur-hydrogen bond length, the sulfur-deuterium bond length, and the angle γ between the bonds as pictured in Fig. 1. The energy equations are assumed purely quadratic functions in the absence of knowledge concerning anharmonic terms.

The three lagrangian equations of motion can be written immediately, and when solutions of the form $e^{i\omega t}$ are assumed, the following secular equation is formed,

$$\begin{vmatrix} a_{11}\lambda^2-k_{11} & a_{12}\lambda^2-k_{12} & a_{13}\lambda^2-k_{13} \\ a_{12}\lambda^2-k_{12} & a_{22}\lambda^2-k_{22} & a_{23}\lambda^2-k_{13} \\ a_{13}\lambda^2-k_{13} & a_{23}\lambda^2-k_{13} & a_{33}\lambda^2-k_{33} \end{vmatrix}=0, \tag{21}$$

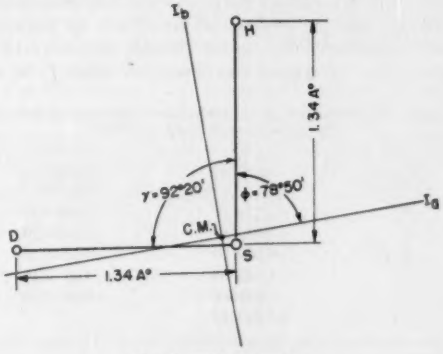

FIG. 1. HDS molecule.

[9] B. T. Darling and D. M. Dennison, Phys. Rev. 57, 128 (1940).
[10] P. C. Cross and G. W. King, private communication.

TABLE IV. Force constants and normal vibration frequencies of HDS[12].

Force constants	Normal frequencies
$k_{11}=4.25\times10^5$ dynes/cm	$\nu_1=1973$ cm^{-1}
$k_{22}=4.33\times10^5$ dynes/cm	$\nu_2=1122$ cm^{-1}
$k_{33}=0.238\times10^5$ dynes/cm	$\nu_3=2723$ cm^{-1}
$k_{13}=0.04\times10^5$ dynes/cm	
$k_{12}=0.05\times10^5$ dynes/cm	

where the λ's are the normal frequencies ($\lambda^2=4\pi^2c^2\nu^2$), the k's are force constants and the a's, reduced masses. The reduced masses are given explicitly by Cross and Van Vleck[11] for the general triatomic nonlinear molecule. The force constants were assumed to be known from the work of Bailey, Thompson, and Hale[12] on H_2S and D_2S, thus the normal frequencies are determined for HDS. This assumption is quite valid in view of the fact that a comparison of the force constants of H_2S and D_2S show differences of the order of magnitude of only one or two percent. The results seem quite reasonable considering the questionable infrared data on HDS. The force constants and zero-order frequencies are given in Table IV.

It is interesting to note that the off-diagonal terms of Eq. (21) are quite small, and thus the actual valence coordinates chosen are essentially the normal coordinates with minor corrections to be made because of the off-diagonal terms. The form of the normal vibrations compared with the original coordinates may be obtained directly from Eq. (21) and will be in the ratio of the first minors of any row in the determinant for each particular normal mode of oscillation. These ratios turn out to be

$$\begin{aligned} &\text{for } \nu_1, \quad q_1 : q_2 : q_3 = -1 \quad : \quad 49 : -2.1 \\ &\text{for } \nu_2, \quad q_1 : q_2 : q_3 = -1.24 : -1 : 150 \\ &\text{for } \nu_3, \quad q_1 : q_2 : q_3 = 109 \quad : \quad 1 : -2, \end{aligned} \tag{22}$$

where $q_1\equiv\pi r_1$, $q_2\equiv\Delta r_2$ and $q_3\equiv\sqrt{2}r\Delta\gamma$. It is immediately obvious that the off-diagonal terms may be neglected with very small effect on the ultimate calculation of Δ, and hence the original coordinates are taken to be the normal coordinates. This is quite reasonable from a physical point of view; there are two stretching vibrations and one bending vibration. Each stretching vibration involves only one of the lighter atoms because of the large mass of the sulfur atom and the complete lack of symmetry in the molecule.

Expressing the normal coordinates in Nielsen's notation, Δ for the ground vibrational state is computed to be

$$\Delta=-0.244\times10^{-40}\text{ g-cm}^2. \tag{23}$$

With Δ and the precise values of $(b-c)$ and $\frac{1}{2}(a-c)$, the effective rotational constants of HDS are determined to be

$$\begin{aligned} &a=9.682\text{ cm}^{-1}; \quad I_{aa}{}^v\equiv2.890\times10^{-40}\text{ g-cm}^2 \\ &b=4.844\text{ cm}^{-1}; \quad I_{bb}{}^v\equiv5.777\times10^{-40}\text{ g-cm}^2 \\ &c=3.140\text{ cm}^{-1}; \quad I_{cc}{}^v\equiv8.910\times10^{-40}\text{ g-cm}^2. \end{aligned} \tag{24}$$

These values can now be used in subsequent work, primarily to predict a $\Delta J=+1$ transition for the microwave spectroscopist and thus the complete experimental determination of the effective rotational constants; and to present considerable aid to the infrared spectroscopist in the analysis of his data. It would be elegant to complete this work by attempting to predict or calculate the equilibrium values of the moments of inertia, but the lack of knowledge of the anharmonic force constants, which give rise to the effects of the same order of magnitude as the effect of harmonic constants, make this task impossible with any degree of accuracy.

TABLE VI. Dipole moments.

$\mu(2_{2,1}\rightarrow2_{2,0})=1.020$ debyes
$\mu(4_{2,2}\rightarrow4_{2,1})=1.017$ debyes
$\mu(7_{4,4}\rightarrow7_{4,3})=1.015$ debyes
$\mu(9_{5,5}\rightarrow9_{5,4})=1.030$ debyes

IV. DISTORTION COEFFICIENTS

The experimental distortion coefficients for HDS are given in Table II. These same coefficients can be calculated utilizing exactly the same data that was needed for the computation of Δ. Hence, the validity of the centrifugal distortion theory, of the calculated effective rotational constants and of the structure of HDS can be quantitatively checked by computing these coefficients. The results of these calculations, compared with the experimental values of the distortion constants, are given in Table V.

While the results are not perfect, the excellent agreement between the calculated and measured values of the distortion constants exceeds expectations in view of the many simplifying assumptions made in the course of the previous work, and completes the cycle providing a check on the analysis presented in this paper.

TABLE V. Comparison of calculated and experimental values of the distortion coefficients of HDS[12].

Distortion coefficient	Calculated value (cm^{-1})	Experimental value (cm^{-1})
R_5	-2.21×10^{-4}	-2.808×10^{-4}
δ_J	$+2.69\times10^{-6}$	$+2.531\times10^{-6}$
D_{JK}	$+9.16\times10^{-4}$	$+9.133\times10^{-4}$
D_K	-1.64×10^{-4}	(-1.64×10^{-4})*
R_6	-1.90×10^{-6}	$+0.695\times10^{-6}$
D_J	$+8.28\times10^{-6}$	

* Assumed.

[11] P. C. Cross and J. H. Van Vleck, J. Chem. Phys. 1, 357 (1933).
[12] Bailey, Thompson, and Hale, J. Chem. Phys. 4, 625 (1936).

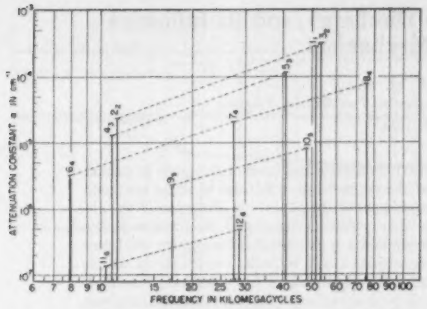

FIG. 2. HDS spectrum.

V. STARK EFFECT ON HDS

The Stark effect was measured for four HDS lines, the $2_{2,1}\rightarrow 2_{2,0}$; $4_{3,2}\rightarrow 4_{3,1}$; $7_{4,4}\rightarrow 7_{4,3}$ and the $9_{5,5}\rightarrow 9_{5,4}$. The dipole moment of each transition was computed, with the results shown in Table VI. In all cases the Stark splitting follows a BM^2 law, where B is a constant depending on the transition. The contributions from terms involving states other than the two participating in the absorption transition cancel to less than 1 percent of the major term value for all transitions except that for $J=2$ where the contribution amounts to 1.2 percent. The latter correction is due entirely to the state $J=2_{1,1}$ mixing with the $J=2_{2,0}$ state.

Within the accuracy with which the measurements were made, the electric dipole moment of HDS is quoted to be

$$\mu=1.02\pm 0.02 \text{ debyes.}$$

It was originally thought that a correlation would be detected between a uniform change in μ and increasing J, i.e., increase of centrifugal distortion of the molecule. Such a change would indicate, on the naive picture of a rotating molecule, whether the hydrogen and deuterium were approaching or receding from each other. Unfortunately, the results are not accurate enough to discern such a trend. From an angular momentum point of view, i.e., $\langle P_i^2\rangle=\partial E/\partial i$, it would seem that with increasing energy the dipole moment should increase.

VI. ABSORPTION COEFFICIENTS AND ISOTOPIC SULFUR TRANSITIONS

The absorption coefficients in cm^{-1} of HDS^{32} absorption transitions are illustrated graphically in Fig. 2 as a function of the frequency, in which form it serves several useful purposes. One, it presents all pertinent experimental data on HDS to the observer at a glance; two, experimentalists in the field may find the data useful as a standard; and three, qualitative predictions can be made regarding additional absorption transitions in HDS by observing the trends of the K families as indicated by the light dotted lines on the graph.

TABLE VII. Absorption frequencies of HDS^{34} and HDS^{33}.

Compound	Transition	Frequency (Mc/sec)
HDS^{34}	$1_{1,1}\rightarrow 1_{1,0}$	50,912.27
HDS^{34}	$2_{2,1}\rightarrow 2_{2,0}$	11,235.45
HDS^{34}	$3_{3,2}\rightarrow 3_{3,1}$	52,979.67
HDS^{34}	$4_{3,2}\rightarrow 4_{3,1}$	10,802.36
HDS^{34}	$7_{4,4}\rightarrow 7_{4,3}$	27,392.00
HDS^{33}	$2_{2,1}\rightarrow 2_{2,0}$	11,258.21

Several absorption lines were observed and measured for the isotopic compounds HDS^{34} and HDS^{33}, and these are tabulated in Table VII for future reference. The intensities of these lines are the same as shown in Fig. 2 but corrected for the natural abundance of the sulfur isotopes. The HDS^{33} line is the weakest line observed ($\alpha\approx 10^{-7}$ cm^{-1}) and was the largest of three lines dispersed over a region of approximately 10 Mc/sec. The poor sensitivity is not attributed to faulty equipment, but to a poor sample of HDS.

VII. CONCLUSION

Within certain restrictions a formula for centrifugal distortion in asymmetric molecules has been presented. The distortion is determined by five calculable constants. As a test of the formula it has been applied to the observed microwave spectrum of HDS. The agreement is sufficiently satisfactory to confirm the general functional dependence of the formula on rotational state. Disagreement does exist, however, between the computed and observed effect both in magnitude and dependence of the contribution resulting from the fourth off-diagonal element, (R_6). Fortunately the effect of this term is minor.

The formula given above compares with the approximate one derived in reference 3, except for a slight difference in the dependence on K. Further discussion of the comparison of the two formulas will be given in paper III of this series.

The Potential Field in and around a Gas Discharge, and Its Influence on the Discharge Mechanism

W. FINKELNBURG AND S. M. SEGAL
Engineer Research and Development Laboratories, Fort Belvoir, Virginia
(Received April 11, 1951)

In the first part of the paper, results on the spatial extension of cathode and anode fall regions in carbon arcs are reported. Potential-probe measurements reveal that the potential drop in front of either electrode is confined to less than one tenth of a millimeter. In the second part of the paper, the distortion of the potential field in and around any discharge, as caused by the non-uniform space charge distribution in the discharge, is discussed for the cases of a low current carbon arc and a negative point corona; for the latter case use was made of data by Loeb. The potential field distortions result in radial electric fields which, depending on their polarity, seem to hinder or support the radial expansion of the discharge. Potential-probe measurements in low and high current carbon arcs are in good agreement with this theoretical analysis and prove the transitional region between the distorted potential field in the arc and the undistorted potential field outside of the discharge to be a fairly thin one.

I. INTRODUCTION

THE potential distribution in and around any electric arc has a considerable influence on the axial as well as radial motion of electrons and ions, and thus on the arc mechanism. The same applies, to an even larger extent, to the potential drop regions immediately in front of the electrodes, i.e., the cathode and anode drops. Surprisingly little experimental evidence has been reported on the potential distribution in and around an arc, and scarcely anything is known about the spatial extension of the cathode and anode drops which determine the electric field strength in front of the electrodes.

In order to improve this situation, we have tried to explore the potential fields of carbon arcs by means of thin metal probes which were covered up to their tips by insulating glass (Fig. 1). These probes were whipped through or shot into the arc, while the potential they picked up in the plasma was recorded by a Hathaway oscillograph. Simultaneously, the position of the probe's tip with respect to some reference point (e.g., the anode surface), as well as the arc current and the arc voltage, were recorded by the same instrument.

One part of our results, published recently,[1] concerns the potential gradient in the high current arc stream and the plasma properties derived from it. In the present paper, results pertaining to two further problems, the spatial extension of the cathode and anode drop regions and the potential fields around the arcs, are presented. For the major part of this investigation, a pure carbon, low current arc was used, in order to permit a sufficiently slow probe motion without the danger of damaging probe tips or insulation. Supplementing experiments with high current carbon arcs, however, proved that all of our results described subsequently apply to the high current arc as well as to the low current arc.

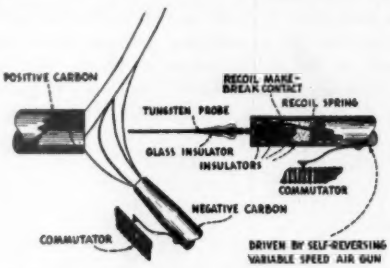

FIG. 1. Probe arrangement for measuring the spatial extension of the anode fall region.

II. THE THICKNESSES OF THE CATHODE AND ANODE DROP REGIONS

In order to measure the spatial extension of the anode and cathode drop regions, the probe, guided by a machined groove, was moved by hand or an air-gun mechanism until it contacted the anode, and was then retracted. A metal contact (Fig. 1), attached to the probe, moved with it over a commutator, and the recorded voltage pulses (trace No. 2 on Fig. 2), corresponding to an actual spacing of 0.45 mm, allowed the determination of the position of the probe and the correlation with the potential record. In a supplementary set of experiments, the negative carbon was used as a probe. It was moved by hand until it made contact with the positive carbon, and was then retracted, while the arc voltage was recorded, together with the arc current, as a function of the distance between the carbon tips. In these experiments, the position indicator (metal contact sliding over commutator of Fig. 1) was attached to the negative carbon.

In both arrangements, a sharp breakdown of the probe potential or arc voltage, respectively (trace No. 1 of Fig. 2), was observed when the probe or the negative carbon pierced a thin plasma sheath immediately in front of the anode, or anode and cathode, respectively, and a corresponding sharp potential rise when the probe broke its contact with the anode. From Fig. 2, where the vertical lines are 1/100-sec marks, it

[1] W. Finkelnburg and S. M. Segal, Phys. Rev. 80, 258 (1950).

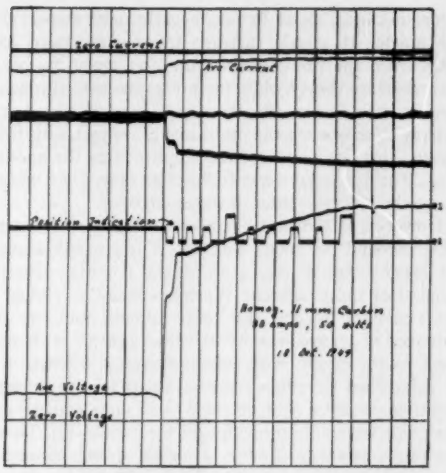

FIG. 2. Sample oscillograph record used for determining the spatial extension of the anode fall region.

is evident that, even with the slowest possible probe motion, the breakdown occurred within a time of the order of 1/1000 of a second, which, unfortunately, was the limit of resolution of our oscillograph elements. Our measurements, therefore, can give only an *upper limit* for the distance d, across which the breakdown occurred. A comparison with the position markers in Fig. 2 showed that the potential drop occurred over a distance which is small compared with that of one marker period (0.45 mm). Careful measurements on a number of records of probes of sufficiently slow motion showed that the thickness of either potential drop region was below 0.1 mm, and in at least one case, even below 0.05 mm. This result seems to be of interest; it means that the increase in temperature by nearly 3000°K from the electrode temperature of scarcely 4000°K to the arc stream temperature (approximately 6800°K for the low current arc stream in air) occurred over a distance of the order of only 10 mean free paths of the electrons.

We shall try to improve our method in order to obtain a better accuracy for this figure which is of decisive importance for any detailed theory of the cathode and anode drop.[2] Quantitative results concerning anode and cathode drop voltages will be given in a later paper for low and high current carbon arcs, after the problem of the contact potential between plasma and probe has been studied in more detail.

III. DISCUSSION OF THE POTENTIAL DISTORTION AROUND AN ARC STREAM

Little consideration seems to have been given in the literature to the distortion of the potential field around a discharge which inevitably is caused by the nonuniform space charge distribution along the axis of the discharge. Only Loeb[3] has pointed to the corresponding radial electric fields and has discussed their effects in relation to the phenomena of the negative point corona discharge.

A sketch of a conventional carbon arc, Fig. 3, may serve to explain the theoretically expected potential field around the arc. Suppose we have a potential difference of 70 volts between the electrodes of a low-current arc; assume, furthermore, a cathode drop of 10 volts and an anode drop of 30 volts. This last figure seems a little high, but we may use it for our example. Knowing, finally, from our probe measurements,[1] that the potential gradient within the arc stream decreases slowly from the cathode towards the anode, we can draw the equipotential lines in the arc stream as indicated in Fig. 3. The potential field distortion with the sharp drops in front of the electrodes is, of course, a consequence of the excess space charges in these regions and thus depends on the current density. In Fig. 3, the potential across the arc stream is assumed to be constant. This is probably not quite true, but is of secondary importance for the present discussion. Far outside of the arc, there is no reason for any distortion of the potential field. Here, therefore, we must have the normal constant distance between consecutive equipotential surfaces.

It follows that in the outer boundary region of the arc stream we must have a transition from the unperturbed potential field, outside of the arc, to that within the arc stream. For theoretical reasons, we believe this boundary region to be rather thin. The temperature decreases fairly rapidly with increasing distance from the apparent arc stream surface. The electric conductivity, moreover, depends exponentially on the temperature and thus decreases even faster with increasing distance from the arc surface. The arc

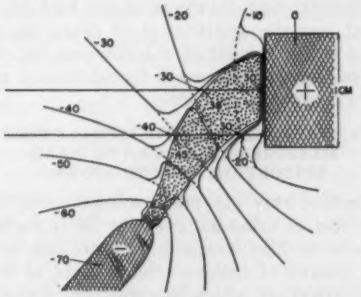

FIG. 3. Schematic sketch of the potential distribution in and around a carbon arc. The arrows indicate the directions of the probes piercing through the arc in anode drop measurements.

[2] W. Finkelnburg, *Hochstromkohlebogen* (Springer-Verlag 1948), p. 172 f. W. Finkelnburg, J. Appl. Phys. **20**, 468 (1949).

[3] L. B. Loeb, J. Appl. Phys. **19**, 882 (1948). The senior author is indebted to Dr. Loeb for directing his attention to this work, after the present paper had been presented at the Gaseous Electronics Conference in New York City on October 20, 1950.

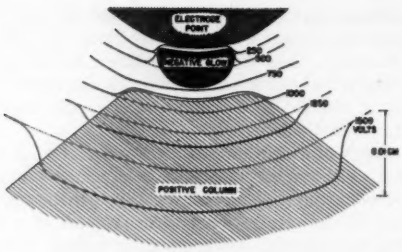

FIG. 4. Schematic sketch of the potential distribution in and around a negative point cornea discharge, based on data by L. B. Loeb.

stream, consequently, is a region of high electric conductivity with a fairly well defined outer boundary. It will be shown in a forthcoming theoretical paper that for such a conductor the surrounding potential field is approximately that indicated in Fig. 3.

Loeb, in his aforementioned paper,[3] had arrived at very similar conclusions, without using the concept of equipotential surfaces, for the entirely different corona discharge. By quantitative considerations about the potential distortions along the discharge axis, to be expected as a consequence of the space charges produced by ionization, and by comparing them with the undisturbed potential, Loeb drew conclusions to the necessary existence of radial electric fields. He further explained the radial contraction of his discharge near the negative point, and its radial expansion farther away from it, as a consequence of these fields. We have used Loeb's data (Figs. 4 and 7 of his paper) to draw a picture (Fig. 4) of the potential distortion in the essential region of a negative point corona. The similarity of Figs. 3 and 4 is striking in spite of the fact that we are dealing with entirely different discharges and different orders of magnitude in linear dimensions and potential gradients.

As potential field distortions of this kind are to be expected near the electrodes of *all* discharges, direct evidence for the correctness of a distortion like that of Fig. 3 and for the thickness of the transitional regions seems of considerable interest.

IV. EVIDENCE FROM POTENTIAL-PROBE MEASUREMENTS FOR THE FIELD DISTORTION AROUND AN ARC

We believe that our probe measurements furnish fairly direct experimental evidence for potential distortions of the kind discussed. To prove this, we compare a number of representative records, of the low current carbon arc, which appeared very surprising at first, with what we expect theoretically from Fig. 3.

Consider first the probe being shot into the arc along the path indicated by the upper arrow. The probe, of course, cannot pick up any potential before it reaches the conducting plasma of the boundary region around the arc stream. The potential here will be, in our assumed example, about 30 volts negative with respect to the anode. It should increase to approximately 38 volts when the probe reaches the arc stream proper, then decrease slowly while the probe proceeds through the arc stream towards the anode, and finally drop sharply to zero when the probe makes contact with the anode—this last potential drop representing the anode drop. This is exactly what is observed (Fig. 5(a)) when the probe hits the center of the anode spot.

However, if the probe happens to reach the outer region around the anode spot, i.e., if it proceeds along the lower arrow in Fig. 3, the probe potential record should look quite different. When reaching the conducting boundary region, the probe should pick up a potential of approximately 40 volts negative with respect to the anode. This potential should increase to 45 volts when the probe reaches the arc stream proper and then exhibit a slow decrease to 35 volts reached at the point where the probe leaves the arc stream. Then the probe proceeds through a region, in our assumed example, where the potential drops suddenly by about 15 volts. In the last few millimeters, before reaching the anode, there should be a second slow decrease and then a final sharp drop of the potential of the order of 10 volts. In this region the conductivity should stem from the high temperature in the neighborhood of the hot anode surface. We may regard the last 10-volt drop as the anode drop corresponding to the small current density in this outer region of the arc; this requires, according to our ideas of the anode drop,[2] a much smaller production of positive ions and thus a smaller anode drop than the arc proper.

This expected probe potential record again agrees well, in all details, with the observed records, such as Fig. 5(c). If the probe hits the anode somewhat closer to the actual anode spot, the spatial distance, in millimeters, between the two sharp potential drops, decreases, as may be seen, for instance, in Fig. 5(b). If, on the other hand, the probe hits somewhat lower, in a regions where the closest equipotential surface begins to move away from the anode surface, this last drop, on our records, becomes much less sharp. To summarize: Depending on the direction of the probe's path with respect to the anode spot, we expect and find a variety of probe potential records which all agree excellently with the theoretical picture presented here. From the steepness of the first potential drop in Figs. 5(b) and 5(c), which was attributed to the potential drop in the boundary region around the arc stream, we conclude that this boundary region is very thin indeed.

There is further evidence for the correctness of our interpretation. By shooting probes through the arc stream, in a direction perpendicular to its axis, and near either the cathode or anode, we find in low current arcs as well as in high current carbon arcs radial changes of the probe potential which agree well with our theoretical picture. Furthermore, simultaneous records of the arc voltage and arc current allow us to determine

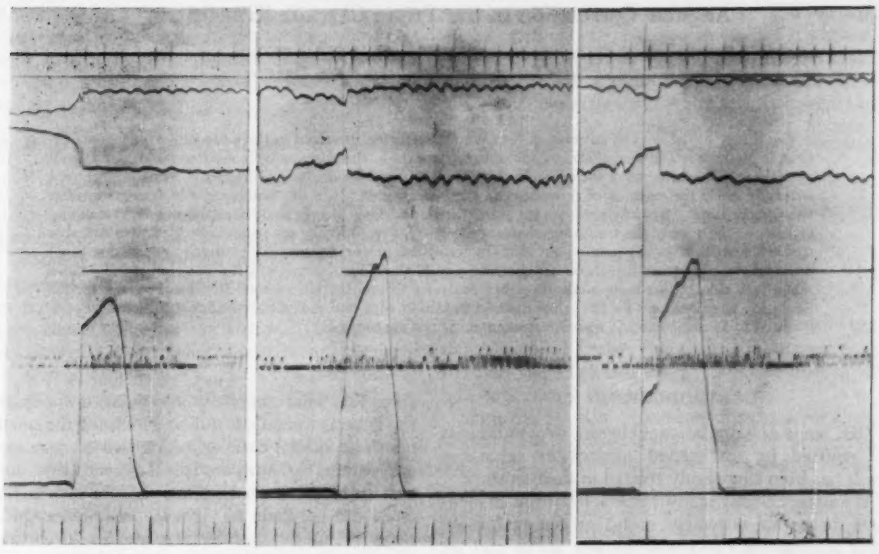

FIG. 5. Oscillograph records of potential probes piercing a carbon arc. (a) Record of probe shot into the arc along the path indicated by the upper arrow in Fig. 3. (b) Record of probe shot into the arc along a path intermediate between the two arrows indicated in Fig. 3. (c) Record of probe shot into the arc along the path indicated by the lower arrow in Fig. 3.

the perturbation of the arc by the probe, and to correlate the probe's position with the occurrence of the perturbation. If the probe follows the upper arrow in Fig. 3, Fig. 5(a) clearly shows a sharp perturbation of the arc at the moment when the probe hits the anode surface, this point being indicated by the step in the third curve from the top in Fig. 5. This perturbation seems to be caused by the fact that the probe here disturbs the anode drop region which is so essential for the production of the positive discharge ions. If, on the other hand, the probe follows the lower arrow in Fig. 3, there is no disturbance of the arc when the probe hits the anode surface, because this outer region of the anode is not essential for the discharge mechanism. Surprisingly, however, in the latter case a strong disturbance of the arc is observed when the probe pierces the sharp potential boundary layer (of Figs. 5(b) and 5(c)), thus apparently upsetting the well-balanced potential and temperature fields in this important region close to the anode.

V. SUMMARY

It is generally known that in all high pressure arc discharges sharp potential drops occur close to the electrodes, called the cathode and anode drops. Our potential probe measurements indicate that these are confined to plasma sheaths of less than 0.1 mm extension, i.e., to distances from the electrode surfaces of the order of only 10 mean free paths of the electrons. We believe to have shown, furthermore, that fairly sharp potential drops exist also in the outer boundary region around an arc stream, at least near the electrodes. These distortions of the potential field should be the more pronounced, the larger the cathode and anode drop voltages are compared with the undistorted potential gradients, and the larger the conductivity of the discharge plasma is. As a result of this potential distortion, the discharge regions close to the electrodes are surrounded by a fairly thin plasma sheath in which a large radial electric field strength exists. Near the cathode, this radial field drives the electrons back toward the axis of the arc stream, and thus changes the normal mechanism of the ambipolar diffusion of the charge carriers, thereby obviously restricting the discharge to a smaller diameter. Near the anode, conversely, the radial electric field attracts the mobile electrons, influences the ambipolar diffusion in the reverse direction and favors a radial expansion of the discharge. These radial fields, to our knowledge, have not been taken into account in all hitherto published theories of arc streams, but we believe they should not be neglected.

Angular Correlation in the Triple Cascade Transitions*

L. C. Biedenharn, G. B. Arfken, and M. E. Rose
Oak Ridge National Laboratory, Oak Ridge, Tennessee

(Received April 23, 1951)

The theory of the angular correlation between the radiations involved in three successive nuclear transitions is presented. The formalism is applicable to the case of three successively emitted radiations as well as to the case in which one of the emission processes is replaced by an absorption process. Thus, applications are made to (1) the emission of three cascade gamma-rays and (2) to the double-cascade gamma-emission following capture of particles with nonzero orbital angular momentum. In some cases the angular correlation depends on the order of the transitions. Under process (2), special results are presented which are applicable to $B^{11}(\rho,\gamma,\gamma)C^{12}$. It is also pointed out that the formalism properly describes the angular correlation in all processes wherein three directions are specified and is therefore applicable when one of these directions refers to a polarization state while the other two refer to propagation vectors. Results are given for the limitation on anisotropy for the triple cascade transition with two radiations parallel or antiparallel and for two radiations in cascade with intervening radiations unobserved.

I. INTRODUCTION

THE angular correlation between two radiations emitted by an excited nucleus in successive cascade has been thoroughly treated in the literature[1–3] and the experimental study thereof has been demonstrated to be an extremely useful procedure for obtaining information concerning nuclear states and for the interpretation of decay schemes.[4] The essential restriction of the theory referred to is the assumption that the sublevels of the initial state are uniformly populated and this may, in fact, be taken as a defining characteristic of the double cascade process.

It is of considerable interest to extend the angular correlation theory to the case in which the above mentioned restriction is removed. This extension is necessary, for example, whenever the initial state is formed by capture of particles with non-vanishing orbital angular momentum (i.e., a propagation vector is defined) and indeed, this capture process followed by the emission of two cascade radiations is a special case of the triple cascade process.[5] In addition, there is considerable interest in the direct triple cascade process in which three radiations are emitted successively. In the following we shall restrict our consideration to two problems: (a) The angular correlation for three gamma-rays emitted in cascade. These results (Sec. II) are readily applied in the case that any one or more of the radiations are spinless particles (α-particles). (b) The angular correlation for the emission of two cascade gamma-rays (or spinless particles) following capture of a particle with spin and orbital angular momentum (Sec. III).[6] For simplicity the detailed applications of the general formalism will be given, for the most part, for those special cases in which two of the radiations are parallel or antiparallel. However, this does not constitute an essential limitation, since such an arrangement can be made to yield the required angular momentum information for the nuclear levels involved just as well as would be the case for the more general and more complicated arrangement. In any case the formalism is presented in such a way as to make clear the procedure to be followed in treating the case of arbitrary directions for the three radiations, and two such applications are given below. In addition the angular correlation between radiations involved in the first and third transitions, with the intervening radiation unobserved, is treated. From the formalism presented, the extension to the angular correlation with any number of unobserved intervening radiations is straightforward.

It should be emphasized that the essential characteristic of the nuclear transitions considered here is the specification of three directions. Thus, so far as the application of the formalism is concerned, we can equally well consider the case that a single radiation is emitted from an initial state which has been formed by capture of polarized particles with a direction of propagation also specified. It is equally true that in this case the substates of the resulting level are not equally populated. Of course, for particle capture this implies the production of a beam of fast polarized particles which is not feasible by present techniques. However, the polarization direction, as one of the three specified directions, need not refer to the initial radiation but may just as well refer to a succeeding radiation observed

* This paper is based on work performed for the AEC at the Oak Ridge National Laboratory.

[1] D. R. Hamilton, Phys. Rev. **58**, 122 (1940).

[2] G. Goertzel, Phys. Rev. **70**, 897 (1946).

[3] D. L. Falkoff and G. E. Uhlenbeck, Phys. Rev. **79**, 323 (1950).

[4] E. L. Brady and M. Deutsch, Phys. Rev. **78**, 558 (1950); J. R. Beyster and M. L. Wiedenbeck, Phys. Rev. **79**, 411 (1950); W. R. Arnold, Phys. Rev. **80**, 34 (1950) and many others.

[5] It follows immediately from the hermitean property of the interaction operator responsible for the capture transition that the distinction between emission and absorption is irrelevant.

[6] An example, to which detailed consideration is given below, is the $B^{11}(\rho,\gamma_1,\gamma_2)C^{12}$ reaction studied by W. M. Good and collaborators in the High Voltage Laboratory, Oak Ridge National Laboratory. The observed anisotropy of γ_1 (12 Mev) relative to the incident proton beam indicates the participation of ρ (or higher) waves for the incident protons. The authors take this opportunity to thank the members of the High Voltage Group for permission to quote their results before publication.

with a polarization sensitive detector. A case in point would be a reaction resulting in the production of fast polarized particles (by spin-orbit coupling, say) or the emission of a second radiation in cascade with the polarized particle.

II. SUCCESSIVE EMISSION OF THREE GAMMA-RAYS

(A) General Formalism

It is instructive to consider first the problem of triple gamma-correlation because this problem contains all the pertinent features of the general problem with few extraneous complications, and is, moreover, not without experimental interest. Consider, therefore, the successive transitions of a nucleus with initial total angular momentum j_0 going through intermediate states of angular momentum j_1 and j_2 to a final state j_3 emitting gamma-rays of multipolarity 2^{L_0}, 2^{L_1}, and 2^{L_2}, respectively. Let us consider a *maximal* experiment,[7] that is, an experiment in which all measurable magnetic quantum numbers are fixed. Then the desired triple transition is from a state j_0, m_0 by successive emission of the three specified gammas with magnetic quantum numbers p_0, p_1, and p_2, respectively, to a final state j_3, m_3. Here p_i is the magnetic quantum number of the gamma-ray measured with respect to its propagation vector $\mathbf{k}_i$. This restricts p_i to the values ± 1 corresponding to left and right circular polarization. The relative probability for this transition is:

$$P(\mathbf{k}_0, \mathbf{k}_1, \mathbf{k}_2) = \Big| \sum_{m_1 m_2} \langle a_0 j_0 m_0 | H(\mathbf{k}_0 p_0) | a_1 j_1 m_1 \rangle \times \langle a_1 j_1 m_1 | H(\mathbf{k}_1 p_1) | a_2 j_2 m_2 \rangle \times \langle a_2 j_2 m_2 | H(\mathbf{k}_2 p_2) | a_3 j_3 m_3 \rangle \Big|^2. \quad (1)$$

It is understood that $P(\mathbf{k}_0, \mathbf{k}_1, \mathbf{k}_2)$ also depends on the polarization parameters p_i and on m_0 and m_3. In Eq. (1) a_i are all the quantum numbers, besides the angular momentum j_i and its projection m_i, which are necessary to characterize the ith level. The interaction operator $H(\mathbf{k}_0 p_0)$ corresponds to the emission of a gamma-ray in the direction $\mathbf{k}_0$ with polarization p_0. Following Goertzel,[2] we may write the matrix elements in the form:

$$\langle a_i j_i m_i | H(\mathbf{k}_i p_i) | a_{i+1} j_{i+1} m_{i+1} \rangle = \sum_{L_i M_i} A_i (j_i L_i m_i M_i | j_{i+1} m_i + M_i) D_{M_i p_i}^{(L_i)}(\alpha_i \beta_i \gamma_i). \quad (2)$$

Here A_i is the part of the nuclear matrix element which is independent of magnetic quantum numbers; it is a function of all other quantum numbers including the multipolarity and parity of the radiation. The $(j_i L_i m_i M_i | j_{i+1} m_i + M_i)$ are the Clebsch-Gordan or vector-addition coefficients corresponding to the addition of angular momenta j_i and L_i to form j_{i+1} with magnetic quantum numbers m_i, M_i and $m_i + M_i$, respectively.[8] The $D_{Mp}^{(L)}(\alpha\beta\gamma)$ are the Mth pth elements of the rotation matrix of dimension $2L+1$, while α, β, γ are the Euler angles of the direction $\mathbf{k}_i$ with respect to the axis of quantization that is used to define the m_i. We restrict our attention to pure multipoles and thereby discard all but the L_ith term in Eq. (2). Substituting Eq. (2) in Eq. (1) yields the result that:

$$P(\mathbf{k}_0\mathbf{k}_1\mathbf{k}_2) = \Big| \sum_{m_1 m_2} (j_0 L_0 m_0 m_1 - m_0 | j_1 m_1) D_{m_1 - m_0 p_0}^{(L_0)}(\alpha_0 \beta_0 0) (j_1 L_1 m_1 m_2 - m_1 | j_2 m_2) D_{m_2 - m_1 p_1}^{(L_1)}(\alpha_1 \beta_1 0) \times (j_2 L_2 m_2 m_3 - m_2 | j_3 m_3) D_{m_3 - m_2 p_2}^{(L_2)}(\alpha_2 \beta_2 0) \Big|^2. \quad (3)$$

We have discarded, in Eq. (3), the "reduced" matrix elements A_i as factors irrelevent for our purposes. In addition the Euler angles, γ_i, have been set equal to zero as is clearly legitimate.

Since the *physical* experiment we consider[9] does not measure the quantum numbers m_0, m_3, p_0, p_1, p_2, we shall sum over these to obtain the desired (relative) probability $W(\mathbf{k}_0\mathbf{k}_1\mathbf{k}_2)$. Upon summing over m_0, m_3 which defined our original axis of quantization, this reference axis becomes arbitrary. It is convenient to take one of the three directions, say $\mathbf{k}_0$, as the z axis of the new reference system since

$$D_{\mu\nu}^{(L)}(000) = \delta_{\mu\nu} \quad (4)$$

and this eliminates the summation over m_1 in Eq. (3). This gives the result

$$W(\mathbf{k}_0, \mathbf{k}_1, \mathbf{k}_2) \equiv w(\vartheta_1 \vartheta_2 \varphi) = \sum_{m_1 m_2 p_0 p_1 p_2} (j_0 L_0 m_1 - p_0 p_0 | j_1 m_1)^2 \times \Big| \sum_{m_2} (j_1 L_1 m_1 m_2 - m_1 | j_2 m_2) D_{m_2 - m_1 p_1}^{(L_1)}(0 \vartheta_1 0) \times (j_2 L_2 m_2 m_3 - m_2 | j_3 m_3) D_{m_3 - m_2 p_2}^{(L_2)}(\varphi \vartheta_2 0) \Big|^2. \quad (5)$$

Here the angle ϑ_1 is the polar angle of $\mathbf{k}_1$ with respect to $\mathbf{k}_0$ and analogously for ϑ_2; $\varphi (= \alpha_1 - \alpha_2)$ is the dihedral angle between the $(\mathbf{k}_0, \mathbf{k}_1)$ and $(\mathbf{k}_0, \mathbf{k}_2)$ planes.

This result shows a number of significant features: (a) The first factor is effectively the population of the m_1 sublevel of state j_1. It will therefore be possible to remove the restriction that the first radiation is a gamma-ray by substituting the appropriate population function for the desired radiation. This will be discussed in Sec. III. (b) The sum over m_2 in Eq. (5) is coherent, a feature of all correlation problems involving more than two directions. This coherency makes the actual reduction of Eq. (5) to an algebraic form in the three angles, ϑ_1, ϑ_2 and φ a very laborious task. However, its application in special cases is quite straightforward. As an illustration, Eq. (6) gives the general solution for

[7] B. A. Lippmann, Phys. Rev. **81**, 162 (1951).

[8] The notation $(j_i L_i m_i M_i | j_i L_i j_{i+1} m_i + M_i)$ is used in E. U. Condon and G. H. Shortley, *Theory of Atomic Spectra* (Cambridge University Press, London, 1935), Chapter III.

[9] If linearly polarized gammas are to be detected the changes in the formalism are minor. See, for example, I. Zinnes, Phys. Rev. **80**, 386 (1950), and Biedenharn, Rose, and Arfken, ORNL Report No. 986 (unpublished).

the case $\{1Q2D1D0\}$ where the numbers stand for the values of j_0, j_1, j_2, j_3, respectively, reading from left to right, and the letters give the multipolarity of the radiations (D dipole, Q quadrupole) reading from left to right in the order of emission.

$$w(\vartheta_1\vartheta_2\varphi)=2(13-5\cos^2\vartheta_1-5\cos^2\vartheta_2+9\cos^2\vartheta_1\cos^2\vartheta_2)$$
$$-3\sin 2\vartheta_1\sin 2\vartheta_2\cos\varphi+2\sin^2\vartheta_1\sin^2\vartheta_2\cos 2\varphi. \quad (6)$$

It should be mentioned that the results obtained above apply equally well to any one or more of the radiations being a spinless particle, restricting attention to a single value of the relative angular momentum L_i for the transition. The value of p_i for this case is then zero instead of ± 1 as for the gamma-transition.

(B) Special Cases

Because of the complexity of Eqs. (5) and (6) and the tedious nature of the calculations it is of interest to note that the cross terms of the coherent sum can be made to vanish whenever any two of the gammas are parallel or antiparallel.[10] Consider γ_0 and γ_1 parallel.[11] Then the elements of the rotation matrix referring to γ_1 become Kronecker delta symbols as in Eq. (4). This eliminates the cross terms and gives for the distribution function

$$w(0\vartheta_2)=\sum_{m_1M_2p_0p_1}(j_0L_0m_1-p_0p_0|j_1m_1)^2(j_1L_1m_1p_1|j_2m_1+p_1)^2$$
$$\times(j_2L_2m_1+p_1M_2|j_3m_1+p_1+M_2)^2F_{L_2}{}^{M_2}(\vartheta_2), \quad (7)$$

where

$$F_L{}^M(\theta)=\sum_{p=\pm 1}|D_{Mp}{}^{(L)}(0\theta 0)|^2 \quad (8)$$

is the classical angular distribution of the 2^L multipole radiation in the notation of Falkoff and Uhlenbeck.[3] As expected the azimuthal dependence of the angular correlation has disappeared.

If the first and third radiations are parallel, a similar reduction yields

$$w(\vartheta_1 0)=\sum_{m_1M_1p_0p_1}(j_0L_0m_1-p_0p_0|j_1m_1)^2$$
$$\times(j_1L_1m_1M_1|j_2m_1+M_1)^2$$
$$\times(j_2L_2m_1+M_1p_2|j_3m_1+M_1+p_2)^2F_{L_1}{}^{M_1}(\vartheta_1). \quad (9)$$

The case of the second and third radiations parallel or antiparallel may be obtained from Eq. (7) by interchange of subscripts.

Because of the large number of parameters it is not practical to tabulate the results for the above cases in as much detail as has been done for the double correlation. Instead it is suggested that the functions be calculated as needed using the published $F_L{}^M$[12] and Clebsch-Gordan[8] coefficients. As an illustration of the simplicity and directness of the calculation consider the case $\{1Q2D1D0\}$ treated above and let γ_0 and γ_1 be parallel, their common direction defining the polar axis. The third γ will be observed at an angle ϑ_2.

Referring to Eq. (5) the populations of the j_1 magnetic substates m_1 are given by $\sum_{p_0}(j_0L_0m_1-p_0p_0|j_1m_1)^2$ with $p_0=\pm 1$. From a table of Clebsch-Gordan coefficients it is seen that the relative populations a_i of the substates of j_1 are 2, 1, 6, 1, and 2 for $i=2,\cdots,-2$, respectively. (This is equivalent to determining the intensities of the unpolarized Zeeman components.) The populations of the m_2 sublevels are calculated in the same manner except that the transition intensities given by $(j_1L_1m_1p_1|j_2m_2)^2$ are to be weighted by the populations of the m_1 substates. Since $p_1=\pm 1$, two terms at most can contribute to the population of any m_2 sublevel. Renormalizing to avoid fractions the population of the substates are given in terms of

$$b_1=6a_2+a_0=b_{-1}=18, \quad b_0=3(a_1+a_{-1})=6 \quad (10)$$

where a_i and b_j are proportional to the populations of the substates $m_1=i$ and $m_2=j$, respectively. For the final transition $\{1D0\}$ the vector addition coefficients are all equal and

$$w(0\vartheta_2)\sim 3F_1{}^1(\vartheta_2)+F_1{}^0(\vartheta_2)+3F_1{}^{-1}(\vartheta_2). \quad (11)$$

Since

$$F_1{}^1(\vartheta)=F_1{}^{-1}(\vartheta)=\tfrac{1}{2}(1+\cos^2\vartheta) \quad (12a)$$

$$F_1{}^0(\vartheta)=1-\cos^2\vartheta \quad (12b)$$

then

$$w(0\vartheta_2)=1+\tfrac{1}{2}\cos^2\vartheta_2. \quad (13)$$

This result may be verified by setting $\vartheta_1=0$ in Eq. (6). However, it is believed that the calculation by substate populations is the more direct and by far the easier method of obtaining the angular correlation functions for these special cases.

III. PARTICLE CAPTURE FOLLOWED BY TWO GAMMA-RAYS

(A) Formation of First Intermediate State

We consider the capture of a particle with spin and orbital angular momentum forming a compound state which decays by emitting two gamma-rays in cascade. It has already been pointed out that this is actually a special case of Eq. (3). The significant new feature of this process is the possibility of forming the state j_1 in more than one way, corresponding to the "channel spin degeneracy." The incident particle with spin i and relative orbital angular momentum L_0 is unpolarized as is the target nucleus with angular momentum j_0. The channel spin s is the vector sum of i and j_0, and j_1 is the vector sum of L_0 and s. The population of the

[10] This is in agreement with the analysis of S. P. Lloyd, Phys. Rev. **80**, 118 (1950) and J. A. Spiers, Phys. Rev. **80**, 491 (1950) for double correlation.

[11] For unpolarized radiation, the parallel and corresponding antiparallel angular correlation functions are identical. This is a consequence of the relation $D_{Mp}{}^{(L)}(000)=(-1)^LD_{M-p}{}^{(L)}(\pi\pi 0)$.

[12] See reference 1. The $F_L{}^M$ through $L=5$ are tabulated by W. R. Arnold, Phys. Rev. **80**, 34 (1950).

m_1 substate becomes

$$\sum_{m_0}|\sum_s A(s)(j_0 m_0 m_1-m_0|sm_1)(sL_0m_10|j_1m_1)|^2$$
$$=\sum_s|A(s)|^2(sL_0m_10|j_1m_1)^2, \quad (14)$$

where $A(s)$ is the part of the matrix element for the capture process exclusive of the Clebsch-Gordan coefficient representing the magnetic quantum number dependence. The cross terms in Eq. (14) have vanished upon summation over m_0 since

$$\sum_{m_0}(j_0 m_0 m_1-m_0|sm_1)(j_0 m_0 m_1-m_0|s'm_1)=\delta_{ss'}. \quad (15)$$

This is in agreement with the results of Devons and Hine.[13] The desired angular correlation function may be written by substituting this population function into Eq. (5).

$$w(\vartheta_1\vartheta_2\varphi)=\sum_{m_1m_2p_1p_2}|A(s)|^2(sL_0m_10|j_1m_1)^2$$
$$\times|\sum_{m_2}(j_1L_1m_1m_2-m_1|j_2m_2)D_{m_2-m_1p_1}^{(L_1)}(0\vartheta_10)$$
$$\times(j_2L_2m_2m_3-m_2|j_3m_3)D_{m_3-m_2p_2}^{(L_2)}(\varphi\vartheta_20)|^2. \quad (16)$$

(B) Example $B^{11}(\hat{p},\gamma,\gamma)C^{12}$ Reaction[6]

As already mentioned, the anisotropy of the first gamma-ray relative to the proton beam ($\sim 1+0.15\cos^2\vartheta$) demonstrates that $L_0=0$ is not alone effective. Since the proton energy, 163 kev, is appreciably smaller than the barrier height it follows that only $L_0=1$ or 2 (depending on the relative parities of the initial and compound states) can make an appreciable contribution. However, it does not appear likely that the observed anisotropy can be accounted for by a mixture of s and d waves and the choice $L_0=1$ is the most probable one for this reaction. With the two possible channel spins, $s=1$ or 2, one has the possibilities $j_1=0$, 1, 2 or 3. The anisotropy eliminates the possibility $j_1=0$ and the break-up of this state into $Be^{8*}+He^4\rightarrow 3He^4$ and $Be^8+He^4\rightarrow 3He^4$ makes the choice $j_1=2$ most plausible. This conclusion follows strictly if the α-particle decay competes with the γ-emission.[14] Of the remaining C^{12} states the angular momentum j_2 of the intermediate state only is in doubt and would presumably be fixed by comparison of experimental results with calculations like the following. Therefore, as an illustration we consider $j_2=2$ and the transition scheme is $\{2D2Q0\}$. The result for the angular correlation function $w(\vartheta_1\vartheta_2\varphi)$ is found, after a somewhat lengthy calculation, to be

$$w(\vartheta_1\vartheta_2\varphi)=47-26x-12(2-3x)\cos^2\vartheta_2$$
$$-3(1-2x)\cos^22\vartheta_2+3\{18x-11+12(1-x)\cos^2\vartheta_2$$
$$+3(1-2x)\cos^22\vartheta_2\}\cos^2\vartheta_1+3\{(3-2x)\sin2\vartheta_2$$
$$+(1-2x)\sin4\vartheta_2\}\sin2\vartheta_1\cos\varphi+3\{1+2x-4x\cos^2\vartheta_2$$
$$-(1-2x)\cos^22\vartheta_2\}\sin^2\vartheta_1\cos2\varphi. \quad (17)$$

The unknown parameter x denotes the fractional contribution of channel spin $s=1$,

$$x=|A(1)|^2/[|A(1)|^2+|A(2)|^2]. \quad (18)$$

As in the case of the triple gamma-cascade, it is highly desirable to restrict attention to the special cases discussed in Sec. II. One might, for example, measure the coincidence rate for γ_1 and γ_2 as a function of angle between them, with γ_1 being detected along the direction of the proton beam. This can also be done with γ_2 being detected along the direction of the beam. In addition the angular distributions of either γ-ray with the beam, the other γ-ray unobserved, may be measured. The corresponding distribution functions are denoted by $w_i(\vartheta_i)$. From such data it will, in many cases, be possible to determine the angular momenta of

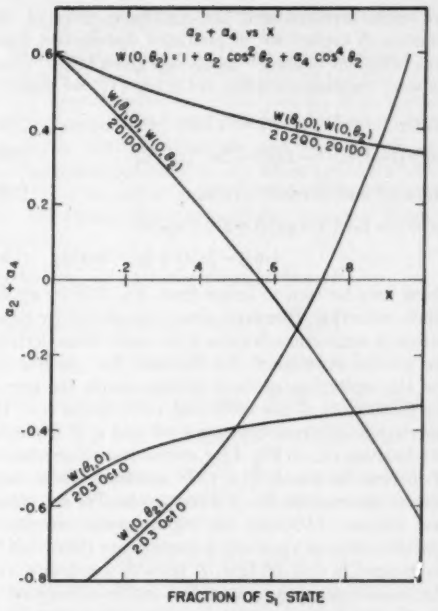

FIG. 1. The degree of anisotropy, $w(\vartheta_i=0)-w(\vartheta_i=\pi/2)$ for the emission of two gamma-rays following $\hat{p}$-particle capture by a nucleus of spin $\frac{1}{2}$ as a function of x, the fraction of channel spin $s=1$. The transition schemes considered are designated by the symbols beneath the respective curves. The topmost curve refers to four cases corresponding to either transition scheme with either first or second gamma parallel to the beam.

[13] S. Devons and M. G. N. Hine, Proc. Roy. Soc. (London) A 199, 73 (1949).

[14] Compare G. B. Arfken and L. C. Biedenharn, Phys. Rev. 83, 238(A) (1951). The existence of an *isotropic* 16-Mev γ-ray indicates the presence of two levels excited in the reaction. Despite the energy coincidence (γ_1=12 Mev, γ_2=4 Mev) the 16-Mev radiation is apparently not a cross-over. See also W. M. Good *et al.*, Phys. Rev. 83, 211(A), 241(A) (1951).

the levels involved and the multipole order of the gammas. A typical set of predicted distribution functions pertinent to the B^{11} reaction is given below. Using the same transition scheme as for Eq. (17) we obtain

$$w_1(\vartheta_1)=1-21(1-2x)(47-14x)^{-1}\cos^2\vartheta_1 \tag{19a}$$

$$w_2(\vartheta_2)=1-3(1-2x)(9-2x)^{-1}\cos^2\vartheta_2 \tag{19b}$$

$$w(\vartheta_1 0)=1+3(5+4x)^{-1}\cos^2\vartheta_1 \tag{19c}$$

$$w(0\vartheta_2)=1-3(1-4x)(5+4x)^{-1}\cos^2\vartheta_1 +6(1-2x)(5+4x)^{-1}\cos^4\vartheta_2. \tag{19d}$$

These may be seen to follow from Eq. (17) by appropriate reduction. However, direct calculation by populations of magnetic substates is far easier than deriving the general expression. To illustrate the possible use and the limitations of these measurements, the sum of the coefficients of the $\cos^2\vartheta$ and $\cos^4\vartheta$ terms (i.e., the correlation difference between $\vartheta=0$ and $\pi/2$) is plotted as a function of x in Fig. 1 for several transition schemes of interest in the $B^{11}(p,\gamma,\gamma)C^{12}$ reaction. These cases assume the capture of a p-wave proton. For the transition scheme $\{2D3Oc0\}$ the triple angular correlation functions depend upon which gamma-ray (identified by its energy) is emitted first. A possible ambiguity with the transition scheme $\{2Oc1D0\}$ can be eliminated on physical grounds so that in this case it would be possible to make a unique identification of multipolarity, or order of emission, for the two gamma-rays. For the two cases $\{2D2Q0\}$ and $\{2Q1D0\}$ the presence of $\cos^4\vartheta$ terms, which occur when the quadrupole radiation is observed at the variable angle, will be sufficient to remove the ambiguity if the order of the gammas is known or if j_2 is known from independent evidence. The transition $\{2D1D0\}$ will be distinguished from the other cases by the absence of $\cos^4\vartheta$ terms. In this case it is not possible to determine the order of the gammas by angular measurements. It is clear in this reaction that the triple correlation experiment can provide more information than the simple correlation of the first gamma with the proton beam which allows all four of the transition schemes mentioned above.

The presence of $\cos^4\vartheta$ in the angular distribution function of a cascade initiated by a p-wave proton may appear surprising. However, this result is not in contradiction with the theorem of Eisner and Sachs[15] and Yang[16] which applies to the angular distribution of a single (observed) outgoing radiation. The limits of anisotropy for triple correlations are discussed in detail in Sec. IV. The theorem does apply to $w_1(\vartheta_1)$ and $w_2(\vartheta_2)$ and it is seen that no contradiction arises. In the present case when $x=\frac{1}{2}$ the contributions of the two channel spins combine to form the state $j_1=2$ with randomly populated magnetic substates. This means that the triple correlation reduces to the familiar double correlation. It is seen that $w_1(\vartheta_1)$ and $w_2(\vartheta_2)$ do indeed vanish while

$$w(\vartheta_1 0)_{x=\frac{1}{2}}=w(0\vartheta_2)_{x=\frac{1}{2}}=1+(3/7)\cos^2\vartheta, \tag{20}$$

which is just the value given by Hamilton.[1]

IV. LIMITATIONS ON ANISOTROPY

(A) Correlation of Two Radiations

The angular correlation between two radiations can always be expressed as a power series in $\cos^2\vartheta$, under the foregoing assumptions. As emphasized elsewhere it is useful to predict the maximum power of $\cos^2\vartheta$ which may enter the distribution function and we refer to the existence of such a maximum power as a limitation on anisotropy. We also refer to the degree of anisotropy and in what follows this phrase may equally well refer to the maximum power of $\cos^2\vartheta$ or to some measure of the departure from isotropy, such as $|1-w(0)/w(\pi/2)|$.

While the limitations in the case of two successive radiations have been completely discussed,[1,2] the limitation in the case of correlating two radiations, with intervening transitions unobserved, has not been treated in detail and the previously determined limits[15,16] for such transitions can be more narrowly restricted. For the case of particle capture followed by a cascade of gamma-rays it has been suggested that the degree of anisotropy, correlating individual gamma-transitions with the initial beam, decreases as one proceeds down a cascade. It is easily seen from the formalism and from investigation of special cases that this is not necessarily so. In particular, it is not difficult to see that the coefficients of the various powers of $\cos^2\vartheta$ may increase or decrease and the highest power of $\cos^2\vartheta$ may also increase or decrease. The treatment of this problem is a special case of triple correlation in which one averages over the directions of intervening radiations. Using the orthogonality property of the rotation matrices

$$\int D_{\lambda_\beta}^{(L)}(\alpha\beta 0)D_{\nu_\beta}^{(L)*}(\alpha\beta 0)d\Omega_{\alpha\beta}=4\pi(2L+1)^{-1}\delta_{\lambda\nu} \tag{21}$$

cross terms in Eq. (5) vanish and

$$w_2(\vartheta_2)=\sum_{m_1 m_2 s M_2}|A(s)|^2(sL_0 m_1 0|j_1 m_1)^2 \times(j_1 L_1 m_1 m_2-m_1|j_2 m_2)^2 \times(j_2 L_2 m_2 M_2|j_2 m_2+M_2)^2 F_{L_2 M_2}(\vartheta_2). \tag{22}$$

The limitations on anisotropy may be shown explicitly by using the methods developed by Racah.[17] Using the properties of the rotation matrices, Eq. (8) may be transformed to give

$$F_L{}^M(\vartheta)=(-)^{L+1}4\pi^{\frac{1}{2}}(2L+1)^{-\frac{1}{2}}\sum_{\nu=0}^{L}(L2\nu M0|LM) \times(LL1-1|2\nu 0)Y_{2\nu}{}^0(\cos\vartheta) \tag{23}$$

[15] E. Eisner and R. G. Sachs, Phys. Rev. **72**, 680 (1947).
[16] C. N. Yang, Phys. Rev. **74**, 764 (1948).
[17] G. Racah, Phys. Rev. **62**, 438 (1942); Phys. Rev. **63**, 367 (1943).

where the $Y_{2\nu}^{0}(\cos\vartheta)$ are the usual normalized spherical harmonics. Consider the case in which the second γ-ray (γ_2) is not observed and the distribution of γ_1 relative to the incident particle beam is investigated. Substituting the form of F_L^M given by Eq. (23) into Eq. (22) and using the Racah coefficients, $W(abcd;ef)$, to change the coupling schemes, it is possible to carry out the summation over magnetic quantum numbers. The derivation is given in Appendix I and the result is

$$w_2(\vartheta_2)=\sum_{s\nu}|A(s)|^2(L_2L_21-1|2\nu0)(2\nu L_000|L_00)\times W(j_12\nu sL_0;j_1L_0)W(j_2L_12\nu j_1;j_1j_2)\times W(L_22\nu j_2j_2;L_2j_2)Y_{2\nu}^{0}(\cos\vartheta). \quad (24)$$

For γ_2 unobserved the angular distribution of γ_1 relative to the beam is given by

$$w_1(\vartheta_1)=\sum_{s\nu}|A(s)|^2(L_1L_11-1|2\nu0)(L_02\nu00|L_00)\times W(L_12\nu j_2j_1;L_1j_1)\times W(sL_0j_12\nu;j_1L_0)Y_{2\nu}^{0}(\cos\vartheta) \quad (25)$$

as is easily verified by the methods of Appendix I.

It is a property of the Racah coefficients that $W(abcd;ef)$ vanishes unless the four triads (abe), (cde), (acf) and (bdf) satisfy triangular inequalities.[17] It follows that the maximum power of $\cos^2\vartheta$ in Eq. (25) is $\mathfrak{M}(L_0, j_1, L_1)$ as has been shown previously.[1,2] Here $\mathfrak{M}(a, b, \cdots)$ denotes the largest integer equal to or less than the smallest member of the set $(a, b, \cdots)$.[18] In a similar manner the maximum power of $\cos^2\vartheta$ in Eq. (24) is seen to be $\mathfrak{M}(L_0, j_1, j_2, L_2)$. This result extends previous statements[15,16] to show explicitly the additional restrictions which exist when intervening levels are present. It will be noted that the multipolarity of the unobserved radiations does not enter this limit.

As an illustration of the foregoing, consider the case of capture of a spin $\frac{1}{2}$ particle with $L_0=2$ (d wave) by a nucleus with spin $\frac{3}{2}$ (as in the proton capture by B^{11}) and, for $x=0$ and the transition scheme $\{3D2Q0\}$, the distribution of γ_1 with γ_2 unobserved is

$$w_1(\vartheta_1)=1-(9/73)\cos^2\vartheta_1 \quad (26a)$$

while the distribution of γ_2 with γ_1 unobserved is given by

$$w_2(\vartheta_2)=1-(42/31)\cos^2\vartheta_2+(55/31)\cos^4\vartheta_2. \quad (26b)$$

Here the degree of anisotropy of the second gamma, by either of the above definitions, is clearly greater than that of the first.

[18] In rare cases the maximum power of $\cos^2\vartheta$ may not be realized due to the possible vanishing of one of the Racah coefficients. Tables of these coefficients are now in process of preparation and will be circulated at a later date. Of the cases investigated thus far there occurs only one case, of physical interest, in which a Racah coefficient vanishes. This corresponds, in Eq. (25) to $L_0=1$, $L_2=2$ and $j_1=j_2=\frac{1}{2}$ which gives an isotropic $w_1(\vartheta_1)$ and for Eq. (24) to $L_2=2$, $j_2=j_3=\frac{1}{2}$, and $\mathfrak{M}(L_0, j_1)\geq 1$ which gives an isotropic $w_2(\vartheta_2)$.

(B) Special Cases of Triple Correlation

As mentioned in Sec. III the maximum power of $\cos^2\vartheta$ that enters in the distribution for the case of two of the three observed radiations parallel or antiparallel may be greater than that allowed for a simple double correlation. To determine the new limit for the first two radiations parallel it is only necessary to transform Eq. (7) by the use of Racah coefficients (see Appendix II). The summation over magnetic quantum numbers leads to

$$w(0\vartheta_2)=\sum_{l'\nu}(2l+1)^{\frac{1}{2}}(2l'+1)^{\frac{1}{2}}(L_22\nu10|L_21)\times[(L_0L_111|l2)(L_0L_111|l'2)(ll'2-2|2\nu0)+(L_0L_11-1|l0)(L_0L_11-1|l'0)(ll'00|2\nu0)]\times W(j_0L_0j_2L_1;j_1l)W(j_0L_0j_2L_1;j_1l')W(ll'j_2j_2;2\nu j_0)\times W(L_2L_2j_2j_2;2\nu j_2)Y_{2\nu}^{0}(\cos\vartheta_2). \quad (27)$$

Again the properties of the Racah coefficients, W, enable one to set an upper limit to the powers of $\cos^2\vartheta$. In this case it may be written as

$$\mathfrak{M}[\mathfrak{M}(L_0, j_1)+L_1, j_2, L_2]. \quad (28)$$

It is quite possible to use Eq. (27) for calculating angular correlation functions. However, for this purpose, the expressions given in Sec. II are more direct and, in the absence of tables of the Racah coefficients, somewhat simpler.

The upper limit on the power of $\cos^2\vartheta$ may be determined in a similar way for the case of the first and third radiations parallel but the analysis is rather lengthy. The result is

$$\mathfrak{M}[\mathfrak{M}(L_0, j_1)+\mathfrak{M}(L_2, j_2), L_1]. \quad (29)$$

It is clear that these limits hold also when the first transition is the capture of an unpolarized particle, L_0 referring then to the relative orbital angular momentum.

There is a very simple physical interpretation of all of these results which makes them somewhat more transparent. It is clear that a 2^L order multipole has an angular distribution containing no powers of $\cos^2\vartheta$ greater than L. This sets a limit to what may be called the "angular information" of a given radiation. It is also clear that a level $j=0$ or $j=\frac{1}{2}$ can contain or transmit no angular information in the sense that all emitted radiation from such a state is isotropic. This is a special case of the result that the highest power of $\cos^2\vartheta$ that can appear in radiation from a level with angular momentum j is just $\mathfrak{M}(j)$ as can be shown quite readily. Then it is possible to schematize the above results as follows: Consider the case of the first and second radiations parallel. The observation of each of these transitions may be interpreted as putting angular information into the system. The first observation limits the powers of $\cos^2\vartheta$ to L_0 and of this no more than $\cos^{2j_1}\vartheta$ can be emitted by the state j_1. The

observation of the second transition then adds angular information limited by $\cos^{2L_1}\vartheta$. Of this angular information no higher power than $\cos^{2j_2}\vartheta$ can be passed by the level j_2 and no higher power than $\cos^{2L_2}\vartheta$ can appear in the final radiation. Hence, the maximum power of $\cos^2\vartheta$ that can appear in the angular distribution is just that given by the foregoing result (28). For the case of the first and third radiations parallel one considers angular information as being introduced into the system by these two transitions. The information transmitted is limited by the j values of the levels as in the previous case. The result is that the maximum power of $\cos^2\vartheta$ that can appear in the angular distribution is that given by (29). It is to be emphasized that this schematization is presented primarily as a mnemonic. The formal justification of the results is found through the application of Racah functions as illustrated in Appendix II.

APPENDIX I

We consider a special case of the triple correlation problem where a particle is captured and two successive gamma-rays are emitted, but only the second gamma-ray is observed. The desired angular distribution of the observed gamma-ray with respect to the propagation direction of the incident particle, $w_2(\vartheta_2)$, is given by Eq. (22). As mentioned earlier, it is possible to perform explicitly the summations over all magnetic quantum numbers that appear in Eq. (22). To do this, we substitute for $F_{L_2}{}^{M_2}(\vartheta_2)$ the result given in Eq. (23) and obtain

$$w(\vartheta_2)\sim\sum_{sm_1M_1M_2\nu}|A(s)|^2(sL_0m_10|j_1m_1)^2$$
$$\times(j_1L_1m_1M_1|j_2m_1+M_1)^2$$
$$\times(j_2L_2m_1+M_1M_2|j_3m_1+M_1+M_2)^2(L_2L_21-1|2\nu0)$$
$$\times(L_22\nu M_20|L_2M_2)Y_{2\nu}{}^0(\cos\vartheta_2). \quad \text{(A1)}$$

Now we perform the summation over M_2 using the result that

$$\sum_{M_2}(j_2L_2m_1+M_1M_2|j_3m_1+M_1+M_2)^2(L_22\nu M_20|L_2M_2)$$
$$=(2j_2+1)(2L_2+1)^{\frac{1}{2}}(2j_2+1)^{-\frac{1}{2}}$$
$$\times(2\nu j_20m_1+M_1|j_2m_1+M_1)$$
$$\times W(L_22\nu j_3j_2;L_2j_2). \quad \text{(A2)}$$

The summation over M_1 can now be performed, namely,

$$\sum_{M_1}(j_1L_1m_1M_1|j_2m_1+M_1)^2(2\nu j_20m_1+M_1|j_2m_1+M_1)$$
$$=(2j_2+1)^{\frac{1}{2}}(2j_1+1)^{-\frac{1}{2}}(j_12\nu m_10|j_1m_1)$$
$$\times W(j_2L_12\nu j_1;j_1j_2). \quad \text{(A3)}$$

This leaves only the summation over m_1 which is done in the same way.

$$\sum_{m_1}(sL_0m_10|j_1m_1)^2(j_12\nu m_10|j_1m_1)$$
$$=(2j_1+1)^{\frac{1}{2}}(2L_0+1)^{-\frac{1}{2}}(2\nu L_000|L_00)$$
$$\times W(j_12\nu sL_0;j_1L_0). \quad \text{(A4)}$$

The final result for $w_2(\vartheta_2)$ is given in Eq. (24), discarding irrelevant factors. It should be mentioned that the specialization to particle capture for the first transition is not essential. Had we desired to calculate a similar problem for a triple gamma-cascade we merely omit the channel spin sum, replacing s by j_0 (the angular momentum of the initial state) and introduce the polarization index p_0 for the magnetic quantum number of the first radiation. For unpolarized gammas this index is summed.

If we observe the first gamma and not the second, the angular distribution of the observed gamma with respect to the beam direction, $w_1(\vartheta_1)$, is given by the usual results for double correlation as

$$w_1(\vartheta_1)=\sum_{sm_1M_1}|A(s)|^2(sL_0m_10|j_1m_1)^2$$
$$\times(j_1L_1m_1M_1|j_2m_1+M_1)^2F_{L_1}{}^{M_1}(\vartheta_1). \quad \text{(A5)}$$

Using Eq. (23), $w_1(\vartheta_1)$ takes the form,

$$w_1(\vartheta_1)\sim\sum_{s\nu m_1M_1}|A(s)|^2(sL_0m_10|j_1m_1)^2$$
$$\times(j_1L_1m_1M_1|j_2m_1+M_1)^2(L_12\nu M_10|L_1M_1)$$
$$\times(L_1L_11-1|2\nu0)Y_{2\nu}{}^0(\cos\vartheta). \quad \text{(A6)}$$

We can perform the summation over M_1 as previously using the equation,

$$\sum_{M_1}(j_1L_1m_1M_1|j_2m_1+M_1)^2(L2\nu M_10|L_1M_1)$$
$$=(2j_2+1)(2L_1+1)^{\frac{1}{2}}(2j_1+1)^{-\frac{1}{2}}(j_12\nu m_10|j_1m_1)$$
$$\times W(L_12\nu j_2j_1;L_1j_1). \quad \text{(A7)}$$

The sum over m_1 can now be done similarly to Eq. (A4).

$$\sum_{m_1}(sL_0m_10|j_1m_1)^2(j_12\nu m_10|j_1m_1)$$
$$=(2j_1+1)^{\frac{1}{2}}(2L_0+1)^{-\frac{1}{2}}(L_02\nu00|L_00)$$
$$\times W(sL_0j_12\nu;j_1L_0). \quad \text{(A8)}$$

The final result, aside from irrelevant multiplicative constants, is given by Eq. (25).

APPENDIX II

It is desired to find the limits on the anisotropy in the case where the first two gamma-rays in a triple cascade are parallel. For this case we find from Eqs. (7) and (23) that the angular correlation for the third gamma has the form,

$$w(0\vartheta_2)\sim \sum_{m_0m_1p_0p_1p_2\nu} (j_0L_0m_0p_0|j_1m_0+p_0)^2$$
$$\times(j_1L_1m_0+p_0p_1|j_2m_0+p_0+p_1)^2$$
$$\times(j_2L_2m_0+p_0+p_1m_3-m_0-p_0-p_1|j_3m_3)^2$$
$$\times(L_22\nu m_3-m_0-p_0-p_10|L_2m_3-m_0-p_0-p_1)$$
$$\times(L_2L_2p_2-p_2|2\nu 0)Y_{2\nu}{}^0(\cos\vartheta_2). \quad \text{(A9)}$$

The summation over m_3 can be carried out in Eq. (A9), exactly as in Appendix I, leading to

$$w(0\vartheta_2)\sim \sum_{m_0p_0p_1p_2\nu} (j_0L_0m_0p_0|j_1m_0+p_0)^2$$
$$\times(j_1L_1m_0+p_0p_1|j_2m_0+p_0+p_1)^2$$
$$\times(j_22\nu m_0+p_0+p_10|j_2m_0+p_0+p_1)(L_2L_2p_2-p_2|2\nu 0)$$
$$\times W(L_22\nu j_3j_2;L_2j_2)Y_{2\nu}{}^0(\cos\vartheta_2). \quad \text{(A10)}$$

To perform the sum over m_0 we use the result that

$$(j_0L_0m_0p_0|j_1m_0+p_0)^2(j_1L_1m_0+p_0p_1|j_2m_0+p_0+p_1)^2$$
$$=(-)^{j_0-j_2}(2j_1+1)(2j_2+1)^{\frac{1}{2}}\sum_{ll'l''}(2l+1)^{\frac{1}{2}}(2l'+1)^{\frac{1}{2}}$$
$$\times(2l''+1)^{\frac{1}{2}}W(j_0L_0j_2L_1;j_1l)W(j_0L_0j_2L_1;j_1l')$$
$$\times W(j_2ljj_2l';j_0l'')(L_0L_1p_0p_1|lp_0+p_1)$$
$$\times(L_0L_1p_0p_1|l'p_0+p_1)(ll'-p_0-p_1p_0+p_1|l''0)$$
$$\times(j_2l''m_0+p_0+p_10|j_2m_0+p_0+p_1). \quad \text{(A11)}$$

The sum over m_0 can now be performed and the result is just Eq. (27).

Using the property that the Racah coefficient $W(abcd;ef)$ vanishes unless a triangular inequality is satisfied for each of the four triads (abe) (cde) (acf) (bdf), we can conclude that value of ν in Eq. (27) is limited by the triangular inequalities on the triads $(2\nu j_2j_2)$ $(2\nu L_2L_2)$, $(2\nu JJ')$, while J (and J') are limited by similar conditions on the triads (j_0j_2J), (L_0L_1J). We can further conclude from this that ν is limited by the condition: $\nu\leq\mathfrak{M}(j_2;L_2;L_1+\mathfrak{M}(L_0,j_1))$.

The case where the first and third radiations are parallel is treated in a similar fashion and results in a product of six Racah functions. The condition on the maximum power (ν) of $\cos^2\vartheta_1$, is then found to be Eq. (29).

In order to see that exactly the same results apply for antiparallel gammas, we note that $D_{\nu\mu}{}^{(L)}(\pi,\pi-\beta,0)=(-1)^LD_{\nu-\mu}{}^{(L)}(0,\beta,0)$, and hence (since the $(-1)^L$ is immaterial here) we merely reverse the polarization of the antiparallel gamma. Since we sum over the polarizations the results are clearly unchanged.

The Capture and Decay of Mesons in Photographic Emulsions*

W. F. Fry
Department of Physics, Iowa State College, Ames, Iowa
(Received March 19, 1951)

Meson events have been studied in Eastman NTB-3 plates which were exposed to cosmic radiation in the stratosphere by means of balloons. It is found that 68±7 percent of the mesons ending in the emulsion which do not produce stars or without associated secondary mesons decay with the emission of a high energy electron. Of these mesons, 11.6±1.5 percent (presumably 23.2 percent of the negative mesons) have associated electrons with energies in the interval from 15 to 70 kev. The energy distribution of these electrons is well represented by a simple exponential with a mean energy of 17 kev. Electrons with energies in the interval from 15 to 70 kev are observed from 19.6±4.0 percent of the stars caused by negative π-mesons.

INTRODUCTION

IN the electron sensitive emulsions recently available, even the minimum ionizing tracks due to charged particles traveling with relativistic velocities can be seen. Because of the high stopping power, comparatively large thicknesses, and the long sensitive time, very infrequent events can be studied. These characteristics make nuclear emulsions very suitable for the study of phenomena associated with mesons. However, the high stopping power has a disadvantage, in that particles of very low energies do not produce a well defined track. The practical lower energy limit for electrons in Eastman NTB-3 plates is about 15 kev. Electrons of energy less than 15 kev occasionally produce a clump of silver grains in these emulsions.

The emulsion consists of a group of heavy elements, mainly silver and bromine in the form of crystals, and a group of lighter elements, principally hydrogen, oxygen, nitrogen, and carbon in the form of gelatin. It is evident that photographic emulsions are not suitable for the detailed study of the capture of negative mesons by any one particular element.

This paper describes the study of certain phenomena associated with the decay and capture of mesons in photographic emulsions.

PROCEDURE

Eastman NTB-3 plates of 200-micron thickness, were exposed in the stratosphere by means of meteorological balloons. Since the sensitivity of nuclear emulsions is reduced at low temperatures, the plates were enclosed in Dewar flasks in order to maintain the maximum sensitivity of the plates. The plates were developed by the temperature method devised by Dilworth, Occhialini, and Payne.[1] A systematic search was made for meson tracks ending in the emulsion. Meson tracks were distinguished from proton tracks by two characteristics. Meson tracks have a greater rate of change of grain density with residual range, and a larger amount of small angle scattering. Tracks shorter than 200 microns were not considered.

On searching 47 plates, containing some 10^7 tracks mainly protons and alpha-particles, 659 tracks which stopped in the emulsion were identified as meson tracks. Of these mesons, 500 are presumably μ-mesons, 118 are negative π-mesons causing stars, and 41 are π-mesons which decay into μ mesons.

μ-MESONS

All mesons ending in the emulsion, without associated particles other than electrons, are classified as μ-mesons. Using this criterion, some negative π-mesons are included as μ-mesons. It has been shown that 26.8 percent of the negative π-mesons ending in the emulsion do not produce stars.[2] Since only 118 negative π-mesons were found in the same plates as the 500 μ-mesons, then approximately 43 of the 500 mesons, classified as μ-mesons, are negative π-mesons.

Of the 500 μ-mesons, only 462 μ-mesons were found in plates which were suitable for observing the decay electrons. The decay electron was observed from 122 μ-mesons out of the 462 μ-mesons. The grain density is very low along the tracks of the decay electrons. Tracks of those electrons which make a large angle with the plane of the emulsion will not be seen. The angles made by the observed decay electrons with the plane of the emulsion were measured. The number of decay electrons which were not seen due to their large angle with the plane of the emulsion, can be estimated from the angular distribution of the observed electrons. A histogram was made of the number of observed decay electrons in a given angular interval, as a function of the angle made with the plane of the emulsion. A calculated curve based on an equal number of electrons per unit solid angle and having the same height as the experimental curve, was superimposed on the experimental histogram. The area between the two curves indicated that about 166 electrons should not have been seen. Thus out of $462-43(462/500)=423$ actual μ-mesons a total of $122+166=288$ decayed in the emulsion (68±7 percent). This result is in agreement with the work of Cosyns, Dilworth, Occhialini, and Schoenberg[3] and

* Supported in part by grants from the Research Corporation and the Iowa State College Research Foundation.
[1] Dilworth, Occhialini, and Payne, Nature **162**, 102 (1948).
[2] F. L. Adelman and S. B. Jones, Phys. Rev. **75**, 1468A (1949).
[3] Cosyns, Dilworth, Occhialini, and Schoenberg, Proc. Phil. Soc. A **62**, 801 (1949).

Bonetti,[4] who found 63±4 percent and 68 percent, respectively. These percentages include as μ-mesons the negative π-mesons which did not produce stars in their plates.

The result is also in agreement with crude theoretical predictions based on the following arguments. Assuming that the stopping power of the various constituents of the emulsion for low energy mesons is proportional to the atomic number, it is estimated that 81 percent of the mesons stopped in silver bromide crystals and that 19 percent stopped in gelatin. It has been shown that negative mesons stopped in a material of $Z=10$ have about equal probability of capture and decay.[5] If it is also assumed[6] that the probability of capture of negative mesons is proportional to Z^4, then nearly all of the negative μ-mesons which end in silver bromide crystals will not decay, while essentially all of those ending in the gelatin will decay. If it is further assumed that there are equal numbers of positive and negative μ-mesons in the low energy spectrum from cosmic rays,[7] then of the 423 μ-mesons considered, 212 are negative, of which $(212)(0.19)=40$ should give rise to a decay electron. From these considerations, $212+40=252$ (60 percent) of the mesons decayed. A total of 288 (68 percent) is observed.

A careful search was made for low energy electrons at the end of the μ-meson tracks. All of the plates were suitable for the study of low energy electrons. In these plates 500 μ-mesons were found, of which 46 (9.2 percent) have one associated low energy electron in the energy interval between 15 and 70 kev. Ten (2 percent) have two low energy electrons. Two mesons (0.4 percent) give rise to three low energy electrons. In only one case were a high energy and a low energy electron observed from the same meson. These results are corrected for the contribution of the negative π-mesons in the following section. A study of low energy electrons from μ-mesons has been made by Cosyns *et al*,[3] who found 7.2±1.3 percent of the μ-mesons give rise to one or more electrons of energy greater than 20 kev. A similar study was made by Bonetti[4] who found that 7.2 percent of the μ-mesons give rise to a low energy electron.

It is difficult to estimate the number of electrons in the interval from 15 to 70 kev that were not seen. Many background electrons of energies less than 100 kev were observed in the plates. Many of these tracks were nearly perpendicular to the plane of the emulsion. From this study, it seems that very few electrons in the interval from 15 to 70 kev were missed.

A typical example of an electron originating from a μ-meson is shown in Fig. 1.

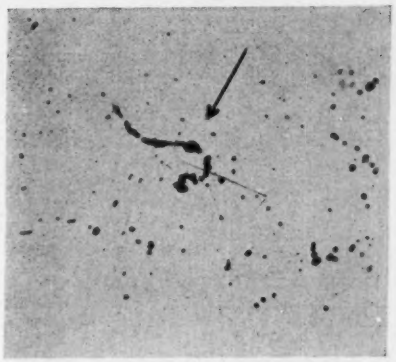

FIG. 1. Mosaic of a μ-meson and an associated low energy electron. The meson track goes to the right and down. A clump of silver grains can be seen at the end of the meson track which is indicated by an arrow. The track of a 45 kev electron can be seen below the meson track.

The energy distribution of the low energy electrons from μ mesons is shown in Fig. 2. There is no evidence of line structure. The spectral energy distribution of these electrons can be approximated by the equation; $N(E)\sim\exp(-E/E_a)$, where E_a is a mean energy and has a value of about 17 kev.

A low energy electron is considered as being associated with a meson only if it originates within two microns from the end of the meson track. Using this criterion, the number of background electrons erroneously counted as being associated with the mesons, can be estimated in the following way. A total of 300 proton tracks were found which stopped in the emulsions. Using the aforementioned criterion, only two cases were found where a low energy electron would have erroneously been considered as having originated from the proton; hence the background can be neglected.

At the end of 32 μ-meson tracks, a clump of silver grains was observed. These "blobs" are not observed

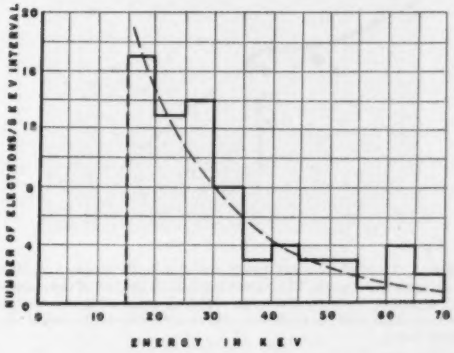

FIG. 2. Energy histogram of 72 electrons from μ-mesons.

[4] A. Bonetti, University of Genoa, Genoa, Italy, private communication.
[5] T. Sigurgeirsson and K. A. Yamakawa, Revs. Modern Phys. **21**, 124 (1949).
[6] J. Wheeler, Phys. Rev. **71**, 462 A (1947).
[7] C. Franzinetti, Phil. Mag. **41**, 86 (1950).

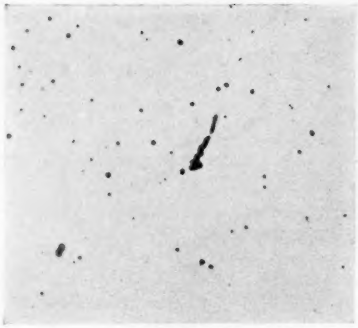

FIG. 3. Photomicrograph of a meson track which has a clump of silver grains at the end.

at the end of the 122 μ-mesons which decay, nor at the end of the 41 π-mesons which decay into μ-mesons. From this, one concludes that the "blobs" are associated only with the capture of negative mesons, rather than with large angle scattering near the end of the meson tracks.[7,8] The "blobs" are thought to be due to one or more electrons of energy below 15 kev. A typical meson track with a clump of grains at the end is shown in Fig. 3.

σ-STARS

Meson tracks were found to end in stars in 118 cases. One or more low energy electrons are observed to originate from 22 stars (18.6 percent). In 4 cases, two low energy electrons are observed from the same star. A typical star with a low energy electron is shown in Fig. 4. The energy distribution of the electrons from meson stars is given in Fig. 5. No correlation was found between the number of low energy electrons and the number of prongs in a star. No minimum ionizing tracks were observed from meson stars. The probability of observing these tracks can be estimated from the study of the number of electrons from μ-meson decays. Since 122 decay electrons were observed out of a total of 288, the probability of observing a minimum ionizing track is about 0.4. Since no minimum ionizing tracks were seen from negative π-stars, the β-activity of the residual nuclei which result in high energy electrons ($E>0.2$ Mev) must be small.

An estimate of the contribution to the number of low energy electrons from negative π-mesons classified as μ-mesons can now be made. Since 18.6 percent of the negative π-mesons have an associated low energy electron, of the estimated 43 π-mesons classified as μ-mesons, on the average only $(43)(0.18)=8$ cases of ejection of low energy electrons are due to negative π-mesons. Of the 58 mesons classified as μ-mesons which have an associated low energy electron, on the average only 50 are actually μ-mesons.

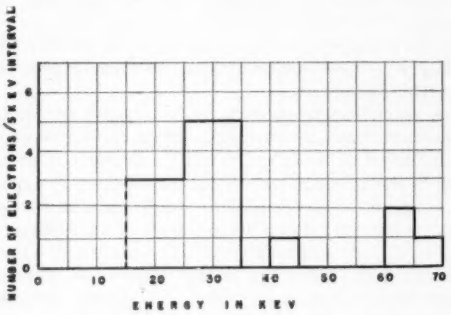

FIG. 5. Energy histogram of electrons from negative meson stars.

Since 118 meson induced stars were found in the same plates along with 41 π–μ-decays, it would appear that the ratio of low energy negative to positive π-mesons in the cosmic radiation is $(118)/(41)(0.73)=4$.

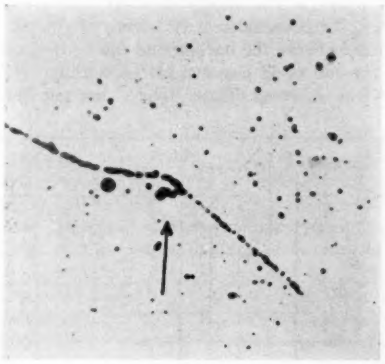

FIG. 4. A mosaic of a one-prong star due to the nuclear capture of a negative π-meson. The meson track is to the left of the mosaic and a proton track to the lower right. A track of a low energy electron, indicated by an arrow, can be seen below the end of the meson track.

[8] H. Bradner, Univ. of Calif. Rad. Lab. Report No. 486 (1949).

RANGE-ENERGY RELATIONSHIP

Electron sensitive NTB-3 plates were exposed to monoenergetic electrons in an electron microscope and an instrument built by General Electric for electron diffraction studies. The ranges of groups of monoenergetic electrons were determined. The results are shown in Table I.

The numbers listed under the last column are estimates of the probable error in energy of a single electron from a measurement of its range.

The ranges of the individual tracks were measured. The average range was then found. A range energy curve was then made. The apparent energy of each electron was then determined from this curve and a

TABLE I. Mean range of electrons in electron sensitive NTB-3 plates.

Energy in kev	Number of tracks measured	Mean range in microns	Spread in energy
50	35	17.5	±6 kev
30	50	7.0	±4 kev
20	50	3.7	±4 kev

histogram drawn. The results are shown in Fig. 6. It is apparent that detailed line structure could not be detected by range measurements for electrons of energy less than 30 kev.

CONCLUSIONS

Since essentially all of the low energy electrons are associated with μ-mesons which do not decay, it is reasonable to assume that these mesons are negative. It also seems reasonable to assume from energy and radiation considerations that the low energy electrons are not due to atomic capture of the mesons in the lighter elements in the emulsion. Of the 457 μ-mesons, on the average 228 are negative, of which 185 were presumably captured by silver and bromine atoms. Thus the probability is 0.20 ± 0.04 that a negative μ-meson eject one electron in the energy interval from 15 to 70 kev upon capture by an atom of silver or bromine. The probability that two electrons in this energy range are ejected is 0.054 ± 0.015. For three electrons, the probability is about 0.01.

The probability of ejection of low energy electrons by negative π-mesons upon capture by silver or bromine is, within the statistical limits, the same as for negative μ-mesons; namely, 0.19 ± 0.04 for one electron and about 0.04 for two electrons. Also the energy distribution of the low energy electrons from negative μ-mesons and negative π-stars seems to be the same. These facts indicate that the low energy electrons are probably due to some type of interaction of the meson with the electronic shell, such as Auger transitions, rather than a nuclear phenomenon.

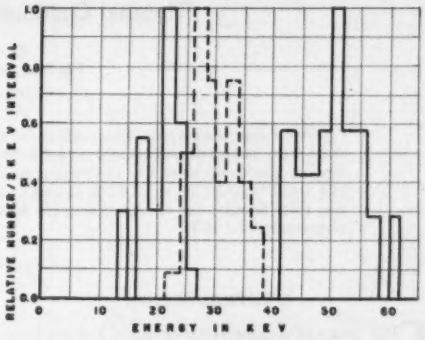

FIG. 6. Apparent energy distribution of three groups of monoenergetic electrons.

The author would like to express his gratitude to Professor J. K. Knipp for suggesting the problem and for the many interesting and helpful discussions, and to Professor G. W. Fox for his continued interest and encouragement.

Thermal Conductivity of Liquid Helium. I

CLAUDE GRENIER
The Rice Institute, Houston, Texas
(Received April 9, 1951)

Direct measurements have been made of the thermal conductivity of liquid helium over the temperature range from its normal boiling point at 4.2°K to a temperature within a few hundredths of a degree of the λ-point. The results show that the thermal conductivity decreases linearly with temperature from a value of 6.5×10^{-5} cal/deg cm sec at 4.2°K to about 4.5×10^{-5} cal/deg cm sec close to the λ-point. No large deviation from linearity can be detected in the heat conductivity until about 0.2 degree from the transition temperature of 2.18°K.

I. INTRODUCTION

THE thermal conductivity of liquid helium between 2.2°K and its normal boiling point at 4.2°K was first studied by Keesom and Keesom.[1] These authors only reported one quantitative result, *viz.*: 6×10^{-5} cal/deg cm sec at the temperature 3.3°K. The experiments by Pellam and Squire[2] on the ultrasonic absorption in liquid helium make it possible to calculate the dependence on temperature of the heat conductivity if the classical theory of sound attenuation is assumed valid over the entire temperature range of liquid helium I. Such a calculation predicts an enormous increase of the thermal conductivity starting at 3°K as the temperature is lowered to the transition point of liquid helium II. Thus, it was of interest to make a direct investigation of the thermal conductivity. The results clearly indicate that the heat conductivity remains nearly constant with temperature even quite close to the transition point.

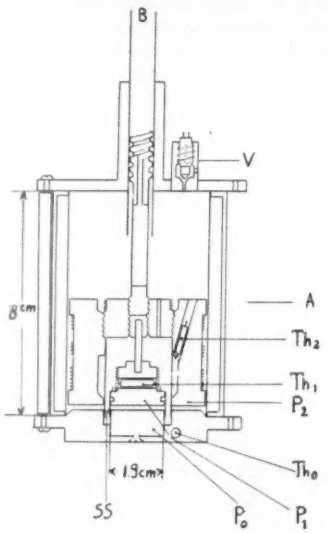

FIG. 1. Experimental apparatus for heat conductivity of liquid helium I: *A*—level of the effective temperature; *B*—tube leading to helium ballast tank; *V*—valve; *SS*—stainless steel walls; P_1—central plate; P_2—guard ring; P_0—lower plate; Th_0, Th_1, Th_2—carbon resistance thermometers.

II. APPARATUS

For this research an apparatus, Fig. 1, with horizontal plates P_0 and P_1 was constructed with a guard ring P_2. This is different from the apparatus of Ubbink and de Haas[3] in that the guard ring, P_2, extends around the sides of the central plate, P_1, as well as on top of it. Both P_0, P_1, and P_2 are made from aluminum whose thermal conductivity at these low temperatures is about 10^3 greater than liquid helium I. The liquid helium column between P_0 and P_1 is confined by a thin stainless steel wall, marked *SS* in Fig. 1. The wall thickness is 0.003 inch and the metal is 18–8 stainless steel. A similar stainless steel wall connects the base plate with P_2.

The central plate, P_1, was heated during the measurements by means of current passing through a coil of wire whose resistance at these low temperatures was 210 ohms. The wire was small diameter (size No. 35) cupron metal, and its resistance is very nearly independent of temperature in the liquid helium region. The guard ring, P_2, was similarly heated with a 450-ohm coil. Good thermal contact between the coil and aluminum metal was assured by a coat of lacquer. The coils were insulated thermally from the liquid helium by a layer of paper.

All these aluminum plates and guard rings are housed in a brass can having double walls (see Fig. 1). Between the walls there is helium gas at very small absolute pressure so that there is adequate thermal insulation across the double wall container. At the top of the brass can is a valve *V* which makes it possible to open the experimental chamber into contact with the liquid helium bath in the outer surrounding Dewar flask. The calibration of the carbon thermometers was done with the helium around P_0, P_1, P_2, in contact with the outer bath through the open valve. During the experiments the valve was closed and the pressure on the

[1] W. H. Keesom and A. P. Keesom, Physica **3**, 359 (1936).
[2] J. R. Pellam and C. F. Squire, Phys. Rev. **72**, 1245 (1947).
[3] I. B. Ubbink and W. J. de Haas, Physica **10**, 451, 465 (1943).

liquid helium inside the experimental chamber was kept very accurately constant. Most of the experiments were made with a pressure of 76 cm (barometric conditions) even though the temperature of the bath in the outer Dewar was cooled well below 4.2°K. In this way, the heat conductivity studies were made on the liquid helium between P_0 and P_1 in such way that the liquid helium was well away from the liquid-vapor transition. Thus no heat supplied to the liquid could produce a vapor. Some studies were made in which the pressure was held constant on the experimental liquid at as high as 3 atmospheres and for this a large tank (approximately 500 liters) was placed in the supply line so that fluctuations of pressure would be at a minimum.

The vapor pressure of the liquid helium in the outer bath was kept constant to 0.1 mm of Hg by means of a hand operated manostat and a differential oil manometer. These techniques are commonly practiced in low temperature laboratories.

The distance, d, between the plates was controlled from the outside by means of a screw having a pitch of $\frac{1}{32}$ inch per revolution (distances given by number of turns are to be multiplied by 0.79 mm). The rod from the top of the apparatus to the movable plate P_1 was of necessity a thin wall tube and so was flexible. This made the zero distance, corresponding to contact between P_0 and P_1, a little uncertain. Thus, when the outside vernier scale read zero, the plates were actually separated a distance, d_0.

The apparatus was constructed with the following factors in mind: (a) the thermometers must be sensitive and reliable, (b) the separation of plates P_0 and P_1 must be accurately known and must be parallel, (c) the flow of heat energy must be accounted for.

III. TEMPERATURE MEASUREMENT

The thermometers were of standard type resistors used in electronic circuits and which are composed of carbon surrounded by a ceramic or by an insulating lacquer. These thermometers are shown in Fig. 1 as Th_0, Th_1, and Th_2 where they give the temperature of the aluminum plates P_0, P_1, and the guard ring P_2. Simple wheatstone bridges were used to measure their resistance and the current was kept small; with a current of 10^{-5} ampere the heating was negligible and current fluctuations caused no trouble. The current was maintained constant by using compensatory resistances in the bridge. Thermal contact between the thermometer and the aluminum metal was made with paraffin.

Two factors limit the accuracy of the calibration curve, Fig. 2, giving electrical resistance as a function of temperature; (a) hysteresis effects when the thermometer is warmed back up to room temperature and then cooled to liquid helium, (b) precision of determining the temperature from the vapor pressure of the helium bath and taking into account the hydrostatic head of liquid helium above the location of the thermometer. As shown in Fig. 3, marked "B," there is a

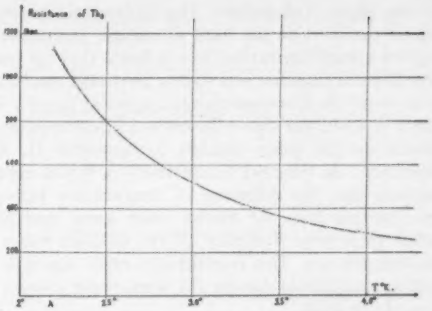

FIG. 2. Calibration curve of the carbon-resistor thermometer Th_2.

change of 30 ohms out of 1200 ohms at 2.17°K if the thermometer has been warmed back up to room temperature between measurements. The thermometers were therefore freshly calibrated each time they were cooled to liquid helium temperatures. After more than twenty different experiments the deviations due to hysteresis are only ±0.01°K. Any hysteresis effects while keeping the thermometers within the temperature range of liquid helium were too small to be significant.

In order to avoid any errors during an experiment, it was preferable to calibrate the thermometers at a given temperature over a range of approximately 0.1°K and make all heat measurements in this range. Under these conditions the electrical resistance thermometers are so accurate and reproducible that their error is smaller than other factors which enter into the heat flow measurements. We refer to Appendix I for more details on the thermometers.

The vapor pressure at the surface of the bath of liquid helium was measured by a mercury manometer and cathetometer. The vapor pressure determined the absolute temperature by using the 1947 tables prepared

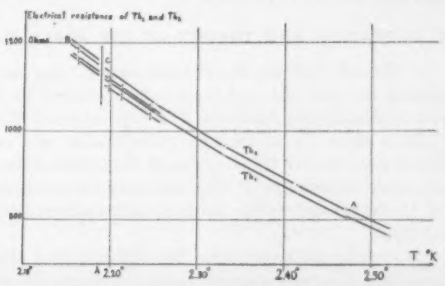

FIG. 3. Calibration curves of the thermometers Th_1 and Th_2 near the lambda-point. The dots represent experimental points. The dots marked with vertical bars represent a later measurement. (The thermometers returned to 290° between measurements.) *A*. Jump: bridge current changed from 5×10^{-6} to 10^{-5} amp. *B*. Hysteresis in carbon resistance thermometer (Sec. III). *C*. Jump in temperature: effect of hydrostatic pressure in liquid helium 1.

by the Mond Laboratory. The hydrostatic pressure due to the level of the bath above the thermometer requires a small correction. It was found that the brass experimental chamber was such a good heat conductor as to cause the thermometers to appear at an effective height of 4 to 5 cm above the bottom of the apparatus. Details on this point are left to Appendix II. The experiment on the heat conductivity of liquid helium requires that the difference of temperature between two thermometers be known with great precision, rather than great accuracy on the absolute value of the temperature. This considerably eased the task of making corrections due to the very slight change in level of the bath.

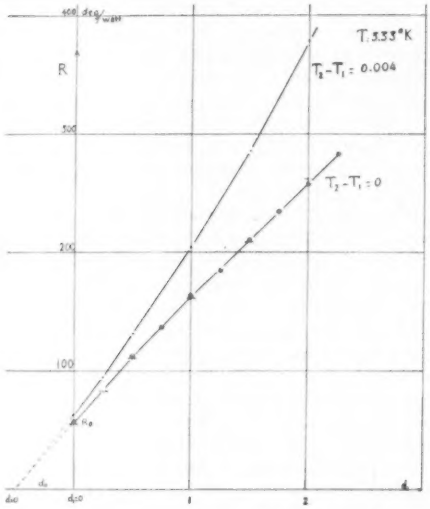

FIG. 4. Thermal resistance between the plates P_1 and P_0. The points on the lower curve are for $T_2-T_1=0$. The points on the upper curve are for $T_2-T_1=0.004°K$.

IV. OPERATION AND THEORY OF THE APPARATUS

As Ubbink and de Haas[3] have shown, one must measure the heat flow and temperature gradient for at least three different distances, d, of separation of plate P_1 from plate P_0, so that by extrapolation one can deduce the effective cross section of the helium column and other parameters of heat loss may be accounted for. In the present work a series of such measurements was made.

An experiment began with the calibration of thermometers. If a measurement on heat conductivity was to be made at a constant bath temperature, θ_0, then the thermometers were calibrated from a temperature 0.06°K above the final temperature on down to θ_0. With the pressure on the liquid helium within the experimental chamber held constant at 76 cm of Hg, the plates P_1 and P_2 were electrically heated until they remained at a constant temperature 0.06° above the temperature θ_0 of the plate P_0. The distance, d, was then changed and a new set of values of electric power in the heating coils, of temperatures, etc., was taken.

If the temperature of the guard ring, P_2, is equal to the temperature of the central plate, P_1, then all the power, E_1, generated in P_1 will flow to the bottom plate P_0. The gradient of temperature between P_1 and P_0 is $(T_1-T_0)/d$ and the effective cross-sectional area of the helium column is S so that the heat conductivity coefficient is:

$$K=\frac{E_1/S}{(T_1-T_0)/d} \text{ watts/deg cm.} \tag{1}$$

The effective cross section, S, depends on the distance, d, and the latter has an uncertainty in absolute value. Let us examine this difficulty.

We define the thermal resistance between plates P_1 and P_0 by:

$$R=(T_1-T_0)/E_1 \tag{2}$$

which from the above equation defining the heat conductivity is also the ratio:

$$R=d/SK. \tag{3}$$

Now the distance $d=d_0+d_1$, so that we may write the ratio as:

$$R=d_0/SK+d_1/SK=R_0+R_1. \tag{4}$$

The distance, d_1, on the vernier scale of the movable screw mechanism is zero when the gap between the plates P_1 and P_0 is just d_0, which we shall see is about 0.5 mm. For d_1 equal to zero the thermal resistance is R_0 as is shown in Fig. 4 where we have plotted R against d_1. Extrapolation of R to zero defines experimentally the distance d_0 which is shown in Fig. 4.

The actual geometric area of plates P_0 and P_1 is S_1 which is smaller than the effective cross section, S, used in the expression for the heat conductivity, K. We shall define a preliminary heat conductivity, K_1, by use of the geometric cross section, S_1, as follows:

$$R_1=d_1/S_1K_1=\left(\frac{T_1-T_0}{E_1}\right)_{d_1}-\left(\frac{T_1-T_0}{E_1}\right)_{d_1=0}. \tag{5}$$

This preliminary value, K_1, is listed in Table I.

Examining Fig. 5 which shows schematically the two plates P_1 and P_0 with the stainless steel wall, we see the heat flux lines drawn for one-half of the cylinder. Some of the heat is conducted straight across the area S_1, some is conducted down the stainless steel wall, and some of the heat passes by the fringe of flux shown in the drawing. In this way we can write the heat conductance:

$$\frac{1}{R_1}=\frac{S_1K_1}{d_1}=\frac{S_1K}{d_1}+\frac{sK_s}{d_1}+\frac{\Delta SK}{d_1} \tag{6}$$

where "s" is the area determined by the product of the stainless steel wall thickness by its circumference, K_{ss} is the heat conductivity of the stainless steel,[4] and "ΔS" is the equivalent cross section of the fringe flux. The term, K, is the true heat conductivity of liquid helium. Thus we write simply:

$$K_1 = K + (s/S_1)K_{ss} + (\Delta S/S_1)K. \tag{7}$$

We now assert that as the plates P_1 and P_0 get closer together the last term in the above expression becomes relatively less important. Thus for the plates touching, $d=0$, which is to say, $d_1 = -d_0$:

$$K_1 = K + (s/S_1)K_{ss}. \tag{8}$$

The true value of the liquid helium heat conductivity, K, is thus obtained by the extrapolation of K_1 to the distance $d=0$, and the small correction (10 percent at 4.0°K) term due to the stainless steel is then used.[5] Such extrapolation, as shown in Fig. 6, has the additional advantage of reducing to a minimum any error in the results caused by the guard ring, P_3, being at a slightly different temperature than the plate P_1. This latter point is brought out in Appendix III.

We are now in a position to understand why the stainless steel wall was used to confine the helium column. In the first place it cuts down on convection currents which for a liquid with such small viscosity can become a large disturbing factor in heat flow measurements. Less important reasons are that (a) it permits the plates P_0 and P_1 to be more nearly parallel, and (b) the fringe flux is reduced.

V. RESULTS

The values of the heat conductivity, K, for liquid helium between the temperatures 4.15°K and 2.27°K are given in Table I and they are plotted in Fig. 7. These values come from the extrapolation of the experimental results with the correction of the stainless steel wall taken into account as explained in Sec. IV of this paper. Taking into account the errors involved in extrapolating experimental values and the errors discussed in the Appendix, the absolute values of the heat conductivity are within 10 percent accurate. Figure 7 shows that the heat conductivity decreases with temperature to 2.4°K and shows a very small increase below that temperature towards the transition point at 2.18°K. The points on the curve of Fig. 7 have lines to each side and parallel to the temperature axis which indicate the range of temperature over which the measurement was made.

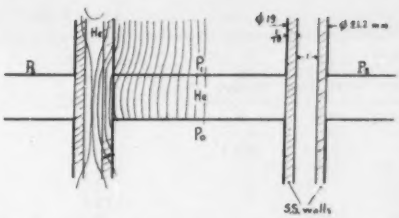

FIG. 5. Schematic representation of the thermal flux lines between P_1 and P_0.

VI. DISCUSSION AND CONCLUSIONS

At the temperature 3.3°K we have very good agreement with the value given by Keesom and Keesom.[1] The experimental values of K are in accord with the calculated values from the classical theory of sound absorption used by Pellam and Squire[2] for liquid helium above 3.0°K. Below 3.0°K the ultrasonic absorption becomes so large that the heat conductivity would have to increase enormously and the present experiments indicate that this does not happen. We must conclude that the classical theory of sound attenuation, which permits the sound energy to be absorbed by viscosity and by heat conduction, is no longer valid for liquid helium in the temperature range below 3.0°K. Table II compares these results.

In Table II the gas theory is used to compute the heat conductivity; $K = 2.5\eta c_v$, where the specific heat per gram at constant volume is taken from the work of Keesom and Clusius[6] and the viscosity, η, is taken from the recent results of Bowers and Mendelssohn.[7] The best agreement, so far as temperature dependence is concerned, is between the gas theory and the experimental work reported here. As this manuscript was being prepared, the preliminary results of Bowers and

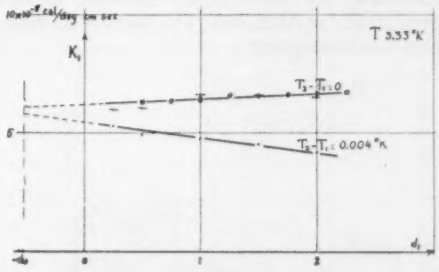

FIG. 6. Uncorrected conductivity of liquid helium and extrapolation to the distance $d=0$. The points on the upper curve are for $T_2 - T_1 = 0$. The points on the lower curve are for $T_2 - T_1 = 0.004$°K.

[4] The values of the heat conductivity of stainless steel 18–8, K_{ss}, were reported by J. E. Zimmerman of The Carnegie Institute of Technology at the Cryogenics Conference held by the ONR at the Georgia Institute of Technology, March 1950. These values are reproduced in Table I.

[5] The distance, d_1, used for the stainless steel wall is slightly shorter than the actual distance because of the construction of the apparatus. The correction for the heat conduction by the stainless steel is, therefore, an upper limit and the helium heat conductivity in Table I represents a lower limit.

[6] W. H. Keesom and K. Clusius, Comm. Leiden 192; W. H. Keesom, *Helium* (Elsevier Press, New York (London), 1942), p. 218.

[7] R. Bowers and K. Mendelssohn, Proc. Phys. Soc. (London) A62, 394 (1949).

TABLE I. Heat conductivity in liquid helium.

$\frac{T_0+T_1}{2}$ °K	T_0-T_1 in °K/1000	T_2-T_1 in °K/1000	Pressure in cm of Hg	R_0 °K/w	K_1 in cal/°K cm sec, d_1 in turns—1 turn =0.79 mm ½	½	1	1½	2	3	K_0, cal °K cm sec	K cal °K cm sec
2°.24−	37	0	76	80.5		5.51	5.75		5.85		15	4.8
···	···	+1.6	···	75.4		5.63	6.05		6.53		···	4.9
···	···	+3.2	···	70.5		6.32	6.58		7.58		···	5
2°.24+	50	(−)	···	78.7		4.67	4.23		4.60	4.59	···	4.4
2°.30	70	(−)	···	74.4		5.07	5.13		5.04		16	4.6+
2°.38	75		···	75.1		5.04	5.17		5.05		17	4.6−
2°.45	53		···	74.2		4.85	5.13		5.24	5.11	18	4.4
2°.50	47		···	71.9		5.23	5.50	6.00	5.51	5.77	19	4.6
2°.85	19		···	67.0	6.05	5.67	6.14		5.96		25	5.2
2°.86	37	(+)	···	60.0	5.82	6.01	6.31	6.58	6.68		···	5.0
2°.87	57		···	61.6	5.91	5.99	6.00	6.07	6.14		···	5.2
2°.88	80		···	60.1	5.83	5.81	6.14	6.39	6.39		···	4.9
3°.33	80		95	57.7		6.27	6.37		6.39	6.75	33	5.4−
···	···		140	58.6		6.37	6.85		6.82	6.83	···	5.8
···	···		76	57.7		6.31	6.43	6.62	6.75		···	5.4
···	20		···	68.7	6.51	6.26	7.17	6.93	6.79		···	5.6
3°.34	52	−4.	···	62.6	5.29	4.90	4.74	4.52	4.24		···	5.1
3°.35	70		···	54.9	5.94	5.97	6.66	6.55	6.52		···	5.2
3°.65	31		···	55.1		7.34	7.03		7.30		38	6.4
3°.63	64		···	51.0		7.34	7.26		7.18		···	6.5
4°.18	50		205	47.7		7.23	7.41		7.34		48	6.3
···	···		145	46.1		7.10	7.10		7.10		···	6.1
···	···		115	46.3		7.15	7.05		7.05		···	6.2
···	67		93	42.6		7.72	8.70		9.43	10.13	···	

Mendelssohn[8] on the heat conductivity of liquid helium appeared in *Nature*. Their work is in agreement with our experimental values.

We have indicated in the text of Sec. IV that the plates P_0 and P_1 are separated by a very small distance, d_0, which is about 0.5 mm when the vernier scale reading on the external screw is zero. If we take the average value of d_0 to be 0.53 mm then the thermal resistance R_0 can be considered to be caused by the liquid helium in that distance. The heat conductivity, K_0, which gives this value of R_0 for the distance d_0, is listed in the last row of Table II. These values are in good accord with the values K obtained by the experimental methods described in Sec. IV. At temperatures below 2.4°K, the values of K_0 may even be more accurate than the values of K. The values of K_0 appear on Fig. 7 as single points.

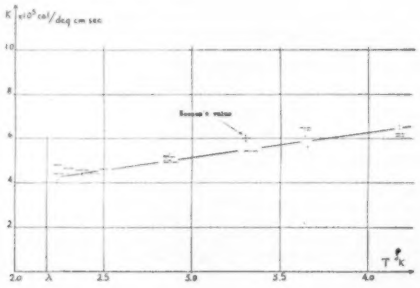

FIG. 7. Heat conductivity of liquid helium I. The horizontal bar through an experimental point indicates the temperature range in which the measurement was made.

[8] R. Bowers and K. Mendelssohn, Nature **167**, 111 (1951).

Table I shows that with a change of pressure on the liquid there was no observable change in the heat conductivity. In most respects liquid helium between 2.2°K and 4.5°K behaves more like a gas than a normal liquid. It is well understood that this is caused by quantum effects of the uncertainty principle which tend to keep the atoms separated from one another.

The author is pleased to acknowledge the research guidance of Professor Charles F. Squire and for the very considerable assistance given generously by the members of the low temperature laboratory. During the research period, the author held a fellowship given by The Rice Institute to a student from France.

APPENDIX I

Referring to Fig. 4 which gives the thermal resistance as a function of the distance of separation of the plate P_0 and P_1, we see that the values obtained have a very small scatter about the curve for $T_2-T_1=0$. One obtains an entirely different curve, for example, with the guard ring temperature slightly higher than the central plate P_1; thus with $T_2-T_1=0.004$°K a new curve is shown in Fig. 4. We may therefore conclude that the stability of the thermometers as indicated by the small scatter of points on the ideal curve is such that the same scatter could be produced by the guard ring being about 0.0004°K higher than the plate P_1.

APPENDIX II

Referring to Fig. 3 which gives the electrical resistance of the carbon thermometer as a function of temperature, we see that at the λ-point of the liquid helium there is a sudden shift of the value of the electrical resistance. The magnitude of this shift was found to be dependent on the height of the liquid helium in the Dewar flask. One may understand that the temperature of the thermometer is influenced by the hydrostatic head of liquid helium, and that when the superfluid is obtained at the λ-point the enormous heat conductivity of the bath brings the thermom-

eter to the temperature of the surface of the bath. Temperature gradients simply cannot be supported in the superfluid bath. Indirectly the shift in the resistance of the carbon thermometers was a measure of the height of the helium level. Observing the height of the level through the clear windows of the Dewar flasks made it clear that the actual level of the carbon thermometers was effectively raised to about 5 cm above the bottom of the brass apparatus because of the high heat conductivity of the brass metal.

APPENDIX III

Suppose that not all of the power, E_1, produced in plate P_1 went to the plate P_0, but that a small quantity, e, went to the guard ring because of a temperature difference T_2-T_1. The error caused by this heat flux will be minimized as the distance of separation of the plates P_1 and P_0 vanishes. To see this let us define the thermal resistance of the path between P_1 and the guard ring as "r," such that:

$$r=(T_2-T_1)/e. \tag{9}$$

The ratio of the power, e, which goes to the guard ring to the power, E_0, which goes to the plate P_0 will then be:

$$e/E_0=[(T_1-T_2)/r]\times[R/(T_1-T_0)]. \tag{10}$$

As the thermal resistance R of the helium column between P_1 and P_0 vanishes with the distance $d=0$, we may conclude that the ratio becomes small and that the relative importance of the small heat leak to the guard ring is minimized. The apparatus was constructed in such a way as to make the thermal resistance, r, as large as possible.

TABLE II. Comparison of results on heat conductivity.

T°K	$10^3\times K$(exp) cal/deg cm sec	K Keesom	K Sound absorb.	$2.5c_v\eta$ Elementary gas theory	K_0 Zero resistance
2°.24−	4.8				4.05
2°.24+	4.4			3.7	4.15
2°.30	4.6+		100		4.4
2°.38	4.6−				4.35
2°.45	4.4				4.4
2°.50	4.6			3.2	4.6
2°.58			17		
2°.86	4.9 5.2				5.2 5.3
3°.08			5.5	3.3	
3°.35	5.1 5.7	6	6		5.4 5.3
3°.50			7	3.6	
3°.63	6.4		6.7		5.6 6.1
4°			5.5	4.4	
4°.2	6.1 6.3		5		6.4 6.6

PHYSICAL REVIEW VOLUME 83, NUMBER 3 AUGUST 1, 1951

Injected Light Emission of Silicon Carbide Crystals

K. LEHOVEC, C. A. ACCARDO, AND E. JAMGOCHIAN
Signal Corps Engineering Laboratories, Fort Monmouth, New Jersey

(Received April 5, 1951)

Recombination of carriers injected through $P-N$ boundaries in silicon carbide crystals may lead to light emission ("injected light emission"). This light emission was investigated as a function of temperature and of current through the crystal by use of a photomultiplier. The emission spectrum extends from 4500A to 6500A at room temperature and is found to be nearly independent of current from 0.1 ma to 50 ma. The light intensity increases approximately proportionally to current (efficiency about 10^{-8} quanta per electron at room temperature for a particular crystal).

I. INTRODUCTION

SOME silicon carbide crystals emit "cold" light while current passes.[1-7] Two types have been reported: (a) a bluish light and (b) a yellow light, the type emitted depending on the direction of current flow. The parts of the crystal that emit yellow light do not coincide, in general, with those emitting blue light on current reversal; nor does the same crystal necessarily emit both types. We conclude that the mechanism of excitation differs for the two cases.

Previously published data on the intensity and spectral distribution of the light are of a qualitative nature. In this paper quantitative information is presented on the spectral distribution of the yellow light and its dependence on current density and temperature.

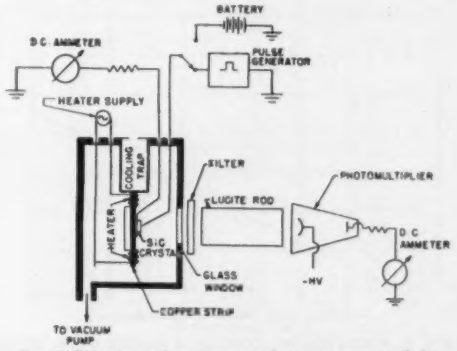

FIG. 1. Experimental arrangement for measurement of the light emission from silicon carbide crystals.

[1] O. Lossew, Wireless World and Radio Review **271**, 93 (1924).
[2] O. Lossew, Z. Fernmeldetechnik **7**, 97 (1926).
[3] O. Lossew, Phil. Mag. **6**, 1028 (1928).
[4] O. Lossew, Physik. Z. **30**, 920 (1929).
[5] O. Lossew, Physik. Z. **32**, 692 (1931).
[6] O. Lossew, Physik. Z. **34**, 397 (1933).
[7] B. Claus, Ann. Physik **11**, 331 (1931).

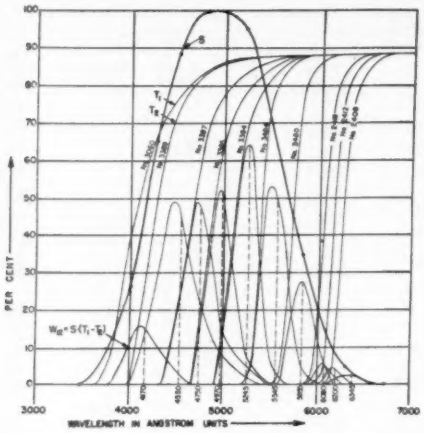

FIG. 2. Transmissivity "T" of Corning Glass Filters (No. of filter indicated in figure), photomultiplier No. 5819 sensitivity "S," and correction factor $W=S(T_1-T_2)$ as functions of wavelength.

An explanation is proposed for the mechanism of the yellow light emission.

II. EXPERIMENTAL ARRANGEMENT

The experimental arrangement is shown diagramatically in Fig. 1. The current source for the crystal consisted of either a battery or a pulse generator. The silicon carbide crystal was silver-plated on one side and attached by silver paste to a brass plate mounted on a copper strip extending from a Kovar coolant container. Two heating coils insulated by mica from the copper strip permitted measurements at elevated temperatures. The light emission was studied under vacuum to prevent water condensation at low temperatures. The light was guided by a Lucite rod to an RCA 5819 photomultiplier tube. The spectral response of the photomultiplier was calibrated against a thermopile by using a prism monochromator. The relative sensitivity curve of the photomultiplier is shown in Fig. 2 (curve S). Its maximum sensitivity was

$$S_{\max}=14{,}900\ \mu\text{amp}/\mu\text{watt}$$

for a wavelength of 4800A. In Fig. 2 the transmissivities (e.g., curves T_1, T_2) are shown for various Corning glass filters. These were inserted between crystal and photomultiplier in order to determine the spectral distribution of the emitted light. The bell-shaped curves are the differences between the transmissivities of two successive filters multiplied by the photomultiplier sensitivity, e.g., $W_{12}=S(T_1-T_2)$.

The following procedure was used to calculate the light intensity per unit wavelength from the photomultiplier readings. Let the reading with filter 1 inserted be I_1, and with a filter 2 be I_2. The average light energy per unit wavelength in the range of W_{12} is then

$$E_\lambda=\left[(I_1-I_2)\Big/\int S(T_1-T_2)d\lambda\right]\cdot f/S_{\max}. \qquad (1)$$

(f is a numerical factor of the order of 10 resulting from the geometry of the optical arrangement). The application of Eq. (1) is justifiable if E_λ does not change much over the range of the integration. E_λ is the spectral density of the emitted light at the value of λ which halves the area of W_{12}. The values of λ so chosen for each of the bell-shaped curves are indicated by dotted lines in Fig. 2.

TABLE I. "Efficiency" and threshold current for three temperatures. The "efficiency" is defined as the ratio of the photomultiplier current to the crystal current in excess of the threshold current.

Temperature	25°C	−45°C	−150°C
"Efficiency"	0.45×10^{-3}	1.0×10^{-3}	2.5×10^{-3}
Threshold current for light emission from the crystal	325 μa	190 μa	40 μa

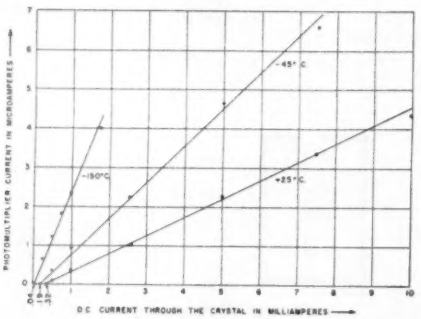

FIG. 3. Photomultiplier current as a function of the crystal current for various temperatures. The photomultiplier current is proportional to the intensity of the light emitted from the crystal.

The silicon carbide crystals obtained through the courtesy of the Carborundum Company were grown in a commercial pile. The crystals used were bluish in color and had a surface oxide layer which was removed by etching with hydrofluoric acid.[8] Emitting areas were found by placing the crystal on a brass plate and probing the surface with a point contact 22 volts negative with respect to the plate. The crystals passed currents of the order of 10 ma at this voltage. Suitable crystals were silvered by evaporation and then mounted on the brass plate with silver solder or silver paste. In some cases the base of the crystal was coated with zirconium by heating zirconium hydride in contact with the crystal in vacuum. Silver soldering to the zirconium layer is possible.[9]

[8] H. G. Heine and P. Scherrer, Helv. Phys. Acta 13, 489 (1940).
[9] C. S. Pearsall and T. K. Zingeser, *Metal to Non-Metallic Brazing* (Research Laboratory of Electronics, M.I.T., April 5, 1949), Technical Report 104 (unpublished).

III. EXPERIMENTAL RESULTS

In this paragraph observations on a particular crystal are described. The light intensity varies approximately linearly with current above a certain threshold current (see Fig. 3). Values of the threshold current and of the "efficiency" (defined as the ratio of the photomultiplier current to the crystal current in excess of the threshold current) are listed in Table I for three temperatures. "Efficiency" of the light emission is not very sensitive to change in temperature. Shift in "efficiency" with temperature is due in part to a change in the spectral distribution of the emitted light. This has to be taken into account along with the sensitivity of the photomultiplier to obtain the absolute efficiency. No light was emitted from this particular crystal upon reversal of current.

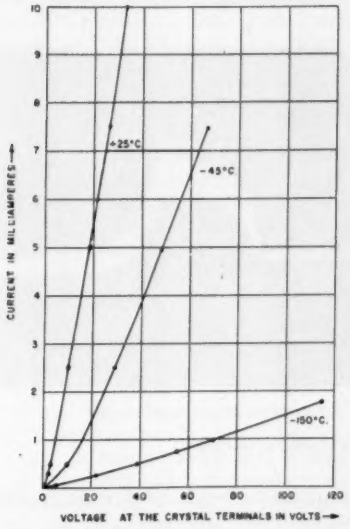

FIG. 4. Current-voltage characteristic at various temperatures.

The curves of Fig. 3 may be translated into curves giving the photomultiplier current as a function of the voltage applied to the crystal by means of the current-voltage characteristic given in Fig. 4. The choice of current as the independent variable in Fig. 3 was made for the following reason. The voltage measured between the electrode of the crystal is the sum of the voltage drops at various parts of the crystal and the electrode contacts. The light emission occurred around the cats-whisker contact in a zone of about 1 mm diameter and of limited depths. Thus the voltage at the light emitting layer was only a fraction of the voltage between the electrodes, whereas the current given in Fig. 3 was actually flowing through the light emitting layer.

The spectral distribution of the emitted light was investigated with filters, as described previously. Figure

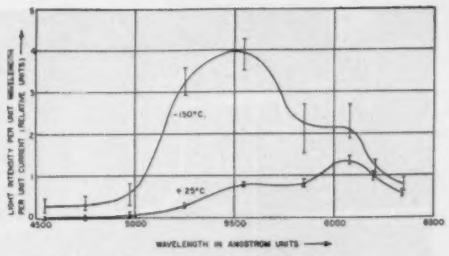

FIG. 5. Light intensity per unit wavelength per unit current as a function of wavelength at 25°C and −150°C. The spread of the values obtained for various currents is indicated in the figure.

5 shows the spectral distribution at room temperature and −150°C. Each curve is the average of about 5 measurements at various current densities. Most of the light emission at room temperature occurs between 5000A and 6500A with a maximum at 6100A. At −150°C, there is a maximum at about 5500A. On the basis of the multiplier sensitivity, an efficiency at room temperature of 10^{-6} light quanta emitted per electron passing was calculated for this particular crystal.

It should be pointed out that the spectral emission curves may vary to a certain extent from crystal to crystal. This was to be expected, since the light comes from zones of various depths and is therefore subject to the filter action of silicon carbide layers of various thicknesses. Also, the transparency of the crystals was influenced by their particular impurity content.

Figure 6 shows the difference between the multiplier currents for two consecutive filters divided by the read-

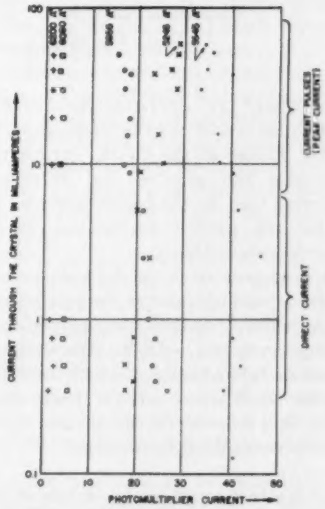

FIG. 6. Light emission in a given wavelength range as function of the current through the crystal.

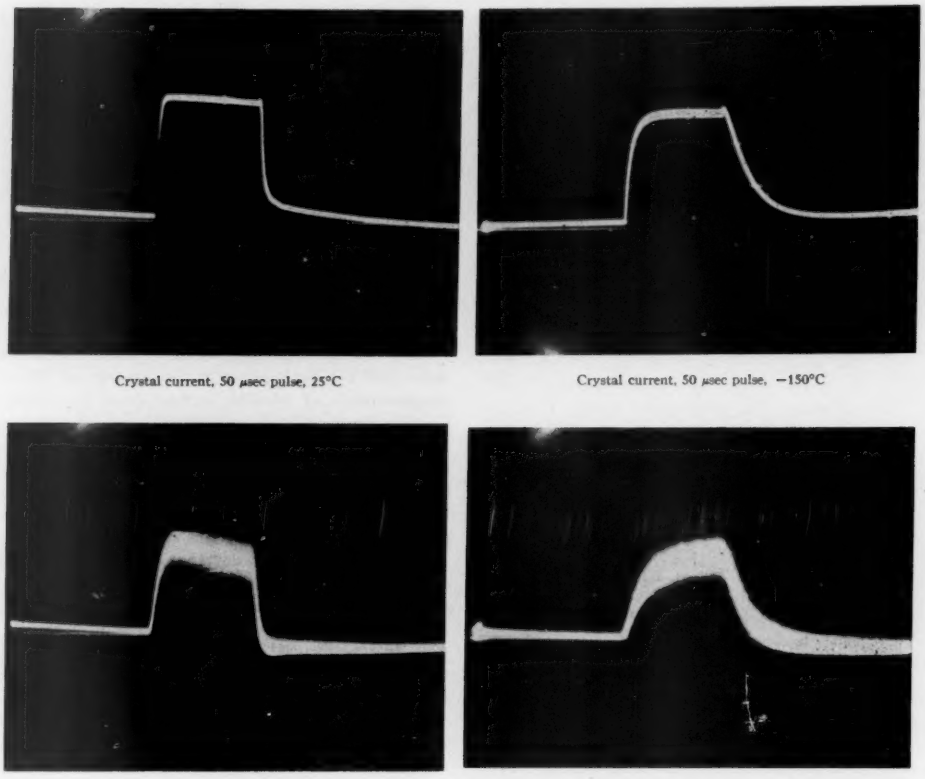
Crystal current, 50 μsec pulse, 25°C
Crystal current, 50 μsec pulse, −150°C
Photomultiplier current, 25°C
Photomultiplier current, −150°C

FIG. 7. Light response of silicon carbide to an applied current pulse.

ing without filter,[10] $(I_1-I_2)/I_0$, as a function of the current through the crystal at room temperature. In order to decrease heating of the crystal, current pulses of repetition rate 200 cycles/sec and 50 microseconds duration were used at the higher currents. Figure 6 shows that the spectral distribution changes only slightly with current density.

Figure 7 compares the wave shape of a current pulse through the crystal with that of the emitted light pulse showing high fidelity up to the megacycle range at both room temperature and −150°C. The features of the silicon carbide light emission which are most promising for possible applications are the linear dependence of emitted light intensity on current, and the high frequency response of the light emission.

[10] I_0 is taken to be 10 percent less than the value of the intensity measured in the absence of a filter. This correction is introduced to take into account the reflection losses present with a filter inserted.

IV. ON THE MECHANISM OF THE LIGHT EMISSION

In the early literature the light emission was related to the presence of an "active layer" on the surface of the crystal. Lossew removed the "active layer" by grinding and measured the resistance between two probes placed on the surface at various intermediate stages of the grinding process.[6] The resistance was found to increase by several orders of magnitude with progressive removal of material and then to drop sharply after 12 microns had been removed. Probing the potential distribution while current was passing from the surface into the crystal showed the presence of a rectifying junction at the boundary of the active layer and the bulk silicon carbide. Yellow light emission occurs when the current passes through the boundary in the forward direction. In a later paper[11] it is mentioned that the active layer consists of an *N*-type layer, whereas the bulk consists of *P*-type material.

[11] O. Lossew, Compt. rend. acad. sci. U.R.S.S. **29**, 363 (1940).

We have investigated the potential distribution over the surface of a crystal in the neighborhood of a "catwhisker" passing current both in the blocking and the forward directions. When the "catwhisker' was made negative, light was emitted from a well-defined area around it. This polarity characterized the forward direction of the current flow. No pronounced inhomogeneity of the potential distribution was found at the boundaries of the light emitting area with the current flowing in the forward direction. When the direction of current was reversed ("catwhisker" positive), the yellow light emission disappeared. However, there was a pronounced potential drop along a certain line. This line was found to coincide with the boundary of the light emitting zone when current passed in the forward direction. The observed potential distribution can be explained by assuming the bulk of the crystal to be P-type with an N-type surface layer. When current passes in the blocking direction, the N-type layer is separated by a highly blocking $P-N$ barrier from the bulk of the crystal and acts therefore like an equipotential electrode.

On some crystals it was observed that the yellow light emission did not occur from a well-defined area around the point contact, but rather from a small region in which the intensity decreased with increasing distance from the point. This may be ascribed to a rather low conductivity in the N-type layer. It may be, however, that the light emission is not connected with a $P-N$ barrier in some of these cases but rather with a metal-semiconductor barrier. In all cases, the yellow light emission was observed with current passing in the forward direction.

The light emission has been attributed to the bremsstrahlung of electrons.[12,13] This theory does not explain the fact that the spectral distribution is nearly independent of the applied field strength. We propose that the light is emitted as a result of recombination of carriers injected across barrier layer by a voltage in the forward direction (Fig. 8). Figure 8 shows the energy level diagram of a $P-N$ type boundary. On one side of the barrier, conduction is due predominantly to electrons, on the other, conduction is due predominantly to holes. A voltage applied to the barrier layer in the forward direction drives both the electrons and the holes toward the barrier and at the same time lowers the height of the barrier. This may lead to an injection of electrons and holes across the barrier as is known from studies of the transistor effect.[14] The injected carriers (holes in the N-type part, electrons in the P-type part) disappear with increasing distance from the barrier due to recombination. In the recombination process an amount of energy equal to the width of the forbidden band of the silicon carbide is released.[15] This energy can be either emitted as light or dissipated as heat (lattice vibration). We have no detailed knowledge whether the recombination process leading to light emission in silicon carbide takes place at impurities (activators), lattice defects, or at the surface. The emission band of the silicon carbide is located at a slightly longer wavelength than the absorption edge ($\lambda_0=0.44$ micron at room temperature) of the silicon carbide lattice. Thus, the energy of the emitted light quanta is somewhat smaller than the forbidden band width, $hc/\lambda_0=3$ electron volts, of the silicon carbide lattice.

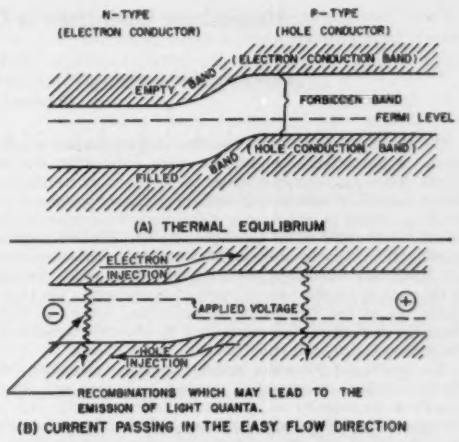

FIG. 8. Energy diagrams for a $P-N$ boundary. The recombination of electrons and holes that leads to light emission may occur at impurities (activators).

The luminescence from silicon carbide crystals under current flow as compared with that of phosphors under x-radiation, uv-radiation, or electron bombardment differs in the mechanism of the excitation process rather than of the emission process. Electrons in excited states are necessary for any case of light emission. In phosphors recombination takes place in the same locality where the electrons are excited. In the case of silicon carbide light emission, electrons are injected into the elevated energy states from distant parts of the crystal ("injected light emission"). This difference between phosphor light emission and injected light emission is analogous to that between photoconductivity and the increased conductivity due to carrier injection.

Acknowledgment is made to Dr. W. Ramm and Mr. J. Rothstein for valuable discussion, and to Mr. E. L. Geissinger for some of the preliminary measurements.

[12] O. Lossew, Physik Z. **32**, 695 (1931).
[13] B. Claus, Ann. Physik **11**, 331 (1931).
[14] For a review of the work on transistors see W. Shockley, *Electrons and Holes in Semiconductors* (D. Van Nostrand Company, Inc., New York, 1950).
[15] The forbidden band width may be identified with hc/λ_0 for structures of the diamond type, as has been proved for germanium and silicon from considerations of the optical absorption and intrinsic conduction.

PHYSICAL REVIEW VOLUME 83, NUMBER 3 AUGUST 1, 1951

Heisenberg Operators in Quantum Electrodynamics. II

F. J. DYSON
Department of Mathematical Physics, University of Birmingham, Birmingham, England
(Received March 29, 1951)

The equations of motion of quantum electrodynamics are set up in the interaction representation, using a formalism due to Gupta. A new representation, called the intermediate representation, is defined by constructing explicitly a unitary operator $S(t)$, which transforms the state-vector of the interaction representation into the state-vector of the new representation. The intermediate representation is intermediate in behavior between the interaction and Heisenberg representations. In it the low frequency changes in the state of a system are represented by changes in the state-vector, as in the interaction representation, while the high frequency fluctuations are represented by the time-variation of the field operators, as in the Heisenberg representation.

The program of this and a forthcoming paper is to prove that the intermediate representation provides a complete and divergence-free formulation of quantum electrodynamics, with a divergence-free Schrödinger equation which describes accurately the behavior of any physical system. In this paper the mathematical technique is developed which will enable the divergences to be eliminated from the Schrödinger equation. For simplicity, the technique is explained by applying it first to the analysis of the electromagnetic potential operators. The greater part of the paper is occupied with a proof that any fourier component of an electromagnetic potential operator in the intermediate representation is divergence-free after renormalizations have been consistently carried out. The cancellation of the divergences by appropriate compensating terms arising from $S(t)$ is an extremely intricate process, the success of which could not be foreseen without carrying through the calculations in detail.

In a final section, it is explained how Heisenberg operators are to be regarded as a special limiting case of intermediate representation operators. It follows from the preceding analysis, that averages over finite space-time regions of Heisenberg field operators in quantum electrodynamics are divergence-free after renormalization.

I. INTRODUCTION

ONE aim of this paper is to carry through in detail the renormalization program for Heisenberg operators in quantum electrodynamics, as promised in an earlier paper.[1] Since that paper was written, the scope of the whole investigation has been widened by considering instead of Heisenberg operators a more general class of operators, intermediate representation operators, of which the Heisenberg operators are a special limiting case. The physical meaning and purpose of the intermediate representation have been described in a separate publication,[2] in a qualitative way. The second aim of the present paper is to give an exact mathematical definition of the intermediate representation, and to show how a renormalization program can be consistently carried out in it. The greater part of the paper will be occupied with the proof that averages of certain intermediate representation operators over finite space-time regions are divergence-free after renormalization. At the end will be a discussion of the way in which Heisenberg operators can be obtained as limiting forms of intermediate representation operators, and this will complete the proof of the finiteness of Heisenberg operators. The second main step in the program described in RM, the proof that the Schrödinger equation in the intermediate representation is divergence-free, is left for later publication.

II. THE GUPTA FORMALISM

The starting point of the analysis is a formulation of quantum electrodynamics due to Gupta,[3] which differs from the usual formulation in the treatment of charge-renormalization. The Gupta formulation describes charge-renormalization from the beginning as a renormalization of the unit in which the electromagnetic field is measured, and not as a renormalization of the coupling constant e. In conforming correctly to the physical interpretation and logical structure of the theory, the point of view of Gupta has substantial advantages; it is therefore not surprising to find that the use of the Gupta formalism is also demanded in order to make the renormalization of intermediate representation operators mathematically manageable.

The idea of Gupta is to distinguish at the outset between the unrenormalized fields $\mathbf{F}_{\mu\nu}^*$, which appear in the field equations of electrodynamics in the Heisenberg representation, and the renormalized fields $\mathbf{F}_{\mu\nu}$, which are physically observable. Here, as always, heavy type is used for Heisenberg operators. The $\mathbf{F}_{\mu\nu}$ are defined by

$$\mathbf{F}_{\mu\nu}=\theta\mathbf{F}_{\mu\nu}^*, \quad \theta=(e/e_1), \tag{1}$$

where e is the unrenormalized electronic charge and e_1 the renormalized charge. The definitions of e and e_1 have been given elsewhere.[4]

The complete lagrangian density in quantum electrodynamics may be written, with the usual notations, as

$$L^*=-\tfrac{1}{4}\mathbf{F}_{\mu\nu}^*\mathbf{F}_{\mu\nu}^*-\tfrac{1}{2}(\partial\mathbf{A}_\mu^*/\partial x_\mu)^2+L_D +ie\mathbf{A}_\mu^*\bar{\boldsymbol{\psi}}\gamma_\mu\boldsymbol{\psi}+\delta mc^2\bar{\boldsymbol{\psi}}\boldsymbol{\psi}. \tag{2}$$

Here L_D is the lagrangian for a free Dirac field with the observed electronic rest-mass. The second term in

[1] F. J. Dyson, Phys. Rev. **82**, 428 (1951), referred to hereafter as HO.I (Heisenberg Operators. I.).
[2] F. J. Dyson, Proc. Roy. Soc. (London) A**207**, 395 (1951), referred to hereafter as RM (Renormalization Method).
[3] S. N. Gupta, Proc. Phys. Soc. (London) A**64**, 426 (1951). The author wishes to thank Dr. Gupta for letting him see this paper before publication; he is also greatly indebted to Mr. Abdus Salam, who first informed him that Gupta's formalism existed and would be effective in overcoming some serious difficulties which had arisen in the analysis.
[4] F. J. Dyson, Phys. Rev. **75**, 486 and 1736 (1949). These papers will be referred to as I and II.

L^* is zero according to the supplementary condition; it is inserted in order to obtain independent dynamical equations for the potentials $\mathbf{A}_\mu^*$, without changing the physical content of the theory.[5] Gupta proposes to use instead of L^* the lagrangian

$$L=L_0+L_1, \tag{3}$$

$$L_0=-\tfrac{1}{4}\mathbf{F}_{\mu\nu}\mathbf{F}_{\mu\nu}-\tfrac{1}{2}(\partial\mathbf{A}_\mu/\partial x_\mu)^2+L_D, \tag{4}$$

$$L_1=ie_1\mathbf{A}_\mu\bar{\psi}\gamma_\mu\psi+\delta mc^2\bar{\psi}\psi+\tfrac{1}{4}f\mathbf{F}_{\mu\nu}\mathbf{F}_{\mu\nu}, \tag{5}$$

$$f=1-\theta^{-2}. \tag{6}$$

Note that L is not exactly equal to L^* expressed in terms of renormalized fields and potentials. The inserted term, the second term in L_0, differs by a numerical factor from the second term in L^*. The difference in the inserted term, while not affecting the physical consequences of the formalism, causes a substantial difference in the mathematical details of calculations carried out with the two lagrangians.

In the usual treatment of electrodynamics,[6] the interaction representation is set up as follows. The interaction representation potentials A_μ, ψ are operators satisfying field equations derived from the free-field lagrangian L_0. The operators $\mathbf{A}_\mu^*$ and ψ are related to A_μ and ψ by a contact transformation

$$\mathbf{A}_\mu^*=(S^*)^{-1}A_\mu S^*, \quad \psi=(S^*)^{-1}\psi S^*, \tag{7}$$

because both sets of operators satisfy the same canonical commutation relations. An equation of motion for S^* is derived, by means of which S^* can be expressed explicitly in terms of interaction representation operators.

In the Gupta formalism the interaction representation is introduced by finding a unitary operator S directly relating the renormalized potentials $\mathbf{A}_\mu$ to the free-field potentials A_μ, thus:[7]

$$\mathbf{A}_\mu=S^{-1}A_\mu S, \quad \psi=S^{-1}\psi S. \tag{8}$$

The equation of motion for S is found to be

$$ih(\partial S/\partial t)=H_1S, \tag{9}$$

$$H_1=H_1(t)=\int H^I(x)d_3x, \tag{10}$$

$$H^I(x)=H_i(x)+H_s(x)+H_p(x), \tag{11}$$

$$H_i(x)=-ie_1A_\mu(x)\bar{\psi}(x)\gamma_\mu\psi(x), \tag{12}$$

$$H_s(x)=-\delta mc^2\bar{\psi}(x)\psi(x), \tag{13}$$

$$H_p(x)=-\tfrac{1}{4}fF_{\mu\nu}(x)F_{\mu\nu}(x)-\tfrac{1}{2}\theta^2f^2F_{\mu4}(x)F_{\mu4}(x). \tag{14}$$

Equation (9) can be formally integrated, and then Eq. (8) gives the series expansions of renormalized Heisenberg operators directly in terms of interaction representation operators. Thus, one obtains

$$\mathbf{A}_\mu(x)=\sum_{n=0}^{\infty}\left(\frac{i}{hc}\right)^n\int_{-\infty}^{t}dx_1\int_{-\infty}^{t_1}dx_2\cdots\int_{-\infty}^{t_{n-1}}dx_n \times[H^I(x_n),[\cdots[H^I(x_1),A_\mu(x)]\cdots]]. \tag{15}$$

The extra term (14) in the interaction hamiltonian compensates exactly all charge-renormalization effects produced by the radiation interaction (12). Accordingly, the operator (15) will be found to be divergence-free as it stands, without any further renormalization of the unit of potential. Just for this reason, the Gupta formalism is the appropriate one to use for a proof of finiteness of Heisenberg operators.

III. THE INTERMEDIATE REPRESENTATION

Let $g(a)$ be a function of the real variable a, defined for $a\geq 0$, with the following properties:

$$g(a)=\int_0^\infty G(\Gamma)e^{-c\Gamma a}d\Gamma, \tag{16}$$

where $G(\Gamma)$ is a function of the real variable Γ, the integral $\int_0^\infty|G(\Gamma)|d\Gamma$ being finite, so that Eq. (16) is uniformly convergent for all $a\geq 0$:

$$g(0)=\int_0^\infty G(\Gamma)d\Gamma=1, \tag{17}$$

$$g'(0)=-c\int_0^\infty \Gamma G(\Gamma)d\Gamma=0, \tag{18}$$

$$g(a)\to 0 \quad \text{as} \quad a\to\infty. \tag{19}$$

The convergence (19) is supposed sufficiently rapid, so that all integrations in which $g(a)$ appears as a factor will be convergent at infinity. The function $G(\Gamma)$ is allowed to have singularities at most of a simple δ-function character at a set of discrete values of Γ.

Let the interaction $H^I(x)=H^I(x, e_1)$ given by Eq. (11) be written explicitly as a function of the true electronic charge e_1. According to Eq. (104) of II, $(\delta m/m)$ is a power series in e_1, with coefficients which are divergent integrals formally independent of e_1. Also,

$$f=[(e^2-e_1^2)/e^2], \quad \theta^2f^2=[(e^2-e_1^2)^2/e^2e_1^2] \tag{20}$$

may be written as power series of the same kind, in virtue of Eq. (105) of II. Let x' be any space-time point with time-coordinate t' not later than t, the time-coordinate of x. Then the operator H_g^0, a function of the two points x' and x, is defined by

$$H_g^0(x, x')=H^I(x', e_1g(t-t')) =H_{gi}+H_{gs}+H_{gp}, \tag{21}$$

[5] Following E. Fermi, Revs. Modern Phys. 4, 87 (1932). See also G. Wentzel, *Einführung in die Quantentheorie der Wellenfelder* (F. Deuticke, Wien, 1943), p. 112.

[6] J. Schwinger, Phys. Rev. 74, 1439 (1948).

[7] It may appear at first sight paradoxical that the operators $\mathbf{A}_\mu^*$ and $\mathbf{A}_\mu$ should both satisfy the same canonical commutation relations, since they differ essentially by a factor not equal to unity. The commutation relations between the $\mathbf{A}_\mu$ and their derivatives $(\partial\mathbf{A}_\mu/\partial t)$ are not the same as the corresponding commutators of $\mathbf{A}_\mu^*$ with $(\partial\mathbf{A}_\mu^*/\partial t)$. The solution of the paradox is that the momenta conjugate to $\mathbf{A}_\mu^*$ and $\mathbf{A}_\mu$ in the two formalisms are different functions of the time-derivatives.

$$H_{\varrho 1}=-ie_1 g(t-t')A_\mu\bar{\psi}\gamma_\mu\psi(x'), \tag{22}$$

$$H_{\varrho 2}=-\delta_\varrho mc^2\bar{\psi}\psi(x'), \tag{23}$$

$$H_{\varrho 3}=-\tfrac{1}{4}f_\varrho F_{\mu\nu}F_{\mu\nu}(x')-\tfrac{1}{2}\theta_\varrho^2 f_\varrho^2 F_{\mu 4}F_{\mu 4}(x'). \tag{24}$$

Writing explicitly the expansions of the coefficients,

$$\delta_\varrho=\sum_{d=2}^{\infty}A_d[e_1 g(t-t')]^d, \tag{25}$$

$$f_\varrho=\sum_{d=2}^{\infty}B_d[e_1 g(t-t')]^d, \tag{26}$$

$$\theta_\varrho^2=[1-f_\varrho]^{-1}. \tag{27}$$

Up to this point, $H_\varrho^0(x, x')$ is identical, apart from notations, with the $H_\varrho(t, t')$ described in RM. However, as was already remarked in RM, the correct definition of $H_\varrho(x, x')$ contains additional terms

$$H_\varrho(x, x')=H_\varrho^0(x, x')+H_{\varrho a}(x, x')+H_{\varrho b}(x, x'), \tag{28}$$

where $H_{\varrho a}$ is of the form of a transient photon self-energy appearing only while $g(t-t')$ is varying. The precise definitions of $H_{\varrho a}$ and $H_{\varrho b}$ are

$$H_{\varrho a}=-\frac{1}{2c^2}\left[\frac{d}{dt}\left(\frac{g'}{g}(t-t')f_\varrho\right)-\left(\frac{g'}{g}(t-t')\right)^2 f_\varrho\right]A_j A_j(x'), \tag{29}$$

$$H_{\varrho b}=-\frac{i}{c}\left[\frac{g'}{g}(t-t')f_\varrho\right]A_4(x')\left(\frac{\partial}{\partial x_j'}\right)A_j(x'). \tag{30}$$

In Eqs. (29) and (30) the index j is summed over the values 1, 2, 3 only.

The intermediate representation is set up by constructing the operator $U(t, t')$, which satisfies the initial condition,

$$U(t, -\infty)=I, \tag{31}$$

and the differential equation for $t'\leq t$,

$$ih(\partial U(t, t')/\partial t')=\left[\int H_\varrho(x, x')d_3x'\right]U(t, t'). \tag{32}$$

Let $\Psi(t)$ be the state-vector of the interaction representation. Then the state-vector of the intermediate representation is $\Phi(t)$, where

$$\Psi(t)=S(t)\Phi(t) \tag{33}$$

and

$$S(t)=U(t, t). \tag{34}$$

By Eqs. (31) and (32), $S(t)$ has the formal expansion

$$S(t)=\sum_{n=0}^{\infty}\frac{1}{n!}\left(\frac{-i}{hc}\right)^n\int_{-\infty}^{t}dx_1\cdots\int_{-\infty}^{t}dx_n \times P(H_\varrho(x, x_1), H_\varrho(x, x_2), \cdots, H_\varrho(x, x_n)), \tag{35}$$

the P representing a chronological product as defined in I, and the fourfold integrals dx_r extending over the whole of space-time previous to the time t. Note that the operator factors in $H_\varrho(x, x_m)$ refer to the point x_m and not to the point x, so that the chronological ordering is with respect to x_m.

The meaning of $S(t)$ has been explained in some detail in RM. A formal proof will now be given of the statement made there that

$$S(t)=\exp[iH_0t/\hbar]S\exp[-iH_0t/\hbar], \tag{36}$$

where H_0 is the hamiltonian of the noninteracting fields and S is a time-independent operator. Imagine each operator $H_\varrho(x, x_m)$ to be expanded as a sum of products Π_m of particle emission and absorption operators multiplied by appropriate exponential factors representing plane waves in the variable x_m. Then $S(t)$ is a sum of terms each having a structure similar to

$$A\int_{-\infty}^{t}dt_1\int_{-\infty}^{t_1}dt_2\cdots\int_{-\infty}^{t_{n-1}}dt_n[(g(t-t_1))^{a_1}\cdots(g(t-t_n))^{a_n}] \times[\Pi_1\exp(-it_1\Delta E_1/\hbar)]\cdots[\Pi_n\exp(-it_n\Delta E_n/\hbar)] =AJ[\Pi_1\Pi_2\cdots\Pi_n]\exp[-it(\Delta E_1+\cdots+\Delta E_n)/\hbar], \tag{37}$$

where J is an absolutely convergent integral over the variables $(t-t_1)$, $\cdots$, $(t-t_n)$, and is independent of t. Since ΔE_m is just the energy difference between initial and final states in a transition effected by the operator Π_m, Eq. (37) may be written

$$\exp[iH_0t/\hbar]\{AJ\Pi_1\cdots\Pi_n\}\exp[-iH_0t/\hbar]. \tag{38}$$

Since $S(t)$ is a sum of terms (38), it is of the form (36) as required. It is important that this argument fails completely in the limiting case $g(t-t')=1$, when $S(t)$ becomes the transformation function leading from the interaction to the Heisenberg representation. In that case the integrals J diverge whenever real energy-conserving processes are occurring, and $S(t)$ depends on t in a much more complicated way than is indicated by Eq. (36).

The electromagnetic potentials in the intermediate representation are given by

$$A_{\mu\varrho}(x)=S^{-1}(t)A_\mu(x)S(t), \tag{39}$$

and other intermediate representation operators are defined similarly. As in HO.I, averages of such operators over finite space-time regions are the primary object of study. These averages are linear superpositions of fourier-transformed operators such as

$$A_{\mu\varrho}(p)=(2\pi)^{-4}\int A_{\mu\varrho}(x)\exp(-ip\cdot x)dx. \tag{40}$$

The main program of the present paper is to prove that $A_{\mu\varrho}(p)$ is free of divergences. This will be accomplished in Secs. IV–X. A similar analysis can be applied to the matter-field operator $\psi_\varrho(p)$ or to the current-operator

$j_{\mu\varrho}(p)$, leading to results which are discussed in Sec. XI. It is found that $\psi_\varrho(p)$ is a divergence-free expression multiplied by a constant divergent renormalization factor. In general, $j_{\mu\varrho}(p)$ does not have a similar property; only in the limit, as the intermediate representation tends to the Heisenberg representation, does $j_{\mu\varrho}(p)$ become divergence-free after renormalization.

IV. GRAPHICAL REPRESENTATION OF OPERATORS

Let $A_{\mu\varrho}(p)$ be expanded into its normal constituents according to the rules given in Sec. II of HO.I. As in Sec. IV of HO.I, let M be the coefficient in the expansion multiplying a particular normal product

$$N(\bar{\psi}_\alpha(p_1)\cdots\psi_\beta(p_i)\cdots A_\lambda(p_j)\cdots A_\nu(p_l)). \quad (41)$$

The objective of Secs. IV–V is to obtain an expression for M in terms of integrals in momentum-space, making use of the results summarized in Sec. VIII of HO.I.

By the definitions (35), (39), and (40), one has

$$A_{\mu\varrho}(p)=\frac{1}{(2\pi)^4}\sum_{n=0}^{\infty}\frac{1}{n!}\left(\frac{i}{\hbar c}\right)^n\int_{-\infty}^{\infty}e^{-ip\cdot x}dx \times\int_{-\infty}^{\infty}dx_1\cdots\int_{-\infty}^{\infty}dx_n S_\varrho, \quad (42)$$

$$S_\varrho=\sum\theta(x-x_1)\theta(x_1-x_2)\cdots\theta(x_{n-1}-x_n) \times[H_\varrho(x,x_n),[\cdots[H_\varrho(x,x_1),A_\mu(x)]\cdots]], \quad (43)$$

the summation in Eq. (43) being over the $(n!)$ permutations of the points $x_1,\cdots,x_n$. Each of the factors $H_\varrho(x,x_i)$ in Eq. (43) is a sum of a great variety of terms, according to Eqs. (21)–(30). By a "term" here is meant either Eq. (22), or a single term of a particular order in e_1 chosen from one of the infinite series occurring in Eqs. (23), (24), (29), and (30). With this meaning of the word "term," let S_ϱ be split up into parts

$$S_\varrho=\sum_Z S_Z, \quad (44)$$

where

$$S_Z=\sum\theta(x-x_1)\cdots\theta(x_{n-1}-x_n) \times[Z_n(x,x_n),[\cdots[Z_1(x,x_1),A_\mu(x)]\cdots]]. \quad (45)$$

For each i, $Z_i(x,x_i)$ is a single term derived from $H_\varrho(x,x_i)$. The summation in Eq. (44) is over the possible ways of choosing one Z_i for every i. The summation in Eq. (45) is over the $(n!)$ permutations of the indices $1,\cdots,n$, the permutation being applied simultaneously to the indices of the Z_i and of the x_i.

Each Z_i consists of an operator Y_i referring to the point x_i, multiplied by a coefficient which contains e_1 raised to a certain power m_i. If Z_i is taken from Eqs. (22), (23), or (24), then one has

$$Z_i=Q_i[e_1g(t-t_i)]^{m_i}Y_i(x_i), \quad (46)$$

where Q_i is a numerical coefficient. If Z_i is taken from Eq. (30), then one has

$$Z_i=Q_ie_1^{m_i}(g'(t-t_i))(g(t-t_i))^{m_i-1}Y_i(x_i), \quad (47)$$

and if from Eq. (29),

$$Z_i=Q_ie_1^{m_i}[g''(t-t_i)g(t-t_i)+(m_i-2)(g'(t-t_i))^2] \times(g(t-t_i))^{m_i-2}Y_i(x_i). \quad (48)$$

Let

$$N=\sum m_i \quad (49)$$

be the degree of S_Z in e_1. Then, one obtains

$$S_Z=Q_Ze_1^N\Pi_\varrho S_Y, \quad (50)$$

$$S_Y=\sum\theta(x-x_1)\cdots\theta(x_{n-1}-x_n) \times[Y_n(x_n),[\cdots[Y_1(x_1),A_\mu(x)]\cdots]], \quad (51)$$

where Q_Z is the product of the Q_i, and Π_ϱ is the product of functions g, g', g'' occurring in Eqs. (46), (47), and (48).

Let the factors in Π_ϱ be expanded by means of the integral representation (16). Then, one obtains

$$\Pi_\varrho=\int_0^\infty G(\Gamma_{10})d\Gamma_{10}\cdots\int_0^\infty G(\Gamma_{N0})d\Gamma_{N0}E_\Gamma F_\Gamma. \quad (52)$$

Here E_Γ is a product of factors Γ_{j0} and Γ_{j0}^2 arising from the differentiations in Eqs. (47) and (48). If no terms of the form (47) or (48) occur in S_Z, then one has $E_\Gamma=1$. The last factor in Eq. (52) is

$$F_\Gamma=\exp[\Lambda_1\cdot(x-x_1)+\cdots+\Lambda_n\cdot(x-x_n)], \quad (53)$$

arising from the exponential factors in Eq. (16). As in Sec. IV of HO.I, each Γ_{j0} is regarded as the fourth component of a vector

$$\Gamma_j=(0,0,0,\Gamma_{j0}), \quad (54)$$

and each Λ_i is a sum of m_i vectors Γ_j arising from the m_i factors g, g', g'' in Z_i.

Summarizing the results of the analysis so far,

$$A_{\mu\varrho}(p)=\frac{1}{(2\pi)^4}\sum_{n=0}^{\infty}\left(\frac{i}{\hbar c}\right)^n\sum_Z Q_Ze_1^NJ_Z, \quad (55)$$

$$J_Z=\int_0^\infty G(\Gamma_{10})d\Gamma_{10}\cdots\int_0^\infty G(\Gamma_{N0})d\Gamma_{N0}E_\Gamma I_n(\Lambda,p), \quad (56)$$

$$I_n(\Lambda,p)=\frac{1}{n!}\int_{-\infty}^{\infty}dx\int_{-\infty}^{\infty}dx_1\cdots\int_{-\infty}^{\infty}dx_n e^{-ip\cdot x}F_\Gamma S_Y. \quad (57)$$

This $I_n(\Lambda,p)$ is of precisely the same form as the $I_n(\Gamma,p)$ defined in Sec. IV of HO.I, bearing in mind the remarks at the end of Sec. III of HO.I. There is only the important difference that the exponential damping factors (53) now appear naturally instead of being arbitrarily inserted. The results of HO.I are now directly applicable to the evaluation of $A_{\mu\varrho}(p)$.

The normal constituents of the multiple commutator S_Y will be enumerated by means of Feynman graphs G

with $(n+1)$ vertices $x, x_1, \cdots, x_n$. These graphs are slightly different from those which were used in HO.I and in earlier papers for two reasons. First, only a single operator A_μ acts at the point x, and therefore only a single photon line is incident at the vertex x of G. Second, the operators Y_i may be of six distinct forms, namely,

$$A_\mu\bar{\psi}\gamma_\mu\psi,\quad \bar{\psi}\psi,\quad F_{\mu\nu}F_{\mu\nu},\quad F_{\mu 4}F_{\mu 4},\quad A_iA_i,\quad A_4\,\mathrm{div}A_4. \tag{58}$$

The first two of these forms for Y_i occurred also in earlier calculations. The corresponding vertices x_i in G were, respectively, vertices with two electron lines and one photon line incident, and vertices with only two electron lines incident. Now, whenever Y_i has one of the last four forms (58), the corresponding vertex x_i is of a new type, having two photon lines and no electron line incident.

The coefficient M is a sum of contributions M_Z from the various terms in the sum (55). Each M_Z is a sum of contributions $M'(G)$ from the various graphs which represent possible factor pairings of S_T and which have the correct external lines to give rise to normal constituents with the operator factor (41). Each $M'(G)$ is further subdivided into contributions $M(G)$ with a particular association of each factor in (41) to one external line of G, so that each external line represents a particle carrying a certain definite momentum p_r.

In order to evaluate $M(G)$ by the methods of HO.I, it is not necessary to enumerate all the doubled graphs G_T derived from G. It is necessary only to choose arbitrarily one doubled graph, which will remain fixed throughout the subsequent discussion; the results are independent of which doubled graph is chosen. Therefore, the notation G_T may now be dropped, and G will denote either the original Feynman graph or the chosen doubled graph derived from it. The doubled lines in G form a "tree," which is connected and simply connected. Regarding the vertex x as the "root" of the tree, a unique "up" direction is fixed in every doubled line, namely, the direction pointing away from x. Every line of G has, independently of the doubling, an inherent direction which is supposed to be marked in it by an arrow. For each doubled line λ_j, there is defined the index η_j which takes the value ± 1 according as the arrow in λ_j points down or up. Further, for each λ_j there is defined the vector Δ_j, which is the sum of the Λ_i corresponding to all the vertices x_i on that part of the tree which is "above" λ_j. This definition of Δ_j corresponds to Eq. (40) of HO.I.

V. MOMENTUM-SPACE INTEGRALS

By Eq. (56), $M(G)$ may be written in the form,

$$M(G)=\int_0^\infty G(\Gamma_{10})d\Gamma_{10}\cdots \times\int_0^\infty G(\Gamma_{N0})d\Gamma_{N0}E_\Gamma M(G,\Lambda). \tag{59}$$

The rules for expressing $M(G,\Lambda)$ as a momentum-space integral will now be formulated. Consider the corresponding coefficient $M^F(G)$, which is obtained from $M(G,\Lambda)$ by replacing the factors $F_\Gamma S_T$ in Eq. (57) by a chronological product

$$P(Y_1(x_1),\cdots,Y_n(x_n),A_\mu(x)) \tag{60}$$

simply. This $M^F(G)$ is a coefficient of the kind which arises in the evaluation of the S-matrix; it can immediately be expressed as a momentum-space integral by following the rules given in II. Certain complications, which arise from the presence of time-derivatives in the third and fourth of the operators (58), are here temporarily ignored and will be discussed in the following section. The form of the integral representation of $M^F(G)$ is

$$M^F(G)=A\int_{-\infty}^{\infty}dk_{n+1}\cdots\int_{-\infty}^{\infty}dk_b\Phi(k_{n+1},\cdots,k_b), \tag{61}$$

where A is a numerical coefficient and the integration is over the $(b-n)$ independent 4-vectors $k_{n+1},\cdots,k_b$, one corresponding to each undoubled internal line of G. The function Φ is a product of factors contributed by the various vertices and lines of G individually. An undoubled internal electron line contributes a factor

$$(k_{a\mu}\gamma_\mu-\mathrm{im})^{-1}. \tag{62}$$

An undoubled internal photon line contributes a factor

$$(k_a^2)^{-1}. \tag{63}$$

A doubled electron line λ_j contributes a factor

$$(l_{j\mu}\gamma_\mu-\mathrm{im})^{-1}, \tag{64}$$

where l_j is a certain linear combination of the vectors k_a and the external momenta p_r appearing in (41); in the notations of Sec. V of HO.I, we have

$$l_j=-\eta_j(q_j+u_j). \tag{65}$$

A doubled photon line λ_j contributes a factor

$$(l_j^2)^{-1}. \tag{66}$$

Each external line contributes a certain constant spinor or polarization vector. Each vertex at which the first type of interaction (58) is operating contributes a factor γ_μ. All the factors so far enumerated occur exactly as described in the S-matrix analysis II. Finally, each vertex x_i at which the third or the sixth type of interaction (58) is operating contributes a factor

$$(q^2\delta_{\alpha\beta}-q_\alpha q_\beta)\quad\text{or}\quad(\delta_{\alpha 4}q_\beta-\delta_{\beta 4}q_\alpha), \tag{67}$$

respectively, where q is the momentum vector belonging to both of the photon lines incident at x_i. In the following section it will be shown that the correct treatment of any graphs involving the fourth interaction (58) is to omit them entirely in the calculation of $M^F(G)$. Therefore, Φ is a product of factors (62), (63),

(64), (66), (67), apart from numerical coefficients. The integration in Eq. (61) is to be taken in the usual Feynman sense, i.e., to each of the factors in the denominator of Φ is added a small negative imaginary term $-i\epsilon$, which is made to tend to zero after the integration is performed.

The integral representation for $M(G, \Lambda)$ is obtained from Eq. (61) by making the following three changes. First, the factors (63) and (66) are changed to

$$(k_a^2+\lambda^2)^{-1}, \quad (l_j^2+\lambda^2)^{-1}, \tag{68}$$

where λ is a fictitious photon mass. Second, each vector l_j in (64) and (66) is changed to

$$R_j=l_j+i\eta_j\Delta_j; \quad j=1, \cdots, n. \tag{69}$$

Third, if x_i is a vertex at which the third or the sixth type of interaction (58) is operating, then the two photon lines incident at x_i both carry the same momentum q, and the vertex gives rise to a factor (67) in $M^F(G)$. The factor (67) is now to be written

$$(q'\cdot q''\delta_{\alpha\beta}-q_\beta' q_\alpha'') \quad \text{or} \quad (\delta_{\alpha 4}q_\beta''-\delta_{\beta 4}q_\alpha'), \tag{70}$$

where q' is the momentum vector carried by one of the two lines and q'' is carried by the other. Actually, it is true that $q'=q''=q$; but it is necessary to distinguish formally between q' and q'' in order to specify the third change to be made in Eq. (61) as follows. If q' belongs to a doubled line λ_j so that $q'=l_j$, then q' is to be replaced in Eq. (70) by R_j; if q' belongs to an undoubled line or to an external line, then q' is left unchanged; and similarly for q''.

It is convenient to write

$$R_a=k_a; \quad a=n+1, \cdots, b. \tag{71}$$

Then the integral $M(G, \Lambda)$ becomes

$$M(G, \Lambda)=A\int_{-\infty}^{\infty} dk_{n+1}\cdots\int_{-\infty}^{\infty} dk_b\Phi_\Delta(k_{n+1}, \cdots, k_b), \tag{72}$$

where Φ_Δ is a product containing a factor

$$(R_{s\mu}\gamma_\mu-\text{im})^{-1} \tag{73}$$

for every internal electron line of G, doubled or undoubled, and a factor

$$(R_s^2+\lambda^2)^{-1} \tag{74}$$

for every internal photon line. Also, Φ_Δ contains factors

$$(R_r\cdot R_s\delta_{\alpha\beta}-R_{r\beta}R_{s\alpha}), \tag{75}$$

$$(\delta_{\alpha 4}R_{s\beta}-\delta_{\beta 4}R_{r\alpha}), \tag{76}$$

arising from vertices at which two internal photon lines are incident. The integration in Eq. (72) is defined in the following way. First, the integral is to be evaluated as a Feynman integral, like Eq. (61), with the quantities $(i\Delta_j)$ treated as real numbers and the masses m and λ treated as positive and very large. The result is an analytic function E of m, λ, and the Δ_j. Then, while m and λ are kept large and positive, the Δ_j are continuously varied from imaginary to positive real values; next, while the Δ_j are kept real and positive, m and λ are decreased through real values continuously from their fictitious large values to the physical value of m and the value $\lambda=0$. During these successive variations the function E remains analytic, and the analytic continuation of E obtained in this way defines $M(G, \Lambda)$ for the values of m and Δ_j which are physically of interest.

To summarize the results of this section, the coefficient M is a sum of terms $M(G)$ given by Eq. (59), where $M(G, \Lambda)$ is an integral of the form (72). To evaluate $M(G, \Lambda)$ the analytic continuation method of HO.I is in general required, but it should be remarked that in practice the process of analytic continuation is usually trivial. The evaluation of Eq. (72), treated as a Feynman integral, can be carried out by using the well-known methods of Feynman,[8] leading to an explicit analytic formula. The analytic continuation then consists merely in substituting the physical values of m and the Γ_i into this analytic formula.

VI. DISCUSSION OF DERIVATIVE INTERACTIONS

The Gupta formalism introduces into the interaction lagrangian the term

$$T_1=\tfrac{1}{4}fF_{\mu\nu}(x)F_{\mu\nu}(x), \tag{77}$$

containing time-derivatives of the potentials. This term appears in the interaction hamiltonian together with a supplementary term T_2, given by Eq. (14). T_2 is the familiar "normal-dependent" term which always appears in the interaction hamiltonian in theories with interactions involving derivatives.[9] It is well-known[10] that when the S-matrix is calculated in such theories, the effects of T_2 are always exactly cancelled by certain singular expressions arising from the higher order effects of T_1. In fact, the correct procedure in calculating the S-matrix is to ignore T_2 entirely, at the same time using the simple rules of Feynman to represent the effects of T_1 as integrals in momentum-space, since these rules omit just the singular expressions arising from T_1. Gupta[3] has pointed out that such a procedure can easily be justified in the case of his formalism.

It is generally true that an exactly similar procedure is correct for the calculation of Heisenberg operators or of intermediate representation operators by the methods of HO.I, in all theories with derivative interactions. This will now be demonstrated for the special case of the Gupta formalism.

---

[8] R. P. Feynman, Phys. Rev. **76**, 769 (1949), Appendix.
[9] S. Tomonaga and S. Kanesawa, Prog. Theor. Phys. **3**, 1 and 101 (1948).
[10] P. T. Matthews, Phys. Rev. **76**, 684 (1949).

By Eq. (27), the interaction (24) may be written

$$H_{gp}=H_{gm}+H_{ge}, \tag{78}$$

$$H_{gm}=-\tfrac{1}{4}f_g F_{ij}(x')F_{ij}(x'), \tag{79}$$

$$H_{ge}=-\tfrac{1}{2}f_{4g}F_{\mu 4}(x')F_{\mu 4}(x'), \tag{80}$$

where

$$f_{4g}=[f_g/(1-f_g)]. \tag{81}$$

The term H_{gm} involves only the space-derivatives of the potentials, and gives rise to no singular expressions. Therefore, only H_{ge} need be further discussed. Consider the evaluation of any coefficient $M(G, \Lambda)$ derived from a graph G containing a vertex x_1 at which H_{ge} is operating. Let λ_j and λ_k be the two photon lines incident at x_1. If the ends of λ_j and λ_k remote from x_1 are vertices at which the interactions H_{gi}, H_{gm}, H_{ga}, or H_{gb} are operating, then the operator $H_{ge}(x_1)$ introduces into $M(G, \Lambda)$ only the first time-derivatives of D-functions. Just as in the calculation of the S-matrix, these first derivatives give rise to no singular expressions. Singular expressions will be obtained only when a line λ_j joins two vertices x_1, x_2 at both of which H_{ge} is operating.

In order to determine the nature of the singular expressions, it is necessary to return temporarily to the analysis in Sec. IV of HO.I, where $M(G, \Lambda)$ is expressed as a sum of contributions $M(G_T, \Lambda)$ from all the doubled graphs G_T derived from G. Suppose first that G_T is a doubled graph in which λ_j is an undoubled line. Then λ_j contributes to $M(G_T, \Lambda)$ a factor

$$D(x_1-x_2) \quad \text{or} \quad D^1(x_1-x_2). \tag{82}$$

The derivatives at x_1 and x_2 operate directly on the factor (82), introducing a second time-derivative of (82); but, since no θ-function or ϵ-function is associated with (82), the second time-derivative can be represented by a momentum-space integral of the usual simple form, and no singular term is left over. The singular expressions are obtained only when λ_j is a doubled line.

Suppose now that λ_j is doubled, and write down explicitly the factors in $M(G_T, \Lambda)$ arising from the vertices x_1, x_2 and the line λ_j. These factors are, according to (44) of HO.I,

$$F(\lambda_j)=F_{\mu 4}(x_1)F_{\nu 4}(x_2)\theta(x_1-x_2)\exp(\Delta_j\cdot(x_1-x_2)) \times[\{\delta_{\mu\alpha}(\partial/\partial x_{14})-\delta_{4\alpha}(\partial/\partial x_{1\mu})\}\{\delta_{\nu\beta}(\partial/\partial x_{24}) -\delta_{4\beta}(\partial/\partial x_{2\nu})\}\delta_{\alpha\beta}D(x_1-x_2)]. \tag{83}$$

The part of $F(\lambda_j)$ containing second time-derivatives is

$$-F_{\mu 4}(x_1)F_{\mu 4}(x_2)\theta(x_1-x_2)\exp(\Delta_j\cdot(x_1-x_2)) \times[(\partial^2/\partial x_{14}{}^2)D(x_1-x_2)]. \tag{84}$$

The usual momentum space integral formula for $M(G_T, \Lambda)$ is obtained if one replaces (84) in $F(\lambda_j)$ by

$$-F_{\mu 4}(x_1)F_{\mu 4}(x_2)\exp(\Delta_j\cdot(x_1-x_2)) \times(\partial^2/\partial x_{14}{}^2)(\theta(x_1-x_2)D(x_1-x_2))]. \tag{85}$$

Therefore, the additional singular contribution to $M(G_T, \Lambda)$ is obtained if one replaces $F(\lambda_j)$ by the difference between (84) and (85), which after an integration by parts is

$$F_s(\lambda_j)=F_{\mu 4}(x_1)F_{\mu 4}(x_2)\exp(\Delta_j\cdot(x_1-x_2)) \times[(\partial/\partial x_{14})\theta(x_1-x_2)][(\partial/\partial x_{14})D(x_1-x_2)] \tag{86}$$

$$=F_{\mu 4}(x_1)F_{\mu 4}(x_2)\delta(x_1-x_2). \tag{87}$$

The exponential factor has disappeared from Eq. (87); the δ denotes an ordinary 4-dimensional δ-function. In virtue of Eq. (87), the singular contribution to $M(G_T, \Lambda)$ from the line λ_j is equal to a multiple of $M(G_T', \Lambda)$, where G_T' is the doubled graph obtained from G_T by removing λ_j and replacing x_1 and x_2 by a single vertex at which H_{ge} is operating. The G_T' derived in this way is a correctly constructed doubled graph when λ_j is doubled in G_T, whereas if λ_j were not doubled, G_T' would not be simply connected and would not be admissable.

It is clear from the preceding analysis that the singular contribution to $M(G, \Lambda)$, obtained when two operators H_{ge} occur at adjacent vertices of G, is always a multiple of $M(G', \Lambda)$, where G' is the graph obtained from G by collapsing the two vertices into one. It can be proved by a more detailed calculation that the effect of these singular contributions from $M(G, \Lambda)$ is accurately reproduced, if $M(G', \Lambda)$ is calculated with the coefficient f_{4g}, appearing in H_{ge} according to Eq. (80), changed to the new value

$$f_{4g}-f_{4g}{}^2. \tag{88}$$

However, it may happen that G' itself still contains two adjacent vertices at which H_{ge} operates, which will give rise to further singular contributions. To avoid this complication, it is best to consider from the beginning the possibility that G contains a string of r vertices $x_1, \cdots, x_r$, joined by $(r-1)$ photon lines, the interaction H_{ge} operating at each vertex of the string. Such a string of vertices, if G_T is any doubled graph in which all the $(r-1)$ photon lines are doubled, will make a singular contribution to $M(G_T, \Lambda)$ with the factor

$$F_{\mu 4}(x_1)F_{\mu 4}(x_r)\delta(x_1-x_2)\cdots\delta(x_{r-1}-x_r) \tag{89}$$

analogous to Eq. (87). Arguing in this way, one finds that all singular contributions to $M(G, \Lambda)$ will be correctly allowed for if the nonsingular terms are written down in the usual way, with the coefficient f_{4g} in H_{ge} changed to

$$f_{4g}-f_{4g}{}^2+f_{4g}{}^3-\cdots=f_g, \tag{90}$$

according to Eq. (81).

The change of f_{4g} to f_g in Eq. (80) is equivalent to simply omitting the term $F_{\mu 4}F_{\mu 4}$ in Eqs. (24) and (58). Therefore, the conclusion of this discussion of derivative interactions is to justify the rules which were formulated in Sec. V for the evaluation of $M(G)$. In fact, the formulas (67) and (75), (76) were obtained just by

translating the term $F_{\mu\nu}F_{\mu\nu}$ in (24) into a momentum-space integral, ignoring all singular contributions and at the same time the term in $F_{\mu 4}F_{\mu 4}$.

VII. GENERAL SURVEY OF DIVERGENCES

All the divergences which can arise in the present theory make their appearance in momentum-space integrals of the form (72). The integrals (72) are derived from Eq. (61) by the replacements described in Sec. V, replacements which change neither the general form of the integrals nor their convergence or divergence at large momenta. The integrals (61) are of the kind already discussed in the analysis of the S-matrix. The introduction of new vertices at which the interactions (24), (29), (30) operate does not introduce any new types of divergent integral. Therefore, the possible divergences in the present theory are precisely the same as those which were studied in the theory of the S-matrix developed in II.

Although the divergences are all of a kind which is already familiar from the S-matrix analysis, it is not at all to be expected at first sight that the methods of isolating and removing the divergences, which were adequate for making the S-matrix finite, will prove adequate also here. First, the divergent integrals now involve a multitude of parameters Λ_i, whereas before they depended upon at most two 4-vector parameters. Second, and more important, the relativistic invariance of the S-matrix, which was of decisive importance for the unambiguous separation of renormalization effects, is altogether lacking in the present calculations. However, in spite of these two serious obstacles, it is found that the elimination of divergences can be carried out for intermediate representation operators, in a way which is consistent and unambiguous. This is possible because of the close formal similarity between the integrals (72) and (61). Although Eq. (72) is not an invariant quantity, its lack of invariance lies only in the fact that the vectors Γ_j are of the special form (54). Considered as a function of the vectors Γ_j, Eq. (72) is a formally covariant expression; and therefore the method of separating divergent parts from covariant integrals can still be applied to it. In this way the lack of real invariance in Eq. (72) turns out to be unimportant. The treatment of divergences in Eq. (72) is more complicated in detail than the treatment of the S-matrix because of the greater number of parameters, but no essentially new problems are encountered.

The divergences in a particular $M(G, \Lambda)$ are associated with local features of the graph G, just as in the S-matrix. There are logarithmic divergences arising from vertex parts in G, linear divergences arising from electron self-energy parts, and quadratic divergences arising from photon self-energy parts. It is easy to verify that Furry's theorem[11] applies to integrals of the form (72). Also, the factors in Eq. (72) corresponding to "scattering of light by light" processes[12] give rise only to logarithmic divergences which cancel identically after the contributions from different G are added together. Therefore, the real divergences which have to be isolated and removed from $M(G, \Lambda)$ are limited to the three types already mentioned.

The vertices of G at which the interaction $H_{\sigma i}$ operates will be called "ordinary" vertices. Irreducible proper and improper vertex parts and self-energy parts are defined as in II. The irreducible vertex parts are identically the same as for the S-matrix, consisting always of a network of ordinary vertices only. Also, the irreducible electron self-energy parts are the same as before, either consisting of ordinary vertices, or consisting of a single vertex at which $H_{\sigma s}$ operates. The irreducible photon self-energy parts are the same as before, consisting of ordinary vertices, except that now a new photon self-energy part is added consisting of a single vertex at which either $H_{\sigma p}$, $H_{\sigma a}$, or $H_{\sigma b}$ operates. Vertex and self-energy parts, in which all the vertices are ordinary, will themselves be called "ordinary." Thus, all irreducible vertex and self-energy parts, with the exception of the single-vertex self-energy parts, are ordinary. When x_i is an ordinary vertex, the index m_i defined by Eq. (46) is unity, and the vector Λ_i associated with x_i reduces to a single Γ_i.

In the following three sections, it will be proved that all the divergences arising from ordinary irreducible vertex and self-energy parts are canceled identically by counter-terms arising from $H_{\sigma s}$, $H_{\sigma p}$, $H_{\sigma a}$, $H_{\sigma b}$ operating at the single-vertex self-energy parts. The arguments will apply verbatim not only to ordinary irreducible parts, but also to all ordinary proper reducible vertex and self-energy parts, assuming that the divergences arising from sources interior to these parts have been canceled out previously. By application of the cancellation first to irreducible parts, and then in succession to more and more complicated reducible parts, all the divergences arising from ordinary vertex and self-energy parts will ultimately be canceled by the contributions from the single-vertex parts. Used in this way, the methods of the following three sections are sufficient to eliminate all the divergences from the theory.

It is one of the great advantages of the Gupta formalism that all mass and charge renormalization effects are canceled automatically whenever they appear in the course of the calculations. This is in contrast to the method used in II. There, the mass renormalization terms were removed by an automatic cancellation; but the charge renormalization effects were handled by a much more complicated procedure, being retained through the calculations and finally collected into the coefficients Z_1, Z_2, Z_3, which renormalized the charge explicitly according to Eq. (86) of II. The Gupta formalism works from the beginning with the renormalized charge e_1, and makes unnecessary the elaborate

[11] W. H. Furry, Phys. Rev. 51, 125 (1937). See Sec. IV of II.

[12] See Sec. VI of II.

discussion in Sec. VII of II which justifies the step-by-step removal of divergences arising from reducible graphs. The program of successive removal of divergences is now justified simply by the fact that each divergence from an ordinary self-energy part appears at every stage of the calculations accompanied by a compensating term from a single-vertex part.

The Gupta formalism would not have simplified the renormalization problem so greatly, if Ward[13] had not previously proved that in the S-matrix the renormalization coefficients Z_1 and Z_2 are equal and exactly compensate each other, so that true charge renormalization arises only from Z_3. In consequence of Ward's work, Gupta needed to introduce an explicit counterterm only for the charge-renormalization effects produced by photon self-energy parts. The spurious charge-renormalization effects from vertex parts and electron self-energy parts cancel each other out. In the following sections, it will be proved that this cancellation of divergences without counterterms continues to be valid for intermediate representation operators. In the proof, Ward's identity plays an essential part.

VIII. REMOVAL OF DIVERGENCES ARISING FROM PHOTON SELF-ENERGY PARTS

Let W be an ordinary proper photon self-energy part, irreducible or reducible. Let G be a graph in which W occurs, $M(G)$ and $M(G, \Lambda)$ the coefficients derived from G as explained in Secs. IV–V. If W is reducible, it is supposed that these coefficients have been freed of all divergences arising from internal pieces of W, the internal divergences having been canceled out at an earlier stage of the calculation, as described in Sec. VII. Let λ_1 and λ_2 be the two photon lines adjacent to W in G. Since the special vertex x cannot lie inside W, at least one of the two lines, say, λ_1, must be internal and doubled. Then λ_2 may be either doubled, or internal and undoubled, or external. Let x_1 and x_2 be the vertices at which λ_1 and λ_2 meet W. The line-doubling in G can always be arranged so that a continuous path P of doubled lines runs from x_1 to x_2 within W. Without loss of generality, it will be assumed that the "down" direction runs from x_2 along P to x_1, then along λ_1 and other doubled lines outside W to x. Also, the direction of the arrows is chosen in λ_2 towards x_2, and in λ_1 away from x_1. Then by Eq. (69), the line λ_1 introduces into the integrand of Eq. (72) a factor (74) with

$$R_1 = l + i\Delta_1. \tag{91}$$

If λ_2 is an internal line, there is also a factor (74) in the integrand of Eq. (72) with

$$R_2 = l + i\Delta_2. \tag{92}$$

Here, we have $\Delta_2 = 0$ if λ_2 is undoubled. If λ_2 is external, we have $\Delta_2 = 0$ by definition and l is the momentum carried by the particle corresponding to λ_2. In all cases, we have

$$\Delta_1 - \Delta_2 = \Gamma_1 + \Gamma_2 + \cdots + \Gamma_d, \tag{93}$$

where $\Gamma_1, \cdots, \Gamma_d$ are the Γ-vectors associated with the d vertices of W.

Now consider the product Π_W of all factors in the integrand of Eq. (72) associated with the lines and vertices of W. Apart from fundamental constants, Π_W depends only upon the following quantities: $\Gamma_1, \cdots, \Gamma_d$, $(l + i\Delta_2)$, and the momentum variables $k_\alpha{}^W$ corresponding to undoubled lines in W. The variables $k_\alpha{}^W$ do not appear in any factors of Eq. (72) except Π_W. Also, Π_W is a second-rank tensor with two suffixes α, β, derived from the Dirac matrices γ_α, γ_β operating at the vertices x_1 and x_2. Thus, the integral

$$I^W = I_{\alpha\beta}{}^W(l + i\Delta_2, \Gamma_1, \cdots, \Gamma_d) = \int \Pi_W dk_\alpha{}^W \tag{94}$$

appears as a factor in Eq. (72), and depends only on the parameters written explicitly in Eq. (94).

The integrals (72) and (94) are to be evaluated as Feynman integrals before any process of analytic continuation is applied to them. While Eq. (94) is in the form of a Feynman integral, the method of Sec. VI of II can be used in order to separate it into a convergent part and a divergent part, the divergent part having a very simple form determined by considerations of covariance. The divergence of Eq. (94) is at most quadratic, and divergences arising from integration over subsets of the variables $k_\alpha{}^W$ are supposed already compensated. Therefore, we obtain

$$I^W = I_F{}^W + I_D{}^W, \tag{95}$$

$$\begin{aligned} I_F{}^W = \int dk_\alpha{}^W \{ &\Pi_W - (\Pi_W)_0 - \lambda^2(\partial/\partial\lambda^2)(\Pi_W)_0 \\ &- [(l_\mu + i\Delta_{1\mu})(\partial/\partial l_\mu) + \Gamma_{1\mu}(\partial/\partial\Gamma_{1\mu}) + \cdots \\ &+ \Gamma_{d\mu}(\partial/\partial\Gamma_{d\mu})](\Pi_W)_0 \\ &- \tfrac{1}{2}[(l_\mu + i\Delta_{2\mu})(l_\nu + i\Delta_{2\nu})(\partial^2/\partial l_\mu \partial l_\nu) \\ &+ 2(l_\mu + i\Delta_{2\mu})\Gamma_{1\nu}(\partial^2/\partial l_\mu \partial\Gamma_{1\nu}) + \cdots \\ &+ \Gamma_{1\mu}\Gamma_{1\nu}(\partial^2/\partial\Gamma_{1\mu}\partial\Gamma_{1\nu}) + \cdots \\ &+ 2\Gamma_{1\mu}\Gamma_{2\nu}(\partial^2/\partial\Gamma_{1\mu}\partial\Gamma_{2\nu}) + \cdots](\Pi_W)_0 \}, \end{aligned} \tag{96}$$

this $I_W{}^F$ being an absolutely convergent integral. The notation $(\Pi_W)_0$ means that the parameters λ^2, $(l + i\Delta_2)$, $\Gamma_1, \cdots, \Gamma_d$, but not the variables $k_\alpha{}^W$, are all to be put equal to zero in Π_W and its derivatives, after carrying out the differentiations. The divergent subtracted term $I_D{}^W$ is of the form:

$$\begin{aligned} I_D{}^W = &T_{\alpha\beta} + \lambda^2 T_{\alpha\beta}' + T_{\alpha\beta\mu}(l_\mu + i\Delta_{2\mu}) + \textstyle\sum_\tau T_{\alpha\beta\mu}{}^\tau \Gamma_{\tau\mu} \\ &+ T_{\alpha\beta\mu\nu}(l_\mu + i\Delta_{2\mu})(l_\nu + i\Delta_{2\nu}) + \textstyle\sum_\tau T_{\alpha\beta\mu\nu}{}^\tau (l_\mu + i\Delta_{2\mu})\Gamma_{\tau\nu} \\ &+ \textstyle\sum_\tau \sum_\sigma T_{\alpha\beta\mu\nu}{}^{\tau\sigma}\Gamma_{\tau\mu}\Gamma_{\sigma\nu}. \end{aligned} \tag{97}$$

[13] J. C. Ward, Phys. Rev. **78**, 182 (1950).

Here the $T_{\alpha\beta}$, $T_{\alpha\beta\mu}$, etc., are dimensionless numerical tensors whose components depend only on the shape of W, multiplied by such powers of the fundamental units, $\hbar$, c, and m, as are required to give the correct dimensions to I^W. Since there exist no numerical tensors of third rank, the terms in Eq. (97) linear in l_μ and $\Gamma_{r\mu}$ vanish identically. The only possible form for a numerical tensor of second rank is

$$T_{\alpha\beta}=A\delta_{\alpha\beta}, \tag{98}$$

where A is a scalar. The fourth-rank tensors in Eq. (97) must each be of the form:

$$T_{\alpha\beta\mu\nu}=B\delta_{\alpha\beta}\delta_{\mu\nu}+B'\delta_{\alpha\mu}\delta_{\beta\nu}+B''\delta_{\alpha\nu}\delta_{\beta\mu}, \tag{99}$$

where B, B', and B'' are scalars. When Eqs. (98) and (99) are substituted into Eq. (97), the result may be written

$$I_D{}^W=\delta_{\alpha\beta}[A+A'\lambda^2+Bq^2+\sum_r B_r q\cdot\Gamma_r + \sum_r\sum_s B_{rs}\Gamma_r\cdot\Gamma_s]+B'q_\alpha q_\beta+\sum_r\{B_r'q_\alpha\Gamma_{r\beta} + B_r''q_\beta\Gamma_{r\alpha}\}+\sum_r\sum_s B_{rs}'\Gamma_{r\alpha}\Gamma_{s\beta}, \tag{100}$$

with

$$q=l+i\Delta_2+i\Gamma_2. \tag{101}$$

In order to simplify Eq. (100), it is necessary to group the self-energy parts W into mutually exclusive classes C and to add together the integrals I^W derived from W belonging to a given C. Let I^C be the sum of these I^W. The definition of the classes C is as follows. Given a particular W, the vertex x_2 belongs to a closed loop L of r electron lines in W; the C to which W belongs is the class of self-energy parts obtained from W by moving x_2 to each of the $(r-1)$ possible positions which x_2 can occupy on L, leaving the order of the other vertices on L unchanged. If G is any graph containing W, then G_C is defined to be the class of graphs obtained by substituting for W in G the various members of C. Clearly, all graphs of G_C contribute together to every coefficient M to which G contributes. Therefore, it is convenient to consider the sums $M(G_C)$ formed by adding together the $M(G)$ derived from graphs G in G_C. The removal of divergences will be performed for the sum $M(G_C)$ as a unit; it is unnecessary to cancel divergences in each $M(G)$ separately. Since the factors of Eq. (72), other than Π_W, arise only from the part of G outside W, the function $M(G_C)$ is formed from $M(G)$ by replacing I^W by I^C.

Consider the sum

$$q_\beta I_{\alpha\beta}{}^W. \tag{102}$$

The factors in Π_W arising from the vertex x_2 and the two adjacent electron lines λ_i, λ_j are

$$[(l_{i\mu}+i\eta_i\Delta_{i\mu})\gamma_\mu-\mathrm{im}]^{-1}\gamma_\beta[(l_{j\mu}+i\eta_j\Delta_{j\mu})\gamma_\mu-\mathrm{im}]^{-1}, \tag{103}$$

where

$$l_i-l_j=l, \quad \eta_i\Delta_i-\eta_j\Delta_j=\Delta_2+\Gamma_2, \tag{104}$$

Eq. (104) being a consequence of the structure of W. By Eq. (101), the sum (102) will be obtained if one replaces the factors (103) in I^W by

$$[(l_{j\mu}+i\eta_j\Delta_{j\mu})\gamma_\mu-\mathrm{im}]^{-1}-[(l_{i\mu}+i\eta_i\Delta_{i\mu})\gamma_\mu-\mathrm{im}]^{-1}. \tag{105}$$

Therefore, one obtains

$$q_\beta I_{\alpha\beta}{}^W=E_i{}^W-E_j{}^W, \tag{106}$$

where $E_i{}^W$ is the expression obtained by omitting from I^W the factors arising from the line λ_i and the vertex x_2. Let the vertices of the closed loop L be in order x_2, x_a, x_b, $\cdots$, x_i. Consider the self-energy part W', belonging to C, in which x_2 stands between x_a and x_b instead of between x_i and x_a. Let the two electron lines adjoining x_2 in W' be λ_k, λ_l. Then, we have

$$q_\beta I_{\alpha\beta}{}^{W'}=E_k{}^{W'}-E_l{}^{W'}, \tag{107}$$

in analogy with Eq. (106). But it is easily verified that the factors in the integrand of $E_j{}^W$ are identical with those of $E_k{}^{W'}$, apart from possible differences of notation arising from a different choice of doubled lines in W and W'. The value of $E_j{}^W$, evaluated as a Feynman integral, depends only on W and is independent of the way in which the doubled lines have been chosen. Therefore, $E_j{}^W$ and $E_k{}^{W'}$ are identical. Similarly, when Eq. (106) is summed over all the W in C, each term $E_r{}^W$ appears exactly twice, once with positive and once with negative sign. This leads to the identity

$$q_\beta I_{\alpha\beta}{}^C=0. \tag{108}$$

The above proof of Eq. (108) is not altogether rigorous, since it involves some rearrangements of divergent integrals. The physical significance of Eq. (108) is to express the conservation of the charges and currents occurring as a result of the polarization of the vacuum by an applied field. Mathematically, Eq. (108) is the direct generalization to intermediate representation operators of the identity

$$(\partial/\partial x_\mu)G_{\mu\nu}(x)=0 \tag{109}$$

expressing the same conservation principle in the Schwinger theory.[14] Schwinger's proofs of Eq. (109) have given rise to much discussion;[15] they are nonrigorous from a strict mathematical point of view, but there seems to be no doubt that Eq. (109) is to be accepted as a correct equation, expressing a formal property which the theory must possess in order to be physically consistent. The dubious features in the proof of Eq. (108) are similar to those which occurred in Schwinger's work. Therefore, it is reasonable to accept Eq. (108) as formally correct, just as Eq. (109) is accepted, without here enquiring more deeply into the mathematical difficulties of the proof.

The grouping together of self-energy parts into classes C, by moving the vertex x_2 round a closed loop,

[14] J. Schwinger, Phys. Rev. **76**, 790 (1949), Eq. (A.16) in the Appendix.

[15] See, for example, W. Pauli and F. Villars, Revs. Modern Phys. **21**, 434 (1949).

can be extended by allowing both the vertices x_1 and x_2 to move independently round the loops on which they respectively lie. It will be supposed henceforth that the classes C are enlarged in this way. Then Eq. (108) will still be valid, and in addition the identity

$$q_\alpha' I_{\alpha\beta}{}^C = 0 \tag{110}$$

will hold, with

$$q' = l + i\Delta_1 - i\Gamma_1. \tag{111}$$

Let I^C be divided into its finite and divergent parts $I_F{}^C$, $I_D{}^C$ by summing Eq. (95) with respect to W. $I_D{}^C$ is formally the sum of all terms of degrees 0, 1, 2 in a power-series expansion of I^C in the variables λ, $(l+i\Delta_2)$, $\Gamma_1, \cdots, \Gamma_d$; and the identities (108), (110) are homogeneous in these variables. Therefore, Eqs. (108), (110) hold not only for I^C but also for the parts $I_F{}^C$ and $I_D{}^C$ separately. Since $I_D{}^C$ satisfies Eq. (108) identically, the coefficients when $I_D{}^C$ is written in the form (100) are mostly zero; in fact, we may write

$$A = A' = 0,\ B + B' = 0,\ B_r + B_r' = 0,\ B_r'' = B_{rs} = B_{rs}' = 0.$$

The condition $A = 0$ states that the self-energy of the photon is zero, as in the Schwinger theory. Therefore, we have

$$I_D{}^C = B(q^2\delta_{\alpha\beta} - q_\alpha q_\beta) + \sum_r B_r(q\cdot\Gamma_r\delta_{\alpha\beta} - q_\alpha\Gamma_{r\beta}). \tag{112}$$

When we apply Eq. (110) to Eq. (112), $I_D{}^C$ reduces finally to the compact form:

$$I_D{}^C = B(q\cdot q'\delta_{\alpha\beta} - q_\alpha q_\beta'), \tag{113}$$

depending on the single scalar coefficient B. When λ and all the Γ_i are put equal to zero, Eq. (113) agrees with the form in which charge-renormalization effects appear in the calculation of the S-matrix. Therefore, B is to be identified with a certain contribution to the coefficient Z_3 of charge-renormalization defined in II.

Let I^d be the sum of all I^W derived from ordinary proper photon self-energy parts W with d vertices. The divergent part of I^d is

$$I_D{}^d = -B_d(q\cdot q'\delta_{\alpha\beta} - q_\alpha q_\beta'), \tag{114}$$

where B_d is defined as a coefficient in the expansion,

$$f = 1 - Z_3 = \sum_{d=2}^{\infty} B_d e_1{}^d, \tag{115}$$

and is therefore identical with the B_d appearing in Eq. (26). Associated with I^d there is an expression $I_0{}^d$ which describes the effects of the terms of degree $e_1{}^d$ in $H_{\varrho p}$, $H_{\varrho a}$, $H_{\varrho b}$, operating at a single-vertex photon self-energy part W_0. By Eqs. (26) and (75), (76), the contribution to $I_0{}^d$ from $H_{\varrho p}$ is

$$I_p{}^d = B_d[(l+i\Delta_1)\cdot(l+i\Delta_2)\delta_{\alpha\beta} - (l+i\Delta_2)_\alpha(l+i\Delta_1)_\beta]. \tag{116}$$

By Eqs. (29) and (48), the contribution from $H_{\varrho a}$ is

$$I_a{}^d = B_d[(d-2)\Gamma_{i0}\Gamma_{j0} + \Gamma_{i0}{}^2](\delta_{\alpha\beta} - \delta_{\alpha 4}\delta_{\beta 4}). \tag{117}$$

By Eqs. (30) and (47), the contribution from $H_{\varrho b}$ is

$$I_b{}^d = -iB_d(\Gamma_{i\alpha}l_\beta - \Gamma_{j\beta}l_\alpha). \tag{118}$$

In Eqs. (117) and (118), not only the factor arising in Eq. (72) from W_0 is included, but also the factor contributed by W_0 to the product E_{Tr}, which appears in $M(G)$ according to Eq. (59). As explained in Sec. IV, the vectors $\Gamma_1, \cdots, \Gamma_d$ are all associated with the single vertex W_0; Γ_i and Γ_j in Eqs. (117) and (118) are any two of these vectors chosen arbitrarily. Since $M(G, \Lambda)$ involves $\Gamma_1, \cdots, \Gamma_d$ only in the combination $(\Gamma_1 + \cdots + \Gamma_d)$, the value of Eq. (59) is independent of the choice of Γ_i and Γ_j. In particular, Eqs. (117) and (118) may be replaced by the expressions,

$$I_a{}^d = B_d(\delta_{\alpha\beta} - \delta_{\alpha 4}\delta_{\beta 4})[\Gamma_{20}(\Gamma_{10} + \Gamma_{20} + \cdots + \Gamma_{d0}) - \Gamma_{20}\Gamma_{10} + (\Gamma_{20} - \Gamma_{10})\Delta_{20}], \tag{119}$$

$$I_b{}^d = -iB_d[\Gamma_{2\alpha}l_\beta - \Gamma_{1\beta}l_\alpha + l\cdot(\Gamma_1 - \Gamma_2)\delta_{\alpha\beta}]. \tag{120}$$

Adding together Eqs. (114), (116), (119), and (120), one finds

$$I_D{}^d + I_0{}^d = I_D{}^d + I_p{}^d + I_a{}^d + I_b{}^d = 0. \tag{121}$$

Now consider the coefficient M defined at the beginning of Sec. IV. It is a sum of contributions $M(G)$ from various G. Suppose that G is any graph which contains the ordinary proper photon self-energy part W consisting of d vertices. Contributions to M will also be obtained from all graphs G' in which W is replaced, either by any other ordinary proper photon self-energy part with d vertices, or by the single-vertex part W_0 at which the terms of order $e_1{}^d$ in $H_{\varrho p}$, $H_{\varrho a}$, and $H_{\varrho b}$ are supposed to operate. The $M(G')$ derived from all these graphs, as defined by Eqs. (59) and (72), will differ from $M(G)$ only by the substitution of $I^{W'}$ or $I_0{}^d$ for I^W; the factors in $M(G)$ derived from all parts of G outside W are retained unaltered in $M(G')$. Let M_d be the sum of all the $M(G')$ including $M(G)$. Then, M is obtained from $M(G)$ by writing in place of I^W

$$I^d + I_0{}^d = I_F{}^d; \tag{122}$$

by Eq. (121) this $I_F{}^d$ is simply the absolutely convergent integral separated from I^d according to Eq. (96). That is to say, in M_d all the divergences arising from the photon self-energy parts W' have been eliminated. Since this elimination of divergences proceeds independently for self-energy parts situated at all possible places in G, the coefficient M finally involves the integrals I^W only in the convergent combinations $I_F{}^d$. Therefore, M is free of divergences arising from photon self-energy parts. Since M is any coefficient in the expansion of $A_{\mu\varrho}(p)$, the absence of photon self-energy and vacuum polarization divergences in $A_{\mu\varrho}(p)$ is now proved.

In conclusion, some explanation should be made of the role of the analytic continuation process in the above arguments. The $M(G, \Lambda)$ were defined in Sec. V as the analytic continuation of certain Feynman inte-

grals, originally defined for large values of m and λ and imaginary values of Γ_{i0}, into the region of real Γ_{i0} and small m and λ. The proof that the $M(G, \Lambda)$ are analytic functions of this kind was given in HO.I, but the proof of analyticity is certainly invalid and meaningless when the $M(G, \Lambda)$ are divergent integrals. Here is a defect in the argument, which must be remedied as follows. The proof of analyticity will apply correctly to the convergent part of an integral defined by the subtraction procedure (96), provided that the subtracted divergent terms are manifestly and formally analytic functions of m, λ, and the Γ_{i0}. Now in Eq. (96) the subtracted terms are formally analytic; they are quadratic functions of λ and the Γ_{i0}, and they can depend on m only as a constant power m^r because m is the only other parameter involved in them with the dimensions of a mass. Therefore, the convergent parts of all the integrals $M(G, \Lambda)$ are correctly defined by the analytic continuation method. Since eventually only the convergent parts of the integrals appear in $A_{\mu\varrho}(p)$, the use of analytic continuation in the analysis of the coefficients M is fully justified.

IX. SEPARATION OF DIVERGENCES ARISING FROM ELECTRON SELF-ENERGY PARTS AND VERTEX PARTS

In this section the divergences from electron self-energy parts and from vertex parts will be treated together. Let V be an ordinary proper vertex part, irreducible or reducible, with $(d+1)$ vertices. Let W be an ordinary proper electron self-energy part with d vertices. Let G be a graph in which either V or W occurs; let $M(G)$ and $M(G, \Lambda)$ be the coefficients derived from G. As before, it is supposed that divergences arising from internal parts of V or W have already been canceled.

Let λ_1 and λ_2 be the two electron lines adjacent to V or W in G, meeting V or W at the vertices x_1, x_2, with the arrow running in λ_2 towards x_2 and in λ_1 away from x_1. Let λ_3 be the photon line adjacent to V at the vertex x_3. The line-doubling in G can be arranged so that x_1 and x_3 are connected in W or V by a continuous path P of doubled electron lines. Also, x_3 is connected in V to P by a continuous path of doubled lines; but it is no longer possible to arrange that λ_1 is necessarily doubled. The "down" direction may lead out of W to x through either λ_1 or λ_2, and out of V through either λ_1, λ_2, or λ_3. The factors arising from V or W in $M(G)$ will in general depend strongly upon which of these alternative routes the down direction takes. Let Π_V or Π_W be the product of the factors in the integrand of Eq. (72) arising from V or W. Let

$$I^V=\int \Pi_V dk_a{}^V, \quad I^W=\int \Pi_W dk_a{}^W, \tag{123}$$

where the $k_a{}^V$ or $k_a{}^W$ are the momentum variables arising from undoubled lines in V or W. In $M(G)$ the integral (123) appears as a factor, since the variables $k_a{}^V$, $k_a{}^W$ occur only in Π_V, Π_W.

Consider now the parameters upon which I^V can depend. These are indicated by

$$I^V=I_\mu{}^V(R_1, R_2, \Gamma_1, \cdots, \Gamma_{d+1}). \tag{124}$$

Here μ is a vector suffix arising from the operator γ_μ at the vertex x_3. Not shown explicitly in Eq. (124) is the fact that I^V is also a Dirac matrix, with two spinor indices which combine with the factors in $M(G)$ arising from λ_1 and λ_2. The vectors R_1, R_2 are given by Eq. (69) if λ_1 and λ_2 are internal lines; if λ_1 or λ_2 is external, the corresponding R_1 or R_2 is simply the momentum carried by λ_1 or λ_2. The vectors $\Gamma_1, \cdots, \Gamma_{d+1}$ are those associated with the vertices of V. In addition to the parameters already mentioned, I^V depends on m and λ.

Since I^V is only logarithmically divergent,

$$I^V=I_{Dt}{}^V+I_{Ft}{}^V, \tag{125}$$

$$I_{Ft}{}^V=\int dk_a{}^V\{\Pi_V-(\Pi_V)_t\}, \tag{126}$$

this $I_{Ft}{}^V$ being absolutely convergent. The subtracted term $(\Pi_V)_t$ is obtained from Π_V by substituting for $(R_1, R_2, \Gamma_1, \cdots, \Gamma_{d+1}, \lambda)$ the special values $(t, t, 0, \cdots, 0, \lambda_0)$, where t is an arbitrary 4-vector satisfying

$$t^2=-m^2, \tag{127}$$

and λ_0 is an arbitrary fixed positive mass. The divergent $I_{Dt}{}^V$, being a vector Dirac matrix depending only on t, must be of the form,

$$I_{Dt}{}^V=L\gamma_\mu+B\gamma_\mu(t_\alpha\gamma_\alpha-\mathrm{im})+B'(t_\alpha\gamma_\alpha-\mathrm{im})\gamma_\mu +C(t_\alpha\gamma_\alpha-\mathrm{im})\gamma_\mu(t_\beta\gamma_\beta-\mathrm{im}), \tag{128}$$

where L, B, B', C are scalar constants independent of t after Eq. (127) is used. Now the difference between the $I_{Dt}{}^V$ defined with two different vectors t is an absolutely convergent integral. Therefore, the coefficients B, B', C are finite, and only L is divergent. Let $I_D{}^V$ be defined by

$$I_D{}^V=L\gamma_\mu, \tag{129}$$

and write

$$I^V=I_D{}^V+I_F{}^V. \tag{130}$$

Then $I_F{}^V$ is finite and independent of t, and is by definition the finite part of I^V. The above definition of $I_F{}^V$ in two stages is similar to the two-stage definition of $\Lambda_{\mu\varrho}$ in Sec. VI of II. Note, however, that L in (129) is still a function of λ_0. It is necessary to retain a non-zero λ_0 in L in order to avoid introducing a spurious infrared divergence into $I_F{}^V$.

Although I^V depends on the route along which the "down" direction runs out of V, the $I_{Dt}{}^V$ does not. Therefore, L depends only on the shape of V and is independent of the situation in which V appears in G. When $\lambda_0=0$, the constant L becomes the contribution from V to the vertex-renormalization constant Z_1

defined in Sec. VII of II. When $\lambda_0 \neq 0$, the constant L is a contribution to the corresponding coefficient $Z_1(\lambda_0)$, which appears in the calculation of the S-matrix of quantum electrodynamics when a neutral vector field of mass λ_0 replaces the maxwell field. Let G be any graph in which V occurs, so that $M(G)$ contains I^V as a factor. In M, together with $M(G)$, there appear all the $M(G')$ from graphs G' obtained from G by replacing V by any other ordinary proper vertex part with $(d+1)$ vertices. The sum of these $M(G')$ is denoted by M_d.

M_d is obtained from $M(G)$ when I^V is replaced by a certain sum I^d. This I^d will depend not only on d but also on the way in which the "down" direction leads out of V in G. However, in all cases one obtains

$$I^d = I_F{}^d + I_D{}^d, \tag{131}$$

where $I_F{}^d$ is convergent and

$$I_D{}^d = L_d \gamma_\mu. \tag{132}$$

Here, L_d is defined as a coefficient in the expansion,

$$Z_1(\lambda_0) = 1 - \sum_{d=2}^{\infty} L_d e_1{}^d, \tag{133}$$

and is independent of the situation of V.

Next consider I^W. If the down direction leaves W along λ_1, then λ_1 is a doubled line and $\eta_1 = +1$. In the opposite case, λ_2 is doubled and $\eta_2 = -1$. Let $\eta_W = +1$ in the first case and $\eta_W = -1$ in the second. In both cases, the vectors R_1, R_2 according to Eq. (69) are given by

$$R_1 = l + i\eta_W \Delta_1, \quad R_2 = l + i\eta_W \Delta_2, \tag{134}$$

with

$$\eta_W(\Delta_1 - \Delta_2) = \Gamma_1 + \cdots + \Gamma_d. \tag{135}$$

Here, $\Gamma_1, \cdots, \Gamma_d$ are the vectors associated with the vertices of W. The parameters upon which I^W depends are indicated by

$$I^W = I^W(l + i\eta_W \Delta_2, \Gamma_1, \cdots, \Gamma_d). \tag{136}$$

Note, however, that I^W is not the same function of these parameters in the two cases $\eta_W = \pm 1$. Also, I^W is a Dirac matrix.

Since I^W is linearly divergent, one obtains

$$I^W = I_{Dt}{}^W + I_{Ft}{}^W, \tag{137}$$

$$I_{Ft}{}^W = \int dk_a{}^W \{\Pi_W - (\Pi_W)_t - [\Gamma_{1\mu}(\partial/\partial\Gamma_{1\mu}) + \cdots + \Gamma_{d\mu}(\partial/\partial\Gamma_{d\mu}) + (l_\mu + i\eta_W \Delta_{2\mu} - t_\mu)(\partial/\partial l_\mu)](\Pi_W)_t\}, \tag{138}$$

this $I_{Ft}{}^W$ being absolutely convergent. Here $(\Pi_W)_t$ is obtained by substituting for $(l + i\eta_W \Delta_2, \Gamma_1, \cdots, \Gamma_d, \lambda)$, in Π_W and in the derivatives of Π_W after differentiation, the special values $(t, 0, \cdots, 0, \lambda_0)$. The divergent $I_{Dt}{}^W$, being a scalar Dirac matrix depending linearly on the vectors $(l + i\eta_W \Delta_2, \Gamma_1, \cdots, \Gamma_d)$, must be of the form:

$$\begin{aligned} I_{Dt}{}^W = {} & X + Y(t_\alpha \gamma_\alpha - \mathrm{im}) \\ & + \sum_r \Gamma_{r\mu} [E^r \gamma_\mu + B^r (t_\alpha \gamma_\alpha - \mathrm{im}) \gamma_\mu \\ & + B^{r\prime} \gamma_\mu (t_\alpha \gamma_\alpha - \mathrm{im}) + C^r (t_\alpha \gamma_\alpha - \mathrm{im}) \gamma_\mu (t_\beta \gamma_\beta - \mathrm{im})] \\ & + (l_\mu + i\eta_W \Delta_{2\mu} - t_\mu)[E^0 \gamma_\mu + B^0 (t_\alpha \gamma_\alpha - \mathrm{im}) \gamma_\mu \\ & + B^{0\prime} \gamma_\mu (t_\alpha \gamma_\alpha - \mathrm{im}) \\ & + C^0 (t_\alpha \gamma_\alpha - \mathrm{im}) \gamma_\mu (t_\beta \gamma_\beta - \mathrm{im})]. \end{aligned} \tag{139}$$

Suppose temporarily that t is an arbitrary vector, not necessarily satisfying Eq. (127). Then, the coefficients X, Y, E^r, etc., in Eq. (139) are scalar functions of t^2. Let X', Y' be the derivatives of X and Y with respect to t^2. From the identity,

$$\int dk_a{}^W (\partial/\partial t_\mu)(\Pi_W)_t = Y\gamma_\mu + 2X' t_\mu + 2Y' t_\mu (t_\alpha \gamma_\alpha - \mathrm{im}), \tag{140}$$

there follow the relations:

$$E^0 = Y + 2\,\mathrm{im} X' = Y + \mathrm{im}(B^0 + B^{0\prime}). \tag{141}$$

Now, t being restricted to satisfy Eq. (127), the coefficients X, Y, etc., become constants depending only on m and λ_0. Let $I_D{}^W$ be defined by

$$I_D{}^W = X + \textstyle\sum_r E^r \Gamma_{r\mu} \gamma_\mu + E^0 [(l_\mu + i\eta_W \Delta_{2\mu}) \gamma_\mu - \mathrm{im}], \tag{142}$$

and write

$$I^W = I_D{}^W + I_F{}^W. \tag{143}$$

Integrals such as

$$\int dk_a{}^W (\partial/\partial \Gamma_{1\mu})(\Pi_W)_t \tag{144}$$

are only logarithmically divergent, and the difference between two integrals (144) constructed with two different vectors t is convergent. From this it follows that the coefficients B^r, $B^{r\prime}$, C^r, B^0, $B^{0\prime}$, C^0 in Eq. (139) are all finite. Comparing Eq. (143) with Eq. (137), Eq. (142) with Eq. (139), and using Eq. (141), one deduces that $I_F{}^W$ is finite. Being independent of t, $I_F{}^W$ is by definition the finite part of I^W. This definition is similar to the two-stage definition of $\sum_c$ in Sec. VI of II. The λ_0-dependent coefficients X, E^r, and E^0 are, however, retained in Eq. (143) in order to avoid infrared divergences.

I^W, like I^V, depends on the route along which the down direction runs out of W. The coefficients X and E^0, like L in Eq. (129), are independent of this direction and depend only on the shape of W. When $\lambda_0 = 0$, the coefficient E^0 becomes the contribution of W to the electron-line renormalization constant Z_2 defined in Sec. VII of II. When $\lambda_0 \neq 0$, the coefficient E^0 is a contribution to the corresponding coefficient $Z_2(\lambda_0)$

appearing in the S-matrix with a neutral meson field of mass λ_0. When $\lambda_0=0$, the coefficient X becomes the contribution of W to the electron self-energy denoted by $(1/2\pi)A=iZ_2\delta\kappa_0$ in Eqs. (72) and (94) of II. When $\lambda_0\neq 0$, the coefficient X is a contribution to the self-energy

$$(1/2\pi)A(\lambda_0)=iZ_2(\lambda_0)\delta m(\lambda_0) \tag{145}$$

of an electron in a neutral meson field of mass λ_0. However, in Eq. (142) the coefficients $E^1, \cdots, E^d$ will in general depend on the down direction in W. It is necessary to use a special symmetrization procedure, explained in the following paragraph, to eliminate these coefficients.

Consider the electron self-energy part W^*, obtained by reversing the direction of all arrows in W and at the same time reversing the direction "down" in the path P of doubled lines joining x_1 to x_2. If G is any graph in which W occurs, there exists a graph G^* obtained from G by substituting W^* for W. To pass from G to G^*, it is necessary only to perform a "reflection" of W which interchanges the two ends x_1 and x_2. The factors in Π_W are of three kinds, arising from undoubled lines, doubled lines not in P, and lines in P, respectively. Factors from undoubled lines appear unchanged in $\Pi_W{}^*$. Factors from doubled lines not in P appear in $\Pi_W{}^*$ with a vector $(q+i\eta\Delta)$ changed to $(q-i\eta\Delta)$, where q is a certain linear combination of the $k_a{}^W$, and Δ is the sum of a certain subset of $(\Gamma_1, \cdots, \Gamma_d)$. Factors from lines in P appear in $\Pi_W{}^*$ with a vector $(l+q+i\eta_W(\Delta_2+\Delta))$ changed to $(l+q+i\eta_W(\Delta_1-\Delta))$, the sign of η_W being unchanged because both the down direction in P and the direction of arrows are reversed. Also, the order of all factors in Dirac matrix products is reversed in passing from Π_W to $\Pi_W{}^*$. Therefore, we have

$$I^{W^*}(l+i\eta_W\Delta_2, \Gamma_1, \cdots, \Gamma_d) = I^W(l+i\eta_W\Delta_1, -\Gamma_1, \cdots, -\Gamma_d)_R, \tag{146}$$

where the suffix R denotes the reversal of the order of factors. By Eq. (142), the divergent part of I^{W^*} is

$$I_D{}^{W^*}=X-\sum_r E^r\Gamma_{r\mu}\gamma_\mu + E^0[(l_\mu+i\eta_W\Delta_{1\mu})\gamma_\mu-\mathrm{im}]. \tag{147}$$

Now G and G^* always contribute together to any coefficient M. Therefore, the value of M is unchanged if one replaces every I^W by the symmetrized expression $\frac{1}{2}(I^W+I^{W^*})$. Instead of Eq. (142), the symmetrized $I_D{}^W$ has the simple form,

$$I_D{}^W=X+E^0[(l_\mu+i\bar{\Delta}_\mu)\gamma_\mu-\mathrm{im}], \tag{148}$$

with

$$\bar{\Delta}=\tfrac{1}{2}\eta_W(\Delta_1+\Delta_2). \tag{149}$$

The dependence of $I_D{}^W$ on the down direction in W has now disappeared.

Let G be any graph in which W occurs, and G' a graph obtained from G by replacing W by any ordinary proper electron self-energy part with d vertices. The sum of the $M(G')$ is denoted by M_d; and M_d is obtained from $M(G)$ when I^W is replaced by a sum

$$J^{d'}=J_F{}^d+J_D{}^{d'}, \tag{150}$$

where $J_F{}^d$ is convergent and

$$J_D{}^{d'}=iK_d m+E_d[(l_\mu+i\bar{\Delta}_\mu)\gamma_\mu-\mathrm{im}]. \tag{151}$$

Note that the vector $(l+i\bar{\Delta})$ depends only on the part of G outside W, and is the same for all G'. In Eq. (151), K_d and E_d are coefficients in the expansions,

$$Z_2(\lambda_0)\left[\frac{\delta m(\lambda_0)}{m}\right]=\sum_{d=2}^{\infty}K_d e_1{}^d, \tag{152}$$

$$Z_2(\lambda_0)=1+\sum_{d=2}^{\infty}E_d e_1{}^d, \tag{153}$$

in accordance with Eqs. (93) and (94) of II.[16] They are independent of G and of the situation of W in G.

There will also be a contribution to M from the graph G_0 obtained from G by replacing W by a single-vertex electron self-energy part W_0, at which the term of degree $e_1{}^d$ in the interaction H_{ge} is supposed to operate. The addition to $J^{d'}$ from W_0 is

$$J_0{}^d=-iA_d m, \tag{154}$$

A_d being the coefficient appearing in Eq. (25). Note that this does not precisely cancel the term K_d in Eq. (151). The sum J^d of integrals I^W, from proper self-energy parts with d vertices and from W_0, is

$$J^d=J_D{}^d+J_F{}^d, \tag{155}$$

$$J_D{}^d=\mathrm{im}(K_d-A_d)+E_d[(l_\mu+i\bar{\Delta}_\mu)\gamma_\mu-\mathrm{im}]. \tag{156}$$

By Ward's identity,[13] which holds for neutral vector meson fields as well as for the ordinary maxwell field, the renormalization factors $Z_1(\lambda_0)$ and $Z_2(\lambda_0)$ in Eqs. (133) and (153) are equal. Therefore, one obtains

$$E_d=-L_d. \tag{157}$$

To summarize the results of the analysis so far, all the remaining divergences of the theory are comprised in Eqs. (132) and (156), arising, respectively, from proper vertex parts and from proper electron self-energy parts. The divergent coefficients are defined by Eqs. (25), (133), (152), and (153). It remains only to show in the next section how Eqs. (132) and (156) cancel each other exactly in the calculation of M. The physical reason for the cancellation is that these terms are not true renormalization effects but only "wave function renormalization terms" of a kind which are familiar in elementary perturbation theory. In the present paper, thanks to the complex denominators which never

[16] The factors 2π which appeared in II are now dropped because all the integrals $M(G, \Lambda)$ are expressed in terms of the functions $2\pi D_F$, $2\pi S_F$. The inconvenient factors 2π arose originally from Eqs. (44) and (45) of II.

vanish or become indeterminate, the treatment of such wave function renormalization effects is free from the difficulties and ambiguities which arose in earlier discussions.[17]

X. REMOVAL OF REMAINING DIVERGENCES

In this section the divergences (132) and (156) are to be removed. The strategy of the removal is as follows. A supplementary interaction H_q is introduced, which plays the same role for the electron-positron field as the supplementary interaction H_p of the Gupta formalism played for the electromagnetic field. H_p was a real interaction which was introduced into the lagrangian of quantum electrodynamics to take account of the renormalization of electromagnetic fields. But there is no actual renormalization of the electron-positron field, in consequence of Ward's identity, which is essentially a statement of the law of conservation of charge in radiative processes. Therefore, H_q is not a real interaction, but must be introduced artificially into the formalism. This is done by adding to the hamiltonian H^I given by Eq. (11) a term (H_q-H_q). To the interaction (28) there is added a corresponding term $(H_{qq}-H_{qq})$. The definitions of H_q and H_{qq} are

$$H_q(x)=[1-Z_2^{-1}(\lambda_0)]L_D(x),$$
$$H_{qq}=[1-Z_{2g}^{-1}(\lambda_0)]L_D(x'), \tag{158}$$

where

$$L_D(x)=-\hbar c\{\tfrac{1}{2}[\bar\psi\gamma_\mu(\partial\psi/\partial x_\mu)-(\partial\bar\psi/\partial x_\mu)\gamma_\mu\psi]+m\bar\psi\psi\}, \tag{159}$$

$$Z_{2g}(\lambda_0)=1+\sum_{d=2}^{\infty}E_d[e_1g(t-t')]^d, \tag{160}$$

$$Z_{2g}^{-1}(\lambda_0)=1-\sum_{d=2}^{\infty}C_d[e_1g(t-t')]^d. \tag{161}$$

The additional interactions H_{qq} and $(-H_{qq})$ are treated in just the same way as the other terms in H_q. Thus, the possible graphs G giving contributions $M(G)$ to M are made more numerous by allowing two new types of vertex to appear, which will be called P-vertices and N-vertices. Both P- and N-vertices may be inserted in all possible combinations in all the electron lines of every graph. At each P- or N-vertex there are two electron lines and no photon line incident. At each P-vertex one term, of a particular order e_1^d in the series expansion of the interaction H_{qq}, is supposed to operate; at each N-vertex one term in the series expansion of $(-H_{qq})$.

[17] For example, J. Schwinger, Phys. Rev. **76**, 790 (1949), especially p. 795; and Sec. VII of II, Eq. (99). The best published treatment is that of R. Karplus and N. M. Kroll, Phys. Rev. **77**, 536 (1949), p. 542.

Every P- and N-vertex is a single-vertex electron self-energy part which may be denoted by W. The two lines adjacent to W will carry momentum vectors R_1 and R_2 given by Eqs. (134) and (135). Let G be any graph in which W appears. They by Eq. (159) the factor contributed by W to $M(G)$ is for a P-vertex

$$I_P{}^W=C_d[(l_\mu+i\bar\Delta_\mu)\gamma_\mu-\mathrm{im}], \tag{162}$$

and for an N-vertex

$$I_N{}^W=-C_d[(l_\mu+i\bar\Delta_\mu)\gamma_\mu-\mathrm{im}]. \tag{163}$$

Strictly speaking, the time-derivatives in Eq. (159) will introduce singular terms in addition to Eqs. (162) and (163), similar to the singular terms discussed in Sec. VI. But the singular terms produced by H_{qq} and by $(-H_{qq})$ are equal and opposite, and may therefore be dropped without further argument.

Eventually, the P-vertices will cancel the divergences (132), and the N-vertices will cancel Eq. (156). But the cancellation is not immediate, and careful consideration must be given to the reducible vertex parts and self-energy parts which contribute to Eqs. (132) and (156) only after the removal of their internal divergences. It is convenient first of all to make an intensive study of the effects of P-vertices in isolation. This study will occupy the following nine paragraphs.

Consider any graph G_0 without P-vertices. A class C of graphs G may be derived by inserting any number of P-vertices independently into each electron line of G_0. It is desired to find the relation between $M(G_0)$ and the sum $M(C)$ of the $M(G)$ with G belonging to C. Consider first the effect of inserting P-vertices into a single external line λ_E of G_0. Suppose that λ_E is incident at the vertex y of G_0, and let $\eta=\pm1$ according as the arrow in λ_E points towards or away from y. Let l be the momentum carried by λ_E. Since l is the momentum of a real particle whose spin-function appears as a factor in Eq. (41), the Dirac equation,

$$l_\mu\gamma_\mu-\mathrm{im}=0, \tag{164}$$

holds whenever the left side of Eq. (164) operates directly on Eq. (41). Let G be a typical graph derived from G_0 by inserting into λ_E the P-vertices $y_1, \cdots, y_r$, in order reading inwards towards y. At each y_i the term of order $e_1^{d_i}$ in H_{qq} is operating. Let Λ_i be the sum of d_i vectors Γ_j associated with y_i according to Eq. (53). Let

$$\Delta_i=\Lambda_1+\cdots+\Lambda_i, \quad \Delta_0=0. \tag{165}$$

Then, $M(G)$ is obtained from $M(G_0)$ by making two alterations. First, an extra Δ_r is added to the vectors Δ in the denominators of all factors in $M(G_0)$ corresponding to doubled lines of G_0 on the route from y to x. Second, additional factors are inserted in $M(G_0)$,

namely,

$$F=[(l_\mu+i\eta\Delta_{r\mu})\gamma_\mu-\mathrm{im}]^{-1}Cd_r \times[(l_\mu+\tfrac{1}{2}i\eta(\Delta_{r\mu}+\Delta_{r-1,\mu}))\gamma_\mu-\mathrm{im}] \times[(l_\mu+i\eta\Delta_{r-1,\mu})\gamma_\mu-\mathrm{im}]^{-1}\cdots \times Cd_2[(l_\mu+\tfrac{1}{2}i\eta(\Delta_{2\mu}+\Delta_{1\mu}))\gamma_\mu-\mathrm{im}] \times[(l_\mu+i\eta\Delta_{1\mu})\gamma_\mu-\mathrm{im}]^{-1}Cd_1 \times[(l_\mu+\tfrac{1}{2}i\eta\Delta_{1\mu})\gamma_\mu-\mathrm{im}]. \quad (166)$$

The order of factors in Eq. (166) is as written when $\eta=+1$, and is reversed when $\eta=-1$. Let F'' denote the product of the numerical factors Cd_i in Eq. (166), and let F' be the product of the remaining factors.

Let $\sum_j F'$ denote the sum of the $(j!)$ products obtained by permuting $\Lambda_1, \cdots, \Lambda_j$ in F'. In $\sum_1 F'=F'$, the last factor of Eq. (166) may be replaced, using Eq. (164), by

$$[(\tfrac{1}{2}l_\mu+\tfrac{1}{2}i\eta\Delta_{1\mu})\gamma_\mu-\tfrac{1}{2}\mathrm{im}]. \quad (167)$$

This combines with the previous factor to give $(1/2)$ simply. Next, in $\sum_2 F'$ the third from last factor of Eq. (166) becomes

$$[(2l_\mu+\tfrac{3}{2}i\eta\Delta_{2\mu})\gamma_\mu-2\,\mathrm{im}], \quad (168)$$

and using Eq. (164) this may be replaced by

$$[(\tfrac{3}{2}l_\mu+\tfrac{3}{2}i\eta\Delta_{2\mu})\gamma_\mu-\tfrac{3}{2}\,\mathrm{im}] \quad (169)$$

which combines with the previous factor to give $(3/2)$ simply. Continuing in this way, in $\sum_j F'$ the $(2r-2j+2)$th factor of Eq. (166) becomes

$$[(jl_\mu+(j-\tfrac{1}{2})i\eta\Delta_{j\mu})\gamma_\mu-j\,\mathrm{im}], \quad (170)$$

which may be replaced, using Eq. (164), by

$$(j-\tfrac{1}{2})[(l_\mu+i\eta\Delta_{j\mu})\gamma_\mu-\mathrm{im}]. \quad (171)$$

This combines with the $(2r-2j+1)$th factor to give $(j-\frac{1}{2})$ simply. Therefore, finally

$$\sum_r F'=\left[\frac{1}{2}\cdot\frac{3}{2}\cdot\frac{5}{2}\cdots\frac{2r-1}{2}\right]=(r!)f_r, \quad (172)$$

where

$$f_k=\left[\frac{1}{2}\cdot\frac{3}{4}\cdot\frac{5}{6}\cdots\frac{2k-1}{2k}\right], \quad f_0=1. \quad (173)$$

Suppose that n_1 of the d_i are equal to 1, n_2 are equal to 2, and so on. Consider all the graphs G obtained by inserting the P-vertices $y_1, \cdots, y_r$ into λ_E with the given set of indices $d_1, \cdots, d_r$ permuted in all possible ways. Let $\sum M(G)$ be the sum of the $M(G)$ derived from these graphs. In $\sum M(G)$ there appears instead of the factor F the expression,

$$\sum F=(n_1!n_2!\cdots)^{-1}F''\sum_r F' =[r!/(n_1!n_2!\cdots)]f_rC_1^{n_1}C_2^{n_2}\cdots, \quad (174)$$

which is a pure number.

Let

$$d=\sum d_i=\sum jn_j. \quad (175)$$

Consider now all the graphs G obtained by inserting any number of P-vertices with any indices d_i into λ_E, only the value of d being fixed. The sum $\sum_d M(G)$ summed over all such G is obtained by inserting in $M(G_0)$ instead of Eq. (166) the numerical factor F_d, which is the coefficient of e_1^d in the expansion,

$$\sum_{n_1}\sum_{n_2}\cdots[(n_1+n_2+\cdots)!/(n_1!n_2!\cdots)] \times f_{(n_1+n_2+\cdots)}(C_1e_1)^{n_1}(C_2e_1^2)^{n_2}\cdots. \quad (176)$$

By the multinomial theorem and Eq. (161), this expansion is identically

$$1+\sum F_de_1^d=[1-\sum C_de_1^d]^{-1}=Z_2^{\frac{1}{2}}(\lambda_0). \quad (177)$$

In every term of $\sum_d M(G)$ there is, in addition to the factor F, also the extra Δ_r to be inserted into the denominators of factors of $M(G_0)$. This Δ_r is the sum of d vectors Γ_j, and is the same for all terms in $\sum_d M(G)$. Such an added Δ_r would be introduced into $M(G_0)$, in precisely the same way, if the interaction operating at the vertex y of G_0 were multiplied by $[g(l-l')]^d$. Let then $M(G)$ be summed over all graphs G derived from G_0 by inserting all combinations of P-vertices into λ_E, the result being $M(G_0, \lambda_E)$. To obtain $M(G_0, \lambda_E)$ from $M(G_0)$, it is only necessary to multiply the interaction operating at y in G_0 by the factor,

$$1+\sum F_de_1^d[g(l-l')]^d=Z_{2g}^{\frac{1}{2}}(\lambda_0), \quad (178)$$

in virtue of Eqs. (161) and (177). Incidentally, the above derivation of Eq. (178), with the square root appearing as the sum of a multinomial expansion, indicates the lines along which a rigorous mathematical derivation of the square-root renormalization factors in Eq. (99) of II can be constructed.

Next consider the effect of inserting P-vertices into a single internal line λ_s of G_0. Let the ends of λ_s be y and z. The line-doubling in G_0 can always be arranged so that λ_s is doubled. It is supposed that the down direction in λ_s runs from z to y. Let

$$R_s=l+i\eta\Delta \quad (179)$$

be the vector appearing in the factor (73) contributed by λ_s to $M(G_0)$. Let G be a typical graph derived from G_0 by inserting in λ_s the P-vertices $y_1, \cdots, y_r$, in order reading from z to y. Let d_i, Λ_i, and Δ_i be defined for each y_i as before. Then $M(G)$ is obtained from $M(G_0)$ by making two alterations. First, an extra Δ_r is inserted in some factors of $M(G_0)$ precisely as before. Second, new factors are inserted in $M(G_0)$, namely, those obtained by replacing l in Eq. (166) by $(l+i\eta\Delta)$. That is to say, the factor (73) in $M(G_0)$ is replaced by

$$F_\Delta=F''F_\Delta',$$

with

$$F_\Delta' = [(l_\mu + i\eta(\Delta_\mu + \Delta_{r\mu}))\gamma_\mu - \mathrm{im}]^{-1} \times [(l_\mu + i\eta(\Delta_\mu + \tfrac{1}{2}\Delta_{r\mu} + \tfrac{1}{2}\Delta_{r-1,\mu}))\gamma_\mu - \mathrm{im}]\cdots \times [(l_\mu + i\eta(\Delta_\mu + \Delta_{1\mu}))\gamma_\mu - \mathrm{im}]^{-1} \times [(l_\mu + i\eta(\Delta_\mu + \tfrac{1}{2}\Delta_{1\mu}))\gamma_\mu - \mathrm{im}] \times [(l_\mu + i\eta\Delta_\mu)\gamma_\mu - \mathrm{im}]^{-1}. \quad (180)$$

The order of factors in F_Δ' is again to be reversed if $\eta = -1$.

Let $\sum_r F_\Delta'$ be defined as the sum of the products obtained by permuting $\Delta_1, \cdots, \Delta_r$ in F_Δ'. The following identity, which is a generalization of Eq. (172), will be proved by induction on r.

$$\sum_r F_\Delta' = \sum_{j=0}^{r} f_j f_{r-j} \sum_r [(l_\mu + i\eta(\Delta_\mu + \Delta_{j\mu}))\gamma_\mu - \mathrm{im}]^{-1}, \quad (181)$$

with f_j given by Eq. (173). The summation $\sum_r$ is over the $(r!)$ permutations of the Δ_j, on both sides of Eq. (181). To prove Eq. (181) for any value of r, assume it to hold for $(r-1)$. Then we have

$$\sum_r F_\Delta' = \sum_{j=0}^{r-1} f_j f_{r-1-j} \sum_r [(l_\mu + i\eta(\Delta_\mu + \Delta_{r\mu}))\gamma_\mu - \mathrm{im}]^{-1} \times [(l_\mu + i\eta(\Delta_\mu + \tfrac{1}{2}\Delta_{r\mu} + \tfrac{1}{2}\Delta_{r-1,\mu}))\gamma_\mu - \mathrm{im}] \times [(l_\mu + i\eta(\Delta_\mu + \Delta_{j\mu}))\gamma_\mu - \mathrm{im}]^{-1}. \quad (182)$$

The middle factor in square brackets in Eq. (182), when summed over permutations of the Δ_j, is equivalent to

$$[(2r-2j-1)/(2r-2j)][(l_\mu + i\eta(\Delta_\mu + \Delta_{r\mu}))\gamma_\mu - \mathrm{im}] + [1/(2r-2j)][(l_\mu + i\eta(\Delta_\mu + \Delta_{j\mu}))\gamma_\mu - \mathrm{im}]. \quad (183)$$

Substituting Eq. (183) into Eq. (182) gives immediately Eq. (181) with the help of the elementary identity[18]

$$\sum_{i=0}^{r-1} \frac{1}{(2r-2j)} f_j f_{r-1-j} = f_r. \quad (184)$$

This completes the proof of Eq. (181).

Let $\sum M(G)$ denote as before the sum of the $M(G)$ derived from G obtained by inserting the P-vertices $y_1, \cdots, y_r$ with the given set of indices $d_1, \cdots, d_r$ permuted in all possible ways. In $\sum M(G)$ there appears instead of the factor F_Δ the expression

$$\sum F_\Delta = (n_1! n_2! \cdots)^{-1} F'' \sum_r F_\Delta'. \quad (185)$$

Let Q denote any subset of the indices d_i, containing q_1 indices equal to 1, q_2 equal to 2, and so on. Thus, $0 \leq q_i \leq n_i$ for each i. Let

$$p_i = n_i - q_i, \quad j = \sum q_i, \quad r - j = \sum p_i. \quad (186)$$

[18] To prove Eq. (184), equate coefficients of x^r in the identity $(1-x)^{-\frac{1}{2}}(1-x)^{\frac{1}{2}} = 1$.

Using (181), we have for Eq. (185)

$$\sum F_\Delta = \sum_Q [j!/(q_1! q_2! \cdots)][(r-j)!/(p_1! p_2! \cdots)] \times f_j f_{r-j} [C_1^{p_1+q_1} C_2^{p_2+q_2} \cdots] \times [(l_\mu + i\eta(\Delta_\mu + \Delta_{Q\mu}))\gamma_\mu - \mathrm{im}]^{-1}, \quad (187)$$

where Δ_Q is the sum of the Δ_i corresponding to the indices d_i in Q. The part of $\sum M(G)$ arising from a particular term Q in the sum (187) will be denoted by $M_Q(G)$.

Let d' be the sum of the d_i in Q, d'' the sum of the d_i not in Q, and $d = d' + d''$. Let $M_Q(G)$ now be summed over all graphs G obtained by inserting any number of P-vertices into λ_s with any set of indices $d_1, \cdots, d_r$, and over all subsets Q of the d_i, with G and Q being restricted only by the condition that d' and d'' are to have fixed values. Let the double sum be denoted by $\sum_d M_Q(G)$. The Δ_Q appearing in Eq. (187) is a sum of d' vectors Γ_i. Since these Γ_i are equivalent integration variables in $M(G)$ according to Eq. (59), Δ_Q is effectively only dependent on d' and is the same in all terms of the sum $\sum_d M_Q(G)$. Therefore, $\Delta_{d'}$ will be written instead of Δ_Q. To obtain $\sum_d M_Q(G)$ from $M(G_0)$, the factor

$$[(l_\mu + i\eta\Delta_\mu)\gamma_\mu - \mathrm{im}]^{-1}$$

is replaced by

$$F_{d'd''}[(l_\mu + i\eta(\Delta_\mu + \Delta_{d'\mu}))\gamma_\mu - \mathrm{im}]^{-1}. \quad (188)$$

The numerical factor $F_{d'd''}$ is by Eq. (187) the coefficient of $(e_1')^{d'}(e_1'')^{d''}$ in the expansion

$$\sum p_1 \sum p_2 \cdots \sum q_1 \sum q_2 \cdots [(p_1 + p_2 + \cdots)!/(p_1! p_2! \cdots)] \times [(q_1 + q_2 + \cdots)!/(q_1! q_2! \cdots)] f_{(p_1+p_2+\cdots)} \times f_{(q_1+q_2+\cdots)} (C_1 e_1')^{q_1} (C_2 e_1'^2)^{q_2} \cdots \times (C_1 e_1'')^{p_1} (C_2 e_1''^2)^{p_2} \cdots, \quad (189)$$

which is the multinomial expansion of

$$[1 - \sum C_d (e_1')^d]^{-\frac{1}{2}} [1 - \sum C_d (e_1'')^d]^{-\frac{1}{2}} = Z_2^{\frac{1}{2}}(\lambda_0, e_1') Z_2^{\frac{1}{2}}(\lambda_0, e_1''). \quad (190)$$

Let $M(G_0, \lambda_s)$ be the sum of the $M(G)$ obtained from all G derived from G_0 by inserting P-vertices in λ_s in any way whatever. The same argument that was used for $M(G_0, \lambda_E)$ can be applied to $M(G_0, \lambda_s)$, starting from Eqs. (188) and (190). The conclusion is the following. To obtain $M(G_0, \lambda_s)$ from $M(G_0)$, it is necessary only to multiply the interactions operating both at z and at y in G_0 by the same factor (178).

Returning finally to the class C of graphs obtained by inserting P-vertices into all electron lines of G_0, the sum $M(C)$ will be obtained as follows. Let an E-vertex be defined as a vertex at which electron lines are incident. At every E-vertex of G_0 there are incident exactly two electron lines, internal or external, in each

of which P-vertices may be independently inserted. Therefore, $M(C)$ is derived from $M(G_0)$ by multiplying every interaction operating at every E-vertex of G_0 by the factor

$$Z_{2\varrho}(\lambda_0). \tag{191}$$

This completes the discussion of the effects of P-vertices.

To summarize the results, it has been shown that all the effects of P-vertices are exactly taken into account, if the P-vertices themselves are dropped and the interactions operating at all other E-vertices are multiplied by (191).

There are three types of E-vertex in G_0, namely, ordinary vertices at which $H_{\varrho i}$ operates, S-vertices at which $H_{\varrho s}$ operates, and N-vertices. Consider first the effect of the multiplying factor (191) at an ordinary vertex y. By Eqs. (157) and (160), the term of order d in (191) will precisely cancel the divergent term (132) arising from the insertion of vertex parts with $(d+1)$ vertices into G_0 at y. The cancellation is to be made step by step, first the term $d=2$ in (191) canceling the term $d=2$ in Eq. (132), next the terms $d=4$ canceling, and so on. In this way it is clear that each vertex part is freed from its internal divergences before its own contribution to Eq. (132) is canceled. Therefore, it was correct to calculate L_d in Eq. (132) assuming the internal divergences to have been previously removed.

Next consider the effect of the multiplying factor (191) at an N-vertex. By Eq. (158), the interaction operating at N-vertices is thereby changed into

$$[1-Z_{2\varrho}(\lambda_0)]L_D(x')=-\sum_{d=2}^{\infty} E_d[e_1 g(t-t')]^d L_D(x'). \tag{192}$$

Let W be any N-vertex in G_0 at which the term of order $e_1{}^d$ in Eq. (192) is operating. Then the factor contributed by W to $M(C)$ is

$$-E_d[(l_\mu+i\bar{\partial}_\mu)\gamma_\mu-\mathrm{im}], \tag{193}$$

which now replaces Eq. (163). The multiplying factor (191) does not change the contribution (150) to $M(C)$ arising from ordinary proper electron self-energy parts W'; in fact, the effects of (191) were exactly used up in canceling the internal vertex-part divergences from each W' before Eq. (150) was calculated. The contributions (150) and (193) are both correct after the multiplication by (191), and are to be added together as they stand in calculating $M(C)$. Therefore, the term in E_d in Eq. (156) is precisely canceled by the contribution from N-vertices.

Finally, consider the effect of (191) at an S-vertex. By Eqs. (23), (25), and (152), the interaction at S-vertices is changed into

$$-Z_{2\varrho}(\lambda_0)\delta_\varrho mc^2\bar{\psi}\psi(x')$$

$$=-\sum_{d=2}^{\infty} X_d[e_1 g(t-t')]^d mc^2\bar{\psi}\psi(x'), \tag{194}$$

where X_d is a numerical coefficient depending on λ_0, which becomes formally identical with K_d as λ_0 tends to zero. Therefore, the contribution (154) to J_d is changed into

$$-iX_d m. \tag{195}$$

The term $(iK_d m)$ in Eq. (156) is, however, not changed by the multiplication by (191), since this term arose from ordinary self-energy parts in the same way as the other term in Eq. (151) which was discussed previously. The total effect of the multiplication by (191) is thus to replace Eq. (156) by

$$\mathrm{im}(K_d-X_d). \tag{196}$$

If, at the end of the calculation of M, the auxiliary mass λ_0 is put equal to zero, then (196) vanishes. Unfortunately, putting λ_0 equal to zero will introduce infrared divergences into the convergent integrals $I_F{}^d$ and $J_F{}^d$. The best solution of this difficulty is to insert a small photon mass λ_0 into the formalism from the very beginning, so that the self-energy $\delta m(\lambda_0)$ appears already in Eq. (13). Then, according to Eqs. (152) and (194), K_d and X_d are equal, and (196) vanishes without creating infrared divergences anywhere.

All the divergent terms (132) and (156) are now eliminated from M. This completes the proof, which has occupied Secs. IV–X, that the operator $A_{\mu\varrho}(p)$ is divergence-free.

XI. NOTE ON MATTER-FIELD OPERATORS

Hitherto, attention has been concentrated exclusively on the electromagnetic potentials $A_{\mu\varrho}(p)$. This was done not because the $A_{\mu\varrho}(p)$ are in themselves of any special importance, but because they served as a concrete example to illustrate the technique of carrying through the renormalization program in the intermediate representation. The methods which have been developed in Secs. IV–X can be applied with only minor changes to the analysis of any intermediate representation operators. The most important application of these methods will be to the hamiltonian operator $H'(t)$ of the intermediate representation, defined in Eqs. (6) and (7) of RM. The detailed discussion of $H'(t)$ will be published in a separate paper. Here only the results of the renormalization program applied to the matter-field operators $\psi_\varrho(p)$, $j_{\mu\varrho}(p)$ will be described.

The graphs which contribute to the normal constituents of $\psi_\varrho(p)$ are similar to those contributing to $A_{\mu\varrho}(p)$, except that a single electron line, instead of a single photon line, is incident at the special vertex x. The whole analysis of Secs. IV to X applies unchanged to $\psi_\varrho(p)$, except that in Sec. X the vertex x appears as an additional E-vertex at which the multiplying factor (178) will occur. At x there are no vertex part divergences to compensate Eq. (178). Moreover, at x the two times t and t' in Eq. (178) are equal, and by Eq. (17) the factor (178) reduces to the numerical constant

$Z_2^{\frac{1}{2}}(\lambda_0)$, which becomes $Z_2^{\frac{1}{2}}$ when λ_0 is put equal to zero. Hence, one obtains the result that the operator $\psi_\sigma(p)$ is a divergence-free expression multiplied by the renormalization factor $Z_2^{\frac{1}{2}}$. The same is true of $\bar{\psi}_\sigma(p)$.

The graphs contributing to $j_{\mu\sigma}(p)$ have the property that two electron lines are incident at x. In this case the analysis of Secs. IX–X applies without change, for x behaves like an ordinary E-vertex at which vertex part divergences cancel the multiplying factor (178). However, the cancellation of Sec. VIII fails for the divergences produced by a proper photon self-energy part W one of whose end-vertices is x. The divergence (113) arising from W is not removed by any compensating terms (116), (117), (118). In the intermediate representation operator $j_{\mu\sigma}(p)$, the divergences (113) occur in a rather complicated way. This operator is in general not made finite by renormalization.

However, in the special case of the Heisenberg representation, $g(t)=1$ and all the Γ_i tend to zero. The Heisenberg charge-current operator $\mathbf{j}_\mu(x)$ is defined in the Gupta formalism by

$$\mathbf{j}_\mu(x)=ie_1c\bar{\psi}(x)\gamma_\mu\psi(x). \tag{197}$$

In $\mathbf{j}_\mu(p)$, the divergence (113) arising from a photon self-energy part W incident at x takes the form

$$I_D{}^C=-cB(p^2\delta_{\mu\nu}-p_\mu p_\nu). \tag{198}$$

In $\mathbf{A}_\mu(p)$, the photon line incident at x contributes a factor $(p^2)^{-1}$, and the remaining factor is what remains of $[(1/c)\mathbf{j}_\mu(p)]$ after all the divergences (198) are removed. Also, the divergences (198) in $\mathbf{j}_\mu(p)$ multiply an expression which is identical with $[-c\mathbf{A}_\mu(p)]$. Therefore, altogether, using Eq. (26), one obtains

$$\begin{aligned}(1/c)\mathbf{j}_\mu(p)&=p^2\mathbf{A}_\mu(p)-[\textstyle\sum B_d e_1{}^d](p^2\delta_{\mu\nu}-p_\mu p_\nu)\mathbf{A}_\nu(p)\\&=p^2\mathbf{A}_\mu(p)-f(p^2\delta_{\mu\nu}-p_\mu p_\nu)\mathbf{A}_\nu(p).\end{aligned} \tag{199}$$

This shows that $\mathbf{j}_\mu(p)$ is divergence-free except for the single constant f appearing in Eq. (199). The above derivation of Eq. (199) confirms the consistency of the renormalization method because Eq. (199) is identical with the field-equation for $\mathbf{A}_\mu$ obtained from the lagrangian (3). When the supplementary condition $(p_\nu\mathbf{A}_\nu(p)=0)$ is imposed, Eq. (199) becomes

$$(1/c)\mathbf{j}_\mu(p)=Z_3p^2\mathbf{A}_\mu(p), \tag{200}$$

so that $\mathbf{j}_\mu(p)$ is a divergence-free expression multiplied by the constant $Z_3=(e_1/e)^2$.

XII. THE TRANSITION TO HEISENBERG OPERATORS. CONCLUDING REMARKS

The transition from the intermediate to the Heisenberg representation is to be made by letting the function $g(t)\to1$. To define the limiting process precisely, it is convenient to replace $g(t)$ by $g(t/T)$, where T is a parameter, and then let $T\to\infty$. The derivatives g' and g'' in Eqs. (29) and (30) tend uniformly to zero as $T\to\infty$. The interaction $H_g(x,x')$ defined by Eq. (28) tends uniformly to $H^I(x')$ given by Eq. (11). Therefore, the transformation operator (35) becomes in the limit identical with Eq. (6) of HO.I, the operator leading from the interaction representation to the Heisenberg representation. Heisenberg operators are limiting cases of intermediate representation operators; this is the exact meaning of the remarks made in Sec. IV of HO.I concerning the relation of Eq. (32) to Eq. (33). The limiting process introduces no difficulties into the formal separation and cancellation of divergences, since all the divergent coefficients are constants independent of $g(t)$. However, it is important to inquire, under what conditions the convergent expressions remaining after renormalization will tend to well-defined limits as $g(t)\to1$, independent of the precise way in which the limiting process is performed. Only when such conditions are satisfied will it be permissible to represent Heisenberg operators by power-series in the interaction hamiltonian, as it is done in HO.I.

When $g(t)$ is a function which is equal to 1 at all recent times t and tends to zero only in the remote past, the intermediate representation operators are equivalent to the Heisenberg operators defined for a theory in which the charge e_1 rises adiabatically from the value zero in the remote past to its actual value at the present time. The power-series expansions of Heisenberg operators in HO.I are by definition the limits of the expansions of Heisenberg operators with the adiabatically varying e_1, supposing the limits to exist as the rate of variation of e_1 is made infinitely slow. The whole discussion of Heisenberg operators has a meaning only when these limits exist. Physically speaking, the limits will exist only if the actual state of the system can be deduced from the state of the system existing in the remote past before the adiabatic switching-on of e_1 was begun, independently of the details of the switching-on process. That is to say, the state of the system must be such that at some time in the past only separate free particles existed; then, each free particle can be considered to have been independently formed from an equivalent "bare" particle when e_1 was switched on. The switching-on process must be finished before the separate free particles converge and interact and give rise to the actual state of the system. The state of the system in the remote past must be free from any groups of particles bound together into stable composite structures by the radiation interaction.

The definition of Heisenberg operators as limits of intermediate representation operators, or the equivalent definition by a limiting process involving the adiabatic switching on of e_1, will thus be meaningful only under the following conditions. Tracing the history of the system back into the past, the radiation interaction must have operated only a finite number of times as a true interaction between different particles; further back than this, the system was in a dissociated state

where the radiation interaction produced only the self-fields of individual free particles.

From the last statement of the condition for the validity of the limiting process there follows an interesting consequence. In the power series expansions of Heisenberg operators, after the cancellation of divergences due to renormalization effects, the terms of order e_1^n represent the processes in which the radiation interaction has operated as a true interaction n times during the whole previous history of the system. If the radiation interaction has operated in this way only a finite number of times, then the terms of very high order in e_1 will make a negligible contribution to the operators. That is to say, the series expansions of Heisenberg operators, after renormalization, will themselves be convergent power series. And conversely, if the previous history of the system involves bound states, so that the radiation interaction has operated an infinite number of times, then the power series will not converge.

The convergence of the power series after renormalization has in no case yet been mathematically proved. The above physical argument only makes it plausible that, under the restricted conditions in which the definition of the series expansions of Heisenberg operators by a limiting process is meaningful, the series will always converge.

It needs to be stressed that the conditions under which the series expansions of Heisenberg operators can be defined are very restrictive. In almost all physical situations, bound states of some kind are involved either actually or virtually, and the expansions are either meaningless or misleading. The same remarks apply *a fortiori* to the series expansion of the S-matrix, which requires the absence of bound states not only in the past but also in the future. Just for this reason, the intermediate representation extends the technique of renormalization to a wide range of problems which could not be satisfactorily treated before.[19,20]

In the power series expansions of intermediate representation operators after renormalization, the terms of order e_1^n represent processes in which the radiation interaction has operated as a true interaction n times during the finite interval of time in which $g(t)$ is appreciable. It is plausible, but not proved, that the total probability of such processes will tend to zero rapidly as n tends to infinity, in all circumstances, whether bound states are involved in the system or not. Thus, not only does the use of the intermediate representation overcome the restrictions on the definability of the series expansions of the S-matrix and of Heisenberg operators, but also it may be hoped with some confidence that intermediate representation operators have power series expansions which are always convergent after renormalization.

---

[19] Another method of treating radiation problems has recently been published by E. C. G. Stueckelberg, Phys. Rev. **81**, 130 (1951), which is similar in its basic idea to the intermediate representation method. Both methods begin by replacing the customary integration over an infinite time-interval by an integration over a finite time-interval. But the two methods are so dissimilar in their subsequent development that a direct comparison between them is hardly possible. See also E. C. G. Stueckelberg and T. A. Green, Helv. Phys. Acta **24**, 153 (1951).

[20] A clear discussion of the limitations of the old series expansion methods is given by B. Ferretti, Nuovo cimento **8**, 108 (1951).

Bipolar Expansion of Coulombic Potentials*

ROBERT J. BUEHLER AND JOSEPH O. HIRSCHFELDER
University of Wisconsin Naval Research Laboratory, Madison, Wisconsin
(Received January 10, 1951)

The calculation classically or quantum mechanically of the coulombic interaction between two charge distributions is greatly simplified by use of the bipolar expansion:

$$\frac{1}{r_{12}}=\sum_{n_1,n_2,m} B_{n_1,n_2}^{|m|}(r_1,r_2;R)P_{n_1}^{|m|}(\cos\theta_1)P_{n_2}^{|m|}(\cos\theta_2)\exp[im(\phi_2-\phi_1)].$$

Here (r_1,θ_1,ϕ_1) are the spherical coordinates at a point referred to the center of the first charge distribution, and (r_2,θ_2,ϕ_2) are the spherical coordinates of another point referred to the center of the second distribution; R is the separation between the centers; r_{12} is the distance between the two points; $P_n^{|m|}(\cos\theta)$ are the associated Legendre polynomials; the $B_{n_1,n_2}^{|m|}(r_1,r_2;R)$ are expansion coefficients given in this paper. There are four functional forms for these coefficients, depending on the ratios of r_1, r_2, and R. Three of these have been given recently by Carlson and Rushbrooke. For quantum-mechanical problems involving overlapping charge distributions, the fourth case, $|r_1-r_2|\leqslant R\leqslant r_1+r_2$, must be considered as well. Here the coefficients have a more complicated form. The solution is expressed as an integral, and a number of the coefficients are tabulated. The expansion permits a simple evaluation of the two center coulombic integrals arising in a large variety of quantum-mechanical problems.

THE problem of calculating the coulombic interactions between two charge distributions in either classical or quantum mechanics can often be simplified by using an expansion of $1/r_{12}$ in terms of products of surface harmonics in the two coordinate systems characteristic of the two distributions. Here r_{12} is the distance between a point in distribution 1 and a point in distribution 2. Let a be an origin located in 1; b be an origin in 2; R be the distance between a and b; θ_1 be the internal angle that a radius vector to a point in 1 makes with the line ab; θ_2 be the internal angle that a radius vector to a point in 2 makes with the line ab; let ϕ_1 and ϕ_2 be the angles which the projections of the radius vector make with an axis perpendicular to ab. Figure 1 shows the geometry. The convenient expansion is, then,

$$1/r_{12}=\sum_{n_1,n_2,m} B_{n_1,n_2}^{|m|}(r_1,r_2;R)P_{n_1}^{|m|}(\cos\theta_1)\times P_{n_2}^{|m|}(\cos\theta_2)\exp[im(\phi_2-\phi_1)]. \quad (1)$$

Here n_1 and n_2 go from zero to infinity and m goes from $-n_<$ to $n_<$, where $n_<$ is the lesser of n_1 and n_2. The $P_n^m(\cos\theta)$ are the associated Legendre polynomials defined by[1]

$$P_n^m(x)=(-1)^m(1-x^2)^{m/2}[d^m/dx^m]P_n(x). \quad (2)$$

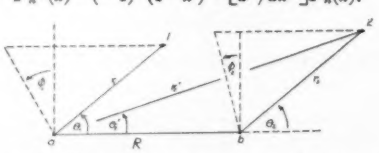

FIG. 1. Coordinates for the bipolar expansion. r_{12} is the distance between points 1 and 2.

Recently Carlson and Rushbrooke[2] have considered this problem. They obtained expressions for $B_{n_1n_2}^{|m|}(r_1,r_2;R)$ provided that $R>r_1+r_2$, $r_2>R+r_1$, or $r_1>R+r_2$. The first condition always applies if the charge distributions do not overlap. However, for overlapping charge distributions such as occur in quantum-mechanical problems it is also necessary to consider another region, $|r_1-r_2|\leqslant R\leqslant r_1+r_2$, which seems to have escaped the attention of Carlson and Rushbrooke. The expressions for the B's are much more difficult to obtain for this region and are the principal subject of attention in the present paper.

An arbitrary charge distribution, $\rho(1;x_1,y_1,z_1)$, can be expressed as the sum of an infinite series of radial functions times surface harmonics:

$$\rho(1;x_1,y_1,z_1)=\sum_{n_1=0}^{\infty}\sum_{m_1=-n_1}^{n_1}\rho_{n_1m_1}(1;r_1)\times P_{n_1}^{|m_1|}(\cos\theta_1)\exp(im_1\phi_1), \quad (3)$$

and a second charge distribution, $\rho(2;x_2,y_2,z_2)$. can be expressed in the form

$$\rho(2;x_2,y_2,z_2)=\sum_{n_2=0}^{\infty}\sum_{m_2=-n_2}^{n_2}\rho_{n_2m_2}(2;r_2)\times P_{n_2}^{|m_2|}(\cos\theta_2)\exp(im_2\phi_2). \quad (4)$$

Here ρ_{00} determines the net charge in the distribution; $\rho_{1,-1}$, $\rho_{1,0}$, $\rho_{1,1}$ determine its dipole moment; $\rho_{2,-2}$, $\rho_{2,-1}$, $\rho_{2,0}$, $\rho_{2,1}$, $\rho_{2,2}$ determine its quadrupole moment; etc. The electrostatic energy of interaction between the two charge distributions is

$$V_{12}=\int\int[\rho(1;x_1,y_1,z_1)\rho(2;x_2,y_2,z_2)/r_{12}]d\tau_1d\tau_2. \quad (5)$$

* This work was carried out under a contract between the United States Navy Bureau of Ordnance and the University of Wisconsin.

[1] The factor $(-1)^m$ is not included by all authors. Our formulas hold if either definition is used consistently.

[2] B. C. Carlson and G. S. Rushbrooke, Proc. Cambridge Phil. Soc. 46, 626 (1950).

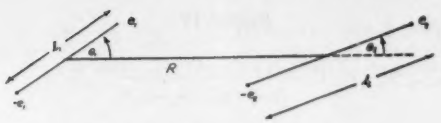

FIG. 2. Interacting dipoles.

Substituting Eqs. (1), (3), and (4) into Eq. (5) and making use of the orthogonality relations between the spherical harmonics, it follows after integrating over the angles that

$$V_{12}=\sum_{n_1=0}^{\infty}\sum_{n_2=0}^{\infty}\sum_{m=-n_<}^{n_<}\frac{16\pi^2}{(2n_1+1)(2n_2+1)}\times\frac{(n_1+|m|)!(n_2+|m|)!}{(n_1-|m|)!(n_2-|m|)!}\cdot\int_0^\infty\int_0^\infty B_{n_1n_2}{}^{|m|}(r_1,r_2;R)\rho_{n_1m}(1;r_1)\times\rho_{n_2m}(2;r_2)r_1{}^2r_2{}^2dr_1dr_2. \quad (6)$$

The problem of evaluating V_{12} is thus considerably reduced by the introduction of the bipolar expansion.

The charge distributions are usually expressed with respect to principal axes located within the charge distribution and oriented so as to diagonalize some tensor property of the system. Thus,

$$\rho(1;x_1,y_1,z_1)=\sum_{n_1=0}^{\infty}\sum_{m_1'=-n_1}^{n_1}\rho_{n_1m_1'}(1;r_1)\times P_{n_1}{}^{|m_1'|}(\cos\theta_1')\exp(im_1'\phi_1'), \quad (7)$$

where θ_1' and ϕ_1' are the angles that the point in question makes with the principal axes. Similarly, a second charge distribution would be expressed in terms of its principal axes:

$$\rho(2;x_2,y_2,z_2)=\sum_{n_2=0}^{\infty}\sum_{m_2'=-n_2}^{n_2}\rho_{n_2m_2'}(2;r_2)\times P_{n_2}{}^{|m_2'|}(\cos\theta_2')\exp(im_2'\phi_2'). \quad (8)$$

But by simple group theory, the radial functions $\rho_{n_1m_1'}(1;r_1)$ can be related to the $\rho_{n_1m_1}(1;r_1)$ of the previous example, Eq. (3), and the $\rho_{n_2m_2'}(2;r_2)$ can be related to the $\rho_{n_2m_2}(2;r_2)$ of Eq. (4). Let S_1 and S_2 be the rotations which turn the two principal axes systems respectively into coincidence with a fixed laboratory reference frame. Then let T be a rotation which turns the Z axis of the laboratory frame into an orientation parallel to the line passing from the origin of the first distribution to the origin of the second. Then TS_1 and TS_2 respectively turn the principal axes of the two distributions into the orientations of Fig. 1. Then if $D^{(n)}(R)_{m'm}$ are the standard rotational representation coefficients, it follows that

$$\rho_{n_1m_1}(1;r_1)=\sum_{m_1'}D^{(n_1)}(TS_1)_{m_1'm_1}\rho_{n_1m_1'}(1;r_1), \quad (9)$$

$$\rho_{n_2m_2}(2;r_2)=\sum_{m_2'}D^{(n_2)}(TS_2)_{m_2'm_2}\rho_{n_2m_2'}(2;r_2). \quad (10)$$

Substituting Eqs. (9) and (10) into Eq. (6) gives V_{12} as a function of the orientations, TS_1 and TS_2, of the two charge distributions.

In quantum mechanics, the charge distributions only involve the first few spherical harmonics and, therefore, expansions of the form of Eq. (6) greatly simplify the work required in the evaluation of the coulombic integrals. As a matter of fact, most of the coulombic integrals are easy to evaluate once the B's are known. It is therefore worthwhile to evaluate the B's once and for all and thereby simplify a great many quantum-mechanical problems. The expansion, Eq. (1), can also be used to good advantage to determine the interaction between two discrete charge distributions. For example, the energy of interaction between two real dipoles as shown in Fig. 2 is given by the equation,

$$V_{12}=4e_1e_2\sum_{n_1=0}^{\infty}\sum_{n_2=0}^{\infty}\sum_{m=-(2n_<+1)}^{2n_<+1}B_{2n_1+1,2n_2+1}{}^{|m|}\times\left(\frac{l_1}{2},\frac{l_2}{2};R\right)\cdot P_{2n_1+1}{}^{|m|}(\cos\theta_1)P_{2n_2+1}{}^{|m|}(\cos\theta_2)\times\exp[im(\phi_2-\phi_1)]. \quad (11)$$

At distances, R, large compared with l_1 and l_2, the $B_{2n_1+1,2n_2+1}{}^{|m|}(l_1/2,l_2/2,R)$ vary as $R^{-3-2n_1-2n_2}$, so that the lead term, corresponding to $n_1=n_2=0$, is just the energy of interaction between two ideal dipoles.

THE FUNCTION $B_{n_1n_2}{}^{|m|}(r_1,r_2;R)$

There are four sets of functional forms of the $B_{n_1n_2}{}^{|m|}$, corresponding to the four regions shown in Fig. 3:

$$\text{I. } R>r_1+r_2, \quad \text{II. } |r_1-r_2|\leqslant R\leqslant r_1+r_2, \quad \text{III. } r_2>R+r_1, \quad \text{IV. } r_1>R+r_2. \quad (12)$$

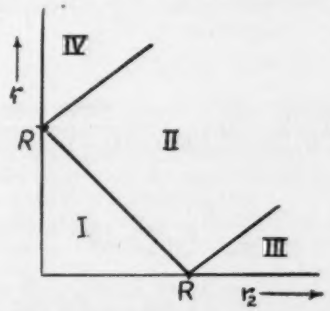

FIG. 3. The four regions of definition of the B's. I: $R>r_1+r_2$. II: $|r_1-r_2|\leqslant R\leqslant r_1+r_2$. III: $r_2>R+r_1$. IV: $r_1>R+r_2$.

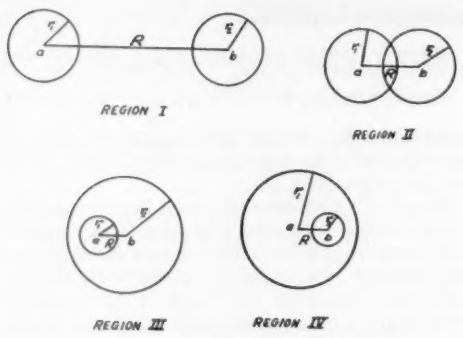

FIG. 4. Alternate description of the four regions. I: $R>r_1+r_2$. II: $|r_1-r_2|\leqslant R\leqslant r_1+r_2$. III: $r_2>R+r_1$. IV: $r_1>R+r_2$.

The geometrical significance of the four regions is shown in Fig. 4.

If the two charge distributions do not overlap, only region I need be considered. Here

Region I

$$B_{n_1,n_2}{}^{|m|}(r_1,r_2;R)=\frac{(-1)^{n_2+|m|}(n_1+n_2)!}{(n_1+|m|)!(n_2+|m|)!}r_1{}^{n_1}r_2{}^{n_2}R^{-n_1-n_2-1}. \quad (13)$$

For overlapping charge distributions it is necessary to consider the other three regions as well. In regions III and IV, the B's are still simple.[3]

Region III

$$B_{n_1,n_2}{}^{|m|}(r_1,r_2;R)=\frac{(-1)^{n_1+n_2}(n_2-|m|)!}{(n_1+|m|)!(n_2-n_1)!}\times r_1{}^{n_1}r_2{}^{-n_2-1}R^{n_2-n_1}\quad(n_2\geqslant n_1)$$
$$=0\quad(n_2<n_1). \quad (14)$$

Region IV

$$B_{n_1,n_2}{}^{|m|}(r_1,r_2;R)=\frac{(n_1-|m|)!}{(n_2+|m|)!(n_1-n_2)!}\times r_1{}^{-n_1-1}r_2{}^{n_2}R^{n_1-n_2}\quad(n_1\geqslant n_2)$$
$$=0\quad(n_1<n_2). \quad (15)$$

In Region II, the $B_{n_1,n_2}{}^{m}(r_1,r_2;R)$ are difficult to obtain. They have the functional form

Region II

$$B_{n_1,n_2}{}^{|m|}(r_1,r_2;R)=\frac{1}{D_{n_1,n_2}{}^{|m|}}\sum_{i,j=0}^{2(n_1+n_2+1)}A_{n_1,n_2}{}^{|m|}(i,j)\times r_1{}^{i-n_1-1}r_2{}^{j-n_2-1}R^{n_1+n_2-i-j+1}. \quad (16)$$

The coefficients $A_{n_1,n_2}{}^{|m|}$ and $D_{n_1,n_2}{}^{|m|}$ for n_1 and $n_2=0$, 1, 2, and 3 together with all of the appropriate values of m are given in Table I. The functions for which $n_1>n_2$ are not given, for they may be determined at once by permuting n_1 and n_2 according to the formula

$$B_{n_1,n_2}{}^{|m|}(r_1,r_2;R)=(-1)^{n_1+n_2}B_{n_2,n_1}{}^{|m|}(r_2,r_1;R). \quad (17)$$

For other values of n_1 and n_2 (not given in Table I), the coefficients may be evaluated by the methods discussed in the appendix.

Substituting Eqs. (13), (14), (15), and (16) into Eq. (6), the energy of interaction between two charge distributions may be written in the form:

$$V_{12}=V_{12}{}^{\mathrm{I}}+V_{12}{}^{\mathrm{II}}+V_{12}{}^{\mathrm{III}}+V_{12}{}^{\mathrm{IV}}, \quad (18)$$

where the $V_{12}{}^{\mathrm{I}}$, $V_{12}{}^{\mathrm{II}}$, $V_{12}{}^{\mathrm{III}}$, and $V_{12}{}^{\mathrm{IV}}$ are the contributions of the various regions:

$$V_{12}{}^{\mathrm{I}}=\sum_{n_1=0}^{\infty}\sum_{n_2=0}^{\infty}\sum_{m=-n_<}^{n_<}\frac{16\pi^2(-1)^{n_2+|m|}(n_1+n_2)!}{(2n_1+1)(2n_2+1)(n_1-|m|)!(n_2-|m|)!R^{1+n_1+n_2}}\cdot\int_0^R\rho_{n_2m}(2;r_2)r_2{}^{n_2+2}dr_2\int_0^{R-r_2}\rho_{n_1m}(1;r_1)r_1{}^{n_1+2}dr_1, \quad (19)$$

$$V_{12}{}^{\mathrm{II}}=\sum_{n_1=0}^{\infty}\sum_{n_2=0}^{\infty}\sum_{m=-n_<}^{n_<}\frac{16\pi^2(n_1+|m|)!(n_2+|m|)!}{(2n_1+1)(2n_2+1)(n_1-|m|)!(n_2-|m|)!D_{n_1n_2}{}^{|m|}}\cdot\sum_{i,j=0}^{2(n_1+n_2-1)}A_{n_1n_2}{}^{|m|}(i,j)R^{n_1+n_2+1-i-j}\left[\begin{array}{l}\displaystyle\int_0^R\rho_{n_2,m}(2;r_2)r_2{}^{j-n_2+1}dr_2\int_{R-r_2}^{R+r_2}\rho_{n_1,m}(1;r_1)r_1{}^{i-n_1+1}dr_1\\ \displaystyle+\int_R^{\infty}\rho_{n_2,m}(2;r_2)r_2{}^{j-n_2+1}dr_2\int_{r_2-R}^{r_2+R}\rho_{n_1,m}(1;r_1)r_1{}^{i-n_1+1}dr_1\end{array}\right], \quad (20)$$

[3] Carlson and Rushbrooke (reference 2) do not express the solution in this form, but Eqs. (14) and (15) follow from their results. An alternate derivation is given in the appendix.

$$V_{12}^{\mathrm{III}}=\sum_{n_2=0}^{\infty}\sum_{n_1=0}^{n_2}\sum_{m=-n_1}^{n_1}\frac{16\pi^2(-1)^{n_1+n_2}(n_2+|m|)!}{(2n_1+1)(2n_2+1)(n_1-|m|)!(n_2-n_1)!}R^{n_2-n_1}\cdot\int_R^{\infty}\rho_{n_2,m}(2;r_2)r_2^{-n_2+1}dr_2\int_0^{r_2-R}\rho_{n_1,m}(1;r_1)r_1^{n_1+2}dr_1, \quad (21)$$

$$V_{12}^{\mathrm{IV}}=\sum_{n_1=0}^{\infty}\sum_{n_2=0}^{n_1}\sum_{m=-n_2}^{n_2}\frac{16\pi^2(n_1+|m|)!R^{n_1-n_2}}{(2n_1+1)(2n_2+1)(n_2-|m|)!(n_1-n_2)!}\cdot\int_0^{\infty}\rho_{n_2,m}(2;r_2)r_2^{n_2+2}dr_2\int_{R+r_2}^{\infty}\rho_{n_1,m}(1;r_1)r_1^{-n_1+1}dr_1. \quad (22)$$

If the first charge distribution is confined to a radius of l_1, and the second charge distribution is confined to a radius of l_2, then if R is larger than l_1+l_2 so that the charge distributions do not overlap, only V_{12}^{I} is different from zero and the energy of interaction has the form:

$$V_{12}=\sum_{n_1=0}^{\infty}\sum_{n_2=0}^{\infty}\sum_{m=-n_<}^{n_<}\frac{(-1)^{n_2+|m|}(n_1+n_2)!}{R^{1+n_1+n_2}}\times Q_{n_1,m}(1)Q_{n_2,m}(2), \quad (23)$$

where

$$Q_{n_1,m}(1)=\frac{4\pi}{(2n_1+1)(n_1-|m|)!}\times\int_0^{\infty}\rho_{n_1,m}(1;r_1)r_1^{n_1+2}dr_1, \quad (24)$$

$$Q_{n_2,m}(2)=\frac{4\pi}{(2n_2+1)(n_2-|m|)!}\times\int_0^{\infty}\rho_{n_2,m}(2;r_2)r_2^{n_2+2}dr_2. \quad (25)$$

In this way the energy of interaction is related to the moments of the charge distributions. Equation (18) is then, the generalization which applies to the overlapping charge distributions which are most common in quantum mechanics.

The authors wish to acknowledge the assistance of Gene Haugh, Marjorie Leikvold, Alice Epstein, Ruth Straus, Dorothy Smith, and Dorothy Campbell in evaluating the integrals for Region II. The derivation presented in the Appendix was shortened considerably by an observation of R. McKelvey. This work was made possible by the financial assistance of the Navy Bureau of Ordnance.

APPENDIX. EVALUATION OF THE EXPANSION COEFFICIENTS

The reciprocal of the distance r_{12} between two points can be expressed by the well-known Neumann expansion.[4] Letting $(r_1, \theta_1, \varphi_1)$ and $(r_2', \theta_2', \varphi_2')$ be the spherical coordinates of the two points (with respect to origin a, as shown in Fig. 1) we have

$$\frac{1}{r_{12}}=\sum_{n=0}^{\infty}\sum_{m=-n}^{n}\frac{(n-|m|)!}{(n+|m|)!}P_n^{|m|}(\cos\theta_1)P_n^{|m|}(\cos\theta_2')\times\exp[im(\phi_2'-\phi_1)]\frac{r_<^n}{r_>^{n+1}}. \quad (26)$$

Here $r_<$ is the lesser of r_2' and r_1 and $r_>$ is the greater of the two. The $P_n^m(\cos\theta)$ are the associated Legendre polynomials as defined by Eq. (2). The Neumann expansion converges provided that $r_{12}\neq 0$. Introducing the new origin, b, and new coordinates $(r_2, \theta_2, \varphi_2=\varphi_2')$ previously described, we may apply three identities given by Hobson:[5]

$$\frac{P_n^{|m|}(\cos\theta_2')}{(r_2')^{n+1}}=\sum_{k=|m|}^{\infty}\frac{(-1)^{|m|+k}(n+k)!}{(k+|m|)!(n-|m|)!}r_2^kR^{-n-k-1}\times P_k^{|m|}(\cos\theta_2)\quad(R>r_2), \quad (27)$$

$$\frac{P_n^{|m|}(\cos\theta_2')}{(r_2')^{n+1}}=\sum_{k=n}^{\infty}\frac{(-1)^{n+k}(k-|m|)!}{(k-n)!(n-|m|)!}r_2^{-k-1}R^{k-n}\times P_k^{|m|}(\cos\theta_2)\quad(R<r_2), \quad (28)$$

$$(r_2')^nP_n^{|m|}(\cos\theta_2')=\sum_{k=|m|}^{n}\frac{(n+|m|)!}{(k+|m|)!(n-k)!}\times r_2^kR^{n-k}P_k^{|m|}(\cos\theta_2). \quad (29)$$

Observing the inequalities, we see that these equations apply respectively in Region I ($r_2'>r_1$ and $R>r_2$), Region III ($r_2'>r_1$ and $R<r_2$), and Region IV ($r_2'<r_1$). On substituting into Eq. (26), we obtain the expansions given by Eqs. (1), (13), (14), and (15).

For Region II the coefficients may be given in terms of an integral. Equating r_{12}^{-1} from the Neumann

[4] See, for example, Eyring, Walter, and Kimball, *Quantum Chemistry* (John Wiley and Sons, Inc., New York, 1944), Appendix V.

[5] E. W. Hobson, *Theory of Spherical and Ellipsoidal Harmonics* (Cambridge University Press, London, 1931), Sec. 89.

TABLE I.* Expansion coefficients with indices ≤ 3 for Region II. $(|r_1-r_2| \leq R \leq r_1+r_2)$.

$$B_{n_1n_2}{}^m(r_1, r_2; R) = \sum_{i,j=0}^{2(n_1+n_2+1)} [A_{n_1n_2}{}^m(i,j)/D_{n_1n_2}{}^m] r_1{}^{i-n_1-1} r_2{}^{j-n_2-1} R^{n_1+n_2-i-j+1}.$$

The summation extends over all entries in the table.

m		0	0	0	1	0	0	1	0
n_1		0	0	1	1	0	1	1	0
n_2		0	1	1	1	2	2	2	3
$D_{n_1n_2}{}^m$		4	16	16	64	32	256	512	256
i	j	$A_{n_1n_2}{}^m(i,j)$							
0	0	−1	3	2	1	−5	−25	−5	35
	1	2	0	0	0	0	0	0	0
	2	−1	−6	−9	−9	5	60	20	−28
	3	0	0	8	16	0	0	0	0
	4	0	3	0	−9	5	−30	−30	−14
	6	0	0	−1	1	−5	−20	20	−28
	8	0	0	0	0	0	15	−5	35
1	0	2	−8	0	0	16	0	0	−128
	1	2	0	0	0	0	0	0	0
	3	0	−8	0	0	0	0	0	0
	5	0	0	0	0	16	0	0	0
	7	0	0	0	0	0	0	0	−128
2	0	−1	6	−9	−9	−15	180	60	140
	2	0	6	0	18	−10	−60	−60	84
	4	0	0	9	−9	−15	60	−60	84
	6	0	0	0	0	0	−180	60	140
3	0	0	0	8	16	0	−256	−128	0
	3	0	0	−16	16	0	0	0	0
	5	0	0	0	0	0	384	−128	0
4	0	0	−1	0	−9	5	90	90	−70
	2	0	0	9	−9	5	−60	60	−84
	4	0	0	0	0	0	−270	90	−70
6	0	0	0	−1	1	−1	20	−20	28
	2	0	0	0	0	0	60	−20	28
8	0	0	0	0	0	0	−9	3	−5

m		0	1	2	0	1	0	1	2
n_1		2	2	2	1	1	2	2	2
n_2		2	2	2	3	3	3	3	3
$D_{n_1n_2}{}^m$		256	1536	12288	256	1024	3072	12288	49152
i	j	$A_{n_1n_2}{}^m(i,j)$							
0	0	−19	−9	−3	21	7	189	49	7
	2	75	50	25	−42	−21	−630	−210	−42
	4	−150	−150	−150	14	14	735	315	105
	5	128	128	256	0	0	0	0	0
	6	−50	0	−150	0	14	−420	−140	−140
	8	25	−25	25	21	−21	315	−105	105
	10	−9	6	−3	−14	7	−294	126	−42
	12	0	0	0	0	0	105	−35	7
2	0	75	50	25	−210	−105	−1050	−350	−70
	2	−100	−100	−100	84	84	1470	630	210
	4	50	0	150	0	42	−420	−140	−140
	6	−100	100	−100	−84	84	−420	140	−140
	8	75	−50	25	210	−105	1470	−630	210
	10	0	0	0	0	0	−1050	350	−70
3	0	0	0	0	384	256	0	0	0
	7	0	0	0	−512	256	0	0	0
4	0	−150	−150	−150	−210	−210	3675	1575	525
	2	50	0	150	0	−126	−1260	−420	−420
	4	150	−150	150	126	−126	−630	210	−210
	6	−450	300	−150	420	−210	−2940	1260	−420
	8	0	0	0	0	0	7875	−2625	525
5	0	128	128	256	0	0	−4608	−2048	−1024
	5	768	−512	256	0	0	0	0	0
	7	0	0	0	0	0	−15360	5120	−1024
6	0	−50	0	−150	0	70	2100	700	700
	2	−100	100	−100	−84	84	1260	−420	420
	4	−450	300	−150	−140	70	2940	−1260	420
	6	0	0	0	0	0	10500	−3500	700
8	0	25	−25	25	21	−21	−525	175	−175
	2	75	−50	25	42	−21	−1470	630	−210
	4	0	0	0	0	0	−2625	875	−175
10	0	−9	6	−3	−6	3	294	−126	42
	2	0	0	0	0	0	630	−210	42
12	0	0	0	0	0	0	−75	25	−5

TABLE I.—(*Continued*).

m		0	1	2	3
n_1		3	3	3	3
n_2		3	3	3	3
$D_{n_1n_2}{}^m$		10240	49152	245760	2949120
i	j	$A_{n_1n_2}{}^m(i,j)$			
0	0	520	131	20	5
	2	−2450	−735	−147	−49
	4	4900	1715	490	245
	6	−7350	−2695	−1225	−1225
	7	5120	2048	1024	2048
	8	0	−735	0	−1225
	10	−1470	539	−245	245
	12	980	−343	98	−49
	14	−250	75	−15	5
2	0	−2450	−735	−147	−49
	2	5880	2058	588	294
	4	−4410	−1617	−735	−735
	6	0	588	0	980
	8	4410	−1617	735	−735
	10	−5880	2058	−588	294
	12	2450	−735	147	−49
4	0	4900	1715	490	245
	2	−4410	−1617	−735	−735
	4	0	294	0	490
	6	−2940	1078	−490	490
	8	14700	−5145	1470	−735
	10	−12250	3675	−735	245
6	0	−7350	−2695	−1225	−1225
	2	0	588	0	980
	4	−2940	1078	−490	490
	6	−19600	6860	−1960	980
	8	61250	−18375	3675	−1225
7	0	5120	2048	1024	2048
	7	−102400	30720	−6144	2048
8	0	0	−735	0	−1225
	2	4410	−1617	735	−735
	4	14700	−5145	1470	−735
	6	61250	−18375	3675	−1225
10	0	−1470	539	−245	245
	2	−5880	2058	−588	294
	4	−12250	3675	−735	245
12	0	980	−343	98	−49
	2	2450	−735	147	−49
14	0	−250	75	−15	5

* This table was checked in three ways: putting $(r_1, r_2; R) = (1, 1; 2)$, $(1, 2; 1)$, and $(2, 1; 1)$ we obtained values for the B's in agreement with those given by Eqs. (13), (14), and (15), respectively.

expansion, Eq. (26), to that from the bipolar expansion, Eq. (1); multiplying both sides of the equation by $P_{n_1}{}^{|m|}(\cos\theta_1) P_{n_2}{}^{|m|}(\cos\theta_2) \exp[im(\phi_2-\phi_1)]$ and integrating over the angles, it follows that

$$B_{n_1n_2}{}^{|m|}(r_1, r_2; R) = \left(\frac{2n_2+1}{2}\right) \frac{(n_2-|m|)!}{(n_2+|m|)!} \frac{(n_1-|m|)!}{(n_1+|m|)!} \cdot \int_{-1}^{1} \frac{r_<{}^{n_1}}{r_>{}^{n_1+1}} P_{n_1}{}^{|m|}(\cos\theta_2') P_{n_2}{}^{|m|}(\cos\theta_2) d(\cos\theta_2). \quad (30)$$

Here $r_<$ is the lesser of r_1 and r_2' as before. In the integration over $\cos\theta_2$ we see that

$$r_2' < r_1 \quad \text{when} \quad -1 < \cos\theta_2 < -\cos\alpha, \quad (31)$$

$$r_2' > r_1 \quad \text{when} \quad -\cos\alpha < \cos\theta_2 < 1, \quad (32)$$

where

$$\cos\alpha = (R^2+r_2{}^2-r_1{}^2)/(2r_2R). \quad (33)$$

This situation is shown in Fig. 5. Thus in Region II,

Region II

$$B_{n_1n_2}{}^{|m|}(r_1, r_2; R)=\left(\frac{2n_2+1}{2}\right)\frac{(n_2-|m|)!}{(n_2+|m|)!}\frac{(n_1-|m|)!}{(n_1+|m|)!}$$

$$\cdot\left\{\int_{-1}^{-\cos\alpha}\frac{(r_2')^{n_1}}{r_1{}^{n_1+1}}P_{n_1}{}^{|m|}(\cos\theta_2')P_{n_2}{}^{|m|}(\cos\theta_2)d(\cos\theta_2)\right.$$

$$+\int_{-\cos\alpha}^{1}\frac{r_1{}^{n_1}}{(r_2')^{n_1+1}}P_{n_1}{}^{|m|}(\cos\theta_2')$$

$$\left.\times P_{n_2}{}^{|m|}(\cos\theta_2)d(\cos\theta_2)\right\}. \quad (34)$$

Here

$$\cos\theta_2'=(r_2\cos\theta_2+R)/r_2', \quad (35)$$

$$r_2'=(R^2+r_2{}^2+2r_2R\cos\theta_2)^{\frac{1}{2}}. \quad (36)$$

We have not discovered a convenient method of evaluating the integrals of Eq. (34). The results given in Table I were determined by direct integration of the special cases. The Hobson expansions, Eqs. (27), (28), and (29) are no help for this purpose.

Convergence of the sum over n_2 follows from the fact that a constant$\times(r_<{}^n/r_>{}^{n+1})P_n{}^{|m|}(\cos\theta_2')$ is a bounded continuous function of $\cos\theta_2$ for $-1\leqslant\cos\theta_2\leqslant 1$ and therefore can be approximated by a series

$$\sum_{n_2} B_{n_1n_2}{}^{|m|}P_{n_2}{}^{|m|}(\cos\theta_2).$$

Convergence of the sum over n_1 follows from convergence of the Neumann expansion.

The rule for permuting n_1 and n_2 in $B_{n_1n_2}{}^{|m|}(r_1, r_2; R)$, Eq. (17), can be derived in the following manner. Reverse the Z axis of the second charge distribution by defining $\theta_2{}^*=\pi-\theta_2$. Defining the new functions

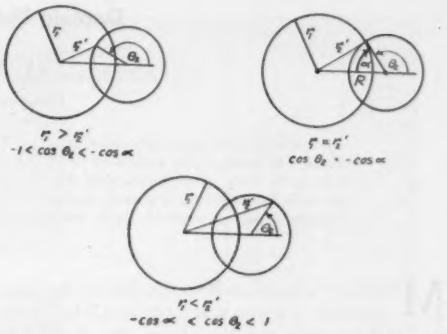

FIG. 5. Behavior of the ratio r_1/r_2' in the integration over $\cos\theta_2$.

$B_{n_1n_2}{}^{|m|*}(r_1, r_2; R)$ by the expansion,

$$\frac{1}{r_{12}}=\sum_{n_1=0}^{\infty}\sum_{n_2=0}^{\infty}\sum_{m=-n_<}^{n_<}B_{n_1n_2}{}^{|m|*}(r_1, r_2; R)P_{n_1}{}^{|m|}(\cos\theta_1)$$

$$\times P_{n_2}{}^{|m|}(\cos\theta_2{}^*)\exp[im(\phi_2-\phi_1)], \quad (37)$$

it follows from symmetry that in Region II

$$B_{n_1n_2}{}^{|m|*}(r_1, r_2; R)=B_{n_2n_1}{}^{|m|*}(r_2, r_1; R). \quad (38)$$

But $\cos\theta_2{}^*=-\cos\theta_2$ and

$$P_{n_2}{}^{|m|}(-\cos\theta_2)=(-1)^{n_2+m}P_{n_2}{}^{|m|}(\cos\theta_2),$$

so that comparing the expansions, Eqs. (1) and (37), and using Eq. (38),

$$B_{n_1n_2}{}^{|m|}(r_1, r_2; R)=(-1)^{n_2+|m|}B_{n_1n_2}{}^{|m|*}(r_1, r_2; R) \quad (39)$$

$$=(-1)^{n_2+|m|}B_{n_2n_1}{}^{|m|*}(r_2, r_1; R) \quad (40)$$

$$=(-1)^{n_2+n_1}B_{n_2n_1}{}^{|m|}(r_2, r_1; R). \quad (41)$$

This is proof of Eq. (17).

Domain Patterns on Nickel*

H. J. WILLIAMS AND J. G. WALKER
Bell Telephone Laboratories, Murray Hill, New Jersey
(Received April 5, 1951)

Domain patterns have been observed on two single crystals of nickel cut in the form of hollow parallelograms. The length of the sides were parallel to the ⟨111⟩ directions in one specimen and to the ⟨110⟩ directions in the other. The crystals show domain structures with the three types of domain boundaries which are to be expected from a material having the directions of easy magnetization along the ⟨111⟩ directions. Domain boundary movement under the influence of an applied magnetic field was observed.

MOST of the previous investigations of the domain structure of ferromagnetic materials by means of the powder pattern technique have been on crystals of material such as silicon iron,[1] which has the directions of easy magnetization parallel to the ⟨100⟩ directions and also has a high anisotropy constant, $K=280{,}000$.

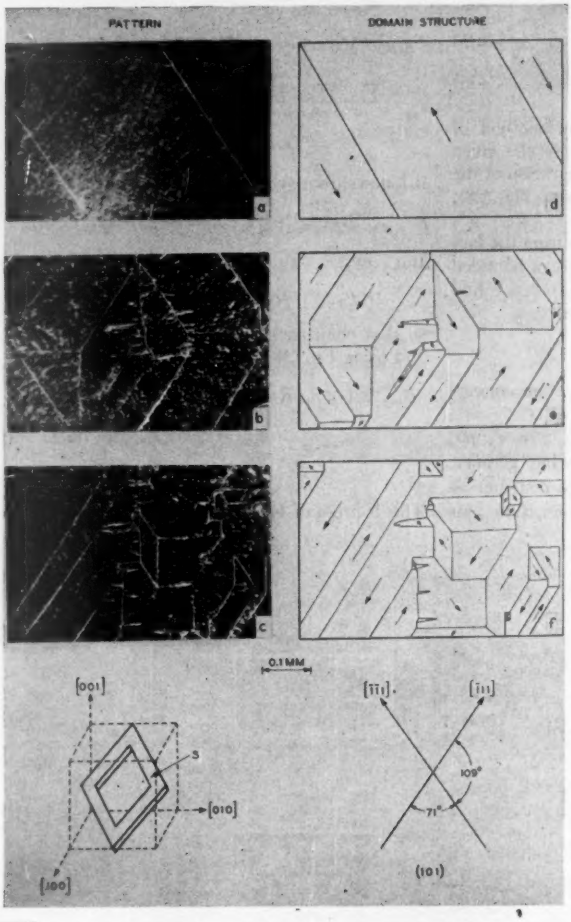

FIG. 1. Domain patterns observed on the (101) surface of a single crystal of nickel. Photographs (a), (b), and (c) show three areas of surface under observation. Interpretation illustrated in (d), (e), and (f). Specimen cut as shown on sketch.

* Since this article was submitted, publications have appeared by M. Yamamoto and T. Iwata, Phys. Rev. **81**, 887 (1951) and Martins, Gow, and Chalmers, Phys. Rev. **82**, 106 (1951).

[1] Williams, Bozorth, and Shockley, Phys. Rev. **75**, 155 (1949); H. J. Williams and W. Shockley, Phys. Rev. **75**, 170 (1949).

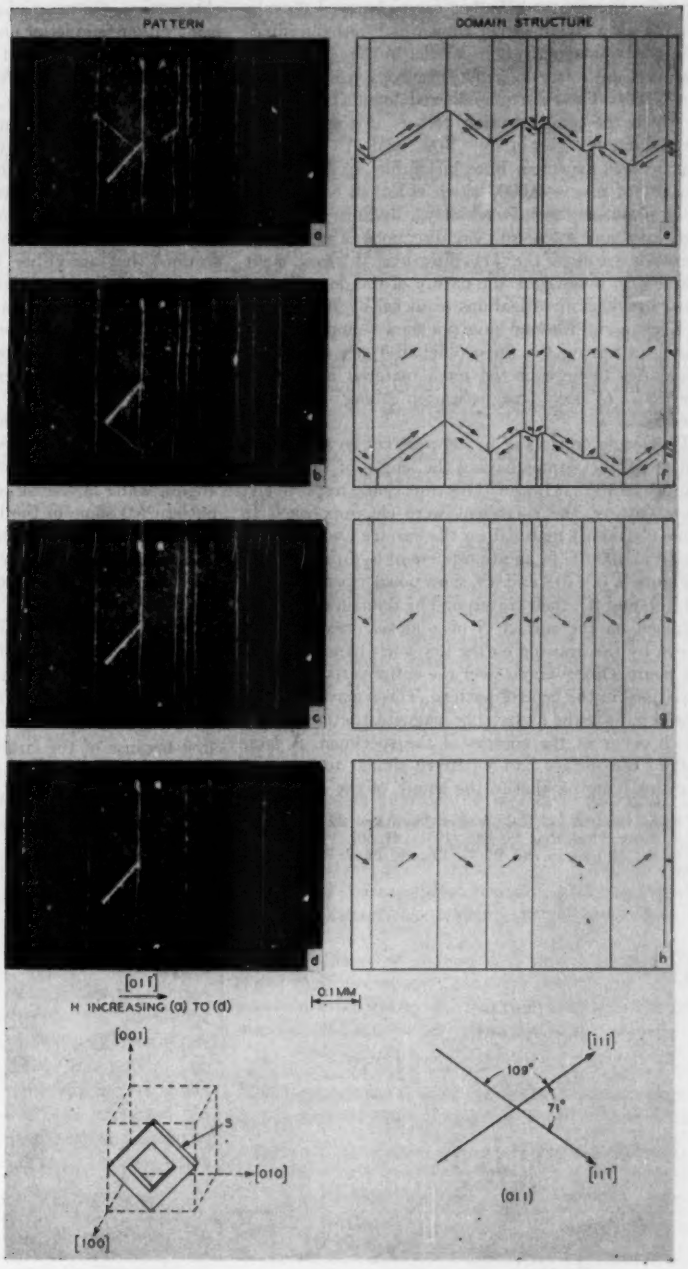

FIG. 2. Patterns showing boundary movement with applied field as observed on the (011) surface of a single crystal of nickel cut as shown in sketch. Field increasing (a) to (d). Interpretation (e) to (h).

Recently, Bozorth and Walker[2] have observed domain patterns on a cobalt-nickel alloy which has the directions of easy magnetization parallel to the ⟨111⟩ directions and also has a high anisotropy constant, $K = -200{,}000$. These patterns showed domain boundaries for which the magnetization vectors in the adjacent domains made angles of 180°, 109°, and 71° with each other as was expected. Pure nickel has an anisotropy constant of $K = -60{,}000$, which is low in comparison to the previously mentioned alloys. Because the anisotropy constant is low and the directions of easy magnetization are along the ⟨111⟩ directions, it was thought desirable to investigate the nature of the domain patterns. Previous investigations of nickel by Bitter[3] and McKeehan and Elmore[4] have not shown simple domain structures having the three different types of domain boundaries to be expected for a material having the directions of easy magnetization along the ⟨111⟩ directions.

Two single crystals of nickel were cut so as to form hollow parallelograms having the length of their sides parallel to the ⟨111⟩ and ⟨110⟩ directions, respectively. After cutting, the specimens were electropolished to remove strained material on the surface and then annealed at 1000°C in an atmosphere of hydrogen.

Figure 1, (a), (b), and (c), show powder patterns, and (d), (e), and (f), their corresponding domain structures, obtained on the surface S of a nickel crystal cut as shown by the drawing on the lower left-hand corner of the figure. Observations over the entire surface showed variations in the type of pattern. These may be due to local strains in the material or magnetostrictive stresses which occur at the corners of the specimen. A large part of the surface had a pattern similar to (a), with domains lying parallel to the length of the side under observation, the magnetization vectors of the domains being either parallel or antiparallel to the $[\bar{1}11]$ direction as shown in (d). In this pattern there are only 180° boundaries. However, in (b) and (c) there are boundaries for which the magnetization vectors in the adjacent domains make angles of 180°, 109°, and 71°.

A fairly uniform type of pattern was obtained over the entire surface S of the specimen cut as shown in Fig. 2. A pattern is shown in Fig. 2(a) and the corresponding domain structure in (e). In this pattern there is a zigzag boundary which is composed of straight sections that are either 180° or 71° boundaries. The upper set of domains carries flux from left to right, and the lower set carries flux in the opposite direction. When the field (H) is increased, the zigzag boundary moves downward as shown in (b), the upper set of domains growing at the expense of the lower set. At (c) the zigzag boundary has moved out of view. A somewhat similar structure has been observed on silicon iron.[1] However, in the case of the silicon iron the magnetization vectors in successive domains make 90° angles, while in the nickel they make 109° angles. In pattern (d) some of the boundaries shown in (c) have disappeared. This is probably because the narrow domains in (c) are shallow domains which cling to the 180° boundary and snap off at higher fields, as has been observed in silicon iron.

It should be noticed that in these patterns some of the domain boundaries are not straight but have slight curves or bends. This may be due to residual strains on the crystal. The patterns for nickel are probably more sensitive to strain than those of 4 percent silicon iron because of the larger magnetostriction and lower anisotropy of nickel. Also, nickel has a lower magnetic saturation, so that a given curvature in a boundary would produce weaker magnetic poles and consequently require less energy for formation in nickel than in silicon iron.

[2] R. M. Bozorth and J. G. Walker, Phys. Rev. **79**, 888 (1950).
[3] F. Bitter, Phys. Rev. **38**, 1903 (1931); **41**, 507 (1932).
[4] L. W. McKeehan and W. C. Elmore, Phys. Rev. **46**, 529 (1934).

Overlap Forces and Elastic Constants of Body-Centered Cubic Metals

IRVIN ISENBERG
Institute for the Study of Metals, University of Chicago, Chicago, Illinois
(Received January 22, 1951)

It is shown that the interactions between neighboring ions which one must postulate for the ordering of β-phase alloys are very similar to the interactions which one must postulate so that these alloys are stable under a (110) $[1\bar{1}0]$ shear. One can then understand why in all known cases the β-phase either disappears at low temperatures or becomes ordered.

The elastic constants of tungsten are also examined; the contribution of ion-ion overlap to these constants is obtained by subtracting estimated values of the other contributions from the experimental values. It is relatively easy to understand the values of the ion-ion overlap contributions if one assumes an antiferromagnetic array in tungsten as proposed by Zener. These values are difficult to understand if one assumes a random spin orientation.

INTRODUCTION

IF a body-centered cubic lattice is sheared in the $[1\bar{1}0]$ direction across a (110) plane, the distance between neighboring atoms will not change in first approximation, while the distance will increase in second approximation. Thus, if one were to imagine copper in body-centered cubic form with one conduction electron per atom, such a shear would lower the exchange interaction between adjacent copper ions. In such a shear Fuchs[1] has shown that the electrostatic energy will increase. However, since Fuchs demonstrated that the exchange interaction is much more important for copper than the coulomb interaction, such a shear would lower the energy of the crystal and a body-centered cubic copper lattice would be unstable.

Zener[2] has used this argument to explain the anomalously low value of the shear coefficient $(C_{11}-C_{12})/2$ of β-brass, where again there are presumably only closed ion shells, copper having contributed one conduction electron and zinc two conduction electrons. The stability of disordered β-brass under a (110) $[1\bar{1}0]$ shear is due in some way to thermal vibrations; the case of the ordered structure will be discussed below.

Fuchs[1] has given a table showing the contribution of the overlap energy[3] to the shear constants. This table is reproduced here (Table I) with certain modifications. The bulk modulus is included, since it will be needed for later work. The next-nearest neighbor interaction energy has been primed to allow for the possibility that next-nearest neighbor interaction may be of a different nature from nearest neighbor interaction, i.e., $w(r)\neq w'(r)$. Finally, certain numerical factors given incorrectly in Fuchs' table have been corrected. In Table I, ρ is the distance between nearest neighbors, δ that between next-nearest neighbors. The derivative $dw/d\rho$ means that the derivative is evaluated at the nearest neighbor distance, with analogous interpretations for the other derivative symbols. N is the density of atoms.

If we neglect, for the moment, next-nearest neighbor interactions and take w to be a short-range repulsive energy, say, something like $w=A\exp[-\alpha(r-\rho)]$, then it can be seen that $dw/d\rho$ is negative. Consulting Table I, we see that the lattice is therefore unstable.

This feature of body-centered cubic metals, which shows up formally as the nonoccurrence of a second derivative in the nearest neighbor contribution to $C_{11}-C_{12}$, makes it possible to discuss profitably certain features of overlap forces in these metals by examining their elastic constants. This will be done qualitatively and semiquantitatively for the β-phase alloys and for the transition body-centered cubic metals, in particular tungsten, for which the elastic constants are known. Tungsten is particularly suited for the type of analysis here presented because the measured values of the elastic constants are high compared with what seem to be reasonable guesses as to the contributions to the elastic constants of the Fermi energy and electrostatic interactions. We can therefore obtain qualitative results for the interactions between neighboring ions in tungsten.

The alkalis are of no interest in this connection. The closed shells are so small that the contribution of the ion-ion overlap energy is small compared with the contribution of the coulomb interaction of the ions.

THE β-PHASE ALLOYS

No β-phase alloy is known to exist at low temperatures in a disordered state. This may be understood on the

TABLE I. Contribution of overlap energy to elastic constants.

	Nearest neighbors	Next-nearest neighbor
$C_{11}-C_{12}$	$(8/3)N\rho dw/d\rho$	$N\delta^2(d^2w'/d\delta^2)+N\delta dw'/d\delta$
C_{44}	$(4/9)N\rho^2(d^2w/d\rho^2)$ $+(8/9)N\rho dw/d\rho$	$N\delta dw'/d\delta$
$\frac{1}{3}(C_{11}+2C_{12})$	$(4/9)N\rho^2d^2w/d\rho^2$	$\frac{1}{3}N\delta^2d^2w'/d\delta^2$

[1] K. Fuchs, Proc. Roy. Soc. (London) **A153**, 622 (1935).
[2] C. Zener, Phys. Rev. **71**, 846 (1947).
[3] The term "overlap energy" used in this paper means the coulomb interaction due to the overlap of the charge distribution of two ions plus the exchange energy due to the same overlap. It should not be confused with the expression of Löwdin (reference 7), who means by overlap energy that energy arising from the nonorthogonality of atomic wave functions of different ions.

TABLE II. Elastic constants with estimated corrections (units of 10^{11} dynes/cm^2).

	Bridgman	Wright	Contribution of overlap forces
C_{11}	51.3	50.1	45.9
C_{12}	20.6	19.8	16.0
C_{44}	15.3	15.1	13.4

basis of the above arguments, namely, the shear instability of these alloys, at least those that have only closed shell ions. The question that arises is that of the stability of the ordered β-phase. It will here be pointed out that the type of forces which one must postulate for the stability of β-brass are very similar to the type of forces which one needs for ordering. One can then understand why, when β-phase alloys do exist at low temperatures, these alloys are ordered.

A term like $\delta^3 d^2w/d\delta^2$ will always dominate $\delta dw'/d\delta$ for short range repulsive forces. Thus, if we assume

$$w'=A' \exp[-\alpha'(r-\delta)/\delta], \tag{1}$$

it follows that

$$(\delta^3 d^2w'/d\delta^2)/(-\delta dw'/d\delta)=\alpha',$$

and $\alpha' \gg 1$ for short-range forces. This, of course, does not depend on the particular form (1). However, it will be convenient to assume Eq. (1) as the ion-ion overlap energy. The energy w' must here be considered to be the average of the zinc-zinc overlap energy and that of copper-copper.

Let us also write the zinc-copper interaction

$$w=A \exp[-\alpha(r-\delta)/\delta].$$

Then, for ordering we have

$$w'(\rho)>w(\rho)$$

or

$$A' \exp(0.134\alpha')>A \exp(0.134\alpha). \tag{2}$$

For stability we have

$$2\delta^3 d^2w'/d\delta^2>|(16/3)\rho dw/d\rho|$$

or

$$\alpha'^2 A'>(4/\sqrt{3})\alpha A \exp(0.134\alpha). \tag{3}$$

It can be seen that while Eq. (2) does not necessarily follow from Eq. (3), and hence we cannot say definitely that in all cases wherever stability exists, there must be ordering, the criterion for stability is quite similar to that for ordering. Both require that either the next-nearest neighbor interaction be sufficiently stronger than the nearest neighbor interaction, i.e., A' sufficiently greater than A or that the ranges be such that α' is sufficiently larger than α. In all known cases it does appear that if Eq. (3) is obeyed, then Eq. (2) is.

THE BODY-CENTERED CUBIC TRANSITION METALS

Zener[4] has recently examined the interactions of the incomplete d shells of the transition metals on the following three assumptions:

1. The interactions between d electrons of a single atom are much the same in the crystal as in an isolated atom. This essentially assumes that the d electrons of an atom in a crystal obey Hund's rule.

2. The exchange integral between d shells of neighboring atoms has the same sign as the exchange integral in the H_2 molecule; i.e., it always tends to produce an antiferromagnetic array of atoms.

3. There is a strong spin coupling between the conduction electrons and the partially filled d shell tending toward a ferromagnetic arrangement. This assumption, while important in discussing ferromagnetism, has no bearing on the subject of this paper and will therefore not be further discussed.

On the basis of assumptions (1) and (2) Zener pointed out that the tendency toward antiferromagnetism should be greatest in those metals where the d shell is roughly half filled. This tendency should be most marked in the metals Cr, Mo, W, V, Cb, Ta. Now all these metals crystallize in a body-centered cubic form and have no other stable structures. A body-centered cubic lattice can be considered as two interpenetrating simple cubic lattices and therefore has the property that an antiferromagnetic array is geometrically possible. Thus, Zener has considered the fact that these metals do crystallize in b.c.c. form as a verification of his hypotheses.

Of these metals only the elastic constants of tungsten are known. These have been determined twice, once by Bridgman[5] and once by Wright.[6] The two sets of values agree quite well, as may be seen from Table II. The values of Wright will be used here.

The object of this section is to show that an analysis of the elastic constants of tungsten supports the concept of antiferromagnetism in tungsten as proposed by Zener.

Following Fuchs,[1] we divide the crystal energy into a number of terms in the following way:

$$W=W_0+W_F+W_L+W_I,$$

W_0 is the energy of the lowest S state, W_F is the Fermi energy of the conduction electrons, and W_L is the interaction energy between different polyhedra of the lattice. It may be written differently:

$$W_L=W_s-W_s,$$

where W_s is the energy of a lattice of positive point charges imbedded in a uniform negative charge distribution and W_s is the self-energy of a Wigner-Seitz sphere.

W_I was taken by Fuchs to be the exchange interaction between neighboring d shells. It will here be taken to

[4] C. Zener, Phys. Rev. **81**, 440 (1951).
[5] P. W. Bridgman, Proc. Am. Acad. Sci. **60**, 305 (1925).
[6] S. J. Wright, Proc. Roy. Soc. (London) **A126**, 613 (1930).

mean the overlap energy which has previously been defined in footnote 3.

W_0, W_F, and W_s are very nearly functions of only the volume, and these terms will therefore make no contribution to the shear constants.

W_L is quite small, since $W_c \simeq W_s$. However, upon the shearing of the lattice W_s does not change, and W_c will make a significant contribution to the shear constants (for the alkalies W_c yields the largest contribution). However, upon hydrostatic compression it remains true that $W_c \simeq W_s$, and consequently W_L will not make a significant contribution to the bulk modulus.

Perhaps the weakest point in this analysis is the neglect of the many body forces which arise from the nonorthogonality of the wave functions of different ions. Löwdin[7] has discussed these forces in the alkali halides and has shown that they explain the deviations from the cauchy relationships in these salts. There seems to be no way of estimating whether these forces will be important in our case. It will simply be assumed that they are negligibly small. Since the results obtained here are self-consistent, this may perhaps be some justification for so doing.

Since we wish to examine only that part of the elastic constants due to overlap forces, we must subtract the other contributions from the values in Table II. This is relatively simple for the shear constants. Since our corrections turn out to be quite small, our results are insensitive to the number of electrons which are assumed to be in the conduction band. For convenience we shall assume that there is one conduction electron per atom. In this case Fuchs[1] has shown that the contribution of W_c to $C_{11}-C_{12}$ is $0.1994Ne^2/2\delta$ and the contribution to C_{44} is $0.7423Ne^2/2\delta$. These are quite small, being 0.4×10^{11} dynes/cm^2 and 1.7×10^{11} dynes/cm^2, respectively.

The corrections to the bulk modulus are also small, and hence our results are insensitive to the assumptions made here. We might simply assume that the contribution of W_0+W_F to the bulk modulus is of the order of magnitude of the bulk modulus of the alkalies, or we might neglect W_0 and take W_F to be given by the Fermi energy of a free electron gas. Since we are interested only in drawing qualitative conclusions, either one would be reasonable. For definiteness we choose the latter procedure. The contribution of W_F to the bulk modulus is then

$$2\pi(\pi/3)^{1/3}(\hbar^2/2m)(N/V)^{5/3}=3.9\times10^{11}\text{ dynes/cm}^2.$$

The values of the elastic constants corrected in the above fashion are shown in Table II.

Our corrections lead us to the conclusion that the major contribution to the elastic constants come from overlap energy. That this is not too unreasonable may be seen by noting that the cauchy relationship ($C_{12}=C_{44}$) is obeyed more nearly by tungsten than by most of the other metals whose elastic constants have been measured (Table III).

[7] Per-Olov Löwdin, *Some Properties of Ionic Crystals* (Upsala, 1948).

TABLE III. Validity of cauchy relationship.[a]

	C_{12} (units of 10^{11} dynes/cm^2)	C_{44}	C_{12}/C_{44}
Copper	12.3	7.52	1.64
Silver	8.97	4.36	2.06
Gold	16.6	4.00	4.15
Aluminum	6.2	2.8	2.21
α-iron	14.1	11.6	1.22
Tungsten	19.8	15.1	1.31

[a] From E. Schmid and W. Boas, *Kristallplastizität* (Verlag. Julius Springer, Berlin, 1935).

Examining Table I we see that we cannot solve for the derivatives of w and w' in terms of the elastic constants because we have three equations for four unknowns. However, it will undoubtedly be true that for second-nearest neighbors we will be in a region where $w'(r)$ is a rapidly varying monotonic function. For such a region it is legitimate to neglect, as a first approximation, $\delta dw'/d\delta$, since it will be true that $\delta^2d^2w'/d\delta^2$ will be of an order of magnitude greater and either $\rho^2d^2w/d\rho^2$ or $\rho dw/d\rho$ will also be of an order of magnitude greater than $\delta dw'/d\delta$. Thus, it becomes possible to solve for the order of magnitude of $\rho dw/d\rho$, $\rho^2d^2w/d\rho^2$, and $\delta^2d^2w'/d\delta^2$:

$$C_{11}-C_{12}=(8/3)N\rho(dw/d\rho)+N\delta^2d^2w'/d\delta^2,$$
$$C_{44}=(4/9)N\rho^2(d^2w/d\rho^2)+(8/9)N\rho dw/d\rho,$$
$$\tfrac{1}{3}(C_{11}+2C_{12})=(4/9)N\rho^2(d^2w/d\rho^2)+\tfrac{1}{3}N\delta^2d^2w'/d\delta^2,$$

or

$$N\rho dw/d\rho=\tfrac{9}{16}[C_{44}-C_{12}],$$
$$N\rho^2d^2w/d\rho^2=(9/8)[C_{44}+C_{12}],$$
$$N\delta^2d^2w'/d\delta^2=\tfrac{1}{2}[2C_{11}+C_{12}-3C_{44}].$$

Numerically, we have

$$N\rho dw/d\rho=-1.5\times10^{11}\text{ dynes/cm}^2.$$
$$N\rho^2d^2w/d\rho^2=33\times10^{11}\text{ dynes/cm}^2,$$
$$N\delta^2d^2w'/d\delta^2=34\times10^{11}\text{ dynes/cm}^2.$$

Several things may be denoted from these values. First, we note that $d^2w'/d\delta^2$ is positive. This implies

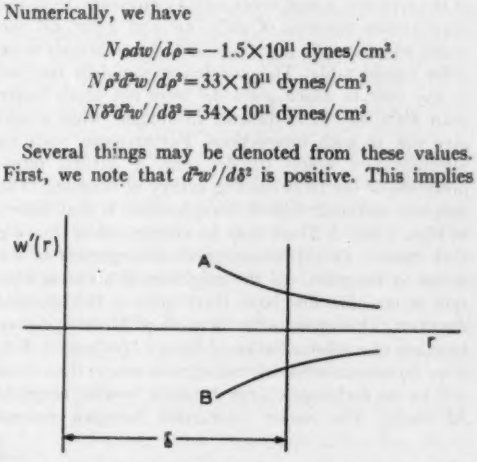

FIG. 1. Two possibilities for $w'(r)$. Curve A is indicated by analysis of elastic constants.

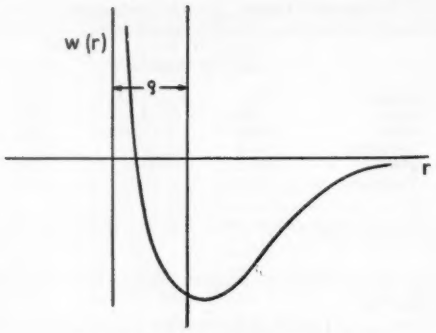

FIG. 2. Nearest neighbor interaction.

that the interaction between second-nearest neighbors is repulsive corresponding to curve A of Fig. 1.

The values obtained for $dw/d\rho$ and $d^2w/d\rho^2$ indicate that the interaction between nearest neighbors is a binding interaction and that we are at a minimum in the $w(r)$ curve as indicated in Fig. 2. Indeed, from our rough calculations it is perhaps more logical to say that

$$N\rho(dw/d\rho)\cong 0$$

than to say that

$$N\rho dw/d\rho = -1.5\times 10^{11}\text{dynes/cm}^2.$$

This picture is consistent with the viewpoint of ascribing the high binding energy to the interaction of neighboring ions. If most of the binding is indeed due to such interaction, we would expect the actual value of ρ to be in the neighborhood of the minimum of $w(r)$.

In a formal sense one could take the values of $dw/d\rho$ and $d^2w/d\rho^2$ as indicating a strong repulsive interaction of the type $w=A\exp[-\alpha(r-\delta)/\delta]$. However, from the approximate equality of $\rho^3d^2w/d\rho^2$ and $\delta^3d^2w'/d\delta^2$ one would still conclude that the w and w' interactions must differ considerably. This conclusion would be reached in any case in which $\rho^3d^2w/d\rho^2$ were not much larger than $\delta^3d^2w/d\delta^2$. It is difficult to imagine what would give rise to such interactions. Furthermore, such an interpretation would conflict with a natural interpretation of the large binding energy of tungsten. The simplest and most logical interpretation is that shown in Figs. 1 and 2. These may be interpreted as showing that there is an antiferromagnetic arrangement of the atoms in tungsten. All the neighbors of an atom with spin in one direction have their spins in the opposite direction. This agrees with the work of Zener[4] and may be taken as a substantiation of Zener's conclusions. For, if we do assume an antiferromagnetic array, then there will be no exchange energy between nearest neighbor $5d$ shells. The major interaction between nearest neighbors will come from the coulomb interaction due to the $5d$ overlap, plus the coulomb and exchange interaction between the $5d$ shell on one ion and the $5p$ shell on its nearest neighbors. On the other hand, there will be a contribution from $5d$ exchange between next-nearest neighbors. Thus, for an antiferromagnetic array, the interaction between nearest neighbors is of a different nature than that between next-nearest neighbors. In spite of the fact that next-nearest neighbors have a larger separation than nearest neighbors, we then obtain approximate equality of $\rho^3d^2w/d\rho^2$ and $\delta^3d^2w'/d\delta^2$. However, if a random distribution of spin were assumed, it would be difficult to understand this equality.

If we started with the assumption that

$$dw/d\rho=0,$$

we could go back to Table I and solve for $\delta dw'/d\delta$. Upon doing this, we find

$$N\rho^3d^2w/d\rho^2=35\times 10^{11}\text{ dynes/cm}^2,$$
$$N\delta^3d^2w'/d\delta^2=32\times 10^{11}\text{ dynes/cm}^2,$$
$$N\delta dw'/d\delta=-2\times 10^{11}\text{ dynes/cm}^2.$$

The ratio

$$\frac{1}{\alpha}=\frac{-\delta dw'/d\delta}{\delta^3d^2w'/d\delta^2}=\frac{1}{16}$$

is a measure of the range of the repulsive interaction between next-nearest neighbors. This value has a reasonable order of magnitude. For example, for copper, Huntington and Seitz[8] used $\alpha=12.5$; Zener[9] used $\alpha=19$.

Fine,[10] in discussing the normal vibrations of tungsten, demanded, as holds true for tungsten, that the isotropy condition $\frac{1}{2}(C_{11}-C_{12})=C_{44}$ hold. He also demanded for his model that the cauchy condition, $C_{44}=C_{12}$, hold, instead of attempting to use the compressibility data. Fine then showed that the force constant for displacement of two nearest neighbors in the direction of a cube edge was half the force constant for two next-nearest neighbors displaced along a cube edge. Such a result, while based on assumptions other than those of this paper, points to the same qualitative features demonstrated here. The relative size of the force constants obtained by Fine is easy to explain if one assumes an antiferromagnetic spin structure, while it becomes difficult to understand if one assumes a structure of uncorrelated spins.

The author wishes to thank Professor C. Zener for his advice and many suggestions during the course of this work.

[8] H. B. Huntington and F. Seitz, Phys. Rev. **61**, 315 (1942).
[9] C. Zener, Acta Cryst. **3**, 346 (1950).
[10] P. C. Fine, Phys. Rev. **56**, 355 (1939).

Thermal Neutron Capture Cross Sections*

H. POMERANCE
Oak Ridge National Laboratory, Oak Ridge, Tennessee
(Received March 5, 1951)

The Oak Ridge pile oscillator has been used for a survey of the thermal neutron capture cross sections of the elements. Sixty-nine elements from atomic number 3 to 82 have been measured by comparison with gold, whose capture cross section is known from other experiments. From the internal consistency of the measurements, the care in selecting samples, and the accuracy of the value for gold, these values are estimated to be accurate within 5 percent. A comparison is made with the results of other pile oscillator measurements and of other methods such as time-of-flight and activation.

THERMAL NEUTRON CAPTURE

Previous Measurements

SYSTEMATIC measurements of the interactions of neutrons with the elements were made almost as soon as the techniques of working with neutrons were known. The first measurements were simple transmission experiments used to determine total cross sections, that is, the sum of scattering and capture cross sections. Since then several methods have been devised for measuring the scattering and capture cross sections separately.

There are several compilations of nuclear data which include thermal neutron capture cross sections. Most charts or tables of nuclear properties which include neutron cross sections contain no evaluation of the probable accuracy of the values. However, in a report by Way and Haines[1] of the thermal cross sections of the 81 stable elements from hydrogen to bismuth known in 1948, estimates of the accuracy are given. Of the 75 elements whose total cross sections had been reported, 16 were probably known within 10 percent; for 15 of the elements there was only one reported experiment. Scattering cross sections had been reported for 61 elements, with 10 of them probably known within 10 percent; for 25 elements only one experiment had been reported. Thermal capture cross sections were known for 73 elements, with 10 of them probably known within 10 percent; for 6 elements only one experiment had been reported, and for 12 elements the cross sections were known only from activation measurements.

With the advent of neutron chain-reacting piles, it became possible to measure the poisoning effects of neutron absorbing materials. Introduction of a neutron absorbing substance into a pile decreases the pile reactivity, and in order to keep the power constant the control rods must be displaced. By proper calibration this displacement may be used as a precision measure of the capture cross section. In this way Anderson *et al.*[2] found the capture cross sections for several elements. About 39 elements in all were measured by Wattenberg by this method, but only four values have been published outside the project reports. The pile oscillator method for determining capture cross sections was developed as a logical refinement of the aforementioned method.

Since 1948 capture cross sections have been measured at several laboratories. From the Oak Ridge National Laboratory, values for 69 elements are included in this report, in the main with an estimated accuracy of 5 percent. These measurements were performed with the pile oscillator which employs the local depletion of neutrons by the sample; the values were included in the volume "Nuclear data."[3] The Argonne National Laboratory has recently reported values for 53 elements[4] using a pile oscillator that effects a measurable change in the pile reactivity. With the same method the laboratory at Harwell has reported values for 40 elements.[5]

Pile Oscillator Method

The ORNL pile oscillator measures the thermal neutron capture cross section of a sample by moving the sample so as to pulse periodically the neutron density within the pile. The theory of pile oscillations has been previously reported by Weinberg and Schweinler,[6] and the instrument has been described by Hoover *et al.*[7] It consists of a mechanical system which oscillates a sample back and forth about once a second through an annular, neutron-sensitive ionization chamber, which is located in a constant and intense neutron flux in the graphite reflector of the pile. The local depletion of neutrons around the capturing sample

* Based on a dissertation presented in partial fulfillment of the requirements for the degree of Doctor of Philosophy at the University of Chicago, Chicago, Illinois.

[1] K. Way and G. Haines, AECD 2138, *Thermal Neutron Cross Sections for Elements and Isotopes* (Oak Ridge, Tennessee, 1948; Technical Information Branch, AEC); also published as Document No. PB-95632, Office of Technical Services, Department of Commerce, Washington, D. C.

[2] Anderson, Fermi, Wattenberg, Weil, and Zinn, Phys. Rev. **72**, 16 (1947).

[3] "Nuclear data," Natl. Bur. Standards (U. S.) Circ. 499 (1950).

[4] Harris, Muehlhause, Rasmussen, Schroeder, and Thomas, Phys. Rev. **80**, 342 (1950).

[5] F. C. W. Colmer and D. J. Littler, Proc. Phys. Soc. (London) **63**, 1175 (1950).

[6] A. M. Weinberg and H. C. Schweinler, Phys. Rev. **74**, 851 (1948).

[7] Hoover, Jordan, Moak, Pardue, Pomerance, Strong, and Wollan, Phys. Rev. **74**, 864 (1948).

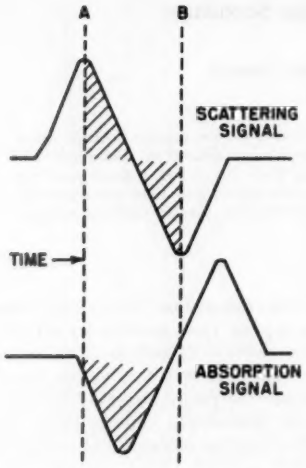

FIG. 1. Scattering and absorption signals (schematic). A (on) and B (off) are the mechanical rectification points. The cross hatched area represents the signal.

depends on the absorption by the sample and can be used to compare absorptions. This transient depletion pulses the ionization chamber current, and these pulses are amplified, and integrated by using the rectified pulses to charge a condenser whose voltage can then be measured. The ratio of the capture cross sections for two samples is found from the weights which experimentally give the same voltage response. In practice all samples were compared with gold, whose capture cross section is rather well known.

The voltage pulse from the ionization chamber is primarily caused by the capture of neutrons in the sample. It is found, however, by oscillating a piece of graphite which has negligible absorption, that a signal is generated by the effects of scattering. Comparison of the scattering and absorption signals (Fig. 1) shows that the scattering signal is opposite in sign, has a steeper rise, and reaches its maximum at an earlier time than the capture signal. This can be explained if one assumes that the scattering signal arises chiefly from neutrons that would have passed through the central hole of the ionization chamber without being detected but instead are deflected into the chamber by the sample which blocks the channel. By phasing the rectifying switch so that the signal integration occurs only during the interval indicated between the two vertical lines, the galvanometer deflection because of a scatterer can be made very small. With 5.5 g of carbon, corresponding to 132 mm² of scattering area and 0.13 mm² of capture area, the adjustment was such that equal capture and scattering areas in the sample gave measured signals in the ratio of about 500 to 1. Under these conditions corrections for scattering need be made only for samples with capture cross sections of a fraction of a barn.

Although thermal neutrons are known to predominate in the region in which the sample is oscillated, a test was made to determine whether neutron capture by resonances above about 1 ev would give a measurable response. The ratio of nonthermal to thermal neutrons at the position of the ionization chamber was determined by measuring the relative activity of two identical 5-mil-thick indium foils, irradiated with and without a cadmium cover. The ratio of activities was 35, indicating that indium captured 35 thermal neutrons to 1 epi-cadmium neutron, about a 3 percent effect for the 1.44-ev resonance, while a regular pile oscillator measurement of indium gave a capture cross section that agreed to about 2 percent with the values found by activation and by velocity selection methods. For higher energy resonances this effect would be even less. Those elements with resonance capture peaks at less than 0.5 ev are so indicated in Table II, because for them the values of the capture cross section are really averages over the pile neutron energy spectrum. For the other elements, which absorb thermal neutrons as $1/(E)^{\frac{1}{2}}$, the dependence of cross section on neutron energy is the same for all, and the particular neutron energy spectrum of the ORNL pile oscillator does not affect the measurement.

The random variations in the readings arise mainly from the variability of the pile neutron flux, and possibly from "noise" in the ionization chamber. The amplifier was checked with a simulated pulse and found to be quite constant. With the average neutron flux at a monitored point in the pile remaining constant within about ½ percent, and with no unusual experimental activity around the pile, the flux at the experimental point is constant within about 1 percent. Short period fluctuations, which can affect the oscillator measurements, cannot be controlled. Empirically the long period constancy of the pile oscillator was established by remeasuring a sample. Short period variations were noted only by seeing that successive two-minute readings during a ten-minute run showed no large variations. For ordinary samples variations corresponding to no more than 0.1 mm² of capture area were permitted. With some weakly absorbing samples it was not possible to introduce a large sample because of volume limitations, and to maintain the same accuracy it was necessary to use longer periods of measurement with the pile held especially constant. In particular, one special sample of 0.07-mm² cross section showed only a 30 percent range of variation in several measurements made on different days.

Samples

The beryllium boat which carried the samples imposed a size limitation of 8×8×64 mm³. The samples were made to cover the full length of the boat and nearly the full width, but the thickness varied with the capture

cross section. For nine-tenths of the samples the thickness was less than that corresponding to 3 percent neutron capture, and no sample had a capture thickness greater than 5 percent. For very strong absorbers the sample was diluted to decrease the possibility of lumps of large capture thickness; sodium carbonate was a satisfactory diluent. The effect of self-protection was about as large as the capture thickness, but the standard gold foils had nearly the same capture thickness as the samples, and no error results in the comparison except for the different shapes of the sample and the gold. Because some of the samples required a wrapper, all the samples were wrapped with a 200-mg piece of 1-mil aluminum foil. The foil could be used as a tube to enclose the powdered samples, as a simple wrapper around solid samples, or as a flat piece to cover the comparison gold foils. The few liquid samples and chemically reactive samples were sealed in quartz tubes and then covered with aluminum.

The chemical states of the samples were chosen so that the foreign atoms had low capture cross sections; thus the oxides (σ_c of oxygen <0.001 barn) or fluorides (σ_c of fluorine $=0.01$ barn) as well as the elemental form were usually used. The composition with respect to strongly absorbing impurities had also to be established. If a sample has an assay of 98 percent, it does not follow that the measurement of the cross section is in error by only two percent. The elements reported here possess capture areas varying from 14,000 mm²/g to 0.05 mm²/g, and for a weak absorber as little as one part per million of strongly absorbing impurity is serious. As an example, about 25 μg (micrograms) of boron are detectible with the pile oscillator; thus the boron impurity should be less than 10 μg per sample or an accurate analysis for boron must be made if a correction is to be calculated. In the range of sample weights that were used, from 100 mg to 5 g approximately, the boron tolerance is from 100 ppm to 2 ppm, respectively.

Samples of the commoner materials were chosen from commercial reagent grade chemicals and most of them were analyzed spectrographically at this laboratory for metallic impurities. Chlorine is the only important nonmetallic impurity that could not be detected spectrographically, the rare earths are not easily detected but they are not generally expected as impurities, and boron may escape detection in amounts that are significant because of its large capture cross section. Normally dry compounds were chosen to avoid dilution of the sample by adsorbed water and carbon dioxide. They were heated, dried, and stored in a desiccator. At least two samples of different origin and preferably of different composition were used for each element.

The rare earths, including scandium and yttrium, are a special case because of their large capture cross sections and because of the difficulties of purifying them in sufficient amounts. Only for three of them—lanthanum, cerium, and neodymium—were two very pure samples available. For the others, the rare earths produced by column extraction methods at the ORNL (by Darwin Harris) and at Iowa State College, were the only ones deemed satisfactory. Their purities are estimated by a study of the extraction techniques, including the use of radioactive rare earth tracers, and verified to the limit of the spectrographic method.

Zirconium and hafnium are similar to the rare earths for difficulty of separation. Because of its large capture cross section relative to zirconium, hafnium is significant if it is present to more than 0.1 percent in the zirconium. This required the preparation of special samples and the development of new analytical methods. Zirconium metal can be made purer than its compounds with respect to impurities other than hafnium, and the final value of the capture cross section in this report is from measurements on metal samples. The measurement of hafnium offered no difficulties.

The ORNL pile oscillator has been used to make measurements of the thermal capture cross sections of 69 of the first 83 elements. Two elements—Tc and Pm—exist only in small quantities that are neither stable nor of any standard isotopic mixture. Five elements are the inert gases—He, Ne, A, Kr, and Xe—whose low density precludes placing sufficient weight in the limited volume of the pile oscillator. Five elements—Be, C, O, F, and Bi—have capture cross sections less than 0.02 barn but scattering cross sections several hundred times larger; any correction for the scattering of neutrons with so large a ratio of cross sections would be an uncertain one. One element—H—not only has a large ratio of scattering to capture but produces slow neutrons by elastic collisions with fast ones, thus counteracting in part its capture of slow neutrons. Gold, the standard for these measurements, was measured by others using direct methods.

TABLE I. Capture cross sections of gold for neutrons at 2200 m/sec.

Reference	Total	Scatter	Capture	Method
[a]	104 b	9 b	95 b	Modulated cyclotron (Los Alamos)
[b]	103.8	10.8	93.0	Mechanical velocity selector (Argonne)
[c]	100			Mechanical velocity selector (Argonne)
[d]	101			Mechanical velocity selector (Argonne)
[e]	103.5	7.6	95.9	Crystal spectrometer (ORNL)
[f]		6.5		Comparison with graphite (Argonne)
[g]		7.5		Neutron diffraction (ORNL)

[a] McDaniel, Sutton, Lavatelli, and Anderson, Phys. Rev. **72**, 729 (1947).
[b] A. Wattenberg, AEC Report ANL-4174 (1949) (unpublished).
[c] T. Brill and H. V. Lichtenberger, Phys. Rev. **72**, 585 (1947).
[d] E. Fermi, quoted by Seren, Friedlander, and Turkel, Phys. Rev. **72**, 888 (1947).
[e] L. W. Cochran, AEC report ORNL-481 (1949) (unpublished).
[f] E. Bragdon, AEC Report CP-2305 (1944) (unpublished).
[g] C. G. Shull and E. O. Wollan, Phys. Rev. **81**, 527 (1951).

Standards

Because the capture cross sections in Table II were determined from ratios with the capture cross section for gold, they are no more accurate than the value used for gold. If 95 b per atom for gold for neutrons at 2200

TABLE II. Thermal neutron capture cross sections (in barns).

Substances examined	Z	Element	ORNL pile oscillator: Final value	ORNL pile oscillator: Estimated error (%)	Comparison data: Pile oscillators: Argonne[a]	Comparison data: Pile oscillators: Harwell[b]	Comparison data: Transmission	Comparison data: Activation[a]
Li_2CO_3; $LiIO_3$	3	Li	67	5		65.5	72.8[d] 65[e]	
BF_3; B_2O_3; Borax	5	B	730	5	(710)	(710)	745[d] 704[f] 722[g] 703[e]	
NaCN; KNO_3; $NaNO_2$	7	N	1.86	5		1.76	2.15[d]	
Na; Na_2CO_3; NaF	11	Na	0.47	5	0.52	0.50		0.63
Mg	12	Mg	0.06	10	0.06	0.057		
Al	13	Al	0.22	5	0.22	0.212	0.23[d]	0.21
SiO_2	14	Si	0.10	20	0.16	0.16		
P red; P_2O_5	15	P	0.15	10		0.193		0.23
S	16	S	0.47	10	0.51	0.49	0.62[d]	
KCl; NaCl; $PbCl_2$	17	Cl	32.7	5	31.5	31.8		
K; KF; K_2CO_3	19	K	2.05	5	2.11	1.89		
CaF_2; CaO; $CaCO_3$	20	Ca	0.41	5	0.43	0.40		
Sc_2O_3	21	Sc	11.8	5	31.8			22
Ti; TiO_2	22	Ti	5.8	5	5.88	5.0		
V_2O_5; VC	23	V	4.7	5	4.93	4.4		4.50
Cr; Cr_2O_3	24	Cr	2.83	5	3.05	3.1	3.42[d]	
Mn; Mn_3O_4; Mn oxide	25	Mn	12.8	5	12.3	12.8	14.2[d]	10.7
Fe; Fe_2O_3	26	Fe	2.39	5	2.48	2.4	2.21[d]	
Co; Co_3O_4	27	Co	34.2	5	35.7	38.2	40.5[d] 39.0[h]	22.4
Ni; NiO	28	Ni	4.5	5	4.37	4.8	4.87[d]	
Cu	29	Cu	3.57	5	3.71	3.6	3.42	2.56
Zn; ZnO	30	Zn	1.00	5	1.09	1.09		
Ga_2O_3	31	Ga	2.77	5	3.10		2.21[d]	2.16
Ge; GeO_2	32	Ge	2.2	10	2.64			
As; As_2O_3	33	As	4.14	5	5.46	4.9		4.2
Se; SrSe	34	Se	12.1	5	12.2	11.4		
Br; $KBrO_3$	35	Br	6.4	5	8.83	8.7	6.40[d]	6.6
Rb_2CO_3	37	Rb	0.70	10				0.55
SrO; $SrCO_3$	38	Sr	1.16	5	1.53	1.35		
Y_2O_3	39	Y	1.38	10				1.24
Zr; ZrO_2	40	Zr	0.18	10	~0.4	0.250		
Nb; Nb_2O_5	41	Nb	1.06	5	1.51	1.26	0.6[d]	~1
Mo; MoO_3	42	Mo	2.40	5	3.04	2.95		
Ru; RuO_2	44	Ru	2.46	5	6.30		2.47[d]	
Rh	45	Rh	150	5	172		141[f] 150[e]	149
Pd	46	Pd	6.6	5	10.3	10.0		
Ag	47	Ag	60	5	90		57.2[d] 59.2[e]	70.7
Cd	48	Cd	3500	res[i]			2300[d]	
In	49	In	191	5			191[f] 189[e]	190
Sn; SnO_2	50	Sn	0.58	5	0.72	0.70		
Sb; Sb_2O_3	51	Sb	5.3	5	8.15	7.6	4.05[d]	4.9
Te	52	Te	4.5	5	5.82			
I; NaI; KI	53	I	6.1	5	9.23	7.4	7.1[d] 6.7[f]	6.25
Cs_2CO_3; CsBr	55	Cs	29.0	5	35.8			25.6
$BaCO_3$; BaF_2	56	Ba	1.05	5	1.35	1.25		
La; La_2O_3	57	La	8.8	5	9.01			8.4
CeO_2	58	Ce	0.80	10	~0.65	<0.92		
Pr_6O_{11}	59	Pr	11.2	5				10.1
Nd_2O_3	60	Nd	44	5	52			
Sm_2O_3	62	Sm	10600	res	~8200			
Eu oxalate	63	Eu	4200	res				
Gd_2O_3	64	Gd	35000	res	36500	37600		
Tb_4O_7	65	Tb	44	10				
Dy_2O_3	66	Dy	890	res				
Ho_2O_3	67	Ho	64	5				59.6
Er_2O_3	68	Er	166	10				
Tm_2O_3	69	Tm	118	5				106
Yb_2O_3	70	Yb	36	10				≥34
Lu_2O_3	71	Lu	108	5				106.9
HfO_2	72	Hf	102	5	171	110		
Ta; Ta_2O_5	73	Ta	21.3	5	36	21.2	19.0[d]	20.6
W; WO_3	74	W	17.7	5	24	20.5	17.2[d]	

TABLE II.—*Continued.*

Substances examined	Z	ORNL pile oscillator Element	Final value	Estimated error (%)	Comparison data Pile oscillators Argonne[a]	Harwell[b]	Transmission	Activation[c]
Re; $KReO_4$	75	Re	84	5	120		100[d]	85.0
Os; OsO_4	76	Os	14.7	5			17[d]	
Ir	77	Ir	440	5	~470		405[d]	467
Pt	78	Pt	8.1	5	13.5	15.0	6.5[d]	
Au	79	Au	95	j	~157			
HgO; HgI_2	80	Hg	341	res	~380		405[d]	
Tl	81	Tl	3.27	5	3.65		3.8[d]	2.28
Pb	82	Pb	0.19	5	0.16	0.28	0.18[d]	

[a] Argonne (reference 4).
[b] Harwell (reference 5).
[c] Seren, Friedlander, and Turkel, Phys. Rev. **72**, 888 (1947).
[d] Columbia University modulated cyclotron, variously reported by Dunning, Rainwater, Havens, Wu, and Melkonian: Phys. Rev. **70**, 136, 154 (1946); **71**, 65, 165, 174 (1947); **72**, 634 (1947); **73**, 733, 963 (1948); **75**, 1296 (1949); **76**, 1750 (1949).
[e] Argonne mechanical velocity selector: Fermi, Marshall, and Marshall, Phys. Rev. **72**, 193 (1947): Fermi quoted in Can. J. Research **A25**, 26 (1947); Fermi quoted in Phys. Rev. **72**, 888 (1947).
[f] Cornell University modulated cyclotron: Bacher, Baker, and McDaniel, Phys. Rev. **69**, 443 (1946); B. D. McDaniel, Phys. Rev. **70**, 832 (1946); W. B. Jones, Jr., Phys. Rev. **72**, 362 (1947); R. R. Meijer, Phys. Rev. **75**, 773 (1949).
[g] Los Alamos modulated cyclotron: Sutton, McDaniel, Anderson, and Lavatelli, Phys. Rev. **71**, 272 (1947).
[h] Oak Ridge crystal spectrometer: Bernstein, Dial, Stanford, and Stephenson, Phys. Rev. **75**, 1302 (1949).
[i] Res indicates a neutron capture resonance at less than 0.5 ev.
[j] The value of 95 barn for gold (for incident neutrons of 2200-m/sec velocity) was the standard for this work.

m/sec is not correct, the list would have to be modified accordingly. The value of 95 barn is an estimated best value based on the cross sections determined by several investigators and listed in Table I. Some recent work done elsewhere indicates that 93 barn is a better value, but the calculated effect of the strong capture resonance at 4.9 ev with the near thermal neutron spectrum used with the pile oscillator is enough to make the "effective" value for gold 94 barn or 95 barn, and thus the values in Table II need not be altered. The pile oscillator work at other laboratories used 710 barn per atom for boron as the standard for comparison; here the preparation of boron samples of about 1 mg that showed no self-protection and were accurately weighed was discarded in favor of the gold foil standard samples.

Accuracy

The thermal neutron capture cross sections reported here have an estimated error of about 5 percent with some exceptions noted in Table II. Measurements on a single sample were reproducible within 2 percent, except for some weak absorbers where the largest usable sample neutron capture areas, for example—magnesium, silicon, and phosphorus, were less than the 2 mm^2 required for good precision. Consideration of response of the pile oscillator to processes other than the capture of thermal neutrons, the accuracy of the value for the gold standards, and, perhaps most important, whether the sample was well identified with respect to all its constituents, together with the reproducibility of results led to the estimate of accuracy.

The pile oscillator measurements at other laboratories involve a change of pile reactivity and thus include some resonance absorption along with the predominant thermal absorption. For some of their values the Argonne group indicates it made a correction for the resonance capture. The values of both other laboratories, when compared with the ORNL results, should be equal if there was no resonance contribution or the correction was made, greater if there was an uncorrected resonance contribution. The Argonne group indicates an accuracy of better than 5 percent in its values; the Harwell group has published only tentative values.

For further comparison, the capture values determined by activation methods and by transmission methods using monoenergetic neutrons are included in Table II. Seren *et al.* state an estimated probable error for their activation cross sections of 20 percent, although their work seems in general to be better than that. Theirs is the largest single report of such cross sections; other activation measurements are to be found in the Bureau of Standards Circular, "Nuclear data."[3] The curves relating neutron transmission with energy have been compiled but not the values of the breakdowns into scattering and capture. The accuracy of the capture values from such work varies, but all such values for $1/v$ absorbers are included in Table II. Other methods of measuring neutron capture such as diffusion, comparison of absorption in a standardized apparatus, and danger coefficients, are in no single published compilation of cross-section values. They are not tabulated here for comparison because the accuracies are generally either unknown or low, and for many of them there is no knowledge of the average neutron energy used in the measurements.

The author is grateful to Drs. A. M. Weinberg, E. O. Wollan, and W. H. Jordan for their continued interest in this project and for their criticisms in the writing of the report.

The Spin of the Pion via the Reaction $\pi^+ + d \rightleftharpoons p + p$

R. DURBIN, H. LOAR, AND J. STEINBERGER
*Columbia University, New York, New York**

(Received June 21, 1951)

It is possible to determine the spin of the pion by comparing the forward and backward rates of the reaction $\pi^+ + d \rightleftharpoons p + p$. The backward rate has been measured in Berkeley. We have measured the forward rate. Comparison of the two results shows the spin to be zero. In the light of other recent experimental results the meson is then pseudoscalar.

DURING the past few years there has accumulated an increasing amount of evidence that the pion is pseudoscalar. This consists chiefly of the following:

(a) The pion has integral spin. This follows from star formation in the capture of π^- mesons in photographic emulsions, as well as from angular momentum conservation in such reactions as $p + p \rightarrow \pi^+ + d$; $p + h\nu \rightarrow \pi^+ + n$.

(b) The neutral pion does not have spin one, since it decays into two γ-rays and such a transition is forbidden for systems with angular momentum $\hbar$.[1]

(c) Because of their similar masses and their similar nuclear production cross sections, as well as from the evidence on charge independence of nuclear forces, it is likely that neutral and charged mesons have the same transformation properties, so that charged pions also cannot have spin one.

(d) The pion is not scalar. This follows from the experiment on the capture of stopped negative pions in deuterium,[2] as well as the results on the production of pions, both charged and uncharged, by γ-rays.[3] Both experiments give best theoretical agreement in the pseudoscalar meson theory. It has therefore appeared quite probable that the pion is pseudoscalar; but the evidence, especially against a spin of two or greater, is poor.

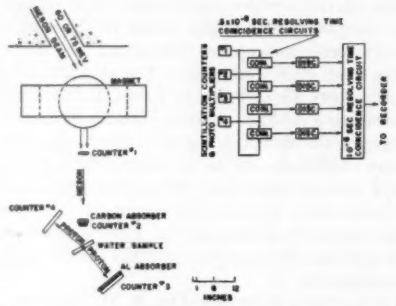

FIG. 1. Arrangement of the beam collimation, water sample, and detectors. Block diagram of circuits.

It has been pointed out by Cheston and Marshak[4] that the reaction $\pi^+ + d \rightleftharpoons p + p$ lends itself to a determination of the spin of the pion. The forward and backward reactions are related by a detailed balancing argument, if one assumes initially unpolarized particles, so that

$$\frac{d\sigma(\rightarrow)}{d\Omega} \Big/ \frac{d\sigma(\leftarrow)}{d\Omega} = \frac{4}{3} \frac{p^2}{q^2(2s+1)},$$

where s is the spin of the meson, and p, q, are the momenta of the proton and meson in the center-of-mass system. The cross sections, of course, are also in the center-of-mass system. The argument is rigorous, independent of meson theory, and in this rests its chief contribution. The reaction $p + p \rightarrow \pi^+ + d$ has been measured by Cartwright, Richman, Whitehead, and Wilcox[5] for 340-Mev protons, corresponding to a meson energy of 21 Mev in the center-of-mass system. We present here results on the inverse reaction.

The experimental arrangement is shown in Fig. 1. The Nevis cyclotron delivers a beam of approximately 20 positive mesons per square centimeter per second outside the concrete shielding. These are produced when the 380-Mev protons strike an internal Be target. The mesons are magnetically analyzed in the fringing field of the cyclotron, and by a small magnet outside the shielding. The energy resolution is ± 4 Mev at 75 Mev and the composition of the beam is 90 percent π^+, and 10 percent μ^+ mesons.[6] The beam is defined by the

* This research has been supported by a joint program of the ONR and AEC.

[1] Steinberger, Panofsky, and Steller, Phys. Rev. **78**, 802 (1950); C. N. Yang, Phys. Rev. **77**, 242 (1950).

[2] Panofsky, Aamodt, and Hadley, Phys. Rev. **82**, 97 (1951); Brueckner, Serber, and Watson, Phys. Rev. **81**, 575 (1951).

[3] Bishop, Steinberger, and Cook, Phys. Rev. **80**, 291 (1950).

[4] R. E. Marshak, Phys. Rev. **82**, 313 (1951); W. B. Cheston, to be published.

[5] Cartwright, Richman, Whitehead, and Wilcox, Phys. Rev. **81**, 652 (1951); V. Peterson, Phys. Rev. **79**, 407 (1950); C. Richman and M. H. Whitehead, to be published. We are most indebted to Professors Richman and Wilcox, Mr. Cartwright, and Miss Whitehead for the privilege of quoting as yet unpublished results, and in particular, the fine meson spectrum shown in Fig. 5.

[6] The beam is analyzed in the following way: Heavy particles and electrons are detected in a measurement of the velocity distribution of the beam particles by means of a time of flight measurement. The mesons have velocities $\sim 0.7c$, the electrons which penetrate the counters have the velocity of light, and heavy particles have smaller velocities. The μ-mesons are measured at the end of their range by means of the delayed coincidences of their electron decay product. This is only possible in the π^- beam, since π^+ mesons at the end of their range are not captured but produce μ^+ mesons and interfere. We have assumed that, since the μ-mesons in the beam are the result of the decay in flight of the π-meson and since π^- and π^+ mesons have at least approximately the same lifetime [Lederman, Booth, Byfield, and Kessler,

crystal scintillation counters 1 and 2, and the energy reduced in the carbon absorber. The liquid scintillation counters 3 and 4 are set with respect to the water sample so that protons emitted 180° apart in the center-of-mass system of the meson and deuteron will be detected.[7] The water sample is 2.5 g/cm² thick. The aluminum absorber in front of counter No. 3 is thin enough to transmit the protons emitted in the meson absorption under study, but stops scattered protons or deuterons. The difference in counting rate using heavy water and light water targets is entirely due to the reaction $\pi^+ + d \rightarrow p + p$. It is in principle quite easy to check that this is so. In actuality, the counting rate is small and only a limited number of checks have been made, to wit: (1) Plateau. In the beginning of each experiment the counters are placed so that the meson beam penetrates all four, and the voltages (amplification) of the phototubes adjusted so that mesons are detected with full efficiency. But the proton pulses in counters 3 and 4 should be larger by a factor two or three than the

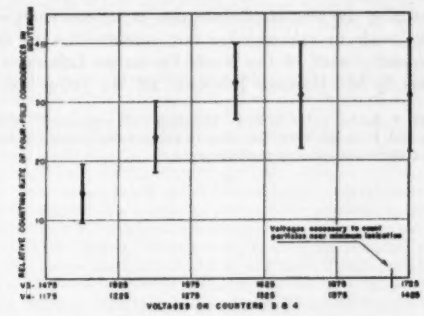
RELATIVE COUNTING RATE OF FOUR-FOLD COINCIDENCES IN DEUTERIUM
Voltages necessary to count particles near minimum ionization
V3- 1475 1525 1575 1625 1675 1725
V4- 1175 1225 1275 1325 1375 1425
VOLTAGES ON COUNTERS 3 & 4

FIG. 2. Counting rate of fourfold events after subtraction, as a function of phototube voltage (amplification) in the proton detection counters 3 and 4.

meson pulses. Figure 2 shows that the pulses responsible for the subtracted fourfold coincidences are large. The $D_2O - H_2O$ difference is counted with full efficiency at voltages 100 volts (i.e., a factor of two in gain) below those necessary to count mesons. (2) When counters 3 and 4 were moved out of line to angles improper for the detection of protons with 180° c.m. angular correlation, no events were observed within statistical accuracy.

Figure 3 shows the energy dependence of the reaction at 45° in the c.m. system. It is sufficiently flat that errors due to energy spread of the meson beam and finite target thickness are small.

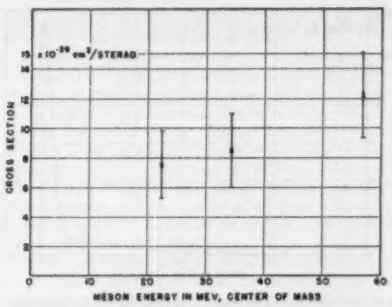

FIG. 3. Differential cross section for the emission of a proton at 45° (and one at 135°) to the meson beam in the c.m. system.

The results on the differential cross section at three angles are shown in Fig. 4. They are the combined results of three determinations, under conditions which varied somewhat. For instance, counters No. 3 and No. 4 were sometimes 4½ in. and at other times 8 in. in diameter. The average meson energy in the target for the three runs was 28 Mev. The data are corrected for the geometrical efficiency of the detecting system which varied from 0.48 to 0.84, for the beam composition (90 percent π^+, 10 percent μ^+), for the nuclear absorption of the mesons and the protons in the target (7 percent), and for an inefficiency of 8 percent in the circuits due to blocking.

The cross sections expected under the assumption of spins zero and one, on the basis of the results of Cartwright, Richman, Whitehead, and Wilcox, and of Peterson[8] are also shown. The Berkeley group has measured the energy distribution of mesons produced in the bombardment of hydrogen by 340 Mev protons.

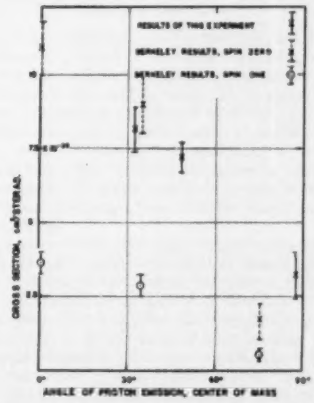
RESULTS OF THIS EXPERIMENT
BERKELEY RESULTS, SPIN ZERO
BERKELEY RESULTS, SPIN ONE
CROSS SECTION, cm²/STERAD.
ANGLE OF PROTON EMISSION, CENTER OF MASS

FIG. 4. Differential cross section of the reaction $\pi^+ + d \rightleftharpoons p + p$ at three angles of emission of the proton in the c.m. system. The average meson energy is 28 Mev in the c.m. system. The dotted points show the cross sections expected for spin one and spin zero pions on the basis of the Berkeley results (see reference 5).

Phys. Rev. 83, 686 (1951)], the μ-contamination is independent of charge.

[7] The center-of-mass transformation is small, approximately 0.05c. The correlation angles in the laboratory system do not differ from 180° by more than 15°. Angular distribution measurements are easier in this reaction than in the inverse, where the large center-of-mass transformation results in a large variation of experimental conditions with angle.

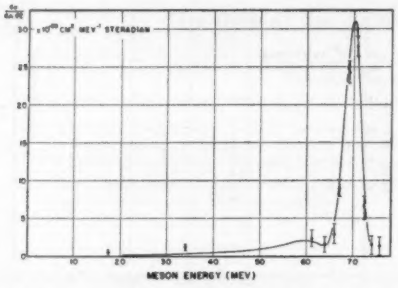

FIG. 5. The spectrum of mesons produced in the collision of 340 Mev protons in the forward direction. This experiment has been performed by Cartwright, Richman, Whitehead, and Wilcox (see reference 5).

(See Fig. 5.) This spectrum consists of a continuum due to the reaction $p+p\rightarrow\pi^{+}+n+p$, and a sharp peak at an energy which exceeds the theoretical limit of the continuum and is due to the reaction $p+p\rightarrow\pi^{+}+d$.[8] The cross section is obtained by integrating the energy spectrum under the peak.

Comparison of the two results shows that the π^{+} meson spin is zero, quite outside the possible limits of error in the two experiments. Combining this result with those of Panofsky[2] and those on the photomeson production,[3] the meson is very likely pseudoscalar.

It is necessary to point out that the same ratio of cross sections could be obtained also for non-zero spin mesons provided that pions were completely polarized both in the $p+$Be and $p+p$ meson production reactions. Such polarization is theoretically possible, but only in the longitudinal mode, that is, in the mode with zero component of angular momentum along the propagation axis. This seems a rather remote possibility.

A similar experiment has been performed by D. L. Clark, A. Roberts, and R. Wilson, who have reached the same conclusions. We are indebted to them for a pre-publication copy of their results.

The experiment is being continued. The reaction is interesting also in other connections. As Bethe[9] has pointed out, the angular distribution is quite perplexing. Furthermore, the energy dependence will shed some light on the momentum dependence of the meson nucleon interaction. We are therefore in the process of measuring the angular distribution at several energies.

We wish to acknowledge our indebtedness to the engineering staff of the Nevis Cyclotron Laboratory, especially Mr. Harrison Edwards and Mr. Julius Spiro.

[8] The actual production of deuterons in coincidence with mesons has been observed by Crawford, Crowe, and Stevenson, Phys. Rev. **82**, 97 (1951).

[9] H. A. Bethe, letter to R. E. Marshak with copies to C. Richman and J. Steinberger. We wish to express our thanks to Professor Bethe for this communication.

Letters to the Editor

PUBLICATION of brief reports of important discoveries in physics may be secured by addressing them to this department. The closing date for this department is five weeks prior to the date of issue. No proof will be sent to the authors. The Board of Editors does not hold itself responsible for the opinions expressed by the correspondents. Communications should not exceed 600 words in length.

Cross Section for the Reaction $\pi^+ + d \rightarrow p + p$, and the Spin of the π^+ Meson*

D. L. CLARK, A. ROBERTS, AND RICHARD WILSON
University of Rochester, Rochester, New York
(Received June 8, 1951)

THE application of detailed balancing to the determination of the spin of the π^+ meson from the reaction $\pi^+ + d \rightarrow p + p$ and its inverse has been suggested by Marshak and Cheston[1] and independently by Johnson.[2] The detailed balancing argument requires the comparison of either differential or total cross sections of both the meson-producing and meson-absorbing reactions at the same energy in the center-of-mass system. The reaction $p + p \rightarrow \pi^+ + d$ has been studied for 340-Mev protons by Richman and others.[3] The best data are for the differential cross section at 0°, and other data are available at 18°, 30°, and 60°. From these data, limits on the angular distribution can be obtained and the total cross section computed. We have now measured the total cross section for the meson-absorbing reaction.

A beam of 40-Mev π^+ mesons was produced from an aluminum target bombarded by the 240-Mev proton beam of the Rochester cyclotron; the mesons were magnetically selected and focused by the fringing field. A threefold scintillation counter telescope[4] in the meson beam counts the mesons and discriminates against other particles by pulse-height measurements in one counter. The transmitted mesons, reduced to 33 Mev by the telescope, enter a D_2O target just thick enough to stop them. Protons produced in the D_2O are detected in coincidence by two large NaI scintillation counters. The ratio of 5-fold coincidences of mesons with protons to meson counts alone determines the cross section for the disintegration, averaged over energy and angle.

Backgrounds were assessed by replacing D_2O by H_2O. Scattering of mesons out of the target and purity of the meson beam were measured in auxiliary experiments. The meson beam was contaminated by not more than 2 percent protons or 6 percent deuterons. It was also shown that even much greater contamination would produce no significant difference between D_2O and H_2O targets.

To find the cross section at 22.7 Mev, which corresponds to 340 Mev in the production experiment, an auxiliary experiment was performed which showed that the average cross section from 23–33 Mev is the same as the average cross section from 0 to 23 Mev, within the statistical error of 10 percent. Since 33-Mev mesons are reduced to 23 Mev after half their range, we conclude that the yield at 23 Mev is equal to the yield averaged from 33 Mev to zero within 5 percent.

The coincidence rate as a function of proton pulse heights in the NaI counters corresponded to those expected for the reaction from the geometry of the apparatus. The NaI counters were calibrated with fast protons of known energy.

TABLE I. Predicted and observed total meson-absorption cross sections.

Angular dependence (c.m. system)	Predicted total cross section (mb) spin 0	spin 1	Measured total cross section (mb)
$\cos^2\theta$	2.55 ±0.6	0.85 ±0.2	5.0 ±0.9
$0.1 + \cos^2\theta$	3.0 ±0.7	1.0 ±0.24	4.7 ±0.9
$0.5 \pm \cos^2\theta$	4.2 ±1.0	1.4 ±0.35	4.2 ±0.8
$0.2 \pm 0.1 + \cos^2\theta$	3.4 ±0.9	1.1 ±0.3	4.5 ±0.8

The detector solid-angle correction to the observed counting rate to obtain total cross section depends upon the angular distribution of the reaction products, and has been calculated assuming an angular dependence of the form $A + \cos^2\theta$ in the c.m. system. The latest data of Cartwright *et al.* (private communication) indicate $A = 0.2 \pm 0.1$. Table I shows the value of the meson-absorption cross section predicted by detailed balancing, using the value 1.3×10^{-28} cm²/ster for the production cross section at 0° in the laboratory system, assuming different values for A. It also shows our observed values for comparison. We conclude that the spin of the π^+ meson is zero.

Kaplon has pointed out[5] that the principle of detailed balancing would not apply if the spin of the π^+ meson were 1, but for some reason only one polarization state appears in both the absorption and production reactions. A statistical weight of 1 would then be observed. For this effect to explain our results, the polarization would have to exceed 75 percent for both reactions, which we regard as very unlikely.

It would be highly desirable to verify further the detailed balancing predictions by a direct comparison of the differential cross sections at several angles. Our meson intensity is too low at present for this to be experimentally feasible.

From the indirect observation of the reaction $\pi^- + d \rightarrow n + n$ by Panofsky *et al.*,[6] Tamor and Marshak[7] have shown that if the π^- meson possesses spin zero, it cannot be scalar. If we assume that π^+ and π^- mesons possess the same spin and parity, we must conclude that the charged π-meson is pseudoscalar.

* This work was supported by the AEC.
[1] R. E. Marshak, Rochester High Energy Conference, December, 1950; W. Cheston, Phys. Rev. (to be published).
[2] M. H. Johnson, private communication.
[3] Cartwright, Richman, Whitehead, and Wilcox, Phys. Rev. **81**, 652 (1951); Crawford, Crowe, and Stevenson, Phys. Rev. **82**, 97 (1951).
[4] Donald L. Clark, Phys. Rev. **81**, 313 (1951).
[5] M. Kaplon, private communication.
[6] Panofsky, Aamodt, and Hadley, Phys. Rev. **82**, 97 (1951).
[7] S. Tamor and R. E. Marshak, Phys. Rev. **80**, 766 (1950).

Energy Distribution of the Primary Cosmic Radiation*

H. V. NEHER
California Institute of Technology, Pasadena, California
(Received June 11, 1951)

THE primary cosmic-ray energy spectrum usually assumed, $N(E) = kE^{-n}$, where n has been assigned various values ranging from 2.5 to 2.9, by different writers obviously cannot hold for small values of the particle energy, E. To assume a cutoff of the primary radiation at an assigned value of, say, 3 or 4 Bev is also unsatisfactory, since a latitude effect at 30,000 ft,[1] as well as at balloon altitudes,[2,3] has been measured down to energies for protons to at least 1 Bev. It therefore appears (at least at the time these experiments were performed) that no definite cutoff occurs, although the energy brought in by these low energy particles must be relatively small.

The B-29 data of Biehl, Neher, and Roesch[3] taken at 310 g cm^{-2} from 64° geomagnetic north to the Equator, along longitude 80°W, has given a means of normalizing the balloon flight curves of Neher and Pickering[4] and of Biehl *et al.*[5] Further, by correlating counter telescope and ionization chamber data it is possible to make use of data at smaller latitude intervals than was possible with ionization chambers.[6] A further requirement is to know the minimum momentum *vs* geomagnetic latitude for the primary particles. This has been done with the help of Vallarta *et al.* by correlating the various geomagnetic effects.[7]

The resulting histogram obtained from the differences of the adjusted counter-telescope balloon curves is shown in Fig. 1. Block 5 is obtained from two high altitude points at 45°E over Peru, and a counts-*vs*-altitude curve is then constructed using the

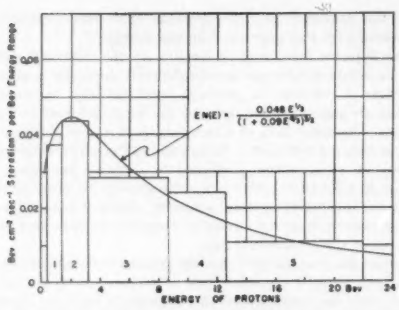

FIG. 1. Blocks 1, 2, 3, 4, and 5 result from differences in adjusted counter-telescope curves at various latitudes. The smoothed curve is a plot of an empirical relationship that fits the ionization data with experimental errors.

extrapolated behavior of known curves for lower minimum momenta of the primaries. This block is admittedly the least well determined of the set. The chief difference between the present results and those published by Bowen, Millikan, and Neher in 1938,[6] is in the abscissas.

An empirical expression that fits the experimental data is as follows:

$$EN(E)=0.048E^{1/3}/(1+0.09E^{4/3})^{3/2}, \tag{1}$$

where E is measured in units of 10^9 ev. $EN(E)dE$ is the energy in Bev cm^{-2} sec^{-1} steradian^{-1} brought to the earth by protons whose energy lies between E and $E+dE$. The differential number distribution is then

$$N(E)=0.048/[E^{2/3}(1+0.09E^{4/3})^{3/2}]. \tag{2}$$

The integral of this last equation, giving the numbers of primary particles with energies larger than E, is plotted in Fig. 2.

In justification of these expressions the following may be cited: (a) The expression (1) may be integrated directly and gives a total energy of 0.418×10^9 ev cm^{-2} sec^{-1} sterad^{-1} for all particles at the vertical in Peru. The experimental value is 0.413 in the same units. (b) A similar integration for Bangalore, India, yields 0.35 as against the experimental value 0.34. (c) From 0.4×10^9 ev to ∞, it gives 0.787 as compared with 0.774 for Saskatoon. (d) It gives a dependence on E of $E^{-2.67}$ for the differential number distribution at very large E. This is within the limits of the exponent found by Hilberry[8] to be necessary to explain extended showers. (e) It gives an effective dependence on E of $E^{-1.1}$ for the integral number spectrum in the range 2 to 12×10^9 ev. This is the distribution found necessary by Van Allen and Singer[9] to explain their results using rockets. (f) It gives a ratio in the total number of particles at 50°N and 30°N of 3.4, as compared with the value of 3.5 found for all primaries by Bradt and Peters.[10]

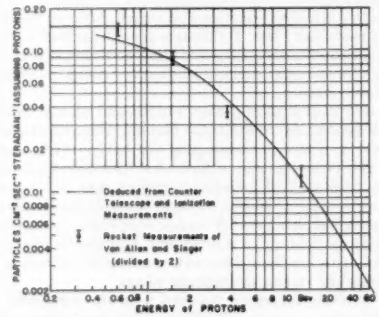

FIG. 2. The integral number distribution of the primary cosmic radiation deduced from the empirical relationship given in Fig. 1. For data of Van Allen and Singer, see reference 9.

The presence of particles heavier than protons in the primary radiation will affect only the constant in the numerator of Eqs. (1) and (2), provided the relative numbers of different particles are not dependent on the momentum, as it seems to be from the work of Bradt and Peters.[10]

The application of Liouville's theorem to be charged particles moving in the magnetic field of the earth implies that the found energy distribution of the primary cosmic-ray particles is also their distribution in space.

As has been pointed out by Van Allen and Singer,[9] and by Winckler *et al.*,[11] a discrepancy of about a factor of 2 exists between the numbers of primary particles determined directly near the top of the atmosphere and that found by taking the area under ionization curves. The, as yet undetermined, albedo effect will tend to make the directly measured value at high altitudes too large, while energy losses due to neutrinos will tend to make the numbers computed from ionization data too small. The small east-west effect measured at very high altitudes[9,11] is good evidence that the albedo, or general background, is important, at least at the Equator.

Further details are being published elsewhere.

* Assisted in part by the joint program of the ONR and AEC.
[1] A. T. Biehl and H. V. Neher, Phys. Rev. **78**, 172 (1950).
[2] M. A. Pomerantz, Phys. Rev. **77**, 830 (1950).
[3] Biehl, Neher, and Roesch, Phys. Rev. **76**, 914 (1949).
[4] H. V. Neher and W. H. Pickering, Phys. Rev. **61**, 407 (1942).
[5] Biehl, Montgomery, Neher, Pickering, and Roesch, Revs. Modern Phys. **20**, 360 (1948).
[6] Bowen, Millikan, and Neher, Phys. Rev. **53**, 855 (1938).
[7] H. V. Neher, Phys. Rev. **78**, 674 (1950).
[8] N. Hilberry, Phys. Rev. **60**, 7 (1941).
[9] J. A. Van Allen and S. F. Singer, Phys. Rev. **78**, 819 (1950).
[10] H. L. Bradt and B. Peters, Phys. Rev. **77**, 66 (1950).
[11] Winckler, Stix, Dwight, and Sabin, Phys. Rev. **79**, 656 (1950).

Observations of Zener Current in Germanium *p-n* Junctions*

K. B. McAFEE, E. J. RYDER, W. SHOCKLEY, AND M. SPARKS
Bell Telephone Laboratories, Murray Hill, New Jersey
(Received June 11, 1951)

IN 1934 Zener[1] published a theory of excitation of electrons directly from the valence band to the conduction band under the influence of high electric fields. For this purpose the energy gap of width $\mathcal{E}_G$ is treated as a region of negative kinetic energy in which the wave function is attenuated, so that the probability of penetrating the gap is approximately

$$f=\exp[-(\pi^2/h)(2m)^{\frac{1}{2}}\mathcal{E}_G^{\frac{3}{2}}/eE], \tag{1}$$

where m is the effective mass and E the electric field; this formula differs from Zener's by being extended to larger energy gaps. The number of oscillations per second in the valence band is

$$\nu=ea\mathcal{E}/h, \tag{2}$$

so that the current per unit cell, containing z/a^3 electrons, is $e\nu fz$. If the field is uniform over a certain region and produces a voltage drop V, then the Zener current per unit area is

$$I=e^2Vzf/a^3h=V\exp[\alpha-(\beta/E)]$$
$$=V10^{(11-10^7/E)}\text{amp/cm}^3, \tag{3}$$

the last form corresponding to the constants for germanium and an effective mass equal to the electron mass, V being expressed in volts, and E in volts/cm.

Measurements of the Zener current have been made across *p-n* junctions in germanium, formed in a single crystal by using arsenic as the donor impurity and gallium as the acceptor.[2-4] Figure 1 shows the reverse $i-e$ characteristic of the junction plotted on a log-log scale over five decades of current. The critical voltage gradient across the junction was measured by determining the behavior of the capacitance of the junction against the reverse bias voltage. The slope of the log$V$ *versus* log$C$ plot for the junc-

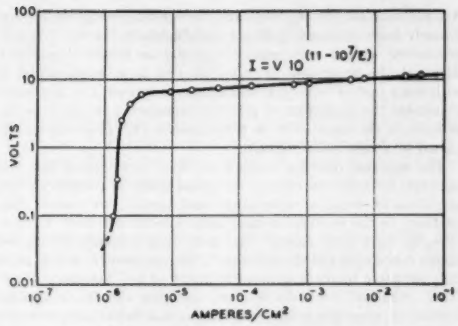

FIG. 1. Current-voltage characteristic for a p-n junction.

tion was 3, as is expected for a constant gradient of impurity concentration across the junction.[5] From the measured capacitance of the junction it is possible to calculate the maximum voltage gradient across the junction, which occurs at the midpoint.

The general behavior of the curve is in agreement with theory, and the rapid increase in current with voltage is consistent with Eq. (3), which gives

$$d\ln I/d\ln V = 1+(2\beta/3E) \tag{4}$$

for $E \propto V^{\frac{1}{2}}$. For $V=8$ and $I=2.5\times10^{-9}$ Eq. (4) becomes 23, whereas the slope in Fig. 1 is 24. In agreement with out observations, the Zener current should cause no permanent damage, since it corresponds to field-induced generation of hole-electron pairs in the junction which are separated by the field, leaving an undisturbed valence bond structure.

The field for appreciable currents deduced from Fig. 2 is 2.2×10^5 volts/cm, whereas Eq. (3) gives 6.9×10^5 volts/cm. The discrepancy may be due to the poorness of the approximation (1). A group of junctions having critical voltages varying from 1 to 10^3 volts due to differences in concentration gradient all have critical fields of about 2×10^5 volts/cm. The high critical voltage junctions were measured under pulse conditions to avoid heating effects; heating is negligible in the low voltage units.

An alternative explanation of the "breakdown" phenomenon might propose the production of secondary electrons by the normal saturation current flowing through a critical field. This mechanism was eliminated by comparing the high field current when the specimen was dark and when illuminated sufficiently to change the low field saturation current[4] by a factor of about two. It was found that the increase in current was the same both below and above the critical breakdown voltage, i.e., that the photocurrent was not multiplied in traversing a barrier biased at greater than critical field strength.

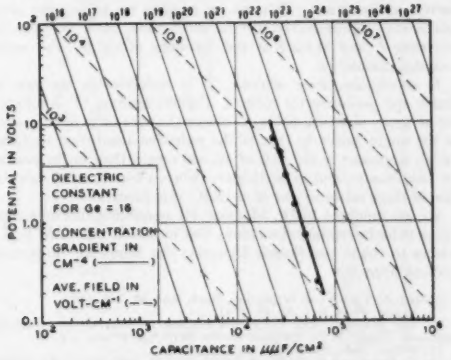
POTENTIAL IN VOLTS
CAPACITANCE IN μμF/CM²
DIELECTRIC CONSTANT FOR Ge = 16
CONCENTRATION GRADIENT IN CM⁻⁴ (———)
AVE. FIELD IN VOLT-CM⁻¹ (— —)

FIG. 2. Capacity-voltage characteristic for a p-n junction. (A dielectric constant of 16 is assumed.)

Investigations are now being carried out to determine to what extent "patch effects" are important and to compare temperature and pressure coefficients with theory.

We are indebted to our colleagues H. R. Moore, G. L. Pearson, W. J. Pietenpol, G. K. Teal, and W. van Roosbroeck in connection with this study and to F. Seitz for a stimulating question regarding secondary currents.

[*] This material was presented on March 9, 1951, at the 304th meeting of the American Physical Society, Phys. Rev. **82**, 765 (1951).
[1] C. Zener, Proc. Roy. Soc. (London) **145**, 523 (1934). See also W. V. Houston, Phys. Rev. **57**, 184 (1940).
[2] Teal, Sparks, and Buehler, Phys. Rev. **81**, 637 (1951).
[3] Goucher, Pearson, Sparks, Teal, and Shockley, Phys. Rev. **81**, 637 (1951).
[4] W. J. Pietenpol, Phys. Rev. **82**, 120 (1951).
[5] W. Shockley, Bell System Tech. J. **28**, 444 (1949).

Erratum: Radioactivity of Ag^{111}, Cd^{111}, In^{111}, and Sn^{111}

[Phys. Rev. **81**, 734 (1951)]

CARL L. MCGINNIS
Department of Physics, University of California, Berkeley, California

THE formulas of Eqs. (1) and (2) should read $N_{ss}/N_{s547}=\Omega x(1-e^{-\lambda t})$ and $N_{ss}/(N_{s172}+N_{s547})=2\Omega xy(1-e^{-\lambda t})/(x+y)$, respectively.

Asymptotic Expression of the Thomas-Fermi Function for a Packed Atom*

KWAI UMEDA
Department of Physics, Faculty of Science, Hokkaido University, Sapporo, Japan

(Received May 28, 1951)

THE Thomas-Fermi function $\phi(x)$ for an atom packed in a finite volume, i.e., the TF function with the initial slope $B<B_0$ ($=1.58808$), has recently become of interest because of its role in the theory of solids under high pressure. Since it is given hitherto merely numerically and only for several values of the atomic radius, its approximate expression in a closed form is strongly desired.

For a free atom ($B=B_0$) as well as for free ions ($B>B_0$), we have indeed the well-known Sommerfeld asymptotic formulas.[1] Now, since a packed atom probably has a finite radius, like an ion, it seems reasonable to treat it by a procedure wholly analogous to that used by Sommerfeld for an ion, provided that the indeterminate constant A in Eq. (36a) of the Sommerfeld paper is determined by means of an alternative boundary condition at the surface, $x=x_0$, of the atom:

$$\phi'(x_0)=\phi(x_0)/x_0. \tag{1}$$

By this method, we have obtained a definitive asymptotic expression for the TF function for a packed atom with a finite radius x_0, in TF units,

$$\phi(x)=[1/(1+z)^{\lambda_1/2}]\{1+A_0[(1+z)/(1+z_0)]^{\lambda_1/\lambda}\}, \tag{2}$$

where

$$A_0=(4z_0+1)/[(\lambda+3)z_0-1], \quad z=(x/12^{\frac{1}{2}})^{\lambda},$$
$$\lambda_1=7.772, \quad \lambda=0.772, \quad \lambda_1/\lambda=10.067.$$

The coefficient A_0 converges to 1.06 with increasing radius and can be taken in practice as 1.2 for $x_0>5$.

In spite of the fact that our method seems at first sight to be not so successful, the values of Eq. (2) for $x_0>5$ are in a surprisingly good accord with the exact solutions computed numerically by Slater and Krutter.[2] For the atom packed as extremely as $x_0<2.5$, however, Eq. (2) departs too much to be useful, as would be expected, since for the smaller values of x_0 the starting assumptions, i.e., the adequacy of the asymptotic treatment and the

smallness of the deviation from the standard TF function for a free atom, are not strictly valid.

Equation (2) yields further an analytic expression for the dependence of the boundary value of the TF function on the radius of the atom,

$$\phi(x_0)=2.060\frac{x_0}{x_0-0.2651}\frac{1}{(1+x_0)^{3.886}}, \tag{3}$$

in place of the tabular form given by Feynman *et al.*[3] Putting Eq. (3) into the equation of state of a solid in the simple TF approximation given by Slater and Krutter,[4] we can transform it into an explicit function of the atomic number Z and the volume v associated with the atom alone,

$$pv=\frac{0.437Z^{7/3}(Zv/a_0^3)^{0.810}}{[0.212(Zv/a_0^3)^{0.257}+1]^{9.72}[0.798(Zv/a_0^3)^{0.257}-1]^{5/2}}\left(\frac{e^2}{a_0}\right), \tag{4}$$

where a_0 denotes the Bohr radius.

Details of this investigation, including the full comparison of Eq. (2) with the Slater-Krutter values, will be published shortly in the *Journal of the Faculty of Science*, Hokkaido University, Japan.

* Assisted by a grant from the Ministry of Education of Japan.

[1] A. Sommerfeld, Z. Physik **78**, 283 (1932); S. Rozental, Z. Physik **91**, 742 (1935); N. H. March, Proc. Cambridge Phil. Soc. **46**, 356 (1950).

[2] J. C. Slater and H. M. Krutter, Phys. Rev. **47**, 559 (1935). The present author wishes to express his appreciation to Drs. Slater and Krutter for their tables, which were sent to him privately.

[3] Feynman, Metropolis, and Teller, Phys. Rev. **75**, 1561 (1949), Table III, which seems, however, to be inconsistent with the Slater-Krutter tables.

[4] Reference 2, p. 564; reference 3, Eq. (6).

π^--Meson Reactions in Tritium

A. M. L. MESSIAH AND E. CAIANIELLO
University of Rochester, Rochester, New York
AND
S. BASRI
Columbia University, New York, New York

(Received June 20, 1951)

IT has been shown that the relative yields of the various possible reactions of slow negative π-mesons with hydrogen[1] and deuterium[2] are very sensitive to the spin and parity of the meson. In fact, the order of magnitude of the branching ratios can be predicted on the basis of angular momentum and parity selection rules. As a consequence, many of the conclusions concerning the spin and parity of the charged and neutral π-mesons which can be drawn on the basis of weak coupling calculations, still hold independently of this assumption. In particular, the results of the absorption experiments in deuterium appear to rule out the scalar and vector fields for the π^--meson.

We report here on a study of the selection rules in the reactions of slow π^--mesons with tritium, namely:

$$\pi^-+H^3\rightarrow 3n, \tag{1}$$

$$\pi^-+H^3\rightarrow 3n+\gamma. \tag{2}$$

Let I (symmetric), A (antisymmetric), U (2-dimensional) be the 3 irreducible representations of the group[3] of permutations of order 3. From the laws of reduction of the direct products of two such representations, one obtains the following symmetry-character for the wave function of a 3-neutron system:

$$\begin{array}{lll} \text{For total spin } S=\frac{3}{2}, & \text{spin part } I & \text{space part } A \\ S=\frac{1}{2}, & \text{spin part } U & \text{space part } U. \end{array} \tag{3}$$

About H^3, we know that it possesses spin $\frac{1}{2}$ and even parity. If one assumes charge-independence of nuclear forces, the experimental values of its magnetic moment leads[4] to the following additional information, in agreement with Wigner's theory of supermultiplets:

(a) Its isotopic spin $T=\frac{1}{2}$; i.e., its spin-space wave function is of type U.

(b) It is mainly ^2S space-symmetrical (type I in space).

A wave function, fitting very well the binding energy of H^3, has recently been obtained by Pease and Feshbach;[5] it is a ^2S space-symmetric with a very small ^4D admixture (about 2 percent). Although the importance of terms of other type (in particular ^2S with space part of type U) is still an open question, it is reasonable to assume the admixture of terms nonsymmetric in space to be, at least, of the same order of magnitude as the ^4D admixture obtained by Pease and Feshbach.

The selection rules for reaction (1) were investigated first. We searched for selection rules in the usual sense, i.e., based on conservation of angular momentum and parity; we found that, contrary to the deuterium case, such rules do not exist. If, however, we take into account the additional information quoted above concerning the ground state of H^3, reaction (1) is seen to be very sensitive to the spin and the parity of π^-. Assuming the π^- to be absorbed from the K-shell, one gets the following nonrelativistic approximations to the interaction in the various meson theories (constants have been omitted):

$$\begin{array}{lccccc} & S & PS & V & PV & \\ \phi_k\times & 1 & \boldsymbol{\sigma}\cdot\mathbf{P} & \mathbf{e}\cdot\mathbf{P} & \mathbf{e}\cdot\boldsymbol{\sigma} & (4) \end{array}$$

(ϕ_k is the wave function of the π^- meson in the K-shell taken at the position of the proton; $\boldsymbol{\sigma}$, $\mathbf{P}$, are the spin and momentum operators acting on the proton; $\mathbf{e}$ is the polarization of the spin 1 meson). ϕ_k varies very slowly inside the H^3 nucleus and may be replaced by its value at the origin and considered as a constant. Then, if the meson is scalar, the interaction is a pure constant and cannot give a transition to final wave functions having another type of symmetry than the initial one, i.e., other than U; thus the reaction is forbidden. If the meson is PV, the interaction does not involve operators acting on the space dynamical variables; one sees from (3) that the final 3-neutron wave function cannot be space symmetric. On the other hand, most of the H^3 wave function is space symmetric; thus, the reaction is practically forbidden. Following the same line of argument, one can even derive selection rules regarding the contribution of the nonsymmetric part, namely:

(1) The ^4D contribution vanishes if the initial system (π^-, H^3) has total angular momentum $\frac{1}{2}$.

(2) The contribution of the ^2S of the type U vanishes if the initial system (π^-, H^3) has total angular momentum $\frac{3}{2}$. However, in view of the smallness of the nonsymmetric admixture, the contribution of such terms is very small anyway, and the relativistic corrections, which have been neglected in our study, may be more important. For a PS or V meson, no such selection rules appear.

We have also investigated reaction (2). There appears no evidence for any selection rules, whatever be the spin and the parity of the meson. This can be verified by taking the nonrelativistic approximation of the interaction, as it is given in reference 2, and looking at the formulas given by the weak coupling calculation.

In conclusion, since reaction (1) is forbidden in the case of scalar and pseudovector mesons, whereas reaction (2) is allowed for all types of meson fields, it follows that the ratio of the yields of the nonradiative to that of the radiative absorption reaction, (n/γ), is greater in the case of an odd meson than in the case of an even meson, and in particular: $(n/\gamma)_{PS}\gg(n/\gamma)_{PV}$. A calculation of those ratios by one of us (S.B.) is in progress.

We are indebted to Dr. Marshak for suggesting this investigation and for interesting discussions. One of the authors (A.M.L.M.) wishes to thank the French Direction des Mines for supporting his stay abroad.

[1] Marshak, Tamor and Wightman, Phys. Rev. **80**, 765 (1950).

[2] S. Tamor, Phys. Rev. **82**, 38 (1951).

[3] v. der Waerden, *Die Gruppentheoretische Methode in der Quantenmechanik* (verlag. Julius Springer, Berlin, 1932), pp. 57 and 134.

[4] F. Villars, Helv. Phys. Acta **20**, 476 (1947).

[5] R. L. Pease and H. Feshbach, Phys. Rev. **81**, 143 (1951). We wish to thank Drs. Pease and Feshbach for kindly communicating to us the explicit form of this wave function.

Ionization of Argon Atoms by Helium or Neon Metastable Atoms

MANFRED A. BIONDI
Westinghouse Research Laboratories, East Pittsburgh, Pennsylvania
(Received June 14, 1951)

IN connection with some studies of electron-ion recombination[1] we have used helium and neon samples containing 0.115 percent argon. Helium (or neon) metastable atoms ionize the argon according to the equation,

$$He^* + A \rightarrow He + A^+ + e^-.$$

The excess energy appears as kinetic energy of the electron. This type of reaction was studied extensively by the Eindhoven group under Penning, and estimates were obtained for the ionizing cross section in Ne–A mixtures.[2] The present experiment, in which microwave techniques are used to measure the electron density following a discharge, affords a more direct means of measuring this cross section.

During the afterglow, helium (or neon) metastable atoms produced in the discharge will be lost by diffusion to the walls, by de-exciting collisions with normal helium (or neon) atoms, and by collisions with argon atoms which result in ionization of the argon. The rate of change of metastable concentration is therefore given by

$$dM/dt = D_m \nabla^2 M - \nu_d M - \nu_i M, \quad (1)$$

where M is the metastable atom concentration, D_m is the metastable diffusion coefficient; ν_d and ν_i are the de-excitation and ionization frequencies, respectively. The solution of Eq. (1) is

$$M = M_0 \exp(-t/T_m),$$

where

$$1/T_m = (D_m/\Lambda^2) + \nu_d + \nu_i. \quad (2)$$

Λ is the characteristic diffusion length of the container. Measurements of D_m and ν_d for pure helium and neon are described in a recent paper.[3]

The electrons and argon ions produced by the metastables will be lost by diffusion to the walls. The rate of change of electron density is

$$dn/dt = D_a^A \nabla^2 n + \nu_i M, \quad (3)$$

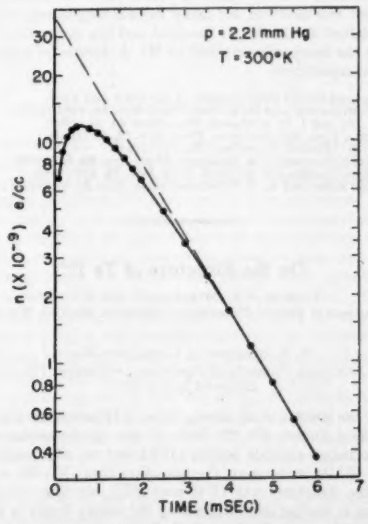

FIG. 1. Production of argon ions by helium metastable atoms.

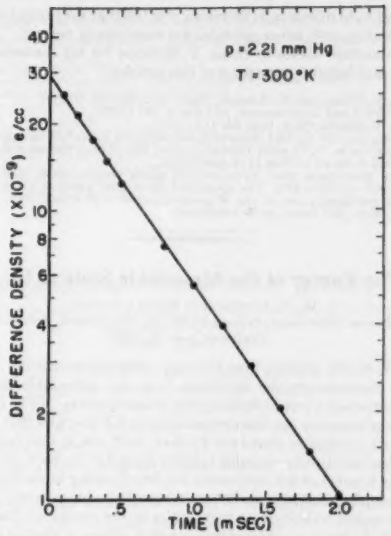

FIG. 2. Decay of metastable helium atoms in a helium-argon mixture.

where n is the electron density and D_a^A is the ambipolar diffusion coefficient of electrons and argon ions in helium or neon. The solution of Eq. (3) is

$$n = A \exp(-t/T_D) - B \exp(-t/T_m), \quad (4)$$

where

$$1/T_D = D_a^A/\Lambda^2. \quad (5)$$

Typical experimental data are shown in Fig. 1. The terminal slope of the curve corresponds to the first term of Eq. (4).[4] The difference between the actual curve and the dashed extrapolated curve yields the second term of Eq. (4), shown plotted in Fig. 2. The slope of the curve is T_m. From T_m and the previously measured values of D_m and ν_d we may calculate ν_i, the frequency of ionization of argon atoms by metastable helium atoms. We define the cross section, σ_i, for this reaction by

$$\nu_i = n_A \bar{v} \sigma_i, \quad (6)$$

where n_A is the argon atom concentration and $\bar{v}$ is the rms velocity of relative motion between helium (or neon) metastable atoms and argon atoms. From data of the type shown in Figs. 1 and 2, taken over the pressure range 1.6–3.2 mm Hg, we find $\sigma_i = 9.3 \pm 0.8 \times 10^{-17}$ cm^2 for the helium-argon reaction.

By a similar procedure, the cross section in neon-argon mixtures between 1.4 and 4.7 mm Hg is calculated to be

$$\sigma_i = 2.9 \pm 0.25 \times 10^{-16} \text{ cm}^2.$$

In this case we may compare our results with earlier estimates by Kruithof and Druyvesteyn.[2] From their data they obtain a value for the ratio of σ_i to the de-excitation cross section of neon metastables by normal neon atoms, σ_d, of $\sigma_i/\sigma_d = 4.1 \times 10^4$. Using the aforementioned value of σ_i and our previously published value[3] of $\sigma_d = 1.2 \times 10^{-19}$ cm^2, we obtain $\sigma_i/\sigma_d = 2.5 \times 10^3$. Thus our value of the ratio of the two cross sections is an order of magnitude smaller than estimates obtained from breakdown data.

The estimate of Kruithof and Druyvesteyn of σ_i/σ_d required lengthy calculations and involved several simplifying assumptions. In the present experiment, σ_i/σ_d is obtained from values of σ_i and σ_d which are calculated from experimental data quite simply. In addition our gas samples are at least as pure[5] as those

referred to in reference 2; therefore, it is felt that the present values of σ_i and σ_d and, hence, of σ_i/σ_d are more nearly correct.

The author wishes to thank T. Holstein for his continued interest and helpful discussions of this problem.

[1] M. A. Biondi and T. Holstein, Phys. Rev. **82**, 962 (1951).
[2] Kruithof and Druyvesteyn, Physica **4**, 462 (1937).
[3] M. A. Biondi, Phys. Rev. **82**, 453 (1951).
[4] Using Eq. (5) we find the ambipolar diffusion coefficient of argon ions in helium to be $D_a{}^A p = 905$ (cm²/sec)–(mm Hg). These measurements are discussed in detail in Part II of reference 1.
[5] The gases used were Airco reagent grade helium, neon, and argon (impurity $\sim 1:10^4 - 10^5$). The vacuum system used pumped to 10^{-6} mm Hg and exhibited a rate of rise of gas pressure of $\sim 10^{-10}$ mm/min. See D. Alpert, Rev. Sci. Instr., to be published.

The Energy of the Metastable State of Ba^{135}

W. H. Cuffey and Robert Canada
*Physics Department, Indiana University, Bloomington, Indiana**
(Received June 18, 1951)

UP to the present time the only information existing in the literature on the radiations from the metastable state of Ba^{135} arises as a result of absorption measurements.[1–3] The energy of the gamma-ray has been reported to be 0.3 Mev and that of the internal conversion electron 0.28 Mev. Ba^{135} lies in that region of the chart of nuclides, running roughly from Ag^{111} to Ba^{137}, in which a large number of isomeric states are found, owing to the fact that the $s_{1/2}$, $d_{3/2}$, and $h_{11/2}$ shells are being filled competitively. Since there appear to be certain regularities in the energy of filling the $h_{11/2}$ shell,[4] it was considered important to obtain an accurate value for the energy of the metastable state of Ba^{135}. The energy of the gamma-ray from Ba^{135} was measured with the help of a scintillation counter and that of the internal conversion electrons in a magnetic lens spectrometer.

The Ba^{135} was made by the bombardment of barium with 11.5-Mev deuterons in the Indiana University cyclotron. After chemical separation for barium the only periods found were the 85-min period of Ba^{139} and the 28.7-hr period of Ba^{135}. The 38.6-hr period of Ba^{133} was not seen.

The gamma-rays were investigated with the help of a scintillation spectrometer consisting of a NaI(Tl) crystal and an RCA 5819 photomultiplier tube. The pulses from the photomultiplier were fed through a cathode follower and then to a linear amplifier. The amplified pulses triggered the sweep of a Tektronix Model 514D oscilloscope. Time exposures[5] of the pulses displayed on the oscilloscope were taken with a camera using Eastman Panchromatic Super XX film. The exposure times varied from 10 seconds to several minutes depending on the intensity of the source.

The instrument was calibrated using the gamma-ray from Cs^{137} at 0.660 Mev and the linearity of the instrument was checked by measuring the 1.12-Mev gamma-ray of Zn^{65}, the 1.33-Mev gamma-ray of Co^{60}, and the two gamma-rays of Os^{185} at 0.878 and 0.648 Mev. The latter two gamma-rays arise from orbital electron capture and were measured in a magnetic lens spectrometer by Bunker, Canada, and Mitchell,[6] and with a scintillation spectrometer using a differential pulse height sorter by Miller and Wilkinson.[7] The photographs in the present experiments show

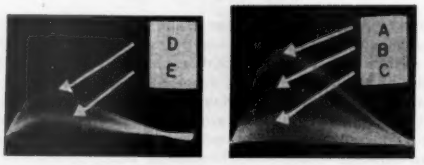

(a) (b)

FIG. 1. (a) Photoline of the 267-kev gamma-ray in Ba^{135} appears at D, and the corresponding Compton distribution appears at E; (b) the photoline and the Compton distribution for the 660-kev gamma-ray in Cs^{137} appear at A and B, respectively. The line at C is due to backscattering of the 660-kev gamma-ray.

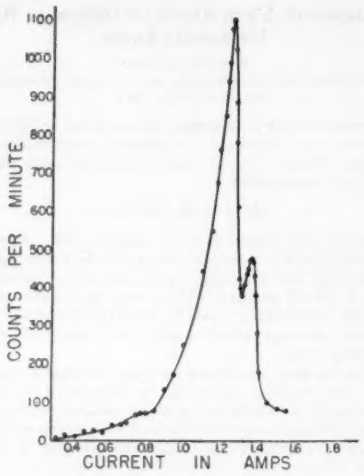

FIG. 2. Internal conversion electrons from Ba^{135}.

strong photo- and Compton peaks for a gamma-ray of 0.620 Mev and a weaker photopeak for a line at 0.870 Mev, together with a strong x-ray line at 60 kev coming about as a result of K-capture.

A photograph showing the results of the Ba^{135} investigation is given in Fig. 1(a) together with a photograph of Cs^{137} [Fig. 1(b)] for comparison. A photopeak and a Compton peak for a line at 0.270 Mev are clearly seen.

A "beta-ray" source of Ba^{135}, rather thick on account of the low intensity, was investigated in the magnetic lens spectrometer. The results are shown in Fig. 2, in which are seen a K- and an L-peak corresponding to the K- and L-conversion for a line of energy 0.267 Mev. The decay of these lines was followed in the spectrograph, and it is certain that they arise from the 28.7-hr Ba^{135}.

The authors wish to thank Professor A. C. G. Mitchell, who suggested this problem, for many helpful suggestions. They are also indebted to Dr. M. B. Sampson and the cyclotron crew for making the bombardments and to Mr. A. Lessor for making the chemical separations.

* Supported by the joint program of the ONR and AEC.
[1] E. E. Robertson and M. L. Pool, Phys. Rev. **76**, 1408 (1949).
[2] F. C. Yu and J. D. Kurbatov, Phys. Rev. **74**, 34 (1948).
[3] Weimer, Pool, and Kurbatov, Phys. Rev. **63**, 59 (1943).
[4] A. C. G. Mitchell, Phys. Rev. **83**, 149 (1951).
[5] R. Hofstadter and J. A. McIntyre, Phys. Rev. **80**, 63 (1950).
[6] Bunker, Canada, and Mitchell, Phys. Rev. **79**, 610 (1950).
[7] M. M. Miller and R. G. Wilkinson, Phys. Rev. **82**, 981 (1951).

On the Structure of Te II*

J. E. Mack,† K. Murakawa,‡ and J. S. Ross
Department of Physics, University of Wisconsin, Madison, Wisconsin
and
F. A. Pick and J. C. van den Bosch
Zeeman Laboratory, University of Amsterdam, Amsterdam, The Netherlands
(Received June 8, 1951)

OF the spectra of all atoms, those of tellurium are among the least known. On the basis of new measurements of lines from a hollow-cathode source (JSR) and an electrodeless discharge (FAP), vacuum-arc Zeeman-effect data (JCvdB), and new hyperfine structure data (KM and JSR), we have made some progress in finding and interpreting the energy levels in the first spark spectrum, as shown in Table I.

TABLE I. Energy levels of singly ionized tellurium, Te II.

Energy (cm^{-1})	Symbol	J	g	Hfs[125] (cm^{-1})
Odd levels				
$5p^5$:				
0	00^o	3/2		
10222	10^o	3/2		
12423	12^o	5/2		
20546	20^o	1/2		
24032	24^o	3/2		
$5p^46p$:				
93978.00	93^o	1/2(3/2)		
96143.84	96^o	3/2	1.3	
97779.13	97^o	1/2	1.2	
99583.68	99^o	3/2	1.30	−0.064
100111.18	100^o	5/2	1.39	0.00
101220.10	101^o	3/2	1.30	−0.061
101370.01	101^o	1/2	2.29	+0.078
102323.61	102^o	5/2	1.33	−0.256
103104.98	103^o	7/2	1.36	−0.246
103935.04	103^o	3/2	1.74	−0.193
105005.21	105^o	3/2	1.18	
105582.14	105^o	5/2	1.29	−0.223
106118.35	106^o	1/2		
107956.82	107^o	5/2		
112271.53	112^o	3/2	1.12	
112547.95	112^o	3/2,5/2		
?117858.18	?117^o	7/2		
?118804.25	?118^o	3/2,5/2		
Even levels				
Energy (cm^{-1})	Symbol	J	g	Hfs[125] (cm^{-1})
$5s5p^4$, $5p^46s$, $5p^25d$:				
71191.66	71	5/2	1.70	
74892.51	74	3/2	1.78	0.00
76299.96	76	1/2	2.71	
78447.25	78	1/2	2.4	−0.228
81894.55	81	3/2	1.12	−0.057
82742.49	82	3/2	1.42	−0.083
83576.56	83	1/2	1.07	+0.082
85048.45	85	5/2		−0.093
85158.81	85	3/2	0.8	0.00
85591.02	85′	5/2	1.49	−0.431
86758.94	86	3/2	0.99	+0.026
87403.64	87	5/2		
88923.83	88	5/2		
88960.18	88	3/2	1.14	
$5p^47s$, $5p^46d$:				
117338.75	117	3/2		−0.010
118008.02	118	1/2(3/2)		
118323.96	118′	1/2(3/2)		
120616.23	120	5/2		−0.25
121173.04	121	3/2		
121518.02	121′	3/2	1.24	−0.044
122195.93	122	3/2(5/2)		
123653.66	123	7/2	1.24	
124081.15	124	1/2		
124645.47	124	5/2	1.27	−0.136

The levels $00^o_{3/2}$, $10^o_{3/2}$, $78_{1/2}$, and $82_{3/2}$ were found by Rao and Sastry[1] from ultraviolet transitions. We are unable to verify the rest of their analysis. We have used the ionization discrimination data of the Blochs,[2,3] which tend to be substantiated by our findings, and we have made tentative use of the ultraviolet wavelengths of the Bloch group.[3,4] Aside from the assignment of configurations or groups of interacting configurations, and J, no quantum numbers are listed here, though some approximate assignments are obvious. In some cases of uncertain J, the less likely value is enclosed in parentheses. The zeros to the right of the decimal point in the energy of level 93^o are arbitrary. The exact values of energy, g-value, and hfs-splitting are subject to slight readjustment in the course of later work. In the "hfs" column, a plus sign means that the energy of the sublevel with $F=J-\frac{1}{2}$ is the lower. The splittings are given only for the isotope 125; those for 123 can be found by dividing by the magnetic moment ratio $\mu^{125}/\mu^{123}=1.208$[5], since both isotopes have the same I-value $\frac{1}{2}$.[5,6]

We are extending the observations in both the infrared and the vacuum ultraviolet, and are systematically searching for more levels. More complete accounts of the general analysis (JCvdB and JEM) will be submitted later to *Physica*, and of the hyperfine structure and isotope shift[5] (JSR and KM) to the *Physical Review*.

* Assisted by the ONR.
† John Simon Guggenheim Fellow, assisted by a grant from the Research Committee of the University of Wisconsin.
‡ On leave from Institute of Science and Technology, University of Tokyo, Tokyo, Japan.
[1] K. R. Rao and M. G. Sastry, Indian J. Phys. 14, 423 (1940).
[2] L. and E. Bloch, Ann. phys. 13, 233 (1930).
[3] L. and E. Bloch, J. Phys. et radium 6, 441 (1935).
[4] M. Lacroute, J. Phys. et radium 9, 180 (1928).
[5] J. E. Mack and O. H. Arroe, Phys. Rev. 76, 1002 (1949).
[6] G. R. Fowles, Phys. Rev. 76, 571 (1949).

Electromagnetic Interactions of μ-Mesons*

W. D. WALKER, J. E. HAMMEL, R. M. SINCLAIR, AND J. D. SORREL
Rice Institute, Houston, Texas
(Received June 8, 1951)

BECAUSE of the finite size of the particles, a deviation from the calculated energy spectrum of electrons knocked on by μ-mesons should occur for collisions with high momentum transfer.[1] A preliminary experiment has been done in an attempt to determine at what electron energy this deviation occurs in order to estimate the size of the charge distributions of the colliding particles.

The collisions were observed in a cloud chamber with carbon plates, and the initiating particles were required to have range between 35 and 37 inches Pb.

The chamber was triggered when counters were struck in rows B, C, and D in anticoincidence with row A of Fig. 1. The counters of row N were connected to neon bulbs to aid in identifying the triggering particle. Other experiments indicate that most of the particles thus selected were μ-mesons.[2,3]

The chamber contained six carbon plates, each 3.16 g/cm², and one lead plate, 15 g/cm². A stereoscopic camera was used. Only pictures with single tracks of counter age with directions such as to strike the counter trays were accepted.

The energy of the knock-on electrons was estimated by the number of carbon plates they traversed. A range-energy curve, obtained by assuming all energy loss to be due to ionization, was corrected for multiple scattering effects and for radiation losses.

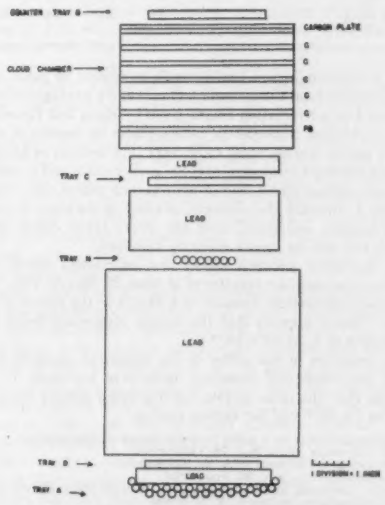

FIG. 1. Experimental arrangement.

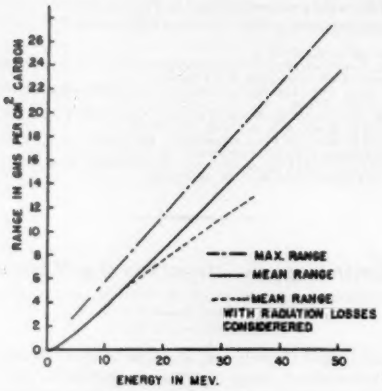

FIG. 2. Range-energy curve.

The correction for the increase of path length caused by multiple scattering was calculated using the approximation that the energy loss per unit path length is constant and equal to 1.8 Mev/g/cm^2.

$$\text{Effective range} = \int_0^{t_{\text{limit}}} \cos(\alpha)dt \approx \int_0^{t_{\text{limit}}} (1-\tfrac{1}{2}\langle\alpha^2\rangle_{\text{Av}})dt,$$

where $\langle\alpha^2\rangle_{\text{Av}} = 441t/E(E-\epsilon t)$ = mean square scattering angle;[4] t-thickness in radiation lengths; $\epsilon = 1.8\times 52$ Mev/radiation length; t_{limit} is chosen such that $\langle\alpha^2\rangle_{\text{Av}} = 2$; E = total energy in Mev at $t = 0$.

Below one-Mev energy the curve was fitted to the expression given by Glendenin.[5] The range-energy curve is shown in Fig. 2.

TABLE I. Number of knock-ons traversing N plates. Total No. of carbon plates traversed = 5439.

Number of electrons observed to traverse	≥ 0 plates	≥ 1 plates	≥ 2 plates	≥ 3 plates	≥ 4 plates	≥ 5 plates
Observed	388	67	19	6	1	1
Calculated	413	65	24	10	4	1.3
Average energy required in Mev	...	16	25	34	43	52

The average radiation loss for each increment of path length was calculated from the formula and curves for average fractional radiation loss per radiation length given by Rossi and Greisen.[6]

The number of traversals of carbon plates by mesons of about 1.2-Bev energy was observed to be 5439. The number of knock-on electrons observed to emerge from one carbon plate and to traverse 0 or more carbon plates, one or more carbon plates, etc., is given in Table I. Beneath the observed number of electrons is the expected number, calculated from the above range curve using a method very similar to one given by Hereford.[7]

The agreement between theory and experiment seems to be good up to momentum transfer of at least 25 Mev/c. This corresponds to a momentum transfer of 5 Mev/c in the center-of-mass system. Thus it appears that the inverse square law holds down to distances of $\hbar/\Delta p = 4\times 10^{-13}$ cm.

Two instances of scattering of the triggering particles in the carbon were observed. However, both were less than 3°. This indicates that the cross section for scattering greater than 4° is less than 3×10^{-27} cm^2 per carbon nucleus.

* Supported in part by a grant from the Research Corporation.
[1] R. P. Feynman, Phys. Rev. **74**, 1430 (1948).
[2] B. Rossi, Revs. Modern Phys. **20**, 537 (1948).
[3] L. Germain, Phys. Rev. **80**, 616 (1950).
[4] Fowler, Lauritsen, and Lauritsen, Revs. Modern Phys. **20**, 236 (1948).
[5] L. E. Glendenin, Nucleonics **2**, 19 (1948).
[6] B. Rossi and K. Greisen, Revs. Modern Phys. **13**, 240 (1941).
[7] F. L. Hereford, Phys. Rev. **75**, 923 (1949).

Inertia of the Carrier of Electricity in Cadmium

G. G. SCOTT
Research Laboratories Division, General Motors Corporation, Detroit, Michigan
(Received March 12, 1951)

THERE has been some attempt to obtain a simple explanation for positive Hall coefficients in metals by assuming a positive carrier for the electric current. Since apparatus was available at the General Motors Research Laboratories for measuring inertia effects of moving electricity, it was decided to set up an experiment[1] to determine both the sign and the mass charge ratio of the carrier of electricity in cadmium, a metal having a positive Hall coefficient. This apparatus and the experimental technique used has recently been described in work on the measurement of the gyromagnetic ratio of iron.[2]

In the present experiment a cylindrical coil was wound from a Nylon insulated cadmium wire. This coil was supported as a torsional pendulum with the axis of rotation coinciding with the mechanical axis of the cylinder. Readings were taken of changes in angular momentum along with the corresponding changes in magnetic moment, and the mass charge ratio of the carrier computed from these values.

The results for five different days on which readings were taken, in May, 1950, are as follows (in units of 10^{-9}g per coulomb): -6.4, -6.0, -5.4, -4.5, and -5.3. The average value obtained for the mass-charge ratio of the carrier in cadmium is -5.5×10^{-9} g per coulomb.

These results show conclusively that the carrier of electricity in cadmium is negative and that the mass-charge ratio is approximately the same as that of the electron.

Similar results have recently been reported by Brown and Barnett[3] for Mo and Zn.

[1] This experiment was suggested by B. Roswell Russell of the Randal Morgan Laboratory of Physics at the University of Pennsylvania.
[2] G. G. Scott, Phys. Rev. **82**, 542 (1951).
[3] S. Brown and S. J. Barnett, Phys. Rev. **81**, 657 (1951).

Erratum: Lithium Ammonium Tartrate Monohydrate, a New Ferroelectric Crystal

[Phys. Rev. **82**, 562 (1951)]

WALTER J. MERZ
Pennsylvania State College, State College, Pennsylvania

THERE was a typographical error in reference 1. The independent discovery of the ferroelectric behavior of $LiNH_4C_4H_4O_6\cdot H_2O$ and $LiTlC_4H_4O_6\cdot H_2O$ was privately communicated to the author by B. T. Matthias and J. K. Hulm in February, 1951, and was reported in the April 1, 1951, issue of *The Physical Review* [Phys. Rev. **82**, 108 (1951)]. Matthias and Hulm did not state that $LiRbC_4H_4O_6\cdot H_2O$ is ferroelectric.

Nuclear Proton Resonance in Related Liquid Hydrocarbons*

R. BRADFORD, C. CLAY, A. CRAFT, E. STRICK, AND J. UNDERHILL
Department of Physics, University of Wyoming, Laramie, Wyoming
(Received June 4, 1951)

A PRELIMINARY investigation of the line-width parameter, T_2,[1] for several long-chain hydrocarbons has been made. These measurements were made as part of an extended program to correlate structure with the line-width parameter in related series of hydrocarbons. The measurements were made with a Bloch crossed-coil type nuclear induction apparatus[1] in our new electromagnet with 12-inch diameter pole faces. The operating

TABLE I. Line widths and line-width parameters.

		ΔH (gauss)	T_2 (seconds $\times 10^{-4}$)
Octadecane	$CH_3(CH_2)_{16}CH_3$	0.37	1.0
Hexadecane	$CH_3(CH_2)_{14}CH_3$	0.29	1.3
Tetradecane	$CH_3(CH_2)_{12}CH_3$	0.15	2.7
Dodecane	$CH_3(CH_2)_{10}CH_3$	0.05	8

frequency was 20 mc. The field was swept sinusoidally at 400 cycles with an amplitude much less than the line width, and the data for the derivative plot[2] of the absorption mode[1] was obtained using a twin-tee narrow band filter in the audio amplifier.

Preliminary measurements have yielded the results given in Table I. T_2 was calculated using the Bloch formulation.[1] All measurements were made at room temperature. The line width for octadecane agrees with that reported by Andrew.[3]

We are now continuing our investigation using proton control of our electromagnet and the steady-state pulsing technique.[4] With this combination of methods, measurements can be extended to narrower line widths. Very narrow line widths (i.e., less than 0.05 gauss) are expected in the short chain hydrocarbons that are being investigated.

* This work was made possible through partial support by the AEC.
[1] F. Bloch, Phys. Rev. **70**, 460 (1946).
[2] Bloembergen, Purcell, and Pound, Phys. Rev. **73**, 679 (1948).
[3] E. R. Andrew, J. Chem. Phys. **18**, 607 (1950).
[4] E. A. Uehling and R. Bradford (unpublished).

New Segregation Phenomena in Metals

M. T. STEWART, R. THOMAS, K. WAUCHOPE, W. C. WINEGARD, AND B. CHALMERS
Radioactive Tracer Laboratory, Department of Metallurgical Engineering, University of Toronto, Toronto, Ontario, Canada
(Received June 18, 1951)

LEAD–BISMUTH alloys containing radioactive bismuth have been examined for segregation of the polonium resulting from the decay of the Bi^{210}. Three types of segregation have been established.

(*1*) *Crystal boundary segregation.*—Bicrystals of bismuth-lead alloys were prepared, a small proportion of the bismuth being the radioactive isotope Bi^{210}. The decay product of Bi^{210} is polonium which, when these experiments were performed, was present in a concentration of approximately one atom of polonium in 10^{10} atoms of bismuth or of the alloy. Autoradiographs of the bicrystals showed that, in spite of its very low concentration, polonium segregates at the crystal boundary. A typical autoradiograph is shown in Fig. 1.

(*2*) *Surface segregation.*—Measurements of the alpha-emission from specimens of similar composition show that the concentration of Po at the surface increases rapidly during annealing, or slowly at room temperature, in alloys of Pb with 10 or 20 percent Bi. The region under examination is restricted to a very thin layer by the extremely short range of alpha-particles. It is concluded that there is a tendency for polonium to segregate at the surface.

(*3*) *Inhomogeneous crystallization.*—When crystals of bismuth containing polonium at a concentration of 10^{-10} are allowed to

FIG. 1. A typical autoradiograph, showing crystal boundary segregation.

FIG. 2. An autoradiograph showing bands transverse to the direction of growth.

to solidify under conditions of linear growth, the concentration of polonium varies periodically; the periodicity is related to variations in the speed of solidification. A similar effect has also been observed in gold-silver alloys; Au^{198} used as a tracer has shown periodic changes of composition in alloys containing 1/10 percent, 10 percent, and 20 percent gold. The autoradiographs show bands transverse to the direction of growth. An example is shown in Fig. 2.

Paramagnetic Resonance Absorption Crystals Containing Color Centers*

MICHAEL TINKHAM AND ARTHUR F. KIP†
Research Laboratory of Electronics, Massachusetts Institute of Technology, Cambridge, Massachusetts
(Received June 14, 1951)

HUTCHISON[1] has published results of microwave absorption experiments on alkali halide crystals (LiF and KCl) which were heavily irradiated with neutrons. This treatment produced a very high density of color centers. The resulting microwave absorption at 9350 Mc showed a peak absorption at a magnetic field giving a g factor of 2.00. This corresponds to the result which would be expected on the basis that the spins of the trapped electrons are nearly free. It is also consistent with the observed paramagnetic susceptibility of crystals containing color centers.[2] A perhaps unexpected result was that the absorption was not symmetrical about the peak. On the highfield side a sloping plateau about 500 gauss wide and about one-quarter the height of the peak was found.

We have measured absorption at a frequency of 9480 Mc on crystals of KBr which may have an appreciably smaller density of color centers. The apparatus used in this work was of high sensitivity as compared with the conventional equipment. The method involves sweeping the external magnetic field and displaying the absorption curve directly on a cathode-ray oscilloscope.[3] Details of the apparatus and measuring techniques will be published in a forthcoming paper. The first sample tried (of volume 0.5 cc) had been electrolytically colored (current being passed through the crystal at about 500°C), and had of the order of 10^{19} centers per cc. This sample was kindly provided to us by J. Gelatis and E. Klokholm of the Laboratory for Insulation Research. Our sensitivity was such that we were able only to detect the peak position and not to study its shape. The g value was found to be 2.00 ± 0.04.

Another sample of KBr was bombarded with high energy electrons and gamma-rays (18-Mev peak energy) on the microwave linear accelerator at the Massachusetts Institute of Technology for about 4 hours. Optical absorption measurements indicated between 10^{19} and 10^{20} centers per cc. The peak of the optical absorption band was at 6300A, indicating that the predominant optical absorption was due to F-centers.[4] In this sample, the microwave absorption was sufficient to allow accurate determination of the shape of the absorption curve as well as its position. In contrast to Hutchison's results, we found complete symmetry of the absorption curve about its peak. Moreover, our sensitivity was such that we could have seen a plateau which was less than 10 percent of the height of the peak absorption. The g

value was the same as for the earlier sample. The width of the curve at the half-power point was 210 gauss at room temperature and 150 gauss at 77°K.

We are tempted to conclude from our results that the plateau observed by Hutchison was a consequence of the extreme treatment given his samples. Clarification of these differences will probably require an increase in the sensitivity of the apparatus.

* This work has been supported in part by the Signal Corps, the Air Materiel Command, and the ONR.
† Now at the Department of Physics, University of California, Berkeley, California.
[1] Clyde A. Hutchison, Jr., Phys. Rev. **75**, 1769 (1949).
[2] Scott, Hrostowski, and Bupp, Phys. Rev. **79**, 346 (1950).
[3] R. Malvano and M. Panetti, Phys. Rev. **78**, 826 (1950).
[4] Henry F. Ivey, Phys. Rev. **72**, 341 (1947).

Effect of Recombinations in Electron Avalanches

G. M. Petropoulos and P. A. Amparіotis
Electrical Measurements and High-Voltage Laboratory, National Technical University, Athens, Greece
(Received June 18, 1951)

THE calculation of the ion number using the equation

$$n=e^{\alpha x} \tag{1}$$

leads to an excessive ion density at the avalanche head which is, in some cases of sparking field strength, higher than the Avogadro constant.[1] This equation is derived without taking into account the possibility of recombinations between ions and electrons during the progress of the avalanche. The following estimate shows that such recombinations would considerably decrease the ion number and consequently the ion density.

If dn_a represents the ion number produced by ionization in a length dx, and dn_c the number of recombinations in time dt required for an avalanche progress by dx, then the actual increase of the ions would be

$$dn=dn_a-dn_c, \tag{2}$$

where $dn_a=n\alpha dx$ and $dn_c=c\rho^2Qdt$, c being the recombination coefficient,[2] ρ the ion density, and Q the volume of a sphere having a radius as given by Meek for the radius of the avalanche head: $r=(0.133x/p)^{\frac{1}{2}}$.

Assuming $\rho=n/Q=3n/4\pi r^3$, Eq. (2) becomes

$$dn=\left[\alpha n-\frac{3cn^2p^{\frac{1}{2}}}{4v\pi(0.133x)^{\frac{1}{2}}}\right]dx, \tag{3}$$

where $v=dx/dt$ is the velocity of the avalanche and p is the pressure in mm Hg. With $k=3cp^{\frac{1}{2}}/4v\pi(0.133)^{\frac{1}{2}}=$ const. the differential Eq. (3) becomes

$$dn+(kn^2x^{-\frac{1}{2}}-n\alpha)dx=0. \tag{4}$$

Its solution is:

$$n=\frac{e^{\alpha x}}{2kx^{\frac{1}{2}}\left(-1+\frac{\alpha x}{1!1}+\frac{\alpha^2x^2}{2!3}+\frac{\alpha^3x^3}{3!5}+\cdots\right)+1}. \tag{5}$$

Comparison of the ion numbers given by Eqs. (1) and (5) shows that the effect of recombinations should reduce $e^{\alpha x}$ by a factor rapidly increasing with x.

In a plane parallel air-gap of $d=1$ cm under breakdown field strength $X_0=31.6$ kv/cm, $\alpha=16.5$ cm^{-1}, $v=1.25\times10^7$ cm/sec, $p=760$ mm Hg, and a recombination coefficient[3] $c=3\times10^{-10}$, the denominator becomes about 1.0000025 for $x=d=1$ cm; i.e., the number of ions is about 0.00025 percent less than that computed from Eq. (1).

In a 5-cm air-gap under $X_0=27.6$ kv/cm, $\alpha=6.5$ cm^{-1}, $v=1.25\times10^7$ cm/sec, $p=760$ mm Hg, and $c=3\times10^{-10}$, the denominator is about 40 for $x=d=5$ cm; i.e., the ion number is about 40 times less than that given by Eq. (1).

Further, in a 10-cm gap under $X_0=26.5$ kv/cm, $\alpha=4.25$ cm^{-} and other values as above, the ion number is about 5×10^4 times less than that given by Eq. (1).

The reduced ion number indicates that the critical lengths[1] (x_k) swept by the avalanches under breakdown conditions are greater than those given when assuming Eq. (1).

[1] G. M. Petropoulos, Phys. Rev. **78**, 250 (1950).
[2] L. B. Loeb, *Fundamental Processes of Electrical Discharge in Gases* (John Wiley and Sons, Inc., New York, 1939), p. 155.

The Crab Nebula as an Observed Point Source of Cosmic Rays

Y. Sekido, T. Masuda, and S. Yoshida
Physical Institute, Nagoya University, Nagoya, Japan
and
M. Wada
Nishina Laboratory, Scientific Research Institute, Tokyo, Japan
(Received May 31, 1951)

STUDY of the diurnal variation of very high energy cosmic rays is considered to be an available method to find the direction of a cosmic-ray source, because lower energy rays are largely scattered in the terrestrial as well as other kinds of magnetic field. For this purpose, the diurnal variation of cosmic rays underground was studied from the data obtained in the Shimizu tunnel by Nishina, Miyazaki, and two of the authors[1] from 1939 to 1944.

The observations contain 1720 incidences detected at 1200 meters water equivalent below the earth's surface during the period from October 27, 1939, to July 4, 1940. No solar-time variation was obtained, only a sidereal-time variation as shown in Fig. 1(a). If the period of observation is divided into three parts as shown in Fig. 1(b), the times of maximum intensity are 4 hr, 5 hr, and 7 hr, respectively. Time differences among these three maxima are not larger than 4 hours, and the probability of getting such a coincidence of maxima by chance is 6.5 percent.

Assuming the rays were not deflected, the effective solid angle of the instrument can be projected on the celestial sphere, as shown in Fig. 2. five hr 20 min local sidereal time corresponds to the mean of the three maxima mentioned above. Near the direction of the axis of the instrument one can find the Crab nebula,

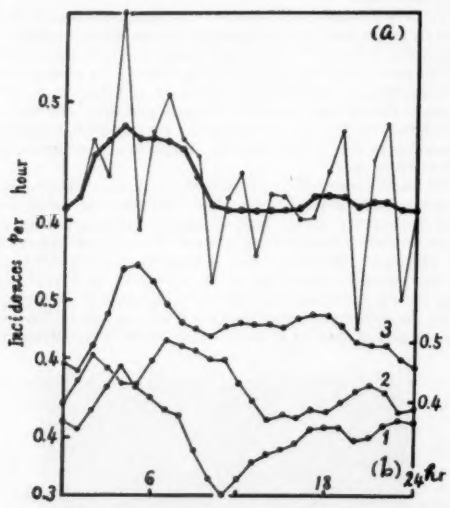

FIG. 1. Sidereal-time variation of cosmic rays at 1400 m H_2O equivalent depth. (a) Total period. Fine line: hourly values. Thick line: weighted (1:2:3:2:1) running average. (b) Weighted running averages. 1: October to December, 1939, 2: January to March, 1940. 3: April to July, 1940.

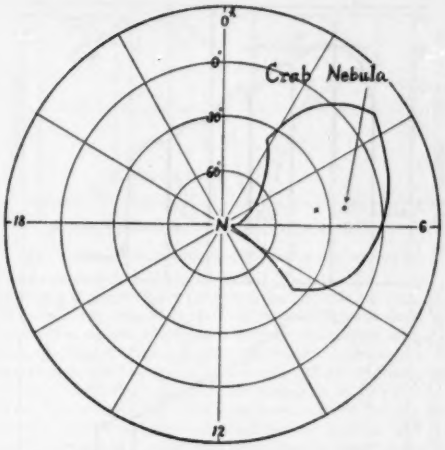

FIG. 2. Projection of the effective solid angle of the instrument on the celestial sphere at 6 hr local sidereal time.

which is a remarkable point source of cosmic noise.[2] Since the distance of the Crab nebula is short and the energy of the rays is high, the deflection of cosmic rays in the galactic magnetic field is negligible. Hence, the above-mentioned assumption is not so unreasonable, if we take the Crab nebula to be the source of cosmic rays. Unsöld,[3] Ryle,[4] and Alfvén *et al.*[5] have theoretically suggested such a possibility. As was shown in Fig. 2, the Crab nebula stays in the solid angle during the period from 2 hr to 8 hr. The intensity of cosmic rays seems to increase in about the same period [see Fig. 1(a)]. The existence of this increase of about 10 percent can be proved with 2 percent significance level.

It must be noticed that there was no considerable effect in cosmic-ray intensity in the directions of Cygnus[6] and other point sources of cosmic noise, which exist on the same latitude band where the instrument has swept. However, the Crab nebula is the most characteristic one among the point sources of cosmic noise, for it is an old supernova and its expansion is still seen.

The authors wish to express their cordial thanks to Mr. Y. Miyazaki for his kind cooperation in this work.

[1] Nishina, Sekido, Miyazaki and Masuda, Phys. Rev. **59**, 401 (1941); Y. Miyazaki, Phys. Rev. **76**, 1733 (1949).
[2] J. G. Bolton, Nature **162**, 141 (1948). J. G. Bolton and G. J. Stanley, Australian J. Sci. Research **A2**, 139 (1949).
[3] A. Unsöld, Nature **163**, 489 (1949).
[4] M. Ryle, Proc. Phys. Soc. (London) **A62**, 491 (1949).
[5] H. Alfvén and N. Herlofson, Phys. Rev. **78**, 616 (1950).
[6] Hey, Parsons, and Phillips, Proc. Roy. Soc. (London) **A192**, 425 (1948).

Measurement of Nuclear Polarizabilities by Nuclear Scattering Experiments*

NORMAN F. RAMSEY
Harvard University, Cambridge, Massachusetts
(Received June 11, 1951)

MOST nuclear scattering experiments are performed with such nuclear charges and energies that the scattering is importantly affected either by the direct interaction of the two nuclei through their specifically nuclear forces, or by electric excitation which leads to inelastic scattering. However, it is the purpose of this note to point out that important nuclear data can also be obtained when the elastic scattering of charged nuclei is carefully measured under circumstances such that the scattering is almost exclusively electrical and elastic. In particular, if the nuclei are polarizable, i.e., if they can be distorted by the strong electric fields which arise in the scattering of charged nuclei, the change in the nuclear charge distribution associated with the distortion will modify the electrical scattering and give rise to a departure from the Rutherford scattering law. Such a nuclear polarizability is to be expected according to current nuclear theory and has already been assumed by Breit and Townes to explain some of the phenomena observed in spectroscopic isotope shifts,[1] and in microwave measurements of nuclear quadrupole moments.[2] The scattering experiments suggested in this letter should provide an independent means for measuring the polarizabilities of a number of different nuclei.

The departures from the Rutherford scattering which arise from nuclear polarizabilities are usually small when the direct nuclear interactions and inelastic scatterings are negligible, since the penetrability of the coulomb barrier and acceleration magnitudes must then be kept low. As a result, the classical closest distance of approach of the two nuclei is large and the polarizability interaction potential, which varies as r^{-4}, is small. However, it should be possible to measure the departures in many cases. For example, changes in the Rutherford scattering of a few percent due to nuclear polarizability should be expected with 2.1-Mev deuterons scattered from copper due to the deuteron polarizability, and with 9-Mev C^{12} or 32-Mev Cl^{35} scattered by Cl^{35} due to a Cl^{36} polarizability of the magnitude assumed by Townes.[2] According to present theories,[3,4] the effects of nuclear interactions and inelastic scatterings should be less than the polarization effects, although this would not be true in all cases if one attempted to increase the magnitude of the polarizability effect by considerably increasing the energy of the scattered particle.

Since the electric field in the scattering process is present for only a short time, the nuclei may not respond sufficiently rapidly for them to achieve their full polarization as they would for a static electrical field. However, in most of the cases considered the duration of the pulse is sufficiently long that the problem is at least approximately adiabatic for the internuclear motions. Scattering experiments with different charges and energies of the bombarding nuclei may indicate the frequency dependence of the nuclear polarizability. Likewise, with the strong electric fields and small distances present in scattering, the dependence of the nuclear polarizability upon the field and its variations across the nucleus may be observable. The author is now planning some experiments of this type. Data on electric excitation[1] and the incidence of direct nuclear effects should be obtainable in the same experiments.

* This work was assisted by the joint program of the ONR and AEC.
[1] C. J. Mullin and G. Guth, Phys. Rev. **82**, 141 (1951).
[2] Breit, Arfken, and Clendenin, Phys. Rev. **77**, 568 (1950). Gunther-Mohr, Geschwind, and Townes, Phys. Rev. **81**, 289 (1951).
[3] H. A. Bethe, Phys. Rev. **53**, 39 (1938).

Thermionic Emission from (Ba-Sr)O Cathodes Illuminated by the Incandescent Lamp

TADATOSI HIBI AND KAZUO ISHIKAWA
Research Institute for Scientific Measurements, Tôhoku University, Sendai, Japan
(Received May 29, 1951)

ACCORDING to the aggregation theory of impurity centers in semiconductors,[1] the variation of the work function of BaO from 1.6 to 1.0 ev due to activation could be explained quantitatively to some extent, taking the trapping energy of an electron in an isolated impurity centers as 1.32 ev. From this theory, one expects the appearance of a lower work function than 1.0 ev by means of methods other than pure thermal activation (for example, an illumination by light of about 1.3 ev at high cathode temperature), or the existence of a trapping energy higher than 1.32 ev for an electron in an isolated impurity center. In order to establish which of the two is experimentally true, the following studies were carried out.

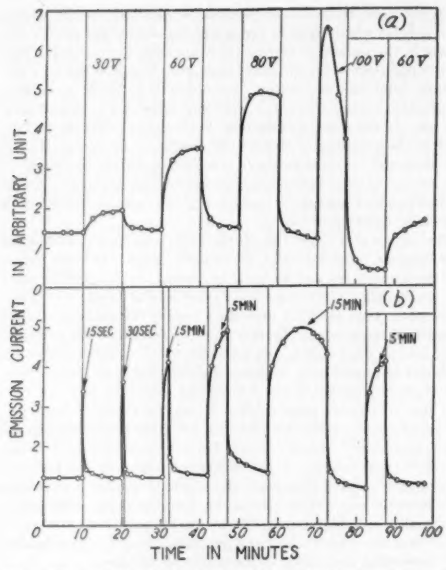

FIG. 1. The variation of thermionic emission with time depending on (a) the intensity of light (in this figure voltages show the heating inputs of the lamp) and (b) the illuminating period.

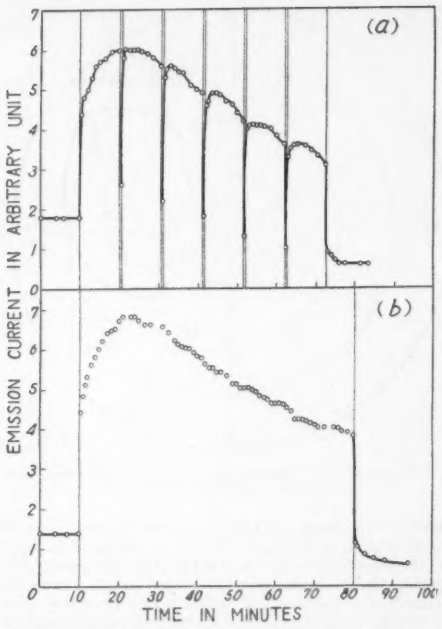

FIG. 2. The variation of thermionic emission with time in (a) the case of interruption of the illuminating light every 30 seconds and (b) the case of continuous illumination.

An incandescent lamp of 500w/100v was used as the light source, and (Ba−Sr)O cathodes of commercial diodes "KX-142" were used as the specimen. At an anode voltage of 30 volts and a cathode temperature of about 800°K, the variation of thermionic emission due to the white light was observed with a Braun tube by the initial emission current.

Figure 1(a) shows the variation of thermionic emission of oxide cathodes with the light intensity. From this figure it is found that (1) the change of thermionic emission depends on the light intensity, (2) a maximum emission current appears even during the period of the light illumination, (3) the earlier the saturated emission current is reached, the quicker the decay characteristic of thermionic emission begins, and (4) the decayed emission current increases or decreases, respectively, relative to the initial state through the interception of light before or after the maximum. The above-mentioned phenomena are very similar to the density-exposure curve of AgBr at room temperature[2] and also to the production of C-centers in KCl.[3] The same relation between initial emission current and decayed emission current was observed when the illuminating periods were changed, as seen in Fig. 1(b).

Figure 2(a) shows the effect on thermionic emission of interruption of the illuminating light every 30 seconds. It is seen that Fig. 2(a) shows the same behavior as seen in the case of continuous illumination in Fig. 2(b). This phenomenon is strikingly similar to the experimental result observed on the change of the induced absorption of light with the time of exposure of an MgO crystal to 40-kv x-rays.[4] In addition, it is very interesting and noteworthy that, as seen in Fig. 2(b), the thermionic emission due to light illumination changes step by step.

The increase of thermionic emission due to the light illumination may be attributed to a secondary origin, for example, the rise of the cathode temperature due to the heat radiation from the light source, or the lowering of the vacuum because of the outgassing from the glass wall of the tube. However, from Richardson plots taken before, during, and after illumination on the same cathode, it was clear that these were hardly likely, because the activation energy of the cathode decreased due to the light illumination. A lower work function than 1.0 ev, as expected previously, did not appear in this experiment. It is suggested, therefore, that the trapping energy of an electron in an isolated impurity center is higher than 1.32 ev.

In conclusion, in support of the correctness of the aggregation theory, it should be emphasized that the variation with lapse of time of thermionic emission due to the illumination of an incandescent lamp is strikingly similar to the production of color centers in alkali halides.

[1] T. Hibi and T. Matsumura, Phys. Rev. **81**, 884 (1951).
[2] W. F. Berg, Trans. Faraday Soc. **35**, 445 (1939).
[3] S. T. Petroff, Z. Physik **127**, 443 (1950).
[4] J. P. Molnar and C. D. Hartman, Phys. Rev. **79**, 1015 (1950).

Neutron Resonances of Tellurium

C. HEINDL AND I. W. RUDERMAN
Columbia University, New York, New York
(Received June 1, 1951)

NEUTRON transmission data obtained with the Columbia neutron velocity spectrometer[1] reveal a large number of resonances in tellurium.[2] Figure 1 shows the cross section of a cast sample of normal isotopic tellurium, 49.2 g/cm² thick, over the neutron energy range 0.06 to 2000 ev. There are well-defined resonances at 375 ev, 62 ev, 20 ev, 7.2 ev, and 2.2 ev, and several probable resonances below 2 ev. If these resonances could be assigned to the proper isotopes, and if the strength of the resonances were more accurately known, an interesting comparison of the level densities of tellurium isotopes could be made. An investigation designed to achieve this objective is now under way.

Enriched samples of the eight stable tellurium isotopes obtained from Oak Ridge have been electroplated onto thin platinum disks

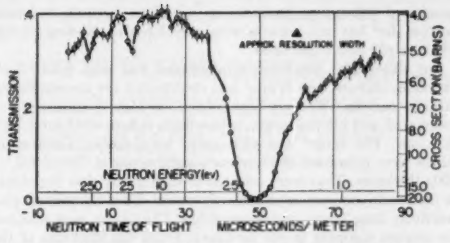

FIG. 1. Neutron cross section of 49.2 g/cm² normal isotopic Te.

2 inches in diameter. Since the quantities available are very small (24 to 3000 mg), these electropolated deposits form extremely thin transmission targets which are effectively transparent at all but resonant energies. Figure 2 shows the energy dependence of the cross section of a 7.9-mg/cm² sample of tellurium containing 60.9 percent of Te^{125}. There are probable resonances at 1.7 ev, 1.4 ev, 1.2 ev, 1.1 ev, and 0.9 ev. The large resonance at 2.2 ev has been assigned to Te^{125} as a result of the following analysis. The best possible theoretical Breit-Wigner single-level resonance curve was fitted[3] to the experimental curves obtained from both the enriched and the normal isotopic tellurium. Taking into account the abundance of each isotope in these two samples, two values of $\sigma_0\Gamma^2$ were calculated for each isotope. For only one isotope was good agreement obtained, namely, for Te^{125}, for which $\sigma_0\Gamma^2$ was found to be 900 ± 100 barns ev. Assignment of the remaining resonances is being carried out in this way with the use of a thinner sample of normal tellurium and better resolution of the spectrometer.

The total cross section of normal isotopic tellurium has also been determined for neutron energies at which there are neither resonances nor diffraction effects, and is given by the equation $\sigma=3.9+0.70E^{-\frac{1}{2}}$ (Fig. 3). This gives a value for the capture cross section at 0.025 ev of 4.43 ± 0.15 barns, in good agreement with that of 4.53 barns found by the pile oscillator method at Oak Ridge.[4] If 78 percent of the thermal cross section is attributed to Te^{125}, as indicated by Pomerance and Arnette,[4] the capture slope for this isotope becomes $0.55E^{-\frac{1}{2}}$. The value of $\sigma_0\Gamma^2$ corresponding to this slope is 825 barns ev, agreeing with the $\sigma_0\Gamma^2$ value obtained from curve fitting in the area of the 2.2-ev resonance.

The incoherent scattering cross section of normal tellurium was determined using the neutron velocity spectrometer and a forward scattering apparatus.[5] The latter consists of two annular rings of BF_3 counter tubes at 18° and 33°, respectively, from the incident neutron beam. For neutrons of sufficiently long wavelength, Bragg reflections fall outside the counter tubes. Thus, only the isotropic incoherent scattering is measured. After correction for multiple scattering, the incoherent scattering cross section was found to be 0.6 ± 0.15 barn.

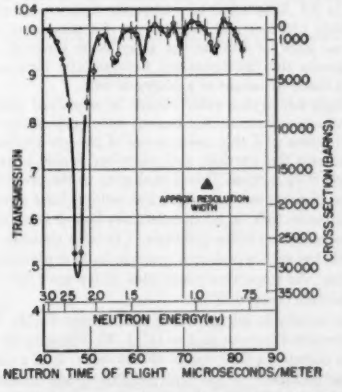

FIG. 2. Neutron cross section of 7.9 mg/cm² enriched Te^{125}.

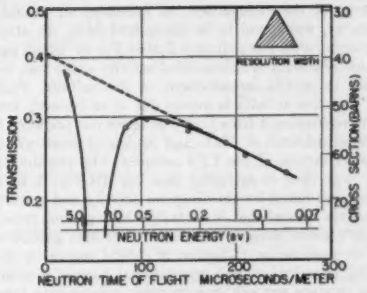

FIG. 3. Neutron cross section of 49.2 g/cm² normal isotopic Te.

We are indebted to Miss Estelle Marder for the preparation of the tellurium isotope samples, and to Drs. W. W. Havens, Jr., L. J. Rainwater, and R. J. Weiss for advice and suggestions in the course of this work.

Thanks also are due to the U. S. Atomic Energy Commission which aided materially in the support of this object.

[3] J. Rainwater and W. W. Havens, Jr., Phys. Rev. **70**, 136 (1946); Rainwater, Havens, Wu, and Dunning, Phys. Rev. **71**, 65 (1947).
[3] Heindl, Ruderman, and Weiss, Phys. Rev. **81**, 325 (1951).
[3] W. W. Havens, Jr., and J. Rainwater, Phys. Rev. **70**, 154 (1946).
[4] H. Pomerance and T. Arnette, ORNL Report 940, Series A, p. 43 (March 15, 1951), unpublished.
[5] Bendt, Rainwater, and Havens, Phys. Rev. **83**, 235 (A) (1951).

Isomeric State of Y^{89} and the Decay of Zr^{89}

M. GOLDHABER, E. DER MATEOSIAN, G. SCHARFF-GOLDHABER, AND A. W. SUNYAR
Brookhaven National Laboratory, Upton, New York†
AND
M. DEUTSCH AND N. S. WALL
Laboratory for Nuclear Science and Engineering and Department of Physics, Massachusetts Institute of Technology, Cambridge, Massachusetts‡

(Received June 18, 1951)

THE decay of Zr^{89} (78 hr) is accompanied[1] by the emission of a partially converted 0.92-Mev gamma-ray which does not coincide with the positrons or with the x-rays due to K capture. This suggests the existence of a metastable state with 0.92-Mev excitation either in Zr^{89} or in its product Y^{89}. In this mass region the longest lived states expected from the shell model and empirical evidence[2] are those which combine with the ground state by transitions of the type $g_{9/2}\leftrightarrow p_{1/2}$ yielding magnetic 2^4-pole ($M4$) radiation. For such transitions the semi-empirical formula[2] $\tau_\gamma=10^4(2I+1)/A^3E^9$ gives an approximate mean life in seconds as a function of the mass number A, the energy E in Mev, and the angular momentum I of the excited state. For $A=89$ and $E=0.92$ Mev, we expect half-lives of $T_{1/2}\simeq18$ sec if $I=9/2$ or $T_{1/2}\simeq3.5$ sec if $I=1/2$.

These considerations make it unlikely that we are dealing with a metastable state of Zr^{89} with $T_{1/2}=78$ hr. In addition, an isomeric state of Zr^{89} with a 4.5-min half-life is already known. On the other hand, if the transition takes place in Y^{89}, where the ground state is known to have $I=\frac{1}{2}$, the expected half-life of 18 sec should permit observation separate from the zirconium parent. We have succeeded in observing Y^{89m} in several ways.

The production of Y^{89m} by excitation with fast neutrons was demonstrated in a very pure, cadmium-covered, sample of Y_2O_3 exposed to fast neutrons from the Brookhaven reactor. A strong gamma-ray activity with a half-life of 16 ± 3 sec was established.

The energy of the gamma-rays, as measured on a scintillation spectrometer, was found to be about 0.92 Mev. An attempt to excite yttrium with x-rays from a 2-Mev Van de Graaff generator yielded an indication of a short-lived activity which was, however, too weak to permit measurement of the half-life. Finally we showed that this activity is indeed due to an isomeric transition in Y^{89} by separating it from Zr^{89}. The latter was prepared by deuteron bombardment of Y_2O_3 and separated from yttrium by repeated extraction of the *TTA* complex. The yttrium daughter activity was then re-extracted into $2M$ $HClO_4$. A half-life of 13 ± 2 sec was found for the daughter activity and a scintillation spectrometer showed that it emits 0.92-Mev gamma-rays.

The Zr^{89} parent activity showed the 0.92-Mev gamma-ray and 0.51-Mev annihilation radiation. A careful search by means of magnetic, scintillation, and proportional counter spectrometers failed to produce any evidence for other gamma-rays ascribed to the decay of Zr^{89} by Hyde and O'Kelley.[2] The relative numbers of yttrium K x-rays and 0.92-Mev gamma-rays from Zr^{89} were compared with the corresponding numbers for Y^{88} which emits close to one 0.91-Mev gamma-ray per strontium K x-ray. Scintillation and proportional counter spectrometers were used for this comparison. The results showed that there are about 1.3 times as many 0.92-Mev gamma-rays as K x-rays in the decay of Zr^{89}. A similar comparison, using calibrated sources of Y^{88} and Na^{22} as intensity standards showed that there are about four times as many nuclear gamma-rays as positrons from Zr^{89}. These results show that the isomeric state of Y^{89} is indeed formed by the positron decay as well as by electron capture. The approximate ratio 3:1 for electron capture to positron emission deduced from these data is in good agreement with the theoretical value[4] for an allowed transition after a small correction for L electron capture. The ft value of 1.2×10^6 also indicates that the transition is allowed, unfavored.[4]

From the observed ratios of 0.04:1 of conversion electrons to positrons[1] and 4:1 of gamma-rays to positrons we obtain the value 10^{-2} for the total conversion coefficient. Allowing for a small contribution from the L-shell we find good agreement with the theoretical value for the K conversion coefficient of 8×10^{-3} for an $M4$ transition.[5]

The transition in Y^{89} is the most energetic $M4$ transition definitely identified as such. The excellent agreement of the observed lifetime of 14 ± 2 sec with the semi-empirical formula derived mostly from data at much lower energies gives strong support to the E^9 dependence[6] over the E^{11} law implied in older formulas.[7] The $g_{9/2}-p_{1/2}$ separation in Y^{89} (0.92 Mev), which contains 50 neutrons, is greater than in either[3] Y^{87} (0.39 Mev) or Y^{91} (0.61 Mev). It seems reasonable that the contraction of the core for a magic number of nucleons leads to a smaller binding energy for orbits of high angular momentum.

We wish to thank Dr. A. O. Allen of the Chemistry Department of Brookhaven National Laboratory for kindly placing the Van de Graaff x-ray generator at our disposal. Thanks are also due to Mr. A. Smith for help with the neutron exposures, and to the MIT cyclotron crew for the deuteron bombardments.

† Research carried out under auspices of the AEE.
* Research supported in part by the joint program of ONR and AEC.
[1] K. Shure and M. Deutsch, Phys. Rev. **82**, 122 (1951).
[2] M. Goldhaber and A. W. Sunyar, Phys. Rev., (to be published).
[3] E. K. Hyde and G. D. O'Kelley, UCRL 1064 (1950), unpublished.
[4] E. Feenberg and G. Trigg, Revs. Modern Phys. **22**, 399 (1950).
[5] Rose, Goertzel, Spinrad, Harr, and Strong, privately circulated tables.
[6] V. F. Weisskopf and J. Blatt, private communication.
[7] P. Axel and S. M. Dancoff, Phys. Rev. **76**, 892 (1949).

Production Ratio of Photomesons from Beryllium*

HEINRICH A. MEDICUS†
Radiation Laboratory, University of California, Berkeley, California
(Received June 18, 1951)

BY the irradiation of targets with a high energy x-ray beam, both negative and positive π-mesons are produced. An investigation was made to determine the ratio of the numbers of mesons of either sign produced in beryllium, because its single isotope $_4Be^9$ has one neutron with only 1.6-Mev binding energy which might affect this ratio.

For this study, the same arrangement was used with which Peterson, Gilbert, and White[1] had determined the corresponding ratio for carbon. The x-ray beam of the 320-Mev synchrotron was collimated and hit the target, a beryllium sphere of about $\frac{1}{2}$-inch diameter. The target was surrounded by a copper absorber in which were imbedded the nuclear emulsion plates, Ilford C2, of 200μ thickness. They were oriented in such a way that the planes of the emulsions were approximately radial. Thus the mesons give relatively long tracks in the emulsion. The plates were scanned for mesons stopping in the emulsion. From the thickness of the traversed material (beryllium, copper, glass, and emulsion) and the energy-range relation one can determine the initial energy of the mesons. The discrimination between negative and positive mesons was made by observing their type of endings. As in the work of Peterson *et al.*, the fact was used that in emulsions negative π-mesons are captured by nuclei and form stars with visible prongs 73 percent of the time; the remaining 27 percent stop without showing a visible track at their end.[2] Positive mesons are not captured and decay to μ-mesons. By counting the meson-produced stars and the π-μ decays, one therefore can calculate for each energy interval the π^-/π^+ ratio. Only mesons emitted at an angle of $90°\pm7°$ to the x-ray beam and in the energy range of 30 to 70 Mev were investigated in this experiment. Because stars are much more conspicuous events in emulsions than π-μ decays, the probability of missing stars in the scanning process is slightly lower than that of overlooking π-μ decays. For this reason, a correction in the ratio of 5 percent, derived from scanning certain areas of the emulsions twice, was applied. Only mesons ending more than 5 microns away from the surface of the emulsion after processing were counted. The ratios were determined from a total of 661 π-μ decays and star forming mesons. The errors given include standard deviations and estimated systematic errors.

TABLE I. π^-/π^+ ratio of mesons produced by x-rays on beryllium.

Meson energy (Mev)	π^-/π^+ ratio
30–40	2.5 ± 0.6
40–55	2.0 ± 0.3
55–70	2.2 ± 0.3
30–70	2.2 ± 0.25

The results are given in Table I. It is seen that the ratio of negative to positive mesons depends little, if any, on the energy in the investigated range. The over-all ratio for mesons of 30 to 70 Mev is 2.2. This value is, within the limits of accuracy, the same which Littauer and Walker[3] got for mesons of about 50 Mev at an angle of 135° to the x-ray beam direction. In their measurements the discrimination between the mesons of both signs was made by means of a magnetic field.

This high minus-plus ratio cannot be explained only by the fact that the beryllium nucleus has one more neutron than protons. Rather it seems as if this one neutron of the low binding energy would act as a free particle, and, therefore, would have a higher production cross section. This is analogous to the case of the production of positive mesons, where free protons have a higher production cross section for π^+ mesons than bound ones, because of the action of the exclusion principle.[4,5] In light elements in which no particle has such a preferred position, as in deuterium, helium, and carbon, the respective minus-plus ratios are 1.0,[6] 1.0 (angle 45°),[6] and 1.06 (angle 135°).[3]

I want to express my gratitude to Professor E. M. McMillan for his continued interest and to Dr. J. M. Peterson for his valuable help during the first stages of this work. It is a pleasure to thank the members of the film program group under Dr. W. Barkas, in particular Mrs. W. R. Gaffey, who did a part of the

scanning. I am particularly grateful to Professor E. O. Lawrence for the privilege of visiting and working at the Radiation Laboratory.

* This work was performed under the auspices of the AEC.
† Fellow of the Swiss Arbeitsgemeinschaft für Stipendien in Mathematik und Physik.

[1] Peterson, Gilbert, and White, Phys. Rev. **81**, 1003 (1951).
[2] F. L. Adelman and S. B. Jones, Science **111**, 226 (1950).
[3] R. M. Littauer and D. Walker, Phys. Rev. **82**, 746 (1951).
[4] J. Steinberger and A. S. Bishop, Phys. Rev. **78**, 494 (1950).
[5] R. F. Mozley, Phys. Rev. **80**, 493 (1950).
[6] Jakobson, Schulz, and White, private communication.

On the Binding Energies of Light Nuclei

JYUMPEI SANADA AND YASUKAZU YOSHIZAWA
Department of Physics, Faculty of Science, Osaka University, Osaka, Japan
(Received April 5, 1951)

IT has been recognized from many empirical facts and theoretical considerations that the magic numbers with which neutron or proton nuclear shells close are 2, 8, 20, 50, 82, and 126. The numbers 14 and 28 have also been proposed from some considerations. To obtain further information on light nuclei, we studied the binding energies of the last nucleon[1] or the last neutron-proton pair using the most accurate part of the mass data,[2] namely, the masses of nuclei having neutron excess $T=N-Z=0$ or 1, where N and Z are the number of neutrons and protons, respectively. While for the light nuclei other effects, e.g., the effects of α-clustering,[3] may be predominant, we attempted to find evidence for the shell structure.

The results are shown in Figs. 1 and 2. The binding energies calculated were corrected for the effect of coulomb interactions, which was estimated from the difference of binding energies of mirror nuclei. We compared nuclei which have the same neutron excess T, to reduce the even-odd variations. Curve I shows the binding energies of the last neutron for nuclei which have $T=1$, even N, and odd Z. Curve II shows those of the last proton for nuclei which have $T=0$, even N, and even Z. Curve III shows the binding energies of the last neutron-proton pair for nuclei which have $T=0$, even N, and even Z. The larger binding energies and the discontinuities like shell closing are seen at N or $Z=6$ and 14. These seem to be emphasized in curve III. Curves IV and V show the binding energies of the last neutron-proton pair for nuclei which have $T=1$ and 5, respectively. The latter was calculated from the masses of nuclei in the neighborhood of $_{28}Ni^{61}$ determined by Duckworth.[4] The larger binding energies at $A=27$ or 29 in curve IV are probably due to the shell closing at N or $Z=14$, respectively; and at $A=61$ in curve V there is an indication of the shell closing at $Z=28$. The situation in the region containing N or $Z=6$ and 8 must be investigated more closely in connection with the α-particle model and displacement of the $2s$ orbit in the shell model.

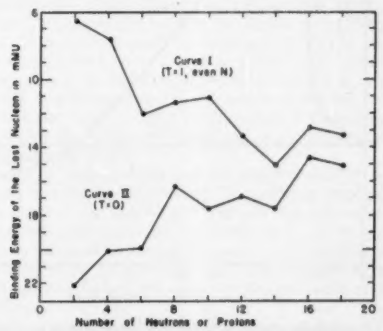

FIG. 1. The binding energy of the last neutron or proton *vs* number of neutrons or protons.

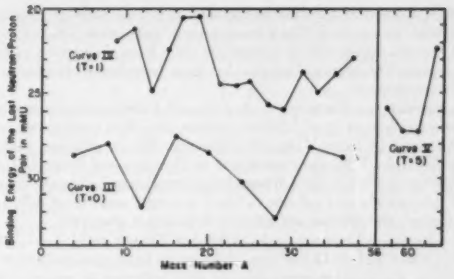

FIG. 2. The binding energy of the last neutron-proton pair *vs* mass number.

Low and Townes[5] showed recently that closing of a major shell at 20 nucleons appears questionable. They thought that the large isotope spread of Ca was probably due to the exceptional stability of Ca^{40} and a shell at 28 neutrons. We calculated the binding energies using their mass data (from $_{18}P^{31}$ to $_{21}Sc^{42}$) and also found no evidence of shell closing at 20 nucleons. It is interesting to note that in the spin orbit coupling model[6] the numbers 6, 14, and 28 discussed above appear after filling the $j=l+\frac{1}{2}$ orbits which have the largest l values in each of the oscillator groups like the numbers 50, 82, and 126. A more detailed account will be published in *Journal of the Physical Society of Japan*.

[1] K. Way, Phys. Rev. **75**, 1448 (1949).
[2] J. Mattauch and A. Flammersfeld, "Isotopic report", Z. Naturforsch. (1949).
[3] L. R. Hafstad and E. Teller, Phys. Rev. **54**, 681 (1938).
[4] Private communication to Dr. K. Ogata. H. E. Duckworth and R. S. Preston, Phys. Rev. **79**, 402 (1950).
[5] W. Low and C. H. Townes, Phys. Rev. **80**, 608 (1950).
[6] M. G. Mayer, Phys. Rev. **78**, 16 (1950).

Scintillation Counter Studies of Neutron Capture Gamma-Ray Spectra

BERNARD HAMERMESH AND VIRGINIA HUMMEL
Argonne National Laboratory, Chicago, Illinois
(Received June 8, 1951)

THE methods[1,2] that have been used to study neutron capture gamma-ray spectra have been limited by low energy detection cutoffs. These cutoffs are usually in the region of 3 Mev. Since [3] there undoubtedly are capture gamma-rays of energy well below this value, we have begun a study using[4] a NaI crystal and photomultiplier. Such a detector has a very high sensitivity to gamma-rays down to the lowest energies.

A beam of neutrons from the thermal column of the Argonne heavy-water-moderated reactor impinges upon a target which gives rise to capture gamma-rays. The crystal and photomultiplier are inside a thick shield consisting of borated paraffin, cadmium, and bismuth. The gamma-rays from the target pass through an opening in the shield to the detector. A thickness of boron covers the opening so as to absorb slow neutrons that are scattered by the target.

The pulses from the detector are sent into a twenty-channel pulse-height discriminator. The pulses that occur in the crystal will be caused by photoelectric effect, Compton effect, or pair production. For the lowest energy gamma-rays, only the first process is important, whereas, for the highest energies, only the last is important. In intermediate ranges two or even all three processes may give separable pulse distributions. The apparatus is calibrated by using Au^{198}, Cs^{137}, and Na^{24} gamma-rays.

We have studied the spectra of several elements and are reporting on the results found in the energy range 300 kev to 10

Mev. Below 300 kev, the background problems near the reactor become very serious. There is evidence of lines below 100 kev but it requires special efforts to separate them from the various backgrounds. The principal results that have been found thus far are discussed below.

Aluminum.—There is a single peak at 6.6 Mev corresponding to pair production by a 7.6-Mev gamma-ray. This corresponds to the binding energy of the last neutron in Al^{28}. In addition, peaks at 1.4 and 1.7 Mev are found due to Compton and photoelectric effect of a 1.7-Mev line. When the neutron beam is shut off, these decay quickly and are due to the 2.3-minute activity of Al^{28}. In all cases, the 500-kev annihilation radiation is observed.

Chlorine.—There are peaks at 500 and 850 kev and 1.2, 1.7, 2.1, 4.5, and 5.2 Mev. In addition, there seems to be even more structure at the higher energies than we have been able to resolve thus far. The two highest peaks are due to pair production by 5.5- and 6.2-Mev lines. The interpretation of the other peaks is not clear-cut. For example, the 2.1- and 2.5-Mev peaks could be the pair and Compton edge of a 3.1-Mev line. The photo peak is negligible at this energy. The 1.7- and 2.1-Mev peaks could be the Compton edge and photo peak of a 2.1-Mev line. The 850-kev and 1.2-Mev peaks have a similar relation to a line at 1.2 Mev. Finally, the 500-kev annihilation radiation could obscure a Compton edge of an 850-kev line.

Iron.—There are three high energy peaks corresponding to pair production by 6.0-, 7.4-, and 8.6-Mev gamma-rays. The 8.6-Mev peak is very weak compared with the others and is probably due to Fe^{57} going to Fe^{58}. The 6.0- and 7.4-Mev lines have about the same intensities. A very careful search from 6.0 Mev down to less than 300 kev has revealed no other peaks. There is no evidence of a line of energy 1.4 Mev.[5]

Manganese.—There are only two peaks corresponding to lines at 5.0 and 7.2 Mev. There is no evidence of a line at 2.2 Mev. The gamma-rays from the 2.59-hour Mn^{56} activity are observed.

The results on iron and manganese are surprising. If the 6.0- and 7.4-Mev lines arise from excited Fe^{57}, then the lack of a 1.4-Mev line means that this energy must be distributed among several very low energy lines. For Mn^{56}, where the 2.2-Mev line does not appear, a similar conclusion is reached. If one believes that the two high energy lines arise from transitions from the originally formed excited state, the transitions could lead to one state of lower spin than this state and one of higher spin. The intercombination transition could then be highly forbidden, since it would require a large spin change to occur. This interpretation is satisfactory for Mn^{56}, since the spin of Mn^{55} is 5/2. For iron this argument does not help since, Fe^{56} (even, even) presumably has spin = 0 so that the two states could not differ markedly in spin. In this case, one requires that the 6.0-Mev line be sandwiched between several of the very low energy transitions, i.e., at least one low energy transition must occur before the 6.0-Mev line can be emitted.

[1] Kinsey, Bartholomew, and Walker, Phys. Rev. **77**, 723 (1950); **78**, 77 (1950); **79**, 218 (1950).
[2] B. Hamermesh, Phys. Rev. **76**, 182 (1949); **80**, 415 (1950); **81**, 487 (1951).
[3] C. O. Muehlhause and C. Hibdon, Phys. Rev. **82**, 235 (1951).
[4] R. Hofstadter and J. A. McIntyre, Phys. Rev. **80**, 631 (1950).
[5] Meyerhof, Roderick, and Mann, Phys. Rev. **82**, 1203 (1951).

A New Magnetic Transition of Mn Ferrite

TOSHIHIKO OKAMURA AND JUNZO SIMOIZAKA
Research Institute for Scientific Measurement, Sendai, Japan
(Received May 7, 1951)

THERE have been many studies on the physical properties of spinel-type oxides. From the results of magnetic measurements, Rengel[1] and Weiss[2] first discovered a magnetic transition of magnetite at a temperature of −160°C. Recently, Guillaud and Grevaux[3] observed a decrease in magnetization with varying temperature for cobalt ferrite in a temperature range of −180°∼−188°C. We have also discovered[4] a magnetic transition

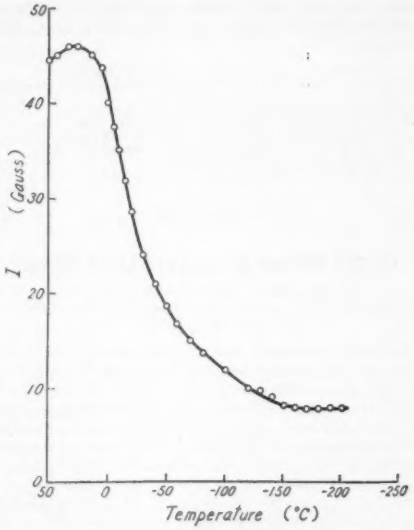

FIG. 1. Intensity of magnetization as a function of temperature. Applied field strength = 1.2 oersted.

of nickel ferrite which occurs from −120°C and seems to be finished at a lower temperature than −195°C. Thus, all complete inverted spinels seems to have a magnetic transition in some temperature range.

In order to ascertain whether a transition in mangan ferrite exists, the magnetic intensity was measured precisely as a function of temperature by using a ring-formed specimen.

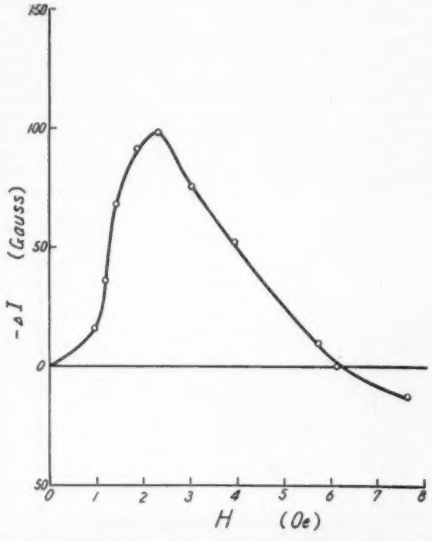

FIG. 2. Temperature change of intensity of magnetization, as a function of applied magnetic field. The ordinate represents the difference in intensity of magnetization between room temperature and liquid nitrogen temperature, and the abscissa is the applied field.

To begin with, the intensity of magnetization was measured in a weak field of 1.2 oersted in the temperature range +50°C to −200°C and is shown in Fig. 1. From the results of this experiment, it was confirmed that a gradual increase of the intensity of magnetization with decreasing temperature is interrupted by a fall in the range +20°C to −150°C, below which temperature the magnetization remains constant. During heating, these changes take place almost reversibly. Moreover, with increasing field the magnitude of the drop in intensity of magnetization (from room temperature to liquid nitrogen temperature) at first increases, up to a field of 2.25 oersted, and afterwards diminishes; it disappears at about 6.1 oersted, at which field the intensity of magnetization shows a value of 216 gauss. When the field is increased further, the intensity of magnetization increases with decreasing temperature. These changes of magnetization due to temperature are shown in Fig. 2 as a function of applied field.

From these results, it can be concluded that the mangan ferrite undergoes a transition like other complete inverted ferrites in the temperature range of +20°C to −150°C.

The electrical resistivity was also observed in the same temperature range and was found to increase considerably with decreasing temperature.

Details of the present experiment will be published in *Scientific Reports of the Research Institute of Tōkohu University*.

The writers wish to express their thanks to Miss Kōko Takahashi for her assistance during the course of the experiments.

[1] Rengel, thesis Zürich (1913).
[2] P. Weiss and R. Forrer, Ann. Physik **12**, 279 (1929).
[3] C. Guillaud and H. Grevaux, Compt. rend. **230**, 1256 (1950).
[4] T. Okamura and J. Simoizaka, to be published.

The Existence of Wheeler-Compounds

AADNE ORE
University of Bergen, Bergen, Norway
(Received June 19, 1951)

RECENT experiments by Deutsch have revealed that significant information concerning the interaction of positrons with the constituents of ordinary matter can be obtained from a study of the annihilation of positrons in gases.[1] In particular, it has been demonstrated in a striking manner that the phenomena of positronium formation and conversion can have pronounced effects upon the observed values of the mean life of the positrons.

The progress in this field of physics has added interest to the question of whether a positron can attach itself to an atomic or to a molecular structure, to become a member of a short-lived system of the kind first envisaged by Wheeler.[2]

The first question with which one is confronted when inquiring into the properties of these "Wheeler-compounds" is, clearly, that of whether such structures can exist at all, i.e., whether they will be energetically stable. Theoretical evidence has already been published, which strongly suggests that some systems of this kind, e.g., Cl^-e^+, actually possess this dynamical stability.[3,4] However, it is hardly justified to say that, in any single case considered up to the present, the stability has been established in a mathematically entirely convincing way. It may be of interest, therefore, to report one case, *viz.*, that of the simple Wheeler-compound H^-e^+, where the variational method can be applied and furnishes an unambiguous proof.

One might perhaps argue that the stability of H^-e^+ is to be expected because the structure of this particular compound lies somewhere between that of the hydrogen molecule and that of the positronium molecule, both of which are known to be stable. However, this qualitative argument would carry but little weight, on account of the fact that the symmetry in positive particles characteristic of each of the latter two systems is not present in the hybrid.

In attempting to establish the dynamical stability of H^-e^+, we first considered the feasibility of deriving the desired result by means of trial wave functions which would describe the system roughly in terms of a positron moving in the field of a polarized negative hydrogen ion. Utilizing mathematical techniques well known, particularly from early works by Hylleraas, functions can be handled which contain as independent variables the three distances from the proton to the light particles, in addition to the two angles which the direction from the proton to the positron forms with those to the two electrons. However, this approach led to approximate energy values which were too high to guarantee against a dissociation of H^-e^+ into a hydrogen atom and a positronium atom—which represents the critical mode of disintegration.

A better approximation will be one which describes the system more closely as a positronium atom coupled to a hydrogen atom. The following symmetrized, simple trial wave function will be of this kind:

$$\psi=\exp[-k(r_{1a}+\alpha r_{2a}+\beta r_{2b})]+\exp[-k(r_{2a}+\alpha r_{1a}+\beta r_{1b})]. \quad (1)$$

The subscript a refers to the proton, b to the positron, and 1 and 2 to the respective electrons. The parameter k permits a variation with respect to a change in scale. For $\alpha=0$, $\beta=0.5$, the function (1) describes the dissociated system correctly. In general, the parameter α introduces a coupling of the negative member of the positronium atom to the hydrogen atom.

The above function can be handled essentially by the method which has proved to be successful for treating the positronium molecule.[5] While the high degree of symmetry of the latter system permitted an exclusive use of the volume element

$$d\tau\sim dr_{ab}r_{1a}dr_{1a}r_{1b}dr_{1b}r_{2a}dr_{2a}r_{2b}dr_{2b}, \quad (2)$$

some of the terms in the energy integral now have to be evaluated by introducing in addition the analogous volume element

$$d\tau\sim dr_{1b}r_{1a}dr_{1a}r_{1b}dr_{1b}r_{2a}dr_{2a}r_{2b}dr_{2b}. \quad (3)$$

The determination of the optimum values of α and β is facilitated if one first considers the idealized system in which the proton mass is taken to be infinitely large. In the dissociated state this system has the energy $E_0=-1.5R_\infty k$. Using the same unit of energy one finds for the compound

$$E_{\min}=-1.50502; \quad \alpha=0.25, \quad \beta=0.5 \quad (4)$$

corresponding to a lower limit of the binding energy of

$$E_0-E_{\min}=0.0050R_\infty k=0.07 \text{ ev}. \quad (5)$$

The correction due to the kinetic energy of the proton can easily be determined, but it will not affect the value (5), for the corrections to E_0 and to $E_{\min}$ are, naturally enough, found to be practically equal. Hence, we conclude that H^-e^+ will be stable against dissociation by at least the value given by (5), and this value is already sufficient even to prevent the system from breaking up in an ordinary thermal collision process.

The author is greatly indebted to Professor E. A. Hylleraas for most valuable discussions and suggestions. He also wants to thank Mr. K. Nybö, who assisted in the computational work.

This investigation was supported by L. Meltzers Höyskolefond and by Det Videnskapelige Forskningsfond av 1919. An extended and more detailed report will be published elsewhere.

[1] M. Deutsch, Phys. Rev. **82**, 455 (1951).
[2] J. A. Wheeler, Ann. N. Y. Acad. Sci. **48**, 219 (1946).
[3] L. Simons, Soc. Sci. Fennica, Commentationes Phys.-Math. **24**, No. 2 (1948); **24**, No. 9 (1949); **24**, No. 12 (1949).
[4] A. Ore, Phys. Rev. **73**, 1313 (1948).
[5] E. A. Hylleraas and A. Ore, Phys. Rev. **71**, 493 (1947).

On the Relative Intensities of First-Order Stark Components

SHU-MU KUNG
Department of Astronomy, University of Michigan, Ann Arbor, Michigan
(Received April 9, 1951)

1. *Error in Gordon's formula.* The relative intensities of the first-order Stark components of a spectral line are given sep-

arately by Schroedinger[1] and Gordon.[2] Both give the same result. Since Gordon's formulas are readily applicable, his formula is commonly used. In the discussion of Stark effect, Bethe[3] also quotes Gordon's formula. Unfortunately, a factor of 2 was inadvertently omitted from the term $(n_1'-n_2')(n^2+n'^2)/(n+n')^2$ in Gordon's formula for the intensity of p-component (light polarized parallel to the field). The error becomes evident when one checks through his intermediate formulas (9), (19), (24), and (29′).

2. *Statistical Weight.* A particular Stark component is specified by a set of values n_1, n_2, m, n_1', n_2', m'. Each of n_1, n_2, $|m|$, n_1', n_2', and $|m'|$ can take any positive integral value with the following restrictions:

$$n=n_1+n_2+|m|+1, \quad n'=n_1'+n_2'+|m'|+1,$$

where n, n' are, respectively, the total quantum number of the upper and the lower state of a spectral line in question. Since m, m' can each take a positive or a negative integral value and their difference can have only the value 0 or 1, only the components with both m and m' equal to 0 have a statistical weight 1. Any other component has a statistical weight 2.

In a table for the intensity of Stark components of $H\alpha$, Bethe[3] gave the two cases $\{(1, 1, 0), (0, 0, 1)\}$ and $\{(2, 0, 0), (0, 0, 1)\}$ a weight 1. Both should have a weight 2. Actually, the intensities calculated by Gordon's formula for the two cases are, respectively, 441 and 9, just half of the values given in his table. With a weight 2 for them, the right values are obtained. The reason he gave weight 1 to these two cases might arise from the fact that the initial state of each of them has a m-value 0. Were the weight to depend only on the initial state, the above Stark components in emission would have different intensities in absorption.

3. *Control Check.* Gordon's two formulas for p- and s-component (light polarized perpendicular to the field) are lengthy, each containing four hypergeometric functions. Fortunately, for each set of values of n_1, n_2, m, n_1', n_2', and m' ($m=m'$ for the p-component), the formula can be computed in two ways, i.e., $I_{n_1,\ n_2,\ m}^{n_1',\ n_2',\ m}$ or $I_{n_1',\ n_2',\ m}^{n_1,\ n_2,\ m}$, with different values of the hypergeometric functions and their respectively different coefficients. The agreement of the results obtained by the two methods guarantees the computation to be free from error.

From the nature of the problem, the sum of the intensities of the p-components should be equal to that of the s-components. However, in taking the sum, the value of the intensity of the unshifted component should be taken half of its value, because the unshifted component belongs to both sides of a symmetrical distribution.

[1] E. Schroedinger, Ann. Physik **80**, 437 (1926).
[2] W. Gordon, Ann. Physik **394**, 1031 (1929).
[3] H. Bethe, Handbuch der Physik **24** (1) (1933).

On Low Energy X-Ray Absorption by Nuclei

ROBERT H. MCFARLAND
Department of Physics, Kansas State College, Manhattan, Kansas
(Received June 11, 1951)

DURING the past several months a series of experiments have been performed to determine the possibility of resonance absorption of low energy x-rays by nuclei. In the event this were observed, it would have an application in the unraveling of decay schemes. Several different approaches have been followed in this work.

Guggenheimer[1] proposed that nuclear rotational energy levels existed according to the relationship

$$E=2.5B_0A^{-5/3}K(K+1),$$

where B_0 is 5.06 million electron volts, A is the mass number, and K is a positive integer or zero. Thus nuclei with A greater than 28 should have excited energy levels under one hundred kilovolts. This includes such elements as nickel, copper, iron, zinc, and calcium whose characteristic x-ray spectra do not overlap the regions in question. Early survey experiments[2] using photographic procedures for measuring the absorption of x-rays, passed through these materials as absorbers, seemed to indicate some correlation between experiment and theory. Later measurements with electronic recording did not verify these earlier results.

A second approach was through the use of silver. Ag^{109} exists in nature with an abundance of 48.1 percent and exhibits an isomeric transition of half-life 40.5 sec and energy 0.087 Mev which has previously been excited by x-rays of greater than 1 Mev.[3] Ag^{107} is reported to have a corresponding isomeric transition of 44.3-sec half-life and an energy of 0.093 Mev. In the current experiment, the region from 80 to 100 kilovolts was explored carefully to determine whether a resonance absorption could be detected. If such an absorption exists, it should be small because ΔI in the transition is considered to be 4 and as such the multipole order is 2^4 or 2^5. In addition to the ordinary absorption methods used for most parts of this experiment, the silver specimen was itself examined for radioactivity after a prolonged x-ray exposure. However, none was observed.

Lastly, Rb^{87} and Sr^{87}, both of which exist in nature with abundances of 27.2 percent and 7.02 percent respectively, were surveyed in an attempt to excite the gamma-rays of 0.034, 0.053, and 0.082 Mev which have been associated with Rb^{87} decay. Since the half-lives of these gamma-radiations are so short that they have not been measured, it is assumed that the transitions are more nearly dipolar. No absorption was observed which could be attributed to resonance transitions within the nucleus.

The negative results of the experiment with silver may lend limited credence to the hypothesis that the silver isomeric transitions are not to the ground state, but to an excited state of less than 2 kilovolts above the ground state. This previously has been postulated to make the silver decay scheme agree with allowed transitions predicted from the Meyer nuclear shell model. A similar situation may exist for rubidium.

Statistical probable errors in the above experiments were kept to less than 1 percent. However, fluctuations in the output of the x-ray unit were observed to cause deviations as great as 2 percent. When absorption, other than mass absorption, was indicated by the results, sufficient additional readings were taken at the same wavelengths to dispel errors due to machine behavior.

If one accepts 1 percent error as the limit of the above experiment, it follows that any nuclear resonance absorption which exists must be less than 1 percent of the total absorption. Consequently, for the cases cited above, the cross sections for nuclear resonance absorption are less than fifty barns.

Acknowledgments are due C. S. Clay, F. Aschenbrenner, and R. B. Edwards for their assistance in obtaining much of the above information and to Professor J. G. Winans of the University of Wisconsin for his interest in this problem.

[1] K. M. Guggenheimer, Proc. Roy. Soc. (London) **A181**, 169 (1942).
[2] C. S. Clay, *Determination of the Existence of Low Lying Rotational Nuclear Energy Levels*, Master's Thesis, Kansas State College (1947), unpublished.
[3] M. L. Wiedenbeck, Phys. Rev. **67**, 92 (1945).

On the Diurnal Variation of Extensive Air Showers of High Density at 3500 m above Sea Level

C. BALLARIO, B. BRUNELLI, A. DE MARCO, AND G. MARTELLI[4]
Istituto di Fisica dell'Università, Roma Centro di Studio per la Fisica Nucleare del C.N.R., Roma, Italy
(Received June 20, 1951)

DURING the last year we have included a series of experiments on extensive air showers at the Laboratorio della Testa Grigia (3500 m above sea level; magnetic latitude 47°N), of which the principal results will be communicated later. In this letter we give a brief account of an analysis of the diurnal variation of the rate of extensive showers, based on a series of measurements taken during the period June-August 1950.[1]

TABLE I. Experimental results.

t_0 (hours)	$C_S^{t_0}$ (coinc/min)	$C_S^{t_0+12}$ (coinc/min)	$C_s^{t_0}$ (coinc/min)	$C_s^{t_0+12}$ (coinc/min)	$C_{S+s}^{t_0}$ (coinc/min)	$C_{S+s}^{t_0+12}$ (coinc/min)	$R_S(t_0)$	$R_s(t_0)$	$R_{S+s}(t_0)$	H^{t_0} (mm Hg)	H^{t_0+12} (mm Hg)
0	3.002 ±0.029	3.074 ±0.031	0.0632 ±0.0047	0.0547 ±0.0042	0.0152 ±0.0021	0.0081 ±0.0016	0.976 ±0.014	1.16 ±0.12	1.88 ±0.46	508	507
2	3.015 ±0.029	3.006 ±0.037	0.0620 ±0.0041	0.0750 ±0.0058	0.0152 ±0.0020	0.0087 ±0.0020	1.002 ±0.016	0.83 ±0.09	1.75 ±0.47	507	508
4	3.102 ±0.044	3.025 ±0.038	0.0545 ±0.0059	0.0572 ±0.0052	0.0171 ±0.0033	0.0076 ±0.0019	1.025 ±0.015	0.95 ±0.13	2.24 ±0.70	508	508
6	3.051 ±0.039	2.994 ±0.035	0.0543 ±0.0052	0.0577 ±0.0048	0.0152 ±0.0027	0.0089 ±0.0019	1.019 ±0.018	0.94 ±0.12	1.70 ±0.47	509	507
8	3.055 ±0.038	3.004 ±0.027	0.0569 ±0.0051	0.0610 ±0.0039	0.0139 ±0.0025	0.0105 ±0.0016	1.016 ±0.015	0.93 ±0.10	1.32 ±0.31	509	507
10	3.113 ±0.026	2.999 ±0.032	0.0542 ±0.0050	0.0609 ±0.0056	0.0099 ±0.0021	0.0122 ±0.0018	1.038 ±0.014	0.89 ±0.13	0.81 ±0.21	508	507

The experimental arrangement for detecting the showers consisted of 3 sets, *ABC*, of Geiger counters placed in a horizontal plane at the vertices of an equilateral triangle of side 6 m: each set had an area $S=8\times10^{-2}$ m². In addition, 3 sets, *DEF*, of counters are placed one above the other near the center of the triangle *ABC*; set *D* was of ordinary Geiger counters, while sets *E* and *F* were of low efficiency counters, (efficiency $r=3$ percent). The area of each set *DEF* was $s=10^{-2}$ m².

Above the counters there was only the roof of the laboratory, of thickness 1.4 g/cm² of light material, and we have neglected correcting any errors resulting from this.

We recorded simultaneously threefold coincidences between the sets $ABC(C_S)$, threefold coincidences $DEF(C_s)$, and sixfold coincidences $ABC+DEF(C_{S+s})$.

In order to analyze the experimental results, from the point of view of diurnal variations, we divided into two groups the three types of coincidences, the threefolds C_S and C_s and the sixfolds C_{S+s}. The first group contained the events recorded between the hours t_0 and (t_0+12), (middle European time), and the second, those recorded between (t_0+12) and (t_0+24). We use $C_S^{t_0}$, $C_s^{t_0}$ and $C_{S+s}^{t_0}$ to refer to events of the first group, and $C_S^{t_0+12}$, $C_{S+s}^{t_0+12}$ to events of the second, and we have calculated the experimental ratios

$$C_S^{t_0}/C_S^{t_0+12}=R_S(t_0),\quad C_s^{t_0}/C_s^{t_0+12}=R_s(t_0),$$
$$C_{S+s}^{t_0}/C_{S+s}^{t_0+12}=R_{S+s}(t_0).$$

In Table I we give the experimental results, including also in column 8 the weighted mean values of the atmospheric pressure. It will be seen from this table that, while $R_S(t_0)$ and $R_s(t_0)$ remain constant at a value near unity, within the experimental errors, $R_{S+s}(t_0)$ is greater than unity for t_0 between 0 and 8 hours, and less than unity for t_0 greater than 8 hours.

This rather large variation of R_{S+s} with t_0, is rendered somewhat uncertain by the large statistical errors, but, assuming that it is significant, we can exclude the possibility that it is due to instrumental effects (casual coincidences, interference, etc.) or to barometric effects. Furthermore, from a rough evaluation of its magnitude, it seems that an effect due to the diurnal variation of temperature of the atmosphere would produce, if at all, a variation of R_{S+s} opposite to that observed.

In an endeavor to explain these experimental results, we observe that:

(a) the coincidences C_S, as is well known, are caused chiefly by showers of density $\Delta\simeq1/S=12$ m^{-2};

(b) the coincidences C_s are due chiefly[2] to heavily ionizing particles, to groups of particles locally associated and to extensive showers of density much greater than 12 m^{-2};[3]

(c) the coincidences C_{S+s} are caused by simultaneous events of type (a) and (b), and chiefly by high density showers,[3] as can be seen from an examination of the function

$$F(\Delta)=K\int_0^{\Delta}(1-\exp[-S\Delta])^3\times(1+\exp[-s(2r-r^2)\Delta])\cdot\Delta^{-(\gamma+1)}d\Delta, \quad (1)$$

which gives the number of coincidences due to showers of density less than Δ, and is written under the usual hypotheses applicable to arrangement similar to ours.

To explain the results, we make the tentative assumption that the showers of density greater than a certain value Δ_1, have an intensity zero during the 12 hours from 4 P.M. to 4 A.M., during which time, in fact, the ratio R_{S+s} is less than unity. On this hypothesis,

$$F(\infty)/F(\Delta_1)=2.2$$

and using this and Eq. (1) we calculate $\Delta_1\simeq500$ m^{-2}.

Such a density cutoff during 12 hours is perfectly compatible with the values found for R_S since, as has been said, these are due mostly to showers of density less than Δ_1, and even with the values found for R_S as only a small fraction of the coincidences C_S are due to showers of high density.

It is generally assumed that the energy of primaries responsible for showers of mean density $\Delta\simeq500$ m^{-2} is of the order 10^{16} ev. We consider it reasonable to assume that the diurnal effect observed for the showers refers to primaries of energy greater than 10^{16} ev.

A similar analysis applied to the results of other experiments,[4,5] carried out at the Laboratorio Della Testa Grigia, gives independent indication of a diurnal variation of the type described above.

We are continuing further experiments in order to examine more closely this effect, and we hope shortly to communicate these additional results, together with a fuller discussion of the problem.

* Now at the Istituto di Fisica dell'Università di Pisa.

[1] We were prompted to this analysis by a suggestion of Professor E. Amaldi, after his recent talk about this subject with Professor H. Alfvén.

[2] De Marco, Martelli, and Salvetti, Nuovo Cimento (to be published).

[3] This was confirmed by a cloud chamber which was placed, originally for other purposes, beneath the sets *DEF*.

[4] Amaldi, Castagnoli, Gigli, and Sciuti, Nuovo Cimento 7, 401 (1950).

[5] G. Martelli and G. Stoppini, to be published.

Momentum Representation of the Coulomb Scattering Wave Functions*

E. GUTH AND C. J. MULLIN
University of Notre Dame, Notre Dame, Indiana
(Received June 14, 1951)

IN a recent paper[1] it was pointed out that a matrix element of the form

$$M=\int\psi_2^*V\psi_1 d\tau \quad (1)$$

where ψ_1 and ψ_2 are the coulomb scattering wave functions of the type introduced by Gordon[2] and used extensively by Sommerfeld,[3] often can be evaluated rather easily if ψ_1 and ψ_2 are expanded in terms of momentum wave functions $\phi_1(\mathbf{k}')$ and $\phi_2(\mathbf{k}'')$. The mo-

mentum wave functions are the fourier amplitudes in the expansions:

$$\psi_1=\int\phi_1(\mathbf{k}')\exp(i\mathbf{k}'\cdot\mathbf{r})d\mathbf{k}';\quad \psi_2^*=\int\phi_2(\mathbf{k}'')\exp(-i\mathbf{k}''\cdot\mathbf{r})d\mathbf{k}''. \quad (2)$$

Expressed in terms of the momentum functions, the matrix element of Eq. (1) is given by

$$M=\int\int d\mathbf{k}'d\mathbf{k}''\phi_1(\mathbf{k}')\phi_2(\mathbf{k}'')M_{\text{Born}}(\mathbf{k}',\mathbf{k}''), \quad (3)$$

where $M_{\text{Born}}(\mathbf{k}',\mathbf{k}'')$ is the value obtained for the matrix element in the Born approximation (expressed in terms of $\mathbf{k}'$ and $\mathbf{k}''$). Because of the properties of the momentum wave functions, a simple evaluation of the integrals occurring in Eq. (3) can be made in many important problems. For example, suppose the coulomb interaction is weak; then $\phi_1(\mathbf{k}')$ and $\phi_2(\mathbf{k}'')$ are "sharply peaked" at $\mathbf{k}'=\mathbf{k}_1$ and $\mathbf{k}''=\mathbf{k}_2$, respectively (where $\mathbf{k}_1$ and $\mathbf{k}_2$ are the asymptotic values of the wave numbers for the particles described by ψ_1 and ψ_2). Consequently, unless $M_{\text{Born}}(\mathbf{k}',\mathbf{k}'')$ is a very rapidly varying function of $\mathbf{k}'$ or $\mathbf{k}''$, Eq. (3) reduces to

$$M=M_{\text{Born}}(\mathbf{k}_1,\mathbf{k}_2)\int\phi_1(\mathbf{k}')d\mathbf{k}'\int\phi_2(\mathbf{k}'')d\mathbf{k}''$$
$$=M_{\text{Born}}(\mathbf{k}_1,\mathbf{k}_2)\psi_1(0)\psi_2^*(0) \quad (4)$$

where $\psi_1(0)$ and $\psi_2(0)$ are the coulomb scattering wave functions evaluated at the origin. This simple procedure explains the frequent occurrence of coulomb correction factors of the type given by Eq. (4).

To extend the usefulness of this method of evaluating matrix elements, we have derived explicit expressions for the momentum wave functions. These wave functions, which we have been unable to find in the literature, are of considerable interest for various atomic and nuclear problems. $\phi(\mathbf{k}')$ may be obtained directly from $\psi(\mathbf{r})$ by fourier (or laplace) transformation. In coordinate space

$$\psi(\mathbf{r})=\exp(i\mathbf{k}\cdot\mathbf{r})F(-in,1,i\rho), \quad (5)$$

where F is the confluent hypergeometric function, $\rho=kr-\mathbf{k}\cdot\mathbf{r}$, $\mathbf{k}$ is the asymptotic value of the wave number, and $n=zZe^2/\hbar v$. Using a real k', the fourier transformation yields[4]

$$\phi(\mathbf{k}')=-\frac{1}{2\pi^2}\lim_{\epsilon\to 0}\frac{d}{d\epsilon}\left\{\frac{[k'^2+(\epsilon-ik)^2]^{in}}{[\epsilon^2+(\mathbf{k}'-\mathbf{k})^2]^{1+in}}\right\}. \quad (6)$$

The terms which correspond to the incident and scattered waves may be identified readily since an undistorted plane wave and an undistorted scattered wave have the fourier transforms:[5]

$$T\{\exp(i\mathbf{k}\cdot\mathbf{r})\}=\delta(\mathbf{k}-\mathbf{k}')=\frac{1}{\pi^2}\lim_{\epsilon\to 0}\frac{\epsilon}{[\epsilon^2+(\mathbf{k}'-\mathbf{k})^2]^2} \quad (7)$$

$$T\{\exp(ikr)/r\}=1/[2\pi^2(k'^2-k^2)] \quad (8)$$

where $T\{f\}$ means the three dimensional transform of f. From (8) it may be seen that the asymptotic representation of the coordinate wave function corresponds to the point $k'=k$ in momentum space. From (6) and (8) it follows that the amplitude of the scattered wave is given by

$$-2nk/(\mathbf{k}'-\mathbf{k})^{2+2in} \quad (9)$$

with $|\mathbf{k}'|=|\mathbf{k}|$. For $|n|\ll 1$, Eq. (6) acquires the form of the Born result previously treated by Dirac.[6]

The relative simplicity of the momentum wave function given by Eq. (6) results from the fact that the confluent hypergeometric function which occurs in the expression for $\psi(\mathbf{r})$ is expressible in terms of a single parabolic coordinate. Thus, the total momentum function may be obtained, by the convolution theorem, from the fourier transforms of a plane wave and a relatively simple function of a single coordinate. The general coulomb wave function, on the other hand, does not have this essentially one-dimensional character and, consequently, its fourier transform[7] is relatively complicated. The simple character of the one-dimensional fourier (or laplace) transforms (in which only one component of the momentum, e.g., the radial component, is used in the transformation) of many types of wave functions has been emphasized by Dirac;[6] independently, one dimensional laplace transforms have been employed extensively by Kallman and Päsler.[9] Simple transforms are obtained whenever the coordinate wave function satisfies a differential equation of the laplace type.

We are applying both one- and three-dimensional momentum representations of the coulomb scattering wave function to a number of atomic and nuclear problems and will report the results in the near future.

* Supported in part by the ONR.

[1] C. J. Mullin and E. Guth, Phys. Rev. **82**, 141 (1951).
[2] W. Gordon, Z. Physik **48**, 180 (1928).
[3] A. Sommerfeld, *Atombau und Spektrallinien* (F. Vieweg und Sohn, Braunschweig, 1939), II band.
[4] Convergence of the integrals may be insured without the explicit use of convergence factors by taking a complex k'. The momentum functions obtained by this procedure are valid for all k' in the lower half of the complex plane. This method has been applied to a discussion of one-dimensional problems by P. A. M. Dirac, Proc. Roy. Soc. (London) **160**, 48 (1937).
[5] Dirac adds to (8) a δ-function which automatically selects the principal value.
[6] P. A. M. Dirac, *Quantum Mechanics* (Oxford University Press, London, 1935), second edition, pp. 195–200.
[7] V. Bargmann, Z. Physik **99**, 576 (1936). The three dimensional transform of the radial part of the coulomb wave function is given by M. Levy, Proc. Roy. Soc. (London) **204**, 145 (1950).
[8] P. A. M. Dirac, see reference 4 and Z. Physik **44**, 585 (1927).
[9] H. Kallmann and M. Päsler, Ann. Physik (6) **2**, 292 (1948).

The Influence of Magnetization on Ultrasonic Attenuation in a Single Crystal of Nickel or Iron-Silicon*

SHELDON LEVY AND ROHN TRUELL
Metals Research Laboratory, Brown University, Providence, Rhode Island
(Received June 7, 1951)

IT has been found that in ferromagnetic single crystals there is an interesting connection between measurements of ultrasonic attenuation[1] (frequency range 5 to 50 megacycles) and the values of a constant magnetic field applied at some fixed direction with the ultrasonic beam direction.

With a single crystal of nickel attenuation measurements were made with the ultrasonic beam direction at approximately 12° to the ⟨111⟩ direction of the crystal. The measurements were made with various values of a constant applied magnetic field applied at right angles to the direction of the ultrasonic beam. The values of the applied magnetic field were varied from zero to saturation in steps as indicated in Fig. 1.

The main features seem to be the magnitude of the change, approximately a factor of nine near 50 megacycles, and the fact that at saturation field the ultrasonic attenuation seems to be quite low and independent of frequency in this range of frequencies.

The photograph of the changes in the pulse amplitude as a function of time, or distance in the material, is shown (at 25 megacycles) in Fig. 2, where the bottom trace is that with saturation field and the top trace is that with zero applied magnetic field. The intermediate stages correspond to the steps shown in Fig. 1.

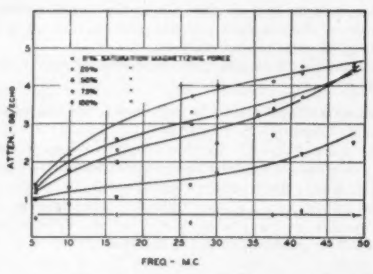

FIG. 1. Attenuation *vs* frequency for nickel at various magnetic field intensities.

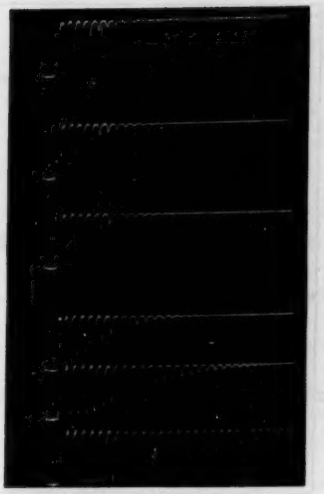

FIG. 2. Changes in the pulse amplitude (at 25 Mc) as a function of time, or distance in the material, at the magnetic field intensities of Fig. 1. The top trace is that with zero applied magnetic field, and the bottom trace is that with saturation field.

Similar effects have been observed in iron-silicon single crystals (3.8 percent Si) but the magnitude of the effect is much smaller. Cobalt has not been examined.

Although the equipment used is capable of detecting velocity changes of less than 0.1 percent, no velocity changes were observed with applied magnetic field corresponding to the above attenuation changes.

Additional experiments with nickel have been made in which the applied magnetic field is directed along the axis of the ultrasonic beam. The result of these observations is that qualitatively the variations of attenuation with magnetic field follows the same pattern as that just described with the applied magnetic field perpendicular to the ultrasonic beam. In the latter case it does not make any appreciable difference what angular position the applied magnetic field has around the beam axis.

The effect of the magnetic field in orienting the magnetic moments appears to be directly coupled to the lattice in such a way that attenuation of the ultrasonic energy is reduced when a saturation field is applied. It may be that the large change observed is a change in the scattering of the ultrasonic radiation by the lattice which is affected by the magnetic domain orientations, hence by the applied magnetic field. It may also be that there are magnetic losses caused by induced currents within the domains—currents which might arise from the passage of a mechanical wave through a magnetostrictive medium. The remaining attenuation value at saturation is probably caused by the absorption of energy by the lattice because of work done on it. The ultrasonic waves were compressional, and the wavelength in the nickel varied from approximately 0.1 cm at 5 mc to 0.01 cm at 50 megacycles. The magnetic domain size in nickel falls within this range of wavelengths. Anisotropy properties of single crystals are being investigated by this method.

* The work described here was supported by the Research Corporation of New York and by the Office of Air Research.

[1] Ultrasonic attenuation is measured by a pulsed system using microsecond pulses with a 300 rep. rate. The attenuation values are free of any effects of boundary conditions or beam spreading, and are characteristic only of the material. Details of such measurements are described in a report entitled "On the measurement of ultrasonic attenuation in solids" by R. L. Roderick and R. Truell (to be published).

Correlation Phenomena and Capture of Polarized Neutrons

OTTO HALPERN
University of Southern California, Los Angeles, California
(Received June 14, 1951)

IN a recent note,[1] attention was called to the fact that the capture of a polarized neutron when followed by the emission of a single gamma-quantum leads to certain polarization effects in the final nucleus as well as in the emitted radiation. A special simple example was discussed, while the treatment of more complicated cases and the question of the design of a gamma-ray analyzer was left to a more detailed paper.

This transfer of polarization has considerable influence, also, in such cases in which the transition to the final state is carried out in two (or more) steps. One can here expect the occurrence of very significant changes in the theory of correlation. This may perhaps best be illustrated if we apply the statistical interpretation[2] of a general group-theoretical result[3] concerning correlation effects to the present case.

The absence of interference effects between the transition amplitudes to and from the intermediate state of the final nucleus was ascribed[2] to the fact that the projection of the angular momentum on the direction of propagation of the emitted quantum is a good quantum number provided that spatial degeneracy allows resolution of the angular momentum along any direction, and in particular, along the wave vector of an emitted particle. This condition no longer obtains if the initial state is formed through capture of a polarized neutron. Depending upon the angular momentum of the original nucleus, the initial state of the final nucleus is totally or partially polarized. The description of the process of emission is no longer invariant under rotation around the direction of propagation, since a preferred direction is established through the axis of polarization. Simple relations are again encountered if, e.g., the direction of emission of the quantum coincides with the axis of polarization of the incident neutron.

A quantitative discussion is reserved for a later publication.

[1] O. Halpern, Phys. Rev. **82**, 753 (1951).
[2] B. A. Lippmann, Phys. Rev. **81**, 162 (1951).
[3] S. P. Lloyd, Phys. Rev. **80**, 118 (1950).

On the Goldberger Model for the Interaction of High Energy Nucleons with Heavy Nuclei*

G. BERNARDINI, E. T. BOOTH, AND S. J. LINDENBAUM
Columbia University, New York, New York
(Received May 24, 1951)

GOLDBERGER[1] considered as a model for the inelastic interaction of 90-Mev neutrons with a heavy nucleus (Pb) the generation of an internal nucleonic cascade in a zero temperature Fermi gas of nucleons. The Monte Carlo method was employed to treat the cascades which were developed in accordance with free nucleon-nucleon scattering cross sections (appropriately reduced by the Pauli exclusion principle).

An experimental check of Goldberger's[1] evaluation by Hadley and York[2] was interpreted to be at best only in partial qualitative agreement. The discrepancies may have been due to the failure of the model at these low energies for which pick-up effects, multiple nucleon interactions, and refraction effects could be important. The use of erroneous cross sections ($p-p$, $n-n$) and some approximations in the calculations also are at least partially responsible for the discrepancy.

To check the model at higher energies (~400 Mev), the nuclear interactions induced by 350- to 400-Mev protons[3] in β-sensitive nuclear emulsions were compared to the model predictions. This technique is particularly well suited for this study, because all charged particles from the individual nuclear events are visible,

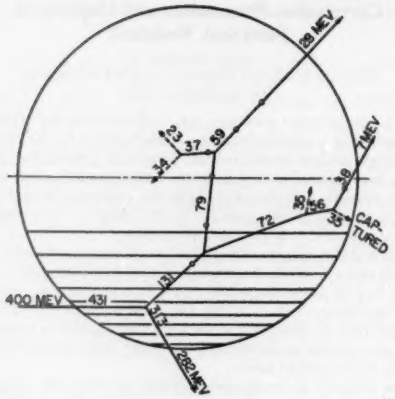

FIG. 1. A Goldberger model work diagram. Cross section of nucleus of mass number 100, using for the radius $R=1.4\times A^{\frac{1}{3}}\times 10^{-13}$ cm. Thermal excitation = 66 Mev.

and hence a detailed comparison with the calculations can be made. About 80 percent of the inelastic events in emulsions occur in Ag–Br nuclei of average mass number 100, and hence the calculations were performed for $A=100$.

A two-dimensional circular geometry ($R=1.4A^{\frac{1}{3}}\times 10^{-13}$ cm) was employed for the nucleus. The true three-dimensional location of the first interaction was preserved by dividing the two-dimensional circle into segments which when rotated present equal normal ring area to the incident nucleon (see Fig. 1). Equal numbers of nucleons were then considered incident upon each segment.

The individual properties of protons and neutrons were replaced by an average nucleon gas with a maximum kinetic energy of 22 Mev in a nuclear barrier (including coulomb) of 35 Mev. The average mean free path inside the nucleus as a function of energy was determined from published experimental $n-p$ and $p-p$ cross-section measurements, and the assumption $\sigma_{n-n}\approx\sigma_{p-p}$. The Monte Carlo calculations follow the general Goldberger technique, and a typical calculation is illustrated in Fig. 1. Of 90 incident nucleons only 60 produced inelastic events.

For a comparison with the experimental results the ejected nucleons were grouped into the energy intervals designated[3] as gray (>100 Mev), sparse black (30 to 100 Mev), and black (<30 Mev). The calculated two-dimensional angular distributions are compared with the experimental projected angular distributions in Fig. 2. The agreement is clearly reasonable within statistics and experimental errors in the values of prong energies.

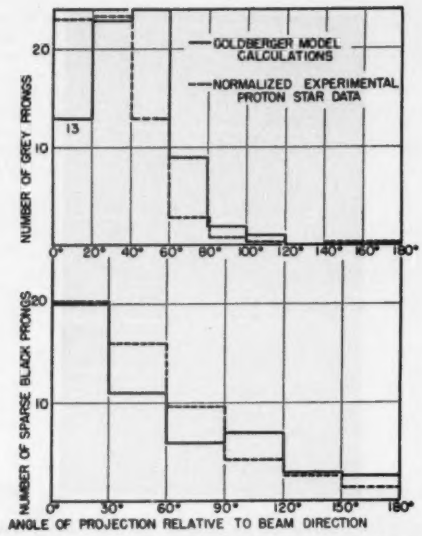

FIG. 2. A comparison of the Goldberger model angular distributions with the experimental proton star data.

An analysis of the calculations revealed that a reasonable estimate of the fraction of ejected nucleons which are protons is $\frac{1}{4}$.

The comparison of experimental and predicted mean prong numbers is made in Table I. The thermal excitation is calculated from the conservation-of-energy equation. The average value is 50 Mev and the maximum value about 200 Mev illustrating that the knock-ons carry away most of the incident energy.

The value of 35 Mev per black prong[4] was used to estimate the mean evaporation black prong number in Table I. This gave the correct (within the errors) total mean prong number as well as a percentage (28±7 percent) of knock-on black prongs which agrees with the experimental determination of at least 25 percent.

Table II is a comparison of the distribution of events with various numbers of gray protons (>100 Mev) and fast protons (<30 Mev). The agreement is clearly reasonable for this rather sensitive

TABLE I. Comparison of experimental and calculated mean prong numbers.

A. Gray and sparse black prongs

	Gray (>100 Mev)	Sparse black (30–100 Mev)
Calculated mean No. of protons	0.6 ±0.12	0.42 +0.1
Experimental mean No. of protons	0.42±0.04	0.35±0.04

B. Black prongs

	Black prongs (>30 Mev)
Calculated mean No. of directly ejected protons	0.58±0.12
Estimated mean No. of evaporation prongs	1.5 ±0.2
Estimated mean No. of visible black prongs	2.1 ±0.4
Experimental mean No. of black prongs	2.5 ±0.2

TABLE II. Comparison of experimental and calculated distribution of gray (>100 Mev) and fast (>30 Mev) proton events.

A. Gray proton events

No. of gray protons	% of events calculated	% of events experimental
0	46±11	57 ±4
1	48±11	40 ±4
2	7±4	2.5±1

B. Fast proton events

No. of fast protons	% of events calculated	% of events experimental
0	30±7	35 ±3
1	48±8	54 ±4
2	21±7	9 ±2
3	3±1.5	1.7±0.7

test of the cascade nature of the process. A detailed report to be published shortly will show that all the results of the 400-Mev proton interactions can be satisfactorily explained by the model.

A similar investigation at 150 Mev is now in progress.

The authors wish to thank Mr. Leon Landowitz and Mr. Jack Leitner for their excellent work on the Monte Carlo calculations.

* This project was jointly supported by the ONR and AEC.
[1] M. L. Goldberger, Phys. Rev. **74**, 1269 (1948).
[2] J. Hadley and F. York, Phys. Rev. **80**, 345 (1950).
[3] Bernardini, Booth, and Lindenbaum, Phys. Rev. **80**, 905 (1950).
[4] Bernardini, Cortini, and Manfredini, Phys. Rev. **79**, 952 (1950).

A Note on the U Operator*

MAURICE NEUMAN
Brookhaven National Laboratory, Upton, Long Island, New York
(Received June 8, 1951)

IT is usually assumed that the operator $U(t)$ transforming the state vector from the interaction to the Heisenberg representation satisfies the relation

$$\bar{U}(t)=U^{-1}(t), \tag{1}$$

where the dash denotes the hermitian adjoint. One then infers from Eq. (1) that

$$\bar{S}=S^{-1}. \tag{2}$$

Here

$$S=\lim_{t\to\infty}U(t). \tag{3}$$

It is the purpose of this note to show that Eq. (2) is implied by the formal structure of the theory; statement (1), however is not. Its use amounts to an additional assumption. The failure of (1) need not be related to convergence or renormalization difficulties

We consider the operator equation

$$i\partial W(t)/\partial t=H(t)W(t) \tag{4}$$

and its hermitian adjoint

$$i\partial\bar{W}/\partial t=-\bar{W}(t)H(t). \tag{5}$$

$H(t)$ is assumed to be hermitian. Two physically interesting implicit solutions of (4) are

$$U^r(t)=1-i\int_{-\infty}^{t}dt'H(t')U^r(t') \tag{6r}$$

$$U^a(t)=1-i\int_{+\infty}^{t}dt'H(t')U^a(t'). \tag{6a}$$

The solution $U^r(t)$ is to be identified with the $U(t)$ mentioned in the introduction, but the symbol $U(t)$ without a superscript will henceforth refer to both $U^r(t)$ and $U^a(t)$. The corresponding solutions of (5) are the hermitian adjoints of (6). An identity:

$$i\frac{\partial}{\partial\tau}[\bar{U}(\tau)-1][U(\tau)-1]=\bar{U}(\tau)H(\tau)-H(\tau)U(\tau) \tag{7}$$

constructed from (4) and (5), is now integrated between $-\infty$ and t for $U^r(t)$ and between $+\infty$ and t for $U^a(t)$. This operation yields directly

$$\bar{U}(t)U(t)=1 \tag{8}$$

and in the limit as $t\pm\infty$,

$$\bar{S}^rS^r=1;\quad \bar{S}^aS^a=1. \tag{9r, a}$$

Equations 8 and 9 are not sufficient to insure (1) or (2). Statement (2) can, however, be deduced from another identity. We integrate

$$i\frac{\partial}{\partial\tau}[\bar{U}^r(\tau)-1][U^a(\tau)-1]=\bar{U}^r(\tau)H(\tau)-H(\tau)U^a(\tau) \tag{10}$$

between the limits $-\infty$ and $+\infty$. This leads to an expression

$$\bar{S}^r=S^a \tag{11}$$

or together with (9)

$$S^r\bar{S}^r=1;\quad S^a\bar{S}^a=1. \tag{12r, a}$$

Relations (12) and (9) then imply (1). Equation (10) integrated between $-\infty$ and a finite time t gives in conjunction with (11)

$$S^r=\bar{U}^a(t)U^r(t) \tag{13r}$$

$$S^a=\bar{U}^r(t)U^a(t), \tag{13a}$$

which may be taken as the defining equations for S^r and S^a even if the limits $U^r(+\infty)$, $U^a(-\infty)$ do not properly exist.[1]

A somewhat better insight into the nature of these relations is gained by connecting $U^r(t)$, $U^a(t)$ with another special solution of (4):

$$U^a(t)=1-\frac{i}{2}\int_{-\infty}^{+\infty}dt'\epsilon(t-t')H(t')U^a(t') \tag{14}$$

where $\epsilon(x)$ denotes the signum function of x. The operator $U^a(t)$ may be used to construct the Cayley representation of S.[2] Its essential properties,

$$\bar{U}^a(t)U^a(t)=\bar{U}^a(\infty)U^a(\infty)=\bar{U}^a(-\infty)U^a(-\infty) \tag{15}$$

$$\int_{-\infty}^{+\infty}dt'H(t')U^a(t')=\int_{-\infty}^{+\infty}dt'\bar{U}^a(t')H(t') \tag{16}$$

readily follow from the integration of the identity

$$i\frac{\partial}{\partial\tau}[\bar{U}^a(\tau)-1][U^a(\tau)-1]=\bar{U}^a(\tau)H(\tau)-H(\tau)U^a(\tau) \tag{17}$$

and its product with $\epsilon(t-\tau)$ between the limits $-\infty$ and $+\infty$. The relations we are interested in are obtained from

$$i\frac{\partial}{\partial\tau}[\bar{U}^a(\tau)-1][U(\tau)-1]=\bar{U}^a(\tau)H(\tau)-H(\tau)U(\tau) \tag{18}$$

when this is integrated over the interval $(-\infty, t)$ for $U(t)=U^r(t)$ and $(+\infty, t)$ for $U(t)=U^a(t)$.

With the aid of (16) we then get[3]

$$\bar{U}^a(t)U^r(t)=U^a(\infty) \tag{19r}$$

$$\bar{U}^a(t)U^a(t)=\bar{U}^a(\infty). \tag{19a}$$

A sufficient condition for the unitarity of $U(t)$ is now seen to be the existence of $[U^a(t)]^{-1}$ in the sense of a right inverse. In that case

$$U^r(t)=[\bar{U}^a(t)]^{-1}U^a(\infty) \tag{20r}$$

$$U^a(t)=[\bar{U}^a(t)]^{-1}\bar{U}^a(\infty) \tag{20a}$$

and

$$\begin{aligned}U^r(t)\bar{U}^r(t)&=[\bar{U}^a(t)]^{-1}U^a(\infty)\bar{U}^a(\infty)[U^a(t)]^{-1}\\&=[\bar{U}^a(t)]^{-1}\bar{U}^a(t)U^a(t)[U^a(t)]^{-1}\\&=1.\end{aligned} \tag{21}$$

The transition from the second to the third member of (21) involved the use of

$$\bar{U}^a(\infty)U^a(\infty)=U^a(\infty)\bar{U}^a(\infty) \tag{22}$$

which is an immediate consequence of (16). The reciprocal of $U^a(t)$ will exist in general only in the limit $t\to\pm\infty$ when the operator $i[U^a(t)-1]$ becomes hermitian on account of (16). In this limit (20) leads to the Cayley representations of S^r and S^a as given in reference 2. A unitary $U(t)$ can however always be expressed in the form

$$U^r(t)=U^a(t)[\bar{U}^a(\infty)]^{-1} \tag{23r}$$

$$U^a(t)=U^a(t)[U^a(\infty)]^{-1} \tag{23a}$$

since the reciprocal of $U^a(\infty)$ is known to exist on account of (16).

The hermiticity of $i[U^a(t)-1]$, even though sufficient, is by no means necessary to insure the unitarity of $U(t)$. To see this we assume that $i[U^a(t)-1]$ is anti-hermitian and show that in this case too $U(t)$ is a unitary operator. Starting from (15) we have

$$\begin{aligned}\bar{U}^a(\infty)U^a(\infty)&=U^a(t)U^a(t)=\bar{U}^r(t)U^a(t)U^a(t)U^r(t)\\&=\bar{U}^r(t)\bar{U}^a(\infty)U^a(\infty)U^r(t)\\&=\bar{U}^r(t)U^a(t)U^a(t)\bar{U}^a(t)U^a(t)U^r(t)\\&=\bar{U}^a(\infty)U^a(t)\bar{U}^a(t)U^a(\infty).\end{aligned} \tag{24}$$

In writing the second member of (24) use is made of the fact that $U^a(t)$ is hermitian. The third member re-expresses the first with the aid of (19r) and its adjoint. The transition to the fourth involves (15). The fifth is reached with the aid of (19a) and its adjoint. Exploiting again Eq. (19r) we get to the sixth member of (24). Since $U^a(\infty)$ has always a reciprocal, we infer from (24) that

$$U^a(t)\bar{U}^a(t)=1. \tag{25a}$$

Applying the same identities in a somewhat different order and using (22) one similarly arrives at

$$U^r(t)\bar{U}^r(t)=1. \tag{25r}$$

Equations (25) and (8) imply the statement made at the beginning of the paragraph.

The author has enjoyed several instructive conversations with Dr. Hartland Snyder regarding the question discussed in this note.

* Research carried out at Brookhaven National Laboratory, under the auspices of the AEC.

[1] Equation (13) rather than (3) is essentially the definition adopted by Yang and Feldman for their "Heisenberg S-matrix." (Phys. Rev. **79**, 972, 1950.) The expressions

$$F(x)=U^r(t)F^{\rm in}(x)\bar{U}^r(t)=F^{\rm in}(x)-i\int_{-\infty}^{t}dt'U^r(t')\,[H(t'),\,F^{\rm in}(x)]\,\bar{U}^r(t')$$

$$F(x)=U^a(t)F^{\rm out}(x)\bar{U}^a(t)=F^{\rm out}(x)-i\int_{+\infty}^{t}dt'U^a(t')\,[H(t'),\,F^{\rm out}(x)]\,\bar{U}^a(t')$$

for the various Heisenberg field operators are equivalent to the integral equations employed by these authors. This may be seen by evaluating the commutator brackets explicitly for the various fields. The relation between $F^{\rm out}(x)$ and $F^{\rm in}(x)$ is then $F^{\rm out}(x)=\bar{U}^a(t)U^r(t)F^{\rm in}(x)\bar{U}^r(t)U^a(t)$.

[2] J. Schwinger, Phys. Rev. **74**, 1439 (1948).

[3] Equations (19) may be regarded as the definitions of the "Heisenberg reaction operator" in the same sense as (13) is taken to define the "Heisenberg collision operator." See reference 1.

The Mechanism of nD Capture

NORMAN AUSTERN*
University of Wisconsin, Madison, Wisconsin
(Received June 18, 1951)

THE thermal neutron-deuteron capture cross section has long been known to be very small (0.46×10^{-27} cm^2 for neutrons of velocity 2200 m/sec.[1] Several attempts at its calculation have been published, and the values obtained are: 3×10^{-27} cm^2 by Schiff,[2] 0.17×10^{-27} cm^2 by Höcker,[3] 0.73×10^{-27} cm^2 by Burhop and Massey,[4] while Verde[5] indicates that the cross section is very small but declines to give any numerical value.

It is generally considered that the H^3 wave function is mostly of ^2S character, and that capture from the continuum ^2S and ^4S states proceeds by the emission of a magnetic dipole gamma-ray. There are strong selection rules on this process. Two types of ^2S wave function must be distinguished, "symmetric," in which the neutrons are in a relative singlet state, and "antisymmetric," in which the neutrons are in a relative triplet state. Now if the radiation interaction involves only the spin magnetic moments of the nucleons then the transition can only link wave functions having the same neutron spin symmetry. Further, since ^2S wave functions of different energies are orthogonal, the magnetic transition must take place from the continuum ^4S state. Only the antisymmetric ^2S part of the ground-state wave function then has the neutron spin symmetry of the quartet state and can contribute to the matrix element of the transition. As this part of the ground state is believed to be very small, the capture cross section is correspondingly small. The above-mentioned authors all based their calculations on estimates of the amount of admixture. It is the purpose of the present note to indicate that their interpretation of the capture process is not a unique one.

Two additional mechanisms seem important: Magnetic dipole capture via the interaction moment[6] does not obey the selection rules which limited the possible transitions via the spin moments; electric quadrupole capture can occur from the continuum ^4S state to ground state ^4D terms.[7]

The capture cross section produced by the spin-antisymmetric interaction moment was computed for the present communication on the assumption that the ground state is a pure symmetric ^2S state. The matrix element for a transition between this state and the ^2S continuum state can be compared with the corresponding matrix element which appears in the calculation of the three-body magnetic moment anomaly. Then the numerical value of the capture matrix element follows from the known value of the three-body magnetic moment anomaly simply by renormalizing one wave function to an amplitude appropriate in the continuum. This method of approximation avoids any detailed assumptions about the interaction moment operator. The necessary renormalization was effected by comparison of the continuum and ground-state wave functions at the point of zero particle separation, a criterion which is reasonable because of the short-range nature of the interaction moment. In this manner a capture cross section was computed which was found to have about one-quarter of the experimental value. The transition involving the continuum ^4S state seems to contribute as much again, although its estimation is less reliable. Thus, in a first estimate, interaction moment magnetic dipole transitions to the main part of the H^3 wave function seem to yield about half the observed nD capture cross section.

The electric quadrupole capture cross section has been estimated very crudely, using the Gerjuoy-Schwinger value of 4 percent ^4D function. It is found nearly to equal the magnetic cross section, so that adding the two just gives the experimentally observed cross section. While this is certainly fortuitous, it does indicate that it is unnecessary to postulate an antisymmetric ^2S term in the ground state as the explanation of the capture process.

Accurate calculation of the quadrupole cross section would show what upper bound the small empirical value can set on the amount of ground-state ^4D function. It may be rather low. It is interesting that the interaction moment model of the three-body magnetic anomaly does not lead to any contradiction with the known small capture cross section.

This investigation was carried out as a direct consequence of conversations with Professor R. G. Sachs.

* AEC Predoctoral Fellow.

[1] Sargent, Booker, Cavanagh, Hereward, and Niemi, Can. J. Research **A25**, 134 (1947).

[2] L. I. Schiff, Phys. Rev. **52**, 242 (1937).

[3] G. Höcker, Physik. Z. **43**, 236 (1942).

[4] Burhop and Massey, Proc. Roy. Soc. (London) **A192**, 156 (1947).

[5] Verde, Helv. Phys. Acta **XXIII**, 453 (1950); Nuovo cimento **7**, 283 (1950); **8**, 152 (1951).

[6] N. Austern and R. G. Sachs, Phys. Rev. **81**, 710 (1951); N. Austern, Phys. Rev. **81**, 307(A) (1951).

[7] The existence of such terms is known theoretically. Gerjuoy and J. Schwinger, Phys. Rev. **61**, 138 (1942); Pease and Feshbach, Phys. Rev. **81**, 142(L) (1951), also private communications from Dr. Pease.

Nuclear Magnetic Resonance Measurements on Be^9, Al^{27}, and Si^{29} in Beryl

J. HATTON, B. V. ROLLIN, AND E. F. W. SEYMOUR
The Clarendon Laboratory, Oxford, England
(Received June 15, 1951)

MEASUREMENTS have been made of nuclear magnetic resonance absorption in a single crystal of beryl ($Be_3Al_2Si_6O_{18}$) at a frequency of 2.3 Mc/sec and a temperature of 20°K.

The five lines due to electric quadrupole splitting of the Al^{27} resonance were clearly observed. With the hexagonal axis of the crystal parallel to the magnetic field, the separation between adjacent lines was 0.45 Mc/sec. Three lines due to Be^9 have been found. With the axis parallel to the field, the separation between the lines was 0.13 Mc/sec. A search was made for other lines in the regions where they would be expected to appear, if present, but nothing was observed. Since the signal-to-noise ratio for the outer lines of the triplet was greater than thirty to one, it seems certain that there were no other lines. This result is in agreement with the recent measurements of Schuster and Pake[1] and confirms the value $I=\frac{3}{2}$ for the spin of Be^9.

It is unfortunately not possible to obtain the quadrupole moment of Be^9 from the observed splitting since the electric field gradient at the nucleus is unknown. Since the observed quadrupole interaction energy $eQ\partial^2V/\partial z^2$ is about ten times smaller for Be than Al, and since the nuclei occupy fairly similar positions in the crystal,[2] it seems reasonable to suppose that the quadrupole moment of Be^9 is appreciably smaller than that of Al^{27} and probably of the order of 0.02×10^{-24} cm^2.

In addition to the lines due to Al and Be, a very weak resonance was also observed at a field corresponding to a g factor of 1.11. As there was no detectable shift of the resonance on rotation of the crystal axis with respect to the magnetic field it was due to a nucleus with very small or zero quadrupole moment. We have also observed the same resonance in two specimens of glass and we think it is probably the result of Si^{29}. According to the theory of Mayer[3] the spin of Si^{29} should be $\frac{1}{2}$, and experiments by Townes *et al.*[4] have shown that the quadrupole moment is small or zero. If we assume $I=\frac{1}{2}$, the magnetic moment is 0.55 nuclear magnetons which is in very good agreement with the value predicted for Si^{29} by the theory of Schawlow and Townes.[5]

[1] N. A. Schuster and G. E. Pake, Phys. Rev. **81**, 886 (1951).
[2] W. L. Bragg and J. West, Proc. Roy. Soc. (London) **A111**, 691 (1926).
[3] M. G. Mayer, Phys. Rev. **78**, 16 (1950).
[4] Townes, Mays, and Dailey, Phys. Rev. **76**, 700 (1949).
[5] A. L. Schawlow and C. H. Townes, Phys. Rev. **82**, 268 (1951).

The Effect of Scattering on Angular Correlation Measurements

SHERMAN FRANKEL
Randal Morgan Laboratory of Physics, University of Pennsylvania, Philadelphia, Pennsylvania
(Received June 13, 1951)

THE purpose of this note is to describe a simple method for correcting measurements of angular correlations (involving electrons) for multiple scattering in the source and for the finite solid angle of the detectors, which will allow the experimenter to determine specific activities needed for such measurements.

Consider an e-γ-experiment, where $W(\theta)$ is the correlation function and $F(\alpha)$ is the scattering function. The probability that a γ-ray will enter $d\Omega_1$ and that any electron correlated to it by $W(\theta)$ will be scattered through an angle α and enter $d\Omega_2$ is

$$P=d\Omega_1 d\Omega_2\int d\Omega_\theta W(\theta)F(\alpha). \tag{1}$$

The experimental correlation may be determined by the tedious process of evaluating $F(\alpha)$ numerically, expressing α in terms of θ, φ, etc., and carrying out the integral (1) numerically. However, in general,

$$W(\theta)=(1/2\pi)\Sigma\tfrac{1}{2}(2l+1)a_lP_l(\cos\theta) \tag{2}$$

$$F(\alpha)=(1/2\pi)\Sigma\tfrac{1}{2}(2k+1)b_kP_k(\cos\theta). \tag{3}$$

By expressing $P_k(\cos\alpha)$, via the addition theorem, in terms of θ and of β, the angle between $d\Omega_1$ and $d\Omega_2$, one obtains

$$P=d\Omega_1 d\Omega_2[(1/2\pi)\Sigma\tfrac{1}{2}(2l+1)a_lb_lP_l(\cos\beta)]. \tag{4}$$

Similar expansions of $P_l(\cos\beta)$ and integrations over $d\Omega_1$ and $d\Omega_2$ yield:

$$P=S_1S_2(1/2\pi)\Sigma\tfrac{1}{2}(2l+1)a_lb_lg_lh_lP_l(\cos\theta), \tag{5}$$

where now θ is the angle between the centers of two circular counters of solid angle S_1 and S_2 and half-angles g_0 and h_0 respectively, and

$$g_l=\int_0^{g_0}P_l(\cos\alpha)d(\cos\alpha)\Big/\int_0^{g_0}d(\cos\alpha) \tag{6}$$

with a similar definition for h_l. We note that S_1g_l is the coefficient in (3) for $F(\alpha)=1$, $0\leq\alpha\leq g_0$; $F(\alpha)=0$, $g_0\leq\alpha\leq\pi$, so that the solid angle correction is identical with a scattering correction. The bracket in (4) represents a new correlation function so that similar treatment extends the result to many "scatterings." Thus, given n events such that the $k+1$th event is correlated to the kth event by $W_k(\theta_k)=(1/2\pi)\Sigma\frac{1}{2}(2l+1)a_{lk}P_l(\cos\theta)$, then the correlation between the first and the nth event is just

$$W_n(\theta_n)=\frac{1}{2\pi}\Sigma\frac{2l+1}{2}\Big(\prod_{k=1}^{n-1}a_{lk}\Big)P_l(\cos\theta_n) \tag{7}$$

where θ_n is the angle between the first and the nth events.

(1) Equation (7) extends (5) to $e-e$ angular correlations. (This formula is valid only if the correlation between the $k+1$th and kth events, W_k, is independent of the previous events. Thus it should not give the angular correlation between the first and last events of a cascade transition.)

(2) The form of the correlation is unaffected by the presence of scattering or finite φ-asymmetric detectors. For example, if only P_2 appears in the experimental data, (say $W(\theta)=1+A\cos^2\theta=1+aP_2$) then only P_2 is present in the correlation function. This is of interest since often the highest power of l appearing in $W(\theta)$ is of importance even when the a_l are not accurately known. (Where lens spectrometers are used to detect the electrons the form is still unaltered but g_1 and g_2, the acceptance angles of the spectrometer, replace 0 and g_0 in the limits in (6).)

(3) The multiple scattering coefficients b_l are just the correction factors for a_l so that one need not evidence $F(\alpha)$ explicitly. Usually only b_2 or b_2 and b_4 are needed. In the Goudsmit and Saunderson[1] treatment of multiple scattering

$$b_l=\exp[-q(1-C_l)/b_1]=\exp(-mt) \tag{8}$$

where $q=Nst$ (N=atomic density; s=total single scattering cross section; t=effective source thickness) and c_l is just the coefficient of the P_l expansion of $f(\theta)$, the single scattering function. The reader is referred to this treatment for a discussion of assumptions inherent in (8) and for simple expressions for b_l in terms of electron energy, source thickness, atomic number, etc.

(4) Electrons originating near the surface of a source are scattered less than Eq. (8) indicates. (8) applies to a collimated electron beam traversing a foil. A first-order approximation valid when (8) is valid and applicable to thin sources would replace b_l by $(1-b_l)/mt$.

(5) Order of magnitude results using the above approximations: for a source thickness of 200 micrograms ($Z=52$; $A=120$; $E=100$ kev) $b_2=0.9$, $b_4=0.77$. For a half-angle of 18° $g_2=0.9$, $g_4=0.75$.

[1] S. Goudsmit and J. L. Saunderson; Phys. Rev. **57**, 24 (1940); **58**, 36 (1940).

Emission of Long-Range Particles in the Fast Neutron Ternary Fission of U-238 and Th-232

E. W. TITTERTON
Research School of Physical Sciences, Australian National University, Canberra, Australia*
(Received June 19, 1951)

FOLLOWING a detailed investigation of the long-range particles emitted in the slow neutron ternary fission of U-235 by the photographic plate method,[1] experiments were undertaken to determine whether similar phenomena occur in the fast neutron fission of U-238 and Th-232. Although Tsien *et al.*[2] reported that U-238 gave no such long-range particles when irradiated by neutrons from the bombardment of beryllium by 6.7-Mev deuterons and Tsien and Faraggi[3] obtained a similar result for Th-232, yet the observation of such a mode of photofission in uranium by Titterton and Goward[4] and in thorium by Titterton and Brinkley[5] threw doubt on the validity of the argument used by the French group to explain the absence of the long-range particles in their experiments.

In the present experiments two sets of plates, each including Ilford C_2 and D_1 emulsions, were loaded with uranium acetate and thorium nitrate respectively, as described elsewhere[4,5] and were exposed to neutrons of energy 2.5 Mev obtained from the

Harwell 200-kev $D-D$ source. Because of the low values of the fission cross sections concerned, long irradiations (~8 hours) were necessary and, as both types of emulsion were used under conditions where they recorded protons of 2.5-Mev energy, a large background of recoil protons and natural radioactive α-particles was present in the processed emulsions. A high rate of chance superposition of tracks was therefore to be expected. However, since the maximum range of the recoil protons was 56μ while the maximum α-particle range in the uranium case was 39μ and in the thorium case 48μ, it was certain that any fission events having light fragments of range in excess of 60μ could not be due to a chance juxtaposition of tracks.

As normal isotopic uranium was used in the experiment, the plates loaded with this material were wrapped in thin cadmium foils to reduce the chance of slow neutron fission in the U-235 component resulting from the slight background of scattered neutrons. The fission cross sections of U-235 and U-238 at 2.5 Mev are such that fission events resulting from the rarer isotope could not be more than a percent or two of those resulting from the U-238. Search of the uranium loaded emulsions yielded 8 cases of ternary fission with the emission of a light, charged fragment of range greater than 60μ among 12,000 binary fissions. The greatest range observed was 202μ. In addition there were 8 events having light particles lying in the range interval 20 to 60μ and which, in the light of experience gained in earlier experiments,[1,4,5] appeared to be ternary fission.

In the case of the thorium-loaded emulsion 14,000 fission events were examined; all of these were fast neutron induced since the threshold is at 1·1 Mev. Seven events were found having light fragments of range 60μ and five where the range of the light fragment lay between 20 and 60μ. The longest range observed in this case was 243μ.

The general character of the events in all cases was similar to those observed in the slow neutron[1] and photofission experiments[4,5] i.e., the light particle appears to be an α-particle and is emitted preferentially near to 90° from the heavy fragments.

Deductions as to the relative frequency of binary and ternary fission in these experiments cannot be drawn with confidence since, with such a high background of tracks, it is not certain that the observers would find all ternary events. However, it appears that the frequency of ternary fission is similar to that observed in the slow neutron fission of U-235.

These experiments therefore throw further doubt on the theory advanced by Tsien[6] which suggests that the emission of the long-range fragments is connected with the excitation of the compound nucleus, being less favored the greater the value of the excitation energy.

* Part of this work was carried out while the author was still at AERE, and thanks are due to the Director, Sir John Cockcroft, for permission to use this material.

[1] E. W. Titterton, Nature (to be published).
[2] Tsien, Ho, Chastel, and Vigneron, J. phys. et radium **8**, 165 (1947).
[3] Tsien and Faraggi, Compt. rend. **225**, 294 (1947).
[4] E. W. Titterton and F. K. Goward, Phys. Rev. **76**, 142 (1949).
[5] E. W. Titterton and Brinkley, Phil. Mag. **41**, 500 (1950).
[6] S.-T. Tsien, J. phys. et radium **9**, 6 (1948).

Energy Storage and Light Stimulated Phosphorescence in Activated NaCl Crystals Induced by Gamma-Rays*

HARTMUT KALLMANN AND MILTON FURST
New York University, New York, New York
(Received June 6, 1951)

IN a previous paper[1] experiments on fluorescence, phosphorescence, and light stimulation in sodium chloride crystals activated with 1 percent silver chloride were described. Three different decay times occur with these crystals. First, immediately after excitation by high energy radiation, the emitted light decays quite slowly with a period (designated by lifetime of instantaneous phosphorescence) of minutes, hours, or even days, depending on the period, rate, and type of high energy radiation. Second, if such a crystal is then irradiated with light of the near ultraviolet or the visible region, even after its phosphorescent light emission has considerably decreased, a new light emission is stimulated mostly in the ultraviolet region around 2400 to 3000A which again decays rather slowly after the stimulating light has been switched off (designated by lifetime of stimulated phosphorescence). Third, if the stimulation of the crystal is deferred for a considerable period of time it should be expected that the amount of stimulated light decreases since the storage qualities of the crystal may not be perfect (designated by lifetime of storage).

This letter is concerned principally with experiments trying to link these processes to the phenomenon of color centers in alkali-halide crystals. It was found that the lifetime of instantaneous phosphorescence and that of stimulated phosphorescence are closely connected to each other and probably originate from the same energy levels. The lifetime of the instantaneous phosphorescence increases considerably with increasing time of irradiation applied at the same rate. This lifetime is also considerably longer if the same total amount of high energy radiation is applied during a long period than during a short period of irradiation. The same is true for the phosphorescence of the stimulated light. If the same total amount of stimulating light is applied during a short period, the decay of the stimulated light is shorter than the decay when the same stimulation is applied during a longer period. For instance, with a short-time gamma-irradiation (5 minutes) the instantaneous phosphorescence decreased to 14 percent of its original value within eight minutes, with a long-time irradiation (12,000 minutes) applied at the same rate the same percentage decrease was reached only after eight thousand minutes.

These increased lifetimes with extended periods of irradiation indicate that electron traps of different depths are responsible for this phosphorescence. The deeper traps which give a longer lifetime are filled to an equilibrium value only after the time of irradiation is extended for a time longer than the lifetime associated with these traps. Thus, with increased times of irradiation the deeper traps are filled to a higher degree and the lifetime is thus extended, whereas the shallower traps are already filled to an equilibrium level after a shorter time of irradiation.

It is noteworthy that the amount of stimulated light, however, is essentially independent of the time of irradiation by high energy radiation but depends mostly on the total dosage. This indicates that in those traps responsible for the observed phenomenon of long-time decay only a relatively small part of the energy which can be released as light is stored.

The third lifetime, namely, that of storage could not yet be determined very accurately. The amount of energy stored, which is indicated by the intensity of the stimulated light, does not decrease by more than two or three percent during one day under normal laboratory conditions according to our observations. This means a lifetime of the order of weeks or longer.

The idea presents itself that this long-time storage is in some way connected to the formation of color centers in alkali-halide crystals since it is known that these persist for long periods of time. It was observed that the crystals of high storage qualities show a considerable coloration after a gamma-dose of 1000 roentgens and more. The color was in this case brownish; the spectrum is similar to the absorption spectrum of the pure colored centered sodium chloride crystals.[2] This coloration increased with increasing doses and was thus as indicated above parallel to the stimulability of the crystal, and the color disappeared under constant irradiation with visible light as did the stimulability. Other crystals of the same kind but made differently, which also show a considerable fluorescence but a much smaller stimulability, exhibited a much smaller coloration. Repeated gamma-irradiation of the crystal up to 10,000 roentgens makes the crystal quite brown, but this color can be made to disappear by continued irradiation by the stimulating light, at which time the light stimulated intensity is very small.

As a result of these experiments the following tentative explanation for the process involved may be proposed The electrons removed from the negative ions in the crystal by high energy radiation are partly trapped (about 5 percent according to our experiments)[4] in lattice vacancies just as in normal alkali-halide crystals. From these it can be concluded that an energy of 2 to 3 electron volts is needed to remove the electron from color centers to the conductivity band. This large energy of more than 2 volts provides the reason for the stability of these excited states (color centers) for long periods of time. The stimulating light brings these electrons into the conductivity band from where either they fall down to a lower state which is connected with the activator and which transition produces the light emission, or they are trapped in electron traps close to the conductivity band (perhaps identical with the F' centers).[3] These traps are responsible for the instantaneous phosphorescence and for the phosphorescence of the stimulated light. Since the lifetimes for both decay processes are essentially the same, these lifetimes are both attributed to electron traps near the conductivity band. The stimulated light and the high energy radiation both bring the electrons in the conductivity band and their further behavior is independent of whether the electrons get into this band by stimulation or by high energy excitation.

Thus the color centers are responsible for the observed storage and explain its long persistence. The stimulating light produces an effect equivalent to the bleaching effect known to occur in alkali-halide crystals. The difference of the crystals investigated from the unactivated ones lies in the ability of their electrons in the conductivity band to go over, with a relatively high probability, to a special ground state (activator) with emission of light instead of recombining without light emission with the normal ground state.

The process which gives rise to the ultraviolet light emission in the silver activator has still to be explored in more detail. It may be that the activators create states near the valence band, which trap, as in the case of the zinc sulfides, the holes produced in the valence band.

* This work was sponsored by the Signal Corps Engineering Laboratory, Fort Monmouth, New Jersey.

[1] M. Furst and H. Kallmann, Phys. Rev. **82**, 964 (1951).

[2] N. F. Mott and R. W. Gurney, *Electronic Processes in Ionic Crystals* (Oxford University Press, England, 1940), Chapter IV.

[3] To be published soon.

A Comparison of the Experimental and Computed Fast Neutron Efficiencies of a Scintillation Counter*

GEORGE E. OWEN, JOHN NEILER, AND WILLIAM RAY
University of Pittsburgh, Pittsburgh, Pennsylvania
(Received May 21, 1951)

SCINTILLATION counters employing hydrogenous crystals or fluorescent hydrogenous liquids have been used by many investigators to detect fast neutrons.[1] Because the proton cross sections for neutrons are well known,[2] the efficiency of such neutron counters can be calculated.

The purpose of the following experiment was to compare the calculated counting rate for a one-inch cube of anthracene with the experimental counting rate. To perform this comparison a standarized PoBe neutron source was employed.

The neutrons from PoBe have a continuous energy distribution extending from zero to 11 Mev. The theoretical analysis in the following discussion utilizes the neutron energy distribution of Whitmore and Baker.[3]

If the total neutron intensity of the standard PoBe source is N', the number of neutrons incident upon the counter crystal is $N'\Omega=N$, where Ω is the fractional solid angle which the crystal subtends at the source. Then

$$N=C_1\int_0^\infty N(E)dE, \tag{1}$$

where $N(E)$ is the energy distribution of the PoBe neutrons.[3]

If the discriminator setting of the amplifier is E_D,[4] the number of neutron interactions in the counter crystal corresponding to neutron energies greater than E_D is

$$n=C_1\int_{E_D}^\infty Kl\sigma_H(E)N(E)dE; \tag{2}$$

l is the length of the crystal in cm, K is the number of hydrogen atoms per cm per barn,[5] and σ_H is the hydrogen cross section in barns.

Equation (2) does not give the number of neutrons which are counted. Consider a neutron interacting with a proton at an energy, $E>E_D$. The recorded pulse is produced by recoil proton, and all energies from 0 to E are possible for this proton. Therefore, the probability that an interaction will record is given by the ratio of the solid angle in which the protons have energies, $E_P>E_D$, to the total solid angle.

The solid angle which will not record has angular limits given by $E_P=E_D=E\sin^2\phi_0$; and the fraction of the interactions which will be counted is

$$(4\pi)^{-1}\left\{4\pi-2\pi\int_0^{2\phi_0}\sin\phi_{CM}d\phi_{CM}\right\}=(E-E_D)/E. \tag{3}$$

This assumes that the scattering is isotropic in the center-of-mass system; therefore, one would expect small deviations from Eq. (3) at energies greater than approximately 10 Mev.

The number of counted interactions, N_R, is therefore given by a combination of Eqs. (1), (2), and (3):

$$N_R=N\int_{E_D}^\infty Kl\sigma_H(E)[(E-E_D)/E]N(E)dE\Big/\int_0^\infty N(E)dE. \tag{4}$$

Equation (4) was computed by graphical methods as a function of E_D. The results of this computation for the specific solid angle, Ω, used in the experiment are shown in Fig. 1.

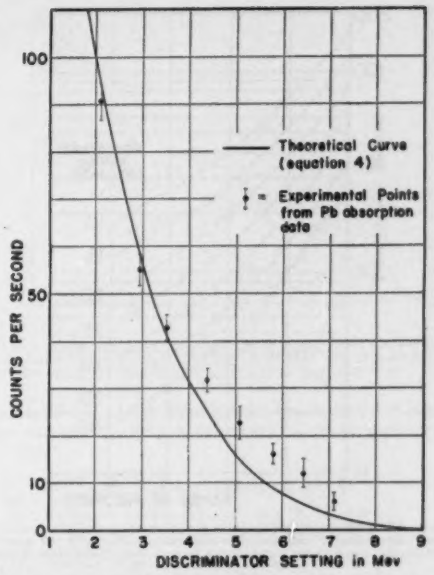

FIG. 1. Integral bias curves for the neutrons from PoBe. The statistical variations shown for the experimental points illustrate the limits of accuracy on the gamma-ray subtraction.

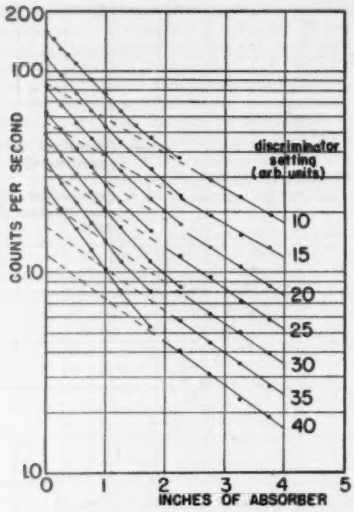

FIG. 2. The Pb absorption curves of the radiations from PoBe, as a function of discriminator settings. The absorption coefficient for the gamma-contribution was 0.59 cm^{-1} and for the neutron contribution is 0.16 cm^{-1}.

The radiations from the standard PoBe source were measured with a one-inch anthracene cube and a 5819 photomultiplier. To avoid as much wall scattering as possible the experiment was performed in the center of a large room.

Since the total counting rate resulted from both gamma-rays and neutrons, a lead absorption curve (using absorbers of area equal to the subtended area of the crystal face) was run at each discriminator setting. The neutron component was obtained by analysis of the absorption curves shown in Fig. 2.

The discriminator was calibrated by measuring the pulse heights from a Po alpha-source. Use was made of the published ratio[6] of Po alpha pulse heights to proton pulse heights and the variation of pulse height with proton energy.[7]

In view of the reliance of this calculation on widely different sources of data, the fit between the calculated curve and the experimental points in Fig. 1 is quite satisfactory and shows a definite correlation.

This experiment illustrates two fundamental points. First, all fast neutron counting performed with scintillation counters must be subjected to the discriminator correction factor of Eq. (3), and second, the correlation between experiment and theory in Fig. 1 suggests that one should be able to measure fast neutron intensities by these methods quite accurately.

We should like to express our gratitude to the Westinghouse Research Laboratories, APD, for the use of their facilities and in particular the PoBe standard. Also we wish to thank Professor A. J. Allen and Professor D. Halliday for their constant aid and many helpful suggestions. In addition we should like to acknowledge gratefully the aid of Mr. S. Levine and Mr. Blair Rhodes.

* Assisted by the joint program of the ONR and AEC.

[1] W. G. Moulton and C. W. Sherwin, Rev. Sci. Instr. **20**, 766 (1949); Jastram, Cleland, Benade, and Hughes, Phys. Rev. **80**, 327 (1950); K. H. Sun and W. E. Shoupp, Rev. Sci. Instr. **21**, 395 (1950); H. B. Frey, Rev. Sci. Instr. **21**, 886 (1950); Poss, Falk, and Yuan, Phys. Rev. **83**, 242(A) (1951); Neiler, Owen and Allen, Phys. Rev. **83**, 242(A) (1951).

[2] Goldsmith, Ibser, and Feld, Revs. Modern Phys. **19**, 259 (1947); R. K. Adair, Revs. Modern Phys. **22**, 249 (1950).

[3] B. G. Whitmore and W. B. Baker, Phys. Rev. **78**, 799 (1950). This distribution was obtained by photographic plate techniques.

[4] E_D is the minimum energy at which a recoil proton in the crystal records.

[5] K is 0.0424 atom per cm-barn in the case of anthracene.

[6] Franzen, Peele, and Sherr, Phys. Rev. **79**, 742 (1950).

[7] Frey, Grim, Preston, and Gray, Phys. Rev. **82**, 372 (1951).

Energy Dependence of the Beta-Gamma Angular Correlation in Sb^{124}

E. K. DARBY AND W. OPECHOWSKI
Department of Physics, University of British Columbia, Vancouver, Canada*
(Received May 28, 1951)

THE theory of the beta-gamma angular correlation developed by Falkoff and Uhlenbeck[1] predicts that this correlation (if any) is a function of the beta-energy. Now, in the case of Sb^{124}, Ridgeway[2] and Beyster and Wiedenbeck[3] have measured the beta gamma-angular correlation integrated over all beta-energies greater than about 1 Mev. Only very recently Stevenson[4] has reported briefly on his measurement of the differential angular correlation (i.e., as a function of the beta-energy) using a beta-lens spectrometer. Here we wish to state the results of a measurement of the differential correlation coefficient $a(E)=[W(\pi, E)-W(\frac{1}{2}\pi, E)]/W(\frac{1}{2}\pi, E)$ by means of a Chalk River design twelve-channel kicksorter,[5] $W(\theta, E)$ being the beta-gamma correlation function for the beta-energy E.

First the integrated angular correlation was determined using as a beta-counter 20 mg/cm^2 of anthracene flakes and as a gamma-counter a half-inch thick crystal of anthracene, both in conjunction with RCA 5819 photomultipliers. The lower energy beta-groups were absorbed by using 260 mg/cm^2 of Al in front of the beta-counter. Measurements were carried out at 10° intervals from 90° to 180°. The source, less than 1 mg/cm^2 in thickness, and the beta-counters were enclosed in a vacuum chamber. Corrections were applied for the gamma-gamma-coincidences and the finite angular resolution of 20°. The results so obtained fitted closely a curve $1-0.23\cos^2\theta$, which is in essential agreement with Beyster and Wiedenbeck.[3]

Next, in order to measure the differential angular correlation, the thin beta-counter was replaced by a half-inch thick anthracene crystal so that pulses proportional to the beta-energy were obtained.[6] The bias was set to accept only pulses corresponding to 1 Mev and over. With this bias the gamma-gamma coincidence rate amounted, on the average, to only 17 percent of the beta-gamma coincidence rate, which is consistent with the accepted decay scheme of Sb^{124}. A coincidence mixer was used to control a gate circuit between the beta-pulses and the twelve-channel kicksorter. We thus measured the energy distribution of only those beta-particles which gave rise to coincidence counts. Measurements were done at 90° and 180°, so that the correlation coefficient $a(E)$ could be obtained for the twelve energy ranges corresponding to twelve kicksorter channels. The channels were evenly spaced from 1 Mev up, the width of each channel being about 0.11 Mev. The energy scale was determined by measuring the beta-spectrum with the kicksorter and assuming the end point of the spectrum to lie at 2.37 Mev. Readings were taken alternatively in the 90° and 180° positions for short times, so that fluctuations in the photomultiplier high tension, amplifier gain, and kicksorter channel definition would tend to average out. The results of four separate series of measurements are plotted in Fig. 1. The points shown in the figure include corrections for the gamma-gamma coincidences, finite angular resolution, and decay of the source. The results are consistent with the two values of $a(E)$ reported by Stevenson.[4]

In Fig. 1 we also show two curves that represent $a(E)$ for two possible assignments of angular momenta of the nuclear states involved: 1→1→0 and 3→2→0. We do not claim that these are the only two possibilities which are not quite inconsistent with out experimental results (see reference 3). The curves have been calculated using Falkoff and Uhlenbeck's formulas and tables,[1] and assuming that the matrix element B_{ij} is the only one which has to be taken into account. This assumption seems to be reasonable in view of Langer's result (quoted by Wu[7]) regarding the forbidden shape of the beta-spectrum of Sb^{124}

When comparing the experimental results with the theoretical curves, one should bear in mind that the points below $E=1.6$ Mev

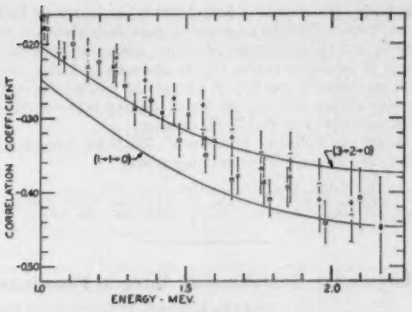

FIG. 1. The beta-gamma correlation coefficient $a(E)$ as a function of the beta-energy E. Experimental points corresponding to different series of measurements are represented by different signs (0, +, ×, −). The full curves are those calculated from the theory mentioned in the text.

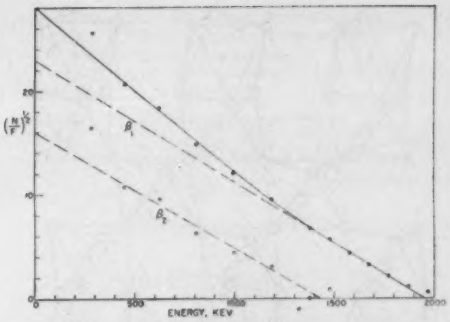

FIG. 1. Kurie plot of the positrons from 24-minute Ag^{106}. The end point of the lower energy spectrum, 1.43 Mev, is obtained after subtracting 515 kev from the 1.945-Mev end point of the higher energy spectrum.

correspond to a superposition of a beta-spectrum with end point at 2.4 Mev and a beta-spectrum with end point at 1.6 Mev. The same holds for the comparison of $a(E)$ with the measured value of the integrated correlation coefficient. A more detailed discussion of fitting the experimental results with the theory and a full report of the experiment itself will be published in the *Canadian Journal of Physics*.

* This work has been supported by the National Research Council of Canada.

[1] D. L. Falkoff and G. E. Uhlenbeck, Phys. Rev. **79**, 323 and 334 (1950).
[2] S. L. Ridgeway, Phys. Rev. **78**, 821 (1950).
[3] J. R. Beyster and M. L. Wiedenbeck, Phys. Rev. **79**, 169 (1950).
[4] D. T. Stevenson, Phys. Rev. **82**, 333 (1951).
[5] Moody, Battell, Howell, and Taplin, N.R.C. of Canada Report CREL 464 (1950).
[6] J. I. Hopkins, Rev. Sci. Instr. **22**, 29 (1951).
[7] Chien-Shiung Wu, Revs. Modern Phys. **22**, 386 (1950).

24-Minute Radiations from Ag^{106}

W. L. BENDEL,* F. J. SHORE, AND R. A. BECKER
Physics Research Laboratory, University of Illinois, Urbana, Illinois†
(Received June 14, 1951)

THE radiations of Ag^{106} have been investigated in this laboratory. The sources were produced by irradiation of thin silver foils (0.1 mil to 1 mil in thickness) with 22-Mev x-rays employing the probe method.[1] The half-life was determined to be 24.0±0.2 minutes.

Using a 180° magnetic spectrometer, two groups of positrons were found with maximum energies of 1.945±0.015 and 1.5±0.1 Mev. A weak conversion line at 0.5 Mev also was found. This is probably the 0.51-Mev transition reported[2–4] in Pd^{106} following the decay of both Rh^{106} and 8-day Ag^{106}. If we assume that the higher energy positron goes to the ground state of Pd^{106}, the data are consistent with the other component going to a 0.51-Mev level. Figure 1 shows the Kurie plot of the positrons obtained with 0.25-mil Ag foils and shows 1.43 Mev as the end point of the lower energy spectrum. After correcting for K-capture, 71 percent of the transitions go directly to the ground state while 29 percent go to the excited state of Pd^{106}. In each case, $\log ft = 4.93$, and the transitions are presumably allowed. This is consistent with the assignment of zero spin to the ground state of Pd^{106}, a spin of two, as suggested by the work of Metzger and others,[4,5] to the excited state of Pd^{106}, and a spin of one for the Ag^{106} parent state. The parity of all three states would be identical.

The magnetic spectrometer also showed a very weak continuous negatron component of approximately 24-minute half-life. If this is assumed to be a beta-minus activity, it has an end point of 0.45±0.10 Mev and represents 2 percent of the disintegrations, $\log ft$ again being 4.9. Both scintillation spectrometer and absorption measurements indicate gamma-rays of energy greater than 0.6 Mev.

* AEC Predoctoral Fellow.
† Aided by the joint program of the ONR and AEC.
[1] R. A. Becker, to be published.
[2] Mei, Huddleston, and Mitchell, Phys. Rev. **79**, 1010 (1950).
[3] Deutsch, Roberts, and Elliott, Phys. Rev. **61**, 389(A) (1942); Alburger, der Mateosian, Goldhaber, and Katcoff, Phys. Rev. **82**, 332(A) (1951).
[4] W. C. Peacock, Phys. Rev. **72**, 1049 (1947).
[5] F. Metzger, Phys. Rev. **79**, 398 (1950); F. Metzger and M. Deutsch, Phys. Rev. **78**, 551 (1950); E. L. Brady and M. Deutsch, Phys. Rev. **78**, 558 (1950); A. H. Williams and M. L. Wiedenbeck, Phys. Rev. **78**, 822 (1950); J. R. Beyster and M. L. Wiedenbeck, Phys. Rev. **79**, 411 (1950).

The Lorentz Correction in Hexagonal Barium Titanate

JACK R. TESSMAN
Department of Physics, University of California, Berkeley, California
(Received June 13, 1951)

THE exact Lorentz correction has been computed previously[1] for the cubic modification of barium titanate and expressions obtained for the actual electric field, at each ion, due to the dipole moments of all the other ions in the crystal. Inserting the known values for the electronic polarizabilities of the Ba, I, and Ti ions, and assuming that only the Ti ions undergo ionic polarization, it was concluded that the ionic polarizability of the Ti ion must have a value of 0.9×10^{-24} cm³ for the crystal to be ferroelectric.

Cubic $BaTiO_3$ has a perovskite structure in which the Ti ions are at the centers of equal regular O octahedra all linked together by sharing corners. In the resulting structure there are infinite linear chains of alternating O and Ti ions, and it has been suggested that the strong dipole interaction of the ions on such a chain makes it possible for the crystal to be ferroelectric.

In the hexagonal modification[2] of $BaTiO_3$, the unit cell contains six units of $BaTiO_3$. The c axis is perpendicular to the rhombic base. The Ti ions are located within O octahedra and every O octahedron is a member of three chains running in directions which are nearly mutually perpendicular and which make equal angles with the c axis. Each chain consists of three octahedra, each octahedron sharing a corner with its neighbor or neighbors in the chain. The octahedron at each end of the chain shares a face with the octahedron at the end of the succeeding chains. The Ba ions are all located outside of the O octahedra. Figure 1 is a schematic representation of the O octahedra. (To simplify the figure further, each octahedron is shown in, at most, only two chains. The arrangement of the third chain in each case is obvious.)

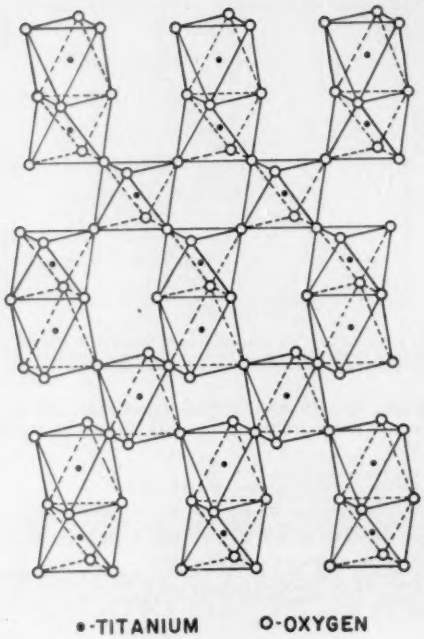

FIG. 1. Schematic idealized representation of the oxygen octahedra in hexagonal barium titanate.

Experimentally, hexagonal $BaTiO_3$ has been found to be nonferroelectric. I have applied the Lorentz local field correction to the hexagonal modification to ascertain if it leads reasonably to the conclusion that the hexagonal modification should be nonferroelectric.

To simplify the calculation a little, the crystal structure was idealized, somewhat. The O octahedra were all taken as equal regular octahedra with the Ti ions at the centers and with dimensions the same as the octahedra of the cubic modification.[2] The directions of the O octahedron chains were taken as mutually perpendicular. The resulting dimensions of the unit cell of the idealized hexagonal structure are $a'=5.68$A, $c'=13.9$A, and $c'/a'=2.45$, compared with the actual dimensions of $a=5.735$A, $c=14.05$A, and $c/a=2.450$.

At the site of each O and Ti ion, the local field was calculated due to the polarization of all the other O and Ti ions contained with a cylinder of infinite length with axis parallel to the c axis and of radius equal to $a'/\sqrt{3}=0.58a'$ circumscribed about the particular site as a center. As in Slater's paper, it was assumed that only the Ti ions undergo ionic polarization. The field due to the polarization of the Ba ions, P_{Ba}, was approximated as the ordinary Lorentz correction of $4\pi P_{Ba}/3$. Ignoring the effect of the material outside of the cylinders, is equivalent to approximating the surrounding material as being uniformly polarized.

The calculation indicated a necessary value of 1.6×10^{-24} cm^3 for the ionic polarizability of the Ti to produce ferroelectricity in the hexagonal modification. This is appreciably greater than the necessary value of 0.9×10^{-24} cm^3 calculated for the cubic modification and presumably just barely attained there at the ferroelectric Curie point temperature of 120°C. Therefore, subject to the assumption that only the Ti ions undergo ionic polarization, it may reasonably be expected that hexagonal $BaTiO_3$ should be nonferroelectric. This is consistent with the experimental finding.

Physically, the absence of ferroelectricity in hexagonal $BaTiO_3$ may be traced to (1) the existence of short finite chains of alternating Ti and O ions instead of infinite chains, and the noncollinearity of successive chains, (2) the absence of a highly polarizable O ion between the two Ti ions at the neighboring ends of successive chains, and (3) the larger distance between these Ti ions as compared with the Ti−O distance.

I should like to thank Professor C. Kittel for proposing this problem and for making helpful suggestions.

[1] J. C. Slater, Phys. Rev. **78**, 748 (1950).
[2] R. D. Burbank and H. T. Evans, Jr., Acta Cryst. **1**, 330 (1948).
[3] Helen D. Megaw, Proc. Roy. Soc. (London) **189A**, 261 (1947).

Note on the Bose-Einstein Integral Functions*

JOHN E. ROBINSON
Chemistry Department, Duke University, Durham, North Carolina
(Received June 18, 1951)

EXPANSIONS of the Bose-Einstein integral functions

$$F(\sigma,\alpha)=[1/\Gamma(\sigma)]\int_0^\infty (x^{\sigma-1}/e^{x+\alpha}-1)dx \qquad (1)$$

in powers of α, which would correspond to well-known developments of the Fermi-Dirac integral functions,[1] are desirable for discussing the behavior of the $F(\sigma,\alpha)$ for small α. However, the power series for the Bose-Einstein functions seems not to be generally known.

The $F(\sigma,\alpha)$ defined in Eq. (1) can be continued analytically for complex σ by an integral, say $G(\sigma,\alpha)$, which is analytic over the entire σ-plane and for all positive α, save for the singularity at $\sigma=1$ when $\alpha=0$, by a procedure similar to that of McDougall and Stoner.[1] Here, however, we seek only a continuation for all σ and *small* positive α, and shall follow a simpler treatment. By the use of Mellin transforms[2] one can express the Bose functions in terms of power series whose functional behavior for small α is translucent, and which are, for those σ of greatest interest, particularly well suited to numerical computation when $\alpha<1$.

In deriving the result it is sufficient to consider the case $\alpha>0$, $\sigma>1$, and $\sigma\neq$integer. The Mellin transform of $F(\sigma,\alpha)$ is then

$$\mathfrak{F}(\sigma,s)=\int_0^\infty F(\sigma,\alpha)\alpha^{s-1}d\alpha=\int_0^\infty \sum_{n=1}^{\infty}\frac{e^{-n\alpha}}{n^\sigma}\alpha^{s-1}d\alpha$$
$$=\Gamma(s)\zeta(s+\sigma), \qquad (2)$$

where $\zeta(s+\sigma)$ is the ordinary Riemann zeta-function. The inverse transformation then gives:

$$F(\sigma,\alpha)=(1/2\pi i)\int_{c-i\infty}^{c+i\infty}\mathfrak{F}(\sigma,s)\alpha^{-s}ds$$
$$=(1/2\pi i)\int_{c-i\infty}^{c+i\infty}\alpha^{-s}\Gamma(s)\zeta(s+\sigma)ds, \quad c>0. \qquad (3)$$

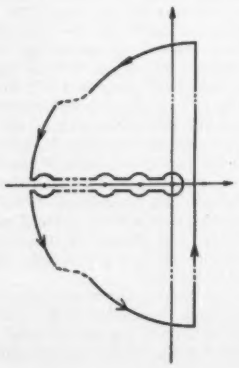

FIG. 1. Contour for evaluating the Mellin integral of Eq. (3).

For $|\alpha|<2\pi$, the contour of Fig. 1, which is indented at the (simple) poles of the integrand, can be used. (The cut along the negative axis of reals makes possible immediate use of the Stirling asymptotic expansion of $\log\Gamma(s)$[3] to show that the integrand vanishes on the arcs as the contour recedes to infinity.) The function $\zeta(s+\sigma)$ has a simple pole at $s=1-\sigma$ with residue $+1$, and $\Gamma(s)$ has simple poles at $s=-n$ with residues $(-1)^n/n!$ Consequently, we have

$$F(\sigma,\alpha)=\Gamma(1-\sigma)\alpha^{\sigma-1}+\sum_{n=0}^{\infty}\frac{(-)^n}{n!}\zeta(\sigma-n)\alpha^n. \tag{4}$$

This is patently an analytic function of σ if $\sigma\leqslant 0$ and for all non-integral σ.

If now $\sigma=m$, a positive integer, although $\Gamma(1-\sigma)\alpha^{\sigma-1}$ and one term of the series in Eq. (4) become infinite separately, their sum remains finite. We have

$$F(m,\alpha)=\lim_{\sigma\to m}\left\{\Gamma(1-\sigma)\alpha^{\sigma-1}+\frac{(-)^{m-1}}{(m-1)!}\zeta(\sigma-m+1)\alpha^{m-1}\right\}$$
$$+\sum_{n=m-1}^{\infty}\frac{(-)^n}{n!}\zeta(\sigma-n)\alpha^n=\frac{(-)^{m-1}}{\Gamma(m)}\left\{C+\frac{\Gamma'(m)}{\Gamma(m)}-\log\alpha\right\}\alpha^{m-1}$$
$$+\sum_{n=m-1}^{\infty}\frac{(-)^n}{n!}\zeta(\sigma-n)\alpha^n,$$

where C is Euler's constant. Therefore, by the principle of analytic continuation, Eq. (4) holds for *all* σ. The series converges absolutely if $|\alpha|\leqslant 2\pi$.

Equation (4) readily yields the differentiation property of the Bose functions:

$$\partial^n F(\sigma,\alpha)/\partial\alpha^n=(-)^n F(\sigma-n,\alpha).$$

When $\alpha\to 0$, it is seen that $F(\sigma,\alpha)$ diverges as $\alpha^{-|\sigma-1|}$ if $\sigma<1$, and as $\log(1/\alpha)$ if $\sigma=1$, and of course converges toward $\zeta(\sigma)$ if $\sigma>1$. If $1<\sigma\leqslant 2$, then $F(\sigma,\alpha)$ has an infinite slope at the origin although the function itself remains finite. Clearly, the origin $\alpha=0$ is a branch point for all the $F(\sigma,\alpha)$.

The series in Eq. (4) converges quite rapidly in the neighborhood of $\alpha=0$ for positive σ which are not too large. For example, with an accuracy of at least 1 percent when $\alpha\leqslant 1$, we have

$$F(\tfrac{1}{2},\alpha)=1.77\alpha^{-\frac{1}{2}}-1.46+0.208\alpha-0.0128\alpha^2,$$
$$F(\tfrac{3}{2},\alpha)=-3.54\alpha^{\frac{1}{2}}+2.61+1.46\alpha-0.104\alpha^2+0.00425\alpha^3,$$
$$F(5/2,\alpha)=2.36\alpha^{\frac{1}{2}}+1.34-2.61\alpha-0.730\alpha^2+0.0347\alpha^3.$$

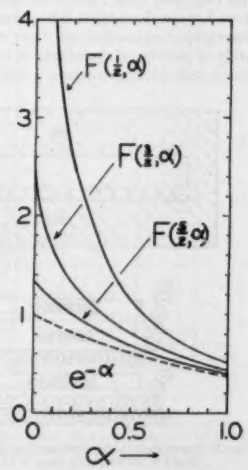

FIG. 2. The Bose-Einstein integral functions $F(\frac{1}{2},\alpha)$, $F(\frac{3}{2},\alpha)$, and $F(5/2,\alpha)$ for the range $0\leqslant\alpha\leqslant 1$.

These functions, together with $\alpha^{-\sigma}$, are shown graphically in Fig. 2 for the range $\alpha\leqslant 1$. For $\alpha>1$, the $F(\sigma,\alpha)$ are conveniently evaluated by the familiar series of exponentials.

The author wishes to thank Professor F. London for his interest in this work.

* This work was done under contract with the ONR.

[3] J. McDougall and E. Stoner, Trans. Roy. Soc. (London) **A237**, 67 (1938).
[3] E. C. Titchmarsh, *Introduction to the Theory of Fourier Integrals* (Oxford University Press, London, 1948), pp. 7 ff., 190 ff. G. G. MacFarlane, Phil. Mag. **40**, 188 (1949).
[3] E. T. Whittaker and G. N. Watson, *Modern Analysis* (Cambridge University Press, London, 1947), p. 276.

Radioactive Decay of I^{131}

E. W. EMERY
Medical Research Council, Radiotherapeutic Research Unit, Hammersmith Hospital, London, England
(Received June 18, 1951)

THE principal radiations emitted in the disintegration of I^{131} have been organized into schemes by Metzger and Deutsch (M.D.)[1] and by Kern, Mitchell, and Zaffarano (K.M.Z.).[2] These are shown in Fig. 1, and it will be seen that they include essentially the same features and differ only in the soft beta-ray branch. However, a number of less prominent features remain to be accounted for. Brosi *et al.*[3] have found that a small fraction of the disintegrations lead to the 12-day metastable level of Xe^{131}; a gamma-ray of an energy approximately 720 kev occurring in about 5 percent of disintegrations has been discovered by Cavanagh[4], and subsequently reported by Cork *et al.*[5], and by Zeldes *et al.*;[6] Cork[5] has produced a convincing photographic spectrum showing K and L conversion lines due to a 177-kev gamma; Zeldes[6] has produced evidence of a weak 810-kev beta-ray. All these radiations, except the 810-kev beta-ray, have been assembled by Cork[5] into a scheme which must, however, be very far from the truth. As the authors point out, there are wide anomalies in the intensities. For instance, in one branch the 600-kev beta-ray which arises from 85 percent of the disintegrations is shown followed by the 723-kev gamma-ray (5 percent) leading to the metastable level (1 percent). Moreover, the scheme places both the 637- and the 364-kev gamma-rays in the soft beta-branch, although M.D. have shown that only the first of these is associated with the soft beta-ray, the other being in the 600-kev beta-

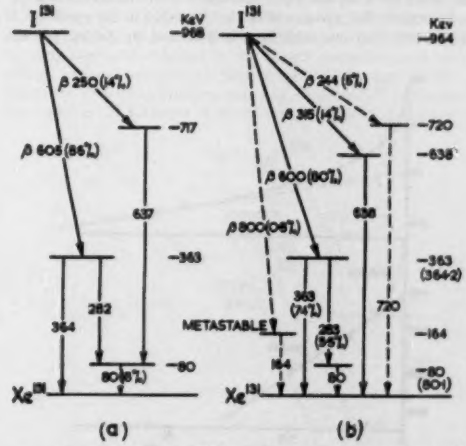

FIG. 1. Decay schemes for I^{131}: (a) Kern, Mitchell, and Zaffarano (K.M.Z.); (b) Metzger and Deutsch (M.D.) with proposed additional branches (dotted).

branch. A further objection to this decay scheme is that it indicates an energy difference between I^{131} and Xe^{131} nuclei of 1.479 Mev, a value which can be shown to be too great. For, since the dose rate in air produced by a gamma-emitting source is closely proportional to the quantum energy over the range 0.1–1.0 Mev, it follows that a measurement of the gamma-ray ionization from a source of known disintegration rate gives an estimate of the energy emitted per disintegration as gamma-rays; and, since the ratio of mean beta-energy to the maximum does not vary greatly among isotopes of a given atomic number, a measurement of the beta-energy emitted from such a source gives an estimate of the total energy carried by beta-particles and neutrinos. The sum of these two quantities is the total energy difference between parent and daughter nucleus. Such energy measurements have been carried out by Gray,[7] and by comparison with the I^{131} samples of the standard disintegration rate now distributed by the National Bureau of Standards, which are based on 4π solid angle beta-counting and are therefore independent of the assumed decay scheme, they yield values of the beta- and gamma-energy which are in complete agreement, within experimental error, with either M.D. or K.M.Z., and demonstrate that the total energy of disintegration cannot differ from 0.964 Mev by more than about 10 percent.

It therefore seems reasonable to assume that either the M.D. or K.M.Z. scheme disposes correctly of the radiations with which they both deal, and that the other radiations are to be accounted for by further branching of the spectrum. It is possible to differentiate between these two schemes by measurement of the 80-kev gamma-ray. Both groups detect this gamma-ray by the conversion line in the beta-spectrum, and they are in substantial agreement as to the number of conversion electrons produced; they do, however, differ widely in the values assigned to the conversion coefficient, K.M.Z. giving 15.5 unconverted quanta per 100 disintegrations and M.D. only 3.4. The actual intensity can be conveniently assessed experimentally by measurement of the ionization in a copper chamber. The effect of the 80-kev radiation is greatly enhanced by the photoelectric effect and can be separated out by absorption in tin (Fig. 2). Correction having been made for the relative stopping power of copper and for the effect of secondary electrons arising within the air cavity, it is found that the intensity is 2.6 quanta per 100 disintegrations. So small a value could not occur if the 80-kev line were in cascade with the 637-kev line, and it follows that the M.D. scheme is to be preferred, even though this rules out the tempting hypothesis that the 720-kev gamma-ray arises from the 717-kev level shown in the K.M.Z. scheme.

As regards the presence of further branches in the spectrum, it is probable that one such branch is formed by Zeldes' 810-kev beta-ray leading to the metastable level at 164 kev. The sum of the energies is correct within reasonable experimental error; and, so far as can be judged, the intensities are in agreement. The author has extracted the Xe^{131} from three I^{131} samples, and by estimating the activity by means of a cavity ionization chamber it was found that the frequency of disintegrations leading to the metastable level is 0.8 ± 0.1 percent. This compares reasonably with the statement in Zeldes' paper that the frequency of the beta-ray is "rather less than 1 percent." Another branch might be formed by the 720-kev gamma-ray associated with a 240-kev beta-ray, for the latter could quite easily have escaped detection in the presence of the more intense 315-kev branch. The inclusion of these features leads to the decay scheme given in Fig. 1(b), and it is suggested that this scheme is in reasonable accordance with the known facts concerning the disintegration of I^{131}. However, the 177-kev gamma-ray is still not accounted for. Its intensity must be quite small, since there is no sign of it in any of the spectra published by M.D. and K.M.Z.; and moreover, if it occurred in more than 5 percent of disintegrations it would certainly have been apparent in the tin absorption curve (Fig. 2). This gamma-ray might conceivably occur in a separate branch with a weak 787-kev beta-ray; or alternatively, if it were in cascade with the 720-kev line, the associated beta-branch would have an energy of 80 kev, and in this region of the spectrum could easily have escaped detection.

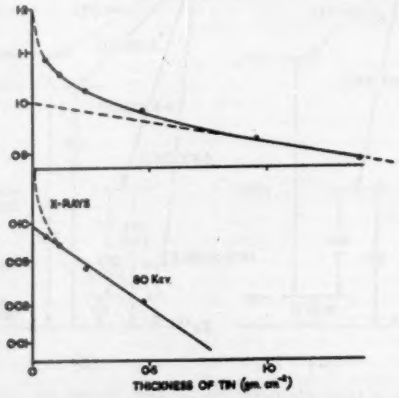

FIG. 2. Absorption of I^{131} gamma-rays in tin.

[1] F. Metzger and M. Deutsch, Phys. Rev. **74**, 1640 (1948).
[2] Kern, Mitchell, and Zaffarano, Phys. Rev. **76**, 71 (1949).
[3] Brosi, DeWitt, and Zeldes, Phys. Rev. **75**, 1615 (1948).
[4] P. E. Cavanagh, private communication (1949).
[5] Cork, Rutledge, Stoddard, Branyan, and Childs, Phys. Rev. **81**, 482 (1951).
[6] Zeldes, Brosi, and Ketelle, Phys. Rev. **81**, 643 (1951).
[7] L. H. Gray, Brit. J. Radiology **22**, 673 (1949).

Capture of μ-Mesons in Heavy Elements*

F. B. HARRISON, J. W. KEUFFEL, AND G. T. REYNOLDS
Palmer Physical Laboratory, Princeton University, Princeton, New Jersey
(Received June 18, 1951)

WE have used large liquid scintillation counters[1] to study the processes associated with the stopping of negative μ-mesons in heavy elements. The reasonable efficiency of the liquid scintillators for gamma-rays and neutrons of a few Mev has permitted us to use the non-ionizing radiations following nuclear capture for mean life measurements in Cu and Sb.

The experimental arrangement is shown in Fig. 1. A coincidence circuit (resolving time 3 μsec) selects events (AS_1S_2-X); and for each such event the relative lag between S_1 and S_2 is measured by photographing an oscilloscope trace on which are presented the scintillator pulses and the output of a chronotron timing circuit.[2] Thus we look for events where a penetrating cosmic-ray particle

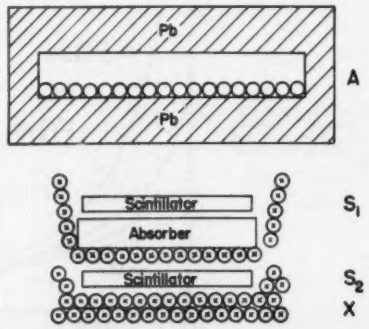

FIG. 1. Experimental disposition: Only the actual volume of scintillator liquid is shown; each tank is 12 in. by 12 in. by 1 in.

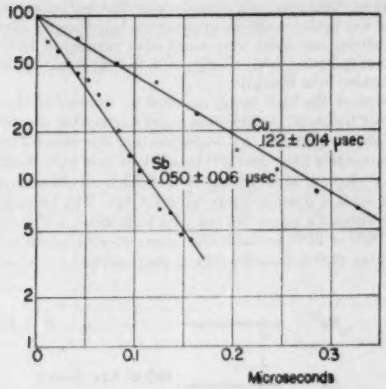

FIG. 2. Integral distributions of delayed counts from the meson capture radiation. The number of counts has been normalized to agree at time zero.

at sea level stops in the absorber, and is followed by a delayed non-ionizing ray which crosses the upper anticoincidence bank and is detected in S_2.

The timing uncertainty was measured by selecting events in which S_1 and S_2 were tripped simultaneously by a fast meson; the resulting lag distribution was approximately gaussian with a mean deviation of 4.5 mμsec. We therefore disregarded events delayed by less than 15 mμsec. Since the total number of instantaneous events selected by our triggering system was only about three times the number of delayed counts, the background due to this source could be ignored.

Integral delay distributions for Cu and Sb are shown in Fig. 2. We have subtracted small backgrounds due to random noise pulses and to the bremsstrahlung of decay positrons from positive mesons stopping in the absorber. The former are due mainly to events where a meson passes obliquely through A and S_1 (but misses the anticoincidence counters X) and is followed by a random noise pulse in S_2. Since noise pulses of this type occur with equal probability before and after the events AS_1, a knowledge of the number of negative lags permits us to correct for the number of positive lags due to noise. The bremsstrahlung background was identified by its characteristic 2.1 μsec decay time, at times long compared to the decay of the negative meson capture radiation, and was corrected for by extrapolation back to the shorter times. For Cu, the combined background rate, per hour of counting and per mμsec of delay, was only 1/10 the maximum counting rate due to meson capture, while for Sb it was only 1/20 the maximum rate.

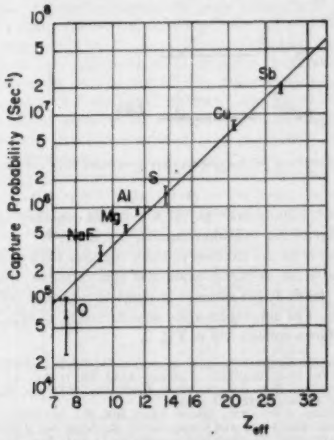

FIG. 3. Capture probability *vs* Z_{eff}. The effective atomic numbers are those calculated by Wheeler. Points for the light nuclei are from Ticho, with the result of Valley for Al averaged in. The line is drawn with a slope corresponding to the Z_{eff}^4 law.

The mean lives given in Fig. 2 have been computed according to the method of Peierls,[5] and the errors quoted are purely statistical. We believe our instrumental errors are smaller than these.

Wheeler[4] has predicted that the capture probability should go as Z_{eff}^4, where Z_{eff} is an effective atomic number defined in his paper. In Fig. 3 we have plotted out values for the capture probability, together with those of Ticho[6] and Valley[6] for the light elements. We find good agreement with the Z_{eff}^4 law. While the earlier results could be fitted fairly well with a simple Z^4 dependence, our results show the need for using Z_{eff} for the heavy elements, where the effect of the finite nuclear radius becomes important.

A knowledge of the capture probabilities permits one in principle to find the value of the coupling constant for the μ-meson-nucleon interaction. An evaluation of this constant more precise than the estimate given by Wheeler and Tiomno[7] awaits, however, a more detailed theoretical analysis of the nucleonic dynamics involved in the meson capture process.

* Supported by the joint program of the AEC and ONR.
[1] Reynolds, Harrison, and Salvini, Phys. Rev. **78**, 488 (1950).
[2] J. W. Keuffel, Rev. Sci. Instr. **20**, 197 (1949).
[3] R. Peierls, Proc. Roy. Soc. (London) **A149**, 467 (1935).
[4] J. A. Wheeler, Revs. Modern Phys. **21**, 133 (1949).
[5] H. K. Ticho, Phys. Rev. **74**, 1337 (1948).
[6] G. E. Valley, quoted by B. Rossi, *Cosmic Rays* (Butterworths, London, 1949), p. 55.
[7] J. Tiomno and J. A. Wheeler, Revs. Modern Phys. **21**, 153 (1949).

Gamma-Radiation Associated with Radium and Daughter Products*

J. M. CORK, C. E. BRANYAN, A. E. STODDARD, H. B. KELLER, J. M. LEBLANC, AND W. J. CHILDS
University of Michigan, Ann Arbor, Michigan
(Received June 14, 1951)

MANY studies have been made of the energies of the gamma-rays emitted by the various decay products of radium. Early spectrometric observations by Ellis[1] and associates and later by Siegbahn[2] have resulted in the correct assignments of many strong, internally converted gamma-rays. Subsequent measurements by various techniques including electron-pair production[3] have shown the existence of additional gamma-rays particularly

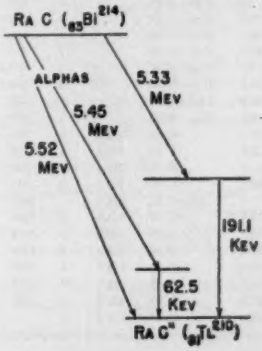

FIG. 1. Decay scheme for RaC to RaC''.

at higher energies. Considerable divergence exists in the reported values by even the same observers using different experimental methods. Since pure radium has a high specific activity, it is an ideal source for calibrating fixed-field magnetic spectrometers provided its gamma-energies are accurately evaluated. On this account a re-survey of the electron lines due to internal conversion and to photoemission from various radiators has been carried out in spectrometers calibrated by the known energies of the iodine 131 gamma-rays with extrapolated field values above 400 kev. A strong source of radium *D* was also available.

The *K-L-M* differences in the observed electron spectra in most cases show clearly the atomic number of the isotope in which each gamma-transition occurred. Generally an adjustment in the previously reported energies of the gamma-rays appears to be warranted. Certain previously unreported gamma-rays have been discovered and conversely, some gamma-radiations do not appear to exist as reported.

In the 0.04 percent branching decay of RaC to RaC″ (Tl^{210}) three alpha-groups with energies as shown in Fig. 1 are known to exist[4] but no gamma-rays had been noted. Conversion lines with *K-L* differences characteristic of $Z=81$, giving energies of 62.5 and 191.1 kev are now observed. Since these energies are compatible with the energy differences of the alpha-rays, the level plan as proposed in Fig. 1 appears justified.

A thorough study has been made of the low energy gamma-radiations in RaE (Bi^{210}) following beta-emission from strong sources of RaD. The magnetic field was reduced so as to give a dispersion of about 3 mm per kev, and the 46.4-kev gamma-ray yielded clearly resolved L_I, L_{II}, L_{III}, *M*, *N*, and *O* electron lines of such intensity that any other similar gamma-ray with intensity 1/100 as great would be detected. No evidence whatever could be found for the existence of the 23-kev gamma as reported[5] by Tsien from cloud-chamber observations nor for his other low energy radiations. Aluminum and critical absorption methods also failed to give any evidence for the presence of these energies. However, fairly strong radiations were found with energies of 13.5 to 9.5 kev corresponding very closely with the expected $L\beta$ and $L\alpha$ x-radiations from bismuth.

Several of the high energy gammas as reported by Latyshev were not observed, perhaps because of our lack of sensitivity in the high energy region, but every electron line reported by Ellis and co-workers plus some additional lines have been found. One pair of electron lines having *K-L* differences characteristic of $Z=82$ yield a gamma-energy of 457.5 kev. The radiation was found with a Ra source but not with RaD alone, and hence may be in Pb^{210} or Pb^{214}, probably the former since the alpha-radiation of Po^{214} to Pb^{210} is complex. The *K* electron line for a gamma-ray reported by Ellis in Bi^{214} at 257.8 kev falls together with the *L* electron line of the 185.6-kev gamma-ray in Rn^{222}.

TABLE I. Summary of observed electron energies, their relative intensities, and their interpretation.

Electron energy (kev)	Assignment	Gamma-energy (kev)	Relative intensity	Electron energy (kev)	Assignment	Gamma-energy (kev)	Relative intensity
30.0	L_I 83	46.3	10	237.3	*M* 83	241.3	4
30.6	L_{II} 83	46.3	4	240.8	*N* 83	241.7	3
33.0	L_{II} 83	46.4	1		Also *L* 83	257.1	
36.6	L_I 83	52.9	9	260.8	*K* 83	350.7	10
37.2	L_{II} 83	52.9	3	278.1	L_I 83	294.4	8
39.5	L_{II} 83	52.9	1	281.2	L_{II} 83	294.6	1
42.4	*M* 83	46.4	8	290.2	*M* 83	294.2	4
45.5	*N* 83	46.4	7	293.4	*N* 83	294.3	2
46.2	*O* 83	46.4	3	334.8	L_I 82	351.1	7
47.2	L_I 81	62.5	1	337.5	L_{II} 83	350.9	1
49.2	*M* 83	53.2	8	346.9	*M* 83	350.9	4
52.2	*N* 83	53.2	5	350.0	*N* 83	350.9	3
52.9	*O* 83	53.1	3	369.6	*K* 82	457.2	3
58.0	$A(\alpha_2-L)$ 83		2	390.4	Unassigned		2
60.9	$A(\alpha_1-L)$ 83		2	442.0	*L* 82	457.6	1
63.3	$A(\alpha_2-L)$ 86		1	516.3	*K* 84	608.8	8
66.0	$A(\alpha_1-L)$ 86		1	572.7	Unassigned		1
70.2	$A(\alpha_2-M)$83		2	592.8	*L* 84	609.0	5
73.4	$A(\alpha_1-M)$83		2	605.0	*M* 84	609.2	1
76.2	$A(\alpha_2-M)$86		1	651	Unassigned		1
79.3	$A(\alpha_1-M)$86		1	676	*K* 84	769	4
87.5	*K* 86	185.3	6	696	*K* 82	784	1
105.9	*K* 81	191.1	4	752	*L* 84	769	1
151.5	*K* 83	241.4	10	842	*K* 84	935	5
168.2	L_I 86	185.5	6	918	*L* 84	935	1
	Also *K* 83	258.1		1029	*K* 84	1122	8
171.3	L_I 86	185.9	4	1105	*M* 84	1122	3
176.2	L_{II} 81	190.9	1	1117	*M* 84	1122	1
181.4	*M* 86	185.9	5	1148	*K* 84	1241	3
184.6	*N* 86	185.7	4	1326	*K* 84	1419	9
204.7	*K* 83	294.6	10	1402	*L* 84	1419	3
225.5	L_I 83	241.8	5	1673	*K* 84	1766	3
228.1	L_{II} 83	241.5	1				

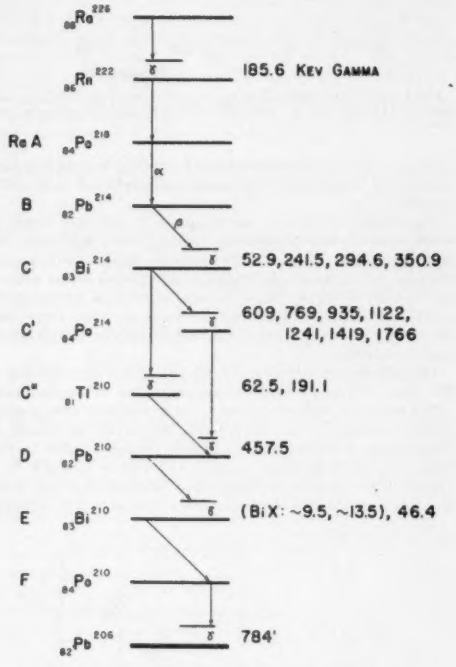

FIG. 2. Summary of the gamma-rays associated with various nuclei.

A summary of the electron energies together with their relative intensities on an arbitrary scale and their interpretation is presented in Table I. No attempt is made to interpret certain very weak lines. The gamma-energies as determined in this investigation are shown collectively in Fig. 2.

* This project received the joint support of the ONR and AEC.

[1] C. D. Ellis, Proc. Roy. Soc. (London) **A143**, 350 (1934); W. Lewis and B. Bowden, Proc. Roy. Soc. (London) **A145**, 235 (1934); G. Briggs, Proc. Roy. Soc. (London) **A157**, 183 (1936).

[2] K. Siegbahn, Arkiv Mat. Astron. Fysik **30A**, No. 20 (1944).

[3] Alichanov, Latyshev, and Dzelepov, C. R. Acad. Sci. URSS **20**, 113, 429 (1938); for more complete bibliography see G. Latyshev, Revs. Modern Phys. **19**, 132 (1947).

[4] W. Chang, Phys. Rev. **74**, 1195 (1948).

[5] S. Tsien, Phys. Rev. **69**, 38 (1946); Curran, Angus, and Cockroft, Phil. Mag. **40**, 36 (1949).

Polarization of Gamma-Radiation Following Capture of Polarized Neutrons*

L. C. Biedenharn, M. E. Rose, and G. B. Arfken
Oak Ridge National Laboratory, Oak Ridge, Tennessee
(Received June 14, 1951)

IN an attempt to utilize polarized neutrons for purposes of nuclear spectroscopy we were led to a consideration of the anisotropy properties of the emitted gamma-rays.[1] It is well known that for the capture of s-neutrons the intensity is isotropic. Therefore, the question arises of obtaining information concerning angular momentum of compound states and/or multipolarity of the γ's by looking for anisotropy with polarization-sensitive detectors.

It can be shown that with ordinary Compton scattering, pair formation, or photoelectric processes as detection devices (all of which measure linear polarization) no anisotropy will occur. The probability that a neutron with polarization $\mathbf{P}_0$ will lead to the emission of a photon with propagation vector $\mathbf{k}$ and polarization vector $\mathbf{e}$ is

$$W(\mathbf{P}_0, \mathbf{k}, \mathbf{e}) \sim \Sigma_{m_0 m m'} |\Sigma_m (A(\mathbf{P}_0, m_0)|H_e|B_m)(B_m|H_\gamma(\mathbf{k}, \mathbf{e})|C_{m'})^*|^2 \quad (1)$$

with A, B, and C representing probability amplitudes of initial, intermediate, and final states, respectively; m_0, m, and m' the magnetic quantum numbers of target, compound, and final nuclear states. The angular momenta of these states are J_0, J, and J', respectively. H_e and $H_\gamma \sim \boldsymbol{\alpha} \cdot \mathbf{A}$ are the capture and γ-emission interaction operators; for the emission of plane polarized radiation the vector potential $\mathbf{A}$ is

$$\mathbf{A}(\mathbf{k}, \mathbf{e}) = \Sigma_{P=\pm 1} e^{-iP\tau} \mathbf{A}(\mathbf{k}, P), \quad (2)$$

where $\mathbf{e}$ makes an angle τ with respect to a fixed direction in the plane normal to $\mathbf{k}$ and $\mathbf{A}(\mathbf{k}, P)$ corresponds to right ($P=1$) and left ($P=-1$) circularly polarized radiation.[2] The result for the intensity, in the linearly polarized case, for emission of a general multipole mixture is

$$W(\mathbf{P}_0, \mathbf{k}, \mathbf{e}) \sim \Sigma_L [(2J'+1)/(2L+1)] |a(JJ'L)|^2 \pm \frac{2|P_0|}{2J_0+1} \sin 2\tau \, \Sigma_{L<L'} \Sigma_M \operatorname{Im}[a(JJ'L) a^*(JJ'L')] \times \Sigma_P P^{L-L'+1} D_{MP}^{(L)}(0\vartheta 0) D_{M,-P}^{(L')}(0\vartheta 0) \times \Sigma_m C_{J'mM}^{JL} C_{J'mM}^{JL'} \quad (3)$$

where the polarization-dependent part arises from the interference between different multipoles (order 2^L and $2^{L'}$). In (3) the $\pm$ corresponds to $J = J_0 \pm \frac{1}{2}$, the a coefficients are reduced matrix elements[3] (independent of magnetic quantum numbers but dependent on parity), the $D^{(L)}$ factors are the rotation matrices of order L, ϑ is the angle between $\mathbf{k}$ and $\mathbf{P}_0$, and the C's are vector addition coefficients.[4] Since the imaginary part of the matrix-element product vanishes,[5] the potentially anisotropic term in (3) disappears.

The detector processes referred to do not distinguish between right and left circular polarization or between these and unpolarized radiation. What is needed is a "nuclear quarter-wave plate." One obtains the desired circular polarization detector by using magnetized iron as a Compton scatterer.[6] Then an azimuthal anisotropy in the Compton scattered intensity will arise because the intensities of the right and left circularly polarized components of the radiation are different. In fact, these intensities for unmixed 2^L-pole radiation are

$$W(\mathbf{P}_0, \mathbf{k}, P) \sim 1 \pm |P_0| P \frac{J'(J'+1) - L(L+1) - J(J+1)}{L(L+1)(2J_0+1)} \cos\vartheta, \quad (4)$$

where $(P = \pm 1)$.

The only essential factor limiting the magnitude of the anisotropy is the relative number of electrons contributing to the magnetization in iron (~ 0.1). As an example of the application of our result we may consider the neutron capture leading to an even-even compound nucleus and a transition leading to the ground state. Such a transition may be identified by using energy-sensitive detectors. Then, since the anisotropy is determined by the coefficient of P in (4) a determination of this sign selects one of the two possibilities $J = J_0 \pm \frac{1}{2}$ and, since $J = L$, the sign measurement determines the multipole order of the radiation as well. It should be noted that there are certain exceptional cases where the anisotropy vanishes. The only cases of interest are $J = 2 \to J' = 3$ with the emission of quadrupole radiation ($L=2$) and, considerably less likely, $J = 5 \to J' = 6$ with octupole radiation ($L=3$). Of course, $J=0$ corresponds to isotropy. So far as dependence on angular momenta is concerned, the anisotropy is maximum when $J'(J'+1) - J(J+1) = \pm L(L+1)(2J_0+1 \pm 1)$. This occurs when $J_0 = 0$, $J = J' = \frac{1}{2}$ and when $J_0 = \frac{1}{2}$, $J' = 0$; in both cases $W \sim 1 \mp |P_0| P \cos\vartheta$ and for these particular cases dipole radiation is expected. Thus, for complete neutron polarization[7] only right, left circular polarization is obtained at $\vartheta = \pi$, $0 (J = J_0 + \frac{1}{2})$ and at $\vartheta = 0, \pi (J = J_0 - \frac{1}{2})$.

A special case of the foregoing considerations was discussed by Halpern.[8]

* This paper is based on work performed for the AEC at the Oak Ridge National Laboratory.

[1] Biedenharn, Rose, and Arfken, AEC Report, ORNL 986 (March 26, 1951).

[2] G. Goertzel, Phys. Rev. **70**, 897 (1946).

[3] E. U. Condon and G. H. Shortley, *Theory of Atomic Spectra* (Cambridge University Press, London, 1935), Chapter III.

[4] E. P. Wigner, *Gruppentheorie* (J. W. Edwards, Ann Arbor, Michigan, 1944), reprint. See also reference 3, pp. 76–77.

[5] S. P. Lloyd, Phys. Rev. **81**, 161 (1951). In obtaining (3) the direction of $\mathbf{P}_0$ was chosen as the axis of quantization. Choosing the latter along $\mathbf{k}$ we obtain only the first term of (3), which is, of course, isotropic. Since none of the factors in the second term of (3) other than $\operatorname{Im}[a(JJ'L)a^*(JJ'L')]$ can vanish identically, we obtain an alternative demonstration of Lloyd's result on relative phases of nuclear matrix elements.

[6] See U. Fano, J. Opt. Soc. Am. **39**, 859 (1949), where this result is implicitly contained.

[7] C. G. Shull, Phys. Rev. **81**, 626 (1951).

[8] O. Halpern, Phys. Rev. **82**, 753 (1951).

Domain Wall Relaxation in Nickel

W. P. Mason
Bell Telephone Laboratories, Murray Hill, New Jersey
(Received June 11, 1951)

RECENT measurements[1] of the decrement δ and the difference between the magnetically saturated and the demagnetized elastic constants (the ΔE effect) of nickel have shown that these effects are much smaller at 10 megacycles than they are in the low frequency range. Complete decrement-frequency and ΔE-frequency curves have been measured on a well-annealed polycrystalline rod with the results shown by Fig. 1. The decrement has reached a maximum value at about 150,000 cycles, while the $\Delta E/E_D$ ratio is decreasing continuously with frequency. It is the purpose of this note to show that this effect is due to a relaxation in the domain wall motion caused by the fact that the wall cannot follow the applied stress at high frequencies, on account of the induced micro-eddy-currents.

The simplest model that will demonstrate the ΔE effect is the 90° wall model shown by Fig. 2. This model applies to iron, since the directions of easy magnetization lie along cube axes. The equation of motion for such a domain wall for a sinusoidally applied magnetic field H, is

$$M'(d^2x/dt^2) + R'(dx/dt) + K'x = HI_s e^{j\omega t}, \quad (1)$$

where M', R', and K' are the effective mass, resistance, and stiffness constants of the wall and I_s is the saturation magnetic intensity. At the low frequencies considered here, M' can be neglected, K' can be evaluated from the initial susceptibility, and R' from power losses.

Taking account of the fact that the domains are distributed in all directions, the average displacement for a field H is

$$\bar{x} = HI_s/3K'. \quad (2)$$

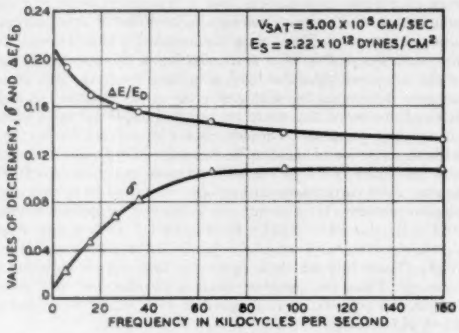

FIG. 1. Values of decrement and $\Delta E/E_D$ plotted as a function of frequency.

The change in intensity of magnetization associated with the domain wall motion is $I=2I_s/D$, so that the susceptibility is

$$\chi_0=I/H=I_s^2/3K'D, \quad \text{or} \quad K'=I_s^2/3\chi_0 D, \tag{3}$$

where D is the domain thickness in the direction of domain motion.

The power loss for a 180° wall has been calculated[2] by Williams, Shockley, and Kittel for a domain whose cross-sectional area is large compared with its thickness. The loss in a 90° wall will be ½ of this; and if we equate this power loss to the rate at which the energy is supplied, we have

$$16D^2I_s^2v^2/\pi R=HI_svD, \quad \text{or} \quad v=\pi RH/16DI_s, \tag{4}$$

where R is the resistivity of the material and v the velocity of the wall. From Eq. (1), if the dissipative term is controlling, we obtain

$$dx/dt=v=HI_s/R'; \quad \text{hence} \quad R'=16DI_s^2/\pi R. \tag{5}$$

Hence, from Eqs. (1), (2), and (3) the complex susceptibility is

$$\chi=\chi_0/[1+jf/f_0],$$

where f_0, the relaxation frequency, is

$$f_0=K'/2\pi R'=R/96\chi_0D^2=\pi R/24\mu_0D^2, \tag{6}$$

μ_0 being the initial permeability. This is the same relaxation frequency as that obtained by calculating the eddy current shielding for a plate the same thickness as the domain.

It is difficult to observe this relaxation of the domain wall motion magnetically, since it is obscured by eddy current damping of the whole specimen. However, by using domain wall movements caused by mechanical stresses, no over-all flux is generated and as shown by Fig. 1, this relaxation can be observed. The magnitude

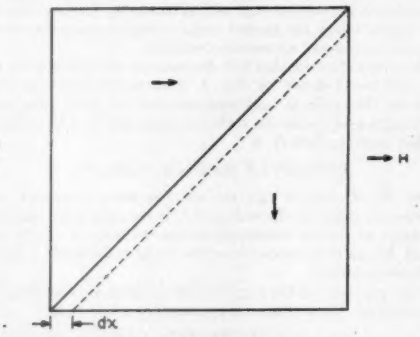

FIG. 2. Domain wall motion for a 90° domain wall.

of the change in the elastic constant (ΔE) and the damping can be calculated by inserting the complex value of the susceptibility in Becker and Döring's expression[3] for the ΔE effect. This results in

$$\Delta E/E_D=9\lambda^2E_s\mu_0/20\pi I_s^2(1+jf/f_0)$$
$$=9\lambda^2E_s\mu_0(1-jf/f_0)/20\pi I_s^2(1+f^2/f_0^2). \tag{7}$$

The real part of this equation represents the difference between the saturated Young's modulus E_s and the demagnetized Young's modulus, E_D, as a function of frequency. The imaginary part represents the dissipation associated with the domain wall motion, and the "Q" of the motion is given by taking the ratio of the real and imaginary parts of the complete elastic constant, i.e., $E_s-\Delta E$. Since the decrement δ is π/Q, we have

$$\delta=\frac{9}{20}\left(\frac{\mu_0\lambda^2E_s}{I_s^2}\right)\left(\frac{f/f_0}{1+f^2/f_0^2}\right). \tag{8}$$

The 90° wall model does not represent nickel, which has its easy direction of magnetization along the [111] directions. Döring,[4] in considering the $\Delta E/E_D$ effect, has shown that the result of this modification is to replace $(3/2)\lambda$ by $\lambda_{111}[5c_{44}/(c_{11}-c_{12}+3c_{44})]$, where λ_{111} is the magnetostrictive constant along [111] direction and c_{11}, c_{12}, and c_{44} are the three elastic constants of nickel. For $\lambda_{111}=-25\times10^{-6}$, $I_s=484$, $c_{11}=2.53\times10^{12}$ dynes/cm^2, $c_{12}=1.58\times10^{12}$, $c_{44}=1.23\times10^{12}$, and the measured values of $\mu_0=340$ and $E_s=2.22\times10^{12}$ dynes/cm^2, the calculated low frequency value of $\Delta E/E_D$ is 0.224 and the maximum value of δ is 0.353. From the initial slope, $\delta/f=2.5\times10^{-6}$ and the frequency of maximum decrement $f_0=150{,}000$ cycles, the average domain size is about 0.05 mm. The actual shape of the $\Delta E/E_D$ curve of Fig. 1 indicates a distribution of domain sizes from 0.15 mm to 0.02 mm, which is in good agreement with the optical measurements of Williams.[5]

I wish to thank Dr. R. M. Bozorth and Dr. C. Kittel for helpful conversations.

[1] Bozorth, Mason, and McSkimin, Phys. Rev. **83**, 220 (A) (1951). A fuller account is to be published in the October issue of the *Bell System Technical Journal*.
[2] Williams, Shockley, and Kittel, Phys. Rev. **80**, 1090 (1950).
[3] M. Becker and W. Döring, *Ferromagnetismus* (Verlag. Julius Springer, Berlin, 1930), p. 343.
[4] W. Döring, Z. Physik 114, 579 (1939).
[5] H. J. Williams, to be published.

Electron Penetration and Scattering in Phosphors

L. R. KOLLER AND E. D. ALDEN
General Electric Research Laboratory, Schenectady, New York
(Received May 15, 1951)

THERE is very little experimental data on the loss of energy of electrons in phosphors. The availability in this laboratory of thin uniform chemically deposited layers of phosphors afforded an opportunity of making such measurements. The preparation of these films of zinc sulfide is described in a Letter to the Editor.[1] The films studied were deposited on glass and varied in thickness from about 0.1 to 0.45 micron.

The samples were excited by electron bombardment at voltages from 2 to 40 kv in a demountable post accelerator cathode-ray tube. A film of aluminum 0.01μ thick was evaporated onto the surface of the phosphor to prevent "sticking." Corrections were made for the energy lost by the electrons in this layer. The brightness at constant beam current (current density 0.8 μa/cm^2) as a function of beam voltage was measured with a photomultiplier tube. These quantities were displayed on a cathode-ray oscilloscope and the resulting trace photographed.

A typical voltage brightness relation is shown in Fig. 1. After the initial portion of the curve (not shown here) over which the brightness increases as a power of the voltage, there is a considerable range over which the brightness is a linear function of voltage, after which it passes through a fairly sharp maximum. The point at which the relation deviates from a straight line is interpreted

FIG. 1. A typical voltage-brightness relation. The abscissa is the beam voltage in kv, and the ordinate is the photocurrent.

as the voltage at which electrons pass completely through the phosphor and begin to give up energy in the glass. In the Thompson-Whiddington relation

$$V_0^2 - V^2 = bx,$$

where V_0 = initial energy in electron volts, and V = energy after traveling a distance x, the value of b calculated on this basis is 5.5 kv²/cm.

Since electrons are scattered in passing through the medium, the beam intensity must decrease with depth, and the law of beam energy as a function of depth of penetration in the medium becomes

$$E = i_0[(V_0^2 - bx)/V_0^2]^{1+a/b},$$

where a is the scattering constant defined by

$$-dN/dx = N^a/V^2,$$

where N is the number of electrons in the beam. The value of a/b determined for ZnS is 2.4. These results indicate a large initial rate of loss of energy by an electron beam passing through a phosphor. Nearly 90 percent of the beam energy is lost in a distance of half the range of the electrons.

[1] Studer, Cusano, and Young, J. Opt. Soc. Am. (to be published).

On the Lifetime of the Negative Pi-Meson*

L. M. LEDERMAN, E. T. BOOTH, H. BYFIELD, AND J. KESSLER
Department of Physics, Columbia University, New York, New York
(Received June 20, 1951)

THREE determinations of the lifetime of the positive pi-meson have recently been made.[1-3] All of these values are significantly higher than the lifetime obtained for negative pi-mesons by Richardson,[4] who first measured this quantity with cyclotron-produced particles. A summary of the reported results is given in Table I.

TABLE I. Summary of π-meson lifetimes.

Author	Meson	Lifetime
Martinelli and Panofsky	π^+	$1.97^{+0.21}_{-0.25} \times 10^{-8}$ sec
Kraushaar, Thomas, and Henri	π^+	$1.65 \pm 0.33 \times 10^{-8}$ sec
Chamberlain, Mozley, Steinberger, and Wiegand	π^+	$2.65 \pm 0.12 \times 10^{-8}$ sec
Richardson	π^-	$1.11^{+0.45}_{-0.35} \times 10^{-8}$ sec

The negative pi-meson lifetime has been redetermined, using the external meson beam of the Nevis cyclotron. The competition of nuclear capture prevents the application of the elegant electronic techniques employed by Chamberlain *et al.* and Kraushaar *et al.* with positive mesons, stopping in scintillation crystals. Instead, the decays are observed in the course of the flight of pi-mesons through a 16 in. magnet cloud chamber. To verify that the process $\pi^- \rightarrow \mu^- + \nu^0$ is actually the mechanism responsible for the negative pi-meson decays observed in the cloud chamber, the previously reported[4] momentum and angle analyses were extended to seventy-five events occurring in favorable regions of the chamber. These gave, for the mass of the neutral decay product, $m_{\nu^0} < 30 m_e$. If the neutrino rest mass is taken as zero, the mu minus mass obtained from these data is

$$M_{\mu^-} = 209.8 \pm 2.2 m_e,$$

where the pi-meson mass is taken as $276.1 \pm 1.3 m_e$.[5]

The mean free path for $\pi \rightarrow \mu$ decay was obtained from the total length of pi-meson track classified as acceptable flux and the corrected number of decay events observed. Particles were allowed as flux if they entered the cloud chamber within a cone of 70° with respect to a fixed reference direction. The momentum interval accepted was 130 to 170 Mev/c. In order to minimize the subjectivity of the flux count, no restriction was placed on the quality of illumination of the track. Instead, all beam tracks were followed until they passed through the chamber or out of the illuminated region.

To reduce the possibility of mistaking a distorted track for a decay, the region of the cloud chamber in which events were counted was rigidly prescribed to be one inch from all vertical surfaces. The flux was then corrected for the reduced path during which decays would be recorded. A map measurer was employed on a full-scale reprojection of the cloud chamber photographs to obtain the actual lengths of the flux tracks.

Decays through angles whose projection is less than 5° in either of the two stereoscopic cameras were not counted. This procedure served to avoid the difficulty of determining the efficiency of stereoscopic scanning for decay events. The correction for the number of decays through angles $<5°$ was made from the geometry of the camera system and the calculated angular distribution of the decays. This yielded 0.33 ± 0.03 as the fraction of $\pi \rightarrow \mu$ decays excluded by the 5° criterion. Finally, a correction was made for the fraction of acceptable flux particles which are not pi-mesons.

The contaminants consist of mu-mesons and electrons. The electron contribution was estimated from the number of multiplication events observed in a 0.6 radiation length lead plate. This was independently checked by the electronic time-of-flight counter telescope.[7] The resultant electron fraction, 10 ± 3 percent, is roughly consistent with that to be expected from the materialization of π^0 decay photons in the $4 \times 4 \times \frac{1}{4}$ in. Be target. The mu-component was determined by an electronic mu-meson detector[8] (counting delayed coincidences between the mu-meson and its decay electron), which yielded a range spectrum of mu-mesons with a geometry designed to simulate that of the cloud chamber. The number of mu's in the proper momentum interval was found to be 9 ± 3 percent.

The mean free path for decay in the laboratory system, based on 188 events, is 9.93 ± 1.10 meters. The error represents the uncertainties in beam composition, efficiency, and statistics, assumed to enter independently. This corresponds to a laboratory mean life of $4.55 \pm 0.52 \times 10^{-8}$ second. If the mean free path is reduced to the rest system lifetime by the time dilation factor of special relativity, $\langle m/cp \rangle_{Av}$, averaged over the momentum spectrum of flux particles, the result is

$$\tau_{\pi^-} = 2.92 \pm 0.32 \times 10^{-8} \text{ second}$$

in satisfactory agreement with the more recent[3] determinations of the positive mean life.

The authors acknowledge with pleasure the important contributions made to this work by Professors G. Bernardini and J. Tinlot.

* Assisted by the joint program of the ONR and AEC.
[1] E. A. Martinelli and W. K. H. Panofsky, Phys. Rev. **77**, 465 (1950).
[2] Kraushaar, Thomas, and Henri, Phys. Rev. **78**, 486 (1950).
[3] Chamberlain, Mosley, Steinberger, and Wiegand, Phys. Rev. **79**, 394 (1950).
[4] J. R. Richardson, Phys. Rev. **74**, 1720 (1948).
[5] Lederman, Tinlot, and Booth, Phys. Rev. **81**, 281 (1951).
[6] Barkas, Smith, and Gardner, Phys. Rev. **82**, 102 (1951).
[7] Chedester, Isaacs, Sachs, and Steinberger, Phys. Rev. **82**, 958 (1951).
[8] The authors are indebted to Professors J. Steinberger and A. Sachs and to Dr. P. Isaacs for performing these measurements.

On Soft Photon Emission in Radiation Processes*

H. Primakoff† and F. Villars
Department of Physics and Laboratory for Nuclear Science and Engineering, Massachusetts Institute of Technology, Cambridge, Massachusetts
(Received June 15, 1951)

In the present note we have investigated the intensity of the soft photon spectrum emitted in ordinary hard photon radiation processes: e.g., x-ray emission and absorption, pair annihilation, etc.[1] The motivation for the work was the reported possibility of a discrepancy between the wavelength of the electron-positron annihilation gamma-ray, λ_{ann}, and $\hbar/mc$: $\lambda_{ann}-\hbar/mc \approx 10^{-9}\ \hbar/mc$, a discrepancy[2] which could conceivably be interpreted on the basis of an extended energy conservation relation: $2mc^2$ = energy of the two hard annihilation photons + energy of all the accompanying soft photons.

We first considered the equivalence of the two possible descriptions of the annihilation process: the configuration space treatment of the electron and positron in the sense of Fock,[3] and the customary one-particle treatment.[4] The two descriptions are essentially identical except for the impossibility of the inclusion of the electron-positron coulomb interaction in the latter. For the soft photon emission problem, the coulomb interaction has the role of determining the velocity spectrum of the annihilating particles; however, an appropriate velocity spectrum can always be assigned to the initial and final electron states in the one particle description. The two modes of treatment then become exactly equivalent and in particular, the intensity of the soft photon energy spectrum turns out to be determined by the average relative velocity v of the electron and positron. Quantitatively, the average energy $\bar{E}_{soft}$ carried off by this spectrum (per individual pair recombination) is approximately given by

$$(2/3\pi)(1/137)(v/c)^2\, 2mc^2 \approx 10^{-7}\, mc^2$$

for v/c values appropriate to the annihilation of slowed down positrons in matter. It is seen, therefore, that the soft photon effect is much too small to account for a discrepancy between hc/λ and mc^2 of the order of magnitude reported, even if the corresponding shift of the intensity maximum in the wavelength distribution of the annihilation line were as large as $\bar{E}_{soft}$ (see below). It is thus very satisfactory that the most recent precise absolute measurements of the energy of the 0.51-Mev ThC'' γ-ray line by Lindström,[5] taken together with the recent precise measurements by Hedgran[6] of the ratio of the energy of this line to that of the annihilation line, yield exact equality of λ_{ann} and $\hbar/mc$ within an experimental error of 3×10^{-4}.

In x-ray emission and absorption the average energy of the accompanying soft photon spectrum (per individual hard photon process) is again given by:

$$\bar{E}_{soft} \approx (2/3\pi)(1/137)(v/c)^2 E_{max}, \tag{1}$$

where E_{max} is the maximum available energy for the soft photons in a single hard photon process and v is the electron velocity appropriately averaged over the initial and final orbits. ($E_{max} \approx h\nu_{hard}$, $v/c \approx Z/137$ for mission; $E_{max} \approx$ photoelectron kinetic energy, $v \approx$ photoelectron velocity, for absorption.) It might therefore be thought that deviations of 1/10 to 1/100 percent could be observed from the Bohr frequency rule, the Ritz combination principle, and the Einstein photoelectric equation in such hard photon emission and absorption. The emitted soft photon spectrum however, is described by the almost flat intensity distribution:

$$\left(\frac{\bar{E}_{soft}}{E_{max}}\right)\left(\frac{E_{soft}}{E_{max}}\right)^{\bar{E}_{soft}/E_{max}} dE_{soft} \tag{2}$$

with the consequence that in the case of emission, for example, the usual hard photon line shape (derived with neglect of the soft photon effect)[7] is multiplied by a correction factor given approximately by

$$1-\pi(\bar{E}_{soft}/E_{max})[(E_{hard}-E_0)/\Gamma]. \tag{3}$$

Here, E_0 is the energy difference between the initial and final states involved in the hard photon emission, and Γ the hard photon natural line breadth. The energy of an emitted hard photon (or in a similar way, the kinetic energy of an ejected photoelectron) suffers, therefore, a most probable net displacement in the direction of lower energy of only

$$\frac{\pi}{8}\frac{\Gamma}{E_{max}}\bar{E}_{soft} \approx \frac{\pi}{8}(\bar{E}_{soft}/E_0)^2 E_0 \approx \frac{1}{50}\left(\frac{1}{137}\right)^3\left(\frac{v}{c}\right)^4 E_0, \tag{4}$$

Γ in the atomic x-ray region being $\approx(1/10)(1/137)(Z/137)^2E_0 \approx \bar{E}_{soft}$. The smallness of this net displacement as compared with $\bar{E}_{soft}$ is due to the extreme flatness of the soft photon energy spectrum.

Equations (3) and (4) show that any measurement of the emitted hard photon or ejected photoelectron energy, by extrapolation of the corresponding line shape on the high energy side, will be independent of the actual presence of the soft photon emission to about one part per million. Essential agreement with the usual energy conservation relations (neglecting soft photons) is thus always to be expected within this precision.

We wish to thank Dr. Martin Deutsch and Dr. Hartland Snyder for very helpful discussions.

* Assisted by the joint program of the ONR and AEC.
† On leave from Washington University, St. Louis, Mo.
[1] We have used the general methods of F. Bloch and A. Nordsieck, Phys. Rev. **52**, 54 (1937); and of W. Pauli and M. Fierz, Nuovo cimento **15**, 167 (1938).
[2] J. W. M. DuMond, Phys. Rev. **81**, 468 (1951). A. Hedgran and D. A. Lind, Phys. Rev. **82**, 126 (1951).
[3] V. Fock, Z. Physik **75**, 622 (1932).
[4] W. Heitler, *The Quantum Theory of Radiation* (Oxford University Press, London, 1944), Chapter 4.
[5] G. Lindström, Phys. Rev. **83**, 465 (1951). We wish to thank Dr. Lindström for sending us a copy of his paper.
[6] A. Hedgran, Phys. Rev. **82**, 128 (1951).
[7] Page 113 of reference 4.

The Isomeric Level of Cd^{111m}

Carl L. McGinnis
Department of Physics, University of California, Berkeley, California
(Received June 12, 1951)

In a previous investigation of the radioactivity of the 111-isobars,[1] spin and parity were assigned to the several levels, with the result that eight of the nine assignments agreed with the predictions of the shell model.[2] The 48-min isomeric level of Cd^{111} at 396 kev was the exception, being given spin 13/2 and even parity rather than the predicted $h_{11/2}$. This assignment was made on the basis of the usual γ-ray half-life formula,[3] row 3, Table I, and the ratio of 149/247 internal conversion electrons, row 4.

Table I. Data for assigning spin and parity to the 396-kev level of Cd^{111}.

	Theory			Expt.
396-kev level	13/2 even	9/2 odd	11/2 odd	
149-kev γ-ray	elec. 4	mag. 2	elec. 3	
149-kev γ, $T_{\frac{1}{2}}$ (sec)	117	8×10^{-4}	8×10^{-4}	2916
149/247 conv. e^-	15.7	10.2	11.4	14.5 ± 1
149/247 γ-rays	0.085	0.43	0.35	0.33 ± 0.06
In^{111} decay ratio	1.9×10^{-3}	2.9×10^{-4}	2.9×10^{-4}	1×10^{-4}

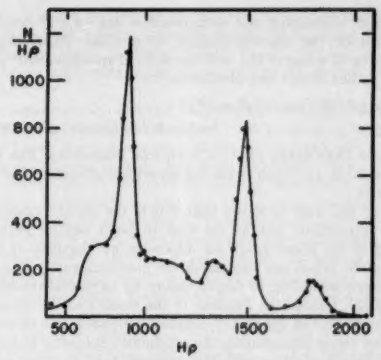

FIG. 1. Cd^{111m} photoelectron spectrum from a 1.1-mg/cm² gold radiator.

As the evidence for spin 13/2 even parity was not conclusive, it was decided to reinvestigate this assignment.

Cd^{111m} decays by the emission of a 149-kev γ-ray followed by a 247-kev γ. The latter is known to be electric quadrupole and 6.0 percent internally converted. The ground state of Cd^{111} is $s_{\frac{1}{2}}$, and this first excited state is $d_{3/2}$. On this basis, spin and parity are assigned to the 396-kev level, row 1, Table I, assuming a multipole order for the 149-kev γ listed in row 2. The possible ratios 149/247-kev γ-rays, row 5, were computed on the basis of the latter being 6 percent internally converted; and the percent the 149-kev γ is converted was computed from the measured K/L ratio, 2.0, and the theoretical K internal conversion coefficients.[4] In a similar manner the possible ratios of 149/247 conversion electrons, row 4, were calculated. It is seen from Table I that the γ-ray ratio is more sensitive to the character of the 149-kev γ than is the ratio of conversion electrons.

This γ-ray ratio was measured by observing the Cd^{111m} photoelectron spectrum from a 1.1 mg/cm² gold radiator, Fig. 1. The measured ratio of 149/247 of photoelectrons was 0.9 ± 0.1. The correction for absorption[5] in an 0.4 mg/cm² Nylon window of the spectrograph increased the ratio to 1.0 and estimating the loss in the gold foil makes the ratio 1.2 ± 0.2. According to the experimental data of Jones[6] a 149-kev γ is 3.67 times more efficient photoelectrically than a 247-kev γ. Hence the γ-ray ratio is 0.33 ±0.06.

This ratio eliminates the possibility that the 396-kev level has spin 13/2 even parity and favors the assignment $h_{11/2}$. The previously measured[1] ratio of conversion electrons, 14.5, is considered to be in error because of the difficulties in making the corrections for scattering and self-absorption in the measurement of such a large ratio.

The $g_{9/2}$ ground state of In^{111} decays by allowed K-capture to the $g_{7/2}$ level of Cd^{111} at 419 kev. The possible ratios (In^{111} transitions to the 396-kev level)/(In^{111} transitions to the 419-kev level), are listed in row 6. The theoretical ratios are those of the Fermi theory f values. The experimental ratio is, within a factor of two, 1×10^{-4}, which was determined by extracting chemically the 48-min Cd from the 2.84-day In. This measurement is consistent with the assignment $h_{11/2}$ to the 396-kev level and is not consistent with the previously assigned spin 13/2 and even parity.

Hence, it is concluded that the 396-kev level of Cd^{111} is $h_{11/2}$. This places the nine levels of the 111-isobars in agreement with the predictions of the shell model.

The usual γ-ray half-life formula assigns a multipole order of four to the 149-kev γ rather than the measured three. This result indicates that such a formula cannot be relied upon to assign a multipole order, despite the apparent correlation with energy and half-life as is shown by the plot of Axel and Dancoff.[3] Sunyar and Goldhaber[7] find that this formula yields spin differences one unit too high for electric 2^3 and 2^4 transitions. The description of the 149-kev γ-ray as electric 2^3 agrees with their conclusion.

I wish to express my appreciation to Professor A. C. Helmholz for his continued guidance.

[1] C. L. McGinnis, Phys. Rev. **81**, 734 (1951).
[2] M. Mayer, Phys. Rev. **78**, 16 (1950).
[3] P. Axel and S. M. Dancoff, Phys. Rev. **76**, 892 (1949).
[4] M. E. Rose *et al.* (table privately distributed).
[5] D. Saxon, Phys. Rev. **81**, 639 (1951).
[6] M. T. Jones, Phys. Rev. **50**, 100 (1936).
[7] A. Sunyar and M. Goldhaber, Phys. Rev. **83**, 216 (1951).

The Anomalous Spin Gyromagnetic Ratio of the Electron*

S. KOENIG, A. G. PRODELL, AND P. KUSCH
Columbia University, New York, New York
(Received June 20, 1951)

PRELIMINARY results of a new measurement of the anomalous spin gyromagnetic ratio[1] of the electron will be presented in this letter.

By a measurement of transitions between Zeeman levels of the hfs of atomic hydrogen in a fixed magnetic field, and a measurement of the precession frequency of protons in a water sample placed in the same magnetic field, it has been possible to find an experimental value for $g_J(^2S_{\frac{1}{2}}, H)/g_I$. Here g_J is the Landé g factor of the electron configuration of the $^2S_{\frac{1}{2}}$ state of hydrogen, and g_I that of the proton, except for small corrections due to diamagnetic effects.

Inasmuch as the ground state of hydrogen is pure to considerably better than a part in a million, it is apparent that g_J equals g_s', the spin g value of the bound electron in atomic hydrogen. It can be shown that application of the correction for the relativistic mass change due to binding yields[2] for the g value of a free electron, g_s:

$$g_s = g_s'(1+\alpha^2/3).$$

Essentially, then, what is measured is the ratio of the spin magnetic moment of the electron to that of the proton.

The recent measurement by Gardner and Purcell[3] of the ratio of the cyclotron frequency of the electron and the nuclear resonance frequency of the proton in a magnetic field establishes the ratio of the orbital gyromagnetic ratio, g_L, of the electron, and g_I, the nuclear g value, of the proton, again within the limits of the internal diamagnetic effects of the hydrogen bearing molecule. A combination of the two results yields a value for g_s/g_L, or effectively the spin magnetic moment of the electron in units of the Bohr magneton.

Preliminary results for the value of g_s/g_I have been obtained. They depend essentially on the measurement of the frequency of the transition ($F=1, m=0 \leftrightarrow F=1, m=-1$) in a field of 1500 gauss, on a prior knowledge[4] of the hyperfine separation, $\Delta\nu(H)$, of hydrogen, and on the measurement of the proton resonance frequency in the same magnetic field. A mechanism is provided in the present experiments for interchanging the positions of the water sample together with the associated rf coil mount and the uhf circuit in which the atomic transitions occur. A crucial point of the experiment is, of course, the accuracy with which the interchange may be made.

A cylindrical water sample is used in the experiment to insure optimum coincidence of water sample and atomic beam. This requires a correction[5] of $+1.5$ parts in 10^6 to the measured value of g_J/g_I, due simply to the bulk diamagnetism of the water. No such correction is necessary for the spherical sample of mineral oil used by Gardner and Purcell. A correction of -0.4 in 10^6 must be applied because of the presence of a known concentration of paramagnetic ions in the water sample. Finally, to combine our result with that of Gardner and Purcell, the known discrepancy between the resonant frequency of the proton in mineral oil and water requires an additional correction of $+2.2$ parts in 10^6.

After the application of the total correction of 3.3 parts in

10^6, we obtain

$$g_J(^2S_{\frac{1}{2}}, H)/g_I = 658.2163,$$

where g_I is the proton g value measured in oil. After applying the relativistic correction, $g_S/g_I = 658.2280$. The probable error of this result from statistical sources alone is about 0.0004. The stated result may, however, be subject to systematic errors of unknown magnitude, presumably arising from effects associated with any inhomogeneity of the magnetic field. We believe that an upper limit to the total uncertainty is about ± 0.0030.

Gardner and Purcell give

$$2g_L/g_I = 657.475 \pm 0.008.$$

A combination of the two results yields

$$g_S/g_L = 2(1.001145 \pm 0.000013).$$

Theoretical calculations of this quantity have been carried out to second order by Schwinger,[6] and more recently to fourth order by Karplus and Kroll.[7] The result is

$$g_S/g_L = 2[1+(\alpha/2\pi) - 2.973\alpha^2/\pi^2] = 2(1.0011454).$$

The rather startling agreement of experiment and theory can only be considered fortuitous at this point, in view of the experimental uncertainties. However, even in their present state the results give very strong evidence of the validity of the higher order quantum electrodynamical calculations. This work is being continued to increase the precision with which g_S/g_I is known.

* This research was supported in part by the ONR.

[1] P. Kusch and H. M. Foley, Phys. Rev. **74**, 250 (1948).
[2] G. Breit, Nature **122**, 649 (1928). H. Margenau, Phys. Rev. **57**, 383 (1940).
[3] J. H. Gardner and E. M. Purcell, Phys. Rev. **76**, 1262 (1949).
[4] A. Prodell and P. Kusch, Phys. Rev. **79**, 1009 (1950).
[5] W. C. Dickenson, Phys. Rev. **81**, 717 (1951).
[6] J. Schwinger, Phys. Rev. **73**, 416 (1948).
[7] R. Karplus and N. Kroll, Phys. Rev. **77**, 536 (1950).

The Electron-Neutron Interaction*

L. L. FOLDY
Case Institute of Technology, Cleveland, Ohio
(Received June 18, 1951)

THE existence of a weak attractive interaction between electrons and neutrons has recently been reported by two groups of workers.[1,2] It was immediately recognized that such an interaction is to be expected on the basis of current meson theories of nuclear forces as a consequence of the partial dissociation of a neutron into a proton and virtual negative meson. Explicit calculations[3] have shown that an electron-neutron interaction of the required character and order of magnitude is indeed obtained on the basis of this assumption.

We wish to show first that an electron-neutron interaction of the desired character and magnitude can also be obtained as a direct consequence of attributing to a neutron an anomalous magnetic moment in the manner suggested by Pauli[4] without any further assumptions. The relativistic (one-particle) hamiltonian for such a neutron in an external electromagnetic field is

$$H = \beta M + \boldsymbol{\alpha}\cdot\mathbf{p} - \mu_N(e/2M)[\beta\boldsymbol{\sigma}\cdot\mathbf{H} - i\beta\boldsymbol{\alpha}\cdot\mathbf{E}],$$

where μ_N is the magnetic moment of the neutron measured in nuclear magnetons. On reducing this by a canonical transformation to the corresponding nonrelativistic hamiltonian by the method of Foldy and Wouthuysen[5] one obtains

$$H = \beta M + (\beta p^2/2M) - \mu_N(e/4M^2)\beta\,\mathrm{div}\mathbf{E} + \mu_N(e/4M^2)\beta\boldsymbol{\sigma}\cdot[\mathbf{p}\times\mathbf{E} - \mathbf{E}\times\mathbf{p}],$$

where we have retained terms up to order $(1/M)^2$. For the coulomb field of an electron located at the point $\mathbf{x}_e$, the above hamiltonian becomes

$$H = \beta M + (\beta p^2/2M) + 4\pi\mu_N(e^2\beta/4M^2)\delta(\mathbf{x}-\mathbf{x}_e) + \cdots.$$

The term[6] containing the delta-function $\delta(\mathbf{x}-\mathbf{x}_e)$ is exactly of the form of the electron-neutron interaction. Expressing the interaction in terms of the well-depth V_0 of an equivalent[7] square well of radius e^2/mc^2, one obtains for V_0

$$V_0 = \pi\mu_N(e^2/M^2)[(4\pi/3)(e^2/mc^2)^3]^{-1} = \tfrac{3}{4}\mu_N(\hbar c/e^2)^2(m/M)^2\,mc^2 = 3900\text{ ev},$$

where we have taken $\mu_N = -1.9$ nuclear magnetons. The above figure is to be compared with the experimental value:[2] $V_0 = 5300 \pm 1000$ ev.

We do not wish to imply that this is the correct explanation of the interaction, but we do wish to point out an important bearing of the above result on meson-theory calculations of the interaction. When one calculates the electromagnetic properties of nucleons according to meson theory by canonical transformations which remove the coupling of the mesons to the nucleon to any given order in the meson coupling constants, one obtains interaction terms representing the anomalous magnetic moment of the nucleon interacting with the magnetic field, together with its relativistic complement expressing the interaction of an electric dipole moment for the nucleon with the electric field, plus an additional term which gives rise to a direct electron-neutron interaction. In the calculations employing this method (Case, and Borowitz and Kohn) only the last term has been compared with the experimental interaction. Actually, the electric dipole moment term gives in second order an additional contribution which is exactly that found above[8] and which must be added to the direct term before the comparison with experiment is made. In the calculations performed by direct computation of neutron scattering by an external coulomb field (Slotnick and Heitler, and Dancoff and Drell) the extra term is automatically included in the computation. We believe that this extra term may account for the discrepancy between the results of Slotnick and Heitler and of Borowitz and Kohn which was noted in a footnote to the paper of the latter authors.

* Supported by the AEC.

[1] E. Fermi and L. Marshall, Phys. Rev. **72**, 1139 (1947).
[2] Rainwater, Rabi, and Havens, Phys. Rev. **72**, 634 (1947); Phys. Rev. **73**, 1295 (1949). Quoted experimental value taken from L. Wilets and L. C. Bradley, III, Phys. Rev. **82**, 285 (1951).
[3] M. Slotnick and W. Heitler, Phys. Rev. **75**, 1645 (1949); K. M. Case, Phys. Rev. **76**, 1 (1949); S. M. Dancoff and S. D. Drell, Phys. Rev. **76**, 203 (1949); S. Borowitz and W. Kohn, Phys. Rev. **76**, 818 (1949).
[4] W. Pauli, Revs. Modern Phys. **13**, 203 (1941).
[5] L. L. Foldy and S. A. Wouthuysen, Phys. Rev. **78**, 29 (1950).
[6] Note the similarity of origin of this term with the "Darwin" term for the hydrogen atom as derived in reference 5.
[7] By the equivalent square well is meant here one having the same volume integral for the potential and consequently giving the same scattering cross section in the Born approximation at very low energies.
[8] In this respect we disagree with the remarks of K. M. Case given at the beginning of Sec. VI of his paper referred to in footnote 3 above. A careful investigation is necessary before discarding terms proportional to the Dirac matrix $\boldsymbol{\alpha}$ on the grounds that they are velocity proportional, since they may give rise to velocity independent contributions in higher order.

4.4-Minute Radiations from Zr^{89}

F. J. SHORE, W. L. BENDEL,* AND R. A. BECKER
Physics Research Laboratory, University of Illinois, Urbana, Illinois†
(Received May 28, 1951)

THE recent findings of Shure and Deutsch[1] regarding 79.3-hour Zr^{89} have been confirmed in this laboratory employing a 180° magnetic spectrometer. The sources were 1-mil foils of zirconium which had been irradiated by means of the probe method[2] in the 22-Mev betatron here. Our results indicate a simple positron spectrum with an allowed shape (at least to 450 kev, where the unfavorable source thickness is apparent), having a Kurie end point at 890 ± 10 kev, and in addition a single K-conversion line at 896 ± 5 kev.[3] The presence of the corresponding gamma-ray was established also by means of a scintillation spectrometer. The ratio of conversion electrons to positrons is 0.023. Deutsch[4] has obtained a conversion coefficient of 8×10^{-3} for this transition and, in addition, has measured the half-life of the ex-

cited state in Y^{89}, thought to be involved, to be 13 seconds. From these two values, together with the energy, he has designated the transition as being magnetic 2^4-pole. Goldhaber[3] has made an independent determination of approximately 16 seconds for this half-life.

The assignment by Deutsch is consistent with the shell theory of Mayer.[6] The measured spin[4,7] of Y^{89} (39 protons) in its ground state is $\frac{1}{2}$, and also is consistent with Mayer's scheme, which would put the odd proton in a $p_{\frac{1}{2}}$ state with odd parity. Similarly, the first excited state is obtained by putting this proton in a $g_{9/2}$ subshell with even parity. This fixes the gamma-transition to be magnetic 2^4-pole, in agreement with the above assignment. In the case of Zr^{89} (49 neutrons) we are concerned with a similar competition between the $g_{9/2}$ and the $p_{\frac{1}{2}}$ subshells for the odd neutron. It is probable from the results of Deutsch and Goldhaber that the 890-kev positron group proceeds from the ground state of Zr^{89} to the excited state (913±5 kev upon adding the K binding energy) of Y^{89}. Thus, if we assume a $p_{\frac{1}{2}}$ state for Zr^{89} the positron group would have to be at least third forbidden. This is not consistent with the ft value of 1.3×10^6 seconds, found in the present investigation with the aid of the curves of Feenberg and Trigg;[8] rather, the transition is either allowed or first forbidden. Accordingly, it is reasonable to assume the levels of Zr^{89} to be inverted relative to Y^{89}, with the odd neutron in a $g_{9/2}$ (even parity) ground state, thus rendering the positron spectrum allowed.

In order to find additional support for this we have investigated the 5-minute isomeric transition in Zr^{89} extensively. The sources employed were formed by irradiation of zirconium foil with 21-Mev x-rays. The half-life was found to be 4.4±0.1 minutes, with less than 1 percent of detectable background present. This is in good agreement with the value of 4.5 minutes found by Dubridge and Marshall.[9] The energy of the gamma-ray was determined with a scintillation spectrometer, by comparison with annihilation radiation at 511 kev and Ba^{137} radiation at 661 kev, to be 588±5 kev. This was confirmed by measurements of the K-conversion line in a 180° spectrometer, which gave 590±5 kev for the gamma-ray energy. The total conversion coefficient was determined, employing the scintillation spectrometer and comparing with that of the 661-kev radiation of Ba^{137}, to be 0.07±0.02. The $K/(L+M)$ ratio was separately determined in the 180° spectrometer to be 7±2. From these the K-conversion coefficient was found to be 0.06±0.02. These results, together with the lifetime, indicate the transition is magnetic 2^4-pole. This is consistent with the assignment of $p_{\frac{1}{2}}$ to the isomeric state of Zr^{89}. Accordingly, one suspects the presence of an allowed positron group going to the ground state of Y^{89}, competing with the 588-kev transition to the ground state of Zr^{89}. Absorption, magnetic spectrometer, and scintillation spectrometer results indicate a weak positron group of approximately 2.5-Mev maximum energy present to the extent of 6 percent of the conversion electrons associated with the 588-kev transition. Since the half-life of these particles was found to be 5±1 minutes, this group was attributed to the expected transition between the metastable state of Zr^{89} and the ground state of Y^{89}. A suggested partial level scheme is shown in Fig. 1. The ft value of the high energy group is 7×10^6 seconds, a value which is of the same order of magnitude as the long-lived group at 890 kev.[10]

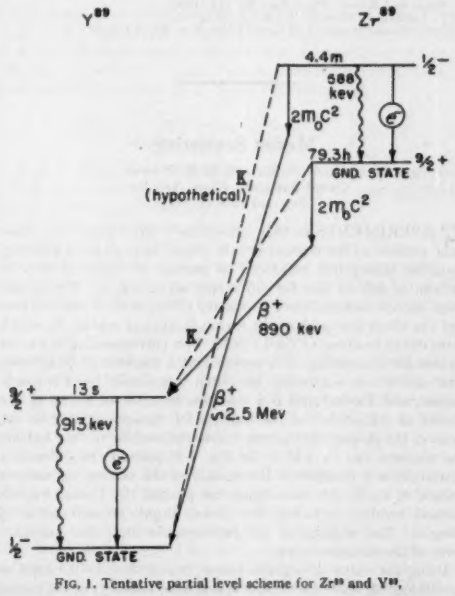

FIG. 1. Tentative partial level scheme for Zr^{89} and Y^{89}.

* AEC fellow.
† Assisted in part by the joint program of the AEC and ONR.
[1] K. Shure and M. Deutsch, Phys. Rev. **82**, 122 (1951).
[2] R. A. Becker, Rev. Sci. Instr. (to be published).
[3] It has been called to the authors' attention that Hyde and O'Kelley (University of California publication UCRL-1064 (1950)) have studied chemically separated Zr^{89} and find, in addition to the conversion line (80-hr activity) mentioned above, lines at 379 kev and 1.256 Mev, of intensity, relative to that of the 896-kev line, approximately 0.2 and 0.03, respectively (as judged from their curves). The weaker of these would not have been observed in the present work; but a careful search for the 379-kev line showed that if it is present at all, it is probably less than 5 percent of the 896-kev line.
[4] M. Deutsch (private communication).
[5] M. Goldhaber (private communication).
[6] M. Mayer, Phys. Rev. **78**, 16 (1950).
[7] H. L. Poss, Brookhaven National Laboratory Report BNL-26 (1949). M. F. Crawford and N. Olson, Phys. Rev. **76**, 10 (1949).
[8] E. Feenberg and G. Trigg, Revs. Modern Phys. **22**, 399 (1950).
[9] L. A. Dubridge and John Marshall, Phys. Rev. **58**, 7 (1940).
[10] The ratio of approximately 5 between the ft values should not be regarded as significant, since sufficient uncertainty attends the higher value to permit the ratio to be anywhere in the range 4 to 7.

The Ionization Loss of μ-Mesons at Relativistic Energies in Anthracene*

THEODORE BOWEN AND FRANCIS X. ROSER†
Department of Physics, University of Chicago, Chicago, Illinois
(Received June 15, 1951)

THE development of scintillation counting techniques has made it possible to measure ionization energy losses of high energy charged particles which pass through a small thickness of material. This makes it feasible to check the validity of the density effect correction to the ionization loss formula which is predicted by several authors.[1-3] μ-mesons in the cosmic radiation at sea-level provide an ideal source of relativistic particles for such an experiment because a wide range of energies is available and absorption by radiation losses and by nuclear collisions is negligibly small.

The arrangement was similar in principle to the one described in a previous paper,[4] except that two identical scintillation crystals (3 cm in diameter and 3 cm long) were used, giving two independent measurements of the energy loss of any particular μ-meson. In order to investigate the ionization loss curve at relativistic energies, lead absorbers were used to determine three energy bands for μ-mesons from (a) 190 to 460 Mev, (b) 460 to 960 Mev, and (c) higher than 960 Mev. Coincidence $ABCD$ (Fig. 1) defines a narrow beam of particles which must traverse practically equal path-lengths through both crystals. Trays E, F, and G cover the solid angle defined by $ABCD$. Counters H detect events accompanied by side showers, which are eliminated from the analysis. According to our knowledge of the energy spectrum of single electrons at sea-level, they should all be stopped in the first 12.7 cm of lead, and, therefore, do not reach tray E. Only events in which the master coincidence $ABCD$ is accompanied by pulses from counters (a) $E-(F+G)$, (b) $EF-G$, or (c) EFG are

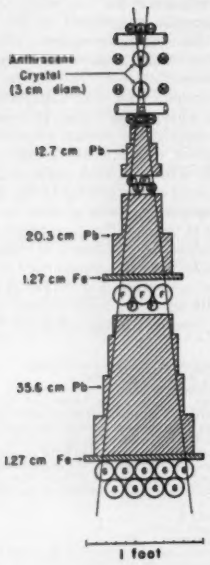

FIG. 1. Experimental arrangement.

used, as these represent the three energy-ranges for μ-mesons. The data is recorded photographically when the master coincidence $ABCD$ initiates the sweep of an oscilloscope. Pulses from scintillation counters (1) and (2), as well as from Geiger-Müller counters E, F, G, and H, are each delayed with respect to the master coincidence by different fixed amounts of time; hence they appear at characteristic positions on the oscilloscope trace. This system makes it possible to obtain the data for all three energy ranges during the same run of the equipment, so that slow time variations in the apparatus cannot affect the results in comparing the data for the various energy ranges. It was estimated that the multiple scattering of mesons out of the solid angle covered by trays F and G was of no consequence for the purpose of this experiment. The pulse-height scale was calibrated in units of energy loss (Mev) with the Compton electron distribution from the 2.62-Mev gamma-line from ThC″. This should yield, in addition to an accurate relative comparison with the theory, a slightly less precise absolute comparison.

The three curves representing frequency *vs* pulse height for each scintillation counter, corresponding to energy ranges (a), (b), and (c), were found to be in agreement within experimental error with the ionization energy-loss distribution calculated by Landau[5] for charged particles traversing thin absorbers. Table I gives the most probable energy loss for each of these distributions.

The averages from the table are also shown in Fig. 2. Two additional points at 40 and 110 Mev in Fig. 2 were taken from the results of a previous experiment.[4] A correction which was made for the change in light output with the specific ionization, as found by Frey *et al.*,[6] and others, was found to be significant only for these two additional points. The solid curve is the theoretically expected

TABLE I. Most probable energy loss for three energy ranges.

Average energy	Most probable energy loss (Mev)		
	Counter 1	Counter 2	Average of 1 and 2
(a) 325 Mev	6.07±0.15	6.14±0.15	6.11±0.10
(b) 710 Mev	6.19±0.12	6.19±0.12	6.18±0.08
(c) 2700 Mev	6.15±0.07	6.15±0.07	6.15±0.05

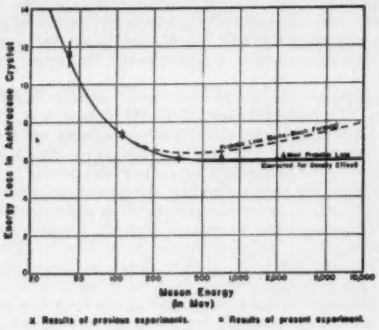

FIG. 2. Energy loss *vs* meson energy.

curve for the most probable energy loss, when corrected for the density effect in anthracene. The density effect correction for anthracene was estimated to be similar to those for light elements as found by Wick,[2] and Halpern and Hall.[3] The uncertainty of the ordinates of the theoretical curve are of the order of 2 or 3 percent. The experimental points are seen to be in good agreement with the theoretical curve, and show, as expected, that the most probable ionization loss in anthracene indicates a relativistic increase of less than 2 percent between 300 and 3000 Mev for μ-mesons. The curve for the most probable energy loss without the density effect correction is shown for comparison. The results of this experiment appear to establish definitely the existence of the reduction in ionization loss caused by the density effect.

We wish to thank Professor Marcel Schein for his continued interest in this work.

* Assisted by the joint program of the ONR and AEC.
† On leave from Universidad Catolica, Rio de Janeiro, Brazil.
[1] E. Fermi, Phys. Rev. **57**, 485 (1940).
[2] G. C. Wick, Nuovo cimento (9) **1**, 302 (1943).
[3] Halpern and Hall, Phys. Rev. **73**, 477 (1948).
[4] Roser and Bowen, Phys. Rev. **82**, 284 (1951).
[5] L. Landau, J. Phys. (U.S.S.R.) **8**, 20 (1944).
[6] Frey, Grim, Preston, and Gray, Phys. Rev. **82**, 372 (1951).

Meson Scattering

H. A. BETHE AND R. R. WILSON
Cornell University, Ithaca, New York
(Received June 11, 1951)

EXPERIMENTS in this laboratory[1,2] have given the cross section σ_a for nuclear events (stars, large-angle scattering, apparent absorption) produced by mesons of about 45 Mev in carbon, as well as that for diffraction scattering, σ_d. The former cross section determines the opacity $O=\sigma_a/\pi R^2$ of the nucleus and the mean free path of the meson in nuclear matter, λ, which turns out to be about $(3.7\pm0.7)\times10^{-13}$ cm corresponding to a cross section for interaction of a meson and a nucleon of 40 ± 8 mb. The diffraction scattering has been calculated by Fernbach, Serber, and Taylor[3] and is a sensitive function of λ and of the "index of refraction" of the nucleus for mesons, defined as the ratio of the propagation vector inside the nucleus to that outside the nucleus, i.e., $(k_1+k)/k$. In Fig. 1 is plotted the diffraction scattering as a function of the opacity of the nucleus for various values[4] of k_1. In the same figure are plotted the Cornell experimental results[1] including the more recent measurements of Shapiro.[2] The rectangular box indicates the statistical standard error of the measurements.

Using the value of λ given above, one finds $k_1\lambda=0.3\pm0.3$ or $k_1=(0.8\pm0.8)\times10^{13}$ cm^{-1}. Now k_1 is related to energy of the meson

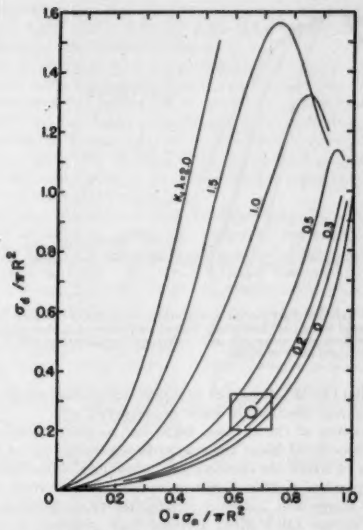

FIG. 1. The diffraction scattering is plotted as a function of the opacity of the nucleus for various values of the parameter $k_1\lambda$ which is related to the index of refraction of the nucleus as is explained in the text. The Cornell data are indicated by the plotted point.

and V_0, the average potential in the nucleus; i.e., $V_0=1.97\times10^{-11}k_1\beta$. The experimental values above imply that V_0 is 11 ± 11 Mev.

The average potential in the nucleus is obviously related to the potential of a meson in the field of one nucleon, $V(r)$, by

$$V_0=\sum_{\text{all nucleons}}\int V(r)d\tau/(4\pi R^3/3). \tag{1}$$

If the potential is the same in the field of a proton and of a neutron, $V_0=\int Vd\tau(4\pi r_0^3/3)$ where[5] $r_0=RA^{-\frac{1}{3}}=1.47\times10^{-13}$ cm. Now the volume integral of the potential is related to the amplitude for scattering of a meson by a nucleon in the forward direction which is, according to the Born approximation,

$$a(10)=-\frac{1}{4\pi}\frac{2\mu}{\hbar^2}\int Vd\tau=-\frac{2\mu}{3\hbar^2}r_0^3V_0=-\frac{2}{3}r_0^3k_1k. \tag{2}$$

It is to be noted that this relation can be derived from general principles of wave interference, without using the average potential or the Born approximation.

The differential cross section for forward scattering of mesons by a nucleon is a^2, and the total scattering cross section is $\sigma_s=4\pi a^2$ if we assume isotropic scattering which may be a resasonable approximation for the energy of 45 Mev. It is convenient to express σ_s in terms of the "geometric cross section of a nucleon," writing

$$\sigma_s/\pi r_0^2=x^2, \quad x=(4/3)k_1kr_0^3. \tag{3}$$

Using the experimental value of k_1 and k, we get $x=0.13\pm0.13$. Thus the observed value of the diffraction scattering from carbon implies as the most probable value for the meson scattering by protons 1.8 percent of the "geometric cross section" πr_0^2 or 1 millibarn, and as the upper limit 7 percent or 5 millibarns.

Such a small cross section has been reported by Shutt *et al.*,[6] who exposed a cloud chamber filled with hydrogen at high pressure to the meson beam from the Nevis cyclotron and found only one recoil proton after scanning 1000 g/cm² of hydrogen. They conclude that the scattering cross section is less than 6 mb. On the other hand, Steinberger *et al.*[7] from transmission measurements, deduced a cross section for proton-meson scattering[8] of $0.2\pi r_0^2=13$ mb. Similarly, Skinner and Richman[9] find a large cross section (17 ± 5 mb/sterad) for the differential scattering of mesons by carbon through 90°; at this angle, the nucleons in carbon should scatter essentially independently (and inelastically); if the nucleon scattering is isotropic, its total cross section would be 18 ± 5 mb. However, the large scattering observed by Skinner and Richman is in contradiction with the experiments of Shapiro[2] who gets for the sum of the nuclear (not diffraction) scattering of mesons plus the emission of fast protons about 6 mb/sterad.

The experimental evidence on meson scattering is thus conflicting. If the small value of Shutt *et al.* turns out to be correct, it would be in agreement with our result from the refractive index. If the larger values turn out to be right, we shall have to assume that the scattered amplitude has the opposite sign for scattering from neutrons and from protons. Since V_0 involves an average over all nucleons, the correct expression for (2) is

$$-(2\mu/3\hbar^2)r_0^3V_0=(Na_N+Za_P)/A, \tag{4}$$

where a_N and a_P are the scattering amplitudes from neutrons and protons, respectively. If these are nearly equal and opposite, V_0 can be small even if a_N and a_P themselves are large.

Theoretically, a_N and a_P should have the same sign for pseudoscalar mesons, now favored by all the experimental evidence, but opposite signs for scalar or pseudovector mesons. This can be seen as follows, e.g., for a positive scalar meson: If the scattering nucleon is a neutron, it must first absorb the incident meson, thus becoming a proton, and then emit the scattered meson. For scattering by a proton, the emission precedes the absorption. In the latter case, then, the intermediate state has a higher energy than the initial, and according to quantum-mechanical perturbation theory, this leads to an attractive potential between proton and meson, so that a_P is positive. Conversely, the potential between positive meson and neutron is repulsive and a_N is negative. For negative mesons, the argument is reversed. Thus for scalar mesons, we have approximately $a_N=-a_P$.

For pseudoscalar mesons, on the other hand, the emission and absorption of mesons is most likely if the nucleon makes, at the same time, a transition from a positive to a negative energy state. Therefore, regardless of the charge of the scattering nucleon, the intermediate state has essentially energy $-2Mc^2$, and the nucleon-meson potential is repulsive in all cases so that $a_N\approx a_P$. In hole theory, this result remains unchanged, just like the Klein-Nishina formula for Compton scattering; one should speak, however, of the creation of a pair of nucleons in the intermediate state. Although the result is based on second-order perturbation theory, it is likely to persist in higher orders because all the important intermediate states involve production of nucleon pairs.

Pseudovector mesons would behave like scalar ones, because their interaction with nucleons involves the nonrelativistic operator $\boldsymbol{\sigma}\cdot$.

The theoretical magnitude of the scattering cross section is, in the pseudoscalar theory,[10]

$$\sigma_s=\pi(g^2/\hbar c)^2(\hbar/Mc)^2=1.3(g^2/\hbar c)^2 \text{ mb} \tag{5}$$

so that a value $g^2/\hbar c$ of 0.9 ± 0.9 would satisfy our result from (3). This is reasonable in view of other evidence, such as the strength of nuclear forces.[11] For the scalar theory,

$$\sigma_s=4\pi(g^2/\hbar c)^2(\hbar/\mu c)^2 \tag{6}$$

and in this case, $g^2/\hbar c$ can be deduced fairly accurately from the binding energy of the deuteron[12] and is 2.39 μ/M, giving $\sigma_s=30$ mb, about twice the highest experimental result. Pseudovector theory would give the same order of magnitude as scalar.

If the cross section for scattering of mesons is small, as the Cornell experiments plus theory would indicate, it becomes harder to understand the result of Bernardini,[13] who finds that most of the mesons scattering in photographic emulsions (presumably by Ag or Br) lose a large fraction of their energy, being degraded from the order of 50 to the order of 5 Mev. This result is most easily interpreted as indicating repeated scatterings by the nucleons in the nucleus; since in one scattering the energy might be reduced by a factor 2 at high and by 10 to 20 Mev at low meson

energy, about 3 scatterings will be necessary to give Bernardini's result. But if the scattering cross section per nucleon is only a few millibarns, such repeated scattering would be most unlikely.

Further experimental evidence on meson scattering, especially by protons and deuterons, is clearly needed.

[1] M. Camac *et al.*, Phys. Rev. **82**, 745 (1951).
[2] A. Shapiro, private communication. See also Bull. Am. Phys. Soc. **26**, No. 4, 10 (1951).
[3] Fernbach, Serber, and Taylor, Phys. Rev. **75**, 1352 (1949).
[4] The *increase* of diffraction scattering due to the refractive index can be calculated by expansion of the formula of Fernbach and others which yields

$$D=\frac{\sigma_d(\lambda, k_1)}{\sigma_d(\lambda, k_1=0)}-1=4(k_1\lambda)^2\left(1-\frac{1}{18}\left(\frac{R}{\lambda}\right)^2+\cdots\right).$$

For carbon, $R/\lambda\approx 1$ so that the second term is only a small correction. The simplified formula, $D=4(k_1\lambda)^2$, was found by numerical calculation to hold within 5 or 10 percent for opacities up to 0.9 and $k_1\lambda$ up to about 1.
[5] This value follows from the energy difference between mirror nuclei which seems to us the most accurate determination of the nuclear radius. The mirror nuclei may be chosen in the neighborhood of carbon.
[6] Shutt, Miller, Thorndike, and Fowler (private communication).
[7] Chedester, Isaacs, Sachs, and Steinberger, post-deadline paper at the Washington meeting of the Am. Phys. Soc.
[8] This cross section was used by Brueckner, Serber, and Watson (Phys. Rev., to be published) to separate the total collision cross section of mesons in nuclear matter, $1/\lambda$, into scattering and star formation. The cross section thus obtained (or star formation is shown by them to be in good agreement with detailed balancing arguments, but this agreement would not be substantially changed if the scattering were reduced to essentially zero because even Steinberger's cross section is only one-third of the total interaction cross section of 40 mb.
[9] M. Skinner and C. Richman, Phys. Rev. **83**, 217 (A) (1951). The cross section quoted is that given at the meeting, not in the abstract.
[10] M. Peshkin, Phys. Rev. **81**, 425 (1951). This paper also shows the signs of the scattered amplitudes, Eqs. (5) to (8), in agreement with the discussion above.
[11] H. A. Bethe, Phys. Rev. **76**, 191 (1949); K. M. Watson and J. V. Lepore, Phys. Rev. **76**, 1157 (1949).
[12] L. Hulthen and K. V. Laurikainen, Revs. Modern Phys. **23**, 1 (1951). Using modern experimental values, their $(-a)^{\frac{1}{2}}$ is 0.236. Their $b=(M/\mu)(g^2/\hbar c)$.
[13] G. Bernardini, Phys. Rev. **82**, 313 (1951).

Ranges of High Energy Electrons in Water

J. S. Laughlin and J. W. Beattie
Department of Radiology, University of Illinois, Chicago, Illinois
(Received June 11, 1951)

RANGE measurements of high energy electrons in various media have customarily been made with Geiger counters or cloud chambers as detectors. With the high intensity homogeneous electron beam available from the betatron, ionization measurements are employed to determine the distribution of dissipated energy in various materials. Such ionization measurements that can be interpreted to supply information on the ranges of high energy electrons in water are reported here.

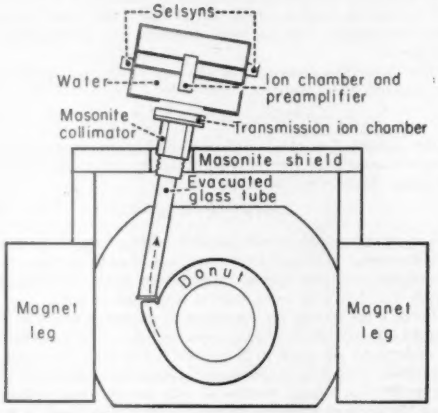

FIG. 1. Top view of betatron and apparatus for measuring ionization as function of depth in water. A parallel beam of electrons passes through transmission monitor chamber (Nylon walls) before entering water tank through thin window.

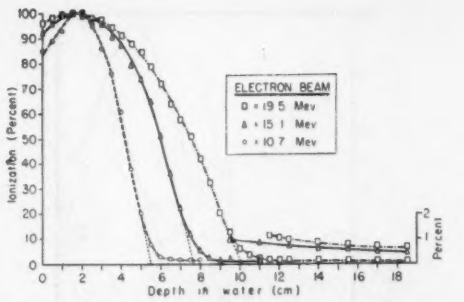

FIG. 2. Relative distribution of ionization as function of depth in water. Extrapolated ranges are indicated. Ionization produced in absorption of the bremsstrahlung was measured with increased amplification and is plotted against ordinate scale at right.

The energy of the electron beam can be varied continuously from 5 Mev to 22 Mev. The energy is determined by controlling the time at which the electrons are "expanded" from their orbit. The expansion timing circuit was calibrated directly against electron energy with known electrodisintegration thresholds. Thin foils of copper (10.9 Mev) and polythene (carbon, 18.7 Mev) were employed with the direct electron beam for this calibration.

A schematic diagram of the apparatus arrangement is shown in Fig. 1. The electron beam emerged from a thin window in the doughnut and passed in an evacuated tube through the fringing field of the magnet. Different field sizes and lengths of evacuated extension tubes were employed, but in all cases the electrons were in a parallel beam at the measuring apparatus. The ionization was measured in a small ion chamber (0.381 cm³) immersed in a water tank. Its position could be accurately varied by remote control. The inside diameter and height dimensions of the chamber were 5 mm. It was mounted on a stem on a preamplifier leading to a dc amplifier. Details of this measuring apparatus have been described elsewhere.[1,2]

Typical distributions of ionization as a function of depth in water produced by a 6-cm diameter electron beam are shown in Fig. 2. The increase in ionization beyond the surface which is due to multiple scattering is less marked with increasing energy. The ionization distribution can be made proportional to the number of electrons by correcting for the specific ionization of the electrons as a function of energy. Brode's plot of specific ionization against energy[3] was used to correct distributions such as those in Fig. 2 to a plot of number of electrons *versus* depth in water. This correction did not prove to be important, and the

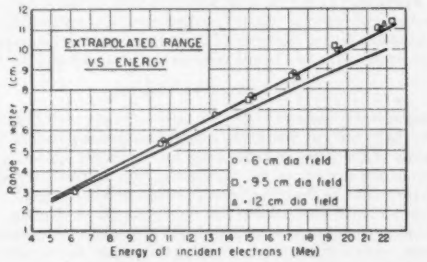
EXTRAPOLATED RANGE
VS ENERGY
○ • 6 cm dia field
□ • 9.5 cm dia field
△ • 12 cm dia field
Range in water (cm.)
Energy of incident electrons (Mev)

FIG. 3. Experimental points are the extrapolated ranges obtained from data plots such as those in Fig. 2. The maximum experimental uncertainty in the points is ±0.2 Mev in energy and ±2 mm in range. The upper curve represents maximum ranges predicted on the basis of Halpern and Hall's equation including density effects. The lower curve represents the predictions of the Bethe-Bloch equation ignoring density effects.

extrapolated ranges obtained from the corrected number plots were not significantly different from those obtained from the original ionization distribution data.

These extrapolated ranges should correspond to the "practical maximum range" defined by Bleuler and Zünti.[4,5] The "absolute maximum range" is greater but is not as easily determined experimentally. In Fig. 3 the extrapolated ranges determined from plots similar to those in Fig. 2 are plotted as a function of the kinetic energy of the electrons. The extrapolated ranges appear to be independent of field size. The "absolute maximum ranges" would be a few millimeters longer.

Fermi[6] and Halpern and Hall[7] have discussed the polarization effect of materials in a condensed state on the energy loss of electrons. The upper curve in Fig. 3 is a plot of the ranges to be expected on the basis of Halpern and Hall's[7] treatment of density effects in water. This curve was constructed from their results for water by numerical integration. The lower curve was constructed in a similar manner from the predictions of the Bethe-Bloch formula as represented by Halpern and Hall.[7] The calculated ranges which include density effects approach the experimental ranges more closely. The experimental "absolute maximum ranges" would, moreover, be slightly greater than the extrapolated range points shown.

[1] J. S. Laughlin and W. D. Davies, Science 111, 514 (1950).
[2] Laughlin, Beattie, Lindsay, and Harvey, Am. J. Roentgenol. Radium Therapy 65, 787 (1951).
[3] R. B. Brode, Revs. Modern Phys. 11, 222 (1939).
[4] E. Bleuler and W. Zünti, Helv. Phys. Acta 19, 375 (1946).
[5] F. L. Hereford and C. P. Swann, Phys. Rev. 78, 727 (1950).
[6] E. Fermi, Phys. Rev. 57, 485 (1940).
[7] O. Halpern and H. Hall, Phys. Rev. 73, 477 (1948).

Low States of F^{17} and Neutrons from $O^{16}+D$

FAY AJZENBERG
University of Wisconsin, Madison, Wisconsin*
(Received June 18, 1951)

A THIN (<80-kev) tungsten oxide target, (prepared by electrolysis) was bombarded by 3.083-Mev deuterons from the Wisconsin electrostatic generator. The resultant neutron spectrum was observed by means of Eastman NTA nuclear emulsions, 100 microns thick, mounted 10 cm from the target and at angles of 0°, 10°, 20°, 30°, and 90° to the direction of the beam. A total of 1700 tracks have been measured. Both the criteria[1] for the measurement of the proton recoil tracks and the range-energy relation[2] have been discussed elsewhere. The data, plotted in 50-kev intervals, and corrected for geometry[2] and for variation of the neutron-proton scattering cross section,[4] are shown as Fig. 1.

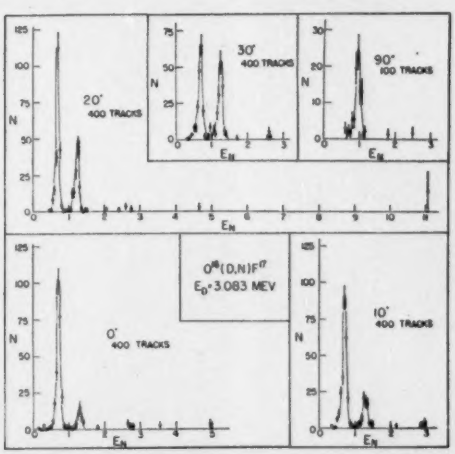

FIG. 1. Neutrons from the deuteron bombardment of O^{16} at 0°, 10°, 20°, 30°, and 90° to the incident beam. N is the relative number of neutrons per 50 kev, and E_n is the neutron energy in Mev.

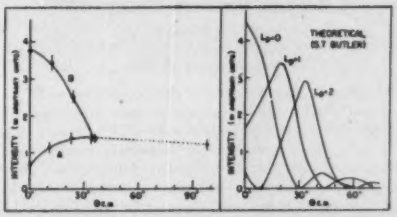

FIG. 2. $O^{16}(d,n)F^{17}$ angular distributions in the center-of-mass system. Curve A is for formation of F^{17} in the ground state, and curve B is for the 536-kev excited state. Butler's theoretical curves for high energy deuterons on O^{16} (see text) are shown for purposes of comparison.

Neutron groups corresponding to a first excited state of F^{17} at 536±10 kev are observed. These groups occur at approximately 0.7 Mev for the 0° to 30° data. The group at 90° corresponding to this first excited state would have an energy less than 0.5 Mev, and no tracks due to neutrons of energy less than 0.6 Mev were measured at that angle. The neutrons of energies 2.5 to 3 Mev at the various angles are possibly from carbon contamination (ground-state neutrons from the $C^{13}(d,n)N^{13}$ reaction). Neutrons from the first excited state of N^{13} would appear well below the lower limit of observation.

Figure 2 shows the relative intensities of the ground-state neutron groups (curve A) and of the 536-kev excited state neutron groups (curve B) as a function of angle in the center-of-mass system. Figure 2 also shows Butler's[5] theoretical curves for angular distributions resulting from a stripping process. These curves are for deuteron energies above the coulomb barrier which for oxygen is about 2.5 Mev. Hence, it is interesting to compare the shape of the experimental intensity *vs* angle curve for the 536-kev level of F^{17} with the $L_p=0$ curve of Butler. If the comparison is valid, this leads to the assignment of $S_{\frac{1}{2}}$ to the first excited state of F^{17}. Burrows, Gibson, and Rotblat[6] have bombarded O^{16} with 8-Mev deuterons, and they have interpreted the angular distribution of the protons from the 0.88-Mev level of O^{17} by means of Butler's theory. This led to their assignment of $S_{\frac{1}{2}}$ to this first excited state of O^{17}. Hence, it appears that the 0.536-Mev level of F^{17} and the 0.88-Mev level of O^{17} are the mirror levels expected from the equality of n-n and of p-p forces.

Alder and Yu[7] have assigned $D_{5/2}$ to the ground state of O^{17} on the basis of a nuclear induction experiment. By mirror nuclei arguments, the ground state of F^{17} should also be $D_{5/2}$. The shape of the experimental intensity *vs* angle curve for the ground state of F^{17}, as shown on Fig. 2, is not inconsistent with such an assignment if it is remembered that for our low deuteron energy compound nucleus formation might be expected to compete appreciably with the stripping process. Compound nucleus formation would probably tend to make the angular distribution more isotropic.

The author is extremely grateful to Professor H. T. Richards for suggesting this experiment, for his aid in the exposure of the plates, and for many helpful discussions. She also wishes to acknowledge the generous assistance of D. R. M. Williamson, and of D. J. Donahue, R. E. Benenson, and D. S. Craig in the running of the generator.

* Supported by the AEC and the Wisconsin Alumni Research Foundation.

[1] Johnson, Laubenstein, and Richards, Phys. Rev. 77, 413 (1950).
[2] Richards, Johnson, Ajzenberg, and Laubenstein, Phys. Rev. (to be published).
[3] H. T. Richards, Phys. Rev. 59, 796 (1941).
[4] R. K. Adair, Revs. Modern Phys. 22, 249 (1950).
[5] S. T. Butler, Phys. Rev. 80, 1095 (1950).
[6] Burrows, Gibson, and Rotblat, Phys. Rev. 80, 1095 (1950).
[7] Alder and Yu, Phys. Rev. 81, 1067 (1951).

A Note on the Beta-Decay of F^{17}

H. T. RICHARDS
University of Wisconsin, Madison, Wisconsin*
(Received June 18, 1951)

THE recent measurement[1] on the beta-decay of F^{17} is very disturbing in that it apparently shows a strong branching (33 ± 5 percent) to the first excited state of O^{17}. Current classification of the pertinent states (see following) would make this branching transition doubly forbidden. Furthermore, the absolute magnitude of the reported transition probability to the first excited state of O^{17} seems anomalous on any possible level classification. Thus, the quoted *ft* value for the excited state transition is only 350 sec. This value is about a factor three or four less than any previously observed *ft* values[2] for odd A nuclei (e.g., neutron, $ft\approx1600$ sec; H^3, $ft=1140$ sec; Ne^{19}, $ft=1950$ sec). These low *ft* values for the mirror nuclei transitions are generally thought to involve the maximum overlap of initial and final wave functions and hence the maximum value of the matrix elements for a single nucleon decay, i.e., $|M|^2=1$. (For He^6 decay $|M|^2=2$, but here two nucleons of He^6 are involved in the decay, since $|N-Z|=2$.) A statistical weight factor[3] $(2I_i+1)/(2I_f+1)$ appears when $I_i<I_f$. For allowed transitions ($\Delta I\leqq1$) this factor could at most be $\frac{1}{3}$ for odd A nuclei, ($\frac{1}{2}$ for even A nuclei). Hence, even with the maximum contribution from both the matrix elements and the statistical weight factor, the low *ft* value for the branching still appears unusual.

It may be worthwhile, therefore, to review both the level classifications and the evidence for the beta-ray branching. It is believed that the ground state of F^{17} and of O^{17} is $D_{5/2}$ and the first excited state of each nucleus is $S_{\frac{1}{2}}$. The evidence comes from several sources: (1) the scattering and capture data[4] of $O^{16}+H$, (2) mirror nuclei arguments, (3) angular distribution data[5,6] of the (d, p) and (d, n) reactions on O^{16} interpreted on a stripping hypothesis,[7] and (4) a nuclear induction experiment.[8] Confirmation of the ground-state character of O^{17} obtained from (3) was recently provided by (4), which definitely fixed the spin of O^{17} as 5/2 and argued for a $D_{5/2}$ orbit for the odd neutron of O^{17}. Partial confirmation of the mirror nuclei argument is indicated in the preceding letter[9] of Ajzenberg.

It would therefore be comforting if the reported low energy positrons did not come from F^{17}. In this connection, one should note that it is of no help to postulate a contaminating activity with a half-life approximately the same as F^{17} (66 sec) since this would again imply an anomalously low *ft* value for the contaminating activity. In fact, it is more reasonable to use the end point of the observed low energy positrons (roughly three-quarters Mev) to guess a possible positron contaminant with a normal allowed *ft* value.[2] C^{11} ($T_{\frac{1}{2}}=20.4$ min, $E_{max}=0.98$ Mev, $ft=4300$ sec) and F^{18} ($T_{\frac{1}{2}}=112$ min, $E_{max}=0.64$ Mev, $ft=4100$ sec) seem to be the only possible positron activities satisfying these requirements.

Since an oxygen gas target with continuous circulation to the spectrometer source was used,[1] much C^{11} contamination is unlikely. Some F^{18} activity would undoubtedly result from (d, γ), (d, n), and $(d, 2n)$ reactions with the appropriate isotopes of the oxygen target. However, the small cross section for the (d, γ) reaction and the low abundance of the other isotopes reduce the importance of these sources. If the 8-Mev cyclotron beam contained much H_3^+ current, the $O^{18}(p, n)F^{18}$ reaction might be of importance. The (d, l) reaction, if fluorine contamination were present, would also be a possible source of F^{18}.

While F^{18} activity would explain the complexity of the beta-ray spectrum, the observed gamma-radiation[1] has a $T_{\frac{1}{2}}=70$ sec and so apparently is associated with the F^{17} activity. One notes, however, that it has an appreciably different energy[1] (0.98 ± 0.05 Mev) than the first excited state of O^{17} which occurs[9] at 0.876 ±0.009 Mev. Moreover, a scintillation counter (hence high gamma-efficiency) was used as a detector; thus, it is just possible that there was sufficient bremsstrahlung from the F^{17} positrons to account for the 70-sec gamma-ray period and to account for the fact that the mean gamma-energy (as measured by Pb absorption)[1] is near the most probable positron energy of the F^{17} decay. It may also be significant that the Pb absorption curve has some suggestion of higher energy gammas.

In view of the anomalously low *ft* value which the alleged branching in F^{17} decay gives and in view of the contradiction to current level classification, it would seem very desirable to have other more conclusive measurements on the radioactivity of F^{17}.

* Supported in part by the AEC and the Wisconsin Alumni Research Foundation.

[1] V. Perez-Mendez and P. Lindenfeld, Phys. Rev. **80**, 1097 (1950).
[2] For a list of *ft* values see A. Feingold, Revs. Modern Phys. **23**, 10 (1951).
[3] R. E. Marshak, Phys. Rev. **61**, 433 (1942).
[4] R. A. Laubenstein, Ph.D. thesis, University of Wisconsin (1950) unpublished; R. A. Laubenstein and M. J. W. Laubenstein, Phys. Rev. (to be published).
[5] Burrows, Gibson, and Rotblat, Phys. Rev. **80**, 1095 (1950).
[6] F. Ajzenberg, Phys. Rev. **83**, 693 (1951).
[7] S. T. Butler, Phys. Rev. **80**, 1095 (1950).
[8] F. Alder and F. C. Yu, Phys. Rev. **81**, 1067 (1951).
[9] Buechner, Strait, Sperduto, and Malm, Phys. Rev. **76**, 1543 (1949).

The Physical Review
Second Series of
Volume Twenty-
Number Twelve
Table of Contents
Description of
Influence of
Effects of Light
Electric Polarizat
Temperature Dep
Dependence of
Conductance of
Optical Absorption
Low Energy
Silver and
Observations
Critical
Optical
Optical
Thermal
Effects of
Elementary
Energy
Double
Overlap Forces
Thermal Energy
Spin of
Letters to the
Cross
Errata
Erratum
Erratum
Erratum